MAGMATIC, STRUCTURAL, AND METALLOGENIC FRAMEWORK OF THE KASSANDRA MINING DISTRICT, CHALKIDIKI PENINSULA, NORTHERN GREECE

A Dissertation

Presented to the Faculty of the Graduate School

of Cornell University

in Partial Fulfillment of the Requirements for the Degree of

Doctor of Philosophy

by

Christopher Russell Siron

May 2018

MAGMATIC, STRUCTURAL, AND METALLOGENIC FRAMEWORK OF THE KASSANDRA MINING DISTRICT, CHALKIDIKI PENINSULA, NORTHERN GREECE

Christopher Russell Siron, Ph.D.

Cornell University 2018

The Kassandra Mining District in northern Greece hosts the Skouries porphyry Au-Cu deposit and intrusion-related carbonate-hosted replacement sulfide orebodies at the Madem Lakkos, Mavres Petres, and Olympias deposits. Igneous suites of late Oligocene (25-27 Ma) and early Miocene (19-20 Ma) age are defined through zircon U-Pb geochronology and whole-rock geochemistry. Both suites exhibit high-K calc-alkaline geochemistry, but the early Miocene porphyries have a shoshonitic affinity. Normalized rare earth element patterns indicate that the late Oligocene suite was influenced by plagioclase fractionation, whereas amphibole-garnet fractionation was important during the early Miocene event.

The location and morphology of the sulfide deposits are controlled by a preexisting ductile structural architecture with ductile to brittle faults interacting with chemically reactive marble host rocks. The sulfide orebodies at the Olympias and Madem Lakkos deposits resulted from the intersection of ductile fabrics and fold hinges with extensional mylonites and semi-brittle shear zones. Ore lenses at the Mavres Petres deposit are restricted to fault-imbricated marbles contained within the Stratoni fault zone. Hydrothermal alteration associated with sulfide deposition occurred between 24 Ma and 22 Ma based on ^{40}Ar-^{39}Ar muscovite ages. Kinematic fault-slip analysis and field relationships suggest that sulfide mineralization within the Stratoni fault zone was controlled by north-south extension, whereas a younger phase of mineralization was influenced by east-west extension. The early Miocene Skouries porphyry stock, hosted by a folded gneiss-schist sequence, was localized within the steeply dipping limb of a preexisting district-scale antiform. Northeast-striking porphyry dikes and sheeted veins within the stock indicate that Au-Cu mineralization occurred in response to northwest-southeast directed extension.

Structural crosscutting relationships, geochronological ages, carbon-oxygen isotopes, fluid inclusions, and metal distribution patterns suggest that the late Oligocene hydrothermal system within the Stratoni fault zone was centered to the southeast of the Madem Lakkos deposit with an isolated hydrothermal system located to the east of the Olympias deposit. Porphyry Au-Cu mineralization culminated about 4 m.y. later, but was restricted to the Skouries stock. Polymetallic carbonate replacement sulfide and porphyry Au-Cu ore formation corresponds to late Oligocene and early Miocene magmatic events that manifested within the back arc environment in a post-collisional tectonic setting.

BIOGRAPHICAL SKETCH

Originally from Fairbanks, Alaska, Chris moved to Colorado in 2002 to pursue an education in the geological sciences, where he graduated from the Colorado School of Mines in 2007 with a B.Sc. degree in geological engineering and in 2010 with a M.Sc. degree in economic geology. Prior to graduate school at Cornell University, he worked as an exploration geologist in the mining and exploration industry, stationed across North America from the Slate Belt of North Carolina to the rugged, wind-swept coastline of the Alaska Peninsula, and many places in between. Chris matriculated to Cornell University after three years in industry, where he began research on what would become this dissertation. In addition to spending his summer months conducting fieldwork in northern Greece, he fulfilled the course requirements necessary for a minor in the graduate field of sustainable energy, and was a teaching assistant for six laboratory-based classes, including the geological summer field camp in Argentina. In the last five years, Chris presented his research findings at four conferences, participated as co-leader on an international fieldtrip to Bulgaria and Greece sponsored by the Society of Economic Geologists, organized a departmental fieldtrip to the western Adirondacks Mountains of New York, and published three peer-reviewed journal articles that included co-authoring a contribution to the Journal of Structural Geology on the best practices of using smart phones as structural data collection devices. Chris is a past-president of the Snee Graduate Student Organization at Cornell University and he is currently the North American representative for the Young Professionals Committee of the Society of Economic Geologists. Chris has maintained an active membership in several professional organizations including the Association for Mineral Exploration British Columbia, Geological Society of America, the Society for Geology Applied to Mineral Deposits, and the Society of Economic Geologists.

DEDICATION

Dedicated to Amy and Verrai, for your unwavering support

ACKNOWLEDGMENTS

First and foremost, I must acknowledge my dedicated advisor John Thompson, who not only proposed this research project, but helped foster the growth of my technical skills and instilled the tools necessary for me to become an objective geoscientist. For this I am especially grateful. I am also appreciative of the efforts of my committee, Louis Derry and Richard Allmendinger, for always being available to discuss research and providing insightful advice.

This project would not have been possible without the financial and logistical aid of Eldorado Gold Corporation. In-depth discussions and time spent in the field with Tim Baker and Peter Lewis (Eldorado Gold), and David Rhys (Panterra Geoservices) were always enlightening and highly valued. Participation in Eldorado's short course in the Golden Quadrilateral of Romania and for the opportunity to facilitate part of their workshop in the Kassandra Mining District of Greece was greatly appreciated. The geologists, technicians, and support staff in the Hellas Gold offices at Madem Lakkos, Olympias, and Skouries were always accommodating. I am indebted to my Greek colleagues, in particular, Lazaros Dalampiras, Panagiotis Daoultzis, Antonis Garezos, Ifigenia Kiriakoglou, Nikos Nestorov, Margarita Sakali, Grigorios Thermos, Pavlos Tsitsanis, Timoleon Xonikis, Ria Vagkli, Theodore Veligrakis, and Evlabia Vougiouka, as well as Scott Randall, Sally Russell, and Tom Sant, for providing assistance while in the field and throughout this study. I hope that we can all reunite again for a Mythos on the patio of the Paraty!

My collaborators at the University of British Columbia (UBC), the State University of New York (SUNY) at Cortland, and the University of Manitoba (UM) were instrumental in making this work possible. Greg Dipple (UBC) and Robert Darling (SUNY) generously opened their labs for my use and provided helpful guidance in using their analytical instruments. Jim Mortensen and Robert Friedman (UBC) assisted with my geochronology study and provided instruction on the laser ablation mass spectrometer and accommodated my many questions regarding zircon geochronology. Alfredo Camacho (UM) and Janet Gabites (UBC) are also acknowledged for providing assistance with my geochronological and isotope analyses, respectively.

Much appreciation goes out to my cohort for sharing unforgettable experiences and friendships over the last five years: Andrés Aguirre, Francisco Delgato, Alida Perez Fodich, Katie Grant, Adam Hawkins, Scott Henderson, Doyeon Kim, John Mason, Dana Peterson, Casey Root, Chelsea Scott, Laura Sinclair, Diego Quiros, Amy Willis, and of course my academic sibling, Irene del Real. The coffee sessions to discuss IOCG deposits with Larry Cathles, and conversations with Dan Karig on Ithaca glaciology and with Richard Allmendinger on topics ranging from the latest mobile geo-app to renewable energy were always thought provoking. I must recognize Savannah Williams and Amy Colvin for accommodating my routine pop-ins and keeping me on the tracks though the years. And of course, all the faculty and staff in the department of Earth and Atmospheric Sciences for providing an intellectually stimulating workplace environment at Cornell.

No words can express the gratitude I have for my stoic wife, Amy, who tolerated my extended field campaigns in Greece and time spent away from home while in Ithaca. I cannot be more thankful for Verrai, whose incessant demands for long muddy runs on the labyrinth of trails in the Ithaca area gave me clarity when I needed it most. And lastly, I am deeply appreciative of the everlasting support of my family.

TABLE OF CONTENTS

LIST OF FIGURES

LIST OF TABLES

LIST OF EQUATIONS

CHAPTER 1

INTRODUCTION

The Kassandra Mining District occupies the southeastern portion of the Serbo-Macedonian Metallogenic Province (Janković, 1997; Serafimovski, 2000; Heinrich and Neubauer, 2002), a northwest-trending Oligo-Miocene magmatic and metallogenic belt containing porphyry Au-Cu, Cu skarn, polymetallic vein and carbonate-hosted replacement mineral deposits that extends from Serbia and Kosovo, through the Republic of Macedonia, and northern Greece (Figure 1.1). Located on the Chalkidiki peninsula (*Place of Copper*) and approximately 100 km east of Thessaloniki, the Kassandra Mining District has been a site of Au and Ag mining since antiquity and remains active today. The measured and indicated resource in the district, current as of December 2016, totals 1.83 Mt of combined Pb-Zn, 1.24 Mt of Cu, 74.43 Moz Ag, and 9.76 Moz Au contained within porphyry and carbonate replacement deposits (Table 1; Eldorado Gold Corp., 2017), thus establishing the Kassandra Mining District as one of the most economically significant mining camps in Eastern Europe.

Bisecting the district, the 12 km-long Stratoni fault zone contains marble-hosted massive and semi-massive sulfide orebodies at the Madem Lakkos (*Deep Valley)* and Mavres Petres (*Black Rock*) deposits, with discontinuous sulfide lenses and an array of Au-bearing quartz-rhodochrosite veins and vein-breccias at the Piavitsa prospect (Figure 1.2). The Olympias deposit occurs in the northern part of the district and contains sulfide orebodies that are similarly hosted by marbles within and adjacent to the Kassandra-East fault zone. In the southern part of the district, the Skouries (*Rust*) porphyry Au-Cu deposit (Figure 1.2) is hosted by porphyry intrusions and wallrock consisting of gneiss and schist. The Skouries deposit is the most important resource in the Kassandra Mining District in terms of contained metal.

Research into the genesis of the ore deposits in the Kasandra Mining District not only places constraints on the complex geodynamic evolution of the north Aegean region, it provides an increased understanding of the controls on mineralization and tools that can be used to promote efficient and

successful exploration, both within the district and globally. The study area has witnessed a long history of metal production with extensive unpublished company data in addition to numerous published studies and applied research. In spite of the extent of previous work, a comprehensive district-scale magmatic, metallogenic, and structural framework and related genetic model for mineralization has not been defined. The purpose of the research that forms this dissertation is to increase the fundamental understanding of ore formation in the Kassandra Mining District and hence, provide the comprehensive framework that has been missing to date.

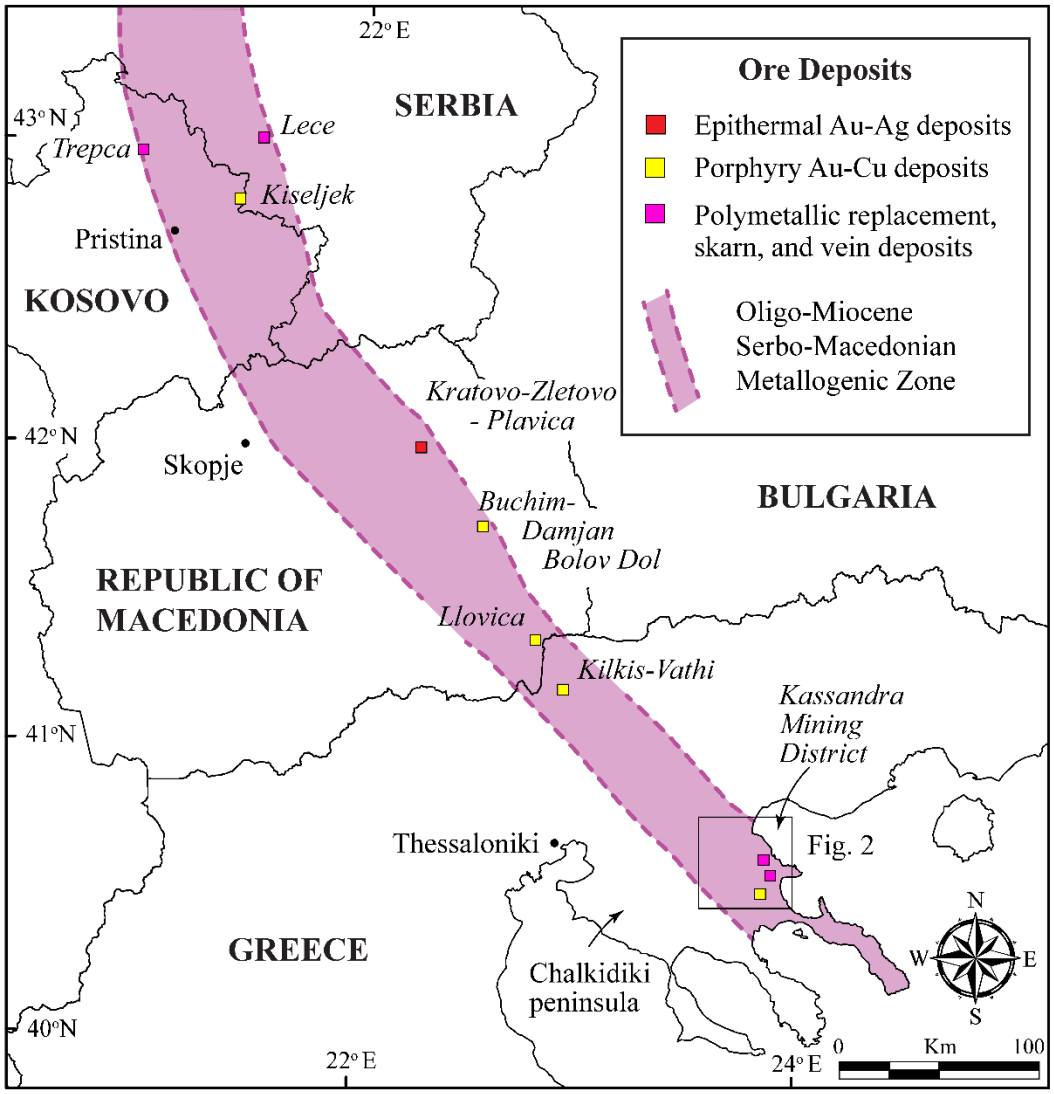

Figure 1.1. Geopolitical map of the eastern Balkans region showing the Oligo-Miocene Serbo-Macedonian Metallogenic Zone highlighted in fuchsia with major ore deposits labeled in italics. Major cities are shown as black circles and labeled in regular font (modified after Janković, 1997; Serafimovski, 2000).

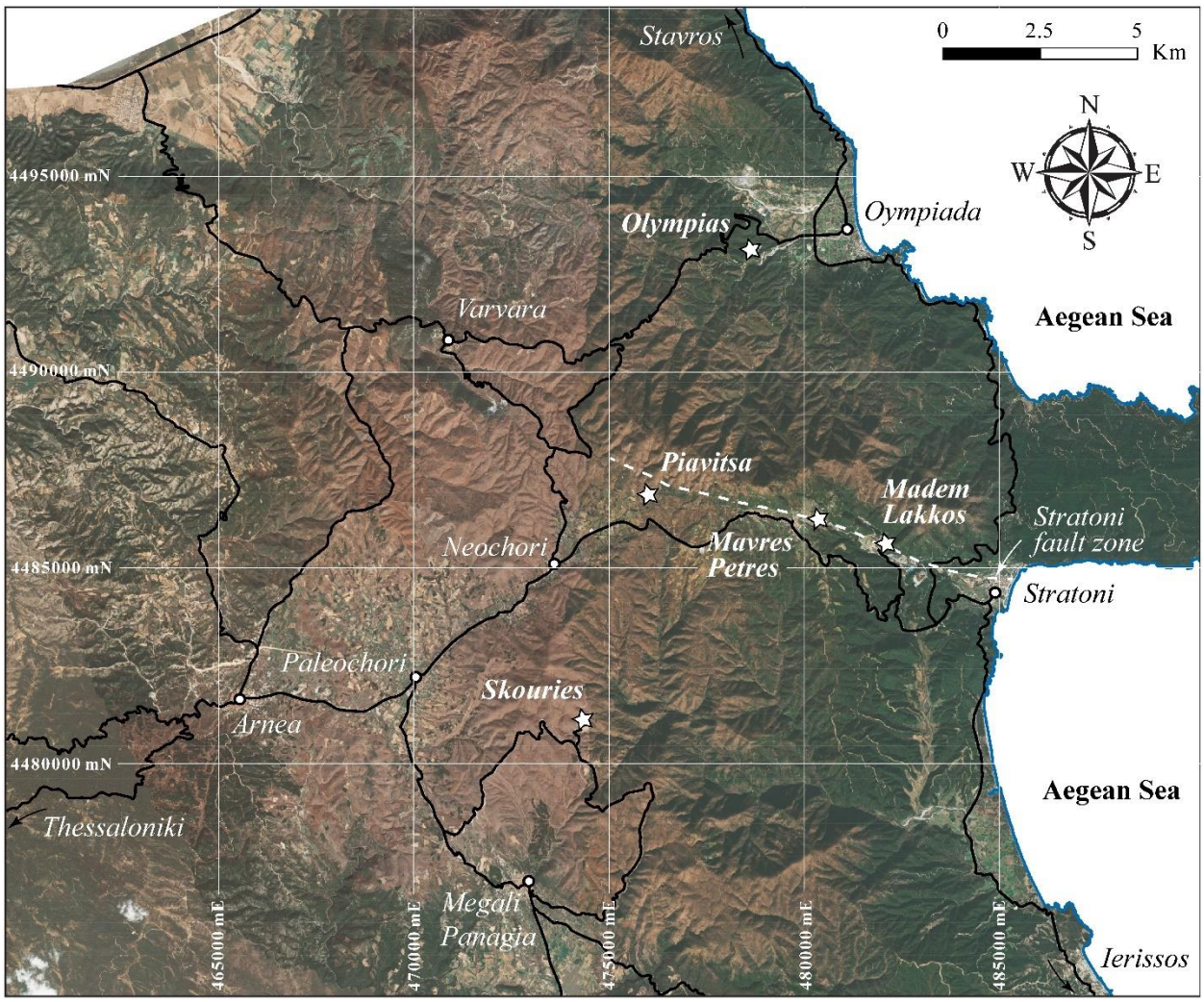

Figure 1.2. Quick Bird satellite image of the eastern Chalkidiki peninsula and the Kassandra Mining District. Major roads are shown as black lines with villages and deposits denoted by white circles and stars, respectively. The approximate location of the Stratoni fault zone is illustrated as a dashed white line. Coordinates are measured using the Greek Geodetic Coordinate System (GGRS 87 Greek Grid).

This chapter serves as an introduction to the dissertation, providing historical context for the study area from a mining perspective and a review of the literature that preceded this work. The chapter begins with an overview of carbonate-hosted replacement and porphyry Cu-Au ± Mo deposits, the two principal ore deposits types that occur within the Kassandra Mining District, and concludes with an outline of the dissertation and the major objectives that were pursued by this research.

Table 1.1. Measured and indicated resources of the of the Kassandra Mining District

Deposit	Tonnage	Grade					Contained metal				
		Au	Ag	Pb	Zn	Cu	Au	Ag	Pb	Zn	Cu
	(Mt)	(g/t)	(g/t)	(%)	(%)	(%)	(Moz)	(Moz)	(Mt)	(Mt)	(Mt)
Skouries	289.3	0.58				0.43	5.4				1.2
Olympias	15.1	8.97	146	4.9	6.5		4.4	70.7	0.74	0.98	
Mavres Petres	0.55		212	8.1	11.0			3.7	0.05	0.06	
Piavitsa[1]	*10.5*	*5.70*	*57*				*1.9*	*19.2*			
Total							**11.7**	**93.6**	**0.79**	**1.04**	**1.2**

Values as of December 31, 2016

[1] Italics indicate an inferred resource estimate

Ore Deposit Models

Carbonate-hosted replacement Ag-Pb-Zn ± Cu ± Au deposits

The marble-hosted sulfide orebodies within the Kassandra Mining District belong to the intrusion-related, carbonate-hosted replacement class of ore deposits that commonly occur within the porphyry environment (Figure 1.3; Sillitoe, 2010). Most carbonate replacement sulfide deposits are generally hosted by limestone or dolostone, but may also occur in volcanic rocks, and rarely within marbles in high-grade metamorphic belts in the North American cordillera and in Eastern Europe (e.g., Marchev et al., 2005; Siron et al., 2010; Bonsall et al., 2011; Moynihan and Pattison, 2011). Carbonate replacement sulfide orebodies generally form at temperatures greater than 200^{o}C in association with economic or sub-economic porphyry mineralization hosted by intermediate-felsic igneous intrusions. Skarn-hosted mineralization may occur proximal or adjacent to the source intrusion (Einaudi et al., 1981), with skarn-free carbonate replacement mineralization being more distal from the intrusion. Carbonate replacement orebodies are commonly strata-bound, forming sub-vertical chimney- or blanket-like ("manto") geometries that are tabular to elongate in shape with sharp wallrock contacts and diffuse alteration halos (Beaty et al., 1990). Carbonate replacement deposits are polymetallic (Ag-Pb-Zn-Mn ±

Cu ± Au ± Sn ± Bi ± W) and contain a wide range of sulfide and sulfosalt minerals including galena, sphalerite, pyrite, pyrrhotite, marcasite, and chalcopyrite, with subordinate arsenopyrite bournonite, digenite, electrum, enargite, jamesonite, and pyrargyrite (Megaw et al., 1988; Nelson, 1996). Most skarn and carbonate replacement sulfide orebodies exhibit a metal zonation pattern from Cu-Zn-Au-W-Mo proximal to a causative igneous intrusion, typically associated with a mineralized skarn, transitioning vertically and/or laterally into Ag-Pb-Zn and Ag-Pb replacement bodies progressively outward from the hydrothermal fluid source (Figure 1.3). Silver-bearing and Mn-dominant replacement zones characteristically define the far-field expressions of the carbonate replacement hydrothermal system (Figure 1.3; Megaw, 1998).

Polymetallic carbonate replacement deposits are distributed throughout the world but are mostly restricted to continental settings, typically along major arcs in association with subduction-related magmatic belts. Metal concentrations (grades) are highly variable but typically range between 5-20% combined Pb-Zn with several hundred g/t Ag (Nelson, 1996). Gold is often absent or present in trace quantities (Megaw et al., 1988) but may exceed 8 g/t in some deposits (e.g., Olympias, Greece). In general, individual deposits contain about 1-2 Mt of ore, but districts comprised of several large deposits may exceed 50 Mt (e.g., Santa Eulalia, Mexico; Megaw et al., 1988). Carbonate replacement deposits that occur in the western United States and northern Mexico are possibly the most studied with notable examples including: Leadville and Gilman, Colorado; Bingham, Marysvale, Tintic, and Park City, Utah; Eureka and Pioche, Nevada; Groundhog and Magdalena, New Mexico; and the silver districts of Santa Eulalia, Naica, and Providencia-Concepcion del Oro in northern Mexico (Prescott, 1916; Lindgren and Loughlin, 1919; Beaty et al., 1986, 1990; Graybeal et al., 1986; Meinert, 1987; Megaw et al., 1988; Vikre, 1998). In addition to the Kassandra Mining District, economically important carbonate replacement deposits occur elsewhere in Eastern Europe including the Madan-Thermes orefield in southern Bulgaria and northern Greece, the Lavrion district in southern Greece, and the Balya deposit in western Turkey (Marchev et al., 2005; Bonsall et al., 2011; Yigit, 2012; Kaiser-Rohrmeier et al., 2013;

Sanchéz et al., 2016; Melfos and Voudouris, 2017). Many of the replacement sulfide orebodies in the eastern Mediterranean region are principally hosted by marbles and are closely associated with inferred detachment faults at the margins of prominent metamorphic core complexes (Melfos and Voudouris, 2017).

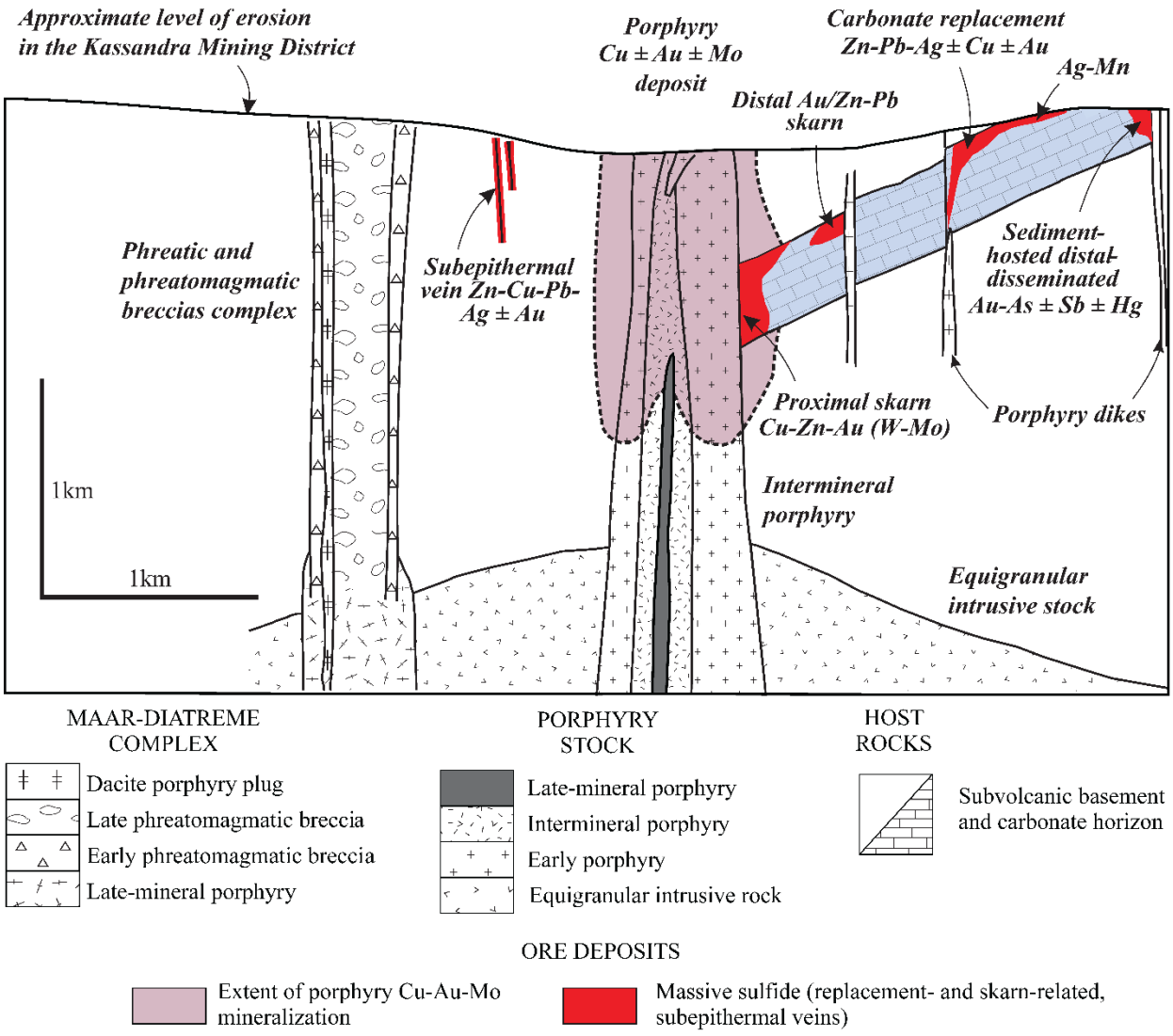

Figure 1.3. Genetic model of ore deposits within the porphyry environment showing the approximate level of erosion in the Kassandra Mining District (modified after Sillitoe, 2010).

Porphyry Cu-Au ± Mo deposits

Copper was exploited at Skouries in Roman times, and in the modern era was recognized to have a significant Cu endowment. Exploration in the last twenty years led to the definition of a resource that is currently under development. In 2002, Kroll et al. recognized that the Skouries deposit closely resembled a shoshonitic-style porphyry Cu-Au system, based on igneous geochemistry, sulfide mineralogy, and alteration mineral assemblages.

Porphyry Cu-Au ± Mo systems occur in magmatic arcs associated with convergent plate margins in continental, oceanic island, and back arc settings (Sillitoe, 2010). Mineralized porphyry systems may form during or after active subduction, for example, in post-collisional tectonic settings (Richards, 2009, 2011). In general, porphyry intrusions related to Cu-Au ± Mo deposits may be classified as calc-alkaline or alkalic, with intermediate types exhibiting characteristics of both (Lang et al., 1995). Porphyritic intrusions associated with Cu-Au ± Mo deposits are exclusively I-type and affiliated with magnetite-series granitoids, and exhibit primitive Sr isotope ratios indicating that the parental magmas were derived from upper mantle or lower crustal sources (Ishihara, 1981; Seedorf et al., 2005; Sillitoe, 2010).

The calc-alkaline and alkalic end-members of mineralized porphyry systems have distinctive igneous geochemistry, and also show contrasting alteration mineral assemblages, metal associations, and styles of mineralization (Wilson, 2003). Calc-alkaline intrusions range in composition from diorite to granodiorite and quartz monzonite, whereas alkalic intrusions are mafic to intermediate in composition, typically ranging from diorite to monzonite, with silica undersaturated (feldspathoid-bearing) syenite occurring in rare instances (e.g., Galore Creek, British Columbia; Sillitoe, 2010).

Mineralized calc-alkaline porphyry systems are dominated by Cu with variable Au-Ag and Mo concentrations. The principal sulfide minerals in calc-alkaline porphyry systems are pyrite and chalcopyrite with variable bornite, digenite, chalcocite, and molybdenite associated with pervasive potassic (K-silicate) alteration and stockwork biotite, K-feldspar, and quartz-sulfide-anhydrite ± magnetite veins (Sillitoe, 2010). Calc-alkaline porphyry systems commonly display an extensive

propylitic alteration halo that variably consists of chlorite, epidote, albite, and calcite with overprinting chlorite-sericite and quartz-sericite-pyrite zones. Sodic-calcic alteration may also be present in deeper parts of some systems (e.g., Yerington, Nevada). Many preserved calc-alkaline porphyry systems display a vertically extensive advanced argillic (quartz-alunite-dickite-kaolinite-pyrophyllite-aluminosilicate) lithocap that may contain pyrite-enargite ± chalcocite-covellite mineralization (Figure 1.4; Holliday and Cooke, 2007; Sillitoe, 2010).

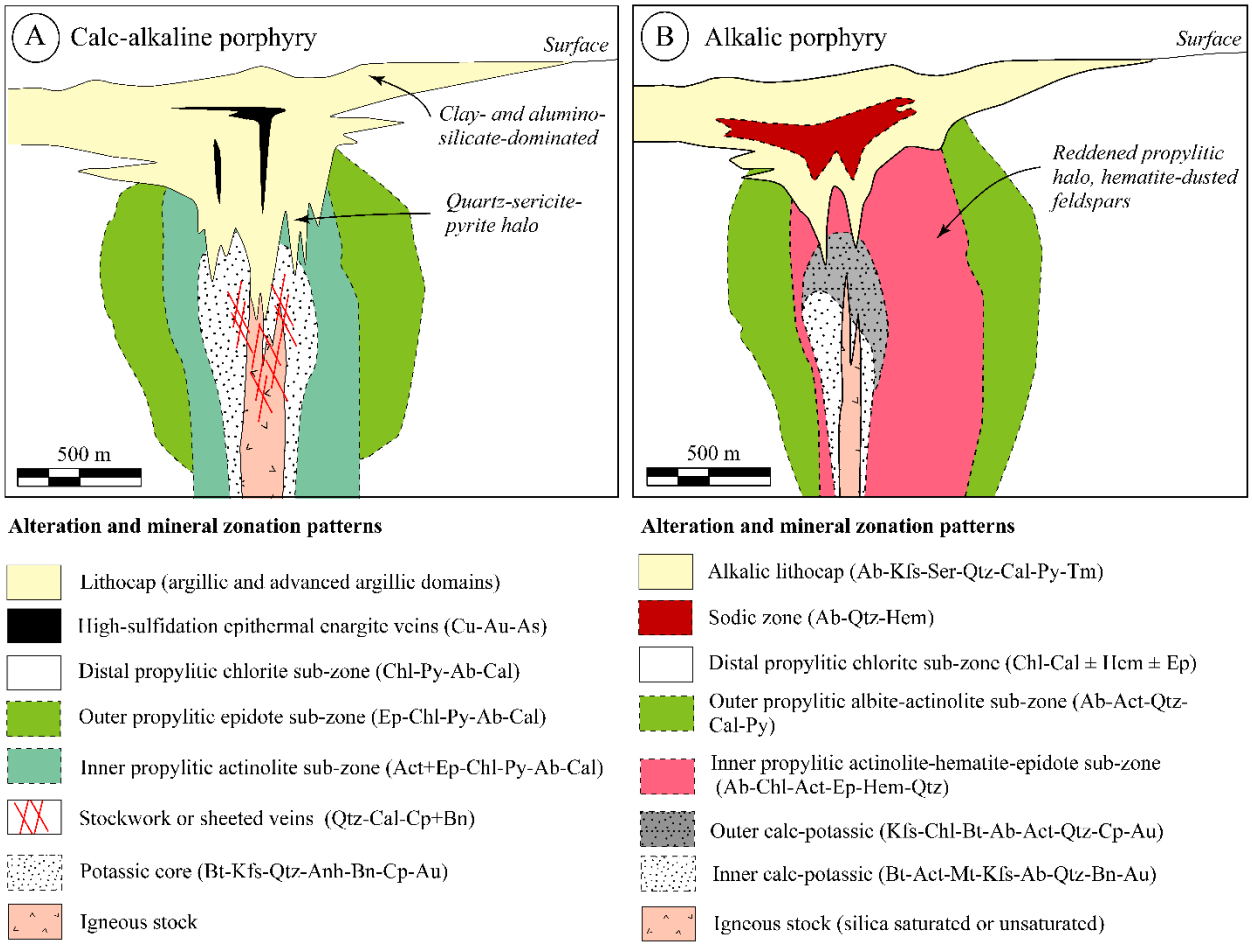

Figure 1.4. Schematic porphyry models illustrating calc-alkaline and alkaline porphyry deposits showing the spatial and overprinting relationships of typical alteration assemblages defined by common mineral occurrences. Note that both models are shown at the same scale (modified from Holliday and Cooke, 2007). Abbreviations are as follows: albite (Ab), actinolite (Act), anhydrite (Anh), arsenic (As), biotite (Bt), bornite (Bn), carbonate (Cal), chlorite (Chl), chalcopyrite (Cp), copper (Cu), epidote (Ep), garnet (Gt), gold (Au), hematite (Hem), K-feldspar (Kfs), magnetite (Mt), pyrite (Py), quartz (Qtz), sericite (Ser), tourmaline (Tm).

In contrast, mineralized alkalic porphyry Cu deposits are Au-rich and may contain elevated concentrations of platinum and palladium (Bissig and Cooke, 2014; McFall, 2016). The principal sulfide minerals are pyrite-chalcopyrite ± bornite associated with an albite-dominated calc-potassic or potassic alteration mineral assemblage that is typically depleted in quartz, particularly within the silica-undersaturated systems (Lang et al., 1995; Wilson, 2003; Holliday and Cooke, 2007). The mineralized porphyry stock is most often surrounded by a propylitic alteration halo consisting of actinolite-epidote-hematite which typically transitions outward into an albite-actinolite and a distal chlorite alteration zone (Figure 1.4). Alkalic porphyry Cu-Au deposits characteristically lack quartz veins and the sericite-, clay-, and aluminosilicate-related alteration facies typical of calc-alkalic porphyry systems (Lang et al., 1995). High-K calc-alkaline, also termed monzonitic or shoshonitic, porphyry systems display characteristics of both calc-alkaline and alkalic deposits (e.g., Lang et al., 1995; Wilson, 2003; Seedorf et al., 2005; Rees et al., 2012). Mineralized high-K calc-alkaline porphyry systems are dominated by Cu with elevated Au grades and low Mo concentrations. The principal sulfide minerals include pyrite-chalcopyrite ± bornite and are commonly associated with stockwork quartz veins and a K-silicate-magnetite potassic alteration mineral assemblage. The alteration patterns developed peripheral to the central potassic core are highly variable and reflect the chemistry of the magmatic-hydrothermal fluids and the host rocks.

Calc-alkaline porphyry Cu-Au ± Mo deposits are prolific in southwest North America, the Andes of South America, and the Apuseni-Banat-Timok-Srednogorie belt of Eastern Europe, whereas alkalic porphyry Cu-Au deposits are restricted to British Columbia and a few locations in Australia, Philippines, Papua New Guinea, and Fiji (Sillitoe, 2010; Bissig and Cooke, 2014). Porphyry Cu-Au ± Mo systems range in size from <10 Mt to 10 Gt with grades ranging between 0.5-1.5% Cu, <0.01-0.04 % Mo, and up to 1.5 g/t Au (Sillitoe, 2010). In general, alkalic Cu-Au deposits are smaller than their calc-alkaline counterparts with the deposits in British Columbia rarely exceeding 150 Mt (Lang et al., 1995). High-K calc-alkaline porphyry Cu-Au deposits are variable in size, typically ranging between 400 Mt to 2.5 Gt (Rees et al., 2012) with examples including: Bajo de la Alumbrera, Argentina; Bingham, Utah; Grasberg,

Indonesia; Oyu Tolgoi, Mongolia; Ok Tedi, Papua New Guinea; Red Chris, British Columbia; and Reko Diq, Pakistan.

Mining and Exploration History in the Kassandra Mining District

Extraction of gold and silver from the Chalkidiki region is believed to have begun during the reign of King Phillip II of Macedon and his successor, Alexander the Great, beginning around 350 B.C. (Sagui, 1928; Neubauer, 1957). Ancient historians Herodotus and Diodorus Siculus document the mines of Potidaea, Mount Pangaeus, and Krissites, the latter is probably the early name for the area referred by Sagui (1928) as the *Cassandra* district. These mines were critical to the Macedonians as the supply of gold and silver financed expansion of their empire throughout the known world. Mining likely continued intermittently during the Byzantine period with a renewed interest from about the 9th to 15th centuries while under Ottoman rule. In the latter half of the 16th century, an estimated 600 furnaces were actively smelting ore principally for Au in the valley between Piavitsa and Stratoni (Figure 1.2; Sagui, 1928). Slag waste is present throughout the district, particularly in areas of known historic artisanal mining, and is evidence for the vast local processing of ore. Arvanitidis and Constantinides (1994) estimated that about 200 kt and 150 kt of ore material was smelted in the Olympias and Mavres Petres areas during this period, respectively. Records show that by the end of the 19th century the district was held in the name of the Paris-based French-Ottoman Company (Nebel, 1989). After the Balkans War (c. 1920), the Hellenic Chemical Products and Fertilizers Company gained ownership of the mining district.

In the Olympias area, an exploration shaft was constructed in 1933 with near-surface extraction known from 1945 (Tsirambides and Filippidis, 2012). Drilling activity occurred between 1954 and 1966, which identified discontinuous sulfide lenses and evidence for ancient underground workings (Forward et al., 2011a). By 1969, the Hellenic Chemical Products and Fertilizer Company had established an exploitable resource. A processing plant was constructed during this time, and by the early 1970s, an access ramp was driven into the west orebody (Forward et al., 2011a). By 1976, lead and zinc concentrate

was produced, while Au-bearing pyrite and arsenopyrite concentrate was stockpiled onsite. The Hellenic Chemical Products and Fertilizer Company went into receivership in 1991 but government subsidies kept the Olympias mine in production until 1995. While under ownership of the Hellenic Chemical Products and Fertilizer Company, the Olympias mine produced approximately 3.6 Mt of ore (Forward et al., 2011a). TVX Gold Incorporated, a Canada-based mining company, took ownership of the Olympias property as part of their successful 1995 bid for the Kassandra properties. After acquisition, production from the Olympias mine was halted to confirm and expand the mineral resource. Within three years, TVX completed over 91,000 m of drilling, produced a resource estimate, and a bankable feasibility study.

Mining in the Stratoni area during the late 19th and early 20th century focused on easily exploitable and oxidized, near-surface Mn-rich material and sulfide ores (Tsirambides and Filippidis, 2012). From the period of 1893 to 1908, the French-Ottoman Company processed approximately 430 kt of Mn ore from the Mavres Petres and Piavitsa areas (Neubauer, 1957; Nebel, 1989). In 1901, the Hellenic Chemical Products and Fertilizer Company began mining near-surface pyritic ore in the Madem Lakkos area with mining operations lasting until 1955 (Nebel, 1989). During this time, approximately 6 Mt of pyrite ore was mined for sulfuric acid. Exploration drilling during the 1940-50s resulted in the delineation of the massive sulfide orebodies, which prompted underground development of the Madem Lakkos and Mavres Petres mines, collectively referred to as the Stratoni mines. In 1952, an enrichment plant was constructed to process the mixed sulfide ore with production beginning at Madem Lakkos in 1953 and Mavres Petres in 1957 (Gilg, 1993). The Hellenic Chemical Products and Fertilizer Company operated the Stratoni Mines until their bankruptcy in 1991. Government subsidies similarly keep the Stratoni mines operational until their procurement by TVX in 1995. The Madem Lakkos mine was finally closed in 2002, after nearly a century of active mining and the production of ~13.5 Mt of sulfide ore from surface and underground operations (Forward et al., 2010).

The earliest documented exploration work in the Skouries area was performed by the Greek state in the late 1950s. Positive exploration results prompted Nippon Mining of Japan to complete a drilling

program in 1960, resulting in the definition of 7 Mt of near-surface Cu-oxide ore that was deemed feasible for open pit recovery (Tobey et al., 1998). The project was subsequently acquired by Placer International, who completed about 11,000 m of drilling from 1962 to 1968 and also developed an exploration adit (Forward et al., 2011b). Their efforts defined a total of 34 Mt of ore grading 0.72% Cu and 1.1 g/t Au (Tobey et al., 1998). The Skouries property was subsequently held by the Hellenic Chemical Products and Fertilizer Company during the early half of the 1970s, however, it is unclear whether work was performed during this time. In 1976, Penaroya conducted a short-lived exploration program that contributed two additional drill holes. Billiton Resources held the property in 1981 and redefined the economic potential of the deposit with a revised resource calculation of approximately 72 Mt of ore grading 0.5% Cu and 0.7 g/t Au (Tobey et al., 1998). Following Billiton's efforts, the government-owned Kassandra Mines Company, performed a 6-hole program expanding known mineralization to depth. In 1995, TVX acquired the project and immediately conducted an infill drilling campaign to test the continuity and extent of high-grade ore at depth. Within three years, TVX conducted over 72,000 m of drilling, advanced development of the existing exploration adit, completed a mineral resource estimate and a bankable feasibility study, and produced an environmental impact study (Forward et al., 2011b).

In 2004, European Goldfields Limited, a junior Canadian exploration company, acquired the Kassandra mining concessions. European Goldfields maintained production of the Mavres Petres mine while revitalizing the Olympias mine infrastructure and advanced development of the Skouries deposit, which included a revised feasibility study. In 2012, Canadian gold miner, Eldorado Gold Corporation, acquired European Goldfields and gained ownership of Kassandra Mining District. Based on historical and current work, the Olympias deposit contains a published measured and indicated resource of 15.1 Mt at 8.97 g/t Au, 146 g/t Ag, 4.9% Pb and 6.5% Zn, the Mavres Petres deposit contains 0.55 Mt at 212 g/t Ag, 8.1% Pb and 11.0% Zn, and the development-stage Skouries deposit contains a measured and indicated resource of 289.3 Mt grading 0.58 g/t Au and 0.43% Cu (Eldorado Gold Corp., 2017).

Previous Research in the Kassandra Mining District

For almost a century, the Kassandra Mining District has attracted explorers and scientists who pursued the economic potential of the region and have attempted to define the origin of the ore deposits. In 1928, Cornelio Sagui published possibly the earliest geologic description of the ores in the district with particular focus on the artisanal mines in the Piavitsa area. Research resumed in the late 1950s with the first geologic assessment of the Madem Lakkos and Olympias deposits by Neubauer (1957). Subsequent studies followed with the geologic description of the Skouries deposit by Zachu (1963) and continued work on the massive sulfide deposits by Nicolaou (1960, 1964, 1969). The apparent economic potential of the eastern Chalkidiki peninsula spurred a regional 1:50,000-scale geologic mapping campaign conducted between 1963 and 1970 by the Greek Institute of Geology and Mineral Exploration (IGME) in cooperation with the German Federal Institute for Geosciences and Natural Resources (BGR). A series of geologic maps accompanied by a number of seminal papers (e.g., Kockel et al., 1971, 1977) were published, establishing the regional geologic framework and providing the basis for the tectonics and ore deposit studies that followed.

This pioneering work undoubtedly motivated a number of early investigations dedicated to unraveling the timing of magmatism and hydrothermal alteration within the district (Papadakis, 1971; Burgarth et al., 1980; Tompouloglou; 1981; Perantonis, 1982; Kalogeropoulos et al., 1990; 1991; Frei, 1992, 1995; Gilg and Frei, 1994). Many of the geochronological studies largely relied on the K-Ar technique, reporting ages from either individual minerals (e.g., biotite or sericite) or whole-rock analyses, with limited use of U-Pb methods (e.g., Frei, 1992). This early research established an Oligo-Miocene timing for magmatism. A wealth of economic geology research was also performed at this time, which largely focused on documenting the genesis of the carbonate replacement sulfide deposits in the Madem Lakkos and Olympias areas (Nicolaou and Kokonis, 1980; Kalogeropoulos and Economou, 1987; Kalogeropoulos et al., 1989; Kilias and Kalogeropoulos, 1989; Mantzos, 1989; Nebel, 1989; Nebel et al., 1991; Gilg, 1993; Gilg and Frei, 1994; Kilias and Madsen, 1994; Kilias et al., 1996; Haines, 1998). The

Skouries porphyry Au-Cu deposit was also the focus of a number of studies documenting the timing and physiochemical conditions of ore formation, and the distribution of platinum group elements within the deposit (Kockel et al., 1975; Eliopoulos and Economou-Eliopoulos, 1991; Frei, 1992, 1995). Later studies investigated the igneous geochemistry of the porphyritic host rocks, comparing the Skouries deposit to other well-known porphyry Cu-Au systems exhibiting similar alkaline-shoshonitic character (Tobey et al., 1998; Kroll et al., 2002). Most recently, McFall (2016) examined the distribution and deportment of platinum group elements in the Skouries deposit.

Geochemical and geochronological studies peripheral to the district refined the understanding of the tectonic basement assemblages that comprise the eastern Chalkidiki peninsula (e.g., Himmerkus et al., 2005, 2011), while other tectonic studies evaluated the thermal evolution and exhumation history of the region (Wüthrich, 2009; Kounov et al., 2015; Kydonakis et al., 2014, 2016). A PhD dissertation from Kingston University (London) recently came available in July of 2017 (Hahn, 2014). This study utilized zircon U-Pb geochronology, as well as whole-rock and isotope geochemistry to evaluate the geodynamic evolution of the Kassandra Mining District with the objective of establishing the tectonic controls on magmatic-hydrothermal ore deposition. Hahn (2014) concluded that Oligo-Miocene magmatism occurred between 20-29 Ma within a post-collisional, supra-subduction zone environment where porphyry and carbonate replacement mineralization occurred coeval with the exhumation of the Rhodope metamorphic core complex. Metal zoning patterns in the district permitted Hahn (2014) to interpret the sulfide orebodies in the Madem Lakkos area as proximal to a source intrusion whereas the deposits in the Mavres Petres, Olympias, and Piavitsa areas were regarded as representing increasingly distal parts of a single hydrothermal system active during the late Oligocene.

Dissertation Outline

Motivation

Decades of research have contributed to the understanding of the metallogeny of the Kassandra Mining District; however, a coherent structural, magmatic and hydrothermal framework for the district was lacking, which hindered the interpretation of ore genesis and exploration. While an Oligo-Miocene timing for syn-mineral magmatism had been established previously, reported ages generally lacked the resolution necessary to separate magmatic episodes. Unfortunately, sample locations were commonly not reported and geochemical analyses rarely accompanied geochronological samples. Despite the number of studies in the district and the reported spatial and temporal association of magmatism with ore, many igneous units remained undated and of uncertain petrologic affiliation, with the source intrusion(s) responsible for carbonate replacement mineralization unresolved. Possibly the most notable deficiency in the geologic understanding of the district was the lack of a structural framework. While an association between ore and folds, faults, and igneous rocks was reported, the structural documentation of these associations was largely absent from the literature. Aside from a few unpublished consulting reports and a deposit-scale study from the Madem Lakkos mine (Haines, 1998), no published record existed for the structural evolution of the district.

These deficiencies in the understanding of ore formation in the Kassandra Mining District were recognized as research opportunities and were the principal motivator for developing the following research goals: i) determine the absolute ages of geologically important igneous intrusions and describe the petrogenesis of Oligo-Miocene magmatism; ii) document the style and timing of structural events within the district and establish a structural model that describes the controls on porphyry and carbonate replacement mineralization; and, iii) identify the origin and source of the hydrothermal fluid(s) responsible for carbonate replacement mineralization in the district.

Methodology

The acquisition of a comprehensive multi-disciplinary database was necessary to meet the research objectives outlined above. Fieldwork was performed from May to August 2013-2015 with a brief field season conducted in September of 2016. District- and deposit-scale geologic mapping covering an area of 250 square kilometers was performed by the author, which improved upon published as well as unpublished company maps. Geologic interpretation was assisted by an unpublished aeromagnetic-resistivity geophysical survey. Geologic map and cross section interpretations presented in this study represent a compilation of these data supported by logging of diamond drill cores and surface structural data principally obtained by the author but including existing data.

Geochronological samples were collected by the author from surface and underground mine exposures. Igneous zircon U-Pb geochronology was conducted at the Pacific Center for Isotopic and Geochemical Research (PCIGR) at the University of British Columbia by Drs. Jim Mortensen and Richard Friedman, with ^{40}Ar-^{39}Ar analysis of hydrothermal mica performed at the University of Manitoba by Dr. Alfredo Camacho. Samples for whole-rock lithogeochemistry were collected by the author from surface exposures and drill core with analyses conducted at ACME Labs in Vancouver, British Columbia. Lead isotope analysis on igneous K-feldspar and sulfide mineral separates were carried out at PCIGR by Dr. Janet Gabites. In addition to detailed petrography, stable carbon-oxygen isotopes, and fluid inclusions were performed by the author at Cornell University, the University of British Columbia, and the State University of New York at Cortland, respectively. A detailed methodology section that describes the field procedures, sampling, and analytical techniques is located in the Appendix. Data tables for each chapter are also presented in the Appendix.

Organization

This dissertation is organized into five chapters consisting of three standalone papers in addition to an introduction (this chapter) and a concluding chapter. Chapter two describes the magmatic and

metallogenic framework of porphyry Au-Cu and polymetallic carbonate-hosted replacement deposits in the Kassandra Mining District. This study was accomplished by means of petrography, whole-rock geochemistry, and igneous zircon U-Pb geochronology. The results presented in this chapter builds upon previous work and places tighter constraints on the timing and petrogenesis of Oligo-Miocene magmatism, thus improving the understanding of the metallogenic evolution of the economic ore deposits in the region. Chapter two was presented at the Society of Economic Geologists annual meeting in Çeşme, Turkey in September of 2016 and published in the Society of Economic Geologists Special Publication Number 19: Tectonics and Metallogeny of the Tethyan Orogenic Belt.

Chapter three describes the structural controls on porphyry Au-Cu and Au-rich polymetallic carbonate-hosted replacement deposits in the Kassandra Mining District. Limited structural studies have been conducted within the district, in spite of the economic significance and demonstrable association of preexisting structures and syn-mineral faults on the location and morphology of ore deposits. Chapter three utilized a comprehensive structural and fault-kinematic database, whole-rock geochemistry, ^{40}Ar-^{39}Ar geochronology, and petrography to describe the structural architecture and deformation history of the district, and to characterize the style, timing, and significance of faulting. This chapter presents a structural model for the evolution of porphyry and carbonate replacement systems within the Kassandra Mining District. Chapter three was published in 2018 (v. 113) of the journal Economic Geology.

Chapter four describes the origin of the carbonate replacement deposits and provides evidence for structurally-controlled and zoned hydrothermal systems occurring within the Stratoni fault zone and in the Olympias area. This chapter evaluated a comprehensive historic drill core database to identify metal zonation patterns at the district- and deposit-scale, and examines fluid inclusion data as well as carbon and oxygen isotopes to model the evolution of the hydrothermal fluid(s) that resulted in carbonate replacement mineralization. Lead isotope data was also investigated to determine the source of metals and to potentially fingerprint source intrusion(s) in the district. These results are combined with previously published data to establish an approximate location for a causative igneous source, and to describe the

origin of the hydrothermal fluid(s) responsible for the carbonate replacement deposits in the Kassandra Mining District. Chapter four is a prepared manuscript intended to be submitted to the journal Economic Geology.

Chapter five summarizes the dissertation and highlights the major conclusions reached from each of the previous three chapters. This chapter also provides recommendations for future research to be undertaken within the Kassandra Mining District and regionally. Supplemental material and data that accompanies each chapter are located in the Appendix.

REFERENCES

Arvanitidis, N.D., and Constantinides, D.C., 1994, Ore geology of the Olympias, Madem Lakkos and Mavres Petres polymetallic deposits: Post-congress 2-day field trip to Chalkidiki peninsula (central Macedonia, northern Greece), Congress of the Geological Society of Greece, 7th, Thessaloniki, Greece, May 27-28, 1994, Guidebook, 17 p.

Beaty, D.W., Cunningham, C.E., Rye, R.O., Steven, T.A., and Gonzales-Urien, E., 1986, Geology and geochemistry of the Deer Trail Pb-Zn-Ag-Au-Cu manto deposits, Marysvale district, west-central Utah: Economic Geology, v. 81, p. 1932-1952.

Beaty, D.W., Landis, G.P., and Thompson, T.B., 1990, Carbonate-hosted sulfide deposits of the central Colorado mineral belt: Introduction, general discussion, and summary, in Beaty, D.W., Landis, G.P., and Thompson, T.B., eds., Carbonate-hosted sulfide deposits of the central Colorado mineral belt: Economic Geology Monograph 7, p. 1-18.

Bissig, T., and Cooke, D.R., 2014, Introduction to the special issue devoted to alkalic porphyry Cu-Au and epithermal Au deposits: Economic Geology, v. 109, p. 819-825.

Bonsall, T.A., Spry, P.G., Voudouris, P.,Ch., Tombros, S., Seymour, K.,St., and Melfos, V., 2011, The geochemistry of carbonate-replacement Pb-Zn-Ag mineralization in the Lavrion district, Attica, Greece: Fluid inclusion, stable isotope, and rare earth element studies: Economic Geology, v. 106, p. 619-651.

Burgath, K., Kockel, F., Mohr, F., Raschka, H., Jung, D., and Mussalam, K., 1980, A complex of sheeted dykes and pillow lavas in the southern part of the Chalkidiki peninsula, Greece [ext. abs.]: International Ophiolite Symposium, 2nd, Nicosia, Cyprus, 1980, Extended Abstracts, p. 20.

Einaudi, M.T., Meinert, L.D., and Newberry, R.J., 1981, Skarn deposits: Economic Geology 75th Anniversary Volume, p. 317-391.

Eldorado Gold Corporation, 2017, Resources and reserves: Accessed October 29, 2017, (http://www.eldoradogold.com/assets/resources-and-reserves/).

Eliopoulos, D.G., and Economou-Eliopoulos, M., 1991, Platinum-group elements and gold contents in the Skouries porphyry copper deposit, Chalkidiki peninsula, northern Greece: Economic Geology, v. 86, p. 740-749.

Eliopoulos, D.G., Economou-Eliopoulos, M., and Zelyaskova-Panayiotova, M., 2014, Critical factors controlling Pd and Pt potential in porphyry Cu-Au deposits: evidence from the Balkan Peninsula: Geosciences, v. 4, p. 31-49.

Forward, P., Francis, A., and Liddell, N., 2010, Technical report on the Stratoni project Pb-Zn-Ag deposit, northern Greece: European Goldfields Limited, NI 43-101 Report, 54 p.

Forward, P., Francis, A., and Liddell, N., 2011a, Technical report on the Olympias project Au Pb Zn Ag deposit, northern Greece: European Goldfields Limited, NI 43-101 Report, 207 p.

Forward, P., Smith, D.J.F., and Francis, A., 2011b, Skouries Cu/Au project, Greece: European Goldfields Limited, NI 43-101 Report, 113 p.

Frei, R., 1992, Isotope (Pb-Rb-Sr-S-O-C-U-Pb) geochemical investigations of Tertiary intrusions and related mineralizations in the Serbo-Macedonian (Pb-Zn, Sb+Cu-Mo metallogenetic) province in northern Greece: Unpublished Ph.D. thesis, Zürich, Switzerland, ETH, 231 p.

Frei, R., 1995, Evolution of mineralizing fluid in the porphyry copper system of the Skouries deposit, northeast Chalkidiki (Greece): Evidence from combined Pb-Sr and stable isotope data: Economic Geology, v. 90, p. 746-762.

Gilg, H.A., 1993, Geochronology (K-Ar), fluid inclusion, and stable isotope (C, H, O) studies of skarn, porphyry copper, and carbonate-hosted Pb-Zn (Ag, Au) replacement deposits in the Kassandra mining district (eastern Chalkidiki, Greece): Unpublished Ph.D. thesis, Zürich, Switzerland, ETH, 153 p.

Gilg, H.A., and Frei, R., 1994, Chronology of magmatism and mineralization in the Kassandra mining area, Greece: The potentials and limitations of dating hydrothermal illites: Geochimica et Cosmochimica Acta, v. 58, p. 2107-2122.

Graybeal, F.T., Smith, D.M., and Vikre, P.G., 1986, The geology of silver deposits, in Wolf, K.H., ed., Handbook of stratabound and stratiform ore deposits: Amsterdam, Elsevier, v. 14, p. 1-184.

Hahn, A., 2014, Nature, timing and geodynamic context of polymetallic mineralisation in the Kassandra mining district, North Greece: Unpublished Ph.D. thesis, London, United Kingdom, Kingston University, 351 p.

Haines, H.S., 1998, A structural synthesis for sector Vb of the Madem Lakkos polymetallic sulfide deposit – Northeast Greece: Unpublished M.Sc. thesis, London, United Kingdom, The University of London, 81 p.

Heinrich, C.A., and Neubauer, F., 2002, Cu-Au-Pb-Zn-Ag metallogeny of the Alpine-Balkan-Carpathian-Dinaride geodynamic province: Mineralium Deposita, v. 37, p. 533–540.

Himmerkus, F., Zachariadis, P., Reischmann, T., and Kostopoulos, D.K., 2005, The mafic complexes of the Athos-Volvi-Zone – a suture zone between the Serbo-Macedonian massif and the Rhodope massif?: Geophysical Research Abstracts, v. 7., p. 10, 240.

Himmerkus, F., Zachariadis, P., Reischmann, T., and Kostopoulos, D., 2011, The basement of the Mount Athos Peninsula, northern Greece: insights from geochemistry and zircon ages: Int. J. Earth Sci., v. 101, p. 1467-1485.

Holliday, J.R., and Cooke, D.R., 2007, Advances in geological models and exploration methods for copper ± gold porphyry deposits, in Milkereit, B., ed., Proceedings of Exploration 07: Fifth Decennial International Conference on Mineral Exploration: Toronto, Prospectors and Developers Association of Canada, p. 791-809.

Ishihara, S., 1981, The granitoid series and mineralization: Economic Geology 75th Anniversary Volume, p. 458-484.

Janković, S., 1997, The Carpatho-Balkanides and adjacent area: a sector of the Tethyan Eurasian metallogenic belt: Mineralium Deposita, v. 32, p. 426-433.

Kaiser-Rohrmeier, M., von Quadt, A., Driesner, T., Heinrich, C.A., Handler, R., Ovtcharova, M., Ivanov, Z., Petrov, P., Sarov, St., and Peytcheva, I., 2013, Post-orogenic extension and hydrothermal ore formation: High-precision geochronology of the central Rhodopian metamorphic core complex (Bulgaria-Greece): Economic Geology, v. 108, p. 691-718.

Kalogeropoulos, S.I., and Economou, G.S., 1987, A study of sphalerite from the carbonate-hosted Pb-Zn sulfide deposits of the eastern Chalkidiki peninsula, northern Greece: Canadian Mineralogist, v. 25, p. 639-646.

Kalogeropoulos, S.I., Kilias, S.P., Bitzios, D.C., Nicolaou, M., and Both, R.A., 1989, Genesis of the Olympias carbonate-hosted Pb-Zn (Au, Ag) sulfide ore deposit, eastern Chalkidiki peninsula, northern Greece: Economic Geology, v. 84, p. 1210-1234.

Kalogeropoulos, S.I., Frei, R., Nikolaou, M., and Gerouki, F., 1990, Origin and metallogenetic significance of the Tertiary Stratoni granodiorite, Chalkidiki, N. Greece: isotope and chemical evidence: Bulletin of the Geological Society of Greece, v. 26, p. 23-38.

Kalogeropoulos, S.I., Gerouki, F., and Papadopoulos, C., 1991, Mineralogy-geochemistry-genesis and metallogenetic significance of lamprophyres from the Stratoni-Olympias area Kerdilia formation, eastern Chalkidiki: Bulletin of the Geological Society of Greece, v. 27, p. 161-173.

Kilias, S.P., and Kalogeropoulos, S.I., 1989, Physiochemical conditions of ore formation of the Olympias Pb-Zn (Au, Ag) sulphide deposit, E. Chalkidiki, based on fluid inclusion studies and arsenopyrite geothermometry. Contribution to metallogeny and exploration: Geological Society of Greece Bulletin, 23/2, p. 271-282.

Kilias, S.P., and Madsen, J. K., 1994, H2O-CO2-NaCl fluid immiscibility in the carbonate-hosted Olympias Pb-Zn (Au, Ag) sulfide deposit, Macedonia, Greece: Bulletin of the Geological Society of Greece, v. 30/1, p. 445-456.

Kilias, S.P., Kalogeropoulos, S.I., and Konnerup-Madsen, J., 1996, Fluid inclusion evidence for the physicochemical conditions of sulfide deposition in the Olympias carbonate-hosted Pb-Zn(Au, Ag) sulfide ore deposit, E. Chalkidiki peninsula, N. Greece: Mineralium Deposita, v. 31, p. 394-406.

Kockel, F., Mollat, H., and Walther, H., 1971, Geologie des Serbomazedonischen massivs und seines mesozoischen Rahmes (Nord-Griechenland): Geologisches Jahrbuch der Bundesanstalt für Geowissenschaften und Rohstoffe, v. 89, p. 529-551.

Kockel, F., Mollat, H., and Gundlach, H., 1975, Hydrothermally altered and (copper-) mineralized porphyritic intrusions in the Serbo-Macedonian massif (Greece): Mineralium Deposita, v. 10, p. 195-204.

Kockel, F., Mollat, H., and Walther, H., 1977, Erläuterungen yur geologischen karte der Chalkidiki und agrenzender Gebiete 1:100000 (Nord-Griechenland): Bundesanstalt für Geowissenschaften Rohstoffe, Hannover, p. 1-119.

Kounov, A., Wüthrich, E., Seward, D., Burg, J.P., and Stockli, D., 2015, Low-temperature constraints on the Cenozoic thermal evolution of the southern Rhodope core complex (northern Greece): International Journal of Earth Science, v. 104, p. 1337-1352.

Kroll, T., Müller, D., Seifert, T., Herzig, P.M., and Schneider, A., 2002, Petrology and geochemistry of the shoshonite-hosted Skouries porphyry Cu-Au deposit, Chalkidiki, Greece: Mineralium Deposita, v. 37, p. 137-144.

Kydonakis, K., Gallagher, K., Brun, J.-P., Jolivet, M., Gueydan, F., and Kostopoulos, D., 2014, Upper Cretaceous exhumation of the western Rhodope Metamorphic Province (Chalkidiki peninsula, northern Greece): Tectonics, v. 33, p. 1113-1132.

Kydonakis, K., Brun, J.-P., Poujol, M., Monié, P., and Chatzitheodoridis, E., 2016, Inference on the Mesozoic evolution of the north Aegean from the isotopic record of the Chalkidiki block: Tectonophysics, v. 682, p. 65-84.

Lang, J.R., Stanley, C.R., and Thompson, J.F.H., 1995, Porphyry copper-gold deposits related to alkalic igneous rocks in the Triassic-Jurassic arc terranes of British Columbia: Arizona Geological Society Digest 20, p. 219-236.

Lindgren, W., and Loughlin, G.F., 1919, Geology and ore deposits of the Tintic mining district, Utah: U.S. Geological Survey Professional Paper 107.

Mantzos, L.A., 1989, Geology and lithogeochemistry of the Olympias carbonate-hosted Pb-Zn sulfide deposit, Chalkidiki, Greece: Unpublished Ph.D. thesis, London, United Kingdom, Imperial College, University of London, 404 p.

Marchev, P., Kaiser-Rohrmeier, M., Heinrich, C., Ovtcharova, M., von Quadt, A., and Raicheva, R., 2005, 2: Hydrothermal ore deposits related to post-orogenic extensional magmatism and core complex formation: the Rhodope massif of Bulgaria and Greece: Ore Geology Reviews, v. 27, p. 53-89.

McFall, K.A., 2016, Critical metals in porphyry copper deposits: Unpublished Ph.D. thesis, Southampton, United Kingdom, University of Southampton, 239 p.

Megaw, P.K.M., 1998, Carbonate-hosted Pb-Zn-Ag-Cu-Au replacement deposits: An exploration perspective, in Lentz, D.R., ed., Mineralized intrusion-related skarn systems: Mineralogical Association of Canada Short Course Series, v. 26, p. 337-258.

Megaw, P.K.M., Ruiz, J., and Titley, S.R., 1988, High-temperature, carbonate-hosted Ag-Pb-Zn(Cu) deposits of northern Mexico: Economic Geology, v. 83, p. 1856-1885.

Meinert, L.D., 1987, Skarn zonation and fluid evolution in the Groundhog mine, Central mining district, New Mexico: Economic Geology, v. 82, p. 523-545.

Melfos, V., and Voudouris, P., 2017, Cenozoic metallogeny of Greece and potential for precious, critical and rare metals exploration: Ore Geology Reviews, v. 89, p. 1030-1057.

Moynihan, D.P., and Pattison, D.R.M., 2011, The origin of mineralized fractures at the Bluebell mine site, Riondel, British Columbia: Economic Geology, v. 106, p. 1043-1058.

Nebel, M.L., 1989, Metamorphism and polygenesis of the Madem Lakkos polymetallic sulfide deposit, Chalkidiki, Greece: Unpublished Ph.D. thesis, Golden, Colorado, Colorado School of Mines, 215 p.

Nebel, M.L., Hutchinson, R.W., and Zartman, R.E., 1991, Metamorphism and polygenesis of the Madem Lakkos polymetallic sulfide deposit, Chalkidiki, Greece, Economic Geology., v. 86, p. 81-105.

Nelson, J.L., 1996, Polymetallic mantos Ag-Pb-Zn, in Lefebure, D.V., and Höy, T., eds., Selected British Columbia Mineral Deposit Profiles, Volume 2: British Columbia Ministry of Energy, Mines and Petroleum Resources, p. 101-103.

Neubauer, W.H., 1957, Geologie der blei-zink reichen kieslagerstätten von Kassandra (Chalkidike, Griechenland): Berg- und Hüttenmännische Monatshefte, v. 102, p. 1-16.

Nicolaou, M.N., 1960, L'intrusion granitique dans la région de Stratoni-Olympiade et sa relation avec la métallogenèse: Annales Géologiques des Pays Helléniques, v. 11, p. 214-265.

Nicolaou, M.N., 1964, The mineralogy and micrography of the sulphide ores of Kassandra mines, Greece: Annales Géologiques des Pays Helléniques, v. 16, p. 111-139.

Nicolaou, M.N., 1969, Recent research on the composition of the Kassandra mines orebodies: Praktika tes Academias Athenon, v. 44, p. 82-93 (in Greek with English abstract).

Nicolaou, M., and Kokonis, I., 1980, Geology and development of the Olympias mine, eastern Chalkidiki, Macedonia, Greece, in Jones, M.J., ed., Complex sulfide ores: London Institute of Mining and Metallurgy, p. 260-270.

Papadakis, A., 1971, On the age of the granitic intrusions near Stratonion Chalkidiki, Greece: Annales Géologiques des Pays Helléniques, v. 23, p. 297-300.

Perantonis, G.I., 1982, Genesis of porphyry copper deposits in the Chalkidiki peninsula and western Thrace, Greece: Unpublished Ph.D. thesis, Athens, University of Athens, 150 p.

Prescott, B., 1916, The main mineral zone of the Santa Eulalia district, Chihuahua: Transactions of the American Institute of Mining Engineers, v. 51, p. 57-99.

Rees, C., Riedell, K.B., Proffett, J.M., Macpherson, J., and Robertson, S., 2012, The Red Chris porphyry copper-gold deposit, northern British Columbia, Canada: Igneous phases, alteration, and controls of mineralization: Economic Geology, v. 110, p. 857-888.

Richards, J.P., 2009, Postsubduction porphyry Cu-Au and epithermal Au deposits: Products of remelting of subduction-modified lithosphere: Geology, v. 37, p. 247-250.

Richards, J.P., 2011, High Sr/Y arc magmas and porphyry Cu ± Mo ± Au deposits: Just add water: Economic Geology, v. 106, p. 1075-1081.

Sagui, C.L., 1928, The ancient mining works of Cassandra, Greece: Economic Geology, v. 23, p. 671-680.

Sánchez, M.G., McClay, K.R., King, A.R., and Wijbrams, J.R., 2016, Cenozoic crustal extension and its relationship to porphyry Cu-Au-(Mo) and epithermal Au-(Ag) mineralization in the Biga peninsula, northwestern Turkey, in Richards, J.P., ed., Tectonics and metallogeny of the Tethyan orogenic belt: Economic Geology Special Publication Number 19, p. 113-156.

Seedorff, E., Dilles, J.H., Proffett, J.M., Jr., Einaudi, M.T., Zurcher, L., Stavast, W.J.A., Johnson, D.A., and Barton, M.D., 2005, Porphyry deposits: Characteristics and origin of hypogene features: Economic Geology 100th Anniversary Volume, p. 251-298.

Serafimovski, T., 2000, The Lece-Chalkidiki metallogenic zone: geotectonic setting and metallogenic features: Geologija, v. 42, p. 159-164.

Sillitoe, R.H., 2010, Porphyry copper systems: Economic Geology, v. 105, p. 3-41.

Siron, C.R., Hitzman, M.W., and McLeod, R., 2010, Geology of the Little Whitman carbonate-hosted replacement Zn-Pb-Ag-(Cu) prospect, western Fortymile district, Alaska, in Goldfarb, R.J., Marsh, E.E., and Monecke, T., eds., The challenge of finding new mineral resources: Global metallogeny, innovative exploration, and new discoveries: Society of Economic Geologists Special Publication Number 15 Volume II, p. 421-436.

Tobey, E., Schneider, A., Algería, A., Olcay, L., Perantonis, G., and Quiroga, J., 1998, Skouries porphyry copper-gold deposit, Chalkidiki, Greece: Setting, mineralization and resources, in Porter, T.M., ed., Porphyry and hydrothermal copper and gold deposits: A global perspective; Adelaide, PGC Publishing, p. 175-184.

Tompouloglou, C., 1981, Les minéralisations tertiares, type cuivre porphyrique, du massif Serbo-Macédonien (Macédoine, Grèce) dans leur contexte magmatique (avec un traitment géostatistique pour les données du prospect d'Alexia): Unpublished Ph.D. thesis, Paris, France, Ecole Nationale Supérieure des Mines de Paris, 204 p.

Tsirambides, A., and Filippidis, A., 2012, Metallic mineral resources of Greece: Central European Journal of Geosciences, v. 4, p. 641-650.

Vikre, P.G., 1998, Intrusion-related polymetallic carbonate replacement deposits in the Eureka district, Eureka county, Nevada: Nevada Bureau of Mines and Geology Bulletin 110, 52 p.

Wilson, A.J., 2003, The geology, genesis and exploration context of the Cadia gold-copper porphyry deposits, NSW, Australia: Unpublished Ph.D. thesis, Hobart, University of Tasmania, 335 p.

Wüthrich, E., 2009, Low temperature thermochronology of the northern Aegean Rhodope Massif: Unpublished Ph.D. thesis, Zürich, Switzerland, ETH, 210 p.

Yigit, O., 2012, A prospective sector in the Tethyan metallogenic belt: geology and geochronology of mineral deposits in the Biga peninsula, NW Turkey: Ore Geology Reviews, v. 46, p. 118-148.

Zachu, K.E., 1963, Discovery of a copper deposit in Chalkidiki peninsula, N-Greece: Geological and Geophysical Research, v. 8, p. 1-26.

CHAPTER 2

MAGMATIC AND METALLOGENIC FRAMEWORK OF AU-CU PORPHYRY AND CARBONATE-HOSTED REPLACEMENT DEPOSITS OF THE KASSANDRA MINING DISTRICT

The Kassandra mining district is located on the eastern Chalkidiki Peninsula approximately 100 km east of Thessaloniki. The cumulative gold endowment, ~12 Moz Au (Eldorado Gold Corp., 2016) in porphyry and carbonate-hosted replacement-style sulfide orebodies, makes this district one of the most economically significant mining camps in the Serbo-Macedonian Metallogenic Province (Hahn et al., 2012). Polymetallic orebodies occur at Olympias, Madem Lakkos, and Mavres Petres, and Au-Cu mineralization is hosted by the Skouries porphyry. Olympias contains a measured resource of 16.3 Mt at 8.6 g/t Au, 146 g/t Ag, 4.9% Pb and 6.5% Zn (Eldorado Gold Corp., 2016) including 1.86 Mt grading 3.4 g/t Au in economically recoverable stockpiles from previous operations. Past mining at Madem Lakkos produced approximately 13.5 Mt of Ag-Pb-Zn ore (Forward et al., 2010). Mavres Petres has a measured resource of 1.1 Mt at 210 g/t Ag, 7.9% Pb and 10.5% Zn (Eldorado Gold Corp., 2016). The Skouries Au-Cu porphyry contains a measured and indicated resource of 283.6 Mt grading 0.6 g/t Au and 0.43% Cu (Eldorado Gold Corp., 2016).

Mining of gold and silver ores in the Chalkidiki region dates from antiquity, about 350 B.C., during the rule of King Phillip II of Macedon and his successor, Alexander the Great. Historic records indicate that the extraction of ores from the mines of Potidaea and Mt. Pangaeus financed expansion of the empire (e.g., Diodorus Siculus). The region experienced limited activity during Roman rule and intermittent development during the 9th and 15th centuries A.D. while under Byzantine and Ottoman occupation, respectively (Haines, 1998). Mineral extraction occurred throughout the 20th century with modern exploration and mining practices established during the 1960s and 1970s when the Hellenic Chemical Products and Fertilizers Company Ltd. operated the Madem Lakkos and Olympias mines, and exploration was undertaken at Skouries by Nippon Mining, Placer International, and Penaroya (Tobey et

al., 1998). Billiton Resources briefly evaluated Skouries in the early 1980s (Tobey et al., 1998). TVX Gold took over mining at Madem Lakkos and Olympias in 1995, and exploration and resource evaluation continued at Olympias and Skouries through 2002. European Goldfields held the concessions prior to acquisition in 2012 by Eldorado Gold Corporation. Currently, Mavres Petres is an operating mine, tailings are being reprocessed at Olympias, and new mine development is underway at Skouries and Olympias.

The objective of this study is to describe the metallogenic framework of the Kassandra mining district based on the structural architecture of the area and the timing and petrogenesis of Oligo-Miocene magmatism. The work was based on mapping approximately 250 km^2, logging representative drill holes, and compilation of drill and exploration data. We present petrography, whole-rock geochemistry, and high-precision zircon U-Pb geochronology defining ages for intrusive rocks belonging to Oligo-Miocene magmatism. These results further constrain the timing of Oligo-Miocene magmatism that builds upon previous work, and improves understanding of the metallogenic evolution of Au-Cu porphyry and Au-rich polymetallic carbonate-hosted replacement deposits of the region. All data from this study including sample location information are presented in the Appendix.

Regional Geologic Framework

The Hellenides of northern Greece form a segment of the Alpine-Himalayan mountain chain connecting the Balkan Peninsula with the Anatolides of Turkey. This section of the orogenic belt resulted from the convergence of the Apulian and Pelagonian microcontinents with the Serbo-Macedonian and Rhodope continental fragments previously accreted to the Eurasian margin during the Late Cretaceous to early Eocene (Pe-Piper and Piper, 2006). Convergence of microcontinents and subduction of oceanic lithosphere led to magmatism resulting from slab detachment or lithospheric delamination assisted by rollback of the subducting slab during post-collisional back arc extension of the subduction wedge (de Boorder et al., 1998; Wortel and Spakman, 2000; Lips, 2002; Neubauer, 2002; Brun and Sokoutis, 2010; Ring et al., 2010; Jolivet et al., 2013; Papanikolaou, 2013).

The Rhodope metamorphic province is described as an amphibolite-grade, crustal-scale, syn-metamorphic accretionary wedge consisting of stacked nappes that lie in the hinterland of the Hellenic subduction zone (Burg et al., 1990, 1996; Ricou et al., 1998; Gautier et al., 1999; Bonev et al., 2006; Krenn et al., 2010). The Greek segment of the Rhodope metamorphic province extends to the southwest to the Vardar Suture Zone (Ricou et al., 1998) and is bound to the northeast by the Maritza strike-slip fault and the Thrace Basin. Kydonakis et al. (2014) divides the Rhodope metamorphic province into three tectonic domains: northern Rhodope complex, southern Rhodope metamorphic core complex, and the Serbo-Macedonian domain. In the Chalkidiki region, the Serbo-Macedonian Vertiskos unit is separated from the southern Rhodope metamorphic core complex by the Kerdilion detachment fault (Figure 2.1; Brun and Sokoutis, 2007; Wüthrich, 2009; Kydonakis et al., 2014).

The Vertiskos unit is a Silurian-age exotic terrane that belonged to a continental magmatic arc of Gondwana-origin that was accreted onto the European margin in the Carboniferous (Himmerkus et al., 2006, 2007, 2009a). The Vertiskos unit consists of leucocratic augen gneisses and kyanite- and staurolite-bearing schist (Himmerkus et al., 2009a) that reached amphibolite-facies metamorphic conditions in the Late Jurassic to Early Cretaceous (Kilias et al., 1999; Lips et al., 2000). The Kerdilion unit originated from a Permo-Carboniferous magmatic arc overlain by Tethyan carbonates, and later witnessed magmatic activity during the Late Jurassic and Cretaceous (Turpaud and Reischmann, 2003; Himmerkus et al., 2011), and again during the early Miocene related to exhumation of the metamorphic dome (Jones et al., 1992; Dinter et al., 1995). Orthogneiss, paragneiss, marbles, micaceous schists, and amphibolite of the Kerdilion unit form the tectonic upper and westernmost portion of the southern Rhodope metamorphic core complex (Burg et al., 1993; Brun and Sokoutis, 2007; Himmerkus et al., 2011).

Triassic rifting of the European arc resulted in the opening of the Vardar Ocean and development of mafic units (Dixon and Dimitriadis, 1984; Himmerkus et al., 2005; Bonev and Dilek, 2010) and intrusion of A-type granites of the Arnea-Kerkini suite (Christofides et al., 2007). This magmatic event is evident in the Chalkidiki region with the Arnea granite that intruded the Vertiskos unit at 228 ± 5.6 Ma

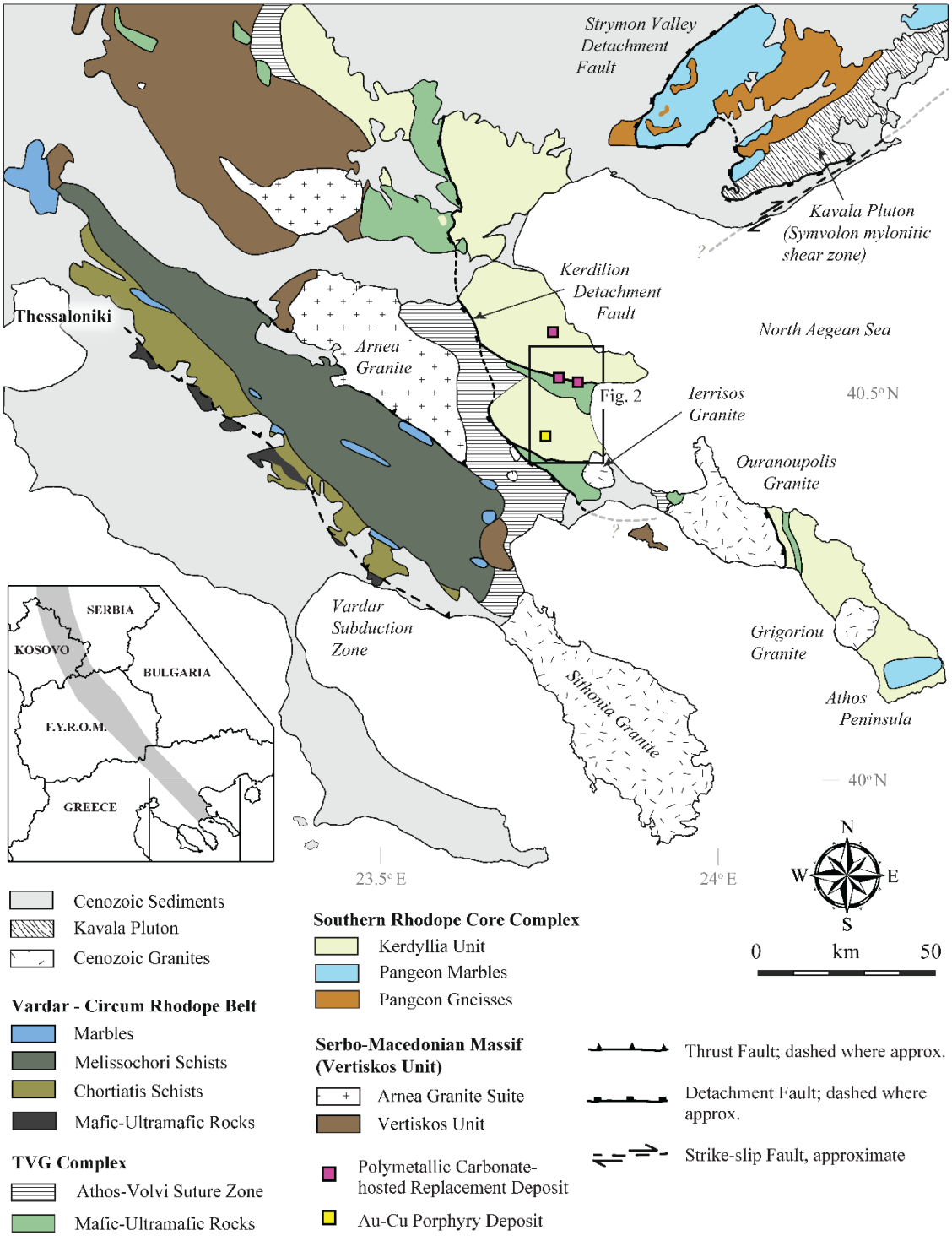

Figure 2.1. Simplified geologic map of the Chalkidiki peninsula after Himmerkus et al. (2011), including the Strymon valley detachment fault adopted from Dinter (1998) and the northern segment of the Kerdilion detachment fault after Brun and Sokoutis (2007) and Wüthrich (2009). The inset map depicts the location of the Oligo-Miocene Serbo-Macedonian Lece-Chalkidiki metallogenic belt (gray) after Janković (1997) and Serafimovski (2000).

(De Wet et al., 1989; Himmerkus et al., 2009b). The Arnea suite is interpreted to have a within-plate tectonic signature characteristic of a rift-dominated environment similar to Triassic-age granites elsewhere in the Aegean (Himmerkus et al, 2009b). Closure of the Vardar Ocean during the Cretaceous Alpine orogeny culminated in amphibolite-grade metamorphism of the Serbo-Macedonian domain and the Triassic rift-related granites (Himmerkus et al., 2009b). Ductile deformation of the Kerdilion unit, however, was accompanied by early to middle Eocene upper greenschist- to lower amphibolite-grade metamorphism, with a retrograde greenschist metamorphic overprint (Wawrzenitz and Krohe, 1998; Lips et al., 2000).

The Vertiskos unit is separated from the southern Rhodope Kerdilion unit by the arcuate Athos-Volvi Suture Zone (Himmerkus et al., 2005) and the Kerdilion fault (Figure 2.1; Kydonakis et al., 2014). Amphibolite, garnet-amphibolite, and serpentinized ultramafic rocks form a tectonic mélange with the adjacent gneisses. Mafic and ultramafic rocks belonging to the Athos-Volvi or Thermes-Volvi-Gomati (TVG) ophiolite complex (Dixon and Dimitriadis, 1984; Bonev and Dilek, 2010) are classified as non-cumulate and cumulate low-K tholeiites of gabbroic to hartzburgitic composition (Himmerkus et al., 2011). Previous geochemical and isotopic studies indicate a within-plate signature consistent with formation in an intra-continental rift or back arc environment within a supra-subduction zone setting (Dixon and Dimitriadis, 1984; Himmerkus et al., 2005; Bonev et al., 2012). These bodies were subsequently emplaced between the crustal blocks of the Vertiskos and Kerdilion units during the Hellenic orogeny (Himmerkus et al., 2005).

Widespread crustal extension in the northern Aegean region began in the mid-Eocene to mid-Oligocene. Approximately 120 km of extensional displacement and 30 degrees of dextral rotation of the Chalkidiki block was imparted by exhumation of the southern Rhodope metamorphic core complex (Dimitriadis et al., 1998; Brun and Sokoutis, 2007). Extensive magmatism and widespread volcanic activity began in the Oligocene (Fytikas et al., 1984; Pe-Piper and Piper, 2002; Ring et al., 2010) in response to plate convergence and crustal extension.

District Geology

The Serbo-Macedonian Metallogenic Province (Janković, 1997) spans the length of the Hellenide orogen (Figure 2.1). Porphyry and carbonate-hosted replacement deposits of the Kassandra Mining District are hosted by the high-grade metamorphic basement rocks of the Kerdilion unit (Brun and Sokoutis, 2007). The west-dipping Kerdilion detachment fault outcrops to the northwest, at the contact of the Kerdilion unit with the imbricated schists and gneiss of the Athos-Volvi Suture Zone (Figure 2.1). This structure is interpreted to have accommodated exhumation of the southern Rhodope core complex beginning in the middle Eocene (Brun and Sokoutis, 2007; Wüthrich, 2009; Kydonakis et al., 2014). A ductile shear zone similar in structural style to the Kerdilion fault occurs within the Athos-Volvi Suture Zone on the Athos peninsula (Himmerkus et al., 2011) southeast of the Kassandra Mining District. This ductile shear zone coalesces with the Kerdilion fault forming a continuous tectonic boundary between the Vertiskos unit to the south and west and the Kerdilion unit to the east and north (Figure 2.1).

Kerdilion Unit

The Kerdilion unit is well exposed north of the Stratoni fault where it consists of migmatitic quartzo-feldspathic biotite gneiss, megacrystic plagioclase-microcline granitic gneiss, amphibolite and marbles. The Stratoni fault is a zone of west-northwest-trending, south- to southwest-dipping normal faults outcropping over 12 km from the village of Stratoni and west to Piavitsa (Figure 2.2). The hangingwall of the Stratoni fault to the south is composed of amphibolite, potentially correlative with the TVG complex of Dixon and Dimitriadis (1984), and a thick sequence of carbonaceous-biotite gneisses and schists interlayered with minor calcareous schists and marble. Kockel et al. (1977) assigned the hangingwall lithologic sequence to the Vertiskos unit and this classification was adopted by subsequent studies in the area (e.g., Kalogeropoulos et al., 1989b; Frei, 1995). Observations from outcrop and drill core suggest a gradational contact between carbonaceous-biotite gneiss and amphibolite hangingwall rocks to the south of the Stratoni fault with footwall quartzo-feldspathic biotite gneiss and marble to the

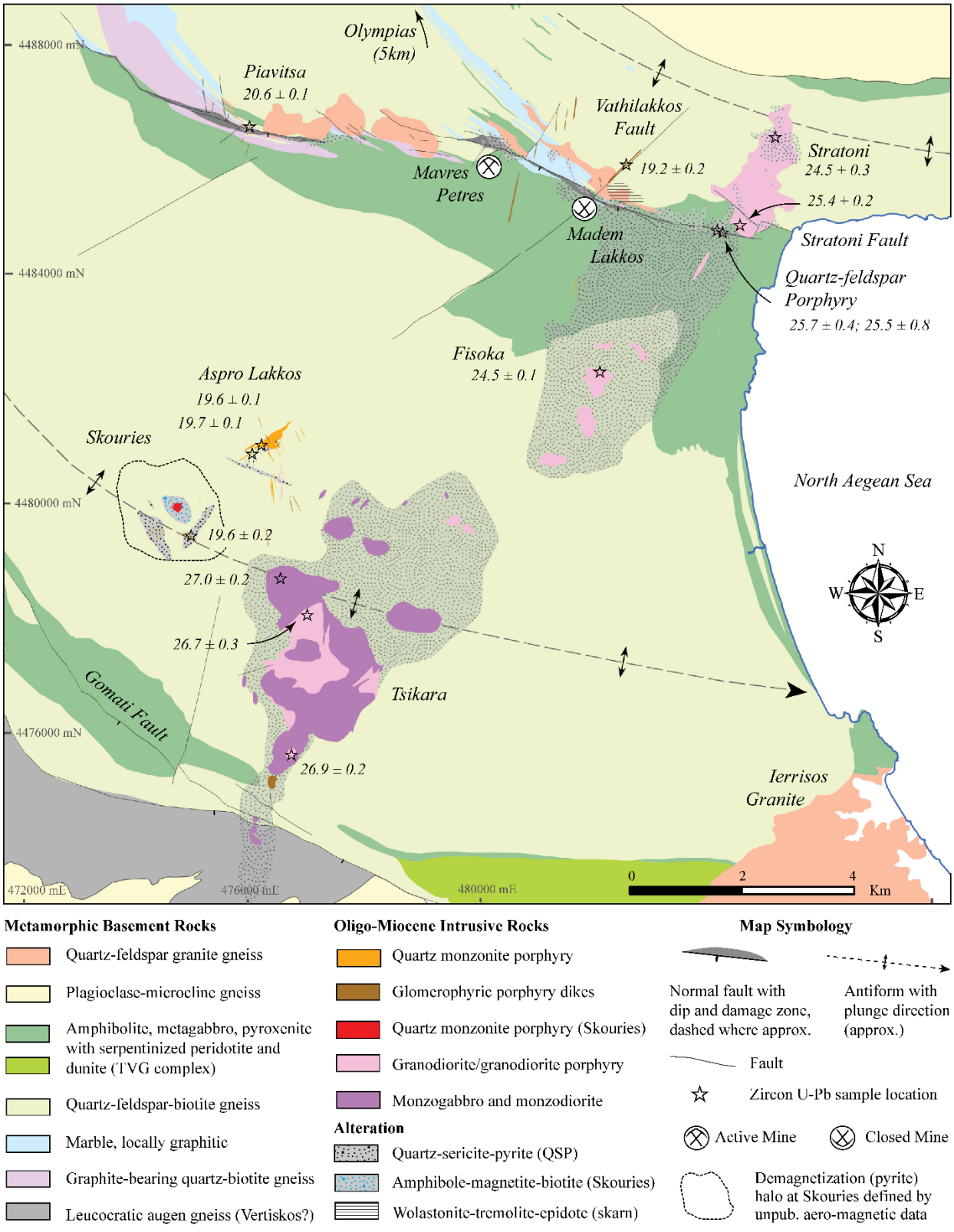

Figure 2.2. Geologic map of the Kassandra Mining District modified after Kockel et al. (1975). Coordinates measured using Greek Geodetic Coordinate System (GGRS 87 Greek Grid).

north. Marble and amphibolite occur on both sides of the fault although marble is prevalent to the north and amphibolite is dominant to the south. Furthermore, interlayered calcareous schists and marble associated with hangingwall gneisses are not characteristic of the Vertiskos unit and are more closely related to the Kerdilion unit (Himmerkus et al., 2011). Therefore, it is proposed that the Kerdilion unit is present on both sides of the Stratoni fault although there are lithologic changes that more or less coincide with the fault zone.

Abundant aplite and pegmatite dikes and sills of Eocene to Oligocene age occur throughout the footwall quartzo-feldspathic gneiss sequence (Kalogeropoulos et al., 1989b). Coarse-grained pegmatites and fine- to medium-grained aplites typically exhibit a discrete penetrative tectonic fabric or boudinage and are likely derived from anatectic processes during deformation (Kalogeropoulos et al., 1989b; Haines, 1998). Some of the aplitic dikes appear undeformed suggesting that anatexis continued post-deformation.

Magmatism

The district has witnessed a protracted magmatic history from the Late Cretaceous to early Eocene (Pe-Piper and Piper, 2002). Magmatism during this period is characterized by subduction-related calc-alkaline granites exposed at Ierissos (Frei, 1992, 1996), Ouranoupolis (De Wet et al., 1989), and Grigoriou (Bébien et al., 2001), which outcrop within the Athos-Volvi Suture Zone and Kerdilion unit (Figure 2.1; Himmerkus et al., 2011). These granitic intrusions exhibit a weak tectonic fabric suggesting emplacement at the waning stages of regional Alpine deformation. Crystallization ages range from 66.8 ± 0.8 Ma and 68 ± 1 Ma for an unnamed intrusion outcropping near the Ouranoupolis granite (Himmerkus et al., 2011) to 53 ± 4 Ma for the Ierissos granite (Frei, 1992, 1996). The latter is similar in age to the Sithonia granite to the south (Christofides et al., 1990). Biotite and muscovite $^{40}Ar/^{39}Ar$ cooling ages from the Ouranoupolis granite are 47 ± 0.7 Ma and 44 ± 1.1 Ma, respectively (De Wet et al., 1989). These ages are consistent with the biotite K-Ar cooling age from the Grigoriou granite of 43 ± 1 Ma (Bébien et al.,

2001). Late Oligocene and early Miocene intrusions outcrop along a northeast-trending belt within the Kerdilion unit and are discussed in detail in subsequent sections.

Structure

The Kerdilion unit of the southern Rhodope core complex displays a regionally consistent flat-lying ductile fabric with a uniform top-to-the southwest sense of shear and northeast-southwest stretching lineations (Eliopoulos and Kilias, 2011). The Kerdilion unit within the Kassandra Mining District similarly exhibits a penetrative shallow dipping S_1 foliation defined by alignment of peak metamorphic minerals (e.g., feldspar and amphibole). A subsequent or co-tectonic high-strain event resulted in tight to isoclinal F_2 folds locally accompanied by subparallel axial planar S_2 cleavage. An ensuing lower-strain deformation event superimposed a spaced and associated steeply dipping S_3 foliation warping previously developed fabrics. This event is associated with kilometer-scale upright and open east-plunging F_3 folds evident as district-scale antiforms in the footwall of the Stratoni and Gomati faults, respectively (Figure 2.2). Both folds mimic the arcuate contact of the Stratoni fault and Athos-Volvi Suture Zone suggesting a geodynamic relationship.

Early movement on the Stratoni fault may have included top-to-the north ductile thrust faulting during compressional tectonism at lower amphibolite metamorphic conditions (Haines, 1998). District-scale F_3 fold kinematics are consistent with this interpretation. The transition from compression to extensional tectonics, probably in the early Oligocene, resulted in southwest-dipping mylonitic ductile shear zones superimposed on the previous thrust fabrics (Haines, 1998). Subsequent late Oligocene semi-brittle deformation consists of cataclastic textures with development of internal foliation and pressure solution fabrics which are overprinted by younger phases of brittle fault gouge (Siron et al., 2014). Sulfide minerals intergrown with and overprinting the tectonic fabric support syn-mineral deformation. Steeply-dipping north-northeast-trending strike-slip faults are kinematically compatible with extension on the Stratoni fault. The Stratoni fault and the massive sulfide orebody at Madem Lakkos, however, are

displaced by the northeast-trending strike-slip fault at Vathilakkos (Figure 2.2; Kalogeropoulos et al., 1991; Nebel et al., 1991; Gilg and Frei, 1994; Haines, 1998) suggesting that movement on these structures persisted after major movement on the Stratoni fault and formation of replacement ore bodies. The Stratoni fault was reactivated in the Neogene by predominately north-south extensional tectonics, which is presently active in the Aegean region (Pavlides and Tranos, 1991; Jolivet et al., 2013).

Ore Deposit Geology

Ore deposits of the Kassandra Mining District belong to the northwest-trending Serbo-Macedonian Metallogenic Province within the intrusive belt of the Lece-Chalkidiki metallogenic zone (Figure 2.1; Janković, 1997; Serafimovski, 2000) that is dominantly associated with Oligo-Miocene magmatism (Heinrich and Neubauer, 2002). Historic and producing economic deposits include the Trepča skarn district of eastern Kosovo (Strmić-Palinkaš et al., 2013) and the Kiseljak Au-Cu porphyry and polymetallic Au-Ag-Pb-Zn vein system of the Serbian Lece Magmatic Complex (Dragić et al., 2014). Pipe-like Au-Cu porphyry deposits occur in the southeastern Republic of Macedonia at the Buchim-Damjan-Borov Dol district and at Llovica (Serafimovski et al., 2010; Barcikowski et al., 2012; Stefanova et al., 2012). Sub-economic porphyry Cu and skarn prospects also occur in the Vathi area of northern Greece (Kockel et al., 1975; Frei, 1992), to the northwest of the economic Au-Cu porphyry and polymetallic Au-Ag-Pb-Zn-Cu carbonate-replacement deposits within the Kassandra Mining District.

Kassandra ore deposits

Olympias: The Olympias deposit was originally described by Neubauer (1957) and Nicolaou (1964), with more recent detailed studies by Kalogeropoulos et al. (1989b) and Kilias et al. (1996). Re-evaluation of the deposit-scale geologic framework has been performed by Eldorado Gold Corporation through extensive drilling and relogging campaigns. The carbonate replacement massive sulfide deposit at Olympias is hosted by a sequence of quartzo-feldspathic biotite gneiss interlayered with graphitic marble

and amphibolite, bounded to the east by a massive body of megacrystic plagioclase-microcline orthogneiss. Contacts between marble and quartzo-feldspathic biotite gneiss are sharp and conformable. The orebody is localized in a structurally complex zone where marble is deformed by ductile and brittle structures. The regional S_1 fabric of the metamorphic sequence in the deposit area strikes to the northwest and dips steeply northeast, and is locally reworked by isoclinal F_2 folds. A distinct L_2 lineation formed by the intersection of S_1 foliation and S_2 axial planar cleavage is evident within marbles north of the deposit. The metamorphic sequence is disrupted by the northwest-trending ductile to semi-brittle Kassandra fault and the north-trending East fault (D. Rhys, pers. commun., 2014). Both faults exhibit a similar geometry with apparent normal relative displacement of hangingwall down to the northeast. Marbles that are structurally bound by the Kassandra and East faults host massive sulfide mineralization. A shallow southeast plunge of pre-mineral F_2 folds and L_2 intersection lineation is coincident with the plunge of the Olympias orebody, suggesting that preexisting structures influenced mineralization. The Olympias deposit has a defined down plunge extent of 1500 m to a depth of approximately 790 m below sea level.

The massive sulfide orebody at Olympias displays a complex sulfide mineral assemblage varying from galena-sphalerite-dominant massive sulfide, to pyrite-rich massive sulfide with traces of arsenopyrite and chalcopyrite. Locally, Zn-Pb-rich sulfide transitions to Au-rich arsenopyrite-bearing massive sulfide, which grades into arsenopyrite- and boulangerite-bearing siliceous breccias. Quartz-rhodochrosite veins containing variable amounts of arsenopyrite and boulangerite occur, particularly in the eastern part of the deposit. Sulfide bodies exhibit coarse- and fine-grained massive and banded textures that cut and replace marble, and are largely discordant to foliation. Locally, however, sulfide banding is concordant with foliation and mimics folded marble layers (Kalogeropoulos et al., 1989b). The latter textures have been interpreted as indicating a pre-deformation timing, but replacement textures cutting foliation are far more common. Well preserved rod textures in pyrite, interpreted to be after marcasite, with a sphalerite-rich matrix (Figure 2.3A) are common and are observed in other carbonate-replacement deposits (e.g., Leadville, Colorado; Thompson and Arehart, 1990). Sulfide minerals are

largely undeformed with some zones showing variable degrees of strain (Kalogeropoulos et al., 1989b). Hahn et al. (2012) constrained the timing of mineralization at Olympias to the Oligo-Miocene based on an arsenopyrite Re-Os age of 26.1 ± 5.3 Ma. This age, along with textural evidence, is consistent with the formation of massive sulfide that post-dates major regional Alpine deformation and is likely related to Oligo-Miocene metallogenesis.

Madem Lakkos: The geology of the Madem Lakkos orebody was originally described by Neubauer (1957) and Nicolaou (1964, 1969). The most recent detailed studies were undertaken by Nebel (1989), Nebel et al. (1991), Gilg (1993), Gilg and Frei (1994), and Haines (1998), and the following description of the Madem Lakkos area is largely taken from these studies. The Madem Lakkos carbonate-hosted deposit occurs in a major strand of the Stratoni fault within a complexly folded and faulted sequence of amphibolite, marble, and lesser hornblende-bearing quartzo-feldspathic biotite gneiss and fine-grained to aplitic granite gneiss. Contacts between units are commonly sheared within the Stratoni fault zone. The S_1 foliation strikes west-northwest and dips moderately to the southwest in the footwall and north-northwest in the hangingwall. Orebodies are hosted in marble, granite gneiss, and aplite. Mineralization is controlled by faults and hinge zones of shallow east-plunging parasitic F_3 folds. The nearby Stratoni stock is displaced by the west-northwest-trending Stratoni fault, and is variably affected by fault-controlled hydrothermal alteration and base metal sulfide-bearing veins. The northeast-trending Vathilakkos fault overprints mineralized strands of the Stratoni fault and massive sulfide bodies at depth (Haines, 1998).

Two stages of sulfide mineralization are recognized at Madem Lakkos. Early replacement-style massive sulfide has sharp and discordant contacts with host rocks and consists dominantly of galena and sphalerite with lesser pyrite, subordinate chalcopyrite, arsenopyrite, tennantite, tetrahedrite, and rare native gold (Gilg, 1993). Evidence based on deformation textures in sulfide minerals from foliation-parallel and folded sulfide lenses was used to infer a pre-deformation syn-sedimentary (syngenetic) origin for mineralization (Nebel et al., 1991). This conclusion has been refuted by Gilg et al. (1992) based on

evidence for replacement textures and crosscutting relationships with respect to tectonic fabric. Moreover, stable and radiogenic isotopes and fluid inclusion data have been used to argue for an epigenetic, post-deformation, replacement origin (Gilg et al., 1992; Gilg, 1993). Nebel et al. (1991) and Gilg (1993)

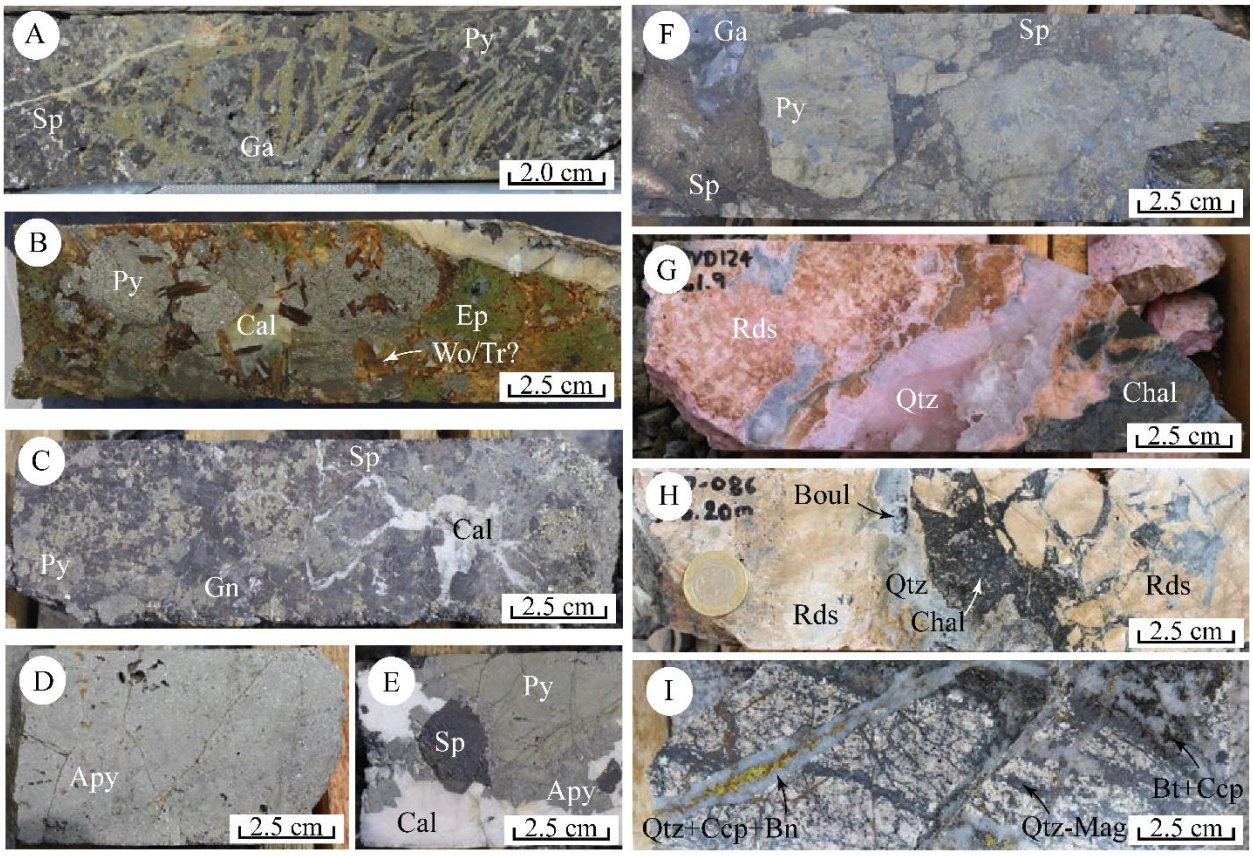

Figure 2.3. Representative mineralization styles from drill core in the Kassandra Mining District: (A) massive sulfide from the Olympias deposit displaying bladed pyrite rod textures with sphalerite and galena matrix; (B) skarn mineralization consisting of pyrite with an intergrown calcite and calc-silicate mineral assemblage of epidote-wollastonite-tremolite from the easternmost drilling at the Madem Lakkos deposit; (C) coarse-grained sphalerite-galena-pyrite massive sulfide with minor calcite gangue from the Mavres Petres deposit; (D) fine-grained arsenopyrite-rich massive sulfide from the westernmost drilling of the Mavres Petres orebody; (E) coarse-grained pyrite-arsenopyrite-sphalerite semi-massive sulfide with calcite gangue from Mavres Petres; (F) massive sulfide breccia from the Piavitsa prospect consisting of pyritic clasts surrounded and overprinted by galena- and sphalerite-rich sulfide mineralization; (G-H) Au-rich crustiform chalcedony-quartz-rhodochrosite vein and vein breccia containing vug-filling and disseminated needle-form boulangerite from the Piavitsa prospect; (I) typical early quartz-magnetite veins cut by main-stage quartz-magnetite-biotite-chalcopyrite ± bornite veins within the intra-mineral porphyry at Skouries. Abbreviations are as follows: arsenopyrite (Apy), biotite (Bt), boulangerite (Boul), calcite (Cal), chalcedony (Chal), chalcopyrite (Ccp), epidote (Ep), galena (Ga), magnetite (Mag), pyrite (Py), quartz (Qtz), rhodochrosite (Rds), sphalerite (Sp), tremolite (Tr), wollastonite (Wo).

describe a second overprinting and volumetrically dominant pyrite-rich disseminated sulfide event that forms the matrix to breccias, and infills or surrounds previous base metal-rich massive sulfide mineralization. The absolute timing of this event is poorly constrained. The sulfide mineral assemblage consists of coarse-grained sphalerite and galena, with lesser chalcopyrite, arsenopyrite, tennantite, tetrahedrite, boulangerite, and a variety of other sulfosalt minerals (Gilg, 1993). Based on K-Ar illite ages, Gilg and Frei (1994) tentatively proposed a late Oligocene age for hydrothermal alteration and mineralization at Madem Lakkos.

East of Madem Lakkos, chalcopyrite-pyrite mineralization is associated with calc-silicate Cu-skarn near the contact with the Stratoni stock and associated northeast-trending quartz-feldspar porphyry dikes (Gilg, 1993). A prograde mineral assemblage consisting of andradite garnet and diopside with variable anhydrite, epidote, and magnetite is overprinted by a retrograde hydrous mineral assemblage, including iron-rich chlorite after garnet and actinolite ± chlorite after pyroxene and epidote (Gilg, 1993). Chalcopyrite is associated with retrograde alteration accompanied by pyrite, calcite, quartz, epidote, and scheelite (Figure 2.3B; Gilg, 1993).

Mavres Petres: The marble-hosted deposit at Mavres Petres occurs 1-2 km west of Madem Lakkos within the Stratoni fault zone. The orebody occurs over a strike length ~1 km with a south-southwest plunging depth extent (defined orebody limit) of about 700 m. The lithologic sequence and S_1 foliation strikes west-northwest subparallel to the Stratoni fault, and becomes northwest-trending to the north in the footwall of the Stratoni fault. The host lithologies are similar to Madem Lakkos with the exception of a thick granite gneiss body that occurs intercalated with marble in the footwall.

A siliceous Mn-oxide gossan forms the surface expression at Mavres Petres and Piavitsa (Gilg, 1993; Arvanitidis and Constantinides, 1994). The orebody at Mavres Petres consists of banded coarse-grained pyrite-sphalerite-galena (Figure 2.3C) with minor accessory stibnite and arsenopyrite overprinted by arsenopyrite-bearing siliceous breccias. In the western part of the orebody, the sulfide mineral assemblage becomes pyrite-sphalerite-dominant, although locally including massive arsenopyrite

intervals (Figure 2.3D-E). Boulangerite occurs as an accessory sulfide mineral interstitial to siliceous breccias, and within quartz-rhodochrosite veins. The partial to complete replacement of fault-bounded marble blocks is evident underground and in drill core from Mavres Petres, documenting the replacement origin of this orebody.

Piavitsa: The Stratoni fault zone becomes concealed west of Mavres Petres, and appears to jog southward along the contact of granite gneiss with graphite-bearing carbonaceous-biotite schists and marbles (Figure 2.2). Drilling at the Piavitsa prospect intersected discontinuous semi-massive to massive sulfide lenses, which have undergone syn-mineral brecciation (Figure 2.3F), and prominent siliceous-rhodochrosite ± rhodonite bodies and veins that partially replace and crosscut the host marble (Arvanitidis and Constantinides, 1994). Well preserved, undeformed Au-bearing rhodochrosite veins display crustiform banded textures (Figure 2.3G) with clear crystalline to black chalcedonic silica intergrown with bladed boulangerite, which also occurs as delicate fibrous mats infilling cavities. Mosaic breccia textures with angular fragments of rhodochrosite set in a black chalcedonic silica matrix (Figure 2.3H) are interpreted to have formed by hydrothermal brecciation during the later stages of the mineralizing event. Vein and breccia textures are typical of epithermal environments and suggest a relatively shallow, low temperature setting for Piavitsa compared to carbonate replacement and skarn mineralization to the east.

Skouries: The Skouries Au-Cu porphyry deposit was originally described by Zachu (1963) with subsequent detailed studies by Eliopoulos and Economou-Eliopoulos (1991), Frei (1992, 1995), Tobey et al. (1998), Kroll et al. (2002), and Hahn et al. (2012). The following descriptions are based on work by the authors, which are largely in agreement with observations from previous studies. The Skouries porphyry exhibits four stages of veining and associated alteration. A $^{40}Ar/^{39}Ar$ hydrothermal biotite age of 19.9 ± 0.9 Ma (Hahn et al., 2012) is interpreted as the timing of potassic alteration and mineralization, and is within error of the U-Pb age of the porphyry (20.56 ± 0.48 Ma; Hahn et al., 2012). Stockwork to sheeted quartz-magnetite and magnetite stringer veins and disseminated magnetite alteration locally obliterate the earliest porphyry phase. The majority of the Au-Cu mineralization is interpreted to have

been introduced with an intra-mineral porphyry phase (see Igneous Petrography section below) that hosts quartz-magnetite-chalcopyrite veins, and a potassic alteration mineral assemblage consisting of K-feldspar, biotite, and magnetite. A later set of quartz-biotite-chalcopyrite-bornite ± magnetite veins occurs as sheeted to wispy veins and veinlets in the upper parts of the deposit. At depth, these veins become thick (up to 3 cm wide) and sulfide-rich, dominated by chalcopyrite ± bornite with envelopes of coarse-grained biotite aggregates (Figure 2.3I). This stage of mineralization locally crosscuts or replaces magnetite-bearing veins and disseminated magnetite associated with earlier stages of veining and alteration (D. Rhys, pers. commun., 2014). Platinum and palladium exists within telluride minerals contained in chalcopyrite and as grains within quartz-chalcopyrite ± bornite veins associated with the intra-mineral porphyry (Eliopoulos et al., 2014; McFall et al., 2016). Gold occurs as inclusions of native metal or electrum in chalcopyrite (Eliopoulos and Economou-Eliopoulos, 1991) or as gold-silver tellurides (McFall et al., 2016).

Post-mineral pyrite-carbonate veins with sericite-carbonate-clay alteration overprint earlier mineralization within the stock and adjacent wallrock. An alteration aureole of quartz, calcite, sericite, and pyrite associated with base metal veins has been mapped up to 600 m from the intrusive center, consistent with observations of Tobey et al. (1998). Within 400 m of the porphyry stock, late-distal sericite-pyrite alteration transitions into an early-stage, and proximal calc-potassic alteration mineral assemblage consisting of amphibole-biotite-magnetite (Tobey et al., 1998; Kroll et al., 2002). Calc-potassic alteration within the schists is overprinted by K-feldspar associated with main-stage chalcopyrite-bearing veins and disseminated chalcopyrite replacing early magnetite. Supergene enrichment is restricted to a 30–40 m-thick zone close to surface consisting of secondary chalcocite and covellite (Tobey et al., 1998).

Igneous Petrology

Previous petrographic studies have been undertaken in the district. The intrusive stock at Stratoni has been previously described by Nikolaou (1960), Tompouloglou (1981), and Kalogeropoulos et al. (1989a, 1990). Frei (1992) further described the Tsikara, Fisoka, and Stratoni stocks and briefly discussed the Aspro Lakkos porphyry intrusion. The Skouries porphyry is described in detail by Frei (1992, 1995), Tobey et al. (1998), and Kroll et al. (2002). The descriptions presented here, while building upon previous studies, are based on field relationships and petrography from 65 thin sections.

Tsikara

The composite monzogabbro–granodiorite intrusion at Tsikara, located south of Stratoni and southeast of Skouries (Figure 2.2), is the southernmost and largest post-deformation intrusion within the district, measuring 4.5 km^2 in area. The Tsikara stock intrudes the quartzo-feldspathic biotite gneisses and schists of the Kerdilion unit and occurs within the south-dipping limb of a major F_3 antiform in the footwall of the Gomati fault. Isolated satellite intrusions occur to the north of the main stock and extend south of the Gomati fault within the tectonic mélange of the Athos-Volvi Suture Zone (Himmerkus et al., 2011). Igneous contacts are sharp, discordant to foliation, and are locally associated with breccias on the western and southwestern margins of the stock. A magnetite-bearing hornfels aureole is variably developed in the metamorphic wallrock. The main stock contains locally abundant sub-angular xenoliths of gneiss and schist, and less abundant cognate igneous clasts (Figure 2.4A).

The main stock consists of fine-grained equigranular monzogabbro to monzodiorite and diorite phases, crosscut by a granodioritic micro-porphyritic phase in the west-central and eastern parts of the Tsikara intrusive complex. The mafic phases have sharp but irregular contacts with the wallrock. The mineralogy of the mafic phases consists of equigranular plagioclase, clinopyroxene, biotite with subordinate microcline, quartz and accessory zircon, apatite, magnetite and ilmenite, and minor pyrite in the groundmass. Chlorite and rare epidote partially replace biotite and clinopyroxene, and plagioclase is

selectively replaced by sericite. The crosscutting micro-porphyry phase (Figure 2.4B) contains relict blocky feldspar phenocrysts which are completely replaced by sericite and set within a fine-grained quartz-sericite-altered groundmass. Unidirectional solidification textures and miarolitic cavities are present within this unit.

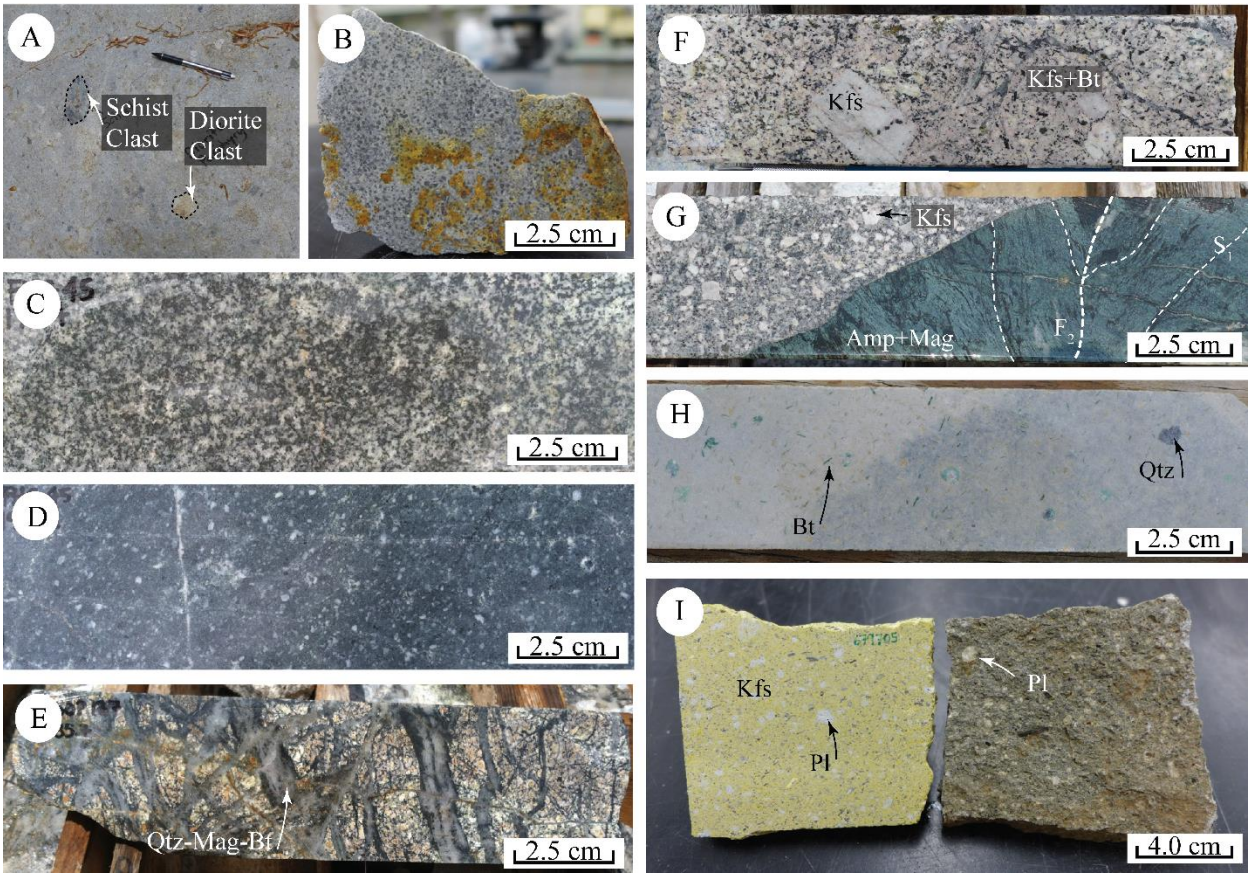

Figure 2.4. Representative surface and drill core examples of Oligo-Miocene intrusive rocks from the Kassandra Mining District: (A) monzodiorite at Tsikara with xenoliths of metamorphic wallrock and cognate diorite clast, pencil for scale; (B) micro-porphyritic granodiorite from Tsikara; (C-D) typical late Oligocene granodiorite and monzodiorite from drill core at Fisoka, respectively; (E) Skouries pre-mineral quartz-monzonite porphyry with characteristic dense network of quartz-magnetite veins; (F) intra-mineral megacrystic K-feldspar quartz-monzonite porphyry at Skouries displaying strong potassic alteration; (G) late-mineral quartz-monzonite porphyry crosscutting folded and amphibole-magnetite-altered gneiss; (H) altered example of the glomerophyric porphyry dike from the Madem Lakkos deposit; (I) black-matrix porphyry dike from the Vathilakkos fault stained with Na-cobaltinitrite to highlight K-feldspar (left) and unstained (right). Abbreviations are as follows: amphibole (Amp), biotite (Bt), K-feldspar (Kfs), magnetite (mag), plagioclase (Pl), quartz (Qtz).

Fisoka

The Fisoka stock belongs to a cluster of igneous intrusions that outcrop in the hangingwall of the Stratoni fault, northeast of Tsikara and southwest of Stratoni (Figure 2.2; Kockel et al., 1975; Tompouloglou, 1981). Each intrusive body is less than 0.2 km^2 in surface area, but the individual pipe-like intrusions may connect at depth. The Fisoka stock is poorly exposed and strongly weathered at surface with limited drilling (7 holes) extending below the weathered zone. The Fisoka intrusions are hosted within variably carbonaceous quartz-biotite gneiss of the Kerdilion unit and interlayered amphibolite. Igneous contacts are largely discordant to metamorphic foliation. Porphyritic phases contain miarolitic cavities similar to those observed in the micro-porphyritic phase at Tsikara.

Porphyritic stocks and dikes commonly have clast-supported brecciated contacts with wallrock. Breccias are composed of angular gneiss clasts with increasing porphyry clast content adjacent to the coherent porphyry body, and limited matrix consisting of quartz-sericite and pyrite (largely replaced by goethite at surface). Widespread quartz-sericite-pyrite alteration is developed within the metamorphic wallrock, associated with stockwork to sheeted quartz-pyrite veins. Historic drilling for supergene Cu mineralization intersected pervasively bleached porphyry with minor vein and disseminated chalcopyrite and localized secondary chalcocite enrichment at the base of the weathered zone (Kockel et al., 1975).

A swarm of quartz-plagioclase feldspar porphyry dikes exposed between the Fisoka and Stratoni stocks intrude amphibolite in the hangingwall of the Stratoni fault. Contacts are commonly highly brecciated and consist of polymict clast-supported angular blocks of extremely altered metamorphic wallrock (amphibolite with lesser granitic gneiss) and porphyry in an altered matrix. The spatial association of breccias with dikes and extensive alteration suggest a magmatic-hydrothermal or possibly phreatomagmatic origin for the breccias.

The individual Fisoka intrusions are composed of fine- to medium-grained equigranular diorite and granodiorite (Figure 2.4C-D) with porphyritic phases to the north. The phenocryst mineralogy consists of K-feldspar, plagioclase, biotite, and clinopyroxene with accessory apatite, titanite, zircon,

magnetite, and minor pyrite and subordinate chalcopyrite. Porphyry intrusions are dominated by a crowded interlocking texture consisting of plagioclase ± K-feldspar phenocrysts in a quartz-feldspar-rich groundmass. Chlorite, epidote, titanite and calcite commonly replace primary biotite and clinopyroxene. Drill core from the Fisoka area reveals an alteration mineral assemblage consisting of sparse to abundant magnetite stringer veinlets associated with aggregates of magnetite and biotite and patchy K-feldspar. The mineralogy and textures are consistent with selective potassic alteration related to a poorly developed porphyry system with minor disseminated chalcopyrite mineralization.

Granodioritic quartz-eye plagioclase feldspar porphyry dikes north of Fisoka are fine-grained and consist of plagioclase phenocrysts and rounded quartz phenocrysts displaying resorbed textures. Hydrothermal alteration has resulted in partial replacement of plagioclase phenocrysts and the groundmass by quartz-sericite-pyrite. Clay alteration in surface outcrops may reflect weathering.

Stratoni

The Stratoni stock is a northeast-elongated intrusion located north of the village of Stratoni at the eastern end of the Stratoni fault (Figure 2.2). The stock has an exposed outcrop area of 1.5 km^2 consisting primarily of granodiorite, with a minor porphyritic phase exposed at the topographically highest part of the stock in the Aspro Chomata prospect area (Gilg and Frei, 1994). The Stratoni stock is hosted by a sequence of quartzo-feldspathic biotite gneisses, amphibolites, and marbles of the Kerdilion unit on the south-dipping limb of a major F_3 antiform within the footwall of the Stratoni fault (Figure 2.2). Intrusive contacts are sharp and discordant to metamorphic foliation. Narrow zones of calc-silicate exoskarn locally occur on the western contact of the intrusion within the gneisses. Quartz-sericite-pyrite alteration with pyrite and galena veins occur in the southern half of the stock in proximity to the Stratoni fault. The porphyritic phase of the Stratoni stock exposed at the Aspro Chomata prospect exhibits intense clay-rich alteration related to a dense orthogonal network of quartz-pyrite ± galena veins. Minor secondary malachite staining is present locally on weathered surfaces.

The Stratoni stock is a fine- to medium-grained, equigranular to weakly porphyritic granodiorite with minor diorite phases. Phenocrysts consist of K-feldspar, plagioclase, biotite, and lesser clinopyroxene in a quartz-feldspar groundmass, with accessory apatite, titanite, zircon, magnetite, minor pyrite and rare chalcopyrite. A pale green color is imparted by chlorite, epidote, titanite and calcite alteration of primary clinopyroxene and biotite. Feldspars are variably replaced by sericite.

Skouries

The Skouries Au-Cu porphyry, located 6 km south of the Stratoni fault and approximately 1 km to the north of the Gomati fault, is hosted in quartzo-feldspathic biotite gneisses and schists interpreted to be part of the Kerdilion unit. The stock is a pencil-shaped intrusion consisting of multiple quartz monzonite porphyry phases that intrude the south-dipping axis of a regional F_3 antiform (Figure 2.2). Outcrop and drill holes define a 200 m-diameter steeply south-plunging intrusive body exceeding 900 m in depth, with porphyry dikes radiating outward from the intrusive center. Intrusive contacts are sharp and discordant to metamorphic foliation and are locally brecciated. Polymict breccias occur in association with syn- to late-mineral intrusive phases. These breccias contain altered angular fragments of wallrock and porphyry clasts in a fine-grained dark gray fragmented matrix possibly suggesting magmatic-hydrothermal or phreatic origins.

This study has identified at least four porphyritic intrusive phases at Skouries (Figure 2.5). The interpreted timing and classification of the intrusive units differ slightly from that proposed by Kroll et al. (2002). The earliest phase, defined by crosscutting relationships, is a dark-gray feldspar porphyry which hosts an early set of densely sheeted and stockwork quartz-magnetite veins that partially destroy the original igneous textures (Figure 2.4E). K-feldspar and plagioclase phenocrysts are set in a fine-grained matrix of K-feldspar, quartz, and primary biotite with accessory titanite and zircon. Phenocrysts and groundmass are extensively overprinted by secondary quartz with abundant disseminated fine-grained magnetite ± biotite.

Figure 2.5. Graphic log of a segment of Skouries drill core (SOP137) showing the spatial relationship between porphyry phases. Alteration is represented by a bar plot showing the relative abundance of K-feldspar + biotite (K-silicate) and magnetite (Mag). Thickness of bar indicates increased intensity of respective alteration. The relative density of veins is shown graphically, where black lines reflect magnetite and quartz ± magnetite veins and red lines reflect quartz-and sulfide-rich veins that contain chalcopyrite ± bornite. Representative photographs of quartz monzonite porphyry phases that comprise the Skouries stock: A) typical examples of megacrystic intra-mineral porphyry phase crosscut by quartz-magnetite veins and younger sulfide-rich chalcopyrite veins; B) representative example of the early porphyry phase. Note the original texture is largely obliterated by pervasive quartz-magnetite alteration and veining; C) intra-mineral porphyry containing late fine-grained and potassically-altered intrusive phase.

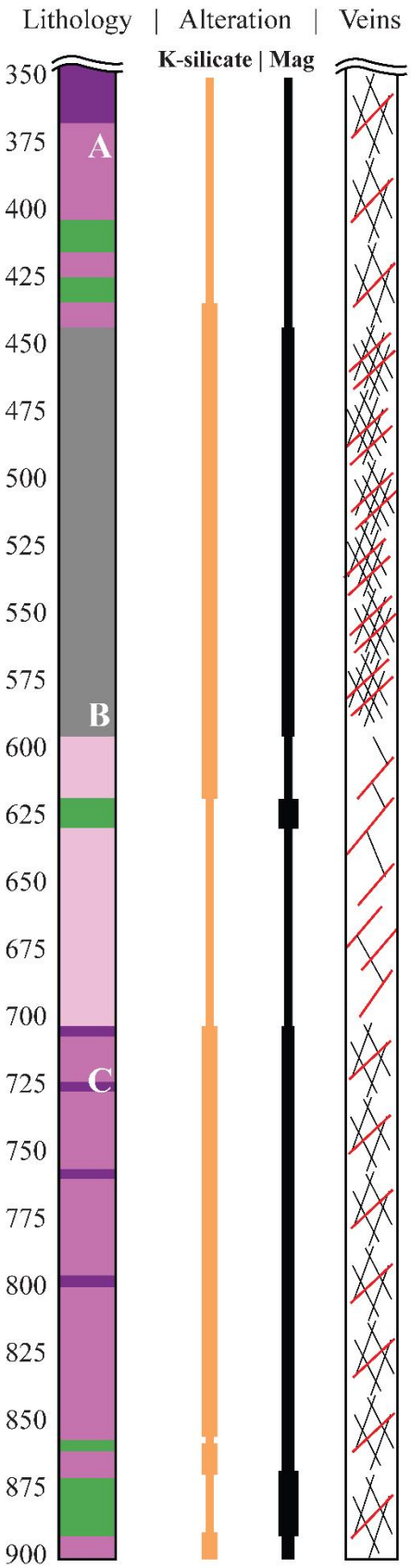

Legend Skouries drill core SOP-137

- Gneiss-schist, pervasive actinolite-magnetite-K-feldspar (calc-potassic) alteration
- Early dark-gray K-feldspar porphyry, stockwork to sheeted quartz and quartz-magnetite, crosscut by younger chalcopyrite-bearing veins
- Intra-mineral megacrystic K-feldspar porphyry, crosscuts earlier porphyry phase; pervasive and intense K-feldspar-biotite-magnetite (potassic) alteration; sheeted quartz-chalcopyrite ± bornite veins
- Fine-grained dark to pinkish-gray K-feldspar porphyry, occurs as phase within intra-mineral porphyry
- K-feldspar porphyry, very similar to the intra-mineral porphyry but lacks megacrysts, exhibits less veins, and has weaker K-feldspar-biotite-magnetite alteration; possibly a younger porphyry phase

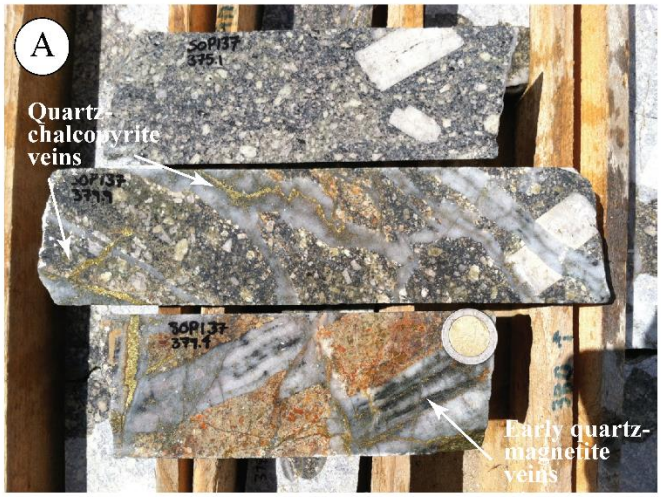

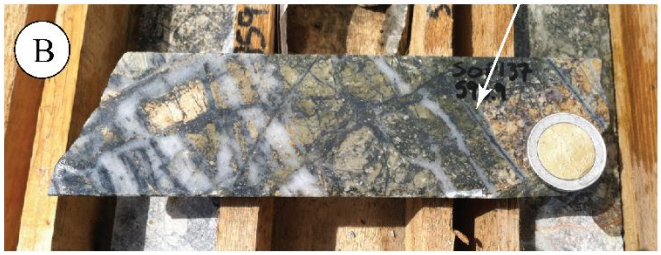

Au-Cu mineralization is spatially and temporally related to an “intra-mineral” K-feldspar porphyry corresponding to the pink or main porphyry phase of Kroll et al. (2002). This intrusive phase exhibits a distinct pink coloration imparted by pervasive K-feldspar alteration. The phenocryst mineral assemblage consists of plagioclase and megacrystic K-feldspar with grains reaching up to 3 cm in length (Figure 2.4F). Phenocrysts are set in a groundmass dominated by K-feldspar, quartz, amphibole, and accessory titanite and zircon. A finer-grained variety of dark pinkish-gray porphyry crosscuts the earlier intra-mineral porphyry defined here, and may correlate to the intra-mineral phase of Kroll et al. (2002). This intrusive phase contains K-feldspar and plagioclase phenocrysts with fine-grained disseminated biotite in a K-feldspar-quartz dominated groundmass, with apatite micro-phenocrysts, titanite, and zircon occurring as accessory minerals. Both porphyry phases are altered by secondary K-feldspar, quartz, fine-grained biotite, and magnetite with associated disseminated chalcopyrite and bornite.

A final post-mineral porphyry phase (Figure 2.4G) crosscuts all earlier intrusive phases and associated alteration and mineralized vein sets. The primary mineralogy of this phase is similar to the intra-mineral porphyry, but veining, potassic alteration, and mineralization are weak to absent. Megacrystic K-feldspar and plagioclase phenocrysts occur in a fine-grained groundmass of K-feldspar, plagioclase, and quartz with accessory titanite, apatite, and magnetite. Pyrite is the dominant sulfide with trace chalcopyrite. Feldspar phenocrysts and groundmass are commonly clouded, with a pale green color imparted by weak but pervasive quartz-sericite-carbonate-pyrite alteration.

Aspro Lakkos

A megacrystic K-feldspar porphyry intrusion outcrops at Aspro Lakkos approximately 1 km northeast of Skouries. Aspro Lakkos is a sill-like body that intrudes the northeast limb of a major F_3 antiform subparallel to foliation (Figure 2.2). Discordant contacts are generally brecciated containing a polymictic suite of angular to sub-angular clasts of sericite-altered schist and porphyry fragments in a fine-grained sericite-altered igneous matrix, suggesting a possible magmatic-hydrothermal origin. Rare

and discrete clast-supported breccia dikes crosscut the Aspro Lakkos body. These breccias are composed of angular to rounded wallrock fragments and porphyry clasts, some of which exhibit irregular shapes, contained in a fine-grained milled schistose matrix, suggesting phreatic brecciation. A weak pervasive sericite overprint with localized zones of strong quartz-sericite-pyrite alteration are common. Porphyry dikes of similar texture and composition are observed splaying from the main body in a northwest-southeast direction along foliation. A late set of fine-grained black-matrix porphyry dikes crosscut the main megacrystic porphyry body in a northwest orientation, also parallel to the regional structural fabric.

The main Aspro Lakkos porphyry is texturally similar to the late porphyry phase at Skouries, with prismatic plagioclase and megacrystic K-feldspar phenocrysts (upwards of 3 cm in length) occurring with fine-grained euhedral biotite books, quartz, and lesser apatite micro-phenocrysts. K-feldspar and quartz comprise the groundmass with accessory zircon, magnetite, and subordinate pyrite. Quartz phenocrysts are generally sub-rounded, and occasionally display irregular embayment textures. Some quartz and carbonate grains display undulose textures suggesting a possible metamorphic xenocrystic origin. Secondary carbonate, sericite, and pyrite variably replace feldspars, biotite and groundmass.

Black-matrix Porphyry Dikes

Porphyritic dikes displaying prominent trachytic (or microlitic) texture were originally described as andesitic-dacites by Neubauer (1957) and reclassified as lamprophyres by Nicolaou (1960) and Kalogeropoulos et al. (1991). Nebel et al. (1991) described andesite and rhyodacite dikes with resorbed quartz phenocrysts at Madem Lakkos. This study documents two sets of porphyritic dikes defined by the presence or absence of a distinct glomero porphyritic (glomerophyric) texture.

Glomerophyric dikes: Glomerophyric dikes outcrop within the Stratoni fault corridor, intercepted in drill core at Piavitsa, and are present underground at Madem Lakkos (Nebel et al., 1991; Haines, 1998) and Olympias (Kalogeropoulos et al., 1989b). They typically range from 1–2 meters in width, trend north-northeast, and have sharp contacts that are discordant to metamorphic foliation. Contacts are commonly

unbrecciated. Dikes display variable degrees of quartz-sericite-carbonate-pyrite alteration or can be unaltered. These dikes contain aggregates of quartz and less commonly K-feldspar phenocrysts (Figure 2.4H). Abundant needle-shape phlogopitic biotite defines a flow banded texture. Accessory euhedral apatite micro-phenocrysts are common. Unaltered groundmass is typically dark gray, consisting of fine-grained quartz and K-feldspar. Quartz phenocrysts are typically rounded, commonly showing corroded, resorbed rims or embayment textures enveloped by fine-grained secondary sericite-carbonate-clay alteration. Chlorite replaces biotite, and sericite-carbonate partially replace the groundmass and feldspar phenocrysts. Most dikes contain disseminated magnetite and trace pyrite, and pyrite content increases systematically with the intensity of quartz-sericite-carbonate alteration. While these biotite-quartz-feldspar porphyry dikes have been previously classified as calc-alkaline lamprophyre minettes by Kalogeropoulos et al. (1991), their felsic phenocryst mineralogy precludes the lamprophyre classification (e.g., Rock, 1991).

Non-glomerophyric dikes: Black-matrix porphyry dikes in the Aspro Lakkos area contain fine-grained K-feldspar and plagioclase phenocrysts, euhedral biotite books and accessory apatite micro-phenocrysts in a dark, near-aphanitic K-feldspar-rich groundmass. Inclusions of rounded to irregularly-shaped fragments of highly strained quartz and carbonate are common, probably representing deformed metamorphic wallrock fragments. Disseminated magnetite occurs in the groundmass along with fine-grained pyrite associated with weak pervasive sericite-carbonate alteration. A black-matrix porphyry dike intrudes the Vathilakkos fault (Figure 2.4I) near Madem Lakkos (Figure 2.2). A prominent flow texture is defined by the alignment of evenly distributed and abundant hornblende and biotite phenocrysts with lesser K-feldspar, plagioclase, quartz and sparse clinopyroxene in a fine-grained dark gray K-feldspar-rich groundmass. Rare and widely dispersed K-feldspar megacrysts are evident. Accessory minerals include apatite micro-phenocrysts, zircon, and titanite. Disseminated magnetite and rare chalcopyrite occur in the groundmass. Minor sericite-carbonate-clay alteration preferentially replaces clinopyroxene and the rims of plagioclase and K-feldspar phenocrysts.

Zircon U-Pb Geochronology

Previously published geochronology within the district was based on the K-Ar dating (Papadakis, 1971; Burgarth et al., 1980; Tompouloglou, 1981) with limited zircon U-Pb ages collected from the Tsikara composite stock, Stratoni stock, and Skouries porphyry (Frei, 1992; Gilg and Frei, 1994; Hahn et al., 2012). Here we present 13 new zircon U-Pb ages of igneous intrusions from the Kassandra mining district. The data are consistent with major magmatic events in the late Oligocene and early Miocene as suggested by previous authors (Figure 2.6).

Tsikara Composite Stock

Three different intrusive phases compose the Tsikara composite stock, and are interpreted, on the basis of geologic mapping and geochemistry, to be part of the same intrusive event. Three samples were collected from each phase to test this hypothesis.

593870: Eighteen zircon grains were analyzed from an unaltered dark clinopyroxene-bearing diorite from the northern half of the composite stock. All analyses fall on or near Concordia with one grain giving a slightly younger age interpreted to be the result of post-crystallization Pb-loss (Figure 2.7A). The remaining 17 analyses yielded a calculated weighted average $^{206}Pb/^{238}U$ age of 27.00 ± 0.19 Ma (Figure 2.7B; mean squared of weighed deviates [MSWD] = 1.4; probability of fit = 0.14). We interpret this age to reflect the crystallization age of the main phase in the Tsikara stock.

593871: Twenty zircons were analyzed from a sericite-altered and weakly porphyritic granodiorite that intrudes the clinopyroxene-bearing diorite. Four grains gave significantly older $^{206}Pb/^{238}U$ ages and are interpreted to be basement-derived xenocrysts. A 602 Ma age marks the oldest zircon recognized in this survey and may be derived from Neoproterozoic basement. Two xenocryst grains yielding $^{206}Pb/^{238}U$ ages of 340 Ma and 250 Ma are consistent with the age of the underlying Permo-Carboniferous Kerdilion unit and Triassic rift-related granites (e.g., Arnea granite), respectively. One zircon grain gave a $^{206}Pb/^{238}U$ age of 39.5 Ma, interpreted as a xenocryst possibly corresponding to

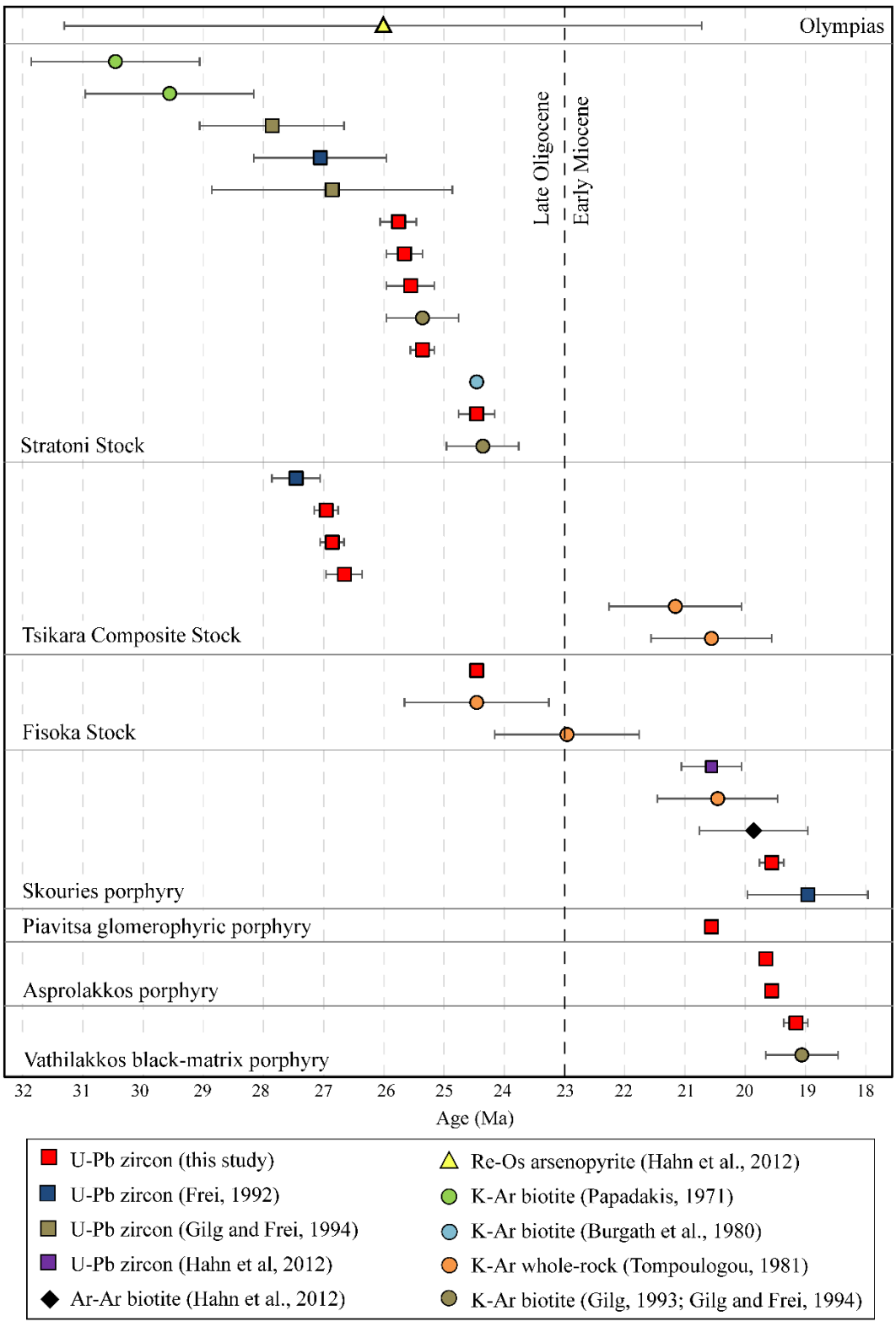

Figure 2.6. Geochronology compilation of Oligo-Miocene intrusive rocks from the Kassandra Mining District sourced from previously published work and this study. Uncertainties for U-Pb, $^{40}Ar/^{39}Ar$, Re-Os, and K-Ar dates are reported at the 2σ level.

the regional pegmatite event within the Kerdilion unit (Kalogeropoulos et al., 1989b). The remaining sixteen zircon grains cluster on Concordia with a weighted average $^{206}Pb/^{238}U$ age of 26.65 ± 0.31 Ma (Figure 2.7C-D; MSWD = 1.3; probability of fit = 0.20). This date is interpreted as the crystallization age of a younger fractionated phase of the Tsikara stock.

593882: Seventeen zircons were analyzed from an unaltered salt-and-pepper-textured diorite phase intruding the clinopyroxene-bearing stock. All analyses plot on or near Concordia yielding a weighted average $^{206}Pb/^{238}U$ age of 26.92 ± 0.20 Ma (Figure 2.7E-F; MSWD = 1.7; probability of fit = 0.047). This date corroborates the other ages and is interpreted as the crystallization age of an intermediate-composition phase within the composite stock.

Fisoka Stock

The Fisoka intrusive cluster is largely granodiorite in composition with porphyritic phases evident to the northeast near Stratoni. On the basis of petrology (see Petrochemistry section below), the Fisoka stock is similar to the Tsikara composite stock to the southwest and the Stratoni stock to the northeast. One surface sample was collected from a porphyritic body in the Fisoka area to test this hypothesis.

279446: Twenty zircons were analyzed from a sericite-altered crowded feldspar porphyry intrusion, coincident with an area of minor supergene Cu mineralization (Kockel et al., 1975). All zircon grains analyzed cluster on or near Concordia resulting in a weighted average $^{206}Pb/^{238}U$ age of 24.47 ± 0.14 Ma (Figure 2.7G-H; MSWD = 0.82; probability of fit = 0.69). This age is interpreted as the crystallization age of the porphyry phase of the Fisoka intrusive cluster.

Stratoni Stock

Gilg and Frei (1994) published zircon U-Pb ages of 27.1 ± 1.1 Ma and 26.9 ± 2.0 Ma for the Stratoni stock, and 27.9 ± 1.2 Ma for the porphyritic phase at Aspro Chomata (Figure 2.6). Low precision and large errors are attributed to a low $^{206}Pb/^{204}Pb$ ratio that necessitated a common lead correction at 30

Ma (Frei, 1992). Thus, re-evaluation of these dates using modern techniques was warranted. This study analyzed two representative samples collected from the equigranular plutonic stock and the internal porphyritic phase from the Aspro Chomata prospect area, respectively.

679714: Twenty zircon grains were analyzed from a weakly porphyritic phase of quartz-feldspar granodiorite exposed at Aspro Chomata (Figure 2.2). The prospect is associated with minor disseminated copper mineralization and poorly developed porphyry-style veins, overprinted by sheeted base metal sulfide-bearing quartz veins and associated intense bleaching and clay alteration. All analyses fall on Concordia; however, the data show considerable scatter ranging from 23.83 Ma to 26.63 Ma (Figure 2.8A). A subset of the 11 youngest grains yielded a weighted average $^{206}Pb/^{238}U$ age of 24.53 ± 0.31 Ma (Figure 2.8A-B; MSWD = 2.0; probability of fit = 0.03). A subset of the 12 oldest grains resulted in a weighted average $^{206}Pb/^{238}U$ age of 25.78 ± 0.31 Ma (Figure 2.8A-B; MSWD = 1.9; probability of fit = 0.04). We interpret these data to represent two stages of magmatism: the older zircons are likely antecrysts recording crystallization of the progenitor granodiorite, whereas the slightly younger zircons may reflect crystallization of the more differentiated porphyritic phase.

593580: Twenty zircon analyses were performed on the topographically lowest exposed portion of non-porphyritic equigranular quartz-feldspar granodiorite. Nearly all the zircon grains fall on Concordia with minor scatter, yielding a weighted average $^{206}Pb/^{238}U$ age of 25.36 ± 0.15 Ma (Figure 2.8C-D; MSWD = 1.4; probability of fit = 0.10). This is interpreted as the crystallization age of the Stratoni granodiorite and is the same age, within error, as the interpreted older age determined from the Aspro Chomata prospect. The age of the Stratoni granodiorite also places an upper age limit on syn-mineral, semi-brittle deformation and associated hydrothermal alteration related to the Stratoni fault.

Stratoni quartz-feldspar porphyry dikes

Granodioritic quartz-feldspar porphyry dikes in the Stratoni area are similar in texture and geochemistry to the porphyry intrusions at Fisoka. Two samples were collected east of the Madem

Lakkos orebody near the contact with the Stratoni stock: one from a brecciated porphyritic body, and a second from a quartz-feldspar porphyry dike that crosscuts the breccia.

679715: Twenty zircons were analyzed from the brecciated and quartz-sericite-pyrite-altered quartz-eye feldspar porphyry. One grain resulted a $^{206}Pb/^{238}U$ age of 153.7 Ma interpreted as a xenocryst likely derived from the Late Jurassic to Early Cretaceous intrusive event that affected the Rhodope basement (Turpaud and Reischmann, 2003; Himmerkus et al., 2011). A second grain yielded a $^{206}Pb/^{238}U$ age of 32.7 Ma which lies outside the expected error and was rejected. The remaining eighteen grains plot very near Concordia and have a weighted average $^{206}Pb/^{238}U$ age of 25.71 ± 0.37 Ma (Figure 2.8E-F; MSWD = 0.87; probability of fit = 0.61). This age is interpreted to be the crystallization age of the dike.

679716: Twenty zircons were analyzed from the altered quartz-eye feldspar porphyry dike cutting the brecciated porphyry previously described. Two older populations of zircons were identified with four grains yielding a range of $^{206}Pb/^{238}U$ ages from 171.0 to 150.8 Ma. These zircons appear to be xenocrystic possibly representing basement of uncertain affinity. Four younger grains resulted in a range of $^{206}Pb/^{238}U$ ages from 49.3 to 41.8 Ma and are interpreted as xenocrysts corresponding to the Late Cretaceous to early Eocene intrusive event (De Wet et al., 1989; Frei, 1996; Bébien et al., 2001). The remaining twelve grains plot on or near Concordia with minor scatter (Figure 2.8G) possibly due to minor Pb-loss as indicated by the elevated MSWD (2.3) and low probability of fit (0.01), and a relatively imprecise weighted average $^{206}Pb/^{238}U$ age of 25.45 ± 0.75 Ma (Figure 2.8H). This date is within error of the older brecciated porphyry suggesting multiple intrusive episodes and brecciation associated with this magmatic event.

Skouries

A previously published LA-ICP-MS single grain zircon U-Pb age of 20.56 ± 0.48 Ma from the Skouries stock (Hahn et al., 2012) probably represents the crystallization age of the syn-mineral porphyry phase. One sample was collected from a distal porphyry dike and, on the basis of petrology, appears to be

similar to the late- to post-mineral porphyry intrusive phases at Skouries. This sample is intended to test the timing relationship of the dike with the published crystallization age at Skouries.

593567: Twenty zircons were analyzed from a quartz-sericite-pyrite-altered megacrystic K-feldspar porphyry dike located 0.5 km south of the mineralized stock. One grain gave an older $^{206}Pb/^{238}U$ age of 44.7 Ma, and is interpreted to be a xenocryst associated with the Late Cretaceous to early Eocene intrusive event (De Wet et al., 1989; Frei, 1996; Bébien et al., 2001). Two grains give older results that lie outside the expected error and were rejected. The remaining seventeen zircon grains plot on or near Concordia (Figure 2.9A), but with significant scatter as indicated by the high MSWD (3.5) and low probability of fit (0.0). The weighted average $^{206}Pb/^{238}U$ age is 19.59 ± 0.17 Ma (Figure 2.9B), but given the scatter in the data the interpreted crystallization age for the porphyry dike is tentative. Nevertheless, the age is likely coeval with other similar dikes emanating from the Skouries stock and the post-mineral megacrystic K-feldspar porphyry observed within drill core at Skouries.

Aspro Lakkos

Geologic mapping identified black-matrix porphyry dikes that crosscut the megacrystic K-feldspar porphyry of Aspro Lakkos. One sample was analyzed from the megacrystic porphyry and one from a crosscutting dike to constrain their absolute age of emplacement and to compare these results to compositionally similar phases at Skouries and Vathilakkos. No published U-Pb data exist from Aspro Lakkos.

593587: Twenty zircon grains were analyzed from the weakly sericite-pyrite-altered megacrystic K-feldspar porphyry at Aspro Lakkos. All twenty grains resulted in overlapping concordant analyses yielding a weighted average $^{206}Pb/^{238}U$ age of 19.71 ± 0.10 Ma (Figure 2.9C-D; MSWD = 1.6; probability of fit = 0.059). This age is interpreted as the crystallization age of the Aspro Lakkos porphyry intrusion, approximately coeval with the emplacement of the late porphyry dike in the Skouries area.

593586: Twenty zircon grains were analyzed from a barren black-matrix K-feldspar porphyry dike crosscutting the main Aspro Lakkos porphyry body. Three grains were rejected on the basis of large analytical errors and skewness. The remaining seventeen grains plot on or near Concordia with minor scatter (Figure 2.9E). The weighted average yielded a $^{206}Pb/^{238}U$ age of 19.58 ± 0.14 Ma (Figure 2.9F; MSWD = 1.9; probability of fit = 0.016), and is interpreted to be the crystallization age of this late-stage dike which is effectively coeval with the porphyry. The age of the dike may represent the age of other texturally similar dikes in the district.

Piavitsa

A series of north-northeast-trending glomerophyric porphyry dikes outcrop within the Stratoni fault zone in the Piavitsa area approximately 5 km north of Aspro Lakkos (Figure 2.2). A surface sample was collected from an unmineralized dike that crosscuts the siliceous-rhodochrosite ± rhodonite body hosted within the Stratoni fault. No known U-Pb data exist for these dikes.

279433: Twenty zircon grains were analyzed from a sericite-pyrite-altered glomerophyric quartz porphyry dike. Six grains returned two older populations: 51.60 Ma to 42.32 Ma, and 26.99 Ma to 24.15 Ma. These zircons are interpreted as xenocrysts consistent with ages from the Late Cretaceous to early Eocene (De Wet et al., 1989; Frei, 1996; Bébien et al., 2001) and late Oligocene intrusive events, respectively. The fourteen remaining analyses plot on or near Concordia with a weighted average $^{206}Pb/^{238}U$ age of 20.62 ± 0.13 Ma (Figure 2.9G-H; MSWD = 0.95; probability of fit = 0.50), interpreted as the crystallization age of the dike. This age suggests that glomerophyric porphyry dikes that occur in the area are similar in age to the Skouries porphyry (within 1 m.y.). The crosscutting relationship of this early Miocene dike with the siliceous-rhodochrosite ± rhodonite carbonate replacement body provides a younger age limit for mineralization at Piavitsa.

Vathilakkos

A black-matrix porphyry dike occurs within the Vathilakkos fault (Figure 2.2), both of which crosscut the massive sulfide orebody at the Madem Lakkos deposit. This dike has been dated previously at 19.1 ± 0.6 by the K-Ar method (Gilg and Frei, 1994).

679705: Seventeen zircon grains were analyzed from the unaltered K-feldspar-hornblende-biotite porphyry dike. Ten zircon grains returned significantly older ages with a population of eight grains that range from 183.3 Ma to 250.8 Ma. These zircons are interpreted as xenocrysts possibly reflecting Triassic to Jurassic age basement. One zircon grain plots at 51.3 Ma (Figure 2.10A) and is interpreted to be a xenocryst consistent with the age of the Ierissos granite (Frei, 1996). One zircon grain lies skewed from the main age cluster at 22.4 Ma and was rejected on this basis. Seven of the remaining zircon grains plot on or near Concordia with a weighted average $^{206}Pb/^{238}U$ age of 19.21 ± 0.19 Ma (Figure 2.10A-B; MSWD = 1.2; probability of fit = 0.28), interpreted as the crystallization age of the Vathilakkos porphyry dike. This provides a younger age limit on mineralization at Madem Lakkos as previously recognized by Gilg and Frei (1994).

Summary

Two intrusive suites have been defined by the new geochronological results, supporting previous geochronology in the region (Frei, 1992). The composite stock at Tsikara and the Fisoka and Stratoni stocks define a late Oligocene igneous suite emplaced in the Kerdilion unit from 27 to 24.5 Ma. The porphyry stocks and dikes at Skouries and Aspro Lakkos, as well as the porphyritic dikes at Piavitsa and Vathilakkos define an early Miocene igneous suite restricted to a period from 20.5 and 19.2 Ma.

Figure 2.7. Zircon U-Pb Concordia and weighted average $^{206}Pb/^{238}U$ age plots of late Oligocene intrusive rocks from the composite Tsikara stock (A-F) and the Fisoka stock (G-H). Data point errors are reported at the 2σ level. Red ellipses correspond to rejected analyses.

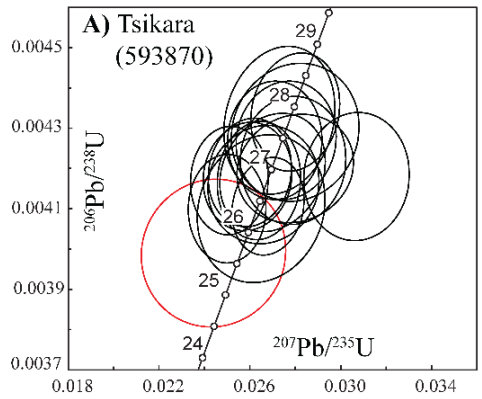
A) Tsikara
(593870)
29
28
27
26
25
24
$^{206}Pb/^{238}U$
$^{207}Pb/^{235}U$
0.0045
0.0043
0.0041
0.0039
0.0037
0.018
0.022
0.026
0.030
0.034

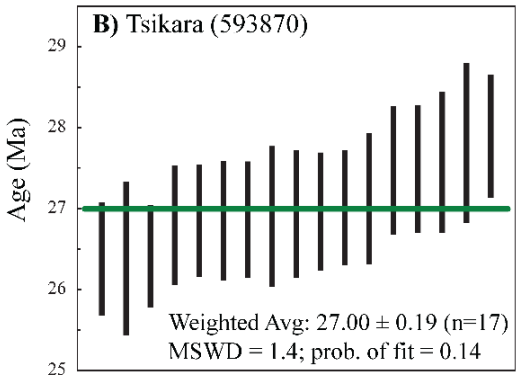
B) Tsikara (593870)
Age (Ma)
29
28
27
26
25
Weighted Avg: 27.00 ± 0.19 (n=17)
MSWD = 1.4; prob. of fit = 0.14

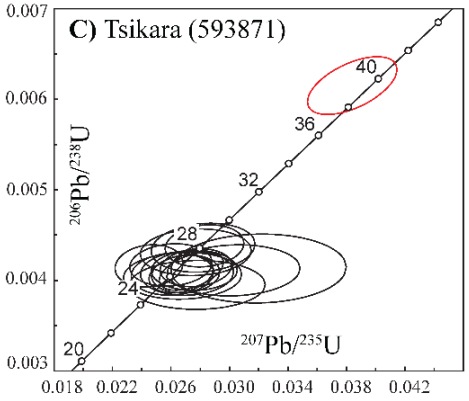
C) Tsikara (593871)
40
36
32
28
24
20
$^{206}Pb/^{238}U$
$^{207}Pb/^{235}U$
0.007
0.006
0.005
0.004
0.003
0.018
0.022
0.026
0.030
0.034
0.038
0.042

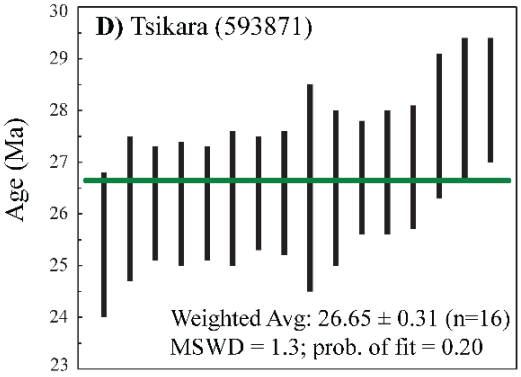
D) Tsikara (593871)
Age (Ma)
30
29
28
27
26
25
24
23
Weighted Avg: 26.65 ± 0.31 (n=16)
MSWD = 1.3; prob. of fit = 0.20

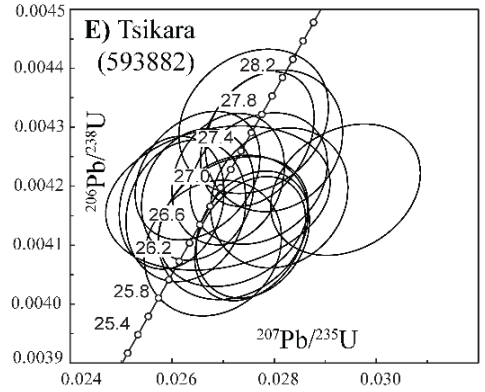
E) Tsikara
(593882)
28.2
27.8
27.4
27.0
26.6
26.2
25.8
25.4
$^{206}Pb/^{238}U$
$^{207}Pb/^{235}U$
0.0045
0.0044
0.0043
0.0042
0.0041
0.0040
0.0039
0.024
0.026
0.028
0.030

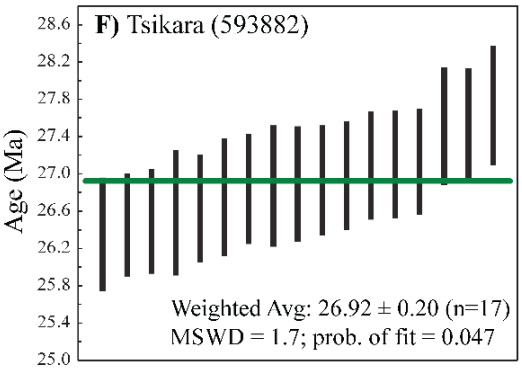
F) Tsikara (593882)
Age (Ma)
28.6
28.2
27.8
27.4
27.0
26.6
26.2
25.8
25.4
25.0
Weighted Avg: 26.92 ± 0.20 (n=17)
MSWD = 1.7; prob. of fit = 0.047

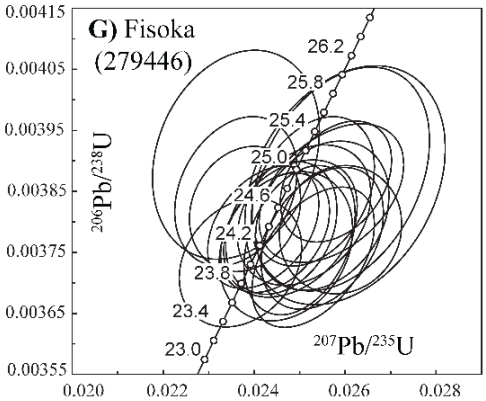
G) Fisoka
(279446)
26.2
25.8
25.4
25.0
24.6
24.2
23.8
23.4
23.0
$^{206}Pb/^{238}U$
$^{207}Pb/^{235}U$
0.00415
0.00405
0.00395
0.00385
0.00375
0.00365
0.00355
0.020
0.022
0.024
0.026
0.028

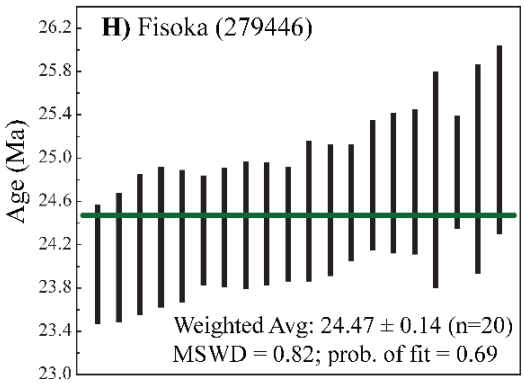
H) Fisoka (279446)
Age (Ma)
26.2
25.8
25.4
25.0
24.6
24.2
23.8
23.4
23.0
Weighted Avg: 24.47 ± 0.14 (n=20)
MSWD = 0.82; prob. of fit = 0.69

Figure 2.8. Zircon U-Pb Concordia and weighted average $^{206}Pb/^{238}U$ age plots of late Oligocene intrusive rocks from the Stratoni stock (A-D) and quartz-feldspar porphyry dikes (E-H) at Stratoni. Data point errors are reported at the 2σ level.

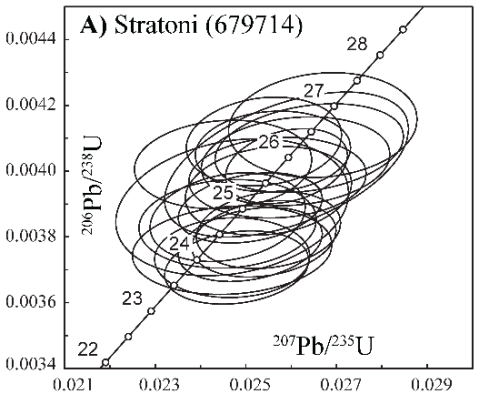
A) Stratoni (679714)
28
27
26
25
24
23
22
0.0044
0.0042
0.0040
0.0038
0.0036
0.0034
$^{206}Pb/^{238}U$
$^{207}Pb/^{235}U$
0.021
0.023
0.025
0.027
0.029

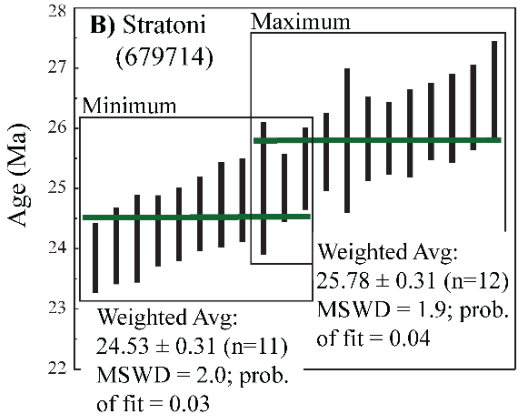
B) Stratoni (679714)
Maximum
Minimum
Age (Ma)
28
27
26
25
24
23
22
Weighted Avg: 25.78 ± 0.31 (n=12)
MSWD = 1.9; prob. of fit = 0.04
Weighted Avg: 24.53 ± 0.31 (n=11)
MSWD = 2.0; prob. of fit = 0.03

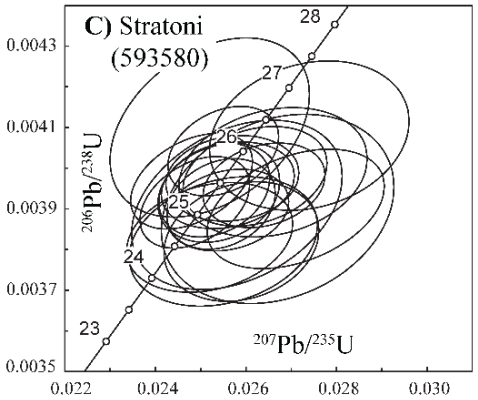
C) Stratoni (593580)
28
27
26
25
24
23
0.0043
0.0041
0.0039
0.0037
0.0035
$^{206}Pb/^{238}U$
$^{207}Pb/^{235}U$
0.022
0.024
0.026
0.028
0.030

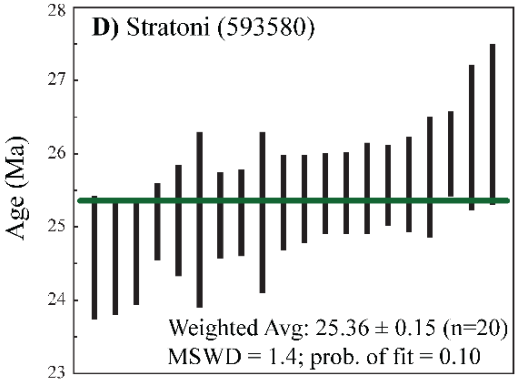
D) Stratoni (593580)
Age (Ma)
28
27
26
25
24
23
Weighted Avg: 25.36 ± 0.15 (n=20)
MSWD = 1.4; prob. of fit = 0.10

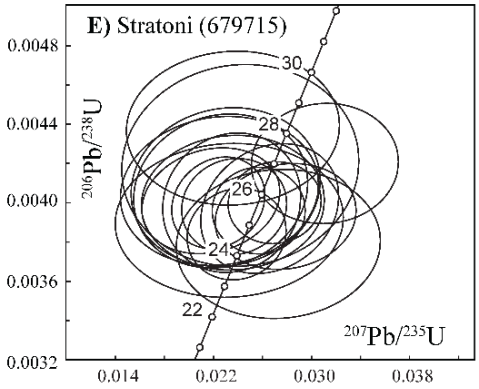
E) Stratoni (679715)
30
28
26
24
22
0.0048
0.0044
0.0040
0.0036
0.0032
$^{206}Pb/^{238}U$
$^{207}Pb/^{235}U$
0.014
0.022
0.030
0.038

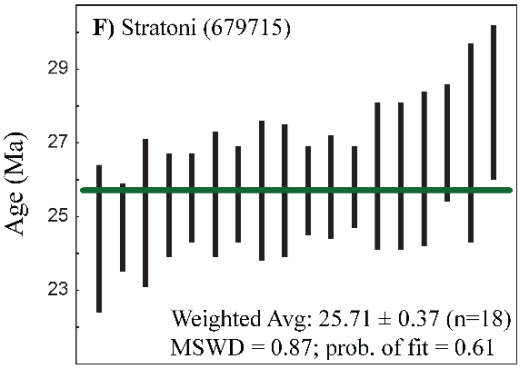
F) Stratoni (679715)
Age (Ma)
29
27
25
23
Weighted Avg: 25.71 ± 0.37 (n=18)
MSWD = 0.87; prob. of fit = 0.61

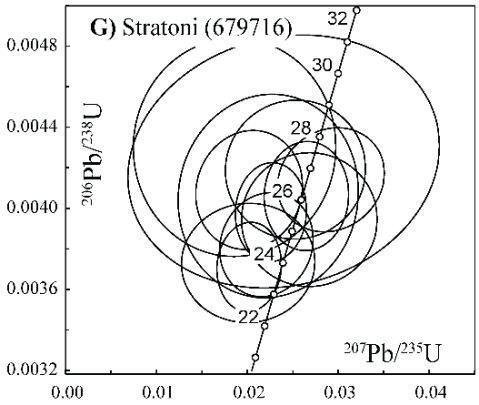
G) Stratoni (679716)
32
30
28
26
24
22
0.0048
0.0044
0.0040
0.0036
0.0032
$^{206}Pb/^{238}U$
$^{207}Pb/^{235}U$
0.00
0.01
0.02
0.03
0.04

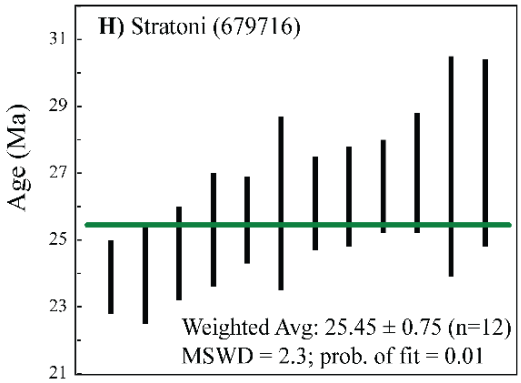
H) Stratoni (679716)
Age (Ma)
31
29
27
25
23
21
Weighted Avg: 25.45 ± 0.75 (n=12)
MSWD = 2.3; prob. of fit = 0.01

Figure 2.9. Zircon U-Pb Concordia and weighted average $^{206}Pb/^{238}U$ age plots of early Miocene intrusive rocks at Skouries (A-B), Aspro Lakkos (C-F), and the glomerophyric porphyry dike at Piavitsa (G-H). Data point errors are reported at the 2σ level. Red ellipses correspond to rejected analyses.

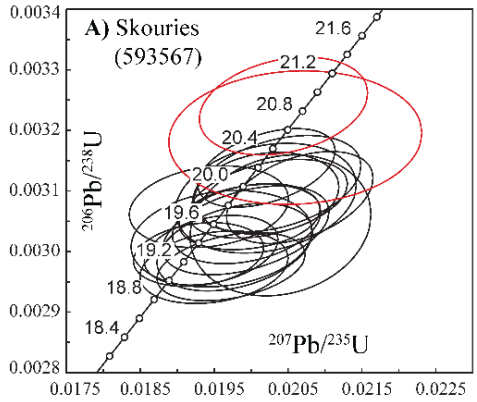
A) Skouries
(593567)
21.6
21.2
20.8
20.4
20.0
19.6
19.2
18.8
18.4
$^{206}Pb/^{238}U$
$^{207}Pb/^{235}U$
0.0034
0.0033
0.0032
0.0031
0.0030
0.0029
0.0028
0.0175
0.0185
0.0195
0.0205
0.0215
0.0225

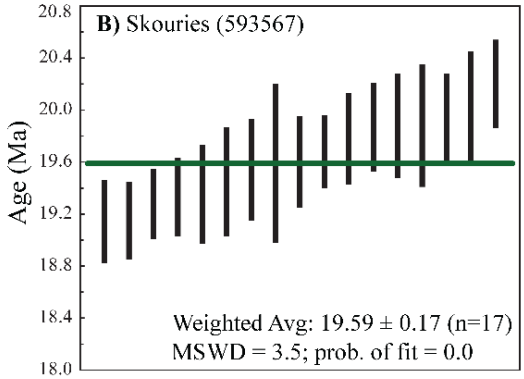
B) Skouries (593567)
Age (Ma)
Weighted Avg: 19.59 ± 0.17 (n=17)
MSWD = 3.5; prob. of fit = 0.0
20.8
20.4
20.0
19.6
19.2
18.8
18.4
18.0

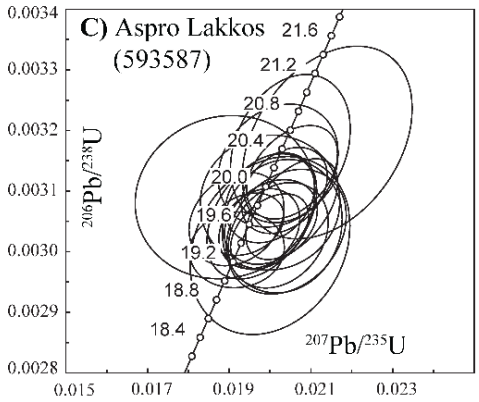
C) Aspro Lakkos
(593587)
21.6
21.2
20.8
20.4
20.0
19.6
19.2
18.8
18.4
$^{206}Pb/^{238}U$
$^{207}Pb/^{235}U$
0.0034
0.0033
0.0032
0.0031
0.0030
0.0029
0.0028
0.015
0.017
0.019
0.021
0.023

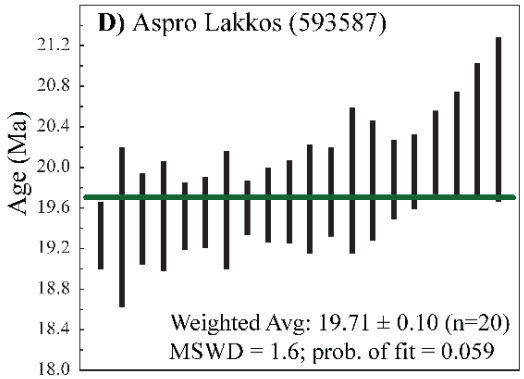
D) Aspro Lakkos (593587)
Age (Ma)
Weighted Avg: 19.71 ± 0.10 (n=20)
MSWD = 1.6; prob. of fit = 0.059
21.2
20.8
20.4
20.0
19.6
19.2
18.8
18.4
18.0

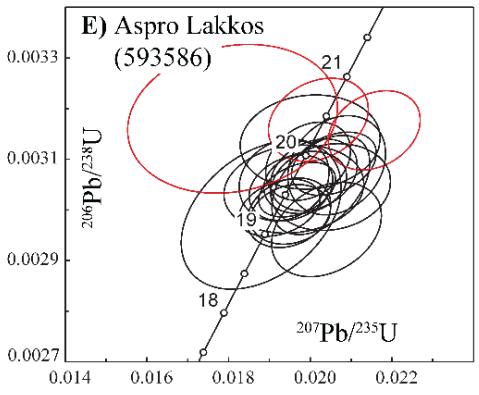
E) Aspro Lakkos
(593586)
21
20
19
18
$^{206}Pb/^{238}U$
$^{207}Pb/^{235}U$
0.0033
0.0031
0.0029
0.0027
0.014
0.016
0.018
0.020
0.022

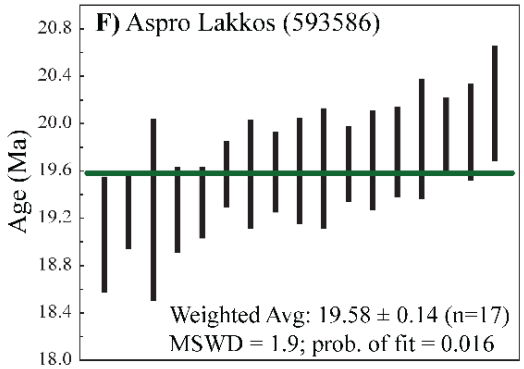
F) Aspro Lakkos (593586)
Age (Ma)
Weighted Avg: 19.58 ± 0.14 (n=17)
MSWD = 1.9; prob. of fit = 0.016
20.8
20.4
20.0
19.6
19.2
18.8
18.4
18.0

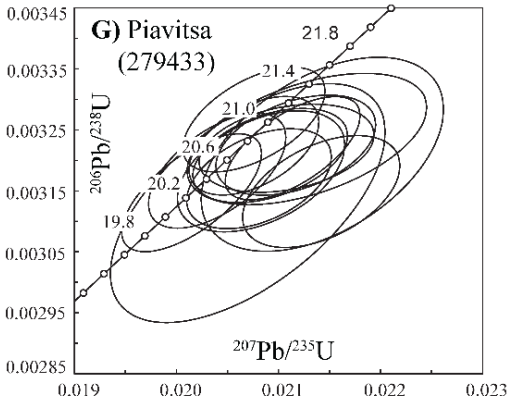
G) Piavitsa
(279433)
21.8
21.4
21.0
20.6
20.2
19.8
$^{206}Pb/^{238}U$
$^{207}Pb/^{235}U$
0.00345
0.00335
0.00325
0.00315
0.00305
0.00295
0.00285
0.019
0.020
0.021
0.022
0.023

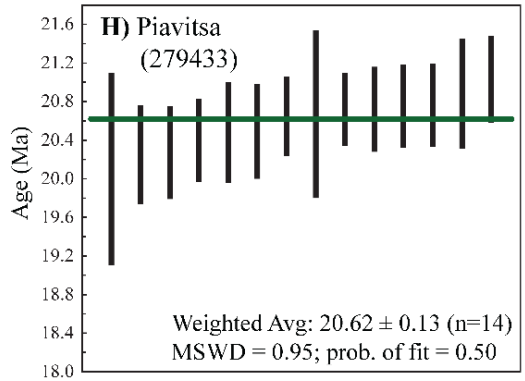
H) Piavitsa
(279433)
Age (Ma)
Weighted Avg: 20.62 ± 0.13 (n=14)
MSWD = 0.95; prob. of fit = 0.50
21.6
21.2
20.8
20.4
20.0
19.6
19.2
18.8
18.4
18.0

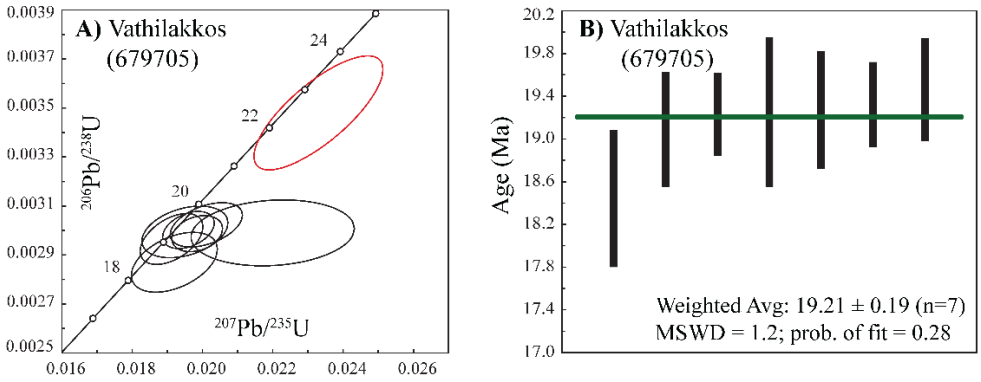

Figure 2.10. Zircon U-Pb Concordia and weighted average $^{206}Pb/^{238}U$ age plots for the early Miocene black-matrix porphyry dike at Vathilakkos (A-B). Data point errors are reported at the 2σ level. Red ellipses correspond to rejected analyses.

Petrochemistry

Major and trace element geochemistry

Late Oligocene Magmatism: Data plotted on the total alkali vs. silica diagram (Figure 2.11A) show a broad distribution of compositions ranging from monzogabbro to monzonite for the main stock at Tsikara, with subordinate monzodiorite to gabbrodiorite phases in the central stock at Fisoka. More evolved compositions range from diorite to granodiorite in the Stratoni and Fisoka stocks, including a granodiorite micro-porphyry phase crosscutting the mafic stock at Tsikara. The data show a negative sloping trend in the granodiorite field interpreted to reflect incipient alteration and weathering of surface samples predominately from the Tsikara micro-porphyry and porphyry dikes at Fisoka. The suite is subalkaline as defined by the classification of Irvine and Baragar (1971) and falls in the high-K calc-alkaline magma series (Figure 2.11C). Petrographic evidence suggests that sericitic alteration in some samples correlates with elevated K_2O concentrations in the granodiorite porphyry at Tsikara as well as porphyry dikes north of Fisoka, resulting in apparent shoshonitic compositions (Figure 2.11C).

The late Oligocene igneous rocks are relatively enriched in light rare earth elements (LREE) whereas heavy rare earth elements (HREE) show flat signatures when normalized to chondritic values (Figure 2.12A-C). The Sm/Yb ratio is utilized to model HREE fractionation (e.g., Kay and Mpodozis, 2001; Bissig and Tosdal, 2009). Sm/Yb ratios from the mafic stock and micro-porphyry at Tsikara (1.23-

3.33) as well as the stocks at Fisoka (1.38-2.66) and Stratoni (1.78-2.36) suggest minimal to no HREE fractionation (Figure 2.13A). The porphyry dikes north of Fisoka show minor HREE fractionation patterns (Sm/Yb = 1.74 to 4.72) with the most fractionated values from aplitic granite dikes. La/Yb ratios are generally <20 for all stocks and slightly elevated (17.46-51.83) for porphyry dikes north of Fisoka (Figure 2.13C). Sr/Y ratios for the late Oligocene intrusive suite range from 0.33 to 69.59, where the most depleted values reflect alteration. The average Sr/Y ratio (37.22) from unaltered Stratoni stock samples is likely representative of the Sr/Y ratio for the late Oligocene suite. A wide range of Eu_n/Eu^* values (0.55-0.96; Figure 2.13A) suggests that the REE pattern was controlled primarily by feldspar fractionation rather than amphibole (Hanson, 1980).

Incompatible large ion lithophile elements (LILE) have high concentrations in the late Oligocene suite. Strontium concentrations are extremely high with respect to average upper crustal abundance (320 ppm Sr; Rudnick and Gao, 2003) reaching values as high as 912 ppm at Stratoni, 897 ppm at Tsikara, and 827 ppm at Fisoka. Barium is similarly enriched with respect to average upper continental crust (624 ppm Ba; Rudnick and Gao, 2003) with concentrations of up to 1136 ppm at Tsikara, 1025 ppm at Stratoni, and 935 ppm at Fisoka. Uranium and Th concentrations are anomalous with respect to average upper continental crust (2.6 ppm U, 10.0 ppm Th; Rudnick and Gao, 2003). The highest U and Th values for the suite occur at Tsikara with concentrations up to 14 ppm and 33 ppm, respectively. The elevated LILE and peraluminous character (alumina saturation index >1) of these intrusive rocks suggest high degrees of crustal contamination.

Early Miocene Magmatism: Skouries and the barren Aspro Lakkos porphyries are quartz monzonites based on their total alkali vs. silica contents (Figure 2.11B). Kroll et al. (2002) interpreted Skouries to be an alkalic porphyry of shoshonitic affinity; however, petrographic evidence indicates K_2O enrichment may reflect intense potassic alteration. Frei (1995) also suggested that potassic alteration at Skouries resulted in a 20-36 relative percent increase in K_2O content. This study proposes a high-K calc-alkaline classification for Skouries and its unaltered equivalent at Aspro Lakkos. A genetic relationship

among both porphyry intrusions at Skouries and Aspro Lakkos is inferred based on petrography and geochemistry as originally proposed by Frei (1992). Lower K_2O contents of quartz-sericite-pyrite-altered porphyry dikes surrounding the Skouries stock are interpreted to be the result of alkali mobility during alteration and surface weathering (Figure 2.11D).

Geochemical data from early Miocene dikes are plotted on the plutonic classification diagram of Middlemost (1994), albeit their texture is more characteristic of trachyandesite to trachydacite volcanic rocks (Figure 2.11B). Glomerophyric porphyry dikes appear to be mildly alkalic to predominately subalkalic high-K calc-alkaline with a tendency toward shoshonitic compositions. Quartz-sericite-carbonate-pyrite alteration is common among glomerophyric dikes, probably explaining the broad range of alkali contents. Unaltered samples from Piavitsa and Olympias drill core represent the least altered chemistry of these dikes (Figure 2.11D). The unaltered black-matrix porphyry dike at Vathilakkos is high-K calc-alkaline, and contains similar alkali contents as the black-matrix porphyry dikes at Aspro Lakkos.

The early Miocene intrusive suite is more enriched in LREE but displays similar chondrite-normalized HREE patterns when compared against late Oligocene igneous rocks (Figure 2.12D-F). However, late Miocene porphyritic stocks and dikes are distinctly HREE fractionated with Sm/Yb ratios of 2.77 to 7.72 at Skouries, 2.79 to 6.20 at Aspro Lakkos, and 6.87 from the black-matrix porphyry at Vathilakkos (Figure 2.13B). Glomerophyric dikes have a wide range of Sm/Yb values (1.77-7.57; Figure 2.13B). High average La/Yb and Sr/Y ratios occur at Skouries (43.42 and 83.6, respectively) and Aspro Lakkos (39.79 and 47.1, respectively) (Figure 2.13D). Weakly negative europium anomalies (Eu_n/Eu^*) are evident at Aspro Lakkos (0.76-0.89) and Skouries (0.70-0.89) with two samples from the Skouries stock exhibiting slightly positive anomalies (1.08 and 1.15) (Figure 2.13B). The black-matrix porphyry dike at Vathilakkos and glomerophyric dikes display weak negative Eu_n/Eu^* anomalies (0.72-0.87) and, combined with the HREE pattern, also suggest fractionation controlled by amphibole or garnet (Figure 2.13B).

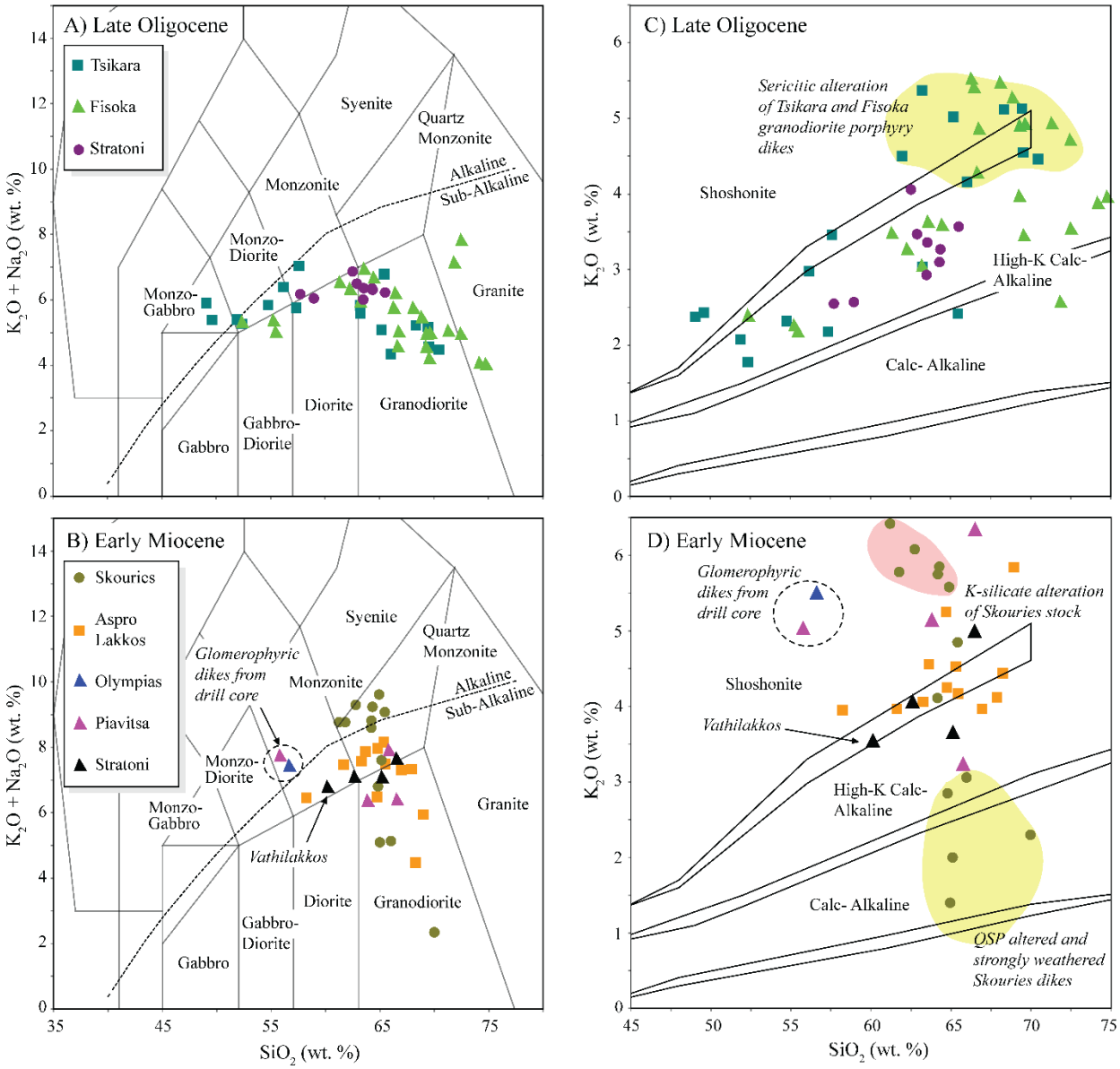

Figure 2.11. Geochemical classification of late Oligocene and early Miocene igneous rocks of the Kassandra Mining District: (A-B) Total-alkali vs. silica diagram for plutonic igneous rocks of Middlemost (1994) with alkaline-subalkaline division represented by dotted line after Irvine and Baragar (1971). Early Miocene porphyry dikes represented by (pink, blue, and black) triangles are referred to by their volcanic equivalents in the text; (C-D) K_2O vs. SiO_2 subalkalic discrimination diagram after Rickwood (1989). Fields shaded in yellow and red correspond to samples that have experienced strong quartz-sericite-pyrite (QSP) alteration or K-silicate alteration, respectively.

Early Miocene porphyries have highly enriched incompatible LILE contents compared to the late Oligocene suite. Sr concentrations exceed 1570 ppm at Skouries and 1446 ppm at Aspro Lakkos, while Ba concentrations reach 2885 ppm and 4190 ppm for Skouries and Aspro Lakkos, respectively.

Extremely high Sr values (3835 ppm) occur within the unaltered glomerophyric dike at Olympias while Sr concentrations (1515 ppm) for the black-matrix porphyry dike at Vathilakkos are similar to Aspro Lakkos. These extremely high Sr contents suggest little to no plagioclase fractionation in the parental magma (Richards et al., 2012). Early Miocene porphyries are strongly elevated in U and Th with highest concentrations at Skouries with 19 ppm and 67 ppm, respectively, consistent with the results from Kroll et al. (2002), suggesting significant crustal interaction.

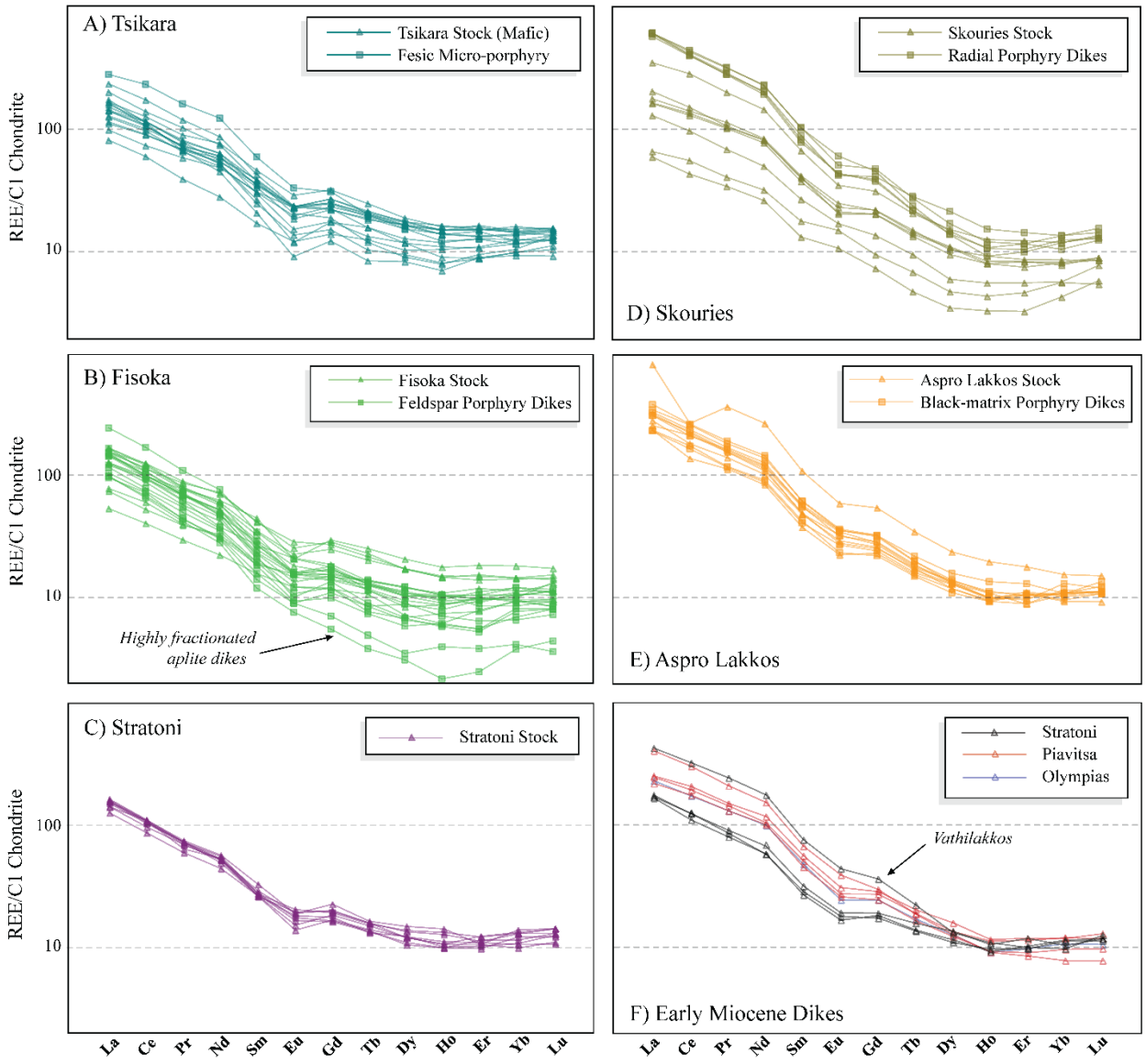

Figure 2.12. Chondrite-normalized REE patterns for (A-C) late Oligocene and (D-F) early Miocene igneous rocks. Normalization values are those of Sun and McDonough (1989).

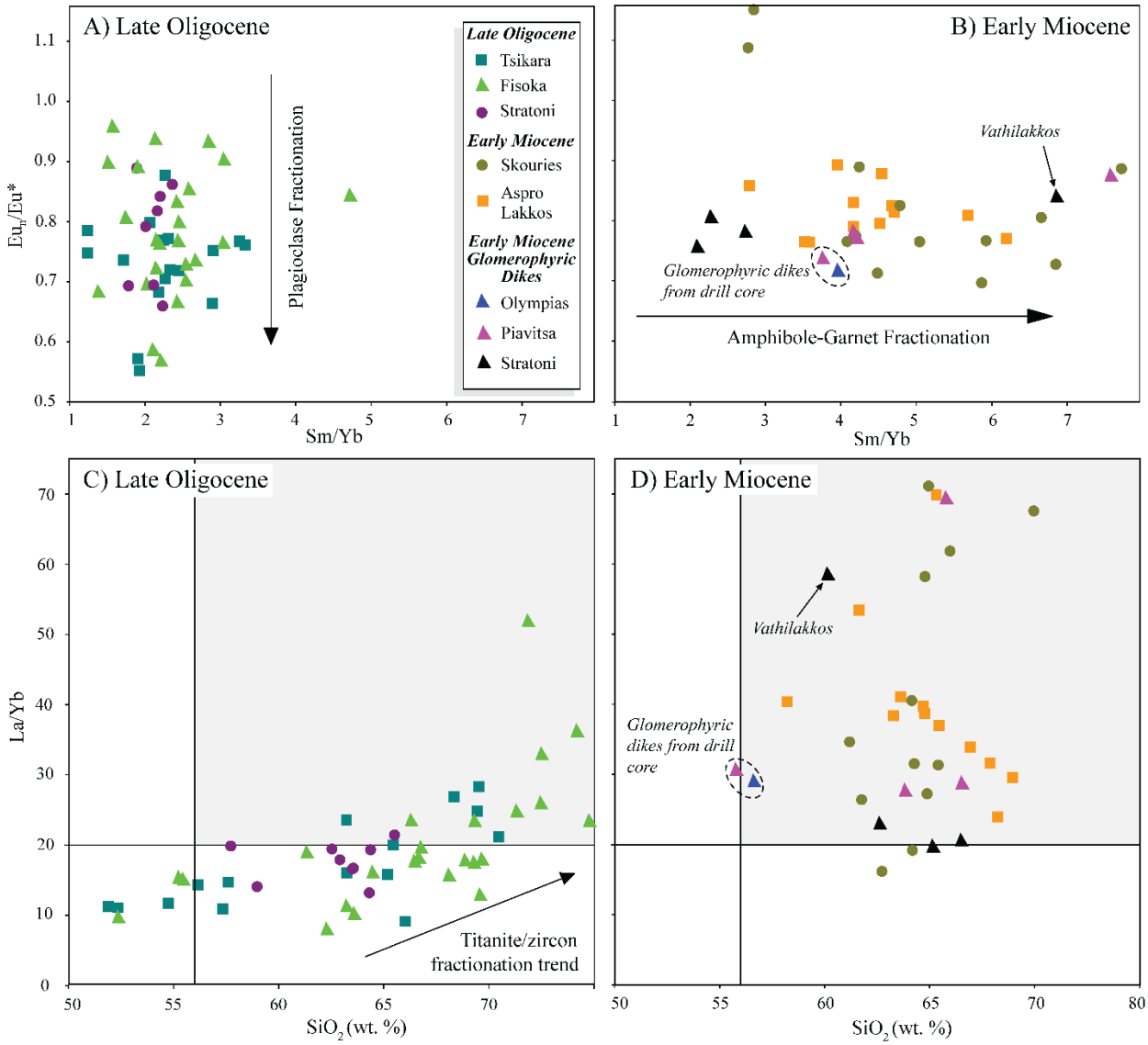

Figure 2.13. Europium anomaly (Eu_n/Eu^*) vs. Sm/Yb fractionation plots for (A) late Oligocene and (B) early Miocene igneous rocks. The europium anomaly is calculated using the equation in Rollinson (1993), and normalized relative to C1 chondrite values (Sun and McDonough, 1989). La/Yb vs. SiO_2 fractionation plots for the (C) late Oligocene and (D) early Miocene igneous suites. Shaded area represents the adakitic field of Richards and Kerrich (2007).

Metallogenic Framework

The regional metallogenic framework of the Serbo-Macedonian Metallogenic Province was strongly influenced by Eocene-Miocene extension and exhumation of the southern Rhodope core complex of northern Greece. Exhumation of the southern Rhodope core complex along the Kerdilion detachment fault (Brun and Sokoutis, 2007; Wüthrich, 2009) is postulated to be the regional tectonic process that

triggered upper crustal magmatism and metallogenesis (Marchev et al., 2005; Eliopoulos and Kilias, 2011; Hahn et al., 2012; Kydonakis et al., 2014).

The penetrative ductile S_1 structural fabric within the district was likely established during regional Cretaceous to Eocene ductile deformation (Kilias et al., 1999). Evidence for an early compressional thrust event in the Stratoni fault area may have been focused on this structural anisotropy associated with rheologically weak marbles (Haines, 1998). Thrust faulting is likely coeval with the development of sub-parallel district-scale F_3 folds. Eocene extensional tectonics and core complex exhumation may have been initiated at the Rhodope-bounding Kerdilion detachment fault (Brun and Sokoutis, 2007; Wüthrich, 2009; Kydonakis et al., 2014). Ductile to semi-brittle extensional reactivation of the preexisting Stratoni thrust fault resulted in the development of a normal fault (Haines, 1998; Siron et al., 2014). Mineralized semi-brittle fault strands crosscutting the Stratoni stock indicate that late Oligocene magmas were emplaced prior to or contemporaneous with extensional deformation within the Stratoni fault zone. The structural relationship between the Kerdilion detachment fault and the mineralized normal fault at Stratoni is unclear.

The northeast-trending axis of Oligo-Miocene intrusive centers in the Kassandra Mining District align with the mid-crustal, northeast-elongated early Miocene Kavala pluton to the northeast of the Chalkidiki peninsula (Figure 2.1; Dinter et al., 1995; Dinter, 1998). Syn-intrusion mylonitic fabrics and stretching lineations within the Kavala pluton indicate a northeast-oriented principal axis of extension along the prominent northwest-trending Symvolon shear zone (Figure 2.1). This crustal-scale rupture developed prior to early Miocene time, and is believed to have localized syn-tectonic magmatism at Kavala (Dinter et al., 1995). Exhumation of the southern Rhodope core complex may have influenced ascent of magmas to shallow crustal levels, preferentially exploiting favorable oblique structural intersections between northeast-trending transtensional, upper crustal faults and west-northwest-trending structures such as the antiform that hosts Skouries and the normal fault at Stratoni.

Magmatic evolution

Late Oligocene magmatism spanned ~2.5 m.y., with emplacement of the Tsikara composite stock at 27.0 Ma followed by variably differentiated high-K calc-alkaline diorite and granodiorite intrusions at Stratoni and Fisoka from 25.8 to 24.5 Ma. The high-K calc-alkaline Skouries quartz monzonite porphyry was emplaced at 20.6 Ma with porphyry-style mineralization inferred to be the same age as the main intrusive phase (Figure 2.6; Hahn et al., 2012). The altered, albeit barren, quartz monzonite porphyry at Aspro Lakkos crystallized at 19.7 Ma, coeval with the post-mineral radial dikes at Skouries and probably synchronous with the compositionally similar late porphyry phases of the Skouries stock. The barren black-matrix porphyry dike at Vathilakkos represents the latest stage of early Miocene magmatism in the district at 19.2 Ma.

Late Oligocene and early Miocene magmatism display distinct compositional differences suggesting different magma sources and/or fractionation and mixing histories. $^{87}Sr/^{86}Sr$ ratios reported from the compositionally diverse Tsikara and Stratoni stocks (Frei, 1992) are consistent with a mafic mantle-derived parental magma potentially with some input from crustal sources. This is in contrast to the more uniform compositions of early Miocene porphyries which may have been derived from a single or well-mixed source. Skouries and Aspro Lakkos have $^{87}Sr/^{86}Sr$ ratios typical of upper mantle or lower crustal sources (Frei, 1995).

The importance of plagioclase fractionation in the late Oligocene igneous suite is indicated by distinct negative europium anomalies and low Sm/Yb ratios (Figs. 11A–C and 12A). However, increasing La/Yb ratios with silica content could indicate fractionation of titanite or perhaps zircon among the most differentiated porphyry phases (Figure 2.13C; Richards et al., 2012).

Petrochemical characteristics of the Miocene suite, including highly fractionated LREE, elevated incompatible LILE including Sr and Ba, and high field strength elements including U and Th suggest involvement of subduction-enriched meta-basaltic continental lithosphere (Pe-Piper and Piper, 2006; Pe-Piper et al., 2009). This suite exhibits elevated Sr/Y (>50), Sm/Yb and La/Yb ratios (Figure 2.13B and

12D) indicating that these melts were controlled by fractionation of amphibole, in an amphibole ± garnet-bearing source (Richards and Kerrich, 2007; Richards et al., 2012; Lu et al., 2015), or achieved through assimilation of crustal material during ascent to shallow crustal levels (Richards and Kerrich, 2007; Richards, 2011). Chondrite-normalized REE patterns, particularly for Skouries (Figure 2.12D), favor fractionation processes that involved amphibole. In order to achieve high Sr/Y and La/Yb ratios, sufficient water must be available to fractionate amphibole and suppress plagioclase in the deep crust or mantle (Richards and Kerrich, 2007; Richards, 2011). The minor to absent europium anomaly suggests oxidizing conditions and/or elevated water content, which will also quell plagioclase crystallization. Abundant amphibole and biotite phenocrysts in the early Miocene porphyries indicate high concentrations of magmatic water. Depletion in Nb, Ta, and Ti further support a hydrous mantle-derived magma (Pe-Piper and Piper, 2006).

The petrologic data document a major change in the physiochemical conditions between the late Oligocene and the early Miocene. Late Oligocene plutonic rocks may reflect the culmination of subduction-related magmatism prior to lithospheric delamination (and slab rollback) resulting in thermal melting of continental lithosphere. Melting of previous subduction-modified meta-basaltic lithosphere would have generated progressively more alkalic (or shoshonitic) magmas in the early Miocene (Pe-Piper and Piper, 2006) possibly resulting in melts more favorable for generating porphyry Au-Cu deposits (Müller and Groves, 2000).

Metallogenesis

As currently known, porphyry Au-Cu mineralization is restricted to a small early Miocene high-K calc-alkaline quartz monzonite porphyry at Skouries, although magmatism of the same age and type is widespread in the area. Skouries shows similarities to silica-saturated, shoshonitic, pencil-shaped porphyry bodies in the Ridgeway-Cadia and North Parkes districts of NSW, Australia (Wilson, 2003). The Skouries porphyry stock intruded a thick sequence of relatively unreactive quartz-rich feldspar-biotite

gneiss close to the axis of a major west-northwest-trending antiform. These lithologic and structural features aided in efficient focusing of magmatic-hydrothermal fluids within a favorable depositional environment (e.g., Wilkinson, 2013). Magmatic-hydrothermal fluid was confined to the stock and immediately adjacent wallrock as dense arrays of stockwork, northeast-trending sheeted veins, and disseminated Au-bearing Cu-sulfide mineralization. Intersections between discrete district-wide northeast-trending structures and fabrics developed in the axis of the regional antiform are postulated to be the principal structural control influencing the upper crustal emplacement and focus of the Skouries magmatic-hydrothermal system.

The brittle-ductile, extensional Stratoni fault zone hosts the Madem Lakkos and Mavres Petres polymetallic carbonate-hosted sulfide orebodies and cuts the late Oligocene (25.8 to 24.5 Ma) high-K calc-alkaline granodiorite at Stratoni. High-temperature Cu-rich skarn occurs adjacent to the Stratoni granodiorite stock and related porphyry dikes, and grades westward into Au-Ag-Pb-Zn massive sulfide at Madem Lakkos, and variably arsenopyrite-rich base metal massive sulfide at Mavres Petres. Massive silica-manganese replacement bodies and epithermal-style silica-rhodochrosite veins at Piavitsa may reflect a continuum of hydrothermal mineralization westward for 12 km from a source region in the Stratoni area coincident with late Oligocene intrusions at Stratoni and Fisoka (Figure 2.2). Zonation from skarn into proximal base metal massive sulfide and distal manganese replacement bodies is a characteristic pattern among intrusion-related, carbonate-hosted replacement systems (Megaw et al., 1988). Enrichment of Au is relatively unusual among these deposit types, albeit a distinguishing feature of the massive sulfide deposits in the Stratoni area and Olympias.

The precise timing of Au-Ag-Pb-Zn-Cu carbonate replacement mineralization within the Stratoni fault zone is uncertain but is constrained by structural and intrusive events. A maximum age of ~25 Ma is constrained by the Stratoni granodiorite stock which is cut by the Stratoni fault and hydrothermal alteration that may represent the eastern extent of the Madem Lakkos ore body. Skarn mineralization near the contact of the Stratoni stock and related porphyry dikes further suggests that mineralization in the

Stratoni fault may be coeval with this igneous event; however, this evidence does not definitively link Madem Lakkos to the Stratoni stock. The minimum age for the marble-hosted mineralization is constrained by the 19.2 Ma black-matrix porphyry dike at Vathilakkos that crosscuts the Madem Lakkos orebody at depth (Nebel, 1989; Haines, 1998), and the 20.6 Ma glomerophyric porphyry dike that crosscuts siliceous-rhodochrosite carbonate replacement mineralization at Piavitsa. Based on these constraints, the orebodies in the Stratoni fault zone formed between 25 and 20 Ma. The spatially associated late Oligocene igneous rocks on eastern end of the Stratoni fault support the older mineralization age. A late Oligocene age was also tentatively proposed by Gilg and Frei (1994) based on K-Ar geochronology.

The precise age of the Olympias deposit is not well constrained. Unaltered glomerophyric porphyry dikes in the Olympias area are geochemically and petrographically similar to those in the Stratoni fault although, at the time of writing this chapter, no crosscutting relationships have been directly observed in the Olympias orebody. The arsenopyrite Re-Os age (26.1 Ma) of Hahn et al. (2012) suggests a minimum Oligo-Miocene age of mineralization at Olympias. Similarities among Olympias, Madem Lakkos, and Mavres Petres, particularly with respect to sulfide mineralogy and replacement textures, strongly suggest that Olympias is similar in age to the Stratoni orebodies, but no direct connection has been established between these deposits.

The close proximity of the Skouries Au-Cu porphyry and polymetallic Au-Ag-Pb-Zn-Cu carbonate-hosted replacement bodies suggest that a similar crustal plumbing system tapped deep fertile source regions that efficiently transported magmas and magmatic-hydrothermal fluids to shallow crustal levels. The nature of the resulting deposits reflects contrasting controls on the release and movement of ore forming fluids and depositional mechanisms within the upper crust. The Kassandra Mining District, therefore, demonstrates the importance of tectonic and magmatic processes working in concert with structures in the shallow environment to generate economic concentration of metal.

Conclusions

Multiple stages of ductile deformation structurally preconditioned the metamorphic basement rocks in the district. Eocene to Miocene exhumation of the southern Rhodope core complex along the Kerdilion detachment fault may have triggered regional magmatism and metallogenesis. Ductile compressional deformation resulted in district-scale folds and the development of thrust faults near the Stratoni fault zone. A regional northeast-southwest axis of extension led to the ductile to semi-brittle formation of the Stratoni normal fault in the late Oligocene. Structural intersections with a west-northwest-trending antiform at Skouries and the Stratoni fault likely influenced the upper crustal emplacement of Oligo-Miocene stocks and dikes and associated magmatic-hydrothermal systems.

Zircon U-Pb geochronology defines two distinct magmatic episodes previously recognized in the district (Frei, 1992). The late Oligocene igneous suite encompasses monzogabbro and granodiorites belonging to the 27 Ma composite stock at Tsikara and the 25.8 to 24.5 Ma diorite to granodiorite stocks at Stratoni and Fisoka. The early Miocene suite includes the 20.6 Ma (Hahn et al., 2012) mineralized quartz monzonite porphyry stock at Skouries and coeval glomerophyric dikes, followed by the 19.7 Ma barren porphyry at Aspro Lakkos. Magmatism concluded with the 19.2 Ma porphyry dike that intrudes the Vathilakkos fault. Both igneous suites belong to the high-K calc-alkaline magmas series, with early Miocene porphyries showing a shoshonitic affinity. Fractionation patterns shown by the Sm/Yb ratio and the Eu_n/Eu^* anomaly indicate plagioclase control for the late Oligocene suite. In contrast, these ratios along with elevated Sr/Y and La/Yb values indicate fractionation of amphibole or garnet for the early Miocene suite of porphyries. Enriched LREE patterns, and extremely elevated LILE concentrations indicate that both magma suites, particularly the early Miocene porphyry event, interacted strongly with subduction-enriched continental lithosphere (Pe-Piper et al., 2006).

Two major mineralizing styles comprise the economic mineral deposits of the Kassandra Mining District. Polymetallic Au-rich sulfide deposits are hosted by marble contained within the semi-brittle Stratoni fault. Mineralization is zoned along a 12 km strike length from Cu-bearing skarn adjacent to the

late Oligocene Stratoni granodiorite stock, through Au-Ag-Pb-Zn-Cu carbonate replacement deposits at Madem Lakkos and Mavres Petres, to distal siliceous-manganese carbonate replacement bodies and associated crustiform Au-rich silica-rhodochrosite veins at Piavitsa. Structural and alteration relationships suggest that carbonate replacement mineralization is syn- to post-emplacement of the late Oligocene Stratoni granodiorite stock (~25 Ma). Unaltered dikes at Vathilakkos and Piavitsa demonstrate that this mineralization pre-dates early Miocene (19-20 Ma) magmatism. The Olympias Au-Ag-Pb-Zn carbonate replacement deposit is located north of the Stratoni fault. Olympias appears to be broadly similar to the Madem Lakkos and Mavres Petres deposits and the Re-Os age (26.1 Ma) of Hahn et al. (2012) suggests a similar timing. Early Miocene Au-Cu mineralization at Skouries, south of the Stratoni fault, is associated with a narrow polyphase porphyry stock. Mineralization is hosted by multiple phases of porphyry-related quartz and quartz-magnetite veins associated with pervasive potassic alteration of the porphyry stock and adjacent wallrock gneiss and schist.

Late Oligocene and early Miocene magmatism overlaps spatially within the district but defines distinct petrogenetic events separated by about 5 m.y. Both episodes are associated with Au-rich mineralization. Carbonate replacement deposits appear to have formed in association with high-K calc-alkaline magmas whereas the Skouries porphyry system has characteristics similar to sub-alkaline and shoshonitic porphyry deposits elsewhere. Carbonate replacement massive sulfide deposition was largely controlled by hydrothermal fluid movement into an extensional fault zone containing receptive host rocks, whereas a major regional antiform localized the Skouries porphyry system. The change in character of mineralization within the Kassandra Mining District may reflect a combination of factors including structural preconditioning, magmatic-hydrothermal processes, and availability of reactive host rocks.

Acknowledgements

The first author would like to thank Eldorado Gold Corporation for providing logistical support while in Greece and financial support for analyses. CRS gratefully acknowledges the unwavering support

from everyone at the Hellas Gold Exploration office at Madem Lakkos. Discussions with Dave Rhys and Peter Lewis contributed to the structural framework and interpretation. Samuel Haines is thanked for providing a copy of his thesis and discussing the evolution of the Stratoni fault from the now closed Madem Lakkos mine. Geochronology support was provided by H. Lin and D. Newton (UBC). A travel grant was generously provided by the Mario Einaudi Center for International Studies at Cornell University. Critical reviews by Nikolay Bonev, Jeremy Richards, and an anonymous reviewer significantly improved this manuscript.

REFERENCES

Arvanitidis, N.D., and Constantinides, D.C., 1994, Ore geology of the Olympias, Madem Lakkos and Mavres Petres polymetallic deposits: Post-congress 2-day field trip to Chalkidiki peninsula (central Macedonia, northern Greece), Congress of the Geological Society of Greece, 7th, Thessaloniki, Greece, May 27-28, 1994, Guidebook, 17 p.

Barcikowski, J., Lehmann, S., von Quadt, A., Heinrich, C., and Serafimowski, T., 2012, The magmatic evolution of the Buchim-Damjan-Borov Dol ore district, in von Quadt, A., and Serafimovski, T., eds., Diversity of copper and gold deposits in the eastern European Balkan, Carpathian and Rhodopean belts: tectonic, magmatic and geochronological investigations: SCOPES Project - International conference, Stip, Macedonia, p. 16.

Bébien, J., Michard, A., Montigny, R., Feinberg, H., and Voidomatis, P., 2001, The Grigoriou plutonic complex (Mt Athos, Greece): a component of the north Aegean Eocene-Oligocene Calc-Alkaline magmatism: European Union of Geosciences Symposium, 11th, Strasbourg, France, 2001, LS03:314.

Bissig, T., and Tosdal, R.M., 2012, Petrogenetic and metallogenic relationships in the eastern cordillera occidental of central Peru: The Journal of Geology, v. 117, p. 499-518.

Black, L.P., Kamo, S.L., Allen, C.M., Davis, D.W., Aleinikoff, J.N., Valley, J.W., Mundil, R., Campbell, I.H., Korsch, R.J., Williams, I.S., and Foudoulis, C., 2004, Improved Pb-206/U-218 microprobe geochronology by the monitoring of a trace-element-related matrix effect; SHRIMP, ID-TIMS, ELA-ICP-MS and oxygen isotope documentation for a series of zircon standards: Chemical Geology, v. 205, p. 115-140.

Bonev, N., Burg, J.-P., and Ivanov, Z., 2006, Mesozoic-Tertiary structural evolution of an extensional gneiss dome – the Kesebir-kardamos dome, eastern Rhodope (Bulgaria-Greece): International Journal of Earth Science, v. 95, p. 318-340.

Bonev, N., and Dilek, Y., 2010, Geochemistry and tectonic significance of proto-ophiolitic metamafic units from the Serbo-Macedonian and western Rhodope massifs (Bulgaria-Greece): International Geology Review., v. 52, p. 298-335.

Bonev, N., Dilek, Y., Hanchar, J.M., Bogdanov, K., and Klain, L., 2012, Nd-Sr-Pb isotopic composition and mantle sources of Triassic rift units in the Serbo-Macedonian and western Rhodope massifs (Bulgaria-Greece): Geological Magazine, v. 149, p. 146-152.

Brun, J.P., and Sokoutis, D., 2007, Kinematics of the southern Rhodope core complex (North Greece): International Journal of Earth Science., v. 96, p. 1079-1099.

Brun, J.P., and Sokoutis, D., 2010, 45 m.y. of Aegean crust and mantle flow driven by trench retreat: Geology, v. 38, p. 815-818.

Burgath, K., Kockel, F., Mohr, F., Raschka, H., Jung, D., and Mussalam, K., 1980, A complex of sheeted dykes and pillow lavas in the southern part of the Chalkidiki peninsula, Greece [ext. abs.]: International Ophiolite Symposium, 2nd, Nicosia, Cyprus, 1980, Extended Abstracts, p. 20.

Burg, J.-P., Ivanov, Z., Ricou, L.-E., Dimor, D., and Klain, L., 1990, Implications of shear-sense criteria for the tectonic evolution of the Central Rhodope massif, southern Bulgaria: Geology, v. 18, p. 451-454.

Burg, J.-P., Ricou, L.-E., Ivanov, Z., Godfriaux, I., Dimov, D., and Klain, L., 1993, Crustal-scale thrust complex in the Rhodope. Structure and kinematics: Bulletin of the Geological Society of Greece, v. 29, p. 71-85.

Burg, J.-P., Ricou, L.-E., Ivanov, Z., Godfriaux, I., Dimor, D., and Klain, L., 1996, Syn-metamorphic nappe complex in the Rhodope Massif. Structure and kinematics: Terra Nova, v. 8, p. 6-15.

Christofides, G., D'Amico, C., Del Moro, A., Eleftheriadis, G., and Kyriakopoulos, C., 1990, Rb-Sr-geochronology and geochemical characters of the Sithonia plutonic complex (Greece): European Journal of Mineralogy, v. 2, p. 79-87.

Christofides, G., Koroneos, A., Liati, A., and Kral, J., 2007, The A-type Kerkini granitic complex in north Greece: geochronology and geodynamic implications: Bulletin of the Geological Society of Greece, v. 40, p. 700-711.

de Boorder, H., Spakman, W., White, S.H., and Wortel, M.J.R., 1998, Late Cenozoic mineralization, orogenic collapse and slab detachment in the European Alpine belt: Earth and Planetary Letters, v. 164, p. 569-575.

De Wet, A.P., Miller, J.A., Bickle, M.J., and Chapman, H.J., 1989, Geology and geochronology of the Arnea, Sithonia and Ouranoupolis intrusions, Chalkidiki peninsula, northern Greece: Tectonophysics, v. 161, p. 65-79.

Dimitriadis, S., Kondopoulou, D., and Atzemoglou, A., 1998, Dextral rotations and tectonomagmatic evolution of the southern Rhodope and adjacent regions (Greece): Tectonophysics, v. 299, p. 159-173.

Dinter, D.A., 1998, Late Cenozoic extension of the Alpine collisional orogen, northeastern Greece: origin of the north Aegean basin: Geological Society of America Bulletin, v. 110, p. 1208-1230.

Dinter, D.A., Macfarlane, A., Hames, W., Isachsen, C., Bowring, S., and Royden, L., 1995, U-Pb and 40Ar/39Ar geochronology of the Symvolon granodiorite: implications for the thermal and structural evolution of the Rhodope metamorphic core complex, northeastern Greece: Tectonics, v. 14(4), p. 886-908.

Diodorus Siculus, Library of history volume VIII, books 16.66-17, Welles, B.C., trans., Loeb Classical Library 422: Cambridge, MA, Harvard University Press, 1963.

Dixon, J.E., and Dimitriadis, S., 1984, Metamorphosed ophiolitic rocks from the Serbo-Macedonian Massif near lake Volvi, north-east Greece, in Dixon, J.E., and Robertson, A.H.F., eds., The geological evolution of the eastern Mediterranean: Geological Society of London Special Publication, v. 17, p. 603-618.

Dragić, D., Mišković, A., Hart, C., Tosdal, R., Dunav, P.F., and Glisic, S., 2014, Spatial and temporal relations between epithermal and porphyry style mineralization in the Lece magmatic complex, Serbia [ext. abs.]: Society of Economic Geologists 2014 Conference: Building Exploration Capability for the 21st Century, Keystone, Colorado, 2014, Extended Abstracts.

Eldorado Gold Corporation, 2016, Resources and reserves: Accessed February 22, 2016, (http://www.eldoradogold.com/assets/resources-and-reserves/).

Eliopoulos, D.G., and Economou-Eliopoulos, M., 1991, Platinum-group elements and gold contents in the Skouries porphyry copper deposit, Chalkidiki peninsula, northern Greece: Economic Geology, v. 86, p. 740-749.

Eliopoulos, D.G., and Kilias, S.K., 2011, Marble-hosted submicroscopic gold mineralization at Asimotrypes area, Mount Pangeon, southern Rhodope core complex, Greece: Economic Geology, v. 106, p. 751-780.

Eliopoulos, D.G., Economou-Eliopoulos, M., and Zelyaskova-Panayiotova, M., 2014, Critical factors controlling Pd and Pt potential in porphyry Cu-Au deposits: evidence from the Balkan Peninsula: Geosciences, v. 4, p. 31-49.

Forward, P., Francis, A., and Liddell, N., 2010, Technical report on the Stratoni project Pb-Zn-Ag deposit, northern Greece: European Goldfields Limited, NI 43-101 Report, 54 p.

Frei, R., 1992, Isotope (Pb-Rb-Sr-S-O-C-U-Pb) geochemical investigations of Tertiary intrusions and related mineralizations in the Serbo-Macedonian (Pb-Zn, Sb+Cu-Mo metallogenetic) province in northern Greece: Unpublished Ph.D. thesis, Zürich, Switzerland, ETH, 231 p.

Frei, R., 1995, Evolution of mineralizing fluid in the porphyry copper system of the Skouries deposit, northeast Chalkidiki (Greece): Evidence from combined Pb-Sr and stable isotope data: Economic Geology, v. 90, p. 746-762.

Frei, R., 1996, The extent of inner mineral isotope equilibrium: a systematic bulk U-Pb and Pb step leaching (PbSL) isotope study of individual minerals from the Tertiary granite of Jerissos (northern Greece): European Journal of Mineralogy, v. 8, p. 1175-1189.

Fytikas, M., Innocenti, F., Manetti, P., Mazzuoli, R., Peccerillo, A., and Villari, L., 1984, Tertiary to Quaternary evolution of volcanism in the Aegean region, in Dixon, J.E., and Robertson, A.H.F., eds., The geological evolution of the eastern Mediterranean: Geological Society of London Special Publication, v. 17, p. 687-699.

Gautier, P., Brun, J.-P., Moriceau, R., Sokoutis, D., Martinod, J., and Jolivet, L., 1999, Timing, kinematic and cause of Aegean extension: a scenario based on a comparison with simple analogue experiments: Tectonophysics, v. 315, p. 31-72.

Gilg, H.A., 1993, Geochronology (K-Ar), fluid inclusion, and stable isotope (C, H, O) studies of skarn, porphyry copper, and carbonate-hosted Pb-Zn (Ag, Au) replacement deposits in the Kassandra mining district (eastern Chalkidiki, Greece): Unpublished Ph.D. thesis, Zürich, Switzerland, ETH, 153 p.

Gilg, H.A., Frei, R., Kalogeropoulos, S.I., Nicolaou, M., 1992, Metamorphism and polygenesis of the Madem Lakkos polymetallic sulfide deposit, Chalkidiki, Greece – a discussion: Economic Geology, v. 87, p. 1184-1193.

Gilg, H.A., and Frei, R., 1994, Chronology of magmatism and mineralization in the Kassandra mining area, Greece: The potentials and limitations of dating hydrothermal illites: Geochimica et Cosmochimica Acta, v. 58, p. 2107-2122.

Haines, H.S., 1998, A structural synthesis for sector Vb of the Madem Lakkos polymetallic sulfide deposit – Northeast Greece: Unpublished M.Sc. thesis, London, United Kingdom, The University of London, 81 p.

Hahn, A., Naden, J., Treloar, P.J., Kilias, S.P., Rankin, A.H., and Forward, P., 2012. A new timeframe for the mineralization in the Kassandra mine district, N Greece: deposit formation during metamorphic core complex exhumation: European Mineralogical Conference, v. 1, 1EMC2012-742.

Hanson, G., 1980, Rare earth elements in petrogenetic studies of igneous systems: Annual Review of Earth and Planetary Sciences, v. 8, p. 371-406.

Heinrich, C.A., and Neubauer, F., 2002, Cu-Au-Pb-Zn-Ag metallogeny of the Alpine-Balkan-Carpathian-Dinaride geodynamic province: Mineralium Deposita, v. 37, p. 533–540.

Himmerkus, F., Zachariadis, P., Reischmann, T., and Kostopoulos, D.K., 2005, The mafic complexes of the Athos-Volvi-Zone – a suture zone between the Serbo-Macedonian massif and the Rhodope massif?: Geophysical Research Abstracts, v. 7., p. 10, 240.

Himmerkus, F., Reischmann, T., and Kostopoulos, D.K., 2006, Late Proterozoic and Silurian basement units within the Serbo-Macedonian massif, northern Greece: the significance of terrane accretion in the Hellenides, in Robertson, A.H.F., and Mountrakis, D., eds., Tectonic development of the eastern Mediterranean region: Geological Society of London Special Publication, v. 260, p. 35-50.

Himmerkus, F., Anders, B., Reischmann, T., and Kostopoulos, D., 2007, Gondwana-derived terranes in the northern Hellenides, in Hatcher, R.D., Jr., Carlson, M.P., McBride, J.H., and Martínez Catalán, J.R., eds., 4-D framework of continental crust: Geological Society of America Memoir, v. 200, p. 379-390.

Himmerkus, F., Reischmann, T., and Kostopoulos, D.K., 2009a, Serbo-Macedonian revisited: a Silurian basement terrane from northern Gondwana in the Internal Hellenides, Greece: Tectonophysics v. 473, p. 20-35.

Himmerkus, F., Reischmann, T., and Kostopoulos, D.K., 2009b, Triassic rift-related meta-granites in the Internal Hellenides, Greece: Geological Magazine, v. 146(2), p. 252-265.

Himmerkus, F., Zachariadis, P., Reischmann, T., and Kostopoulos, D., 2011, The basement of the Mount Athos Peninsula, northern Greece: insights from geochemistry and zircon ages: Int. J. Earth Sci., v. 101, p. 1467-1485.

Irvine, T.N., and Baragar, W.R.A., 1971, A guide to the chemical classification of the common volcanic rocks: Canadian Journal of Earth Science, v. 8, p. 523-548.

Janković, S., 1997, The Carpatho-Balkanides and adjacent area: a sector of the Tethyan Eurasian metallogenic belt: Mineralium Deposita, v. 32, p. 426-433.

Jolivet, L., Faccenna, C., Huet, B. , Labrousse, L., Le Pourhiet, L., Lacombe, O., Lecomte, E, Burov, E, Denele, Y., Brun, J.P., Philippon, M., Paul, A., Salaun, G., Karabulut, H., Piromallo, C., Monie, P., Gueydan, F., Okay, A.I., Oberhansli, R., Pourteau, A., Augier, R., Gadenne, L, and Driussi, O., 2013, Aegean tectonics: Strain localization, slab tearing and trench retreat: Tectonophysics, v. 597-598, p. 1-33.

Jones, C.E., Tarney, J., Baker, J.H., and Gerouki, F., 1992, Tertiary granitoids of Rhodope, northern Greece: magmatism related to extensional collapse of the Hellenic Orogen?: Tectonophysics, v. 210, p. 295-314.

Kalogeropoulos, S.I., Economou, G.S., Gerouki, F., Karamonou, E., Kougoulis, C., and Perlikos, P., 1989a, The mineralogy and geochemistry of the Stratoni granodiorite and its metallogenetic significance: Bulletin of the Geological Society of Greece, v. 25, p. 225-243.

Kalogeropoulos, S.I., Kilias, S.P., Bitzios, D.C., Nicolaou, M., and Both, R.A., 1989b, Genesis of the Olympias carbonate-hosted Pb-Zn (Au, Ag) sulfide ore deposit, eastern Chalkidiki peninsula, northern Greece: Economic Geology, v. 84, p. 1210-1234.

Kalogeropoulos, S.I., Frei, R., Nikolaou, M., and Gerouki, F., 1990, Origin and metallogenetic significance of the Tertiary Stratoni granodiorite, Chalkidiki, N. Greece: isotope and chemical evidence: Bulletin of the Geological Society of Greece, v. 26, p. 23-38.

Kalogeropoulos, S.I., Gerouki, F., and Papadopoulos, C., 1991, Mineralogy-geochemistry-genesis and metallogenetic significance of lamprophyres from the Stratoni-Olympias area Kerdilia formation, eastern Chalkidiki: Bulletin of the Geological Society of Greece, v. 27, p. 161-173.

Kay, S.M., and Mpodozis, C., 2001, Central Andean ore deposits linked to evolving shallow subduction systems and thickening crust: GSA Today, v. 11, No. 3, p. 4-9.

Kilias, S.P., Kalogeropoulos, S.I., and Konnerup-Madsen, J., 1996, Fluid inclusion evidence for the physicochemical conditions of sulfide deposition in the Olympias carbonate-hosted Pb-Zn(Au, Ag) sulfide ore deposit, E. Chalkidiki peninsula, N. Greece: Mineralium Deposita, v. 31, p. 394-406.

Kilias, A., Falalakis, G., and Mountrakis, D., 1999, Cretaceous-Tertiary structures and kinematics of the Serbomacedonian metamorphic rocks and their relation to the exhumation of the Hellenic hinterland (Macedonia, Greece): International Journal of Earth Sciences, v. 88, p. 513-531.

Kockel, F., Mollat, H., and Gundlach, H., 1975, Hydrothermally altered and (copper-) mineralized porphyritic intrusions in the Serbo-Macedonian massif (Greece): Mineralium Deposita, v. 10, p. 195-204.

Kockel, F., Mollat, H., and Walther, H., 1977, Erläuterungen yur geologischen karte der Chalkidiki und agrenzender Gebiete 1:100000 (Nord-Griechenland): Bundesanstalt für Geowissenschaften Rohstoffe, Hannover, p. 1-119.

Krenn, K., Bauer, C., Proyer, A., Klözli, U., and Hoinkes, G., 2010, Tectonometamorphic evolution of the Rhodope orogen: Tectonics, v. 29, TC4001.

Kroll, T., Müller, D., Seifert, T., Herzig, P.M., and Schneider, A., 2002, Petrology and geochemistry of the shoshonite-hosted Skouries porphyry Cu-Au deposit, Chalkidiki, Greece: Mineralium Deposita, v. 37, p. 137-144.

Kydonakis, K., Gallagher, K., Brun, J.-P., Jolivet, M., Gueydan, F., and Kostopoulos, D., 2014, Upper Cretaceous exhumation of the western Rhodope Metamorphic Province (Chalkidiki peninsula, northern Greece): Tectonics, v. 33, p. 1113-1132.

Lips, A.L., 2002, Correlating magmatic-hydrothermal ore deposit formation over time with geodynamic processes in SE Europe: Geological Society of London Speccial Publication, v. 204, p. 69-79.

Lips, A, L.W., White, S.H., and Wijbransb, J.R., 2000, Middle-Late Alpine thermotectonic evolution of the southern Rhodope Massif, Greece: Geodinamica Acta, v. 13, p. 281-292.

Lu, J.Y., Loucks, R.R., Fiorentini, M.L., Yang, Z.M., and Hou, Z.Q., 2015, Fluid flux melting generated postcollisional high Sr/Y copper ore-forming water-rich magmas in Tibet: Geology, v. 43, p. 583-586.

Ludwig, K.R., 2003, Isoplot 3.09 - a geochronological toolkit for Microsoft Excel: Berkeley Geochronology Center, Special Publication 4.

Marchev, P., Kaiser-Rohrmeier, M., Heinrich, C., Ovtcharova, M., von Quadt, A., and Raicheva, R., 2005, 2: Hydrothermal ore deposits related to post-orogenic extensional magmatism and core complex formation: the Rhodope massif of Bulgaria and Greece: Ore Geology Reviews, v. 27, p. 53-89.

McFall, K.A., Roberts, S., Teagle, D., Naden, J., Lusty, P., and Boyce, A., 2016, The origin and distribution of critical metals (Pd, Pt, Te & Se) within the Skouries Cu-Au porphyry deposit, Greece: Mineral Deposits Study Group meeting, 39th, Dublin, Ireland, 2016, Extended Abstracts.

Megaw, P.K.M., Ruiz, J., and Titley, S.R., 1988, High-temperature, carbonate-hosted Ag-Pb-Zn(Cu) deposits of northern Mexico: Economic Geology, v. 83, p. 1856-1885.

Middlemost, E.A.K., 1994, Naming materials in the magma/igneous rock system: Earth-Science Reviews, v. 37, p. 215-224.

Müller, D., and Groves, D.L., 2000, Potassic igneous rocks and associated gold-copper mineralization: New York, springer, 252 p.

Nebel, M.L., 1989, Metamorphism and polygenesis of the Madem Lakkos polymetallic sulfide deposit, Chalkidiki, Greece: Unpublished Ph.D. thesis, Golden, Colorado, Colorado School of Mines, 215 p.

Nebel, M.L., Hutchinson, R.W., and Zartman, R.E., 1991, Metamorphism and polygenesis of the Madem Lakkos polymetallic sulfide deposit, Chalkidiki, Greece, Economic Geology., v. 86, p. 81-105.

Neubauer, W.H., 1957, Geologie der blei-zink reichen kieslagerstätten von Kassandra (Chalkidike, Griechenland): Berg- und Hüttenmännische Monatshefte, v. 102, p. 1-16.

Neubauer, F., 2002, Contrasting late Cretaceous with Neogene ore provinces in the Alipine-Balkan-Carpathian-Dinaride collision belt, in Blundell, D.L., Neubauer, F., and von Quadt, A., eds., The timing and location of major ore deposits in an evolving orogen: Geological Society of London Special Publication, v. 204, p. 81-102.

Nicolaou, M.N., 1960, L'intrusion granitique dans la région de Stratoni-Olympiade et sa relation avec la métallogenèse: Annales Géologiques des Pays Helléniques, v. 11, p. 214-265.

Nicolaou, M.N., 1964, The mineralogy and micrography of the sulphide ores of Kassandra mines, Greece: Annales Géologiques des Pays Helléniques, v. 16, p. 111-139.

Nicolaou, M.N., 1969, Recent research on the composition of the Kassandra mines orebodies: Praktika tes Academias Athenon, v. 44, p. 82-93 (in Greek with English abstract).

Papadakis, A., 1971, On the age of the granitic intrusions near Stratonion Chalkidiki, Greece: Annales Géologiques des Pays Helléniques, v. 23, p. 297-300.

Papanikolaou, D., 2013, Tectonostratigraphic models of the Alpine terranes and subduction history of the Hellenides: Tectonophysics, v. 595-596, p. 1-24.

Paton, C., Hellstrom, J., Paul, B., Woodhead, J., and Hergt, J., 2011, Iolite: Freeware for the visualization and processing of mass spectrometric data: Journal of Analytical Atomic Spectrometry, v. 26, p. 2508-2518.

Pavlides, S.B., and Tranos, M.D., 1991, Structural characteristics of two strong earthquakes in the north Aegean: Ierissos (1932) and Agios Efstratios (1968): Journal of Structural Geology, v. 13, p. 205-214.

Peccerillo, A., and Taylor, S.R., 1976, Geochemistry of Eocene calc-alkaline volcanic rocks from the Kastamonu area, northern Turkey: Contributions to Mineralogy and Petrology, v. 58, p. 63-81.

Pe-Piper, G., and Piper, D.J.W., 2002, The igneous rocks of Greece: Stuttgart, Borntraeger, 645 p.

Pe-Piper, G., and Piper, D.J.W., 2006, Unique features of the Cenozoic igneous rocks of Greece, in Dilek, Y., and Pavlides, S., eds., Postcollisional tectonics and magmatism in the Mediterranean region and Asia: Geological Society of America Special Paper, v. 409, p. 259-282.

Pe-Piper, G., Piper, D.J.W., Koukouvelas, I., Dolansky, L.M., and Kokkalas, S., 2009, Postorogenic shoshonitic rocks and their origins by melting underplated basalts: The Miocene of Limnos, Greece: Geological Society of America Bulletin, v. 121, p. 39-54.

Piercey, S.J., 2014, A review of quality assurance and quality control (QA/QC) procedures for lithogeochemical data: Geoscience Canada, v. 41, p. 75-88.

Richards, J.P., and Kerrich, R., 2007, Adakite-like rocks: Their diverse origins and questionable role in metallogenesis: Economic Geology, v. 102, p. 537-576.

Richards, J.P., 2011, High Sr/Y arc magmas and porphyry Cu ± Mo ± Au deposits: Just add water: Economic Geology, v. 106, p. 1075-1081.

Richards, J.P., Spell, T., Rameh, E., Razique, A., and Fletcher, T., 2012, High Sr/Y magmas reflect arc maturity, high magmatic water content, and porphyry Cu ± Mo ± Au potential: Examples from the Tethyan arcs of central and eastern Iran and western Pakistan: Economic Geology, v. 107, p. 295-332.

Rickwood, P.C., 1989, Boundary lines within petrologic diagrams which use oxides of major and minor elements: Lithos, v. 22, p. 247-263.

Ricou, L.E., Burg, J.-P., Godfriaux, I., and Ivanov, Z., 1998, Rhodope and Vardar: the metamorphic and the olistostromic paired belts related to the Cretaceous subduction under Europe: Geodinamica Acta, v. 11, p. 285-309.

Ring, U., Glodny, J., Will, T., and Thomson, S., 2010, The Hellenic subduction system: high-pressure metamorphism, exhumation, normal faulting, and large-scale extension: Annual Reviews of Earth and Planetary Sciences, v.38, p. 45-76.

Rock, N.M.S., 1991, Lamprophyres: Glasgow, Blackie, 285 p.

Rollinson, H. R., 1993, Using geochemical data: Evaluation, presentation, interpretation: London, Longman, 352 p.

Rudnick, R.L., and Gao, S., 2003, Composition of the continental crust, in Holland, H.D., and Turekian, K.K., eds.: Treatise on Geochemistry, v. 3, p. 1-64.

Serafimovski, T., 2000, The Lece-Chalkidiki metallogenic zone: geotectonic setting and metallogenic features: Geologija, v. 42, p. 159-164.

Serafimovski, T., Stefanova, V., and Volkov, A.V., 2010, Dwarf copper-gold porphyry deposits of the Buchim-Damjan-Borov Dol ore district, Republic of Macedonia (FYROM): Geology of Ore Deposits, v. 52, p. 179-195.

Sláma, J., Košler, J., Condon, D.J., Crowley, J.L., Gerdes, A., Hanchar, J.M., Horstwood, M.S.A., Morris, G.A., Nasdala, L., Norberg, N., Schaltegger, U., Schoene, B., Tubrett, M.N., and Whitehouse, M.J., 2008, Plesovice zircon – a new natural reference material for U-Pb and Hf isotopic microanalysis: Chemical Geology, v. 249, p. 1-35.

Siron, C.R., Thompson, J.F.H., Rhys, D., and Baker, T., 2014, Structural framework of Au-rich porphyry and carbonate-hosted replacement deposits of the Kassandra mining district, northern Greece [ext. abs.]: Society of Economic Geologists 2014 Conference: Building Exploration Capability for the 21st Century, Keystone, Colorado, 2014, Extended Abstracts.

Stefanova, E., Donkova, A., Georgiev, S., Marchev, P., and Waelle, M., 2012, Llovitsa porphyry Cu-Au deposit: sequence of vein formation and sulfide deposition, in von Quadt, A., and Serafimovski, T., eds., Diversity of copper and gold deposits in the eastern European Balkan, Carpathian and Rhodopean belts: tectonic, magmatic and geochronological investigations: SCOPES Project - International conference, Stip, Macedonia, p. 16.

Strmić Palinkaš, S., Palinkaš, L.A., Renac, C., Spangenberg, J.E., Lüders, V., Moldar, F., and Maliqi, G., 2013, Metallogenic model of the Trepča Pb-Zn-Ag skarn deposit, Kosovo: evidence from fluid inclusions, rare earth elements, and stable isotope data: Economic Geology, v. 108, p. 135-162.

Sun, S.S., and McDonough, W.F., 1989, Chemical and isotopic systematics of oceanic basalts: implications for mantle composition and processes, in Saunders, A.D., and Norry, M.J., eds., Magmatism in the ocean basins: Geological Society of London Special Publication no. 42, p. 313–345.

Tafti, R., Mortensen, J.K., Lang, J.R., Rebagliati, and Oliver, J.L., 2009, Jurassic U-Pb and Re-Os ages for the newly discovered Xietongmen Cu-Au porphyry district, Tibet, PRC: Implications for metallogenic epochs in the southern Gangdese belt: Economic Geology, v. 104, p. 127-136.

Thompson, T.B., and Arehart, G.B., 1990, Geology and the origin of ore deposits in the Leadville district, Colorado: Part I. Geologic studies of orebodies and wall rocks, in Beaty, D.W., Landis, G.P., and Thompson, T.B., eds., Carbonate-hosted sulfide deposits of the central Colorado mineral belt: Economic Geology Monograph 7, p. 130-155.

Tobey, E., Schneider, A., Algería, A., Olcay, L., Perantonis, G., and Quiroga, J., 1998, Skouries porphyry copper-gold deposit, Chalkidiki, Greece: Setting, mineralization and resources, in Porter, T.M., ed., Porphyry and hydrothermal copper and gold deposits: A global perspective; Adelaide, PGC Publishing, p. 175-184.

Tompouloglou, C., 1981, Les minéralisations tertiares, type cuivre porphyrique, du massif Serbo-Macédonien (Macédoine, Grèce) dans leur contexte magmatique (avec un traitment géostatistique pour les données du prospect d'Alexia): Unpublished Ph.D. thesis, Paris, France, Ecole Nationale Supérieure des Mines de Paris, 204 p.

Turpaud P., and Reischmann, T., 2003, Zircon ages of granitic gneisses from the Rhodope (N. Greece), determination of basement age evidences for a Cretaceous intrusive event: Geophysical Research Abstracts, 5:04435.

Wawrzenitz, N., and Krohe, A., 1998, Exhumation and doming of the Thassos metamorphic core complex (S Rhodope, Greece): structural and geochronological constrains: Tectonophysics, v. 285, p. 301-312.

Wilkinson, J.J., 2013, Triggers for the formation of porphyry ore deposits in magmatic arcs: Nature Geoscience, v. 6, p. 917-925.

Wilson, A.J., 2003, The geology, genesis and exploration context of the Cadia gold-copper porphyry deposits, NSW, Australia: Unpublished Ph.D. thesis, Hobart, University of Tasmania, 335 p.

Wortel, M.J.R., and Spakman, W., 2000, Subduction and slab detachment in the Mediterranean-Carpathian region: Science, v. 290, p. 1910-1917.

Wüthrich, E., 2009, Low temperature thermochronology of the northern Aegean Rhodope Massif: Unpublished Ph.D. thesis, Zürich, Switzerland, ETH, 210 p.

Zachu, K.E., 1963, Discovery of a copper deposit in Chalkidiki peninsula, N-Greece: Geological and Geophysical Research, v. 8, p. 1-26.

CHAPTER 3

STRUCTURAL CONTROLS ON PORPHYRY AU-CU AND AU-RICH POLYMETALLIC CARBONATE-HOSTED REPLACEMENT DEPOSITS OF THE KASSANDRA MINING DISTRICT

The Serbo-Macedonian Metallogenic Province (Janković, 1997; Serafimovski, 2000) of the Tethyan Mineral Belt forms a northwest-trending zone of porphyry Au-Cu, Cu skarn, and Au-rich polymetallic vein and carbonate-hosted replacement deposits extending from Serbia and Kosovo, through the Republic of Macedonia, and northern Greece. Deposits within this belt are associated with Oligo-Miocene intrusions occurring within a tectonically complex environment (Heinrich and Neubauer, 2002). The most economically significant district in the Greek segment of the Serbo-Macedonian Metallogenic Province is the Kassandra Mining District which contains about 12 Moz Au hosted by porphyry and polymetallic carbonate replacement orebodies. The Skouries porphyry Au-Cu deposit contains a measured and indicated resource of 289.3 Mt grading 0.58 g/t Au and 0.43% Cu. The Olympias carbonate replacement deposit contains a measured and indicated resource of 15.1 Mt at 8.97 g/t Au, 146 g/t Ag, 4.9% Pb and 6.5% Zn (Eldorado Gold Corp., 2017). Approximately 13.5 Mt of Ag-Pb-Zn ore was historically produced from the Madem Lakkos carbonate replacement deposit (Forward et al., 2010) with the nearby and actively producing Mavres Petres mine containing a measured and indicated resource of 0.55 Mt at 212 g/t Ag, 8.1% Pb and 11.0% Zn (Eldorado Gold Corp., 2017).

Zircon U-Pb geochronology defines two magmatic episodes that took place within the Kassandra Mining District during the late Oligocene and early Miocene, each of which corresponds to a major metallogenic event (Frei, 1992, 1995; Gilg, 1993; Gilg and Frei, 1994; Hahn et al., 2012; Siron et al., 2016). Previous studies (e.g., Haines, 1998) recognized the Stratoni fault zone as a major mineralized corridor that hosts the Mavres Petres and Madem Lakkos Au-Ag-Pb-Zn-Cu carbonate replacement style massive sulfide deposit. Based on crosscutting relationships with respect to dated igneous intrusions,

sulfide ore is interpreted to have formed syn- to post-emplacement of the late Oligocene (~25 Ma) Fisoka and Stratoni granodiorite stocks (Siron et al., 2016). The Olympias Au-Ag-Pb-Zn-Cu carbonate replacement deposit, located to the north of the Stratoni fault zone, occurs within a folded marble-gneiss sequence and is closely associated with the Kassandra fault. Sulfide ore from the Olympias deposit shows mineralogical and textural similarities to the Mavres Petres deposit (Siron et al., 2016). These similarities and an arsenopyrite Re-Os age has led previous workers to assign an Oligo-Miocene age to the Olympias deposit (Kalogeropoulos et al., 1989; Hahn et al., 2012; Hahn, 2014).

The Skouries Au-Cu deposit is associated with a narrow, steeply plunging, pipe-shaped and multiphase quartz monzonite porphyry intrusion (Eliopoulos and Economou-Eliopoulos, 1991; Frei, 1992, 1995; Tobey et al., 1998; Kroll et al., 2002; Hahn et al., 2012; Hahn, 2014; McFall et al., 2016; Siron et al., 2016). Published K-Ar whole-rock and zircon U-Pb ages from the Skouries porphyry, and a hydrothermal biotite ^{40}Ar-^{39}Ar cooling age are within error and define a 20-19 Ma age range for Au-Cu mineralization (Frei, 1992, 1995; Hahn et al., 2012; Hahn, 2014). Based on these ages, the Skouries deposit is interpreted to be ~4-5 m.y. younger than the fault-controlled carbonate-hosted replacement massive sulfide deposits to the north (Siron et al., 2016).

In spite of the economic importance of the Kassandra Mining District and the demonstrable association of the Madem Lakkos and Mavres Petres deposits with the Stratoni fault zone, little previous work has been done to assess the structural controls on ore deposit formation. Previous work is limited to a study of the Stratoni fault zone on one level in the now-closed Madem Lakkos mine by Haines (1998), and district-scale reviews in unpublished consulting reports. This study presents the results of research focused on characterizing the kinematic and structural controls on mineralization, and identifying the structural architecture that facilitated faulting and Oligo-Miocene magmatism associated with porphyry and carbonate replacement mineralization. We present detailed geologic maps and cross sections from the Olympias, Madem Lakkos, Mavres Petres, and Skouries deposits based on field and drill core observations, structural measurements and fault kinematic analyses, as well as whole-rock geochemical

data. Procedural and analytical methods, and data tables are located in the Appendix. The location and importance of the Stratoni fault zone as a potential terrane bounding structure is discussed in the context of whole-rock geochemistry and the age of the metamorphic units from previous zircon U-Pb data. The objective of this study is to: (i) define the structural architecture and deformation history of the district, (ii) characterize the style, timing, and significance of faulting, and (iii) identify the major structural controls that focused polymetallic carbonate replacement and porphyry Au-Cu systems within the Kassandra Mining District.

Lithotectonic Setting

The Hellenic orogen of northern Greece originated from the collision of the Apulian and Pelagonian microcontinents with the previously accreted Serbo-Macedonian and Rhodope continental fragments to the Eurasian continental margin during the Late Cretaceous to Eocene (Pe-Piper and Piper, 2006). Convergence of microcontinents and subduction of oceanic lithosphere during this event led to magmatism resulting from slab detachment or lithospheric delamination assisted by rollback of the subducting slab during post-collisional back arc extension of the subducted wedge (de Boorder et al., 1998; Wortel and Spakman, 2000; Lips, 2002; Neubauer, 2002; Brun and Sokoutis, 2010; Jolivet and Brun, 2010; Krenn et al., 2010; Ring et al., 2010; Jolivet et al., 2013; Papanikolaou, 2013). Retreat of the subducting slab resulted in widespread extension that manifested in the unroofing of deep-crustal lithotectonic blocks from the Late Cretaceous through to the late Miocene (Dinter and Royden, 1993; Sokoutis et al., 1993; Wawrzenitz and Krohe, 1998; Krohe and Mposkos, 2002; Brun and Sokoutis, 2007; Brun and Faccenna, 2008; Wüthrich, 2009; Kydonakis et al., 2014; Kounov et al., 2015).

Northeastern Greece is principally underlain by rocks belonging to the Rhodope metamorphic province, defined as a crustal-scale, amphibolite-facies accretionary complex consisting of southwest-verging stacked nappes that lie within the overriding plate of the Hellenic subduction zone (Burg et al., 1990, 1996; Ricou et al., 1998; Gautier et al., 1999; Bonev et al., 2006; Jahn-Awe et al., 2010; Krenn et

al., 2010; Burg, 2012). Bordered by the Maritza dextral strike-slip fault in southern Bulgaria, the Rhodope metamorphic province extends under the Thrace basin of northeastern Greece and is bounded by the ophiolitic Vardar Suture Zone, which outcrops on the western Chalkidiki Peninsula (Figure 3.1; Ricou et al., 1998). The Rhodope metamorphic province comprises the eastern and structurally stacked Thracia and Rhodope lithotectonic terranes, and the western Serbo-Macedonian terrane. The upper tectonic Permo-Carboniferous Rhodope unit, which hosts Late Jurassic orthogneisses, is separated from the lower Thracia terrane by the southwest verging Nestos thrust fault (Figure 3.1; Turpaud and Reischmann, 2010). The Permo-Carboniferous Thracia terrane consists of the lower Pangeon and upper Kerdilion marble-gneiss sequences. On the Chalkidiki Peninsula, the Kerdilion unit is tectonically juxtaposed with Ordovician to Silurian orthogneiss and Triassic leucogranites belonging to the Vertiskos unit of the Serbo-Macedonian terrane (Figure 3.1; Himmerkus et al., 2007).

The Kassandra Mining District is underlain by the Vertiskos and Kerdilion units (Figure 3.1; Kockel et al., 1971, 1977; Brun and Sokoutis, 2007), which are interpreted to be the upper and lower tectonic units respectively of the Serbo-Macedonian terrane (Kockel et al., 1971). The Vertiskos unit is interpreted to be a Gondwanan-derived continental magmatic arc that was accreted onto the European margin in the Carboniferous (Himmerkus et al., 2006, 2007, 2009a). In contrast, zircon ages and whole-rock geochemical data suggest that the Kerdilion unit originated from a Permo-Carboniferous magmatic arc, which was overlain by Paleotethyan carbonates, and was subsequently modified by Late Jurassic to Early Cretaceous arc magmatism related to the Neotethyan subduction zone (Turpaud and Reischmann, 2003; Himmerkus et al., 2007, 2011). The contact between the Vertiskos and Kerdilion units has been interpreted in earlier studies as the Stratoni fault zone (e.g., Nebel et al., 1991; Haines, 1998). Himmerkus et al. (2005), however, reassigned the tectonic boundary between these tectonic units to the Athos-Volvi suture zone located in the west and southwest of the district (Figure 3.2).

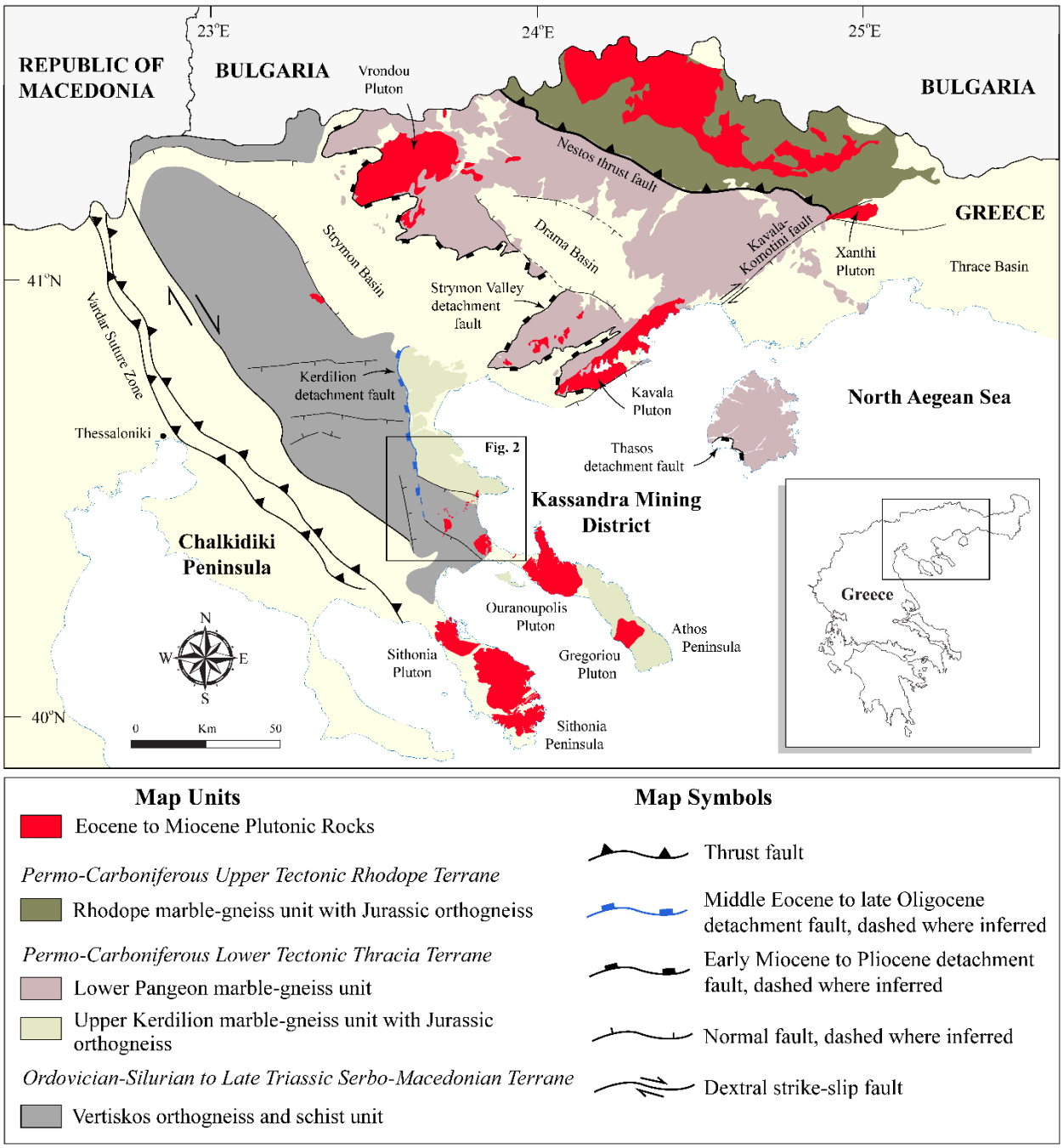

Figure 3.1. Simplified regional geologic map of northeastern Greece modified after Kydonakis et al. (2014). The Maritza fault lies outside of the figure area and only the tectonic units referenced in the text are displayed. The Strymon Valley detachment fault and the Kavala-Komotini fault are after Dinter (1998), the Thasos detachment fault is after Wawrzenitz and Krohe (1998), and the Kerdilion detachment fault is adapted from Brun and Sokoutis (2007).

Ultramafic and mafic rocks outcropping within the Athos-Volvi suture zone belong to the Thermes-Volvi-Gomati ophiolite complex, first described in detail by Dixon and Dimitriadis (1984), and interpreted to represent mantle-derived magmas formed by rifting in a supra-subduction zone setting during the Late Permian to Early Triassic (Himmerkus et al., 2005; Liati et al., 2011; Bonev et al., 2012). Late Triassic anorogenic granites of the Arnea-Kerkini Suite were emplaced within a rift setting that is broadly coeval with the formation of the ophiolitic rocks (Dixon and Dimitriadis, 1984; De Wet et al., 1989; Himmerkus et al., 2005; Christofides et al., 2007; Himmerkus et al., 2009b; Bonev et al., 2012).

Neoproterozoic basement fragments including gneisses of the Arnea-Kerkini Suite, and dismembered segments of the Thermes-Volvi-Gomati ophiolite sequence were incorporated into the Athos-Volvi suture zone during Late Paleozoic to Mesozoic assembly of the European margin during closure of the Neotethyan Vardar Ocean and inception of the Alpine-Hellenic orogeny (Figure 3.2; Dixon and Dimitriadis, 1984; Bonev and Dilek, 2010; Liati et al., 2011).

Accretion of the Vertiskos continental fragment to the European margin was accompanied by regional high-temperature, upper greenschist- to lower amphibolite-facies metamorphism that overprinted an earlier, and discrete high-pressure subduction-related eclogite-facies event (Wawrzenitz and Mposkos, 1997; Lips et al., 2000; Mposkos and Kostopoulos, 2001; Liati, 2005; Turpaud and Reischmann, 2010; Kydonakis et al., 2014, 2016). Syn-metamorphic thrust faulting and exhumation of the Vertiskos unit to mid-crustal levels occurred by early Late Cretaceous time (Kydonakis et al., 2016). The Kerdilion unit, however, underwent amphibolite-facies metamorphism that locally reached anatectic partial melt conditions by the early to middle Eocene, and was subsequently overprinted by retrograde greenschist-facies metamorphism (Kalogeropoulos et al., 1989; Wawrzenitz and Krohe, 1998; Lips et al., 2000). Thermochronological studies suggest contrasting evolutionary paths for the Vertiskos and Kerdilion units (Burg et al., 1995; Brun and Sokoutis, 2007; Kounov et al., 2015; Kydonakis et al., 2016).

Tertiary magmatism and regional extension

Early Eocene subduction-related arc magmatism is evident throughout the Rhodope metamorphic province. Rollback of the subducting slab and back arc extension in the north Aegean region gave way to post-collisional magmatism from the Oligocene to early Miocene (Fytikas et al., 1984; Jones et al., 1992; Dinter et al., 1995; Pe-Piper and Piper, 2002; Ring et al., 2010). A southward migration of the magmatic arc resulted from the retreat of the Hellenic trench from the late Miocene into the Pliocene. This occurred coeval with northward collision of the Arabian plate with Eurasia, facilitating westward extrusion of the Anatolian block into the northern Aegean (Jolivet et al., 2013). Since the middle Miocene, this westward escape of Anatolia has been largely accommodated by regional north-south crustal stretching and dextral displacement on the north Anatolia fault (Armijo et al., 1998; Gautier et al., 1999; Jolivet et al., 2013), which propagated into the north Aegean Sea by approximately 5 Ma (Armijo et al., 1998; Koukouvelas and Aydin, 2002; Allmendinger et al., 2007).

Extensional tectonics have been active in the north Aegean region since the middle to late Eocene beginning with the unroofing of the southern Rhodope core complex in the footwall of the inferred Kerdilion detachment fault (Figure 3.1; Brun and Sokoutis, 2007, 2010). Exposure of the Kerdilion detachment fault is limited and the fault is largely defined by thermochronology. Fission track age patterns from the study area indicate that the footwall Kerdilion unit cooled below the apatite and zircon partial annealing temperatures from 42 Ma through to about 24 Ma coincident with the inferred age of detachment faulting and exhumation of the Kerdilion unit (Wüthrich, 2009; Kounov et al., 2015). A similar conclusion was reached by Brun and Sokoutis (2007) based on the reinterpretation of previously published isotopic cooling ages from the region.

Continued exhumation of the previously unroofed metamorphic dome was accompanied by early Miocene magmatism and accommodated by the Thasos and Strymon Valley detachment faults located northeast of the Kassandra Mining District (Figure 3.1; Dinter and Royden, 1993; Sokoutis et al., 1993; Dinter et al., 1995; Dinter, 1998; Wawrzenitz and Krohe, 1998). Unroofing of the southern Rhodope core

complex continued into the late Pliocene where it was modified by late Pliocene to Quaternary basin-forming normal and strike-slip faults (Dinter, 1998). Exhumation of the southern Rhodope core complex reflects an estimated 120 km of extension accompanied by approximately 30^{o} clockwise rotation of the Chalkidiki block from the middle Eocene to present. Rotation is largely explained by horizontal ductile flow during rise of the metamorphic dome in the area of detachment faulting as inferred from paleomagnetic studies (Dimitriadis et al., 1998; Brun and Sokoutis, 2007).

Regional Structural Framework

The Kassandra Mining District is underlain by metamorphic rocks belonging to the poly-deformed Vertiskos and Kerdilion units (Kockel et al., 1977), including mafic and ultramafic bodies mainly occupying areas around the Gomati and Stratoni fault zones (Figure 3.2). Subduction-related Late Cretaceous to early Eocene calc-alkaline magmatism was followed by the emplacement of post-collisional late Oligocene and early Miocene intrusions along a northeast-trending corridor hosted by both Vertiskos and Kerdilion units (Siron et al., 2016). This section presents lithologic descriptions of these metamorphic basement units based on field and drill core observations, combined with previously published geochronological data. Major deformation events recorded by these rocks are described from structural data collected from surface outcrops.

Metamorphic basement rocks

Metamorphic rocks of the Kerdilion unit to the north of the Stratoni fault zone consist of partially migmatitic quartzo-feldspathic hornblende-biotite gneiss containing intervals of compositionally layered to massive graphite-bearing marble, meta-gabbros composed of massive to strongly layered amphibolite, interspersed bodies of megacrystic plagioclase-microcline orthogneiss, and fine-grained to aplitic granite gneiss (Kockel et al., 1977; Kalogeropoulos et al., 1989; Nebel et al., 1991; Gilg and Frei, 1994). These lithologic units have an arcuate geometry, striking in a north-south direction in the north and becoming

Figure 3.2. Geologic map of the Kassandra Mining District modified after Kockel et al. (1977). The inset map at the top right outlines the northern and southern structural domains referenced in the text. A district-scale cross section along the line A-A' is shown below. Dotted lines represent foliation traces. Coordinates are displayed in the Greek Geodetic Coordinate System (GGRS 87 Greek Grid). Abbreviations are as follows: Aspro Lakkos porphyry stock (As), Fisoka stock (Fs), Madem Lakkos deposit (ML), Mavres Petres deposit (MP), Olympias deposit (OL), Piavitsa prospect (PV), Stratoni stock (St), Skouries deposit (SK), and Tsikara composite stock (Ts).

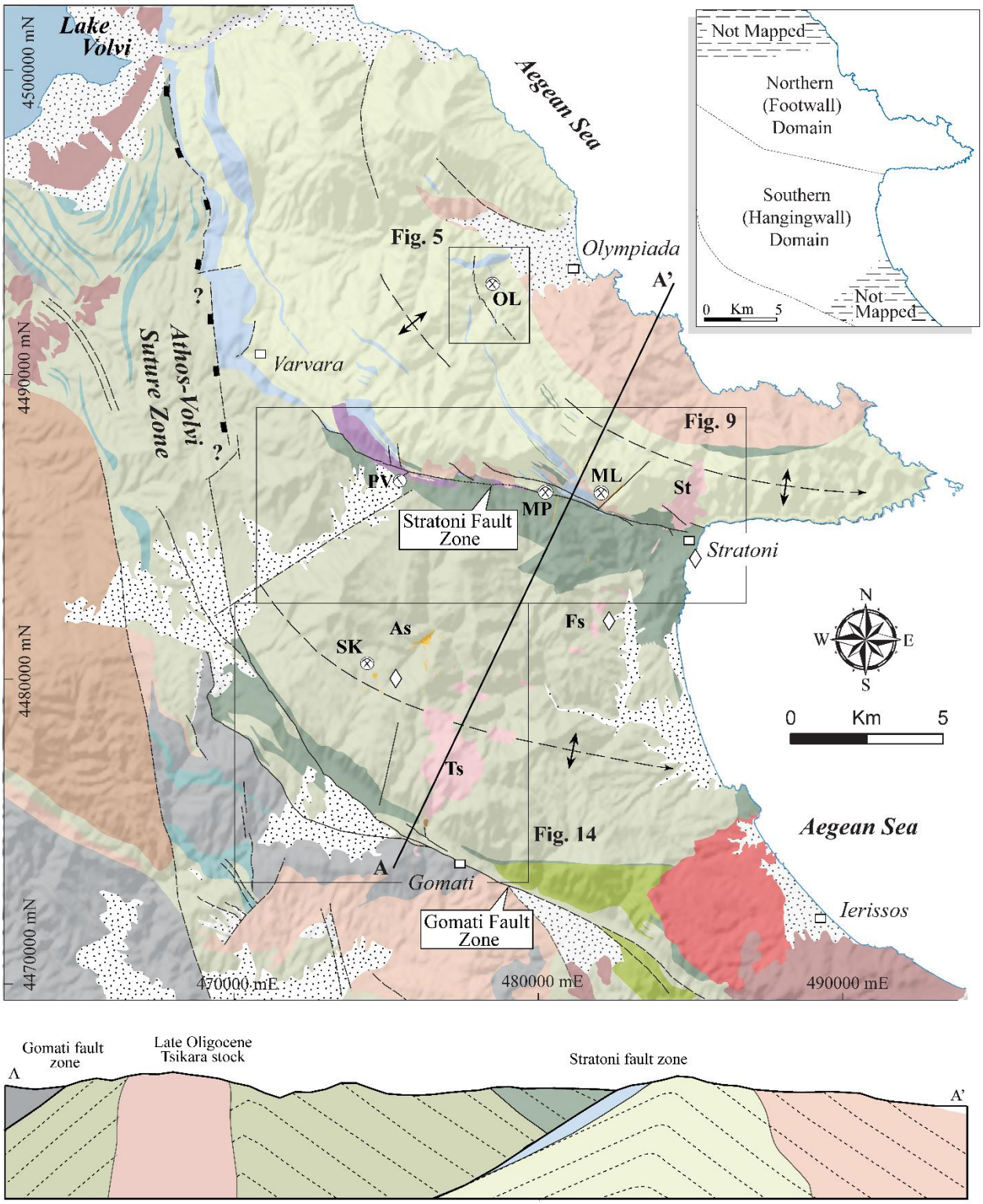
Lake Volvi
Aegean Sea
Not Mapped
Northern (Footwall) Domain
Southern (Hangingwall) Domain
Not Mapped
0 Km 5
Fig. 5
OL
Olympiada
A'
Varvara
Athos-Volvi Suture Zone
?
?
Fig. 9
PV
ML
MP
St
Stratoni Fault Zone
Stratoni
N
W
E
S
0 Km 5
As
SK
Fs
Ts
Fig. 14
A
Gomati
Gomati Fault Zone
Aegean Sea
Ierissos
4500000 mN
4490000 mN
4480000 mN
4470000 mE
470000 mE
480000 mE
490000 mE

Gomati fault zone
Late Oligocene Tsikara stock
Stratoni fault zone
A
A'

Figure 3.2. Continued.

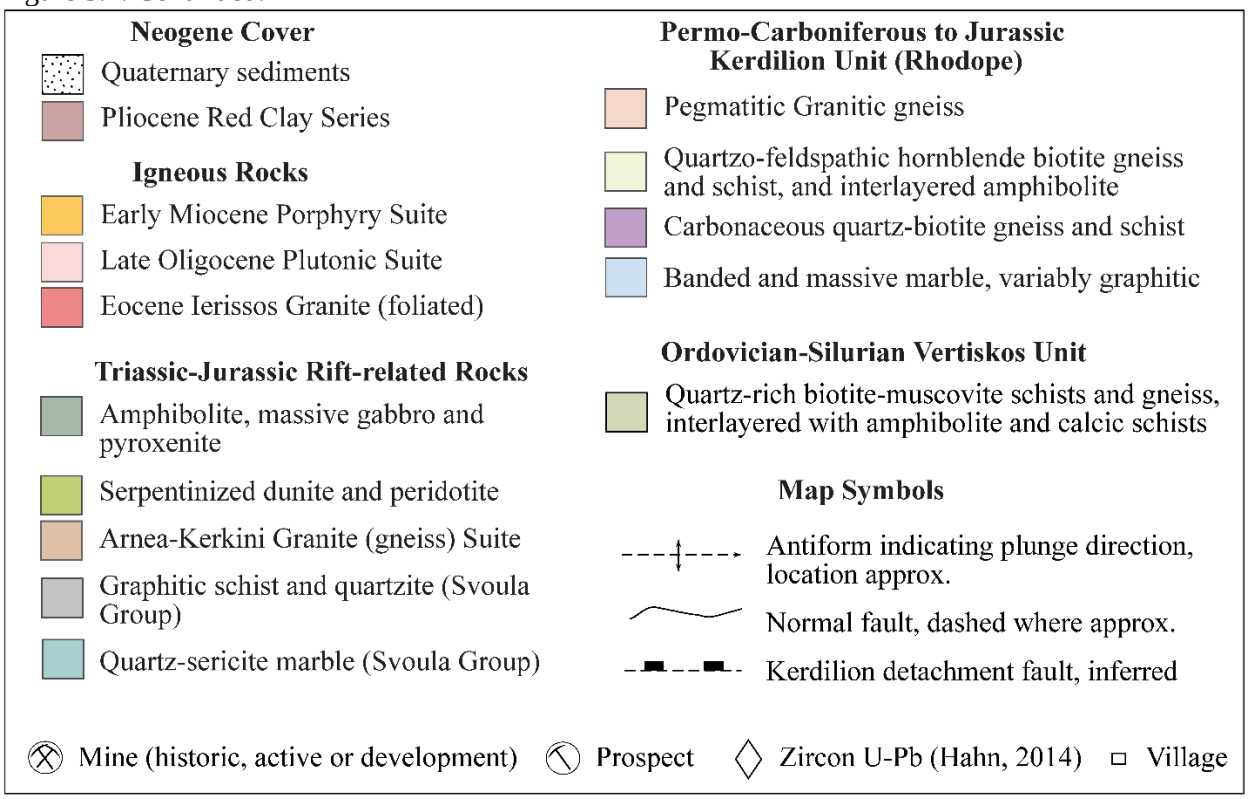

east-west striking near the Stratoni fault zone (Figure 3.2). Middle Jurassic to Early Cretaceous zircon U-Pb and Pb-Pb ages from granitic gneisses of the Kerdilion unit range from 164-134 Ma and are interpreted as primary igneous ages reflecting a period of widespread magmatism within the region (Himmerkus et al., 2011; Hahn, 2014). The hosting lithologies, however, are likely Carboniferous to Permian in age based on inherited zircon cores derived from the orthogneisses (Himmerkus et al., 2011). Pegmatitic dikes and sills occur throughout the Kerdilion unit. These probably represent anatectic partial melts of the metamorphic rock from about the middle Paleocene to middle Eocene (Wawrzenitz and Krohe, 1998; Kalogeropoulos et al., 1989). These dikes commonly contain a penetrative foliation, and may be folded and boudinaged indicating that ductile deformation persisted through at least the middle Eocene (Kalogeropoulos et al., 1989; Gilg and Frei, 1994). Pegmatitic gneisses and dikes are largely absent south of the Stratoni fault zone.

Strongly foliated and variably graphitic garnet-bearing quartz-biotite gneiss and schist (meta-pelites) define a distinct unit that is spatially associated with the Stratoni fault zone (Figure 3.2). This unit

is exposed underground in the Mavres Petres mine and is present in outcrop and drill core at the Piavitsa prospect. Quartz-biotite ± garnet gneiss and schist consist of thinly laminated quartz-rich lenses grading into layers with abundant graphite. Drill core intercepts indicate that the graphitic quartz-biotite gneiss and schist unit is conformable with quartzo-feldspathic biotite gneiss and is interlayered with graphite-bearing marble, calcareous schists, and thin amphibolite layers. The graphitic meta-pelite unit is extensively altered in the Stratoni fault zone where a black, insoluble carbonaceous residue is focused within pressure solution seams, and biotite, feldspar, and garnet are variably altered to white mica-chlorite-carbonate to form a grey, carbonaceous phyllite.

Mafic and ultramafic rocks are exposed to the south and predominately within the hanging wall of the Stratoni fault zone (Figure 3.2), however, thinner mafic layers also occur to the north and extend into the Olympias area. These rocks consist of layered- and massive-textured amphibolite with subordinate pods of variably serpentinized pyroxenite. Amphibolite units that occur to the north of the Stratoni fault zone are interlayered with marble and have contacts that are compositionally gradational with hornblende-bearing quartzo-feldspathic biotite gneisses. Amphibolites in this area are potentially correlative with the Triassic Thermes-Volvi-Gomati ophiolitic complex (Dixon and Dimitriadis, 1984; Bonev and Dilek, 2010; Liati et al., 2011), however, a middle Jurassic zircon U-Pb age of 167 Ma was obtained from feldspar-rich banded amphibolite south of the village of Stratoni (Figure 3.2; Hahn, 2014).

A monotonous sequence of quartz-rich feldspathic to muscovite-biotite-bearing gneiss and schist assigned to the Vertiskos unit occurs to the south of the Stratoni fault zone and the large amphibolite unit described above (Figure 3.2). Minor calcareous calc-silicate schist, marble, and amphibolite are thinly interlayered within the metamorphic sequence. Zircon U-Pb ages (Hahn, 2014) show that the micaceous schist in the Skouries area range from Neoproterozoic (686-576 Ma) to Ordovician (464-450 Ma), which is consistent with the age of the Pan-African Pirgadikia and Vertiskos units of the Serbo-Macedonian terrane, respectively (Himmerkus et al., 2006, 2007). Hahn (2014) additionally identified a broad range of zircon ages from a micaceous schist near the southern amphibolite contact south of the Stratoni fault zone

(Figure 3.2). Three populations of zircon U-Pb ages from Neoproterozoic (699-594 Ma), Ordovician to Silurian (475-428 Ma), and Permian to Triassic (279-228 Ma) correspond to the Pirgadikia unit, Vertiskos unit, and the Arnea-Kerkini granite gneiss suite, respectively (Himmerkus et al., 2006, 2007). This wide distribution of zircon ages, that includes rare Neoarchean zircon cores (2519 Ma), reflects either a complex detrital sedimentary precursor and/or a mélange of structurally imbricated basement units.

In the southernmost parts if the study area, mafic and ultramafic rocks consisting of chlorite-amphibole schist, meta-gabbro, and chromite-bearing serpentinized peridotite and dunite outcrop along the Gomati fault zone (Figure 3.2). These rocks belong to the dismembered Gomati ophiolite body, and are interpreted to be the lowest structural position of the Thermes-Volvi-Gomati ophiolitic complex (Kockel et al., 1977; Dixon and Dimitriadis, 1984; Bonev and Dilek, 2010). This mafic to ultramafic body is mostly hosted by the tectonic mélange of the Athos-Volvi suture zone (Himmerkus et al., 2005).

Tertiary igneous rocks

Three suites of subduction-related and post-collisional igneous rocks outcrop within the Kassandra Mining District. The earliest suite comprises late Paleocene to early Eocene intrusions that are variably deformed. The most significant intrusion from this suite is the c. 53 Ma subduction-related calc-alkaline Ierissos granodiorite (Frei, 1992, 1996; Himmerkus et al., 2011), which outcrops to the southeast of the district (Figure 3.2) and is coeval with the Sithonia, Ouranoupolis and Grigoriou granodiorites located on the Sithonia and Athos peninsulas, respectively (Figure 3.1; De Wet et al., 1989; Christofides et al., 1990; Bébien et al., 2001; Pe-Piper and Piper, 2002). Other intrusions in this suite include foliated granodiorite dikes that outcrop within the Stratoni fault zone between the Stratoni granodiorite stock and the Madem Lakkos deposit. One of these granodiorite dikes yielded a zircon U-Pb crystallization age of 58.0 ± 0.2 Ma (Siron, unpub. data) suggesting that the late Paleocene to Eocene subduction-related igneous event extended to the north into the Kassandra Mining District.

A northeast-trending, 15 km-long belt of post-collisional intrusive rocks of Oligo-Miocene age mostly outcrops between the Gomati and Stratoni fault zones (Figure 3.2), and represents the two youngest intrusive suites in the study area (Gilg and Frei, 1994; Hahn, 2014; Siron et al., 2016). Zircon U-Pb geochronology defines two distinct post-collisional magmatic episodes in the late Oligocene (27-25 Ma) and early Miocene (20-19 Ma). Both igneous suites belong to the high-K calc-alkaline magma series with the younger early Miocene porphyritic intrusions having a more-evolved, shoshonitic geochemistry (Kroll et al., 2002; Siron et al., 2016). The late Oligocene igneous suite includes monzogabbros and granodiorites belonging to the 27.0 ± 0.2 Ma to 26.7 ± 0.3 Ma Tsikara composite stock in the south, and the 25.7 ± 0.4 Ma to 24.5 ± 0.1 Ma variably porphyritic diorite to granodiorite stocks and dikes of Stratoni and Fisoka in the north (Figure 3.2; Siron et al., 2016).

The early Miocene igneous suite includes the 20.6 ± 0.5 Ma (zircon U-Pb; Hahn et al., 2012; Hahn, 2014) Au-Cu-mineralized Skouries quartz monzonite porphyry stock (Figure 3.2). Highly potassic glomerophyric porphyry dikes that crosscut the Stratoni fault zone and the Olympias deposit are interpreted to be early Miocene in age, coeval with the Skouries stock (Siron et al., 2016). Early Miocene magmatism continued with the emplacement of the barren Aspro Lakkos quartz monzonite porphyry stock (19.7 ± 0.1 Ma) and crosscutting trachyandesite black-matrix porphyry dikes dated at 19.6 ± 0.1 Ma (Siron et al., 2016). The youngest stage of magmatism in the district is documented by the 19.2 ± 0.2 Ma trachyandesite black-matrix porphyry dike hosted within the Vathilakkos fault at the Madem Lakkos deposit (Gilg and Frei, 1994; Haines, 1998; Siron et al., 2016).

Deformation events

In this study, the Kassandra Mining District has been divided into two structural domains, north and south of the Stratoni fault zone (inset of Figure 3.2). Structural analyses also focused in the Olympias and Skouries deposit areas to better establish the local structural architecture. Data of ductile structures is displayed in lower-hemisphere, equal-area stereographic projections and is presented in Figure 3.3. Three

deformation episodes are defined here based on the superposition of ductile fabrics. Earlier events may have occurred but are obscured by the intensity of D1 strain and associated metamorphism.

D1 deformation: Gneisses and marbles within the northern domain display a locally preserved compositional layering that is transposed into the plane of a penetrative S1 gneissosity, which affects granitic intrusions as young as 58 Ma (Siron, unpub. data). Foliation is defined by the alignment of peak amphibolite-facies minerals typically consisting of hornblende-biotite-plagioclase ± garnet and feldspathic mineral segregations within quartzo-feldspathic biotite gneiss and amphibolite. In marble, compositional banding is parallel to the plane of S1 foliation (Figure 3.4A). Massive marble that hosts sulfide ore commonly contains aligned graphite flakes that define the S1 fabric. Pegmatites that occupy the metamorphic sequence occur as thin layer-parallel leucosomes within migmatitic intervals of quartzo-feldspathic biotite gneiss and as dikes that crosscut the metamorphic package. Most pegmatites generally exhibit a penetrative S1 foliation (Kalogeropoulos et al., 1989). Within the Olympias deposit area, S1 foliation strikes predominately to the north and uniformly dips to the east as observed from surface outcrops and underground exposures. Orientation of the metamorphic sequence and the S1 foliation abruptly shifts to an east-west strike with a shallow south dip to the north of the deposit area, likely representing a D2 fold (Figure 3.3A). North of the Stratoni fault zone, S1 foliation dips to the north-northeast and south-southwest defining a fold geometry (Figure 3.3B). Asymmetry of granite gneiss and pegmatite boudins within the quartzo-feldspathic biotite gneiss sequence show top-to-the-northeast sense of shear of S1 foliation in the northern domain as similarly noted by Kilias et al. (1999).

Immediately to the south of the Stratoni fault zone, S1 foliation strikes west-northwest and dips predominately toward the north-northeast, discordant to the south dipping Stratoni fault zone (Figure 3.3C). The moderate northeast dip of S1 foliation extends into the Skouries area where S1 becomes south to southwest dipping, thus defining a broad D2 anticlinorium (Figure 3.3D). Foliation traces diverge from the Stratoni fault zone striking north-south parallel to the coastline and roughly following the outcrop pattern of the mafic hanging wall rocks on the eastern margin of the district (Figure 3.2). S1 foliation

Figure 3.3. Lower-hemisphere, equal-area stereographic projections of ductile structural elements subdivided by domain in the study area. Data is contoured at 3σ significance level following the method of Kamb (1959): (A-D) S1 foliation plotted as poles from planes. Best-fit great circle, orthogonal axial distributions, and plunge of the F2 fold axis are plotted as a solid line, black squares, and π symbol respectively; (E-F) S2 cleavage plotted as poles from planes; (G-H) axial planes of F2 folds plotted as poles from planes with corresponding orientation of F2 fold hinges from the Olympias area and Stratoni fault footwall domain; (I-J) axial planes of F2 folds plotted as poles from planes with corresponding orientation of F2 fold hinges from the Skouries area and Stratoni fault hanging wall domain; (K-L) S1-S2 foliation intersection (L2) lineations plotted as lines; (M-N) S3 foliation plotted as poles from planes. Abbreviations are as follows: footwall (FW), hanging wall (HW).

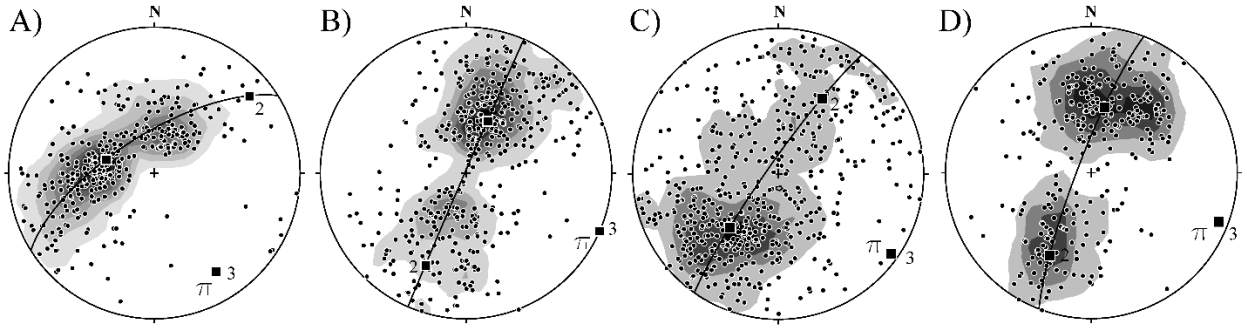

S1 Olympias Area (n=363) | S1 Stratoni FW (n=463) | S1 Stratoni HW (n=568) | S1 Skouries Area (n=310)

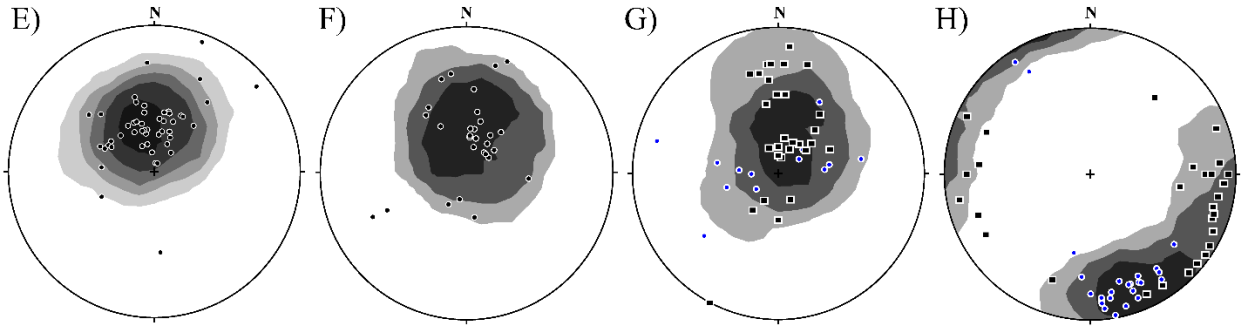

S2 Olympias Area (n=49) | S2 Skouries-Stratoni HW combined (n=31) | F2 Axial Planes Olympias (circle) Stratoni FW (square) combined (n=42) | F2 Fold Hinges Olympias (circle) Stratoni FW (square) combined (n=56)

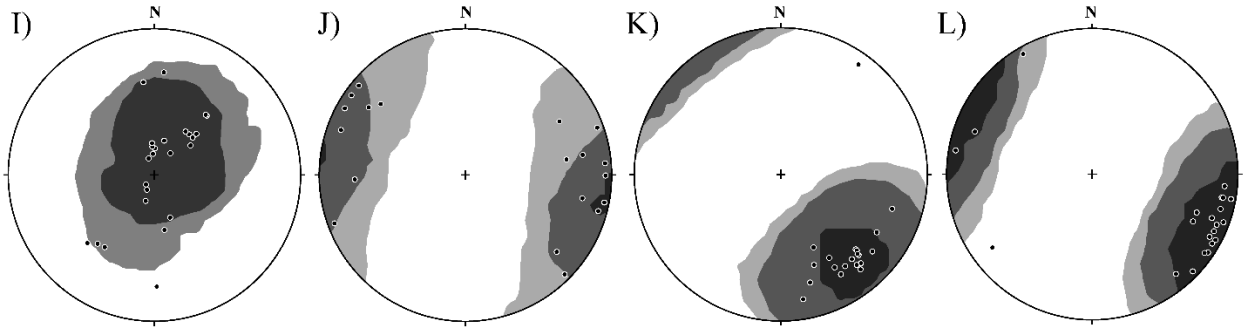

F2 Axial Planes Skouries-Stratoni HW combined (n=26) | F2 Fold Hinges Skouries-Stratoni HW combined (n=19) | L2 Olympias-Stratoni FW combined (n=20) | L2 Skouries (n=22)

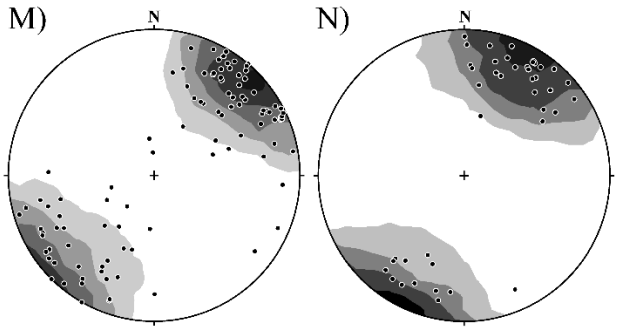

S3 Olympias-Stratoni FW combined (n=103) | S3 Skouries-Stratoni HW combined (n=42)

Figure 3.4. Photos of representative ductile structural elements from the Kassandra Mining District: (A) outcrop of folded Kerdilion marble on the Varvara-Olympiada road north of the Olympias deposit. This outcrop displays the relationship of S1 foliation defined by compositional layering reworked into a tight F2 fold. A ptygmatically folded pegmatite dike is also evident. Sub-horizontal axial planar S2 cleavage and crosscutting sub-vertical S3 cleavage are illustrated and shown in detail in Figure 4G; (B) meta-pelitic lithology within the Vertiskos unit in the Skouries area displaying a pronounced S2 crenulation cleavage associated with parasitic F2 folds; (C) tight F2 folds in quartz-rich biotite gneiss belonging to the Vertiskos unit exposed south of the Piavitsa prospect; (D) tight F2 folds in a granite gneiss sill located within the immediate footwall of the Stratoni fault zone east of Stratoni. A shallow south dipping axial plane is implied. Field of view is approximately 10 m; (E) outcrop exhibiting S1-S2 foliation intersections and the resulting L2 intersection lineation developed within the Kerdilion marble north of the Olympias deposit; (F) L2 intersection lineations developed in quartz-rich micaceous schist of the Vertiskos unit in the Skouries area; (G) close-up of image Figure 4A showing the relationship of steeply dipping S3 pressure solution cleavages with sub-horizontal S2 axial planar cleavage; (H) kink fold warping S1 foliation in quartz-rich biotite gneiss in the Skouries area.

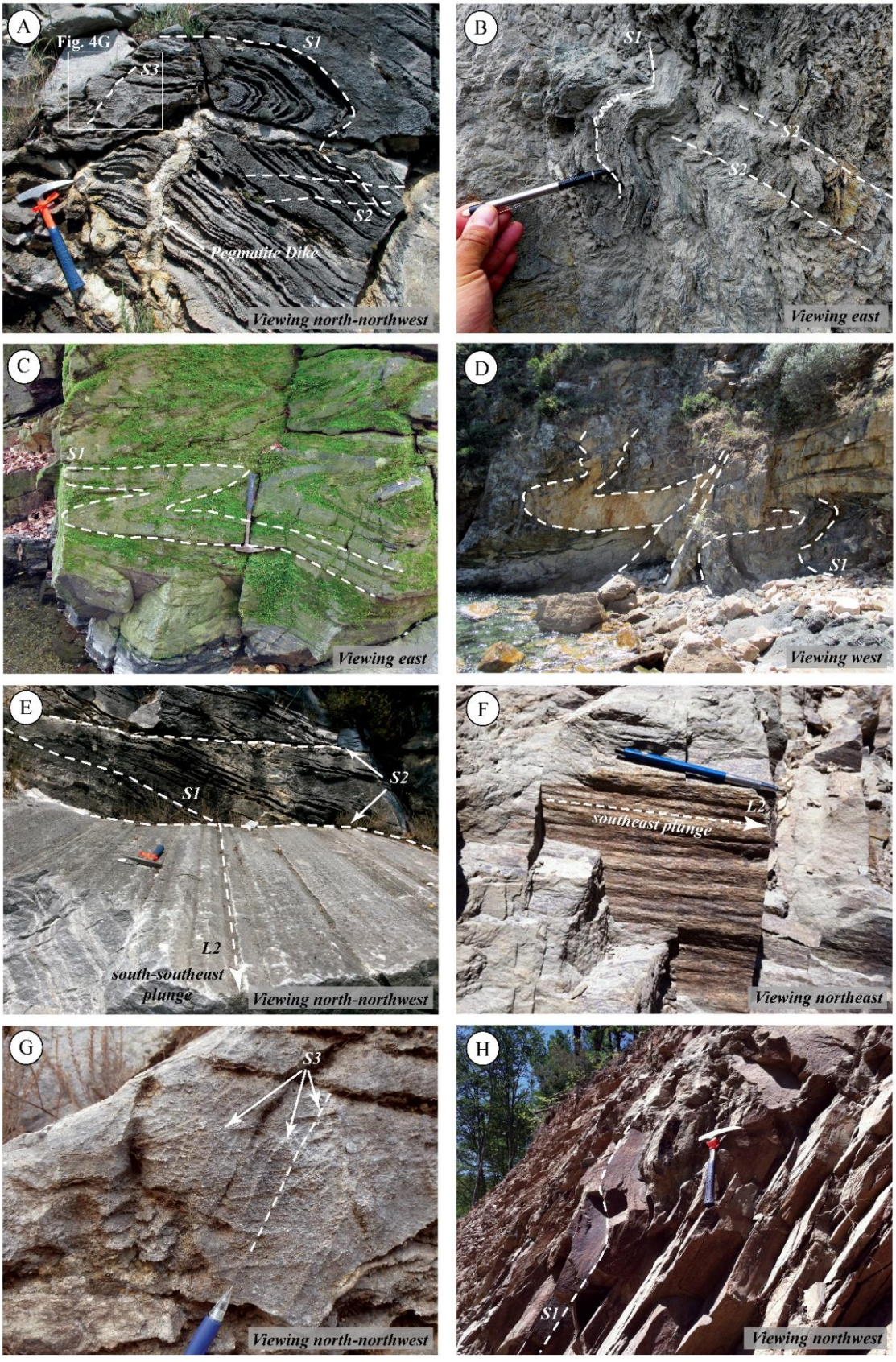
A
Fig. 4G
S1
S3
S2
Pegmatite Dike
Viewing north-northwest
B
S1
S2
S2
Viewing east
C
S1
Viewing east
D
S1
Viewing west
E
S2
S1
L2
south-southeast plunge
Viewing north-northwest
F
L2
southeast plunge
Viewing northeast
G
S3
Viewing north-northwest
H
S1
Viewing northwest

exhibits a northeast strike and southwest dip in the southeast portion of the district. Foliation boudins evident within the well-foliated mafic rocks south of the Stratoni fault zone locally occur as lenticular and symmetrical pyroxenite lozenges within amphibolite, thus recording high degrees of strain during the D1 event.

D2 deformation: A second ductile fabric (S2) overprints and locally transposes the previously developed S1 foliation, and is associated with upper greenschist- to lower amphibolite-facies metamorphism based on the realignment and growth of phyllosilicate minerals (e.g., biotite) into S2 foliation planes. Within the northern domain, the S2 foliation forms a spaced to locally penetrative cleavage that dips gently to the south-southeast (Figure 3.3E). S2 cleavage is present within the axes of folds at the Olympias deposit, where it manifests as a penetrative fabric resulting in the realignment of biotite in the quartzo-feldspathic gneisses, and as thin pressure solution partings and realignment of graphite flakes in marble. S2 cleavage is generally poorly developed within the massive, mica-poor and coarse-grained to megacrystic granitic gneisses that underlies much of the eastern portion of the northern domain. In general, S2 cleavage is subparallel to S1 foliation at the southern margin of the northern domain within the Stratoni fault zone. In the southern domain, the S2 fabric occurs as a tightly-spaced, penetrative crenulation cleavage (Figure 3.4B) that dips moderately to the south (Figure 3.3F) and is commonly localized in the axes of folds best developed in meta-pelitic layers. Poles to axial planar S2 foliation measured in the Skouries area and surrounding parts of the southern domain display a clustered distribution with no evidence of post-D2 folding. This relationship is consistent with the orientation and distribution of F2 axial planes.

Folds associated with the D2 event (F2 folds) affected the metamorphic sequences in the northern and southern domains. Folds have interlimb angles that range from open to tight and commonly have inclined to near-recumbent axial planes (Figure 3.4C-D). In the northern domain, F2 folds in outcrop verge either northeast or southwest and uniformly plunge gently south-southeast to east-southeast (Figure 3.3G-H). S1 foliation poles from the Olympias area form a well-developed girdle distribution that defines

a shallow southeast plunging F2 fold hinge (Figure 3.3A), subparallel to the plunge of F2 folds (Figure 3.3H). Field relationships and a bimodal distribution of S1 foliation poles defining fold limbs within the footwall of the Stratoni fault zone define an upright and shallow east-southeast-plunging F2 antiform (Figure 3.3B; Nebel et al., 1991; Gilg, 1993; Gilg and Frei, 1994; Haines, 1998). Axial planes of parasitic F2 folds mostly dip shallowly to the south (Figure 3.3G). In the southern domain, outcrop patterns and S1 foliation poles show a bimodal distribution that defines a northwest-southeast-striking F2 antiform exhibiting an open geometry with a steep south-southwest dipping axial plane that plunges shallowly to the east-southeast (Figure 3.3D). Parasitic F2 folds display axial planes that mostly dip to the south-southwest on the southern limb with a minor population of steep north-northeast dipping axial planes on the northern limb (Figure 3.3I). Previous identification of a district-scale synform to the south of the Stratoni fault zone (see geologic map of Frei, 1995) is not supported by field observations in this study.

A pronounced L2 lineation resulting from the intersection of S1 foliation with S2 cleavage is evident in the marbles north of the Olympias deposit (Figure 3.4E). This linear fabric forms on S2 cleavage planes and plunges gently to the southeast (Figure 3.3K), subparallel to the orientation of F2 fold axes. Within the southern domain, L2 intersection lineations are commonly developed in meta-pelitic units (Figure 3.4F), and similarly result from the intersection of S1 foliation and S2 axial planar cleavage. L2 intersection lineations in the southern domain also plunge shallowly to the southeast (Figure 3.3L).

D3 deformation: A widely spaced northwest-striking S3 fabric occurs in both northern and southern domains (Figure 3.4G). This low-strain fabric forms as a steep northeast or southwest dipping pressure solution cleavage in marble, or manifests as thin cleavage domains that discretely warp S1 and S2 foliation in meta-pelitic layers, but may also occur as anastomosing fractures in mica-poor granitic gneiss. S3 foliation is best developed in marbles north of the Olympias deposit, and within the meta-pelitic lithologies within the southern domain (Figure 3.3M-N). Locally persistent kink-style folds are evident in the Skouries area and are likely associated with the D3 deformation event (Figure 3.4H).

Mylonitic shear zones: Moderate to shallow dipping ductile mylonitic to protomylonitic shear zones commonly exploit pegmatite and fine-grained granite dikes and sills (referred to as aplite in the mine terminology) that are exposed underground in the Madem Lakkos mine (Haines, 1998) and in the Olympias deposit. These shear zones postdate peak metamorphic fabrics (S1, S2) and have an associated greenschist-facies mineral assemblage of fine-grained muscovite-chlorite. Mylonites exhibit kinematic criteria that imply at least two phases of ductile shear associated with an older contraction and a younger extensional event. The latter is described in context of the Olympias area and Stratoni fault zone in the following sections.

At the Madem Lakkos mine, a south dipping 1.5 m-wide mylonitic shear zone occurs approximately 200 m into the footwall of the Stratoni fault zone and is hosted by a pegmatitic sill at the contact between marble and amphibolite (Haines, 1998). Asymmetric S-C fabrics, isoclinal intrafolial folds, and drag folds at the shear zone margin document reverse top-to-the-north-northeast sense of shear (Haines, 1998). Folded and boudinaged marble and mylonitized granite gneiss are thrust-imbricated toward the north-northeast implying that the fold and boudinage event predated, or was outlasted by mylonitic reverse faulting. Mylonitization at lower amphibolite- to upper greenschist-facies metamorphic conditions is inferred by Haines (1998) based on mineralogy and ductile deformation textures. Rare mylonitic shear zones exhibiting similar characteristics and reverse top-to-the-northeast sense of shear also occur in the Olympias area, although their respective timing is uncertain.

Olympias Area

The Olympias deposit lies 1 km west of the village of Olympiada and approximately 6 km north of the Stratoni fault zone (Figure 3.2). Previous studies on the Olympias deposit have principally described ore mineralogy and the physiochemical conditions of ore deposition (Kalogeropoulos et al., 1989; Kilias et al., 1996), with a limited number of unpublished consulting reports focused on describing the structural framework of the deposit. This section presents a revised deposit-scale geologic map and

cross section (Figure 3.5A-B) with detailed descriptions of ductile and brittle structures combined with kinematic analyses of major faults within the Olympias area.

The Olympias deposit

The Olympias orebodies consist of massive sulfide and silicified cataclastic breccias hosted by a less than 150 m-thick marble unit that is conformably interlayered within a body of garnet-bearing quartzo-feldspathic biotite gneiss of the Kerdilion unit. The marble layer is similar to the marble horizon that hosts the Madem Lakkos and Mavres Petres deposits (Kalogeropoulos et al., 1989; Gilg, 1993; Kilias et al., 1996). Ore mineralogy consists of sphalerite-galena-dominant massive sulfide that grades into pyrite-rich intervals with variable amounts of arsenopyrite and trace chalcopyrite (Figure 3.6A-B). Massive to banded Ag-Zn-Pb sulfide ore locally transitions into Au-rich arsenopyrite-bearing sulfide and arsenopyrite-boulangerite-bearing silicified breccia ore types, with diffuse zones of disseminated pyrite and arsenopyrite associated with quartz-rhodochrosite ± rhodonite alteration of the surrounding wallrock. Auriferous arsenopyrite lenses and silicified breccias containing rhodochrosite-rhodonite mostly occur in the upper northern portions of the Olympias deposit, and generally crosscut the massive sulfide where both ore types occur together. Mineralized breccias include those containing a chalcedonic quartz- or carbonate-dominated matrix with sulfide minerals, and younger cataclastic breccias where the matrix consists of comminuted sulfide grains.

Sulfide bodies occur as coarse-grained lenses of compositionally banded sulfide that have discordant and crosscutting contacts with respect to marble and S1 foliation (Kalogeropoulos et al., 1989; Kilias et al., 1996; Siron et al., 2016). Orebodies commonly display internal banding that locally mimics folded marble layers (Kalogeropoulos et al., 1989). Sulfide intervals that appear folded are largely unstrained, and are therefore interpreted to have formed from the pseudomorphic replacement of pre-existing F2 folds (Siron et al., 2016). Mine data shows that the geometry of the Olympias orebody is strongly influenced by the morphology of the hosting marble-gneiss sequence. Individual sulfide lenses

Figure 3.5. (A) Detailed geologic map of the Olympias deposit area modified after Kockel et al. (1978a, 1978b). Mapping was conducted at 1:5,000-scale and based largely on surface outcrops; (B) cross section A-A' of the Olympias deposit is defined by underground drill core interpretation. Coordinates are displayed in the Greek Geodetic Coordinate System (GGRS 87 Greek Grid). Abbreviations are as follows: relative level (RL).

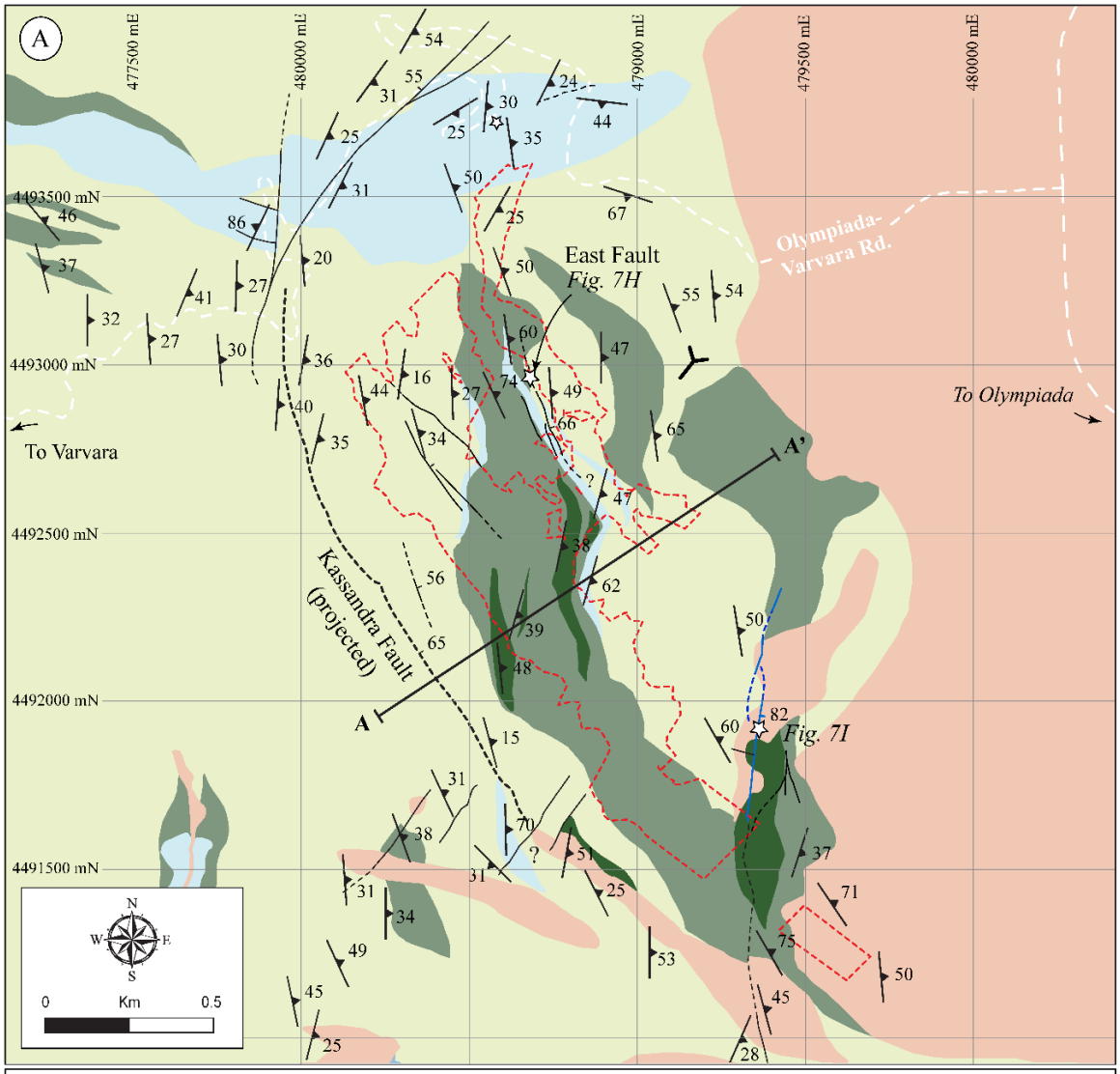

Jurassic (?) Rift-related Rocks

- Gabbro, amphibole-bearing pyroxenite, massive and non-foliated
- Amphibolite, layered and foliated

Permo-Carboniferous to Jurassic Kerdilion Unit

- Quartzo-feldspathic hornblende-biotite gneisses; abundant pegmatites
- Plagioclase-microcline granite gneiss (pegmatitic to aplitic)
- Marble, graphitic, layered to massive

Map Symbols

- Fault, dashed where approx., marker indicating dip
- Quartz-rich breccia, dashed where approx., marker indicating dip
- Strike-dip of S1 foliation
- Olympias portal
- Surface projection of Olympias orebody

Cross Section Symbols

- Massive Sulfide
- Normal fault; mylonitic to brittle cataclastic
- OL-353 — Drill hole, arrow indicates projection of drill hole out of section
- Location of photo (refer to text)

Figure 3.5. Continued.

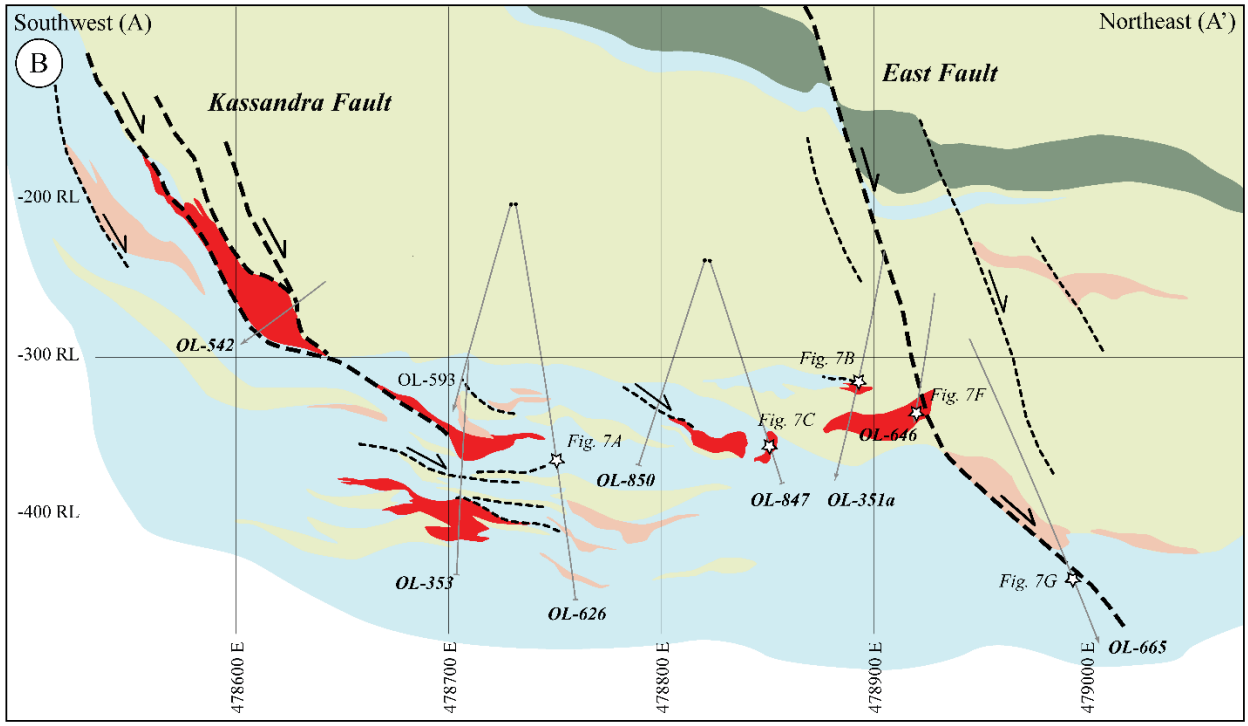

form elongate, cigar-like shapes with their long dimension oriented in a southeast direction (Veligrakis and Dalampiras, 2016). At the deposit scale, the modeled sulfide orebody plunges approximately 19° at an azimuth of 150° southeast, subparallel to the mean plunge of the F2 fold hinge and L2 intersection lineation as shown in Figure 3.3H and 3.3K, respectively.

Olympias sulfide ore is locally associated with a post-deformation igneous breccia within the footwall of the Kassandra fault (Figure 3.6C). This breccia body is composed of granite and quartz-rhodochrosite-altered marble fragments supported by a matrix that is compositionally similar to the granite clasts (Figure 3.6D). Sulfide within the matrix of the breccia suggests a close timing relationship between magmatism, brecciation, and sulfide deposition and is consistent with a magmatic-hydrothermal breccia. The timing of emplacement of this igneous body, however, was not investigated in this study and is currently unconstrained. Glomerophyric porphyry dikes that are geochemically and texturally similar to the early Miocene dikes that crosscut the sulfide orebody at the Madem Lakkos deposit (Gilg and Frei, 1994; Haines, 1998) and the silicified rhodochrosite replacement body at the Piavitsa prospect similarly

Figure 3.6. Photos of representative mineralization styles and structural features from the Olympias and Mavres Petres deposits: (A-B) drill core intercepts from the Olympias deposit showing rod-textured arsenopyrite-pyrite and massive arsenopyrite replacing banded sphalerite (A) and quartz-rich, coarse-grained and banded arsenopyrite-sphalerite-pyrite with calcite infill (B); (C) underground exposure of igneous breccia from the -45 level at the Olympias mine. Field of view is approximately 2.5 m; (C) close-up of image B showing the granitic composition of the breccia matrix; (E) Olympias drill core intercept of altered glomerophyric porphyry dike with phreatic breccia at its margins containing sulfide clasts; (F) underground exposure of undeformed pyrite-rich massive sulfide from the Mavres Petres mine. Note the relict fold textures of the host marble preserved by the sulfide lenses; (G) mineralized quartz-arsenopyrite-stibnite-boulangerite-bearing breccia crosscutting pyrite-sphalerite-rich massive sulfide. Stringer zones of arsenopyrite partially replaces previously deposited sulfide. Image from an underground exposure at the Mavres Petres mine. Field of view is roughly 2 m; (H) northeast-trending late-mineral rhodochrosite-rhodonite veins filling dilatant shear zones at the Mavres Petres mine. These veins crosscut sulfide mineralization and contain minor quantities of sulfide. Abbreviations are as follows: arsenopyrite (Apy), calcite (Cal), galena (Ga), pyrite (Py), quartz (Qtz), sphalerite (Sp).

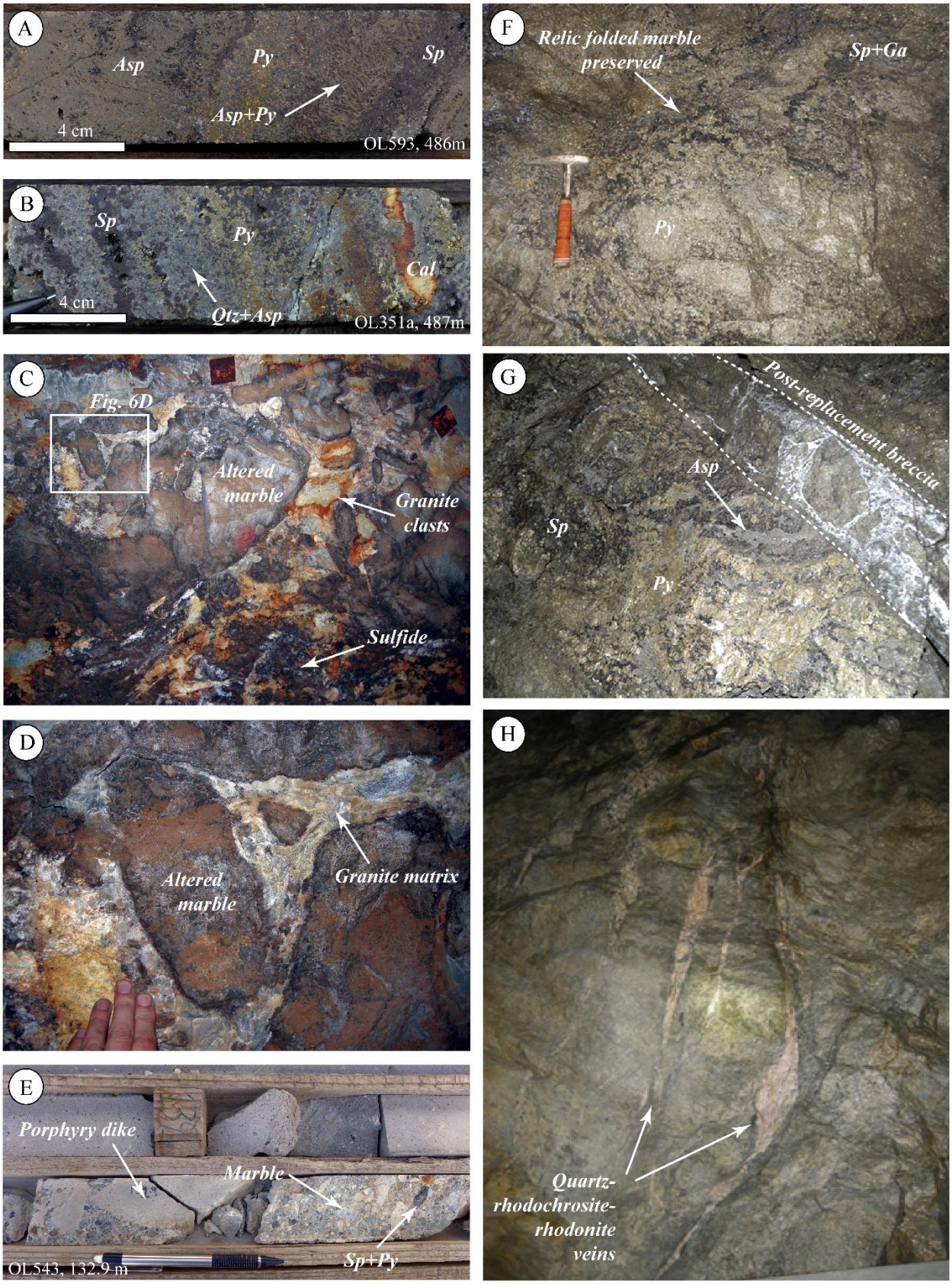
A
Asp
Py
Sp
Asp+Py
4 cm
OL593, 486m
B
Sp
Py
Cal
4 cm
Qtz+Asp
OL351a, 487m
C
Fig. 6D
Altered marble
Granite clasts
Sulfide
D
Altered marble
Granite matrix
E
Porphyry dike
Marble
Sp+Py
OL543, 132.9 m
F
Relic folded marble preserved
Sp+Ga
Py
G
Post-replacement breccia
Asp
Sp
Py
H
Quartz-rhodochrosite-rhodonite veins

crosscut sulfide ore at the Olympias deposit (Figure 3.6E; Kalogeropoulos et al., 1989; Siron et al., 2016). Brecciated contacts locally developed at dike margins consist of angular to subrounded fragments of sericite-carbonate-altered porphyry, quartz-rhodochrosite-altered marble, and sphalerite-pyrite sulfide clasts (Figure 3.6E).

Faults in the Olympias area

Carbonate replacement massive sulfide at the Olympias deposit shows a close spatial relationship with mylonitic to brittle faults in contact with the host marble unit (Figure 3.5A-B; Kalogeropoulos et al., 1989). An array of shallow dipping mylonitic to protomylonitic shear zones occur throughout the Olympias deposit and define the earliest stage of post-peak metamorphic faulting in the area. These ductile shear zones are transitional with, and are overprinted by, younger fault phases along the northwest-striking Kassandra and north-striking East faults. Each fault zone exhibits less than 100 m of normal top-to-the-northeast/east displacement based on the approximate magnitude of offset between marble and the surrounding quartzo-feldspathic biotite gneiss (Figure 3.5B).

Kassandra fault zone: The northeast dipping Kassandra fault zone occurs on the western margin of the Olympias deposit and exploits the lithologic contact between graphite-bearing marble and interlayered quartzo-feldspathic biotite gneiss, pegmatitic granite gneiss, and amphibolite. Underground and surface drilling has delineated an anastomosing fault zone comprising a network of narrow fault strands that vary in thickness from ~1 to 20 m, and is traceable for a strike length greater than 2 km (Figure 3.5A). Displacement on the Kassandra fault diminishes down dip as it dissipates into minor fault strands and *en echelon* steps which coincide with sulfide orebodies in the central parts of the Olympias deposit (Figure 3.5B).

Ultramylonitic to protomylonitic shear zones, hereafter referred to as mylonites, belong to the Kassandra fault and define the earliest stage of fault deformation in the Olympias area. Mylonites generally occur as shallow dipping, less than 1 m-wide shear zones that are typically localized within

pegmatite sills and dikes, and are focused along the upper parts of the main marble unit (Figure 3.5B). Mylonites commonly occur subparallel to the local S1 foliation at the down-dip terminus of the Kassandra fault and central to the Olympias deposit (Figure 3.5B). Deformation textures developed within the pegmatite-hosted mylonites consist of rotated feldspar porphyroclasts that are enclosed by a fine-grained to aphanitic matrix of dynamically recrystallized quartz (Figure 3.7A), whereas those developed in marble display a pronounced shear fabric with thin, laminar carbonaceous pressure solution seams defining slip surfaces. Mylonites generally exhibit a muscovite-chlorite-carbonate mineral assemblage suggesting formation under greenschist-facies temperature conditions (Figure 3.7B). Mylonitic shear zones are laterally transitional with, and commonly superimposed by, semi-brittle shear zones. Undeformed replacement-style sulfide and mineralized silicified breccias locally overprint older mylonitic shear zones, and typically display sharp and discordant contacts with respect to the tectonic fabric (Figure 3.7C).

Foliated, semi-brittle shear zones developed within quartzo-feldspathic biotite gneiss within the Kassandra fault (Figure 3.7D) are polymict and clast-supported, containing sub-rounded fragments of the host lithology and pegmatitic granite gneiss. The shear fabric is typically fine-grained with foliated domains consisting of pale green hydrothermal muscovite-dolomite-quartz and disseminated pyrite with variable amounts of euhedral arsenopyrite (Figure 3.7E). Semi-brittle faults developed in marble are monomict, containing corroded and rotated clasts in between carbonaceous pressure solution fabrics. These shear zones are accompanied by base metal sulfides, which in part define the tectonic fabric. Mineralized semi-brittle faults may become overprinted by younger cataclastic breccias and fault gouge. Silicified cataclastic breccias within the Kassandra fault commonly contain disseminated pyrite ± galena-sphalerite-arsenopyrite or may be composed of a sulfide-dominated matrix resulting from the comminution of preexisting sulfide layers (Figure 3.7F). These mineralized breccias are also spatially associated with quartz-rhodochrosite ± rhodonite veins.

Figure 3.7. Photos of representative fault styles in the Olympias deposit area: (A) mylonitic pegmatite sill located at the base of a massive sulfide interval at the down-dip terminus of the Kassandra fault; (B) example of shear band hosted by a pegmatitic gneiss and composed of sericite-chlorite mineral assemblage; (C) unstrained galena-pyrite semi-massive sulfide and associated Fe-carbonate discordantly replacing the mylonitic shear fabric in marble; (D) underground exposure of the mineralized Kassandra fault from the -203 production level. Direction of tectonic transport is indicated by the arrow; (E) mineralized strand of the Kassandra fault hosted in a pegmatitic granite gneiss. Note the green hydrothermal muscovite with intergrown sphalerite, pyrite, and arsenopyrite; (F) silicified breccia containing clasts of sericite-altered granite gneiss and mineralized arsenopyrite-bearing quartz-matrix breccia, enclosed by a fine-grained and comminuted sulfide-rich matrix; (G) foliated, semi-brittle shear zone in marble containing pyrite localized along graphitic pressure solution fabrics. The lower drill core image represents a semi-brittle fault overprinted by a quartz- and calcite-cemented hydrothermal breccia from the lower section of the East fault; (H) surface exposure of the East fault with dashed line illustrating the principal slip surface; (I) outcrop of quartz vein breccia exposed at the southeast end of the Olympias deposit. Direction of tectonic transport is indicated by the arrow. Abbreviations are as follows: ankerite (Ank), arsenopyrite (Apy), galena (Ga), muscovite (Ms), plagioclase (Pl), pyrite (Py), quartz (Qtz), sphalerite (Sp).

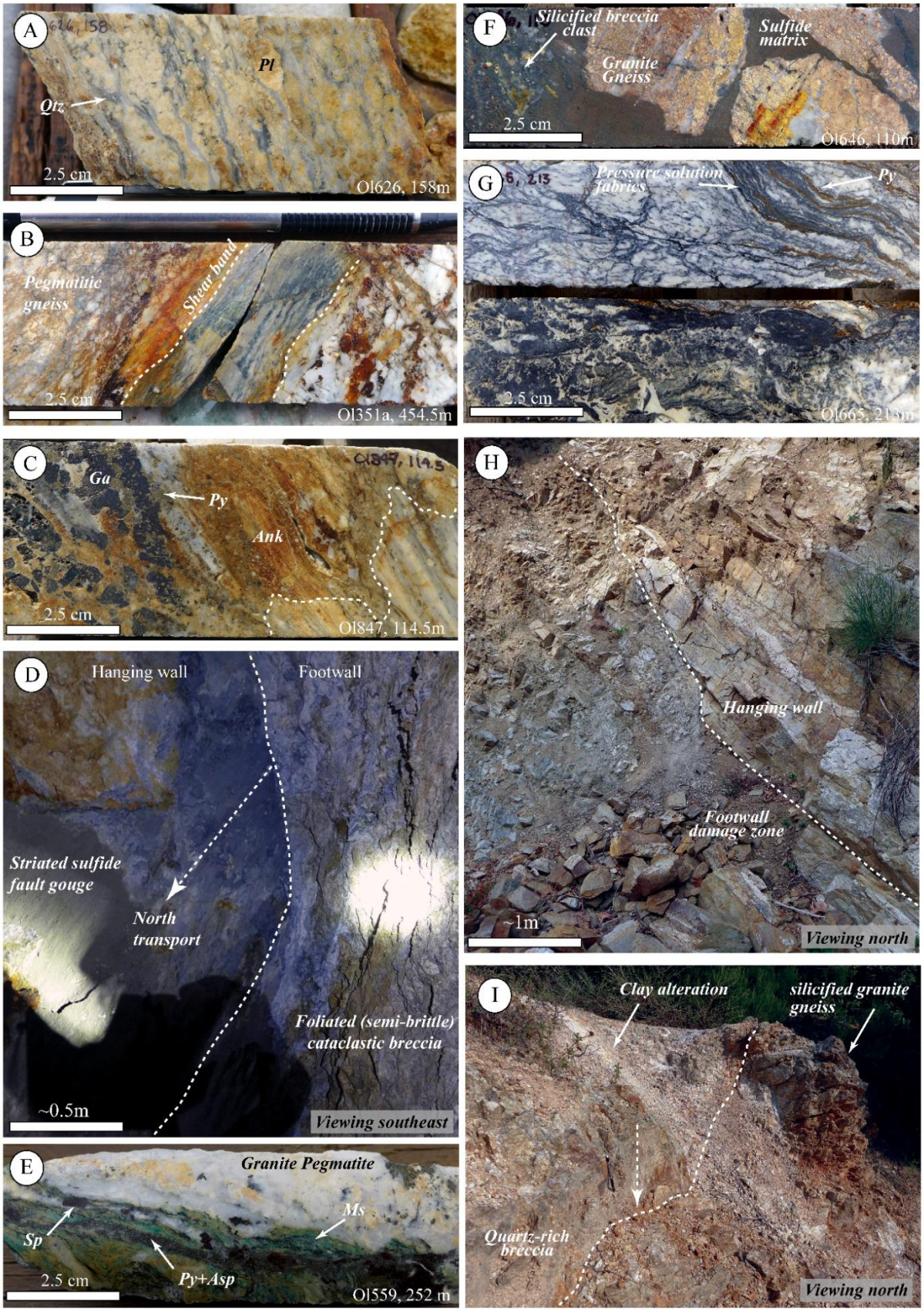
A
Pl
Qtz
2.5 cm
Ol626, 158m
B
Pegmatitic gneiss
Shear band
2.5 cm
Ol351a, 454.5m
C
Ga
Py
Ank
2.5 cm
Ol847, 114.5m
D
Hanging wall
Footwall
Striated sulfide fault gouge
North transport
Foliated (semi-brittle) cataclastic breccia
~0.5m
Viewing southeast
E
Granite Pegmatite
Ms
Sp
Py+Asp
2.5 cm
Ol559, 252 m
F
Silicified breccia clast
Sulfide matrix
Granite Gneiss
2.5 cm
Ol646, 110m
G
Pressure solution fabrics
Py
2.5 cm
Ol665, 213m
H
Hanging wall
Footwall damage zone
~1m
Viewing north
I
Clay alteration
silicified granite gneiss
Quartz-rich breccia
Viewing north

East fault zone: Surface mapping and underground drill holes from the eastern portion of the Olympias deposit define the 5 to 20 m-wide East fault zone with a north-south strike extent greater than 1 km (Figure 3.5B). Mylonites generally occur in the footwall of the East fault but are less abundant than in the Kassandra fault area to the west. Foliated, semi-brittle shear zones and silicified cataclastic breccias similarly define the East fault (Figure 3.7G). North-northwest- to north-striking gouge-filled faults and fracture zones are pervasive within the East fault (Figure 3.7H). Younger clay-altered and gouge-filled faults overprint the older mylonitic and semi-brittle shear zones, as well as the sulfide and silicified cataclastic breccia bodies. Post-mineral faults, while recognized throughout the Olympias area and are particularly evident within the East fault zone, resulted in only minor displacement of the sulfide orebodies toward the east.

Quartz-rich breccias: Silicified, chalcedonic quartz-rich breccias occur as north-south-striking fault-filled structures that outcrop on the southeast margin of the Olympias deposit (Figure 3.7I). These zones are commonly accompanied by quartz-rhodochrosite veins which are typically identified by a sooty, weathered appearance with localized silicification of the adjacent metamorphic wallrock. Quartz-rich breccias are matrix-supported and consist of previously sericite-altered, sub-angular to angular clasts of granitic gneiss that are chaotically interspersed with marble and sulfide fragments. The matrix is composed of dark gray chalcedonic quartz containing fine-grained, disseminated euhedral pyrite and bladed arsenopyrite. Quartz-rich breccias can be Au-rich, locally containing up to 19 g/t Au. The chaotic breccia texture and flinty quartz matrix is distinctive, and broadly similar to the silicified breccias intercepted in drill core and adjacent to the Kassandra and East faults.

Kinematic analysis

Kinematic indictors developed within the mylonitic shear zones, where observed in drill core, imply a normal sense of shear when reoriented with respect to S1 foliation (e.g., drill core was oriented such that foliation was restored to a north-south direction). This is consistent with the normal eastward-

displaced lithological relationships and sense of shear on the Kassandra and East faults (Figure 3.5B). An underground exposure of a mineralized segment of the Kassandra fault displays two sets of slickenlines. One set rakes obliquely across the fault surface (Figure 3.7D) resulting in left-lateral displacement and a northeast-directed principal axis of extension (Figure 3.8A). A younger and more extensive set of slickenlines indicate normal dip-slip displacement resulting from an east-northeast-directed principal axis of extension (Figure 3.8A). At surface, minor faults displaying cm-scale displacement and shear-related drag folds of S1 foliation in quartzo-feldspathic biotite gneiss are kinematically compatible with the younger set of slickenlines observed underground.

The East fault similarly displays normal top-to-the-east movement as indicated by displaced lithological relationships in the cross section in Figure 3.5B. Kinematic fault-slip data collected from surface exposures of the East fault records two generations of fault deformation superimposed on the older lithified cataclastic and mylonitic fault rocks (Figure 3.8B). Slickenlines developed on a clay-altered segment of the East fault at the southern end of the Olympias deposit record oblique left-lateral displacement controlled by a northeast-directed principal axis of extension (Figure 3.8B). A second set of younger (?) gouge-filled faults crosscutting pegmatitic granite gneiss and quartzo-feldspathic biotite gneiss display groove marks that indicate oblique right-lateral displacement controlled by an east-southeast-directed principal axis of extension (Figure 3.8B).

Fault-slip data from auriferous fault-filled quartz-rich breccias collected on surface (Figure 3.7I) exhibit near-vertical slickenlines and quartz mineral fiber growths along vein segments that imply normal movement with a minor component of either left- or right-lateral oblique slip (Figure 3.8C). The shallow southeast-plunging extensional strain axis corresponds to a discrete northwest-southeast extensional event that was associated with this style of mineralization in the Olympias area.

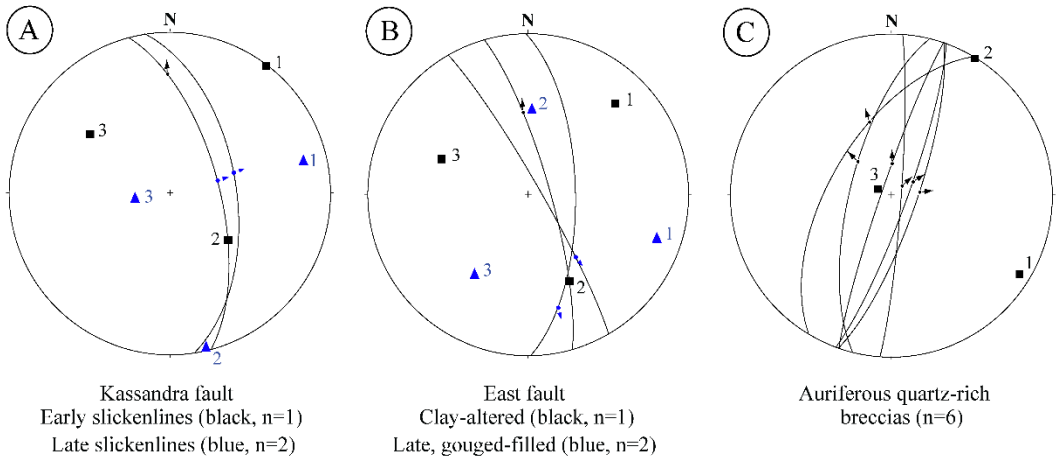

Figure 3.8. Lower-hemisphere, equal-area stereographic projections of fault kinematic data from the Olympias deposit area. Fault planes and slip vectors are represented by great circles and arrows, respectively. Kinematic strain axes are plotted as squares and numbered according to the principal extension axis (1), the principal shortening axis (3), and the orthogonal intermediate axis (2): (A) kinematic strain data from an underground exposure of the mineralized Kassandra fault is plotted as squares. The kinematic axes that describe the latest movement recorded on the Kassandra fault are represented by triangles; (B) kinematic data from a clay-altered (late-mineral?) segment of the East fault is plotted as squares. The kinematic axes that describe the post-mineral segment of the East fault are represent by triangles; (C) fault kinematic data from outcrops of variably mineralized, auriferous quartz-rich breccias.

Stratoni Fault Zone

The Madem Lakkos and Mavres Petres deposits contain marble-hosted replacement Au-Ag-Zn-Pb-Cu massive to semi-massive sulfide, quartz-rich disseminated Au-Ag-As-Zn-Pb-Cu sulfide, minor Cu skarn, and Au-rich quartz-rhodochrosite vein-breccia bodies which occur throughout the Stratoni fault zone but is the dominant style of mineralization at the Piavitsa prospect. These orebodies are temporally and spatially associated with Oligo-Miocene igneous rocks and the ductile to brittle Stratoni fault zone (Figure 3.9; Gilg and Frei, 1994; Haines, 1998). This section describes the sulfide deposits that occur within the Stratoni fault zone with detailed structural observations and kinematic analyses of this fault system.

Ore deposits of the Stratoni fault zone

The Madem Lakkos deposit: The Madem Lakkos deposit lies 2 km northwest of the village of Stratoni (Figure 3.9) and consists of skarn- and replacement-style sulfide hosted mainly within marble of the Kerdilion unit (Nebel, 1989; Nebel et al., 1991; Gilg, 1993; Gilg and Frei, 1994; Haines, 1998; Hahn, 2014; Siron et al., 2016). Unstrained sulfide ore is commonly localized at marble-granite gneiss contacts but may also occur as replacement bodies in gneiss (Haines, 1998). Previous work has shown that sulfide orebodies are spatially related to post-deformation granite dikes, referred to as aplite in the mine terminology. Orebodies are controlled by extensional faults and the closure of a prominent east-southeast-plunging F2 antiform within the footwall of the Stratoni fault zone (Nebel et al., 1991; Gilg, 1993; Gilg and Frei, 1994; Haines, 1998; Siron et al., 2016).

The Madem Lakkos deposit displays a complex mineralization history involving an early phase of carbonate replacement massive sulfide, minor skarn, and a younger phase of quartz-rich sulfide mineralization. Early sulfide consists of galena-sphalerite-pyrite-pyrrhotite-arsenopyrite that forms replacement bodies displaying concordant to irregular contacts with respect to marble layers and S1 foliation (Haines, 1998). Early sulfide ore is partially overprinted by the younger sulfide phase consisting of prismatic quartz-pyrite ± arsenopyrite-sphalerite-galena-chalcopyrite and a variety of sulfosalt minerals (e.g., boulangerite). This style of mineralization was termed disseminated sulfide in previous studies and it contributed the majority of the ore mined from the Madem Lakkos deposit (Nebel et al., 1991; Gilg, 1993; Haines, 1998). Quartz-rhodochrosite ± rhodonite vein and vein breccias crosscut the sulfide orebodies (Gilg, 1993; Haines, 1998), a paragenetic relationship similar to the Olympias deposit. Volumetrically minor pyrite- and Cu-bearing calcic and magnesian skarns are present locally at surface and at depth on the eastern margin of the Madem Lakkos deposit. Skarn-related sulfide ore occurs within marble adjacent to the Vathilakkos fault (Figure 3.10A) and within granitic and quartzo-feldspathic biotite gneisses adjacent to the Stratoni granodiorite stock (Gilg, 1993). The timing relationship between these skarn occurrences and the carbonate replacement sulfide ores remain unclear.

Figure 3.9. Simplified geologic map of the Stratoni fault zone modified after Kockel et al. (1978a, 1978b). The inset map is located in Figure 10A. The thick black line in the Mavres Petres area corresponds to the dip-slope exposures of the Stratoni fault zone. Coordinates are displayed in the Greek Geodetic Coordinate System (GGRS 87 Greek Grid).

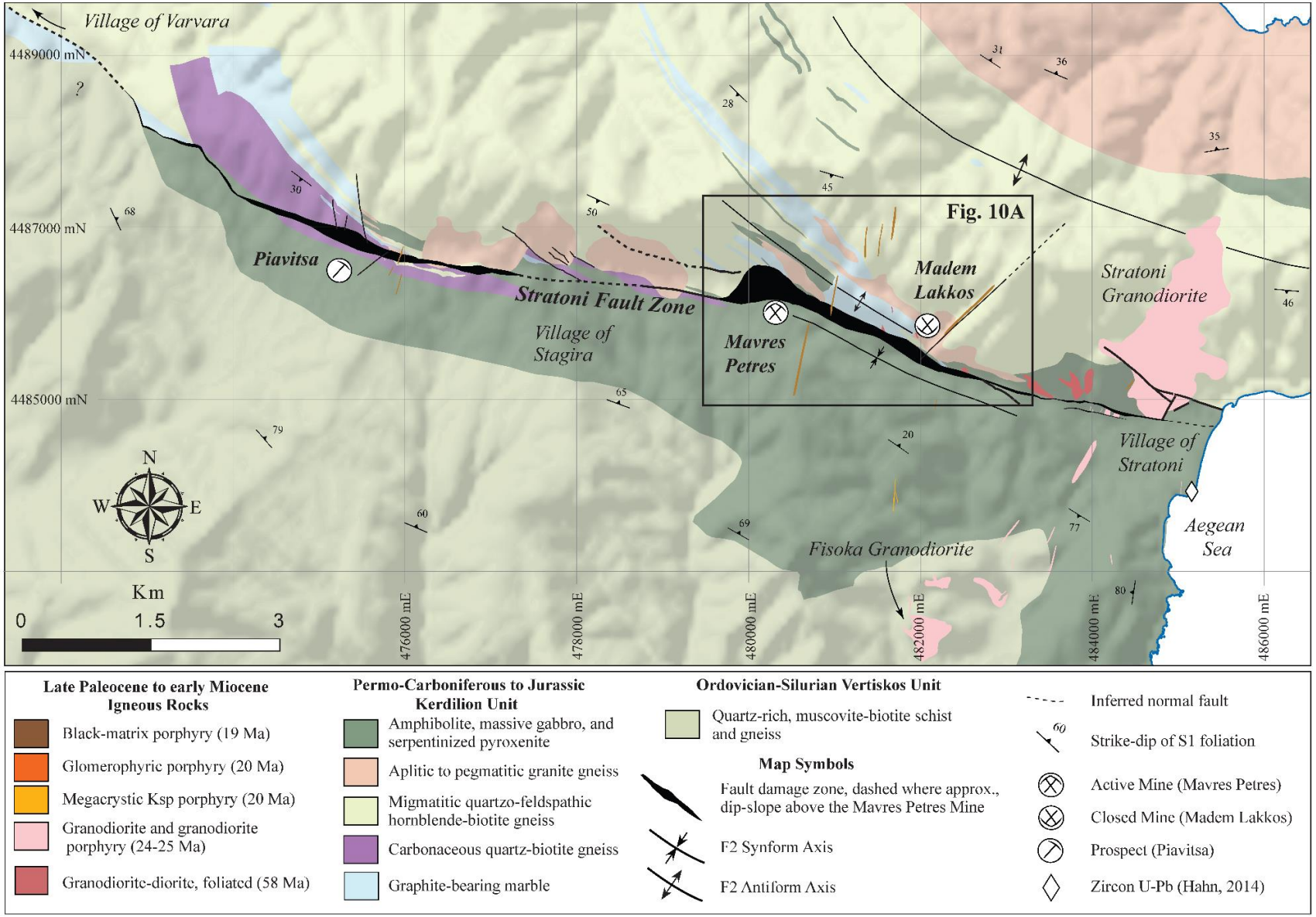
Village of Varvara
4489000 mN
4487000 mN
4485000 mN
Piavitsa
Stratoni Fault Zone
Village of Stagira
Mavres Petres
Madem Lakkos
Fig. 10A
Stratoni Granodiorite
Village of Stratoni
Aegean Sea
Fisoka Granodiorite
N
W
E
S
Km
0
1.5
3
476000 mE
478000 mE
480000 mE
482000 mE
484000 mE
486000 mE
Late Paleocene to early Miocene Igneous Rocks
Black-matrix porphyry (19 Ma)
Glomerophyric porphyry (20 Ma)
Megacrystic Ksp porphyry (20 Ma)
Granodiorite and granodiorite porphyry (24-25 Ma)
Granodiorite-diorite, foliated (58 Ma)
Permo-Carboniferous to Jurassic Kerdilion Unit
Amphibolite, massive gabbro, and serpentinized pyroxenite
Aplitic to pegmatitic granite gneiss
Migmatitic quartzo-feldspathic hornblende-biotite gneiss
Carbonaceous quartz-biotite gneiss
Graphite-bearing marble
Ordovician-Silurian Vertiskos Unit
Quartz-rich, muscovite-biotite schist and gneiss
Map Symbols
Fault damage zone, dashed where approx., dip-slope above the Mavres Petres Mine
F2 Synform Axis
F2 Antiform Axis
Inferred normal fault
Strike-dip of S1 foliation
Active Mine (Mavres Petres)
Closed Mine (Madem Lakkos)
Prospect (Piavitsa)
Zircon U-Pb (Hahn, 2014)

Replacement orebodies in the Madem Lakkos deposit are principally restricted to the footwall of the Stratoni fault zone and are localized at ductile-brittle fault contacts and hinge zones of east-southeast-plunging F2 folds associated with the Madem Lakkos antiform (Figure 3.10A; Nebel, 1989; Nebel et al., 1991; Gilg, 1993; Gilg and Frei, 1994; Haines, 1998). Outcrop patterns and the distribution of S1 foliation poles in the footwall of the Stratoni fault zone demonstrate an upright geometry and a steep south-southwest-dipping axial plane of the Madem Lakkos antiform (Figure 3.3B). Mine data shows that east-southeast-plunging F2 fold hinges, in part, controlled the distribution of sulfide ore within the Madem Lakkos deposit. Sulfide ore overprints thrust-related mylonitic fabrics in the Stratoni fault zone, including the younger and more extensive extensional mylonites. In the southern part of the Madem Lakkos deposit, sulfide orebodies are hosted by steeply south dipping marble lenses which are controlled by south dipping strands of the Stratoni fault zone (Haines, 1998).

Fine-grained to pegmatitic granitic dikes, which have localized mylonitic deformation in the footwall of the Stratoni fault are spatially associated with replacement sulfide ore (Haines, 1998). Granitic intrusions also locally crosscut the massive sulfide orebodies and are reported to have been affected by later stages of alteration and sulfide mineralization within the Madem Lakkos deposit (Gilg, 1993; Haines, 1998). The structural, spatial, and relative timing relationships of sulfide ore with granite bodies at the Madem Lakkos deposit are broadly similar to the Olympias deposit.

The Mavres Petres deposit: The Mavres Petres carbonate replacement sulfide deposit is located ~1 km to the west of the Madem Lakkos deposit (Figure 3.9 and 10A). Sulfide orebodies are largely restricted to the Stratoni fault zone and are hosted by marble lenses that are complexly imbricated with graphite-bearing quartz-biotite gneiss and schists, granite gneiss, and amphibolite. The marble unit is interpreted to be equivalent to the marble that hosts the Madem Lakkos and Olympias deposits (Kalogeropoulos et al., 1989). As currently known, the Mavres Petres deposit has a strike length greater than 1 km and a down-dip extent exceeding 700 m from surface, and forms semi-continuous sulfide replacement bodies that mantle and fully replace marble lenses between strands of the Stratoni fault on

the southwest limb of the Madem Lakkos antiform (Figure 3.10B). Sulfide textures and mineralogy are similar to Madem Lakkos and the Olympias deposits. Silicified Fe-Mn-oxide gossans and pods of massive sulfide form the surface expression of the deposit on the exposed dip-slope segment of the Stratoni fault zone above the village of Stratoniki (Figure 3.10A) in an area that was the focus of ancient mining (Sagui, 1928).

The Mavres Petres sulfide ores consist of massive to banded, coarse-grained pyrite-sphalerite-galena accompanied by minor accessory arsenopyrite-stibnite and trace chalcopyrite (Figure 3.6F). Pyrite-sphalerite-dominant massive sulfide is compositionally gradational with domains of massive arsenopyrite in the western sector of the orebody. Bladed pyrite occurring within sphalerite-rich banded sulfide is developed locally and resembles the rod-textured pyrite that occurs in the Olympias orebody (Siron et al., 2016). Younger cataclastic breccias related to mineralized strands of the Stratoni fault zone locally crosscut sulfide ore (Figure 3.6G). Quartz-rich sulfide pods and silicified breccias containing fibrous to acicular boulangerite and arsenopyrite occur in close association with quartz-rhodochrosite veins (Figure 3.6H) and vein breccias, which commonly exhibit elevated Au grades. Both silicified breccias and quartz-rhodochrosite vein-breccias overprint the replacement sulfide orebodies, demonstrating similar textural relationships and paragenesis to the Madem Lakkos and Olympias deposits.

The Piavitsa prospect: The Piavitsa prospect occurs 3 km west of the Mavres Petres deposit within the Stratoni fault zone (Figure 3.9). Carbonate replacement semi-massive sulfide with more extensive Au-bearing quartz-rhodochrosite vein-breccias occur in the Piavitsa area. Outcrop and drill core intercepts outline a broad west-northwest-striking set of faults with secondary north-striking splays that collectively define the western segment of the Stratoni fault zone. Outcropping quartz-Mn-rich replacement bodies form the surface expression of discontinuous sulfide zones at depth. These sulfide bodies are largely restricted to marble lenses entrained within the Stratoni fault zone in a setting similar to the Mavres Petres deposit. Gold-bearing quartz-rhodochrosite ± rhodonite veins and vein breccias are principally hosted by hanging wall quartz-muscovite-carbonate-pyrite-altered, graphite-bearing quartz-

Figure 3.10. (A) Detailed geologic map of the Madem Lakkos and Mavres Petres deposits. Mapping was conducted at 1:5,000-scale and based largely on surface outcrops; (B) cross section B-B' of the Mavres Petres deposit defined by surface mapping and underground drill core; drill hole traces have been omitted to preserve readability of the section. Inferred displacement on the Stratoni fault zone is shown by offset marble as indicated by dashed lines. Coordinates are displayed in the Greek Geodetic Coordinate System (GGRS 87 Greek Grid). Abbreviations are as follows: relative level (RL).

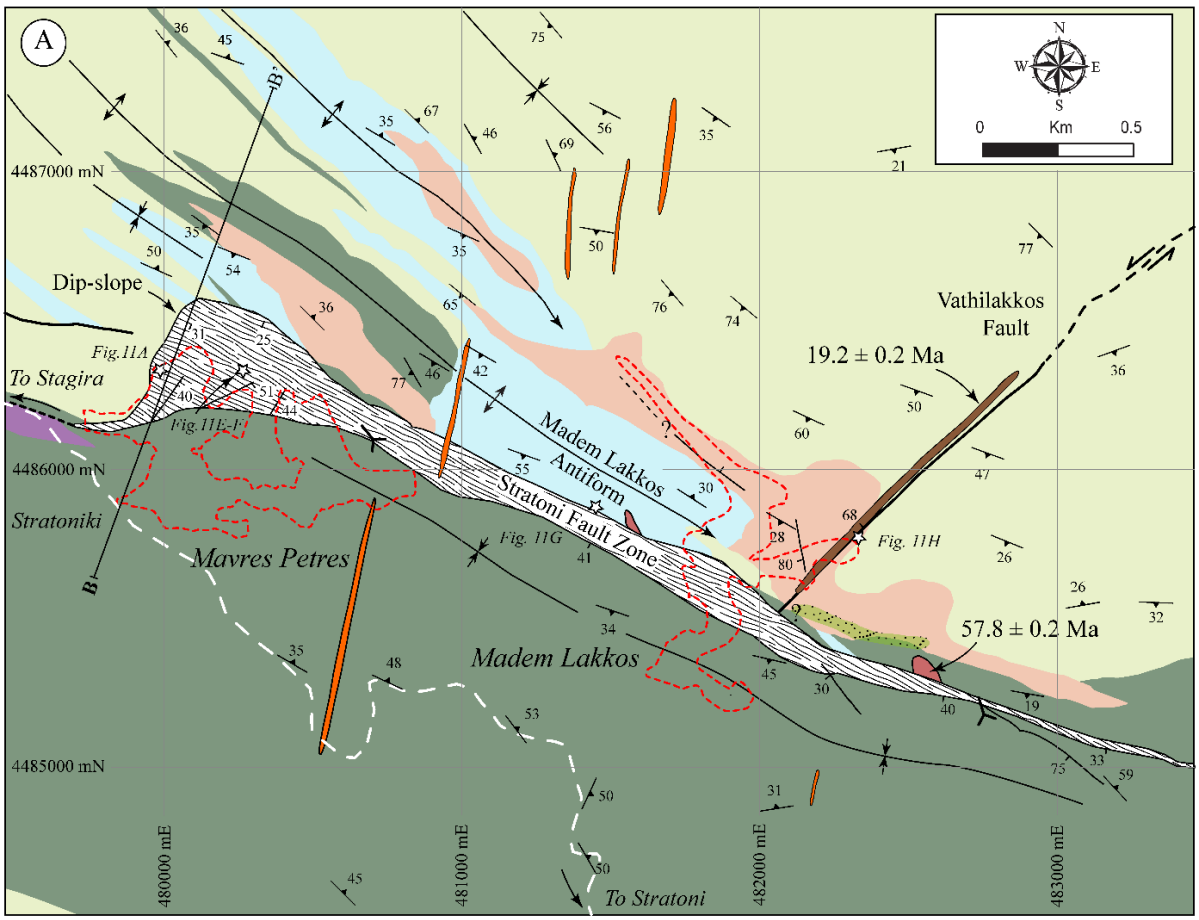

Igneous Rocks

- Black-matrix porphyry dike (19.2 Ma Siron et al., 2016)
- Glomerophyric porphyry (~20 Ma Siron et al., 2016)
- Granodiorite, porphyritic and foliated (Late Paleocene to early Eocene)

Jurassic Rift-related Rocks

- Amphibolite with interlayered gabbro and amphibole-bearing pyroxenite, massive and non-foliated

Permo-Carboniferous to Jurassic Kerdilion Unit

- Quartzo-feldspathic hornblende-biotite gneisses; abundant pegmatites
- Plagioclase-microcline granite gneiss (pegmatitic to aplitic)
- Carbonaceous quartz-biotite gneiss
- Marble, graphite-bearing, layered to massive, locally recrystallized

Alteration and Mineralization

- Wollastonite-tremolite-epidote ± pyrite skarn
- Massive sulfide (cross section)

Map and Cross Section Symbols

- Mylonitic to semi-brittle, and brittle cataclasite (Stratoni fault zone)
- Fault, dashed where approx., marker indicating dip
- Antiform axis indicating plunge direction
- Synform axis indicating plunge direction
- Strike-dip of S1 foliation (plan view)
- Strike-dip of S1 foliation (cross section)
- Underground portal
- Location of photo (refer to text)
- Surface projection of orebody

Figure 3.10. Continued.

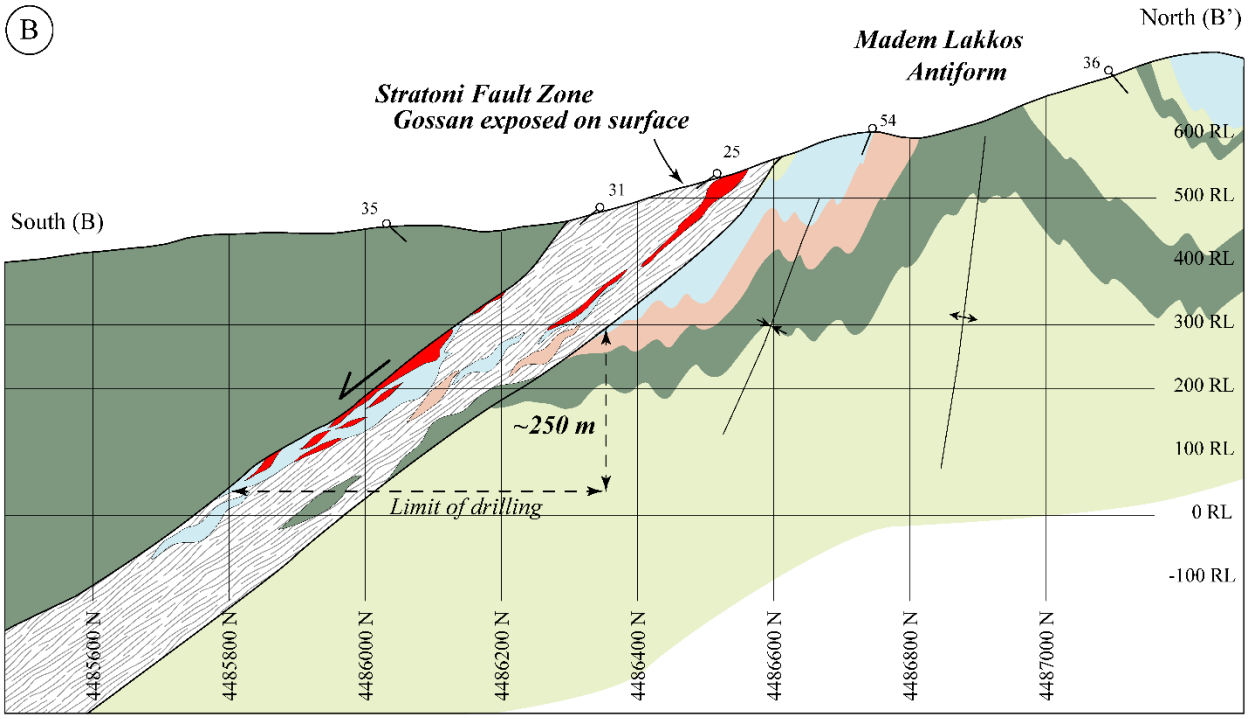

biotite-garnet schists, gneiss, and interlayered amphibolites. Gold mineralization is generally localized where fault splays obliquely intersect major strands of the Stratoni fault zone. Quartz-rhodochrosite veins intercepted in drill core locally exhibit a crustiform texture and commonly contain disseminated pyrite ± galena-sphalerite-arsenopyrite-boulangerite, similar to veins in the upper parts of the Olympias and Mavres Petres deposits. Widely-spaced veins, similar in mineralogy and texture to those in drill core, occur ~2 km south of the Piavitsa prospect in association with steep west and east dipping faults which accommodate cm-scale normal displacement as indicated by offset compositional layers within the gneiss sequence.

Previous tectonic interpretations of the Stratoni fault zone

The area that defines the Stratoni fault zone has been viewed as the tectonic boundary between the Rhodope Kerdilion unit and the Serbo-Macedonian Vertiskos unit (Kockel et al., 1977). Burg et al. (1995, 1996) interpreted the Kerdilion-Vertiskos contact as a south verging thrust fault, whereas Kounov et al. (2015) shows this boundary as the southeastern extension of the Kerdilion detachment fault which

controlled exhumation of the southern Rhodope core complex (e.g., Brun and Sokoutis, 2007). Zircon U-Pb ages from the metamorphic basement rocks (Hahn, 2014) with structural and geochemical data from this study challenge these previous interpretations.

Middle Jurassic amphibolites (Hahn, 2014) of ophiolitic origins that occur to the north in the footwall and to the south in the hanging wall of the Stratoni fault zone (Figure 3.9) exhibit similar structural patterns. Principal component analysis of immobile elements indicates that the amphibolies to the north and south of the Stratoni fault zone are chemically indistinguishable, and therefore have a common origin (see Appendix for details). The geochronological, structural, and geochemical data imply that the amphibolites were tectonically emplaced into the Kerdilion unit by at least the middle Jurassic, either during terrane assembly or after accretion, and later crosscut by normal faults that comprise the Stratoni fault zone. The boundary separating the Kerdilion and Vertiskos units in the Kassandra Mining District is therefore not defined by a middle Eocene detachment fault as suggested by Haines (1998) and inferred by Kounov et al. (2015), but rather an older structure. The terrane bounding structure separating the Kerdilion and Vertiskos units and the tectonic control that imbricated the ophiolitic rocks, however, is currently undefined within the district.

The Stratoni fault zone

The strongly mineralized and south dipping Stratoni fault zone is a continuous mylonitic to brittle fault zone exceeding 12 km in strike length, extending from the Aegean coast at Stratoni to the village of Varvara in the west (Figure 3.9). Marble lenses entrained within the Stratoni fault zone are separated from their likely footwall equivalents by a minimum of 250 m at the Mavres Petres deposit based on drill core data and cross section interpretation (Figure 3.10B). An inflection in the strike direction of the Stratoni fault zone in the Mavres Petres area reflects the linkage between two individual fault segments (Figure 3.9). Underground exploration drill holes within the Mavres Petres mine confirm the western continuation of the Stratoni fault zone as it passes unexposed through the village of Stagira (Figure 3.9). The fault zone

is dominated by strongly carbonaceous rocks toward the west where it is intermittently exposed at surface in the Piavitsa prospect area, and becomes less evident to the northwest where it likely diminishes near the village of Varvara (Figure 3.9).

In general, the Stratoni fault zone separates quartzo-feldspathic biotite gneiss, granite gneiss, marble, and minor amphibolite in the north from amphibolite-dominant units to the south. The fault zone also crosscuts the lower portion of the late Oligocene (25.4 ± 0.2 Ma) Stratoni granodiorite stock in the east (Figure 3.9; Siron et al., 2016). Graphitic quartz-biotite gneiss and schist lay structurally above quartzo-feldspathic biotite gneiss and both are gradationally interlayered with marbles and thin amphibolite units. Fault strands preferentially exploit this graphite-bearing layer particularly within the Mavres Petres and Piavitsa areas. Residual carbonaceous material is localized along pressure solution seams (Figure 3.11A-B), and is spatially associated with the hydrothermal alteration of amphibole, biotite, feldspar, and garnet to muscovite and chlorite within the damage zone. Carbonaceous material derived from the graphite-bearing quartz-biotite layer and marble is concentrated in areas where deformation and alteration is most intense.

Internal structure of the Stratoni fault zone: The Stratoni fault zone contains slivers of amphibolite, marble, quartzo-feldspathic biotite gneiss, granite gneiss, and graphite-bearing quartz-biotite schists in the polyphase damage zone that consists of multiple anastomosing fault strands ranging from several tens of meters and locally in excess of 100 m in width. The south-southwest dipping ductile mylonitic shear zones that define the earliest stage of extension within the Madem Lakkos deposit exhibit textures and relative timing relationships consistent with syn- to post-peak metamorphism. Kinematic indicators including asymmetric S-C fabric, quartz ribbons, and recrystallized feldspar sub-grains associated with strain-related myrmekites and a biotite-hornblende shear fabric imply formation within an extensional stress field at lower amphibolite-facies metamorphic conditions (Haines, 1998). These mylonitic shear zones are extensively overprinted by broad deformation zones exhibiting pressure solution fabrics which show the development of phyllonitic cleavage defined by residual carbonaceous

material, muscovite, and chlorite. Drag folds that warp S1 and S2 foliation into near-parallelism with the shear zone indicate a component of ductile strain whereas the area between individual fault strands is commonly disrupted by fracturing and brecciation, reflecting more brittle styles of deformation.

Overprinting relationships record progressively younger increments of extensional strain. Semi-brittle shear zones are enriched with carbonaceous material and commonly have a variably silicified fault gouge matrix that contains sub-rounded, asymmetrically rotated clasts of marble, amphibolite, and pegmatitic to aplitic granite gneiss (Figure 3.11C). Mineralized fault strands are generally altered to a mineral assemblage consisting of hydrothermal muscovite, Fe- and Mg-rich carbonate, and fine-grained pyrite ± galena-sphalerite-arsenopyrite (Figure 3.11D). Individual shear zones commonly contain asymmetric fault-related shear folds exhibiting an isoclinal geometry with southward dipping axial planes (Figure 3.11E). Second-order Riedel shear fractures occur as an array of synthetic faults that overprint and internally displace previously developed shear fabric (Figure 3.11F). Semi-brittle shear zones and spatially associated sulfide lenses are locally overprinted by fault-hosted veins and clast-supported cataclastic fault breccias containing sub-angular to angular fault-rock fragments cemented by hydrothermal rhodochrosite ± rhodonite. These breccias may transition laterally into quartz-rhodochrosite ± rhodonite veins as recognized at the Mavres Petres deposit and the Piavitsa prospect (Siron et al., 2016).

Fault-slip surfaces that are late with respect to semi-brittle faults and the sulfide bodies form a complex anastomosing fault network internal to the Stratoni fault zone. Late- to post-mineral faults typically strike oblique to the previously developed shear fabric but in general have not accommodated sufficient strain to completely displace principal fault strands. A prominent post-mineral fault surface outcrops in marble above the Madem Lakkos mine and displays a corrugated fault surface with micro-breccia striations consisting of angular to sub-angular marble fragments supported by a fine-grained carbonate groundmass (Figure 3.11G). Similar brittle faults associated with incremental amounts of displacement are reported to crosscut the Madem Lakkos massive sulfide orebody (Haines, 1998) and occur in underground exposures at the Mavres Petres deposit.

Neotectonic activity within the Stratoni fault zone has produced a topographically pronounced range front with distinct south-facing triangular facets (Michailidou et al., 2005). Fault surfaces commonly occupy areas of previous fault deformation and are typified by moderate to steep south dipping fracture arrays and polished slip surfaces. In the Stratoni area, these fault surfaces are encrusted by a clast-supported breccia carapace consisting of hydrothermally-altered and sulfide-bearing metamorphic wallrock and late Oligocene feldspar porphyry dike fragments that are cemented by a ferruginous matrix. These iron-rich scabs are interpreted to be ferricrete breccias that formed by weathering of sulfide-rich rock. Neotectonic faults (see kinematic analysis section below) exposed underground and intercepted in drill core manifest as narrow fault surfaces or gouge-rich zones that crosscut sulfide ore and are superimposed on all previous strain features.

Faults intersecting and oblique to the Stratoni fault zone: Numerous faults merge into or intersect the Stratoni fault zone, and are observed in surface outcrops and within underground exposures. The most notable of these structures is the northwest dipping Vathilakkos fault (Figure 3.10A). This structure is about a 1 m-wide network of fractures and gouge-filled brittle faults outcropping above and within the Madem Lakkos mine (Figure 3.11H). The Vathilakkos fault extends for approximately 2 km to the northeast of the Stratoni fault zone as determined from drill core and surface traces. The intersection of the Vathilakkos fault with the Stratoni fault zone is not exposed but Haines (1998) describes apparent right-lateral displacement of the Madem Lakkos orebody related to post-mineral movement on this fault. An altered glomerophyric porphyry dike and an unaltered black-matrix porphyry dike, the latter dated at 19.2 ± 0.2 Ma by zircon U-Pb methods (Siron et al., 2016), each occur within the Vathilakkos fault. Both dikes crosscut the Madem Lakkos orebody at depth (Nebel, 1989; Gilg and Frei, 1994; Haines, 1998). Strands of the Vathilakkos fault crosscut the black-matrix porphyry dike (Figure 3.11H) indicating that movement continued after crystallization of the dike.

Figure 3.11. Photos of representative fault styles from the Stratoni fault zone: (A) outcrop of the ductile-brittle Stratoni fault zone above the Mavres Petres deposit. Sense of shear is normal and top-to-the-south; (B) drill core intercept from the Piavitsa prospect of graphite-bearing quartz-biotite gneiss crosscut by a semi-brittle carbonaceous shear band bounding quartz-sericite-carbonate-pyrite alteration; (C) foliated, semi-brittle fault showing well-developed pressure solution fabrics within a silicified carbonaceous matrix intergrown with pyrite, dolomite, and crystalline hydrothermal muscovite. Sense of shear is top-to-the-left; (D) drill core intercept from the Piavitsa prospect showing typical pale green muscovite, dolomite, and pyrite alteration replacing graphitic quartz-biotite-garnet gneiss adjacent to a mineralized strand of the Stratoni fault zone; (E) micro-shear folds contained within a major strand of the Stratoni fault zone showing normal sense of shear to the south. Image taken from an outcrop above the Mavres Petres deposit; (F) same outcrop of Stratoni fault zone exhibiting synthetic Riedel shears that crosscut the shear fabric and demonstrate normal southward sense of shear. The pale green mineral is hydrothermal muscovite; (G) outcrop of the post-mineral segment of the Stratoni fault zone above the Madem Lakkos deposit. Micro-breccia streaks and tension fractures developed on the fault surface indicate normal sense of shear in a southwest direction; (H) outcrop of the Vathilakkos fault showing the faulted contact between granite gneiss to the east and an early Miocene black-matrix porphyry dike to the west. Abbreviations are as follows: dolomite (Dol), muscovite (Ms), pyrite (Py).

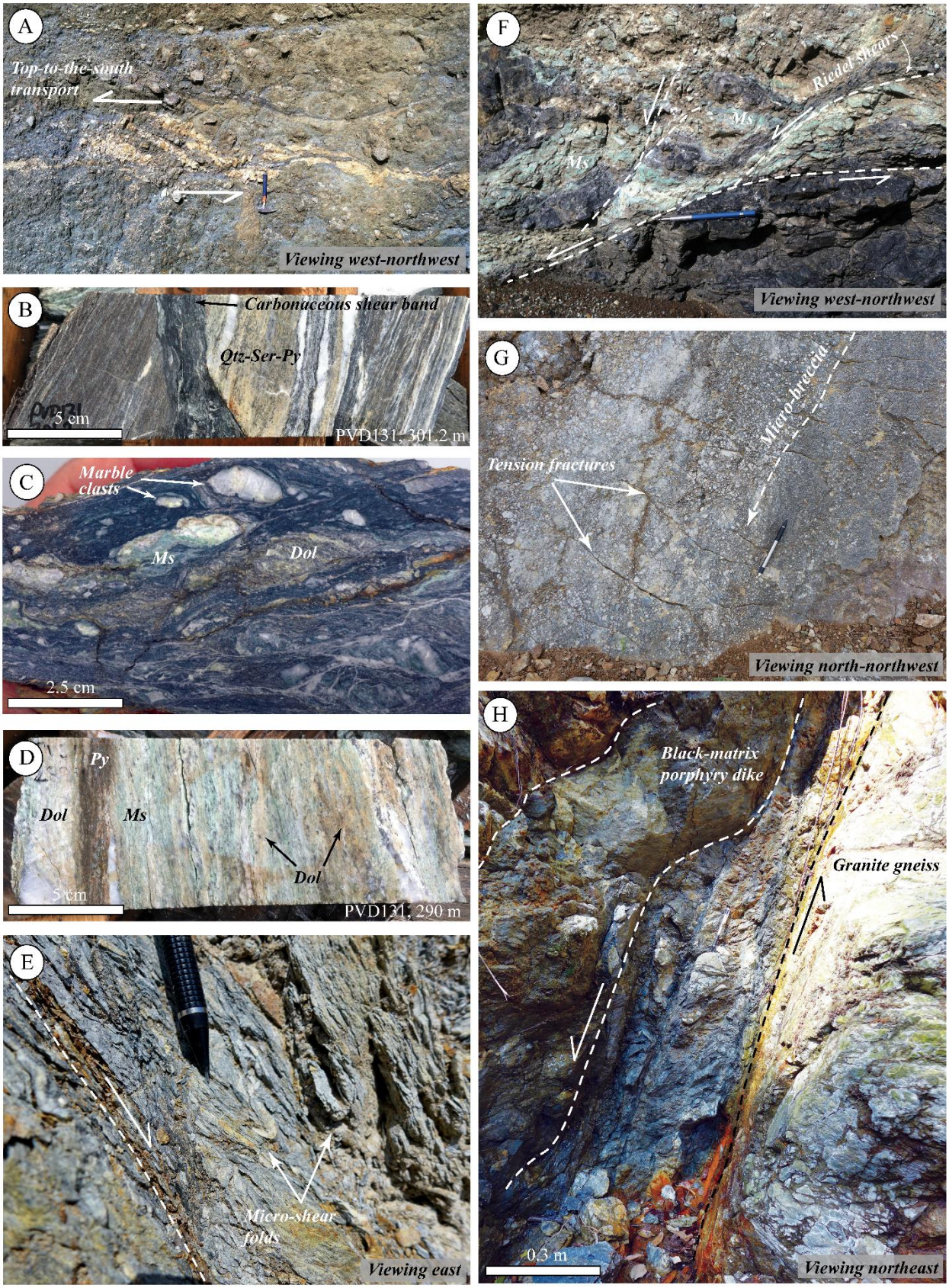
A
Top-to-the-south transport
Viewing west-northwest
B
Carbonaceous shear band
Qtz-Ser-Py
5 cm
PVD131, 301.2 m
C
Marble clasts
Ms
Dol
2.5 cm
D
Py
Dol
Ms
Dol
5 cm
PVD131, 290 m
E
Micro-shear folds
Viewing east
F
Riedel shears
Ms
Ms
Viewing west-northwest
G
Micro-breccia
Tension fractures
Viewing north-northwest
H
Black-matrix porphyry dike
Granite gneiss
0.3 m
Viewing northeast

Kinematic analysis

The Stratoni fault zone mainly displays normal top-to-the-south-southwest sense of shear as evidenced by displaced lithologies (Figure 3.10B) and kinematic criteria (Figure 3.12A). Mineralized west-northwest- and north-northeast-striking foliated, semi-brittle shear zones were likely active at the same time based on textural similarities and the lack of crosscutting relationships, and are therefore treated collectively in this analysis. Kinematic analyses of S-C shear fabrics and Riedel shear fractures developed within the semi-brittle shear zones reveal a bimodal fault-slip distribution that plunges to the south-southeast and south-southwest (Figure 3.12A). Slip vectors developed on north-northeast-striking faults occur at the intersection of the two fault sets (Figure 3.12A) and are interpreted to be strain compatible with the principal west-north-striking faults. While the overall heterogeneous fault-slip behavior of the semi-brittle Stratoni fault zone may be explained by multiple deformation events (e.g., Marrett and Allmendinger, 1990), strain incompatibility is likely best explained by dilation and brecciation processes.

Late- to post-mineral faults within the Stratoni fault zone strike oblique to syn-mineral semi-brittle shear zones or form splays trending to the north-northwest and north-northeast. Northwest-plunging slickenlines on fault surface within the Stratoni fault zone resulted from largely compatible dextral and normal dip-slip movement (Figure 3.12B). Northwest-plunging slickenlines are similarly recorded on a fault surface from the Gomati fault zone to the south of the Skouries deposit (Figure 3.2), which also imply right-lateral displacement. These faults convey a younger extensional episode responding to an east-directed principal axis of extension (Figure 3.12B). The late- to post-mineral and mostly brittle Vathilakkos fault in the footwall of the Stratoni fault zone displays left-lateral displacement on a set of northeast-striking brittle faults resulting from a west-directed principal axis of extension (Figure 3.12C).

Younger cataclastic breccias and gouge-filled faults that overprint earlier ductile and semi-brittle fabrics record increments of normal displacement that postdate carbonate replacement sulfide orebodies.

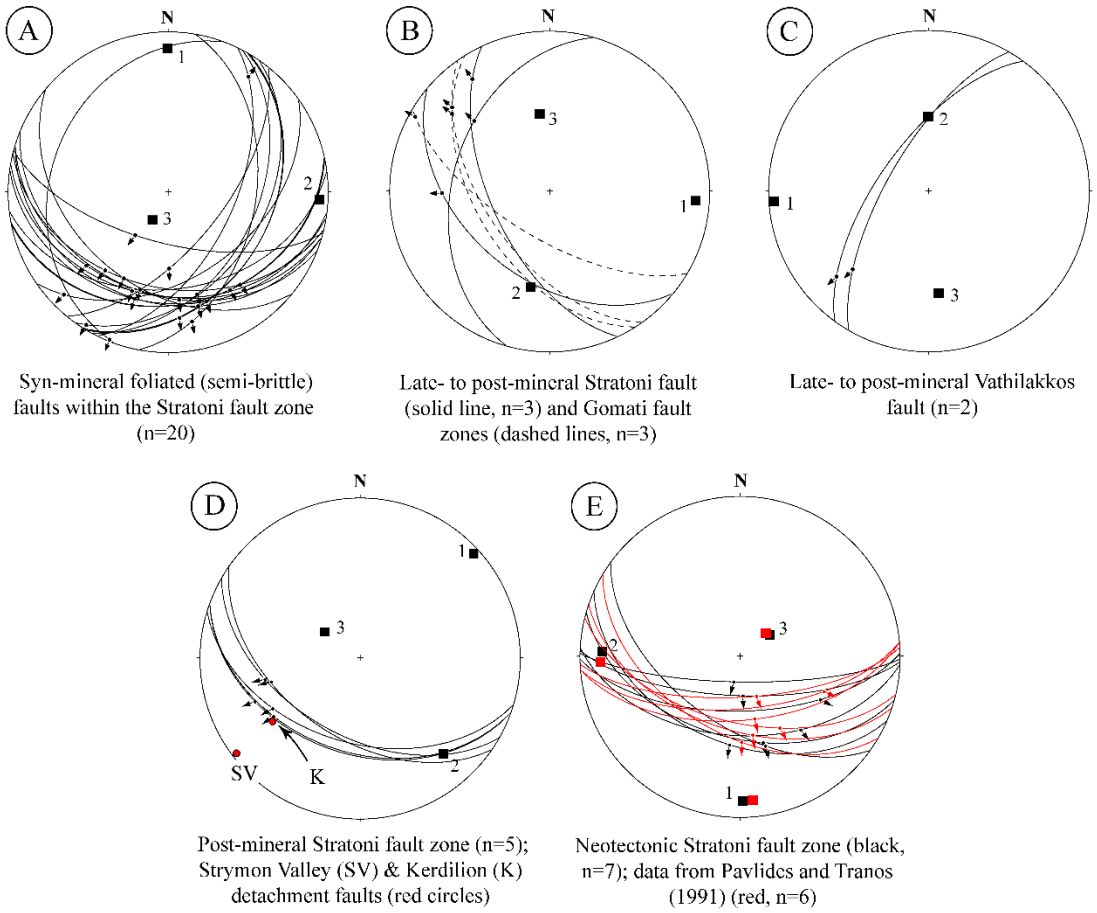

Figure 3.12. Lower hemisphere, equal-area stereographic projections of fault kinematic data from the Stratoni fault zone. Fault planes and slip vectors are represented by great circles and arrows, respectively. Kinematic strain axes are plotted as squares and numbered according to the principal extension axis (1), the principal shortening axis (3), and the orthogonal intermediate axis (2): (A) kinematic data from semi-brittle and syn-mineral segments of the Stratoni fault zone; (B) late- to post-mineral strand of the Stratoni fault zone (solid line) and kinematically equivalent deformation from the Gomati fault zone (dashed lines); (C) late- to post-mineral Vathilakkos fault; (D) post-mineral corrugated fault segment within the Stratoni fault zone at the Madem Lakkos deposit. Kinematic criteria from the Kerdilion (K) and Strymon Valley (SV) detachment faults (Dinter, 1998) are shown as red circles for comparison; (D) neotectonic faults within the Stratoni fault zone from this study are plotted in black with data from Pavlides and Tranos (1991) represented in red. Note the coincident position of the kinematic strain axis for each set of data.

Fluted (corrugated) troughs, micro-breccia streaks, calcite mineral fibers, and extensional tensile fractures developed on the fault surface (Figure 3.11G) indicate normal top-to-the-southwest transport with a component of right-lateral oblique movement produced by a northeast-directed principal axis of extension (Figure 3.12D). The youngest faults occupying the Stratoni fault zone display slickenlines and minor groove marks demonstrating normal top-to-the-south-southeast relative movement with a minor left-

lateral strike-slip component produced by a south-directed principal axis of extension (Figure 3.12E). These data agree with the kinematic axes previously reported from the neotectonic segment of Stratoni fault zone (Figure 3.12E; Pavlides and Tranos, 1991).

^{40}Ar-^{39}Ar Geochronology of the Carbonate Replacement Deposits

Two samples of pale green hydrothermal sericite (white mica) from sulfide-bearing semi-brittle, phyllonitic shear zones of the Kasandra fault at the Olympias deposit and the Stratoni fault zone at the Piavitsa prospect were dated using the ^{40}Ar-^{39}Ar technique (see Appendix for analytical methodology and data). Secondary white mica is spatially associated with sulfide ore at the Olympias, Madem Lakkos, Mavres Petres deposits and the Piavitsa prospect. It occurs within and adjacent to mineralized intervals and extends into the metamorphic wallrock for no more than several meters. Structurally, these micas define the foliation in semi-brittle fault strands within the Kassandra fault and the Stratoni fault zone. Quartz-carbonate ± sulfide veinlets associated with the replacement sulfide bodies crosscut but are also overprinted by mineralized shear fabrics implying a syn-mineral timing to foliation and mica development. While there are general spatial, mineralogical, and structural relationships between hydrothermal white mica with faults and sulfide, correlation with a specific style of mineralization (replacement sulfide or rhodochrosite ± rhodonite vein-breccias) is not well constrained. Shortwave infrared and powder X-ray diffraction analyses indicate that the pale green mica in the two samples investigated is muscovite.

Results

Sample OL559 (252m) was collected from drill core which intercepted a phyllonitic shear band crosscutting pegmatitic granite gneiss associated with the Kassandra fault at the Olympias deposit (Figure 3.7E). Muscovite defines a lenticular shear fabric and forms euhedral to subhedral grains reaching 500 μm in length, and is intergrown with domains of quartz-carbonate and euhedral fine-grained masses of

pyrite, sphalerite, and arsenopyrite (Figure 3.7E; Figure 3.13A). Step-heating analysis of mica yielded an overall flat ^{40}Ar-^{39}Ar spectrum with a plateau age of 22.6 ± 0.3 Ma, including ~80% of total ^{39}Ar released (Mean Square of Weighted Deviates [MSWD] = 4.33; Figure 3.13B). Isotopic disturbance in the initial three steps may be attributed to excess ^{40}Ar or recoil effects possibly due to a fraction of fine-grained mica within the sample. We interpret this date as the crystallization age of the mica, and by association, a minimum age of hydrothermal alteration which was coeval within carbonate replacement sulfide ore at the Olympias deposit.

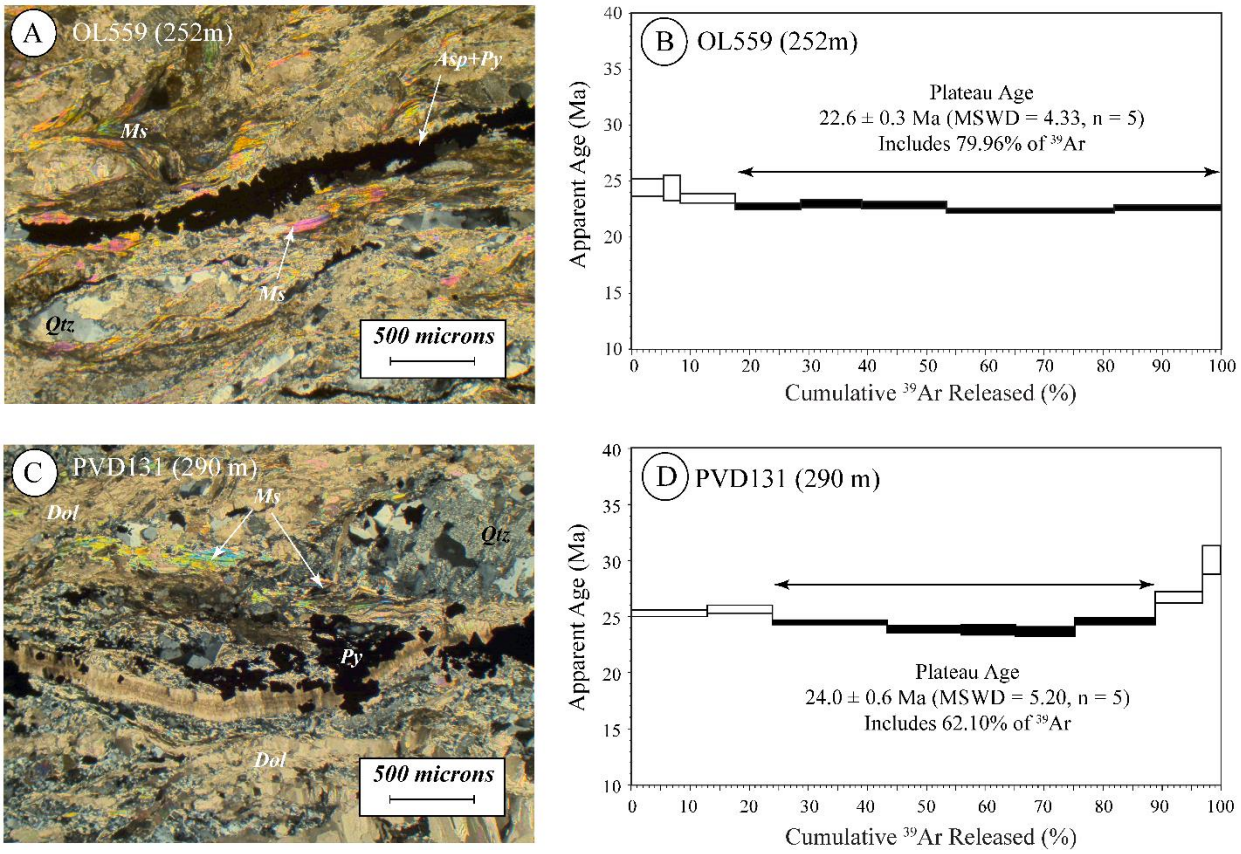

Figure 3.13. Representative photomicrographs and step-heating Ar-release patterns for samples from the Olympias deposit and Piavitsa prospect: (A-B) photomicrograph and Ar-release spectrum of sample OL559 (252 m) from a drill core intercept of the Kassandra fault at the Olympias deposit. An image of this sample is located in Figure 6E; (C-D) photomicrograph and Ar-release spectrum of sample PVD131 (290 m) from a drill core intercept adjacent to a mineralized strand of the Stratoni fault at the Piavitsa prospect. An image of this sample is located in Figure 11D. Abbreviations are as follows: arsenopyrite (Asp), dolomite (Dol), muscovite (Ms), pyrite (Py), quartz (Qtz).

Sample PVD131 (290m) was collected from a drill core intercept of a pervasively altered and mineralized segment of carbonaceous quartz-biotite gneiss immediately adjacent to semi-brittle fault strands within the western segment of the Stratoni fault zone at the Piavitsa prospect (Figure 3.11D). Muscovite occurs as euhedral to subhedral and mixed fine- to coarse-grained (greater than 500 μm) masses that are intergrown with bands of disseminated euhedral pyrite with lenticular quartz and dolomitic carbonate domains that define the shear fabric and alteration associated with sulfide ore (Figure 3.13C). Step-heating analysis of an aliquot consisting of ~15 grains yielded a saddle-shaped ^{40}Ar-^{39}Ar age spectrum with a short, flat segment at its trough (steps 3-7) corresponding to an age of 24.0 ± 0.6 Ma, including ~62% of total ^{39}Ar released (MSWD = 5.20; Figure 3.13D). Increasing ages from the higher temperature steps may reflect inherited ^{40}Ar potentially derived from wallrock micas. The plateau is interpreted as the minimum crystallization age of the mica and a minimum age of hydrothermal alteration associated with the replacement sulfide bodies in the Piavitsa area.

Structure of the Skouries Porphyry Au-Cu Deposit

The Skouries deposit lies 3.5 km north of the village of Megali Panagia and the Gomati fault zone (Figure 3.14A). An early Miocene timing for porphyry emplacement and Au-Cu mineralization is constrained by a 20.6 ± 0.5 Ma zircon U-Pb crystallization age and 19.9 ± 0.9 Ma ^{40}Ar-^{39}Ar hydrothermal biotite age, respectively (Hahn et al., 2012; Hahn, 2014). These radiometric ages agree with the 19.0 ± 1.0 Ma zircon-uranothorite age of Frei (1992). Previous studies on the Skouries deposit have largely focused on the mineralogical and physiochemical conditions of ore deposition (Eliopoulos and Economou-Eliopoulos, 1991; Frei, 1995; McFall et al., 2016). Structural studies from the deposit area are limited to unpublished consulting reports. The following section presents a revised geologic map and cross section of the Skouries area that includes the Aspro Lakkos porphyry, and is based on surface and drill core observation. Structural measurements of ductile metamorphic fabrics in the host gneiss and schist, and vein orientations from the Skouries stock were collected from surface outcrops.

The Skouries deposit

The Skouries porphyry Au-Cu deposit is largely hosted by a composite high-K calc-alkaline to shoshonitic, megacrystic K-feldspar porphyry intrusion that was emplaced into quartz-rich micaceous gneiss and schist of the Vertiskos unit (Figure 3.14A; Eliopoulos and Economou-Eliopoulos, 1991; Frei, 1992, 1995; Tobey et al., 1998; Kroll et al., 2002; Hahn et al., 2012; Hahn, 2014; Siron et al., 2016). The mineralized porphyry intrusion forms a narrow, less than 200 m-diameter, pencil-like stock that plunges steeply to the south-southwest and obliquely crosscuts the moderate to steeply northeast dipping limb of a district-scale F2 antiform (Figure 3.14A-B). Surface exposures and drill data indicate that the porphyry stock has a subtle northeast elongate geometry. Four K-feldspar porphyritic intrusive phases of quartz monzonite composition comprise the Skouries stock and are described in Siron et al. (2016). The relative timing relationships among the porphyry phases are based on mineralogy, texture, and crosscutting relationships (Tobey et al., 1998; Kroll et al., 2002; Siron et al., 2016). Margins of the porphyry stock exhibit sharp and discordant intrusive contacts with respect to S1 foliation and F2 folds developed within the metamorphic host rocks.

Four principal vein stages and associated alteration are recognized at the Skouries deposit. The oldest vein set is a dense stockwork to sheeted array of quartz-only, quartz-magnetite, and magnetite-only stringer veins associated with pervasive disseminated magnetite and secondary K-feldspar alteration (Figure 3.15A-C). Introduction of Au-Cu was accompanied by quartz-magnetite-chalcopyrite veins associated with K-feldspar-biotite-magnetite alteration and by a later crosscutting set of sulfide-rich quartz-biotite-chalcopyrite-bornite ± magnetite veins (Kroll et al., 2002; Siron et al., 2016). Chalcopyrite-bearing magnetite veins and the later set of quartz-biotite-chalcopyrite-bornite ± magnetite veins mainly occur within the early and intra-mineral porphyry phases of the intrusive stock, while younger porphyry phases may host later sulfide-rich chalcopyrite-bornite veins (Siron et al., 2016), particularly deep in the deposit. Mineralized veins also occur within enclaves of schist between porphyry phases and immediately surrounding the composite porphyry stock. A younger assemblage of pyrite-carbonate (ferroan calcite-

Figure 3.14. (A) Detailed geologic map of the Skouries deposit and surrounding area modified after Kockel et al. (1975, 1977). Mapping was conducted at 1:5,000-scale and based largely on surface outcrops; (B) cross section C-C' of the Skouries porphyry and the post-mineral Aspro Lakkos porphyry is based on surface mapping and drill core. Trace of folded S1 foliation is illustrated by the dotted line. Coordinates are displayed in the Greek Geodetic Coordinate System (GGRS 87 Greek Grid).

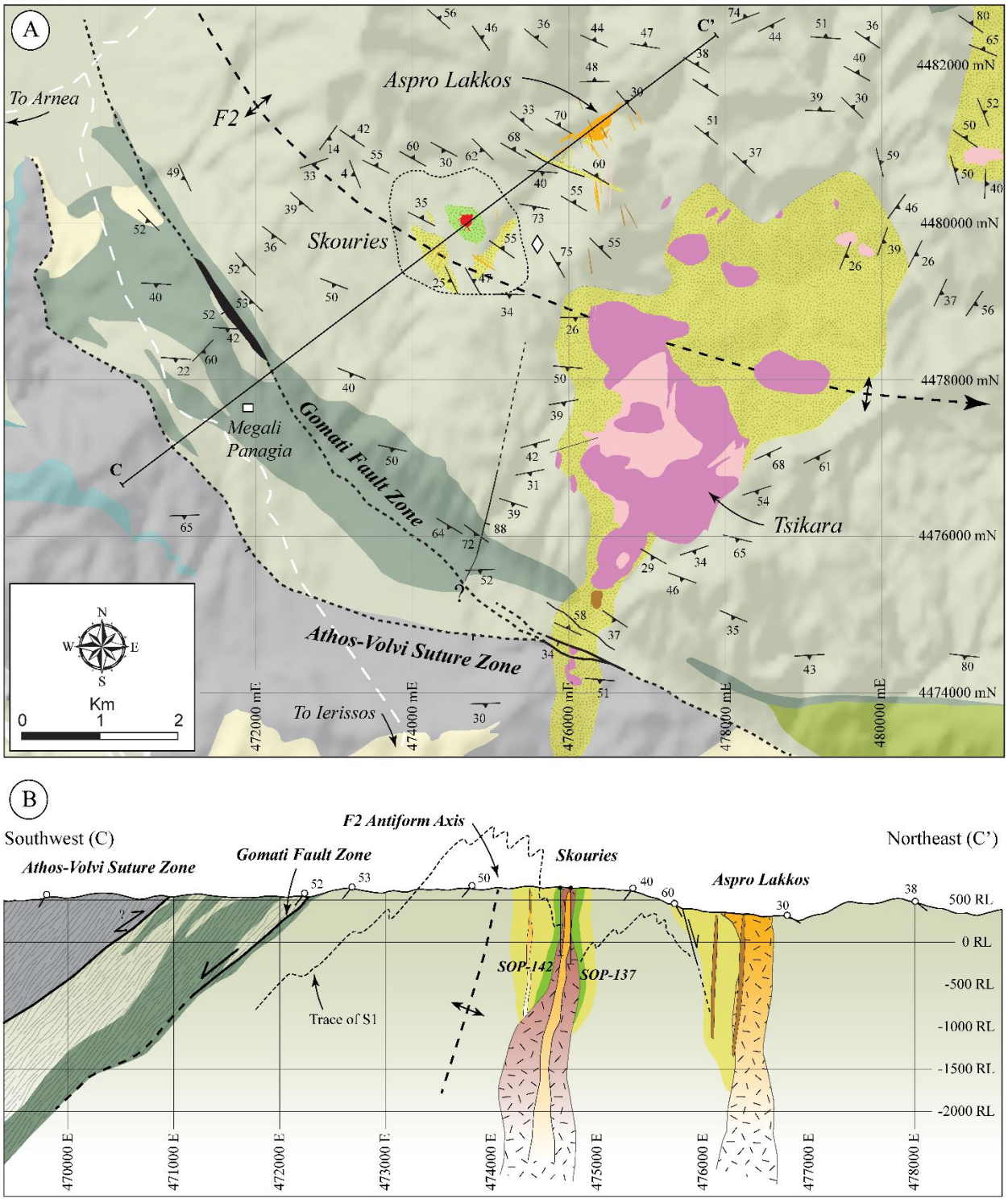
A
To Arnea
F2
Aspro Lakkos
Skouries
C
C'
Megali Panagia
Gomati Fault Zone
Tsikara
Athos-Volvi Suture Zone
To Ierissos
N
S
W
E
Km
0
1
2
4482000 mN
4480000 mN
4478000 mN
4476000 mN
4474000 mN
472000 mE
474000 mE
476000 mE
478000 mE
480000 mE
B
Southwest (C)
Northeast (C')
F2 Antiform Axis
Athos-Volvi Suture Zone
Gomati Fault Zone
Skouries
Aspro Lakkos
SOP-142
SOP-137
Trace of S1
500 RL
0 RL
-500 RL
-1000 RL
-1500 RL
-2000 RL
470000 E
471000 E
472000 E
473000 E
474000 E
475000 E
476000 E
477000 E
478000 E

Figure 3.14. Continued.

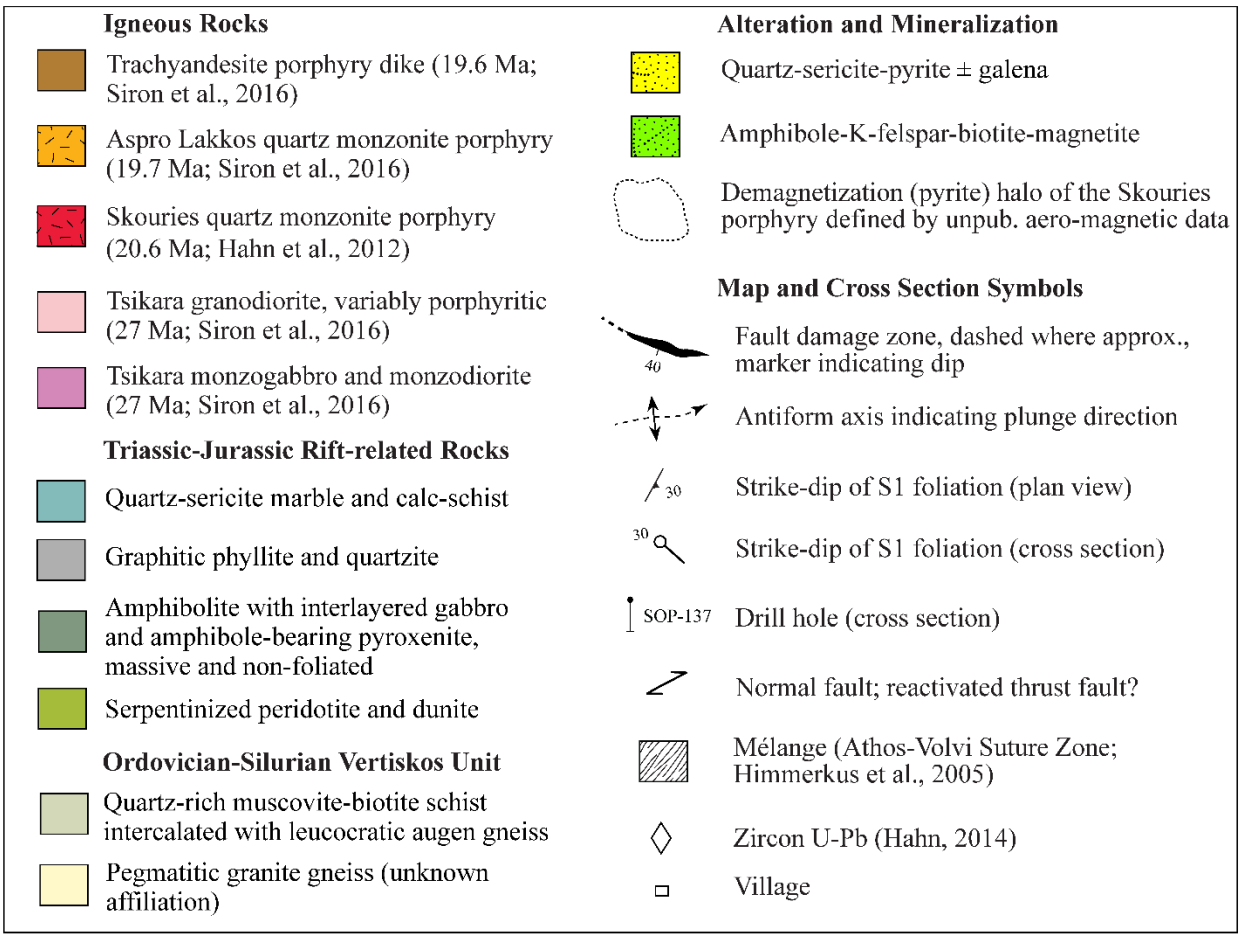

ankerite) ± base metal veins, similar to the D veins described by Gustafson and Hunt (1975), are accompanied by fine-grained white mica-carbonate alteration that envelopes veins and minor fault breccias. These late-stage veins and associated alteration crosscut all porphyry phases within the stock and adjacent wallrock (Figure 3.15D), but are volumetrically minor.

Widely spaced fractures and faults occur within the porphyry stock and the metamorphic wallrock as observed in drill core and surface outcrops. Albeit minor, faults crosscut all porphyry phases, veins, and associated alteration. Faults in the Skouries area occupy steeply dipping, northwest-striking planes that manifest as narrow, gouge-rich shear zones that are generally less than 0.5 m in width. Offset of compositional layers within the metamorphic sequence suggests that these faults accommodate only minor normal displacement.

Geometry of porphyry-related veins and dikes

Outcrops of the early quartz monzonite porphyry phase containing quartz-magnetite and chalcopyrite-bearing magnetite veins and associated pervasive K-feldspar-biotite-magnetite alteration form the surface expression of the Skouries deposit. These veins are steeply dipping and display a preferential north-northeast sheeted orientation (Figure 3.15E). A volumetrically minor population of shallow dipping quartz-only and quartz-magnetite veins associated with K-feldspar-magnetite envelopes (Figure 3.15B) is also present in outcrop and at depth. These shallow dipping veins are crosscut by younger, steeply dipping Cu-bearing quartz-magnetite veins (Figure 3.15B-C). Pyrite-carbonate ± base metal veins that occur within a 1 km radius of the porphyry stock are interpreted to be the distal expression of the Skouries magmatic-hydrothermal system. These young and spatially distal veins strike to the northwest-southeast and north-south (Figure 3.15F), oblique to the direction of S1 foliation and subparallel to the fault-fracture network in the area.

Late-stage megacrystic K-feldspar porphyry dikes hosted by gneiss and schist occur within 0.5 km from the Skouries stock. Porphyry dikes display steeply dipping planar geometries with sharp and discordant contacts with respect to S1 foliation. These dikes typically lack veins, locally exhibit a weak, albeit pervasive sericite-pyrite alteration, and crosscut amphibole-magnetite-altered schist adjacent to the porphyry stock. An anisotropic distribution of porphyry dike orientations is evident from outcrop with northeast-southwest strikes predominating and a subordinate set that strike roughly in an east-west direction (Figure 3.15G).

Discussion

Deformation history and kinematic evolution of extensional faulting in the district

The metamorphic basement rocks belonging to the Permo-Carboniferous to Jurassic Kerdilion unit and the Ordovician-Silurian Vertiskos unit within the Kassandra Mining District were affected by at least three syn-metamorphic deformation episodes beginning with an early D1 event that resulted in a

Figure 3.15. Representative photos of porphyry-style veins and vein measurement data from the Skouries area: (A) early quartz monzonite porphyry phase outcropping in the Skouries open-pit area hosting sheeted quartz-magnetite veins which strike northeast; (B) close-up view of box in Figure 15A showing oxidized Cu-bearing quartz-magnetite veins that crosscut earlier sub-horizontal quartz ± magnetite veins; (C) drill core example of quartz-magnetite veins crosscutting the early quartz monzonite porphyry phase. These veins occur at a high angle to core axis (vertical hole) indicating that they belong to the sub-horizontal set. Note the steeply dipping vein which overprints the shallow dipping set; (D) late pyrite-ferroan calcite vein with a pale green mica-quartz-carbonate envelope replacing biotite-magnetite-altered schist adjacent to the porphyry stock; (E) stereonet of quartz-magnetite and Cu-bearing quartz-magnetite veins measured from the porphyry stock in outcrop; (F) stereonet of pyrite-carbonate veins occurring within the Vertiskos unit in the Skouries area; (G) late-stage K-feldspar porphyry dikes occurring peripheral to porphyry stock. Stereonets display planar data represented as poles in a lower-hemisphere, equal-area projection and contoured at 3σ significance level following the method of Kamb (1959). The rose diagram illustrates azimuth of veins and dikes with petals displayed as axes and scaled by length. Axial distributions are plotted as black squares with numbers corresponding to density concentrations ranging from greatest (1), intermediate (2), and least (3). Abbreviations are as follows: biotite (Bt), calcite (Cal), copper (Cu), magnetite (Mag), pyrite (Py), quartz (Qtz), sericite (Ser).

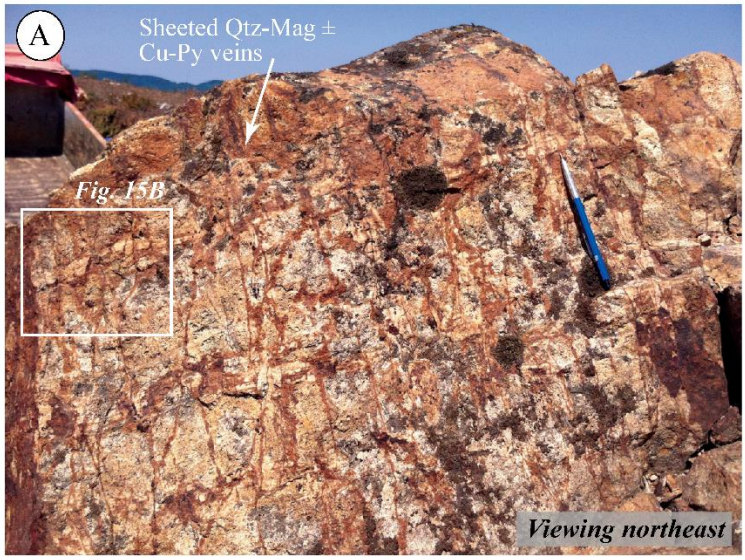

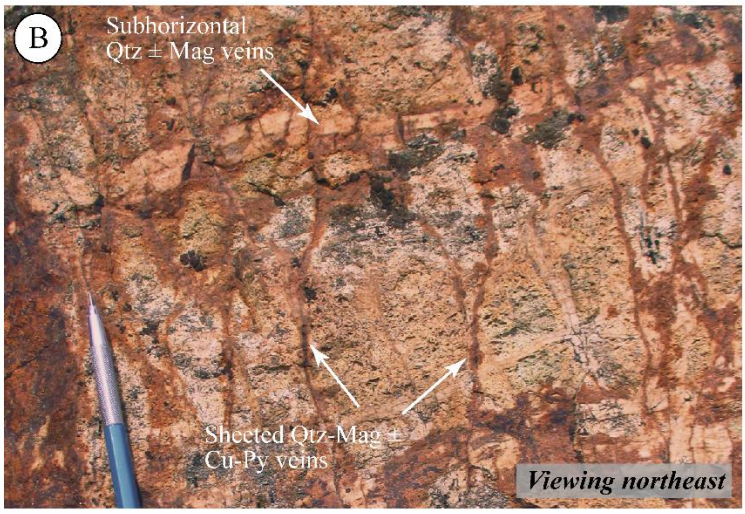

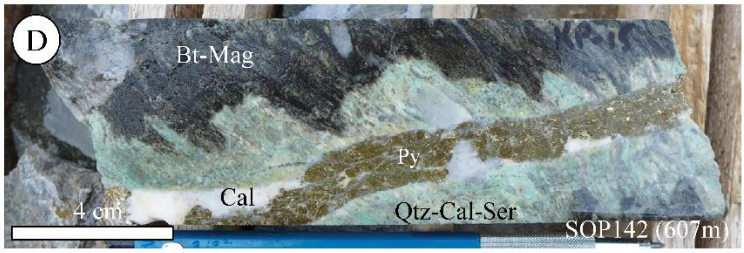

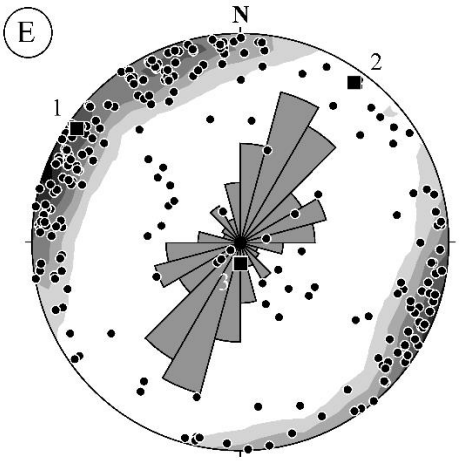

Skouries porphyry Qtz-Mag-Cu veins (n=235), measured within stock

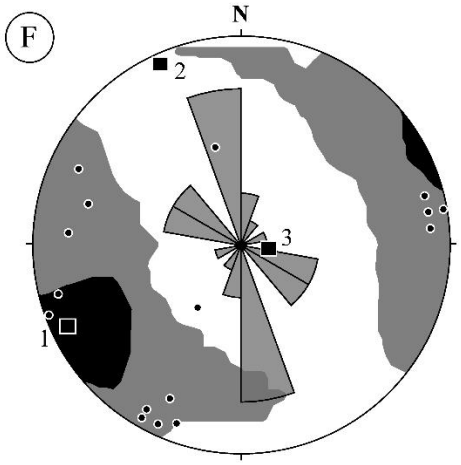

Pyrite-carbonate veins (n=16) in the Skouries area, measured in schist and gneiss

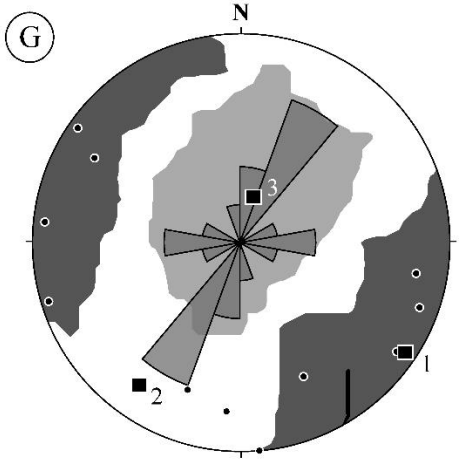

K-feldspar porphyry dikes (n=11) peripheral to the Skouries stock

penetrative S1 foliation accompanied by amphibolite-facies metamorphism. The D2 event reworked the earlier S1 penetrative fabrics into tight to open F2 folds with an associated axial planar S2 cleavage and locally prominent L2 intersection lineation. A younger and lower strain D3 event resulted in a S3 cleavage which overprinted all earlier ductile fabrics. D1 and D2 fabrics both imply top-to-the-northeast vergence possibly representing increments of progressive deformation associated with regional Eocene or older contraction. Contractional ductile deformation likely continued through the Late Paleocene as evidenced by dated intrusions that contain a penetrative S1 foliation.

The Stratoni fault zone originated as a mylonitic normal fault that was active during regional southwest-directed ductile extension as demonstrated at the Madem Lakkos deposit by Haines (1998). Mylonitic shear zones nucleated within a lithologically complex section of the Kerdilion metamorphic sequence where the orientation of ductile structural fabrics were approximately perpendicular to the principal axis of extension. Extensional mylonites preferentially exploited the rheologically weak marble and graphitic meta-pelite unit bounded by massive amphibolite to the south with granite gneiss and quartzo-feldspathic gneisses to the north. Mylonitic shear zones in the Olympias area, however, are less prominent than within the Stratoni fault zone, and are largely restricted to a diffuse shear zone network between the Kassandra and East faults. Sharp rheological gradients between quartzo-feldspathic biotite gneiss and conformably interlayered graphite-bearing marble units with granitic pegmatite sills established a stratigraphic control for localizing extensional strain. Based on textural and kinematic similarities, the mylonitic shear zones within the Olympias deposit were probably coeval with extensional mylonites in the Stratoni fault zone. Mylonitic deformation probably initiated at the onset of regional extension during the middle Eocene based on apatite and zircon fission track ages from the Kerdilion detachment fault located to the west of the Kassandra Mining District (Figure 3.2; Wüthrich, 2009; Kounov et al., 2015).

Semi-brittle faults overprint earlier mylonitic shear zones in the Olympias area and within the Stratoni fault zone. Textures suggest that the formation of ductile-brittle fault fabrics occurred by the

mechanical reduction of grains through cataclastic flow (e.g., Sibson, 1977) whereas carbonaceous fault-slip surfaces and pressure solution (stylolitic) fabric development was facilitated by volume loss through dissolution mass transfer processes. Deformation at this time was likely accelerated locally by the introduction of hydrothermal fluids into the previously developed mylonitic shear zone (e.g., Cox et al., 2001), resulting in the formation of a shear-related foliation. Kinematic fault-strain features showing top-to-the south normal displacement along semi-brittle strands of the Stratoni fault were controlled by north-south extension (Figure 3.16; red circles). Due to limited exposure, however, kinematic control on the syn-mineral fault strands in the Olympias area is less well-defined. Kinematic data from the striated, sulfide-bearing Kassandra fault surface exposed underground in the Olympias mine indicates control by a northeast-directed extensional strain axis (Figure 3.8A), which is consistent with post-mineral deformation.

An east-west extensional event was recorded by a set of incipiently mineralized fault strands that crosscut massive sulfide within the Stratoni fault zone (Figure 3.16; green squares). Kinematic fault-slip data from the Olympias area and the Gomati fault zone in the south (Figure 3.2) also record this tectonic event. Faults demonstrating east-west extension within the district may correspond to a widespread east-northeast–west-southwest extensional episode documented by other workers within the region (e.g., Kilias et al., 1999). This period of extension may have been episodically prolonged through the late Oligocene and early Miocene, controlling the upper crustal emplacement of north-northeast-trending porphyry dikes, as well as the Au-bearing quartz-rhodochrosite veins localized along north- and north-northeast-trending faults. The near perpendicular shift in extension direction, from north-south to east-west, may be explained by fault rotation, although this is unlikely given geological relationships. It is inferred that the shift in extension direction during the period of mineralization was controlled by an inflating magmatic body, or pherhaps the influx of hydrothermal fluids into the Stratoni fault zone.

Subsequent northeast-southwest extension within the district is recorded by brittle faults that crosscut the Mavres Petres and Madem Lakkos sulfide orebodies, and therefore postdate the carbonate

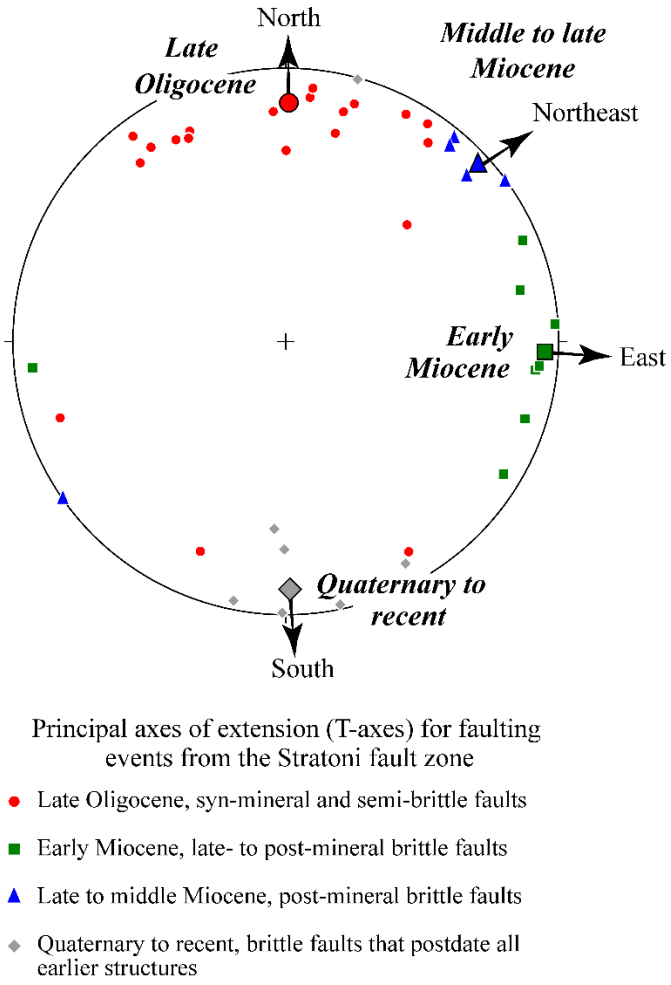

Figure 3.16. Kinematic evolution model for the Stratoni fault zone presented as a distribution of the principal extensional strain axes from individual fault measurements plotted in a lower-hemisphere, equal-area stereographic projection. The principal extensional strain axis for each fault population are plotted as small symbols with the mean represented by large symbols with arrows indicating the extension direction.

replacement event. Post-mineral brittle faults, such as the corrugated fault scarp outcropping above the Madem Lakkos mine, are texturally and kinematically compatible with middle to late Miocene northeast-southwest-directed extension (Figure 3.16; blue triangles) as documented from other fault zones in the north Aegean region (Dinter and Royden, 1993; Sokoutis et al., 1993; Dinter, 1998; Kilias et al., 1999). Fault-slip indicators recording northeast-southwest extension in the Olympias area are kinematically compatible with post-mineral fault strands within the Stratoni fault zone and, by association, also reflect middle to late Miocene extension. This fault set is interpreted to reflect regional extension due to crustal

stretching and exhumation of the southern Rhodope core complex in the back arc of the Hellenic subduction system (e.g., Kilias et al., 1999).

Steeply dipping fault surfaces aligned subparallel to the Stratoni fault zone and displaying south-southeast-plunging slickenlines record a final stage of north-south extension (Figure 3.16; gray diamonds). These faults are differentiated from late Oligocene semi-brittle and mineralized fault strands within the Stratoni fault zone by their brittle textures, unconsolidated gouge fill, and overprinting relationship relative to all earlier fabrics and fault surfaces. Kinematic data that describes this fault set agrees with published results from neotectonic faults within the Stratoni fault zone (Pavlides and Tranos, 1991). Gouge-filled faults and brittle fracture zones that occur at the Olympias deposit are probably coeval with the most recent faults evident in the Stratoni fault zone. This youngest fault set is interpreted to have formed by the Late Quaternary and may be related to active tectonism in the North Aegean (Pavlides and Tranos, 1991; Koukouvelas and Aydin, 2002; Pavlides and Caputo, 2004; Michailidou et al., 2005; Pavlides et al., 2010).

Structural controls and timing of carbonate replacement and vein-style mineralization

The carbonate replacement sulfide deposits in the district exhibit morphologies that are influenced by a preexisting ductile structural architecture and the interaction of syn-mineral faults with marble host rocks. In the Olympias area, pre-mineral, penetrative L2 intersection lineations and F2 folds developed within the gneisses and marbles contribute to a structurally enhanced southeast-plunging permeability network by introducing anisotropy into otherwise impermeable lithologies. Termination of the Kassandra fault at depth into an *en echelon* network of subsidiary shallow dipping mylonitic to semi-brittle fault strands likely resulted from the lateral transfer of strain controlled by the rheologically heterogeneous metamorphic sequence (Figure 3.5B). Permeable pathways developed between the Kassandra and East faults, facilitated by the intersection of shallow dipping mylonites with preexisting

ductile fabrics, were exploited by hydrothermal fluids that reacted with marble to produce replacement sulfide orebodies (Figure 3.17A).

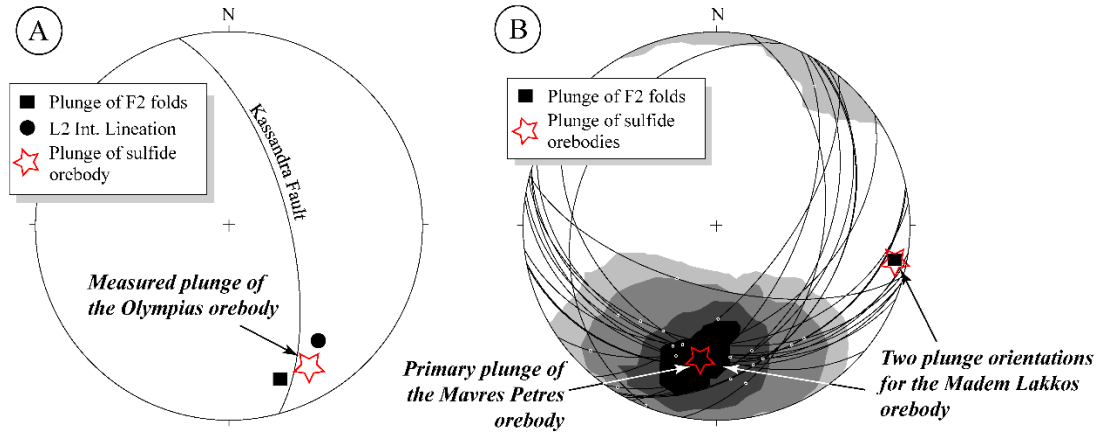

Structural model for the Olympias deposit

Structural model for the Madem Lakkos and Mavres Petres deposits

Figure 3.17. Schematic summary diagram displaying structural data and plunge orientation of carbonate replacement orebodies plotted in a lower-hemisphere, equal-area stereographic projection: (A) measured plunge of the Olympias orebody with the Kassandra fault plotted as a great circle and the mean plunge of F2 fold hinges and (S1, S2) L2 intersection lineations plotted as square and circle, respectively; (B) plunge of the Madem Lakkos and Mavres Petres orebodies plotted with fault surfaces defining the Stratoni fault zone indicated by great circles. Fault-slip vectors are indicated by small circles and contoured using the method of Kamb (1959). The mean plunge of F2 fold hinges from the footwall of the Stratoni fault zone is plotted as a square.

Previous studies have concluded that the sulfide orebodies at the Olympias deposit resulted from magmatic fluids (Kalogeropoulos et al., 1989); however, no definitive source intrusion was identified. A published arsenopyrite Re-Os age of 26.1 ± 5.3 Ma (Hahn et al., 2012; Hahn, 2014) indicates an Oligo-Miocene age of sulfide deposition. An undeformed granitic dike located in the western portion of the Olympias deposit yielded zircon U-Pb ages between 29.2 ± 0.5 Ma and 21.3 ± 0.3 Ma (Hahn, 2014), consistent with a local magmatic event coeval with ore formation. The mineralized magmatic-hydrothermal granite breccia body located in the footwall of the Kassandra fault is similar to the unstrained aplitic granite bodies that are spatially related to sulfide ore at the Madem Lakkos deposit (Gilg, 1993; Haines, 1998), further supporting a close Oligo-Miocene igneous association to ore. The post-mineral timing of glomerophyric porphyry dikes that crosscut Olympias ore and their geochemical

correlation with the early Miocene porphyry suite (Siron et al., 2016) suggest a minimum age of sulfide deposition at ~20 Ma.

Ductile fabrics and folds are also important within the Stratoni fault zone and contributed to the localization of the sulfide ores. Quartzo-feldspathic gneiss and marbles reworked by F2 folds associated with the Madem Lakkos antiform (Figure 3.10A) resulted in an east-southeast-plunging permeability network in the footwall of the Stratoni fault zone (Figure 3.17B). On the south dipping limb of the Madem Lakkos antiform, the rheological contrasts between quartzo-feldspathic biotite gneiss and granite gneiss with marble and massive amphibolite likely localized strain and facilitated the propagation of the eastern segment of the Stratoni fault zone. Mineralized semi-brittle faults displaying south-southwest and east-west fault-slip vectors reported in Haines (1998) from the Madem Lakkos mine are consistent with the kinematic data presented in this study and correspond to the syn- and late-mineral kinematic evolution of the Stratoni fault zone, respectively. Structural evidence combined with field relationships demonstrate that the Stratoni fault zone forms the principal permeability pathways that focused hydrothermal fluids.

In the Mavres Petres and Piavitsa areas, the Stratoni fault zone and contained marble lenses constitute the principal structural and lithologic controls for massive sulfide ore formation. Dismembered marble lenses enclosed by foliated carbonaceous phyllonite and entrained by segments of the Stratoni fault form the elongate down-dip component of the replacement sulfide orebody (Figure 3.17B). The Mavres Petres deposit is broadly coincident with a change in strike orientation of the Stratoni fault zone, which is interpreted to represent the linkage between two overlapping fault segments. The graphitic meta-pelitic unit, evident along the western segment of the Stratoni fault zone, may have provided a structurally weak layer that concentrated deformation potentially aided by fluid-enhanced pressure solution mass transport mechanisms. Localization of strain is interpreted to have been largely controlled by the lithologic anisotropy imposed by the carbonaceous meta-pelite layer juxtaposed to massive amphibolite, and facilitated by the preferred orientation of the Stratoni fault zone with respect to the principal stress field at the time of deformation. Internal fault bifurcations, fault intersections, and incompatible strain

behavior between coeval fault strands, and the high surface area of locally imbricated marble lenses within the Stratoni fault zone contributed to a mechanically-enhanced permeability network which was exploited by migrating hydrothermal fluids.

The late Oligocene Stratoni and Fisoka granodiorite stocks (Figure 3.9), or possibly a concealed intrusion in the area may have been the potential igneous source of mineralizing fluids that resulted in the carbonate replacement sulfide orebodies in the Stratoni fault zone (Gilg and Frei, 1994; Haines, 1998; Hahn, 2014; Siron et al., 2016). The mylonitic and unstrained aplitic granite dikes that are spatially associated with ore at the Madem Lakkos deposit are potentially co-magmatic with the Stratoni and Fisoka granodiorite stocks (Gilg and Frei, 1994). A shift in the direction of extension from north-south to east-west occurred after sulfide deposition and late Oligocene magmatism. The north-northeast- to northeast-striking glomerophyric and black-matrix porphyry dikes within the Stratoni fault zone (Figure 3.10A) support fault kinematic data in suggesting that east-west-directed extension was active through the early Miocene. The Au-bearing quartz-rhodochrosite ± rhodonite vein-breccias crosscut sulfide ore and semi-brittle shear zones in the Mavres Petres and Piavitsa areas, indicating a later timing relative to carbonate replacement mineralization (Figure 3.18). Quartz-rhodochrosite ± rhodonite veins fill north- to north-northeast-striking faults which principally show normal displacement, implying that east-west extension also controlled their emplacement.

The ^{40}Ar-^{39}Ar ages determined from hydrothermal muscovite, spatially and probably genetically associated with sulfide ore, suggests a minimum alteration and mineralization age between 25 Ma and 22 Ma (Figure 3.18). White mica intergrown with sulfide ore, and in part defining the tectonic fabric within semi-brittle strands of the Stratoni fault, suggests that deformation, alteration and mineralization were synchronous. The 24.0 ± 0.6 Ma ^{40}Ar-^{39}Ar age for muscovite at the Piavitsa prospect is interpreted as the timing of the carbonate replacement sulfide event, coeval with semi-brittle extensional faulting and late Oligocene magmatism within the Stratoni fault zone. This timing is supported by field relationships and overlaps, within analytical error, with the zircon U-Pb crystallization age of the Fisoka granodiorite stock

(24.5 ± 0.1 Ma; Siron et al., 2016). Syn-kinematic intergrowths of hydrothermal muscovite-dolomite with sulfide similarly defines the tectonic fabric of semi-brittle shear bands within the Kassandra fault at the Olympias deposit. The 22.6 ± 0.3 Ma ^{40}Ar-^{39}Ar age is interpreted to reflect the timing of carbonate replacement sulfide and semi-brittle extensional faulting in the Olympias area. This minimum ^{40}Ar-^{39}Ar age, while younger than the Piavitsa prospect, is still supportive of late Oligocene mineralizing event possibly driven by the granite that resulted in the igneous breccia or a parent intrusion at depth in the Olympias area.

Structural controls on the emplacement of the Skouries porphyry

The crosscutting relationships observed between intrusive phases with Au-Cu-mineralized veins and associated alteration, supported by published geochronological data, demonstrate that the Skouries deposit was part of an early Miocene magmatic-hydrothermal event (Frei, 1995; Kroll et al., 2002; Hahn et al., 2012; McFall et al., 2016; Siron et al., 2016). Structural data and outcrop patterns indicate that the Skouries stock occupies the steep northeast dipping limb of a major northwest-trending district-scale F2 antiform (Figure 3.14A-B), and is interpreted to be the principal structure that controlled upper crustal emplacement.

The subtle northeast-elongate geometry of the Skouries stock is broadly mimicked by the preferred northeast orientation of related porphyry dikes and Au-Cu mineralized veins contained within the stock. The shallow dipping to flat-lying veins within the porphyry stock imply transient fluid overpressure conditions and hydraulic fracturing of a crystallizing hydrous magma within a fluid saturated magmatic-hydrothermal environment (e.g., Gruen et al., 2010). The lack of sulfide and the early paragenesis of these veins indicate that the sub-horizontal hydraulic fracturing processes occurred relatively early and possibly at higher temperature than the main mineralizing vein events. The younger, steeply dipping and sheeted veins within the porphyry stock dilated in response to northwest-southeast

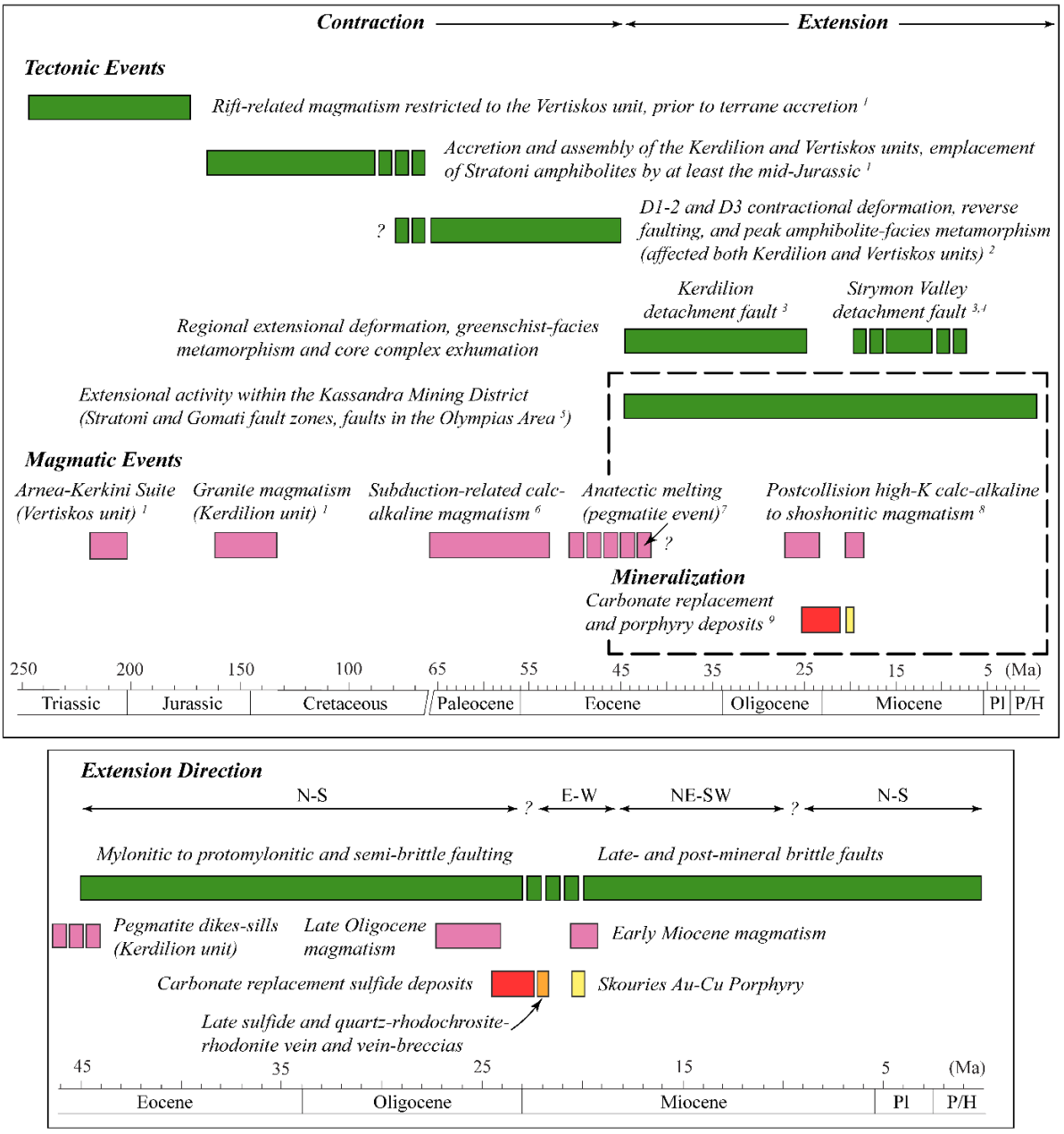

Figure 3.18. Summary diagram illustrating the timing of structural, magmatic, and mineralization events in the Kassandra Mining District. Timing constraints are supported by the following references: (1) zircon U-Pb and Pb-Pb ages (Himmerkus et al., 2006, 2009b, 2011; Hahn, 2014); (2) field relationships (this study); (3) apatite and zircon fission track ages (Brun and Sokoutis, 2007; Wüthrich, 2009; Kounov et al., 2015); (4) ^{40}Ar-^{39}Ar ages of biotite and K-feldspar (Dinter and Royden, 1993, and references therein; Dinter et al., 1995); (5) field relationships (Pavlides and Tranos, 1991; Haines, 1998; this study); (6) zircon U-Pb and Pb-Pb ages (Frei, 1992, 1996; Himmerkus el al., 2011; this study); (7) white mica Rb-Sr ages and field relationships (Kalogeropoulos et al., 1989; Wawrzenitz and Krohe, 1998; this study); (8) zircon U-Pb ages (Siron et al., 2016); (9) K-Ar age of hydrothermal illite (Madem Lakkos: Gilg and Frei, 1994), Re-Os arsenopyrite age (Olympias: Hahn et al., 2012; Hahn, 2014), ^{40}Ar-^{39}Ar age of hydrothermal biotite (Skouries: Hahn et al., 2012; Hahn, 2014), and ^{40}Ar-^{39}Ar ages of hydrothermal muscovite (Olympias and Piavitsa: this study).

and west-northwest-east-southeast extension (Figure 3.15E). Variations in the orientation of steeply dipping veins, however, indicate that dilation of sub-vertical fractures varied spatially within the porphyry stock and may reflect localized, episodic fluctuations in the orientation of the horizontal differential stress axes during Au-Cu mineralization (e.g., Tosdal and Richards, 2001). Pyrite-carbonate ± base metal veins overprint all earlier vein phases and associated K-feldspar and biotite-magnetite alteration suggesting that they developed late with respect to the Skouries magmatic-hydrothermal system.

The preferred northeast orientation of porphyry dikes surrounding the Skouries stock is consistent with the pattern developed by the Au-Cu mineralized veins, as well as the subdued elongation direction of the porphyry stock. The differential horizontal stresses developed within an anisotropic regional stress field likely influenced the northeast orientation of structural elements related to the Skouries porphyry system. The early Miocene and barren Aspro Lakkos porphyry stock located 2 km to the northeast of the Skouries deposit also displays a northeast-southwest elongation (Figure 3.14A). This northeast orientation is similarly shared by the chain of late Oligocene igneous stocks and dikes (Figure 3.2), which likely reflects a crustal-scale structure that acted as a conduit for the shallow emplacement of rising magmas. During the early Miocene, a shift from north-south- to east-west-directed extension, as evidenced by fault kinematic data and crosscutting structural relationships, may have triggered ascent of fertile magmas through the upper crust, localizing the Skouries porphyry stock within the steeply dipping limb of a major district-scale antiform.

Summary and Conclusions

The Kassandra Mining District belongs to the Serbo-Macedonian Metallogenic Province, an Oligo-Miocene magmatic belt developed in a post-collisional and extensional back arc environment that hosts porphyry Au-Cu and polymetallic carbonate replacement deposits, including vein and skarn systems (Janković, 1997; Serafimovski et al., 2010; Heinrich and Neubauer, 2002). Ores hosted by marble along with elevated Au contents distinguish the Madem Lakkos, Mavres Petres, and Olympias deposits from

other carbonate-hosted systems within the belt (e.g., Trepča Mining District of eastern Kosovo; Strmić-Palinkaš et al., 2013). While similarly hosted by marble of Rhodope origins and strongly controlled by extensional faults, the carbonate replacement deposits in the Madan-Thermes district of southern Bulgaria and northeastern Greece are older, closely associated with Late Eocene to early Oligocene magmatism, and are notably deficient in gold (Marchev et al., 2005; Kaiser-Rohrmeier et al., 2013). The early Miocene Skouries porphyry Au-Cu deposit broadly resembles, in terms of chemistry and structural setting, other mineralized porphyry deposits in the Serbo-Macedonian Metallogenic Province such as the early to late Oligocene Kiseljak and Buchim deposits of southern Serbia and the Republic of Macedonia, respectively (Serafimovski et al., 2010; Márton et al., 2013). These porphyry systems, including Skouries, are analogous to economic porphyry deposits developed in post-collisional back arc settings described elsewhere (e.g., Ridgeway-Cadia and North Parkes districts of NSW, Australia; Wilson, 2003).

The Stratoni fault zone has been historically viewed as the tectonic boundary separating the Kerdilion unit from the Vertiskos unit (Kockel et al., 1977). The Kerdilion unit is compositionally gradational with no observable change in metamorphic grade across the Stratoni fault zone. Amphibolites occurring in footwall and hanging wall domains are conformably interlayered in the Kerdilion unit and are geochemically indistinguishable. Ductile structural elements spanning the Stratoni fault zone also display consistent deformation patterns suggesting that footwall and hanging wall lithologies were affected by the same phases of deformation, for which syn-metamorphic fabrics are largely contractional (Figure 3.18). These data suggest that the tectonic boundary between the Kerdilion and Vertiskos units is probably an older structure and not a detachment as previously thought (Haines, 1998; Kounov et al., 2015).

The location and morphology of carbonate replacement sulfide deposits within the Kassandra Mining District is influenced by a preexisting ductile structural architecture, and the interaction of syn-mineral faults with available marble host rocks. The Olympias orebody is controlled by a southeast-plunging L2 intersection lineation and F2 folds interacting with extensional mylonites and semi-brittle

shear zones that link the Kassandra and East faults within a hosting marble unit. Timing of mineralization may have overlapped with igneous activity which locally formed a granite-matrix breccia, and mylonite-associated granitic dikes and sills along ore-controlling faults. To the south, the Madem Lakkos orebody is controlled by marbles localized within the hinge of a footwall antiform and syn-mineral strands of the Stratoni fault zone (Gilg, 1993; Gilg and Frei, 1994; Haines, 1998) in association with granite dikes that may form part of the late Oligocene intrusive suite. The Mavres Petres orebody, however, is hosted by fault-bounded marble lenses entrained within a strongly carbonaceous segment of the Stratoni fault zone.

Carbonate replacement sulfide ore and syn-mineral faults within the district were active from 24.0 ± 0.6 Ma to 22.6 ± 0.3 Ma based on ^{40}Ar-^{39}Ar geochronology of hydrothermal muscovite. The ^{40}Ar-^{39}Ar data suggests a late Oligocene timing for sulfide deposition within the district, consistent with the zircon U-Pb crystallization ages from the Fisoka and Stratoni granodiorite stocks (Siron et al., 2016). Further work, however, is needed to assess the relationship of the granitic intrusions that are associated with mineralization in the Olympias and Madem Lakkos deposits to other Oligocene intrusions in the district.

Kinematic fault-slip data indicates that carbonate replacement mineralization was coeval with north-south extension during the late Oligocene (Figure 3.18) with a later phase of east-west extension as evidenced by the kinematic data and implied by dikes and mineralized veins that occur within north- to northeast-trending faults. Younger Au-bearing quartz-rhodochrosite vein and vein-breccias developed along these structures overprint semi-brittle faults and sulfide within the Stratoni fault zone, suggesting that east-west extension was coeval with the latest phase of hydrothermal activity at the Mavres Petres deposit and the Piavitsa prospect (Figure 3.18). Post-mineral faults produced by northeast-southwest extension crosscut the sulfide orebodies within the Stratoni fault zone, and are kinematically compatible with middle to late Miocene regional extension (Dinter, 1998). A final stage of brittle faulting overprints all earlier deformation events and is characterized by north-south extension typical of the modern tectonic environment (Pavlides and Tranos, 1991).

The early Miocene Skouries porphyry stock is hosted by folded gneiss and schist of the Vertiskos unit, and crosscuts the moderate to steeply dipping limb of a major F2 antiform. Quartz-magnetite and Au-Cu-mineralized quartz-biotite-chalcopyrite-bornite ± magnetite veins contained within the porphyry stock predominately strike to the northeast, consistent with the preferred orientation of related porphyry dikes. Ascent of fertile magmas into the upper crust may have been triggered by a change in the regional extensional stress field as evidenced by fault kinematic data. Polymetallic carbonate-hosted replacement and porphyry Au-Cu ore formation manifested where a preexisting structural architecture juxtaposed reactive host rocks and localized magmatism within an evolving post-collisional, extensional back arc environment.

Acknowledgements

The first author would like to acknowledge Eldorado Gold Corporation in providing logistical and financial support for this study. We are grateful for the thoughtful discussions with Peter Lewis and Hellas Gold geologists Panagiotis Daoultzis, Antonis Garezos, Nikos Nestorov, George Perantonis, Scott Randall, Sally Russell, Grigorios Thermos, Pavlos Tsitsanis, and Timoleon Xonikis (Madem Lakkos), Ria Vagkli (Skouries), and Konstantinos Kydonakis and Panagiotis Zachariadis (Olympias). Samuel Haines is thanked for providing his thoughts on the structural evolution of the Stratoni fault zone from the now-closed Madem Lakkos mine. Richard Allmendinger (Cornell University) is acknowledged for providing assistance in the interpretation and presentation of structural data and Amy Willis (Cornell University) is graciously thanked for assisting with the interpretation of principal component data. A travel grant was awarded to the first author by the Mario Einaudi Center for International Studies at Cornell University. Richard Friedman (University of British Columbia) kindly provided comments on an earlier draft and a critical review by Richard Tosdal significantly improved the quality of this manuscript. Shaun Barker is also acknowledged for providing a careful editorial review of the final version of this manuscript.

REFERENCES

Allmendinger, R.W., Reilinger, R., and Loveless, J. P., 2007, Strain and Rotation Rate from GPS in Tibet, Anatolia, and the Altiplano: Tectonics, v. 26, TC3013.

Allmendinger, R.W., Cardozo, N., and Fisher, D., 2012, Structural geology algorithms: Vectors and tensors in structural geology: Cambridge University Press, 302 p.

Armijo, R., Meyer, B., Hubert, A., Barka, A., 1998, Westward propagation of the North Anatolian fault into the northern Aegean: Timing and kinematics: Geology, v. 27, p. 267-270.

Bébien, J., Michard, A., Montigny, R., Feinberg, H., and Voidomatis, P., 2001, The Grigoriou plutonic complex (Mt Athos, Greece): a component of the north Aegean Eocene-Oligocene Calc-Alkaline magmatism: European Union of Geosciences Symposium, 11th, Strasbourg, France, 2001, LS03:314.

Best, M.G., Christiansen, E.H., Deino, A.L., Grommé, C.S., and Tingey, D.G., 1995, Correlation and emplacement of a large, zoned, discontinuously exposed ash flow sheet; the $^{40}Ar/^{39}Ar$ chronology, paleomagnetism, and petrology of the Pahranagat Formation, Nevada: Journal of Geophysical Research, v. 100, p. 24593-24609.

Bonev, N., Burg, J.-P., and Ivanov, Z., 2006, Mesozoic-Tertiary structural evolution of an extensional gneiss dome – the Kesebir-kardamos dome, eastern Rhodope (Bulgaria-Greece): International Journal of Earth Science, v. 95, p. 318-340.

Bonev, N., and Dilek, Y., 2010, Geochemistry and tectonic significance of proto-ophiolitic metamafic units from the Serbo-Macedonian and western Rhodope massifs (Bulgaria-Greece): International Geology Review., v. 52, p. 298-335.

Bonev, N., Dilek, Y., Hanchar, J.M., Bogdanov, K., and Klain, L., 2012, Nd-Sr-Pb isotopic composition and mantle sources of Triassic rift units in the Serbo-Macedonian and western Rhodope massifs (Bulgaria-Greece): Geological Magazine, v. 149, p. 146-152.

Brun, J.P., and Sokoutis, D., 2007, Kinematics of the southern Rhodope core complex (North Greece): International Journal of Earth Science., v. 96, p. 1079-1099.

Brun, J.P., and Faccenna, C., 2008, Exhumation of high-pressure rocks driven by slab rollback: Earth and Planetary Science Letters, v. 272, p. 1-7.

Brun, J.P., and Sokoutis, D., 2010, 45 m.y. of Aegean crust and mantle flow driven by trench retreat: Geology, v. 38, p. 815-818.

Burg, J.-P., Ivanov, Z., Ricou, L.-E., Dimor, D., and Klain, L., 1990, Implications of shear-sense criteria for the tectonic evolution of the Central Rhodope massif, southern Bulgaria: Geology, v. 18, p. 451-454.

Burg, J.-P., Godfriaux, I., and Ricou, L.-E., 1995, Extension of the Mesozoic Rhodope thrust units in the Vertiskos-Kerdilion Massifs (Northern Greece): Comptes Rendus de l'Académie des Sciences, 320(9), p. 889-896.

Burg, J.-P., Ricou, L.-E., Ivanov, Z., Godfriaux, I., Dimor, D., and Klain, L., 1996, Syn-metamorphic nappe complex in the Rhodope Massif. Structure and kinematics: Terra Nova, v. 8, p. 6-15.

Burg, J.-P., 2012, Rhodope: from Mesozoic convergence to Cenozoic extension. Review of petro-structural data in the geochronological frame: in Skourtsos, E., and Lister, G.S., eds., The Geology of Greece: Journal of the Virtual Explorer, electronic edition, v. 42(1).

Cardozo, N., and Allmendinger, R. W., 2013, Spherical projections with OSXStereonet: Computers & Geosciences, v. 51(0), p. 193-205.

Christofides, G., D'Amico, C., Del Moro, A., Eleftheriadis, G., and Kyriakopoulos, C., 1990, Rb-Sr-geochronology and geochemical characters of the Sithonia plutonic complex (Greece): European Journal of Mineralogy, v. 2, p. 79-87.

Christofides, G., Koroneos, A., Liati, A., and Kral, J., 2007, The A-type Kerkini granitic complex in north Greece: geochronology and geodynamic implications: Bulletin of the Geological Society of Greece, v. 40, p. 700-711.

Cox, S.F., Knackstedt, M.A., and Braun, J., 2001, Principals of structural control on permeability and fluid flow in hydrothermal systems: Reviews in Economic Geology, v. 14, p. 1-24.

Dazé, A., Lee, J.K.W., and Villeneuve, M., 2003, An intercalibration study of the Fish Canyon sanidine and biotite $^{40}Ar/^{39}Ar$ standards and some comments on the age of the Fish Canyon Tuff: Chemical Geology, v. 199, p. 111-127.

de Boorder, H., Spakman, W., White, S.H., and Wortel, M.J.R., 1998, Late Cenozoic mineralization, orogenic collapse and slab detachment in the European Alpine belt: Earth and Planetary Letters, v. 164, p. 569-575.

De Wet, A.P., Miller, J.A., Bickle, M.J., and Chapman, H.J., 1989, Geology and geochronology of the Arnea, Sithonia and Ouranoupolis intrusions, Chalkidiki peninsula, northern Greece: Tectonophysics, v. 161, p. 65-79.

Dimitriadis, S., Kondopoulou, D., and Atzemoglou, A., 1998, Dextral rotations and tectonomagmatic evolution of the southern Rhodope and adjacent regions (Greece): Tectonophysics, v. 299, p. 159-173.

Dinter, D.A., 1998, Late Cenozoic extension of the Alpine collisional orogen, northeastern Greece: origin of the north Aegean basin: Geological Society of America Bulletin, v. 110, p. 1208-1230.

Dinter, D.A., and Royden, L., 1993, Late Cenozoic extension in north-eastern Greece: Strymon Valley detachment system and Rhodope metamorphic core complex: Geology, v. 21, p. 45-48.

Dinter, D.A., Macfarlane, A., Hames, W., Isachsen, C., Bowring, S., and Royden, L., 1995, U-Pb and $^{40}Ar/^{39}Ar$ geochronology of the Symvolon granodiorite: implications for the thermal and structural evolution of the Rhodope metamorphic core complex, northeastern Greece: Tectonics, v. 14(4), p. 886-908.

Dixon, J.E., and Dimitriadis, S., 1984, Metamorphosed ophiolitic rocks from the Serbo-Macedonian Massif near lake Volvi, north-east Greece, in Dixon, J.E., and Robertson, A.H.F., eds., The geological evolution of the eastern Mediterranean: Geological Society of London Special Publication, v. 17, p. 603-618.

Eldorado Gold Corporation, 2017, Resources and reserves: Accessed October 29, 2017, (http://www.eldoradogold.com/assets/resources-and-reserves/).

Eliopoulos, D.G., and Economou-Eliopoulos, M., 1991, Platinum-group elements and gold contents in the Skouries porphyry copper deposit, Chalkidiki peninsula, northern Greece: Economic Geology, v. 86, p. 740-749.

Forward, P., Francis, A., and Liddell, N., 2010, Technical report on the Stratoni project Pb-Zn-Ag deposit, northern Greece: European Goldfields Limited, NI 43-101 Report, 54 p.

Frei, R., 1992, Isotope (Pb-Rb-Sr-S-O-C-U-Pb) geochemical investigations of Tertiary intrusions and related mineralizations in the Serbo-Macedonian (Pb-Zn, Sb+Cu-Mo metallogenetic) province in northern Greece: Unpublished Ph.D. thesis, Zürich, Switzerland, ETH, 231 p.

Frei, R., 1995, Evolution of mineralizing fluid in the porphyry copper system of the Skouries deposit, northeast Chalkidiki (Greece): Evidence from combined Pb-Sr and stable isotope data: Economic Geology, v. 90, p. 746-762.

Frei, R., 1996, The extent of inner mineral isotope equilibrium: a systematic bulk U-Pb and Pb step leaching (PbSL) isotope study of individual minerals from the Tertiary granite of Jerissos (northern Greece): European Journal of Mineralogy, v. 8, p. 1175-1189.

Fytikas, M., Innocenti, F., Manetti, P., Mazzuoli, R., Peccerillo, A., and Villari, L., 1984, Tertiary to Quaternary evolution of volcanism in the Aegean region, in Dixon, J.E., and Robertson, A.H.F., eds., The geological evolution of the eastern Mediterranean: Geological Society of London Special Publication, v. 17, p. 687-699.

Gautier, P., Brun, J.-P., Moriceau, R., Sokoutis, D., Martinod, J., and Jolivet, L., 1999, Timing, kinematic and cause of Aegean extension: a scenario based on a comparison with simple analogue experiments: Tectonophysics, v. 315, p. 31-72.

Gilg, H.A., 1993, Geochronology (K-Ar), fluid inclusion, and stable isotope (C, H, O) studies of skarn, porphyry copper, and carbonate-hosted Pb-Zn (Ag, Au) replacement deposits in the Kassandra mining district (eastern Chalkidiki, Greece): Unpublished Ph.D. thesis, Zürich, Switzerland, ETH, 153 p.

Gilg, H.A., and Frei, R., 1994, Chronology of magmatism and mineralization in the Kassandra mining area, Greece: The potentials and limitations of dating hydrothermal illites: Geochimica et Cosmochimica Acta, v. 58, p. 2107-2122.

Gruen, G., Heinrich, C.A., and Schroeder, K., 2010, The Bingham Canyon porphyry Cu-Mo-Au deposit. II. Vein geometry and ore shell formation by pressure-driven rock extension: Economic Geology, v. 105, p. 69-90.

Gustafson, L.B., and Hunt, J.F., 1975, The porphyry copper deposit at El Salvador, Chile: Economic Geology and the Bulletin of the Society of Economic Geologists, v. 70, p. 857-912.

Haines, H.S., 1998, A structural synthesis for sector Vb of the Madem Lakkos polymetallic sulfide deposit – Northeast Greece: Unpublished M.Sc. thesis, London, United Kingdom, The University of London, 81 p.

Hahn, A., 2014, Nature, timing and geodynamic context of polymetallic mineralisation in the Kassandra mining district, North Greece: Unpublished Ph.D. thesis, London, United Kingdom, Kingston University, 351 p.

Hahn, A., Naden, J., Treloar, P.J., Kilias, S.P., Rankin, A.H., and Forward, P., 2012. A new timeframe for the mineralization in the Kassandra mine district, N Greece: deposit formation during metamorphic core complex exhumation: European Mineralogical Conference, v. 1, 1EMC2012-742.

Heinrich, C.A., and Neubauer, F., 2002, Cu-Au-Pb-Zn-Ag metallogeny of the Alpine-Balkan-Carpathian-Dinaride geodynamic province: Mineralium Deposita, v. 37, p. 533-540.

Himmerkus, F., Zachariadis, P., Reischmann, T., and Kostopoulos, D.K., 2005, The mafic complexes of the Athos-Volvi-Zone – a suture zone between the Serbo-Macedonian massif and the Rhodope massif?: Geophysical Research Abstracts, v. 7., p. 10, 240.

Himmerkus, F., Reischmann, T., and Kostopoulos, D.K., 2006, Late Proterozoic and Silurian basement units within the Serbo-Macedonian massif, northern Greece: the significance of terrane accretion in the Hellenides, in Robertson, A.H.F., and Mountrakis, D., eds., Tectonic development of the eastern Mediterranean region: Geological Society of London Special Publication, v. 260, p. 35-50.

Himmerkus, F., Anders, B., Reischmann, T., and Kostopoulos, D., 2007, Gondwana-derived terranes in the northern Hellenides, in Hatcher, R.D., Jr., Carlson, M.P., McBride, J.H., and Martínez Catalán, J.R., eds., 4-D framework of continental crust: Geological Society of America Memoir, v. 200, p. 379-390.

Himmerkus, F., Reischmann, T., and Kostopoulos, D.K., 2009a, Serbo-Macedonian revisited: a Silurian basement terrane from northern Gondwana in the Internal Hellenides, Greece: Tectonophysics v. 473, p. 20-35.

Himmerkus, F., Reischmann, T., and Kostopoulos, D.K., 2009b, Triassic rift-related meta-granites in the Internal Hellenides, Greece: Geological Magazine, v. 146(2), p. 252-265.

Himmerkus, F., Zachariadis, P., Reischmann, T., and Kostopoulos, D., 2011, The basement of the Mount Athos Peninsula, northern Greece: insights from geochemistry and zircon ages: International Journal of Earth Sciences., v. 101, p. 1467-1485.

Jahn-Awe, S., Froitzheim, N., Nagel, T.J., Frei, D., Georgiev, N., and Pleuger, J., 2010, Structural and geochronological evidence for Paleogene thrusting in the western Rhodopes, SW Bulgaria: elements for a new tectonic model of the Rhodope Metamorphic Province: Tectonics, v. 29, TC3008.

Janković, S., 1997, The Carpatho-Balkanides and adjacent area: a sector of the Tethyan Eurasian metallogenic belt: Mineralium Deposita, v. 32, p. 426-433.

Jolivet, L., and Brun, J.P., 2010, Cenozoic geodynamic evolution of the Aegean region: International Journal of Earth Sciences, v. 99, p. 109-138.

Jolivet, L., Faccenna, C., Huet, B. , Labrousse, L., Le Pourhiet, L., Lacombe, O., Lecomte, E, Burov, E, Denele, Y., Brun, J.P., Philippon, M., Paul, A., Salaun, G., Karabulut, H., Piromallo, C., Monie, P., Gueydan, F., Okay, A.I., Oberhansli, R., Pourteau, A., Augier, R., Gadenne, L, and Driussi, O., 2013, Aegean tectonics: Strain localization, slab tearing and trench retreat: Tectonophysics, v. 597-598, p. 1-33.

Jolliffe, I.T., 2002, Principal component analysis, 2nd ed.: New York, Springer, 487 p.

Jones, C.E., Tarney, J., Baker, J.H., and Gerouki, F., 1992, Tertiary granitoids of Rhodope, northern Greece: magmatism related to extensional collapse of the Hellenic Orogen?: Tectonophysics, v. 210, p. 295-314.

Kalogeropoulos, S.I., Kilias, S.P., Bitzios, D.C., Nicolaou, M., and Both, R.A., 1989, Genesis of the Olympias carbonate-hosted Pb-Zn (Au, Ag) sulfide ore deposit, eastern Chalkidiki peninsula, northern Greece: Economic Geology, v. 84, p. 1210-1234.

Kamb, W.B., 1959, Ice petrofabric observations from Blue Glacier, Washington in relation to theory and experiment: Journal of geophysical research, v. 64, p. 1891-1909.

Kilias, S.P., Kalogeropoulos, S.I., and Konnerup-Madsen, J., 1996, Fluid inclusion evidence for the physicochemical conditions of sulfide deposition in the Olympias carbonate-hosted Pb-Zn(Au, Ag) sulfide ore deposit, E. Chalkidiki peninsula, N. Greece: Mineralium Deposita, v. 31, p. 394-406.

Kilias, A., Falalakis, G., and Mountrakis, D., 1999, Cretaceous-Tertiary structures and kinematics of the Serbomacedonian metamorphic rocks and their relation to the exhumation of the Hellenic hinterland (Macedonia, Greece): International Journal of Earth Sciences, v. 88, p. 513-531.

Kockel, F., Mollat, H., and Walther, H., 1971, Geologie des Serbomazedonischen massivs und seines mesozoischen Rahmes (Nord-Griechenland): Geologisches Jahrbuch der Bundesanstalt für Geowissenschaften und Rohstoffe, v. 89, p. 529-551.

Kockel, F., Mollat, H., and Gundlach, H., 1975, Hydrothermally altered and (copper-) mineralized porphyritic intrusions in the Serbo-Macedonian massif (Greece): Mineralium Deposita, v. 10, p. 195-204.

Kockel, F., Mollat, H., and Walther, H., 1977, Erläuterungen yur geologischen karte der Chalkidiki und agrenzender Gebiete 1:100,000 (Nord-Griechenland): Bundesanstalt für Geowissenschaften und Rohstoffe, Hannover, p. 1-119.

Kockel, F., Mollat, H., and Walther, H., 1978a, Geological map of Greece, Stavros sheet: Athens, Institute of Geological and Mining Research, scale 1:50,000.

Kockel, F., Mollat, H., and Walther, H., 1978b, Geological map of Greece, Stratoniki sheet: Athens, Institute of Geological and Mining Research, scale 1:50,000.

Koukouvelas, I.K., and Aydin, A., 2002, Fault structure and related basins of the North Aegean Sea and its surroundings: Tectonics, v. 21(5), 10.

Kounov, A., Wüthrich, E., Seward, D., Burg, J.P., and Stockli, D., 2015, Low-temperature constraints on the Cenozoic thermal evolution of the southern Rhodope core complex (northern Greece): International Journal of Earth Science, v. 104, p. 1337-1352.

Krenn, K., Bauer, C., Proyer, A., Klözli, U., and Hoinkes, G., 2010, Tectonometamorphic evolution of the Rhodope orogen: Tectonics, v. 29, TC4001.

Krohe, A., and Mposkos, E., 2002, Multiple generations of extensional detachments in the Rhodope mountains (northern Greece): evidence of episodic exhumation of high-pressure rocks, in Blundell, D.L., Neubauer, F., and von Quadt, A., eds., The timing and location of major ore deposits in an evolving orogen: Geological Society of London Special Publication, v. 204, p. 151-178.

Kroll, T., Müller, D., Seifert, T., Herzig, P.M., and Schneider, A., 2002, Petrology and geochemistry of the shoshonite-hosted Skouries porphyry Cu-Au deposit, Chalkidiki, Greece: Mineralium Deposita, v. 37, p. 137-144.

Kuiper, K.F., Deino, A., Hilgen, F.J., Krijgsman, W., Renne, R., and Wijbrans, J.R., 2008, Synchronizing rock clocks of Earth history: Science, v. 320, p. 500-504.

Kydonakis, K., Gallagher, K., Brun, J.-P., Jolivet, M., Gueydan, F., and Kostopoulos, D., 2014, Upper Cretaceous exhumation of the western Rhodope Metamorphic Province (Chalkidiki peninsula, northern Greece): Tectonics, v. 33, p. 1113-1132.

Kydonakis, K., Brun, J.-P., Poujol, M., Monié, P., and Chatzitheodoridis, E., 2016, Inference on the Mesozoic evolution of the north Aegean from the isotopic record of the Chalkidiki block: Tectonophysics, v. 682, p. 65-84.

Liati, A., 2005, Identification of repeated Alpine (ultra) high-pressure metamorphic events by U-Pb SHRIMP geochronology and REE geochemistry of zircon: the Rhodope zone of Northern Greece: Contributions to Mineralogy and Petrology, v. 150, p. 608-630.

Liati, A., Gebauer, D., and Fanning, C.M., 2011, Geochronology of the Alpine UHP Rhodope zone: a review of isotopic ages and constraints on the geodynamic evolution, in Dobrzhinetskaya, L.F., Faryad, S.W., Wallis, S., and Cuthbert, S., eds., Ultrahigh-pressure Metamorphism 25 Years after the Discovery of Coesite and Diamond. Elsevier, Amsterdam, p. 295-324.

Lips, A.L., 2002, Correlating magmatic-hydrothermal ore deposit formation over time with geodynamic processes in SE Europe: Geological Society of London Special Publication, v. 204, p. 69-79.

Lips, A, L.W., White, S.H., and Wijbrans, J.R., 2000, Middle-Late Alpine thermotectonic evolution of the southern Rhodope Massif, Greece: Geodinamica Acta, v. 13, p. 281-292.

Marchev, P., Kaiser-Rohrmeier, M., Heinrich, C., Ovtcharova, M., von Quadt, A., and Raicheva, R., 2005, 2: Hydrothermal ore deposits related to post-orogenic extensional magmatism and core complex formation: The Rhodope Massif of Bulgaria and Greece: Ore Geology Reviews, v. 27, p. 53-89.

Marrett, R. A., and Allmendinger, R. W., 1990, Kinematic analysis of fault-slip data: Journal of Structural Geology, v. 12, p. 973-986.

Márton, I., Dragić, D., Djordjević, B., Fox, P., Tosdal, R.M., van der Toorn, J., and Hasson, S., Intrusion-alteration-mineralization relationships from the porphyry Cu-Au deposit at Kiseljak, Serbia [ext. abs.]: 12th Biennial SGA Meeting: Mineral deposit research for a high-tech world, Uppsala, Sweden, 2013, Extended Abstracts.

McFall, K.A., Roberts, S., Teagle, D., Naden, J., Lusty, P., and Boyce, A., 2016, The origin and distribution of critical metals (Pd, Pt, Te & Se) within the Skouries Cu-Au porphyry deposit, Greece: Mineral Deposits Study Group meeting, 39th, Dublin, Ireland, 2016, Extended Abstracts.

Michailidou, A., Chatzipetros, A., and Pavlides, S., 2005, Quantitative analysis – tectonic geomorphology indicators of the faults in the region of Stratoni-Varvara and Gomati-Megali Panagia (eastern Chalkidiki: Bulletin of the Geological Society of Greece, v. 38, p. 14-29.

Mposkos, E.D., and Kostopoulos, D.K., 2001, Diamond, former coesite and supersilicic garnet in metasedimentary rocks from the Greek Rhodope: a new ultrahigh-pressure metamorphic province established: Earth and Planetary Science Letters, v. 192, p. 497-506.

Nebel, M.L., 1989, Metamorphism and polygenesis of the Madem Lakkos polymetallic sulfide deposit, Chalkidiki, Greece: Unpublished Ph.D. thesis, Golden, Colorado, Colorado School of Mines, 215 p.

Nebel, M.L., Hutchinson, R.W., and Zartman, R.E., 1991, Metamorphism and polygenesis of the Madem Lakkos polymetallic sulfide deposit, Chalkidiki, Greece, Economic Geology., v. 86, p. 81-105.

Nelson, E.P., 2006, Drill-hole design for dilational ore shoot targets in fault-filled veins: Economic Geology, v. 101, p. 1079-1085.

Neubauer, F., 2002, Contrasting late Cretaceous with Neogene ore provinces in the Alipine-Balkan-Carpathian-Dinaride collision belt, in Blundell, D.L., Neubauer, F., and von Quadt, A., eds., The timing and location of major ore deposits in an evolving orogen: Geological Society of London Special Publication, v. 204, p. 81-102.

Papanikolaou, D., 2013, Tectonostratigraphic models of the Alpine terranes and subduction history of the Hellenides: Tectonophysics, v. 595-596, p. 1-24.

Pavlides, S.B., and Tranos, M.D., 1991, Structural characteristics of two strong earthquakes in the north Aegean: Ierissos (1932) and Agios Efstratios (1968): Journal of Structural Geology, v. 13, p. 205-214.

Pavlides, S., and Caputo, R., 2004, Magnitude versus faults' surface parameters: quantitative relationships from the Aegean region: Tectonophysics, v. 380, p. 159-188.

Pavlides, S., Caputo, R., Sboras, S., Chatzipetros, A., Papathanasiou, G., and Valkaniotis, S., 2010, The Greece catalogue of active faults and database of seismogenic sources: Bulletin of the Geological Society of Greece, v. 43(1), p. 486-494.

Pe-Piper, G., and Piper, D.J.W., 2002, The igneous rocks of Greece: Stuttgart, Borntraeger, 645 p.

Pe-Piper, G., and Piper, D.J.W., 2006, Unique features of the Cenozoic igneous rocks of Greece, in Dilek, Y., and Pavlides, S., eds., Postcollisional tectonics and magmatism in the Mediterranean region and Asia: Geological Society of America Special Paper, v. 409, p. 259-282.

Pearce, J.A., 1996, A User's guide to basalt discrimination diagrams, in Wyman, D.A., ed., Trace element geochemistry of volcanic rocks: applications for massive sulfide exploration: Geological Association of Canada, short course notes, v. 12, p. 79-113.

Pearce, J.A., 2014, Immobile element fingerprinting of ophiolites: Elements, v. 10, p. 101-108.

Piercey, S.J., 2014, A review of quality assurance and quality control (QA/QC) procedures for lithogeochemical data: Geoscience Canada, v. 41, p. 75-88.

Renne, P.R., and Norman, E.B., 2001, Determination of the half-life of ^{37}Ar by mass spectrometry: Physical Review, C 63 (047302), 3 p.

Renne, P.R., Swisher, C.C., Deino, A.L., Karner, D.B., Owens, T.L., and DePaolo, D.J., 1998, Intercalibration of standards, absolute ages and uncertainties in $^{40}Ar/^{39}Ar$ dating: Chemical Geology, v. 145, p. 117-152.

Ricou, L.E., Burg, J.-P., Godfriaux, I., and Ivanov, Z., 1998, Rhodope and Vardar: the metamorphic and the olistostromic paired belts related to the Cretaceous subduction under Europe: Geodinamica Acta, v. 11, p. 285-309.

Ring, U., Glodny, J., Will, T., and Thomson, S., 2010, The Hellenic subduction system: high-pressure metamorphism, exhumation, normal faulting, and large-scale extension: Annual Reviews of Earth and Planetary Sciences, v. 38, p. 45-76.

Roddick, J.C., 1983, High precision intercalibration of ^{40}Ar-^{39}Ar standards: Geochimica et Cosmochimica Acta, v. 47, p. 887-898.

Rollinson, H. R., 1993, Using geochemical data: Evaluation, presentation, interpretation: London, Longman, 352 p.

Kaiser-Rohrmeier, M., von Quadt, A., Driesner, T., Heinrich, C.A., Handler, R., Ovtcharova, M., Ivanov, Z., Petrov, P., Sarov, St., and Peytcheva, I., 2013, Post-orogenic extension and hydrothermal ore formation: High-precision geochronology of the central Rhodopian metamorphic core complex (Bulgaria-Greece): Economic Geology, v. 108, p. 691-718.

Sagui, C.L., 1928, The ancient mining works of Cassandra, Greece: Economic Geology, v. 23, P. 671-680.

Serafimovski, T., 2000, The Lece-Chalkidiki metallogenic zone: geotectonic setting and metallogenic features: Geologija, v. 42, p. 159-164.

Serafimovski, T., Stefanova, V., and Volkov, A.V., 2010, Dwarf copper-gold porphyry deposits of the Buchim-Damjan-Borov Dol ore district, Republic of Macedonia (FYROM): Geology of Ore Deposits, v. 52, p. 179-195.

Sibson, R. H., 1977, Fault rocks and fault mechanisms: Journal of the Geological Society, London, v. 133, p. 191-213.

Siron, C.R., Thompson, J.F.H., Baker, T., Friedman, R., Tsitsanis, P., Russell, S., Randall, S., and Mortensen, J., 2016, Magmatic and metallogenic framework of Au-Cu porphyry and polymetallic carbonate-hosted replacement deposits of the Kassandra Mining District, Northern Greece, in Richards, J.P., ed., Tectonics and metallogeny of the Tethyan orogenic belt: Society of Economic Geologists, Special Publication No. 19, p. 29-55.

Sokoutis, D., Brun, J.P., Van Den Driessche, J., and Pavlides, S., 1993, A major Oligo-Miocene detachment in southern Rhodope controlling north Aegean extension: Journal of the Geological Society, London, v. 150, p. 243-246.

Spell, T.L., and McDougall, I., 2003, Characterization and calibration of $^{40}Ar/^{39}Ar$ dating standards: Chemical Geology, v. 198, p. 189-211.

Steiger, R.H., and Jäger, E., 1977, Subcommission on geochronology: Convention on the use of decay constants in geo- and cosmochronology: Earth and Planetary Science Letters, v. 36, p. 359-362.

Strmić Palinkaš, S., Palinkaš, L.A., Renac, C., Spangenberg, J.E., Lüders, V., Molnar, F., and Maliqi, G., 2013, Metallogenic model of the Trepča Pb-Zn-Ag skarn deposit, Kosovo: Evidence from fluid inclusions, rare earth elements, and stable isotope data: Economic Geology, v. 108, 135-162.

Tobey, E., Schneider, A., Algería, A., Olcay, L., Perantonis, G., and Quiroga, J., 1998, Skouries porphyry copper-gold deposit, Chalkidiki, Greece: Setting, mineralization and resources, in Porter, T.M., ed., Porphyry and hydrothermal copper and gold deposits: A global perspective; Adelaide, PGC Publishing, p. 175-184.

Tosdal, R.M., and Richards, J.P., 2001, Magmatic and structural controls on the development of porphyry Cu ± Mo ± Au deposits: Reviews in Economic Geology, v. 14, p. 157-181.

Turpaud, P., and Reischmann, T., 2003, Zircon ages of granitic gneisses from the Rhodope (N. Greece), determination of basement age evidences for a Cretaceous intrusive event: Geophysical Research Abstracts, 5:04435.

Turpaud, T., and Reischmann, T., 2010, Characterization of igneous terranes by zircon dating: implications for UHP occurrences and suture identification in the central Rhodope, northern Greece: International Journal of Earth Science, v. 99, p. 567-591.

Veligrakis, T., and Dalampiras, L., 2016, 3-D modeling contribution for producing near mine exploration targets at Olympias gold-rich polymetallic carbonate replacement deposit, Halkidiki, N. Greece [ext. abs.]: Society of Economic Geologists 2016 Conference: Tethyan Tectonics and Metallogeny, Çeşme, Turkey, 2016, Extended Abstracts.

Wawrzenitz, N., and Krohe, A., 1998, Exhumation and doming of the Thassos metamorphic core complex (S Rhodope, Greece): structural and geochronological constrains: Tectonophysics, v. 285, p. 301-312.

Wawrzenitz, N., and Mposkos, E., 1997, First evidence for Lower Cretaceous HP/HT-metamorphism in the Eastern Rhodope, North Aegean region, North-East Greece: European Journal of Mineralogy, v. 9(3), p. 659-664.

Wilson, A.J., 2003, The geology, genesis and exploration context of the Cadia gold-copper porphyry deposits, NSW, Australia: Unpublished Ph.D. thesis, Hobart, University of Tasmania, 335 p.

Wortel, M.J.R., and Spakman, W., 2000, Subduction and slab detachment in the Mediterranean-Carpathian region: Science, v. 290, p. 1910-1917.

Wüthrich, E., 2009, Low temperature thermochronology of the northern Aegean Rhodope Massif: Unpublished Ph.D. thesis, Zürich, Switzerland, ETH, 210 p.

CHAPTER 4

ORIGIN OF AU-RICH CARBONATE-HOSTED REPLACEMENT DEPOSITS OF THE KASSANDRA MINING DISTRICT, NORTHERN GREECE: EVIDENCE FOR LATE OLIGOCENE, STRUCTURALLY-CONTROLLED, AND ZONED HYDROTHERMAL SYSTEMS

The Serbo-Macedonian Metallogenic Province (Janković, 1997; Serafimovski, 2000) of the greater Tethyan Mineral Belt forms a northwest-trending zone of Oligo-Miocene porphyry Au-Cu, Cu skarn, and Au-rich polymetallic vein and carbonate-hosted replacement deposits that extends from Serbia and Kosovo, through the Republic of Macedonia and into the Kassandra Mining District on the eastern Chalkidiki peninsula of northern Greece. Past mining of the Madem Lakkos deposit produced approximately 13.5 Mt of Ag-Pb-Zn ore (Forward et al., 2010). The actively producing Mavres Petres and Olympias mines contain measured and indicated resources of 0.55 Mt at 212 g/t Ag, 8.1% Pb and 11.0% Zn, and 15.1 Mt at 8.97 g/t Au, 146 g/t Ag, 4.9% Pb and 6.5% Zn, respectively (Eldorado Gold Corp., 2017). Upwards of 12Moz Au is contained within these sulfide orebodies and the Skouries porphyry Au-Cu deposit, making the Kassandra Mining District one of the more economically significant mining camps in Eastern Europe (Siron et al., 2016).

The location and morphology of the polymetallic massive sulfide orebodies at the Olympias, Madem Lakkos, and Mavres Petres deposits are controlled by preexisting ductile structures, but formed during semi-brittle to brittle deformation in the Kassandra and Stratoni fault zones (Siron et al., 2018). Two major magmatic episodes in the late Oligocene and early Miocene also occurred during ductile-brittle faulting and are linked to two distinct metallogenic events (Frei, 1992, 1995; Gilg, 1993; Gilg and Frei, 1994; Hahn et al., 2012; Hahn, 2014; Siron et al., 2016, 2018). Late Oligocene high-K calc-alkaline magmas are closely associated with the carbonate replacement massive sulfide orebodies, whereas porphyry Au-Cu mineralization resulted from early Miocene shoshonitic magmatism in the Skouries area (Siron et al., 2016). The late Oligocene Stratoni granodiorite stock and spatially-related granitic aplite

dikes and sills occurring within the Stratoni fault zone were originally interpreted as the magmatic source intrusions responsible for the sulfide orebodies in the Madem Lakkos area (Neubauer, 1957; Nicolaou, 1960, 1964). This interpretation has been refuted by other studies, which tentatively propose that the porphyritic stocks and dikes in the Fisoka area represent the source of fluids for the replacement sulfide ore deposits (Frei, 1992; Gilg, 1993). Nebel et al. (1991) similarly proposed that either the Fisoka or Stratoni stocks could have contributed to skarn mineralization in the Madem Lakkos area. The sulfide orebodies in the Olympias area were considered the distal expressions of the hydrothermal system responsible for the Madem Lakkos and Mavres Petres deposits (Kalogeropoulos et al., 1989; Hahn, 2014). Regardless, the causative magmatic source for the hydrothermal system(s) resulting in the sulfide orebodies within the Stratoni fault zone and at the Olympias deposit remains uncertain.

This study uses a variety of techniques and data sources to constrain the origin of the carbonate replacement mineralization in the Kassandra Mining District. Detailed petrography on representative ore styles combined with a comprehensive drill core geochemical database were used to identify metal deportment and zonation patterns at the district- and deposit-scale. Fluid inclusion microthermometry of primary, syn-mineral quartz gangue was used to investigate the temperatures of ore formation. Carbon and oxygen isotopic analyses of marble and carbonate associated with the sulfide bodies were determined to identify possible fluid sources and to model the physical processes that resulted in the replacement sulfide and vein-breccia systems in the district. Lead isotope data from the sulfide ore and igneous K-feldspar phenocrysts from selected late Oligocene and early Miocene intrusions were also obtained to investigate possible relationships between intrusions and the sulfide deposits. These results, combined with previously published data, are presented here to provide constraints on the origin and source of the hydrothermal fluid(s) responsible for the carbonate replacement deposits in the Kassandra Mining District.

Geological Framework

Carbonate replacement massive sulfide deposits in the Kassandra Mining District are hosted by a complex metamorphic assemblage of deep-crustal rocks within the hinterland of the Alpine-Hellenic orogen. This segment of the Tethyan Alpine-Himalaya mountain belt formed by the collision of the Apulian and Pelagonian microcontinents, with the previously accreted Serbo-Macedonian and Rhodope continental fragments, to the Eurasian continental margin during closure of the Tethys Ocean in the Late Cretaceous to Early Eocene (Pe-Piper and Piper, 2006). Subduction of oceanic lithosphere and related calc-alkaline magmatism is interpreted to have resulted from slab detachment or lithospheric delamination assisted by rollback of the subducting slab during post-collisional back arc extension beginning in the late Eocene (de Boorder et al., 1998; Wortel and Spakman, 2000; Lips, 2002; Neubauer, 2002; Brun and Sokoutis, 2010; Jolivet and Brun, 2010; Krenn et al., 2010; Ring et al., 2010; Jolivet et al., 2013; Papanikolaou, 2013). Retreat of the subducting slab resulted in widespread extension and the exhumation of deep-crustal lithotectonic blocks from Late Cretaceous through to late Miocene time (Dinter and Royden, 1993; Sokoutis et al., 1993; Wawrzenitz and Krohe, 1998; Krohe and Mposkos, 2002; Brun and Sokoutis, 2007; Brun and Faccenna, 2008; Wüthrich, 2009; Kydonakis et al., 2014; Kounov et al., 2015).

Northeastern Greece is underlain by crystalline metamorphic basement rocks belonging to the Rhodope metamorphic province (Burg, 2012). This crustal-scale, amphibolite-facies accretionary prism consists of a stacked complex of southwest-verging nappes situated within the overriding plate of the Hellenic subduction zone (Burg et al., 1990, 1996; Ricou et al., 1998; Gautier et al., 1999; Bonev et al., 2006; Jahn-Awe et al., 2010; Krenn et al., 2010; Burg, 2012). In the study area, Kockel et al. (1977) subdivided the Rhodope metamorphic province into two lithotectonic domains: the Vertiskos unit and the Kerdilion unit (Figure 4.1). The Vertiskos unit is an Ordovician to Silurian, Gondwanan-derived continental magmatic arc that was accreted onto the European margin in the Carboniferous (Himmerkus et al., 2006, 2007, 2009). The younger Kerdilion unit originated from a Permo-Carboniferous magmatic

arc that was overlain by Paleotethyan carbonates (Himmerkus et al., 2011) and subsequently modified by arc magmatism that lasted from Late Jurassic to Early Cretaceous time (Himmerkus et al., 2007, 2011).

The Kerdilion unit consists of migmatitic quartzo-feldspathic hornblende-biotite gneiss containing intervals of compositionally layered to massive graphite-bearing marble, meta-gabbros composed of massive to layered amphibolite and pyroxenite, and interspersed bodies of megacrystic plagioclase-microcline orthogneiss (Kockel et al., 1977; Kalogeropoulos et al., 1989; Nebel et al., 1991; Gilg and Frei, 1994). A conformably interlayered and compositionally gradational graphite-bearing quartz-biotite ± garnet gneiss and schist unit occurs in close association with graphite-bearing marble, calcareous schists, and amphibolite within the Stratoni fault zone (Siron et al., 2018). Fine-grained to aplitic granite gneiss occurs throughout the Kerdilion unit, likely representing the middle Jurassic to Early Cretaceous magmatic event within the district (Himmerkus et al., 2011; Hahn, 2014). Pegmatitic dikes and sills are prominent within the Kerdilion unit and reflect anatectic partial melts from about the middle Paleocene to middle Eocene (Wawrzenitz and Krohe, 1998; Kalogeropoulos et al., 1989).

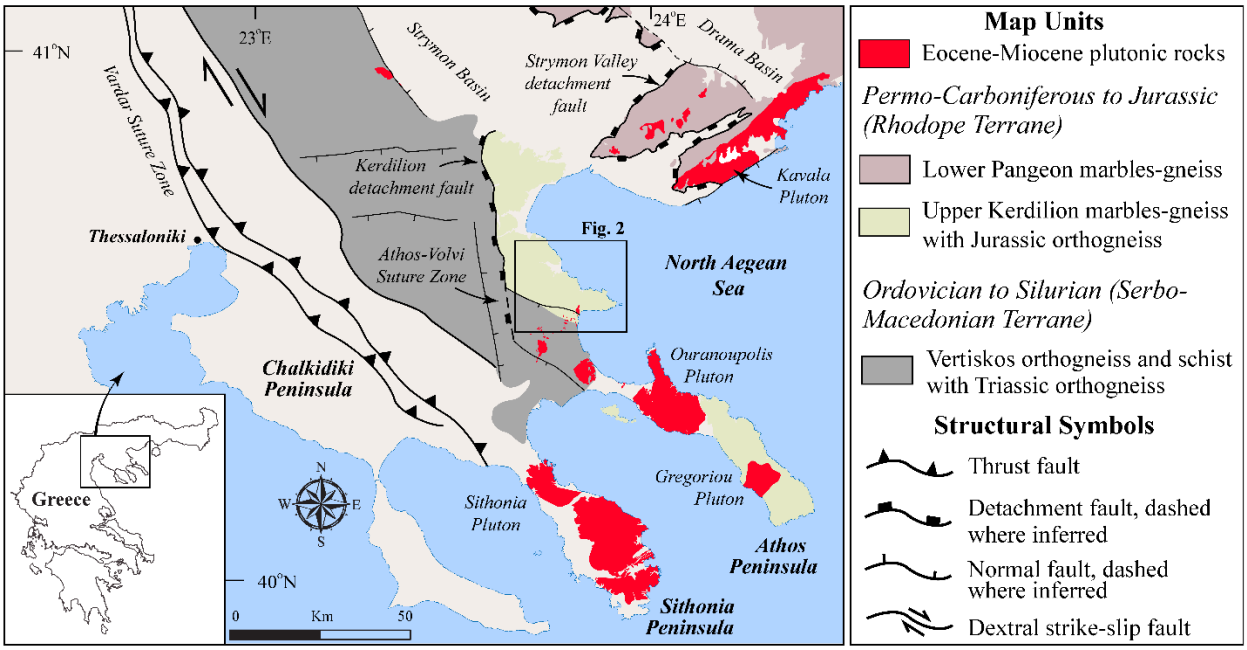

Figure 4.1. Simplified regional geologic map of northeastern Greece modified after Kydonakis et al. (2014) showing the major tectonic units described in the text. The Strymon Valley and Kerdilion detachment faults were adapted from Dinter (1998) and Brun and Sokoutis (2007), respectively. The location of the Athos-Volvi Suture Zone is after Himmerkus et al. (2005).

A package of mafic and ultramafic rocks outcropping mostly within the hanging wall of the Stratoni fault zone separates the Kerdilion unit to the north from the Vertiskos unit to the south (Figure 4.2; Siron et al., 2018). Thin mafic layers within the Kerdilion quartzo-feldspathic biotite gneiss sequence extend north into the Olympias area. These mafic rocks, consisting of layered- and massive-textured amphibolite with subordinate pods of variably serpentinized pyroxenite, are potentially correlative with the Thermes-Volvi-Gomati ophiolitic complex that outcrops within the Athos-Volvi Suture Zone (Figure 4.1; Dixon and Dimitriadis, 1984; Himmerkus et al., 2005; Bonev and Dilek, 2010). However, a middle Jurassic zircon U-Pb age reported in Hahn (2014) suggests that these amphibolites are possibly affiliated with the younger ophiolitic rocks that occur to the west of the district (e.g., Zachariadis et al., 2006).

A monotonous sequence of quartz-rich feldspathic to mica-dominated muscovite-biotite gneiss and schist occurs to the south of the large amphibolite body described above (Figure 4.2). This unit also includes minor lenses of calcareous calc-silicate schist, marble, and amphibolite of uncertain provenance (Siron et al., 2018). An inferred Ordovician to Silurian age for this gneiss package is based on zircon U-Pb geochronology (Hahn, 2014), thus indicating that this lithologic sequence is likely part of the Serbo-Macedonian Vertiskos unit (Kockel et al., 1977).

Oligo-Miocene magmatism

A prominent northeast-oriented intrusive belt of Oligo-Miocene age outcrops within the southern half of the Kassandra Mining District. Zircon U-Pb geochronology defines two distinct post-collisional magmatic episodes with a late Oligocene (27-25 Ma) pulse followed by an early Miocene (20-19 Ma) porphyry episode (Frei, 1992, Frei, 1995; Hahn, 2014; Siron et al., 2016). Both igneous suites belong to the high-K calc-alkaline magma series although an evolved shoshonitic geochemical signature is characteristic of early Miocene porphyry stocks and dikes (Kroll et al., 2002; Hahn, 2014; Siron et al., 2016). The late Oligocene igneous suite exhibits a wide range of compositions from monzogabbro to granodiorite. Crystallization ages tightly cluster from 27.0 ± 0.2 Ma to 26.7 ± 0.3 Ma for the different

phases within the Tsikara composite stock and 25.7 ± 0.4 Ma to 24.5 ± 0.1 Ma for the diorite to granodiorite Fisoka and Stratoni stocks. Granodiorite porphyry dikes that outcrop to the east of the Madem Lakkos deposit in the Stratoni area exhibit similar ages (Figure 4.2; Siron et al., 2016).

The most important member of early Miocene igneous suite is the 20.6 ± 0.5 Ma Au-Cu-mineralized Skouries quartz monzonite porphyry stock (Hahn et al., 2012; Hahn, 2014). Highly potassic glomerophyric porphyry dikes that occur within the Stratoni fault zone and at the Olympias deposit postdate carbonate replacement massive sulfide and are interpreted to be early Miocene based on a zircon U-Pb age of 20.6 ± 0.1 Ma, which is coeval with the Skouries stock (Siron et al., 2016). The youngest early Miocene intrusions documented in the district, also based on zircon U-Pb data, include the barren Aspro Lakkos quartz monzonite porphyry stock (19.7 ± 0.1 Ma), crosscutting trachyandesite porphyry dikes (19.6 ± 0.1 Ma), and the black-matrix trachyandesite porphyry dike (19.2 ± 0.2 Ma) that occurs within the Vathilakkos fault at the Madem Lakkos deposit (Figure 4.2; Gilg and Frei, 1994; Haines, 1998; Siron et al., 2016).

Structural framework

The Kerdilion and Vertiskos basement units were both affected by at least three syn-metamorphic deformation episodes as evidenced by similar peak metamorphic mineral assemblages and structural patterns present in each unit (Siron et al., 2018). Deformation resulting in a penetrative S1 foliation was accompanied by amphibolite-facies metamorphism characterized by an amphibole-biotite ± garnet mineral assemblage. A continuation of D1 deformation, or possibly an unrelated and subsequent D2 event, reworked the S1 foliation into tight to open F2 folds associated with an axial planar S2 cleavage. A locally persistent L2 lineation resulted from the intersection of S1 and S2 fabrics. The D2 event culminated with the development of a district-scale anticlinorium. A final low-strain D3 deformation episode resulted in a steeply dipping S3 cleavage that overprints all earlier ductile fabrics. Mylonitic thrust faults associated with contractional deformation are syn-metamorphic as shown by an amphibolite-

Figure 4.2. Geologic map of the Kassandra Mining District modified after Kockel et al. (1977). Coordinates are displayed in the Greek Geodetic Coordinate System (GGRS 87 Greek Grid).

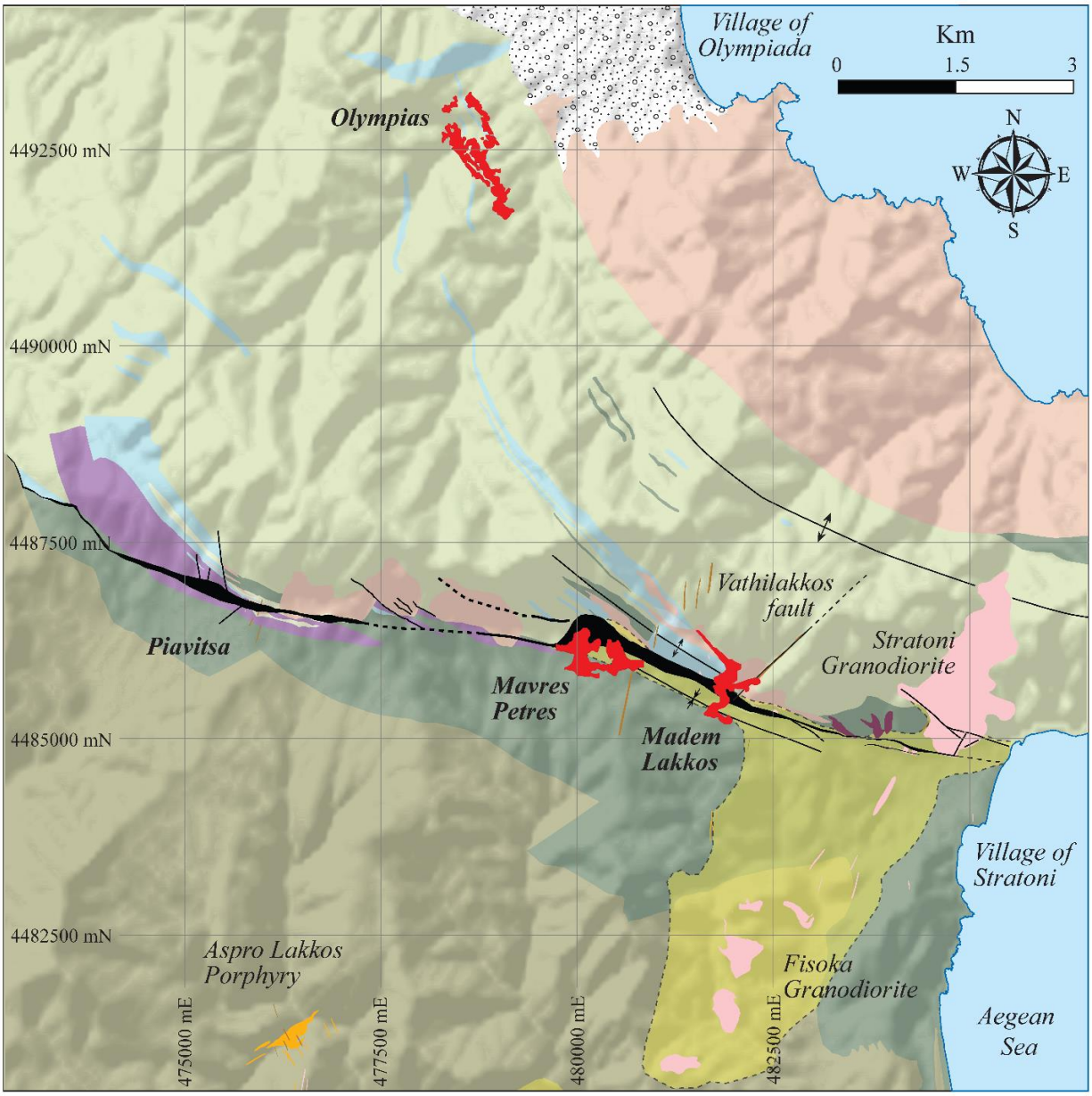

Late Paleocene to Early Miocene Igneous Rocks

- Black-matrix porphyry (19.2 Ma)
- Glomerophyric porphyry (c. 20 Ma)
- Megacrystic Ksp porphyry (c. 20 Ma)
- Granodiorite and granodiorite porphyry (24.5 - 25.4 Ma)
- Granodiorite-diorite, foliated (~58 Ma)

Permo-Carboniferous to Jurassic Kerdilion Unit

- Amphibolite, massive gabbro, and serpentinized pyroxenite
- Aplitic to pegmatitic granite gneiss
- Migmatitic quartzo-feldspathic hornblende-biotite gneiss
- Carbonaceous quartz-biotite gneiss
- Graphite-bearing marble

Ordovician-Silurian Vertiskos Unit

- Quartz-rich, muscovite-biotite schist and gneiss

Hydrothermal Alteration and Mineralization

- Quartz-sericite-pyrite with abundant base metal veins; extent is approximate
- Surface projection of sulfide orebody

Structural Symbols

- F2 Synform Axis
- F2 Antiform Axis
- Fault damage zone (Stratoni fault zone)
- Fault trace, solid line where exposed and dotted where approximate

Quaternary Alluvium

- Unconsolidated sediments

facies metamorphic mineral assemblage that defines the tectonic fabric. Compressive fabrics and thrust faults imply top-to-the-northeast vergence possibly representing increments of progressive deformation associated with regional Eocene or older contraction (Siron et al., 2018).

Regional extensional deformation during the middle Eocene is associated with mylonitic shear zones and ductile-brittle faults that display a normal sense of shear (Brun and Sokoutis, 2007). The mineralized Kassandra and East faults in the Olympias area and the Stratoni fault zone both record a protracted extensional strain history. North-south extension during the late Oligocene was coeval with skarn and carbonate replacement massive sulfide mineralization with syn- to late-mineral east-west extension corresponding to a younger phase of quartz-rich sulfide and quartz-rhodochrosite vein-breccia systems (Siron et al., 2018). Post-mineral brittle faults that crosscut the sulfide orebodies were produced by northeast-southwest extension during the middle to late Miocene (e.g., Diner, 1998). A youngest set of brittle faults overprints all previous ductile fabrics and faults, as well as the sulfide orebodies. These faults are interpreted to have resulted from north-south extension typical of the modern tectonic environment in the northern Aegean region (Pavlides and Tranos, 1991; Siron et al., 2018).

Carbonate Replacement Deposits

The polymetallic (Au-Ag-Pb-Zn-Cu) carbonate-hosted sulfide orebodies within the Kassandra Mining District consist of the past producing Madem Lakkos deposit and the actively producing Mavres Petres and Olympias deposits. These orebodies have attracted research for over ninety years (e.g., Sagui, 1928) with a wealth of mineralogical and physiochemical studies focused on the Madem Lakkos and Olympias massive sulfide deposits (Nicolaou, 1960, 1964; Nicolaou and Kokonis, 1980; Kalogeropoulos and Economou, 1987; Kilias and Kalogeropoulos, 1989; Kalogeropoulos et al., 1989; Mantzos, 1989; Nebel, 1989; Nebel et al., 1991; Gilg, 1993; Gilg and Frei, 1994; Kilias and Madsen, 1994; Kilias et al., 1996; Haines, 1998), as well as a number of unpublished consulting reports. In this section, we

summarize previous mineralogical work aided by petrological observations from polished sections of representative sulfide ore styles from the Olympias, Mavres Petres, and Piavitsa areas.

Olympias deposit

The Olympias deposit is located 6 km north of the Stratoni fault zone (Figure 4.2). Replacement-style massive sulfide orebodies are hosted by graphitic marble interlayered within a sequence of quartzo-feldspathic biotite gneiss, amphibolite, and plagioclase-microcline orthogneiss (Kalogeropoulos et al., 1989; Siron et al., 2016). The massive sulfide orebody plunges shallowly to the southeast, subparallel to F2 fold hinges, and is largely controlled by sub-horizontal, syn-mineral shear zones that occur between the Kassandra and East faults zones. Crosscutting structural relationships and ^{40}Ar-^{39}Ar geochronology indicate that carbonate replacement mineralization occurred by latest Oligocene, coincident with the early stage of post-deformation magmatism in the region (Siron et al., 2018).

Sulfide mineralogy of the Olympias deposit consists of coarse-grained, massive and banded lenses of sphalerite-galena-pyrite that locally transition into pyrite-rich intervals, which become dominated by arsenopyrite locally. Sphalerite-rich sulfide zones commonly display bladed or rod-textured pyrite (Figure 4.3A-B), which may represent the pseudomorphic replacement of marcasite (e.g., Thompson and Arehart, 1990). Similar textures have also been recognized at the Mavres Petres deposit. Chalcopyrite is a common minor mineral in the massive sulfide bodies and typically occurs as inclusions in sphalerite, along sphalerite grain boundaries, or within micro-fractures (Kalogeropoulos and Economou, 1987). Accessory minerals including graphite, pyrrhotite, marcasite, and stibnite occur in trace quantities (Figure 4.3C), with mackinawite, enargite, geocronite, cubanite, bornite, and covellite also reported in previous studies (Nicolaou and Kokonis, 1980; Kalogeropoulos et al., 1989). Unpublished consulting reports identified Ag-tetrahedrite (friebergite) and bournonite intergrowths and inclusions in galena as well as fracture-filling in sphalerite. Gold has also been identified as inclusions in arsenopyrite. Unpublished metallurgical studies, utilizing secondary ion mass spectroscopy, determined

that Ag and Au primarily occupies lattice sites within galena and arsenopyrite (and As-bearing pyrite), respectively.

A quartz-rich sulfide phase is paragenetically younger, and locally overprints, the early replacement massive sulfide ore horizons. These quartz-rich sulfide bodies consist of interlocking, euhedral and growth-zoned quartz accompanied by interstitial bladed to fibrous boulangerite and arsenopyrite with subordinate pyrite, galena, and sphalerite containing minor inclusions of chalcopyrite (Figure 4.3D-E). Boulangerite commonly replaces pyrite and sphalerite (Figure 4.3F). Mineralized silicified breccias also occur within the Olympias deposit and consist of matrix-supported, chaotically arranged sub-angular to angular clasts of sericite-altered granite gneiss, marble, and sulfide (Siron et al., 2018). The breccia matrix consists of dark gray chalcedonic quartz containing disseminated, euhedral pyrite and bladed arsenopyrite. These quartz-rich replacement zones and mineralized silicified breccias are commonly associated with quartz-rhodochrosite alteration of the surrounding wallrock and are most commonly developed on the eastern portions of the Olympias deposit.

Deposits of the Stratoni fault zone

The Stratoni fault zone is a complexly mineralized structural corridor, which hosts the Madem Lakkos and Mavres Petres deposits, and the Piavitsa prospect (Figure 4.2). Skarn and replacement-style orebodies at the Madem Lakkos deposit occur at the eastern end of the Stratoni fault zone, and within 2 km of the Stratoni and the Fisoka granodiorite stocks to the east and south, respectively (Figure 4.2). Previous studies have described a spatial and temporal relationship between aplitic and porphyritic dikes of late Oligocene age and sulfide mineralization (Gilg and Frei, 1994). Massive sulfide in the Madem Lakkos area is hosted by marbles that are localized along faults and within F2 fold hinges associated with a major antiform in the footwall of the Stratoni fault zone (Nebel, 1989; Nebel et al., 1991; Gilg, 1993; Gilg and Frei, 1994; Haines, 1998; Siron et al., 2016, 2018). To the west of Madem Lakkos, massive sulfide orebodies at the Mavres Petres deposit are similarly hosted by marbles contained within a strongly

carbonaceous segment of the Stratoni fault zone (Siron et al., 2018), with discontinuous sulfide lenses and quartz-Mn-rich replacement bodies occurring further to the west (Figure 4.2). Crustiform-textured, Au-bearing quartz-rhodochrosite ± rhodonite vein-breccias persist throughout the district, but are largely concentrated at the Piavitsa prospect. The vein-breccia system in the Piavitsa area is localized in the hanging wall of the Stratoni fault zone and is controlled by east-west extension along north-south faults (Siron et al., 2018).

Madem Lakkos deposit: The Madem Lakkos deposit consists of skarn, massive sulfide, and a younger and volumetrically larger sulfide phase termed "disseminated" sulfide by Nebel (1989) and Gilg (1993). The sulfide mineralogy of the Madem Lakkos deposit described here is adapted from previous work (Nicolaou, 1964; Nebel, 1989; Nebel et al., 1991; Gilg, 1993; Haines, 1998). Early skarn alteration consists of an anhydrous mineral assemblage of andradite garnet, diopside ± anhydrite, epidote, and magnetite. Conversion of primary calcic skarn minerals to hydrous phases (e.g., Fe-bearing chlorite and actinolite) during retrograde alteration is accompanied by pyrite and chalcopyrite with minor pyrrhotite, mackinawite, bismuthinite, cubanite, and scheelite, and trace amounts of galena, tennantite, galenobismuthinite, aikinite, and cosalite. Magnesian skarns are spatially associated with dolomitic marble and consist of a prograde mineral assemblage of forsteritic olivine, magnetite, and pyrite. Retrograde alteration of primary skarn minerals resulted in the conversion of olivine to serpentine and talc and the development of other hydrous mineral phases including tremolite, phlogopite, Mg-chlorite, and the addition of calcite and anhydrite. Pyrite associated with retrograde alteration contains inclusions of pyrrhotite, mackinawite, cubanite, and chalcopyrite.

The mineralogy of the early massive sulfide bodies consists of galena, sphalerite, and pyrite with minor to trace amounts of chalcopyrite, arsenopyrite, and tetrahedrite-tennantite. Pyrrhotite occurs in abundance in association with pyrite-rich replacement bodies (Nicolaou, 1964). The disseminated sulfide phase partially overprints the massive sulfide and is characterized by replacement and breccia textures, veinlets, and open-space cavity fill. This phase of mineralization consists of pyrite with lesser sphalerite,

Figure 4.3. Thin section blanks and corresponding reflected light photomicrographs of representative sulfide samples from the carbonate replacement sulfide deposits of the Kassandra Mining District: A-C) sphalerite-rich massive sulfide with distinctive radiating rod-textured pyrite from the Olympias deposit; B) tarnished pyrite rods penetrating and replacing sphalerite; C) inclusions of relic marcasite and blebs of chalcopyrite within sphalerite; D-E) example of quartz-rich sulfide from the Olympias deposit showing prismatic clear quartz and sulfide-bearing blue quartz intergrown with pyrite, minor sphalerite, and fine-grained boulangerite; E) example of partially replaced cubic pyrite crystal by younger anhedral sphalerite; F) boulangerite (silver color) occurring within voids between quartz grains and invading fractures within sphalerite. Note the abundant chalcopyrite inclusions in sphalerite; G-I) arsenopyrite-rich pyrite-sphalerite >galena massive sulfide from the Mavres Petres deposit; H) arsenopyrite containing inclusions of pyrite and sphalerite and showing a typical brecciated texture caused by syn- to late-mineral calcite; I) partial cross polarized reflected light image of galena in part replaced by boulangerite with quartz forming the matrix to brecciated pyrite; J-L) typical quartz-rich "disseminated sulfide" from the Mavres Petres deposit showing patchy pyrite and fine-grained boulangerite imparting the bluish-gray hue to the quartz; K) common occurrence of boulangerite occupying void space between quartz grains; L) interwoven mesh of boulangerite and quartz with euhedral oscillatory-zoned quartz crystals; M-O) base metal-rich quartz-carbonate vein; N) sphalerite overgrown by euhedral arsenopyrite, quartz and carbonate gangue; O) euhedral pyrite crystals showing arsenopyrite overgrowths on margin of quartz vein; P-R) typical quartz-rhodochrosite vein displaying vibrant pink color and exhibiting domains of clear crustiform quartz and dark chalcedonic quartz hosting fine-grain boulangerite and sphalerite; Q) boulangerite occurring within chalcedonic quartz at margin of rhodochrosite; R) sphalerite showing partial replacement by boulangerite within chalcedonic quartz vein. Abbreviations are as follows: arsenopyrite (Asp), boulangerite (Boul), calcite (Cal), chalcopyrite (Cp), galena (Ga), graphite (Gr), pyrite (Py), quartz (Qtz), reflected light (RL), rhodochrosite (Rds), sphalerite (Sp).

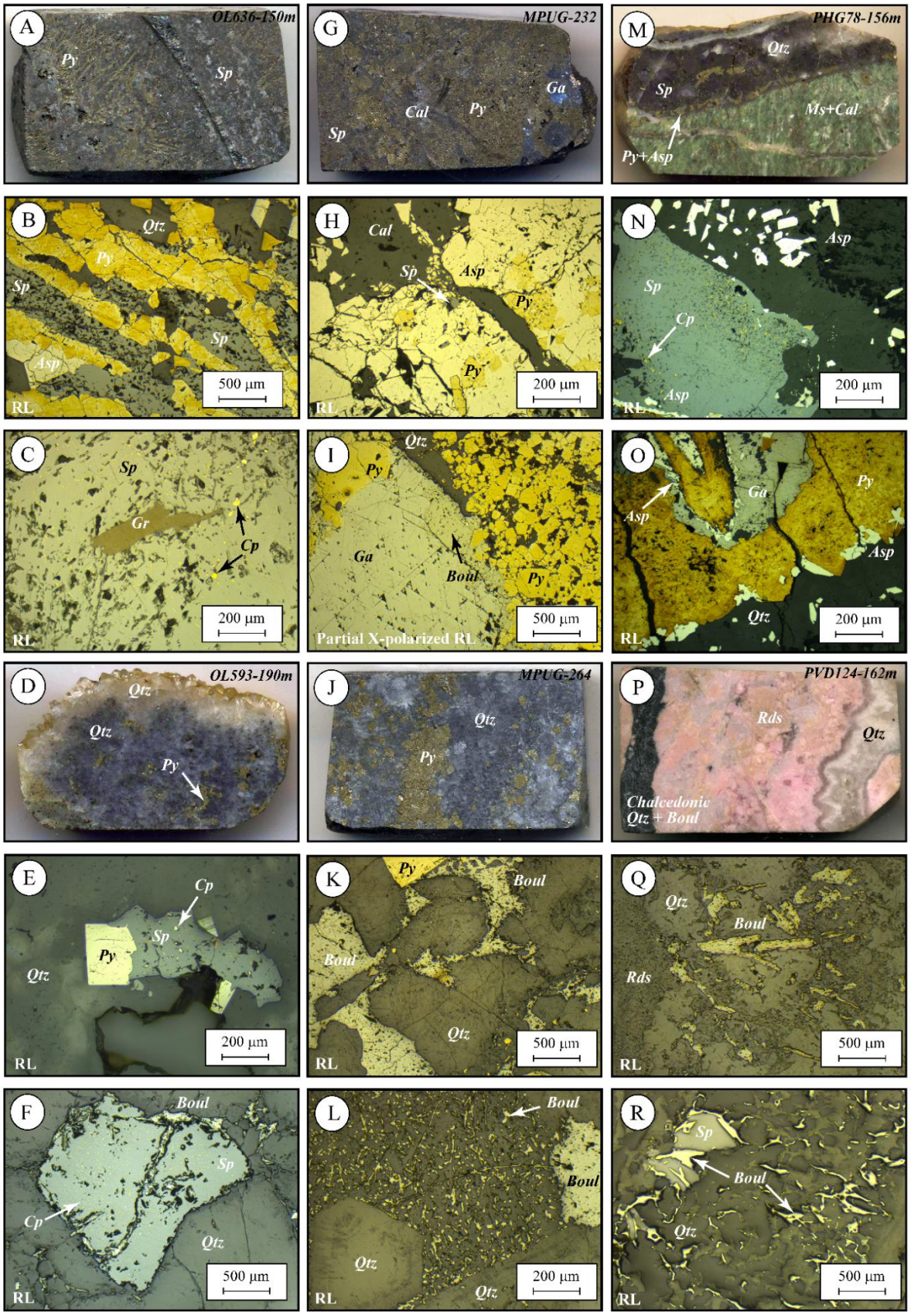
A
OL636-150m
Py
Sp
G
MPUG-232
Ga
Cal
Py
Sp
M
PHG78-156m
Qtz
Sp
Ms+Cal
Py+Asp
B
Qtz
Py
Sp
Sp
Asp
500 µm
RL
H
Cal
Sp
Asp
Py
Py
200 µm
RL
N
Asp
Sp
Cp
Asp
200 µm
RL
C
Sp
Gr
Cp
200 µm
RL
I
Qtz
Py
Ga
Boul
Py
500 µm
Partial X-polarized RL
O
Asp
Ga
Py
Asp
Qtz
200 µm
RL
D
OL593-190m
Qtz
Qtz
Py
J
MPUG-264
Qtz
Py
P
PVD124-162m
Rds
Qtz
Chalcedonic
Qtz + Boul
E
Cp
Sp
Py
Qtz
200 µm
RL
K
Py
Boul
Boul
Qtz
500 µm
RL
Q
Qtz
Boul
Rds
500 µm
RL
F
Boul
Sp
Cp
Qtz
500 µm
RL
L
Boul
Boul
Qtz
Qtz
200 µm
RL
R
Sp
Boul
Qtz
500 µm
RL

galena, arsenopyrite, and chalcopyrite, minor tetrahedrite-tennantite and boulangerite, as well as trace amounts of other sulfosalt minerals. Quartz and rhodochrosite typically occur with the massive and disseminated sulfide phases, and are the principal gangue minerals in the late-mineral vein-breccias (Siron et al., 2018).

Mavres Petres deposit: The Mavres Petres deposit exhibits mineral textures and a sulfide paragenesis that is broadly similar to the Madem Lakkos and Olympias deposits. Replacement-style massive sulfide consists of pyrite, sphalerite, and galena in varying proportions with accessory arsenopyrite, stibnite, and minor boulangerite and chalcopyrite (Figure 4.3G-I; Siron et al., 2016). Massive arsenopyrite occurs locally and is often late in the sulfide paragenesis, infilling fractures and replacing previously deposited sulfide minerals. Massive sulfide is also overprinted by a quartz-rich sulfide phase, characterized by replacement and breccia styles of mineralization with open-space and vuggy textures. The quartz-rich sulfide phase recognized at the Mavres Petres deposit is considered equivalent to the "disseminated sulfide" described at the Madem Lakkos deposit, based on mineralogical similarities and fluid inclusion evidence presented later. The quartz-rich sulfide phase consists predominately of pyrite and is typically accompanied by sphalerite containing chalcopyrite inclusions (Figure 4.3J). Boulangerite also occurs as bladed to fibrous crystals, which commonly form masses and anhedral mosaics that are interstitial to prismatic and zoned quartz (Figure 4.3K-L). Crustiform-textured quartz-rhodochrosite ± rhodonite veins and breccias, similar to those at the Piavitsa prospect discussed below, are incipiently developed in the western portions of the Mavres Petres deposit, and are recognized as the youngest phase of mineralization based on crosscutting relationships (Siron et al., 2018). Quartz-rhodochrosite vein-breccias display a similar mineralogy to the quartz-rich sulfide phase but predominately contain boulangerite ± arsenopyrite.

Piavitsa prospect: Replacement-style sulfide bodies in the Piavitsa area occur as discontinuous lenses, which are typically brecciated, and veins (Figure 4.3M) hosted by marble and graphite-bearing carbonaceous quartz-biotite gneiss and schist within the Stratoni fault zone (Siron et al., 2018). The

sulfide lenses exhibit similar mineralogy to the replacement bodies at the Mavres Petres deposit. Surface outcrops of marble in the Piavitsa area are commonly oxidized where Mn-bearing silicate and carbonate minerals have been converted to oxides including pyrolusite, cryptomelane, nsutite, and ramsdellite (Arvanitidis and Constantinides, 1994). Drill core intercepts show that marble lenses are variably replaced by quartz-rhodochrosite intergrown with pale green mica and patchy replacement sulfide intervals consisting of pyrite, galena, sphalerite, and arsenopyrite (Figure 4.3N-O; Siron et al., 2016). A younger and overprinting event consisting of quartz-rhodochrosite ± rhodonite veins and breccias exhibit a diagnostic pink coloration and crustiform textures with open-space, clear to milky prismatic quartz and black chalcedonic quartz domains (Figure 4.3P). Fine-grained pyrite and arsenopyrite are associated with rhodochrosite and prismatic quartz. Fibrous boulangerite crystals that are characteristic of this later event typically occupy black chalcedonic quartz (Figure 4.3Q). Sphalerite is a minor mineral associated with the black chalcedonic quartz and is commonly replaced by boulangerite (Figure 4.3R). Chalcopyrite is a rare sulfide mineral phase and is generally late in the mineral paragenesis.

Metal Zonation

Carbonate-hosted replacement deposits commonly show metal zonation patterns where Cu-(Au-W-Mo) are elevated proximal to mineral-related igneous intrusions with increased Ag-Mn concentrations in the distal parts of the hydrothermal system (Megaw, 1998). This study utilized a multi-element geochemical database to identify the distribution of metals in and around the orebodies within the Stratoni fault zone and at the Olympias deposit, and evaluate the similarities and differences to other carbonate-hosted replacement deposits. Assay data was collected from 2690 exploration and production drill holes within 2 km north and south of the Stratoni fault zone, and 1103 drill holes from the Olympias deposit area. The database was sorted by element (Ag, As, Au, Sb, Mn, Cu, Pb, and Zn) and filtered based on intercepts that were logged by company geologists as altered and/or mineralized. Metal grades determined from this dataset are not based on economic factors and are therefore not necessarily representative of the

measured and indicated resource estimates reported earlier (Eldorado, 2017). The assay data is plotted on conventional box-and-whisker plots (Figure 4.4A-B) which are suitable for illustrating the distribution and variability of large datasets, with average assay values and metal ratios displayed in Table 4.1. The objective of this study is to map district- and deposit-scale metal zonation patterns that may be indicative of hydrothermal fluid source and flow direction within the Stratoni fault zone and around the Olympias deposit.

Table 4.1. Summary of geochemical assay data (mean values) and metal ratios from the carbonate replacement deposits. Values are reported in parts per million (ppm) with percentages in italics

Deposit	Ag	As	Au	Sb	Mn	Cu	Pb	Zn
Madem Lakkos	146	5995	1.2	234	4808	6040	69402	83378
		0.60			*0.48*	*0.60*	*6.94*	*8.34*
Mavres Petres	198	34397	4.9	1237	21039	405	76704	102706
		3.44			*2.10*	*0.04*	*7.67*	*10.27*
Piavitsa	17	2074	1.2	188	11130	165	3897	6333
		0.21			*1.11*	*<0.02*	*0.39*	*0.63*
Olympias	61	15684	3.7	705	27924	431	19234	21420
		1.57			*2.79*	*0.04*	*1.92*	*2.14*

Table 4.1. Continued.

Deposit	Ag/Au	Cu/Pb	Cu/Zn	Pb/Zn
Madem Lakkos	317	0.9	8.5	5.7
Mavres Petres	78	0.2	0.04	1.5
Piavitsa	24	3.2	0.5	0.5
Olympias	52	0.2	0.1	1.8

The skarn and replacement sulfide orebodies of the Madem Lakkos deposit contain 0.6% Cu, whereas the average Cu grade at the Mavres Petres deposit and Piavitsa prospect are markedly lower at 0.04% and 0.02%, respectively. On average, Pb and Zn grades are highest at the Mavres Petres deposit at

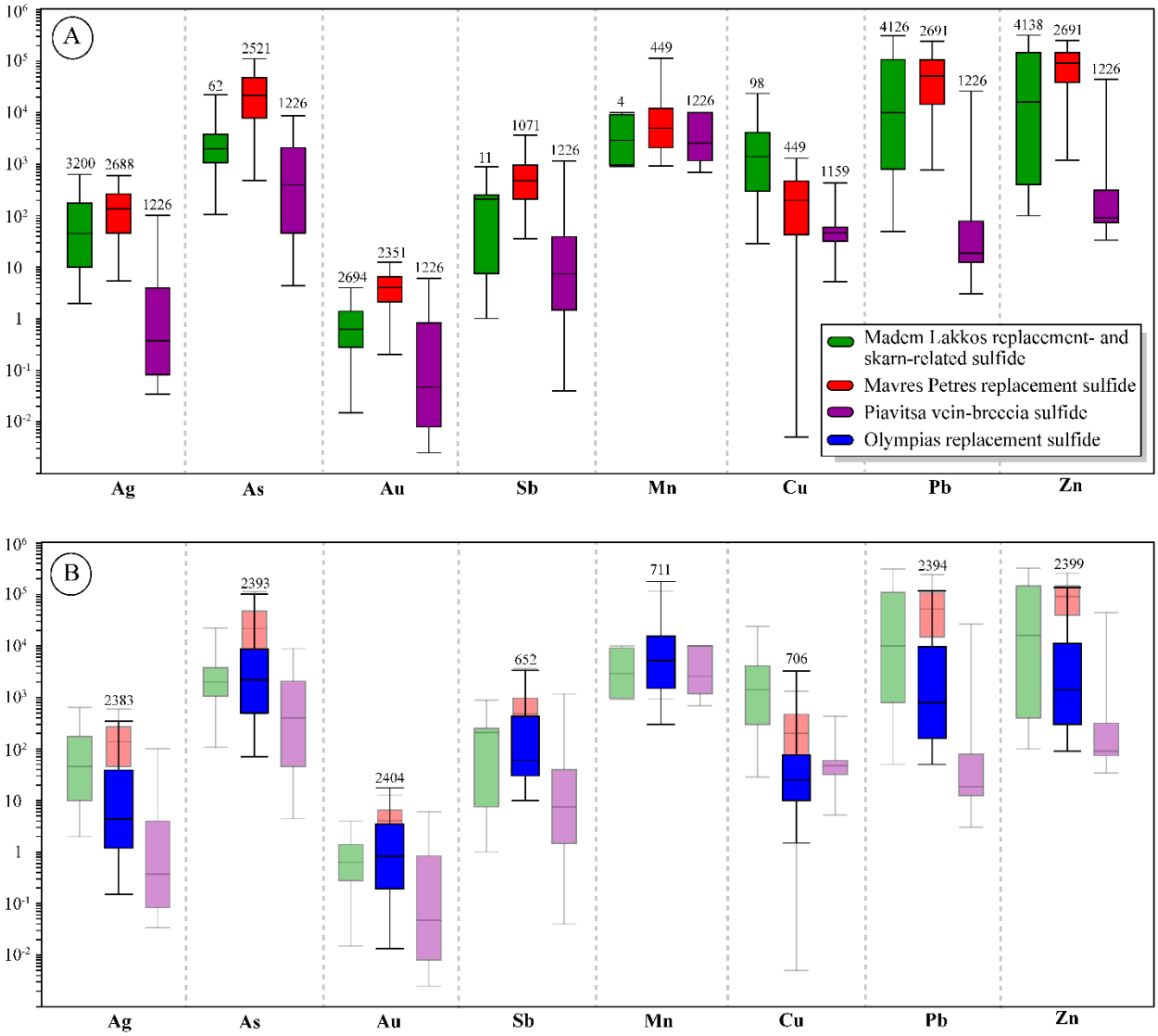

Figure 4.4. Box-and-whisker plots of multi-element geochemical assay data (Ag, As, Au, Sb, Mn, Cu, Pb, and Zn) from surface and underground exploration and production drill holes. The box represents the 25th to 75th percentile range of the data with the 5th and 95th percentile values indicated by the lower and upper whiskers, respectively. Median values are represented by the solid line within each box. The total number of samples for each box-and-whisker plot is shown above the upper whisker: A) data from the Madem Lakkos (green) and Mavres Petres (red) deposits, and the Piavitsa prospect (purple); B) data from the Olympias deposit (blue) is superimposed on image (A).

7.67% and 10.27%, respectively, and lowest for the quartz-rhodochrosite vein-breccias at the Piavitsa prospect (Figure 4.4A). Manganese assay data from the Madem Lakkos deposit is sparse and insufficient to define trends, and the data from Mavres Petres and Piavitsa areas are not distinctly different. The data shows that Ag (197.70 g/t), As (3.44%), Au (4.87 g/t), and Sb (0.12%) are elevated at the Mavres Petres

deposit relative to the Madem Lakkos deposit and the Piavitsa prospect. Sulfide ores at the Olympias deposit to the north contain 0.04% Cu, similar to the Mavres Petres deposit, but with average Pb (1.92%) and Zn (2.14%) values that are much lower than the sulfide deposits within the Stratoni fault zone (Figure 4.4B). Manganese values largely overlap with the Mavres Petres deposit but Ag (61.41 g/t), As (1.57%), Au (3.65 g/t), and Sb (0.07%) consistently exhibit lower concentrations (Figure 4.4B).

Metal ratios also reveal consistent patterns within the Stratoni fault zone. The Pb/Zn ratio decreases westward from the Madem Lakkos deposit to the Mavres Petres deposit and Piavitsa prospect. The Ag/Au ratio displays a similar decreasing trend from Madem Lakkos (317) to Mavres Petres (78) with a minimum value at the Piavitsa prospect (24). The Cu/Pb ratio also decreases toward the west from Madem Lakkos to the Mavres Petres deposit, but it increases sharply at the Piavitsa prospect, albeit lower concentrations. The Cu/Zn ratio decreases substantially from Madem Lakkos to the Mavres Petres deposit, but it also shows an order of magnitude rise at the Piavitsa prospect, again at lower concentrations. Metal ratios from the Olympias deposit are similar in scale to the Mavres Petres deposit as shown in Table 4.1.

Fluid Inclusion Microthermometry

Fluid inclusion microthermometry can aid in understanding the physiochemical conditions of ore formation (Roedder, 1979). Previous fluid inclusion studies from the Kassandra Mining District have focused on the skarn and carbonate replacement sulfide orebodies at the Madem Lakkos and Olympias deposits (Gilg, 1993; Kilias and Kalogeropoulos, 1989; Nebel et al., 1991; Kilias and Madsen, 1994; Kilias et al., 1996), base metal-rich quartz-carbonate veins distal to the Madem Lakkos deposit and igneous quartz contained within the late Oligocene Stratoni granodiorite stock (Gilg, 1993), and the porphyry-style veins associated with the Skouries Au-Cu deposit (Frei, 1992, 1995). Fluid inclusion results reported here expand on previous work from the Olympias and Madem Lakkos deposits and adds new results from the Mavres Petres deposit and the Piavitsa prospect, particularly to evaluate the later

stages of mineralization. Temperatures derived from fluid inclusion analyses are utilized in the modeling and interpretation of carbon and oxygen isotopic data presented in the following section. In addition, the microthermometric data presented here assists in developing a fluid flow zonation model for the Stratoni fault zone. Fluid inclusion data from earlier studies specific to the carbonate replacement deposits in the district are summarized below and are considered in the interpretation of data from this study. The sampling procedure, analytical methodology, and microthermometric data are presented in the Appendix.

Previous studies

Olympias deposit: Previous microthermometric studies at the Olympias deposit were performed on primary and psuedosecondary fluid inclusions contained in quartz associated with sulfide ore (Kilias and Kalogeropoulos, 1989; Kilias and Madsen; 1994; Kilias et al., 1996). Fluid inclusion data presented in these studies were categorized based on sulfide morphology (e.g., Kalogeropoulos et al., 1989) rather than sulfide paragenesis; consequently, it is unclear which stage of sulfide mineralization their data represent. Regardless, three types of fluid inclusions were identified based on the fluid and solid phases present at room temperature, as well as phases present upon heating and cooling. The results from this work are summarized below.

The most abundant fluid inclusions, termed type-1 inclusions, contain a two-phase aqueous liquid-vapor assemblage, which on rare instances produces an optically observable clathrate that melts at temperatures above 0^{o}C. Type-1 inclusions contains a moderately saline fluid (<18 weight percent NaCl equivalent) that always homogenizes to the liquid phase at temperatures between 338.9 ± 26.2^{o}C and 297.0 ± 19^{o}C. Type-2 fluid inclusions contain three-phases consisting of aqueous H_2O liquid coexisting with CO_2 liquid and vapor. Melting of solid CO_2 occurs at -56.5^{o}C with homogenization of liquid CO_2 to the vapor phase occurring between 30.8^{o}C and 21.0^{o}C. Type-2 inclusions are low salinity (<4 weight percent NaCl equivalent) and exhibit total homogenization behavior to either the liquid or vapor phase at temperatures between 350^{o}C and 306^{o}C. Type-3 fluid inclusions are similarly characterized by three

phases, but consist of an aqueous H_2O liquid and vapor with trapped solids that are interpreted as halite and sphalerite. Type-3 inclusions are highly saline (32-28 weight percent NaCl equivalent) and homogenize to the liquid phase at temperatures of 349.0 ± 11.1ºC.

Madem Lakkos deposit: Gilg (1993) performed analyses on fluid inclusions from the massive sulfide, skarn, and disseminated sulfide orebodies at the Madem Lakkos deposit, including distal quartz-carbonate veins hosted by the metamorphic rocks. Three fluid inclusions types (L, S, and V) from sulfide ore were defined based on fluid and solid phases present at room temperature (25ºC), and their heating and cooling behavior. L-type fluid inclusions contain two phases consisting of H_2O liquid and vapor, which homogenize to the liquid phase. Calculated salinities define two populations for L inclusions: <12 weight percent NaCl equivalent for L1 inclusions, and >12% NaCl equivalent for L2 inclusions. S-Type fluid inclusions contain three phases consisting of H_2O liquid and vapor, and a trapped isotropic solid interpreted as halite. S-type fluid inclusions are further divided into S1 and S2 subtypes based on homogenization behavior. S1 inclusions homogenize to the liquid phase before dissolution of the halite crystal, whereas the dissolution of halite before homogenization defines the S2 subgroup. V-type fluid inclusions are CO_2-rich and contain two or three phases consisting of liquid and vapor CO_2, or two liquids and a vapor at room temperature. V-type inclusions homogenize to the vapor phase and are low-salinity based on clathrate melting temperatures.

Skarn-related sulfide contains two fluid inclusion types (L and S2) that occur in quartz, diopside, and garnet. Early anhydrous calcic skarns are characterized by homogenization temperatures ranging from 450ºC to 400ºC with a wide range of calculated salinities from 45 to 14 weight percent NaCl equivalent. L-type fluid inclusions from retrograde hydrous skarns are less saline and display homogenization temperatures that range from 278ºC to 240ºC. L2-, S1-, and V-type inclusions occur within quartz and sphalerite associated with the skarn-free replacement sulfide orebodies. Both L- and S-type inclusions contain 30 to 20 weight percent NaCl equivalent and homogenize to the liquid phase at temperatures from 450ºC to 230ºC (average 370ºC). Coexisting CO_2-rich (V-type) inclusions homogenize

to the vapor phase between 450ºC and 300ºC. Melting of a solid CO_2 phase occurs at -56.6ºC with the melting of clathrate solid from 9ºC to 4.5ºC. Total homogenization of liquid CO_2 to the vapor phase occurs from 29ºC to 20ºC. Fluids associated with the younger disseminated sulfide phase are characterized by L1-type inclusions that contain <10 weight percent NaCl equivalent and exhibit homogenization temperatures from 250ºC to 150ºC.

Microthermometric results

Olympias deposit: Quartz-rich replacement sulfide lenses located in drill core were evaluated from the Olympias deposit (Figure 4.3D). Two samples investigated contain variable pyrite-galena-sphalerite and arsenopyrite with boulangerite interstitial to euhedral interlocking quartz grains. Euhedral and prismatic quartz is generally clear but commonly exhibits clouded growth zones defined by concentrations of submicron-scale fluid inclusions, most of which are unsuitable for microthermometric analysis. While previous work described fluid inclusion types from the replacement sulfide (Kilias and Madsen, 1994; Kilias et al., 1996), it was unclear if the paragenetically younger mineralization was investigated in their studies. Two fluid inclusion types from primary inclusions (as defined by Roedder, 1984) were identified in quartz associated with sulfide. Type-1 fluid inclusions are occasionally euhedral, but are commonly elliptical to irregular in shape and are typically less than about 20 μm in length. These inclusions contain two-phases consisting of aqueous liquid and vapor, which comprise 30 to 40 percent of the inclusion at 25ºC (Figure 4.5A). Small transparent solids were observed in few inclusions. Type-2 fluid inclusions occur in clusters together with type-1 inclusions, and exhibit flat and elongate shapes that range from less than 5 μm to about 30 μm in their long dimension. Two phases are present in the type-2 inclusions, consisting of aqueous liquid H_2O and a CO_2 vapor phase which occupies approximately 60 percent of the inclusion at 25ºC (Figure 4.5B-D). All type-2 inclusions contain small trapped transparent solids, which may be carbonate daughter crystals.

Microthermometry of type-1 fluid inclusions yielded total homogenization temperatures that range from 365.6ºC to 227.8ºC with an average of 309.6ºC ± 31.2ºC (Figure 4.6A). Ice melting depression temperatures range from -1.4ºC to -5.8ºC, which yield an average calculated salinity of 6.4 ± 2.0 weight percent NaCl equivalent (Figure 4.6B). Type-2 fluid inclusions homogenize to the vapor and liquid phase within a narrow range of temperatures from 347.1ºC to 344.5ºC (Figure 4.6A). Liquid CO_2 occurs as a thin film that coats the CO_2 vapor bubble between 17.2ºC and -7.5ºC in type 2 inclusions, the temperature where liquid CO_2 dissolves into the CO_2 vapor phase. Figure 4.5C-D shows the presence of liquid CO_2 in two separate inclusions at 12.8ºC and 13.8ºC. The final melting temperature of the solid CO_2 phase occurs from -56.9ºC to -57.7ºC, below the triple point of pure CO_2 (-56.6ºC), indicating the presence of a trapped gas other than CO_2 (Roedder, 1984). Melting of a clathrate phase occurs from 9.9ºC to 9.2ºC yielding calculated salinities that range from 1.6 to 0.2 weight percent NaCl equivalent (Figure 4.6B), just below the peritectic curve for the system H_2O-CO_2-NaCl (Darling, 1991).

Mavres Petres deposit: Quartz gangue associated with massive sulfide at the Mavres Petres deposit did not yield fluid inclusions amenable for microthermometric study. However, boulangerite-bearing quartz-rich sulfide that displays textural and mineralogical similarities to the younger phase of mineralization at the Olympias deposit were evaluated. Two samples were collected; one from drill core and another from an underground exposure at the 264 m level of the Mavres Petres mine (Figure 4.3J). Each sample displays a distinctive interlocking network of euhedral and prismatic quartz intergrown with pyrite and sphalerite. A fibrous mesh of boulangerite and fine-grained secondary quartz infills open-space between preexisting quartz grains (Figure 4.3K). Coeval boulangerite and quartz also occupy fractures within earlier deposited sulfide.

Analysis of primary fluid inclusions in syn-mineral quartz revealed Type-1 inclusions, similar to those defined at the Olympias deposit. Type-1 fluid inclusions are generally elliptical to irregular in shape and range from less than 5 μm to about 40 μm in length. These inclusions contain an aqueous liquid phase and a vapor phase that occupies 20 to 40 percent of the inclusion at 25ºC (Figure 4.5E). Trapped solids

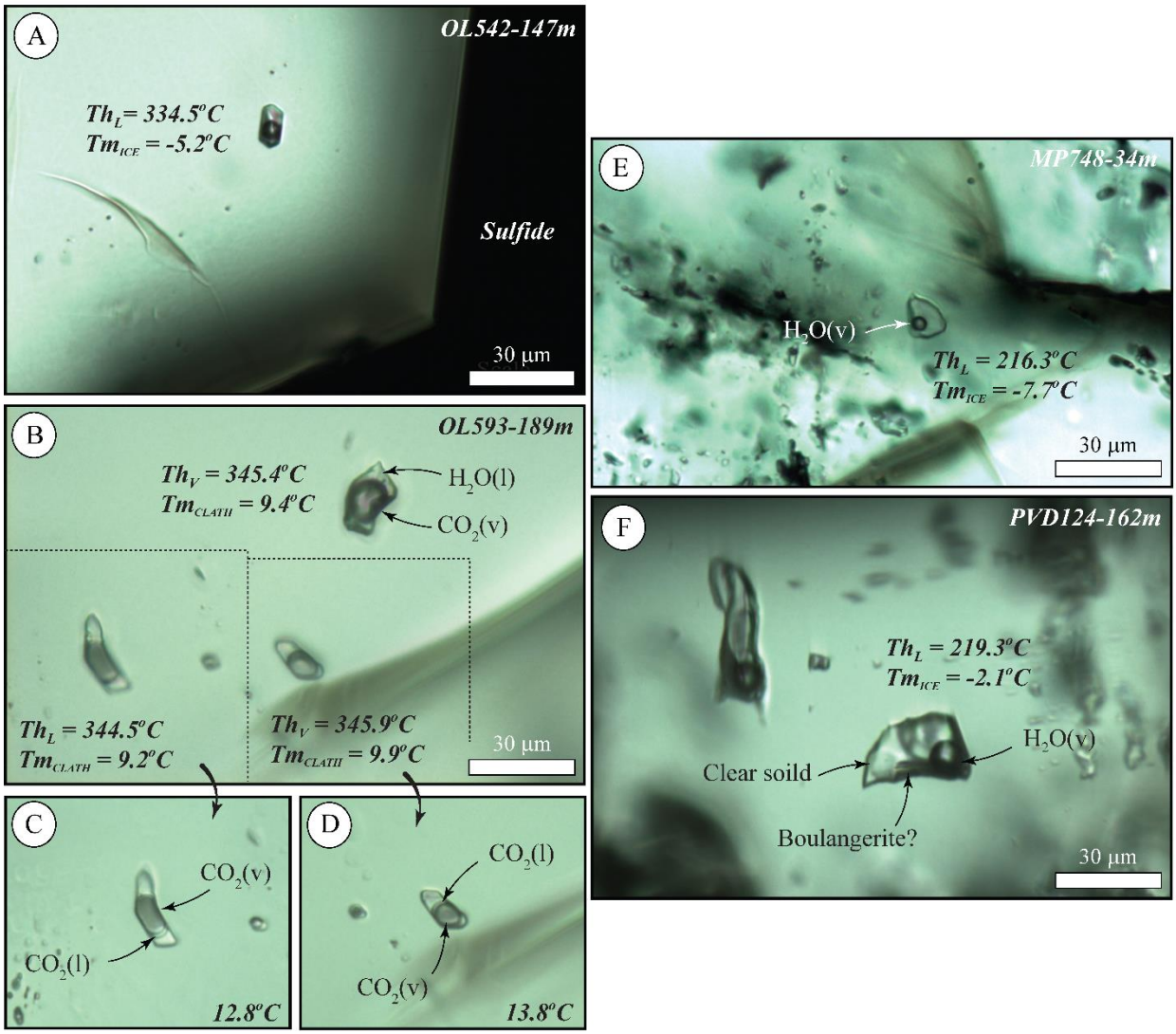

Figure 4.5. Photomicrographs of representative primary fluid inclusions contained in quartz from the quartz-rich sulfide phase at the Olympias and Mavres Petres deposits, and quartz-carbonate veins at the Piavitsa prospect. Microthermometric measurements are indicated on each image: A) type-1 fluid inclusion in quartz from the Olympias deposit imaged at 25ºC. Note the geometry of the inclusion mimics the crystallographic shape of the hosting quartz crystal in contact with sulfide; B) type-2 fluid inclusions imaged at 25ºC trapped at slightly different focal levels in quartz show three phases in the system H_2O-CO_2-NaCl. Bimodal total homogenization behavior is indicated by expansion of the CO_2 bubble to the vapor and by shrinking of the CO_2 bubble to the liquid; C-D) photomicrographs of fluid inclusions outlined in image B taken at 12.8ºC and 13.8ºC document the presence of CO_2 liquid forming a meniscus on the CO_2 vapor bubble; E) typical type-1 fluid inclusion in quartz from the Mavres Petres deposit, imaged at 25ºC; F) type-1 fluid inclusion in quartz-rhodochrosite vein from the Piavitsa prospect, imaged at 25ºC. Note the presence of a clear daughter crystal and needle-shaped opaque minerals interpreted to be calcite (?) and boulangerite, respectively. Abbreviations are as follows: total homogenization temperature to the liquid phase (Th_L) and vapor phase (Th_V), melting temperature of clathrate (Tm_{Clath}) and of H_2O ice (Tm_{Ice}), liquid (l), vapor (v).

Figure 4.6. Histograms of fluid inclusion microthermometric data showing total homogenization temperature (left) and calculated salinity (right) for primary fluid inclusions contained within quartz associated with quartz-rich replacement sulfide from the Olympias deposit (A-B), Mavres Petres deposit (C-D), and the quartz-carbonate veins at the Piavitsa prospect (E-F). Average values and 1σ standard deviations are reported in bold text and represented by the dashed red line and gray bounding box. Published homogenization temperature and salinity ranges for the Olympias and Madem Lakkos deposits are represented by horizontal brackets in images A-B and C-D, respectively.

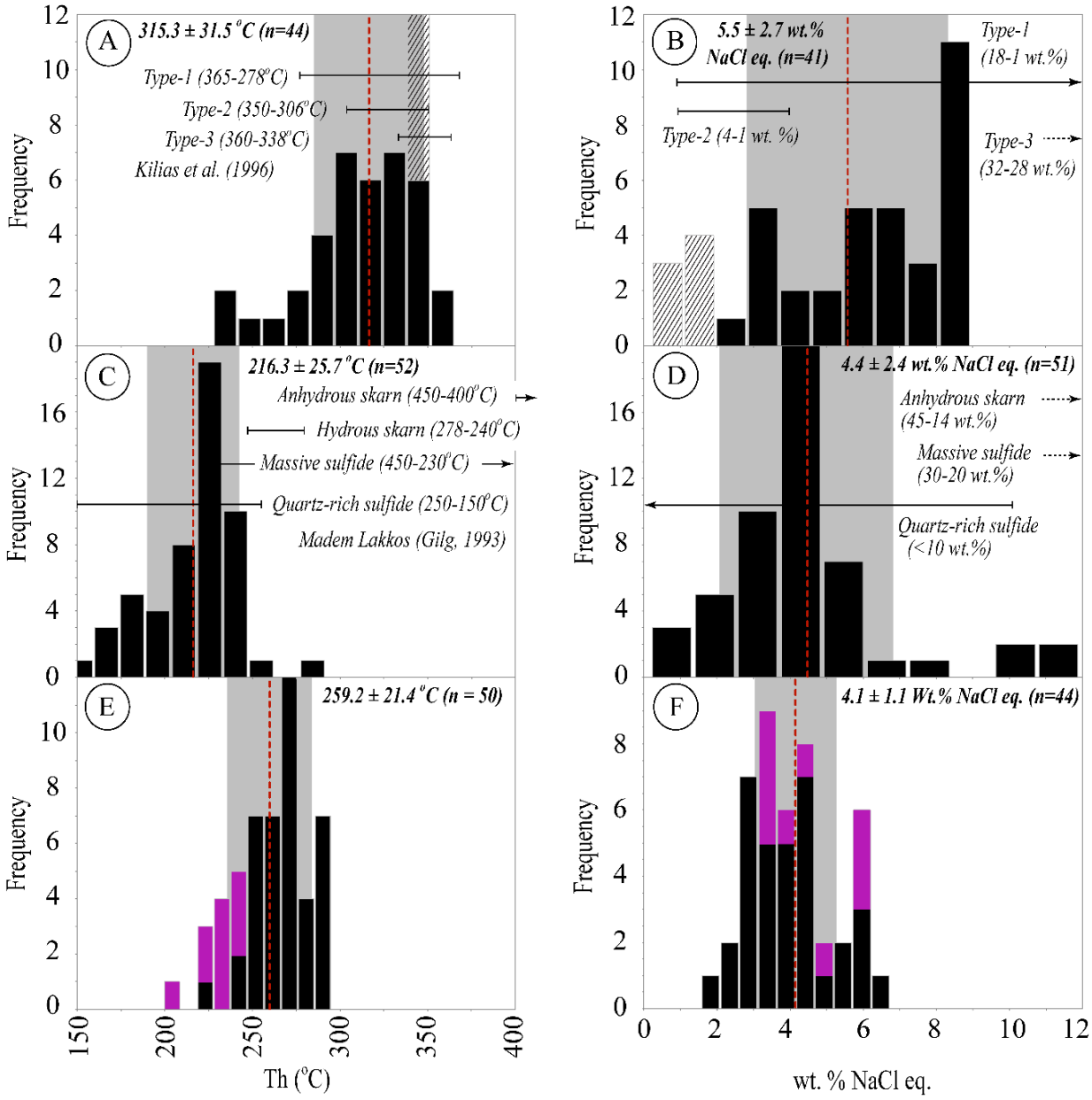
A
315.3 ± 31.5 °C (n=44)
Type-1 (365-278°C)
Type-2 (350-306°C)
Type-3 (360-338°C)
Kilias et al. (1996)
B
5.5 ± 2.7 wt.% NaCl eq. (n=41)
Type-1 (18-1 wt.%)
Type-2 (4-1 wt. %)
Type-3 (32-28 wt.%)
C
216.3 ± 25.7 °C (n=52)
Anhydrous skarn (450-400°C)
Hydrous skarn (278-240°C)
Massive sulfide (450-230°C)
Quartz-rich sulfide (250-150°C)
Madem Lakkos (Gilg, 1993)
D
4.4 ± 2.4 wt.% NaCl eq. (n=51)
Anhydrous skarn (45-14 wt.%)
Massive sulfide (30-20 wt.%)
Quartz-rich sulfide (<10 wt.%)
E
259.2 ± 21.4 °C (n = 50)
F
4.1 ± 1.1 Wt.% NaCl eq. (n=44)
Frequency
Th (°C)
wt. % NaCl eq.
Fluid inclusion types
Type-1: H2O-rich liquid-vapor
Type-1: H2O-rich liquid-vapor (within boulangerite-bearing quartz-rhodochrosite veins)
Type-2: H2O and CO2-rich liquid-vapor (observed at the Olympias deposit)

are uncommon but may include a transparent and equant, and needle-shaped opaque crystals interpreted as carbonate daughter minerals and boulangerite, respectively. Type 1 fluid inclusions display homogenization temperatures that range from 291.6ºC to 144.7ºC with an average of 216.3 ± 25.7ºC (Figure 4.6C). Several fluid inclusions recorded lower homogenization temperatures and are interpreted as either secondary inclusions unrelated to the ore forming fluid, or inclusions that have undergone post-entrapment modification. Salinities calculated from ice melting temperatures range from 11.9 to 0.9 weight percent NaCl equivalent with an average of 4.4 ± 2.4 weight percent NaCl equivalent. A subset of Type-1 inclusions, however, displays salinities >10 weight percent NaCl equivalent (Figure 4.6D).

Piavitsa prospect: Two drill core samples from base metal-rich quartz-calcite veins containing sphalerite-pyrite-galena-arsenopyrite were analyzed (Figure 4.3M). These veins exhibit a distinctive pale green muscovite-quartz-carbonate-pyrite alteration envelope that generally occurs near the replacement sulfide lenses at the Mavres Petres and Olympias deposits. A boulangerite-bearing quartz-rhodochrosite vein intercepted in drill core was also analyzed (Figure 4.3P), although the timing between the two vein styles is uncertain. The quartz-rhodochrosite vein contains clear quartz exhibiting a zoned and crustiform texture, and black chalcedonic quartz that hosts minor sphalerite and pyrite with abundant boulangerite. Fluid inclusions contained within the black chalcedonic quartz are generally <5 μm and unsuitable for microthermometric analysis; consequently, primary fluid inclusions within the coarser-grained clear quartz were examined.

Microthermometry of quartz from the base metal-rich quartz-calcite and the quartz-rhodochrosite veins revealed only type-1 fluid inclusions, similar to those defined above. Type-1 fluid inclusions from both vein styles are elliptical to elongate in shape and commonly exceed about 30 μm in length (Figure 4.5F). Type-1 fluid inclusions contain two-phases consisting of aqueous H_2O liquid and a vapor phase typically occupying 20 to 40 percent of the inclusion. Some inclusions contain needle-shaped opaque solids and euhedral clear crystals that are interpreted to be boulangerite and carbonate daughter minerals based on shape and microthermometric properties. Type-1 fluid inclusions in the base metal-rich quartz-

calcite veins homogenize to the liquid phase at temperatures ranging from 294.9ºC to 226.5ºC, yielding an average temperature of 266.6 ± 16.0ºC (Figure 4.6E). Fluid inclusions in the quartz-rhodochrosite veins homogenize to the liquid phase but at lower temperatures that range from 239.7ºC to 199.3ºC, averaging 229.4 ± 12.3ºC (Figure 4.6E). Combined, the average homogenization temperature of both vein styles is 259.2 ± 21.4ºC. Ice melting depression temperatures for both vein styles correspond to calculated salinities that span 6.7 to 1.6 (average 4.1 ± 1.1) weight percent NaCl equivalent (Figure 4.6F).

Carbon and Oxygen Stable Isotopes

Carbon and oxygen stable isotopes are geochemical tracers that may indicate the nature, evolution and flow of hydrothermal fluids in carbonate environments (e.g., Engel et al., 1958). This study presents the results of 234 coupled carbon-oxygen isotope measurements of carbonate that were determined using a laser infrared absorption technique based on Off-Axis Integrated Cavity Output Spectroscopy (OA-ICOS) developed at the University of British Columbia. The detailed methodology of OA-ICOS and comparisons with conventional Isotope Ratio Mass Spectroscopy (IRMS) is described in Barker et al. (2011) and Beinlich et al. (2017). The objective of the stable isotope study was to investigate the district-scale zonation pattern recorded in gangue and wallrock carbonates, and to model the processes that controlled the isotopic composition of carbonates associated with the carbonate replacement systems in the Stratoni fault zone and in the Olympias area. Carbon-oxygen isotope data are presented in standard δ-notation and displayed on conventional $\delta^{13}C$ vs. $\delta^{18}O$ covariation diagrams. This section describes the isotopic patterns exhibited by carbonate occurring in marble, gangue associated with sulfide ore, and vein-breccias. These data are also discussed with respect to carbonate mineralogy as determined from the qualitative staining technique of Hitzman (1999). Theoretical mass balance calculations that describe the effect of fluid-rock interaction and decarbonation reactions (Taylor, 1974, 1979; Valley, 1986; Bowman, 1998; Baumgartner and Valley, 2001) are presented in the discussion section. Sampling procedures, analytical methodology, carbon-oxygen isotope data, and model calculations are located in the Appendix.

Previous studies

Stable isotope studies have been previously performed on the marble host rocks and carbonate associated with the replacement sulfide orebodies from the Madem Lakkos and Olympias deposits (Kalogeropoulos and Kilias, 1989; Kalogeropoulos et al., 1989; Gilg, 1993). Depleted $\delta^{18}O$ values from marble and ore-related gangue carbonate at the Olympias deposit led Kalogeropoulos et al. (1989) to conclude that isotopic exchange resulted from water-dominated fluid-rock interaction rather than CO_2 decarbonation processes. Gilg (1993) similarly reported $\delta^{18}O$-depleted values in marble and gangue associated with the sulfide orebodies at the Madem Lakkos deposit; however, the mechanism that controlled isotope depletion was not discussed. Hahn (2014) conducted a marble provenance study using carbon and oxygen isotopes collected from the Olympias, Mavres Petres, and Piavitsa areas but an insufficient number of samples (n=7) precluded definitive conclusions. Published carbon and oxygen isotope data from unaltered marbles to the north of the Kassandra Mining District probably accurately represent the isotopic background of Permo-Carboniferous marble in the region. These data are shown as blue diamonds in Figure 4.7A-B and are illustrated by the blue boxes in each subsequent diagram (Varti-Matarangas and Eliopoulos, 2005; Boulvais et al., 2007; Eliopoulos and Kilias, 2011).

Carbon and oxygen isotope composition of marbles and hydrothermal carbonates

The Olympias deposit: Carbon and oxygen stable isotope ratios were determined from marble, stylolites within the hosting marble, coarse-grained carbonate spar associated with replacement sulfide, and late-stage quartz-rhodochrosite vein-breccias (Figure 4.7A-C). The Olympias marble mostly consists of calcite, which exhibits a wide distribution of $\delta^{13}C$ and $\delta^{18}O$ values ranging from 2.37‰ to -6.33‰ and 31.27‰ to 6.12‰, respectively (Figure 4.7A). Stylolites occurring within marble approximately 10 m from known sulfide ore show a restricted range of $\delta^{13}C$ (0.84‰ to 0.26‰) and $\delta^{18}O$ values (28.27‰ to 22.38‰) (Figure 4.7B). Euhedral and coarse-grained carbonate associated with replacement sulfide consists mostly of calcite and rhodochrosite. Calcite $\delta^{13}C$ values range from 2.29‰ to -0.80‰ with $\delta^{18}O$

values spanning 26.74‰ to 2.95‰. Rhodochrosite $\delta^{13}C$ and $\delta^{18}O$ values are similarly depleted, ranging between 1.46‰ to -2.16‰ and 17.49‰ to 10.13‰, respectively (Figure 4.7B). The average $\delta^{18}O$ composition of gangue calcite is more depleted (10.54‰) than rhodochrosite (13.97‰). Rhodochrosite, ferroan calcite, and calcite characterize the carbonate associated with the paragenetically young vein-breccias at the Olympias deposit. Rhodochrosite in veins exhibit a wide range of $\delta^{13}C$ values from 2.64‰ to -1.94‰ with $\delta^{18}O$ values between 16.85‰ to 8.69‰ (Figure 4.7C). The mean $\delta^{18}O$ value (13.66‰) for vein rhodochrosite is broadly similar to the coarse-grained rhodochrosite associated with replacement sulfide. Ferroan calcite veins vary widely with $\delta^{13}C$ values ranging from 2.04‰ to -2.41‰ and $\delta^{18}O$ values spanning 17.71‰ to 4.55‰. A single vein sample composed of calcite yielded a similar $\delta^{13}C$ (0.19‰) and $\delta^{18}O$ (15.56‰) composition.

The Stratoni fault zone: Carbon and oxygen stable isotope compositions were similarly determined from marble and related stylolites, gangue carbonate associated with skarn and replacement sulfide ore, and late-stage quartz-rhodochrosite vein-breccias from the Madem Lakkos and Mavres Petres deposits, and the Piavitsa prospect (Figure 4.7D-F). Marbles within the Stratoni fault zone are predominately composed of calcite with minor ferroan calcite and rhodochrosite (Figure 4.7D). Marble exhibits $\delta^{13}C$ and $\delta^{18}O$ compositions that vary from 3.16‰ to -2.82‰ and 30.50‰ to 3.16‰, respectively. On average, marbles in the Madem Lakkos area have the least depleted $\delta^{18}O$ signature relative to background values whereas the most depleted values occur to the west in the Mavres Petres and Piavitsa areas. Stylolites hosted by marble at the Mavres Petres deposit exhibit a wide range of $\delta^{13}C$ (1.55‰ to -2.03‰) and $\delta^{18}O$ (21.84‰ to 5.86‰) values as shown in Figure 4.7E. Carbonates in skarn and replacement sulfide at the Madem Lakkos and Mavres deposits display a variable mineralogy consisting of calcite, ferroan species of calcite and dolomite, and rhodochrosite. Skarn-related carbonates show a large range of $\delta^{13}C$ values from 0.41‰ to -2.85‰ and a comparatively restricted $\delta^{18}O$ distribution from 15.97‰ to 9.95‰. A similar range of isotopic compositions is shown by carbonate occurring with replacement sulfide ($\delta^{13}C$ = 1.89‰ to -2.49‰ and $\delta^{18}O$ = 17.11‰ to 7.75‰) (Figure

Figure 4.7. Plots of $\delta^{13}C_{VPDB}$ vs. $\delta^{18}O_{VSMOW}$ reported in per mil (‰) for carbonate phases associated with the carbonate replacement deposits from the Kassandra Mining District. Carbonate data is displayed with respect to mineralogy and style of occurrence. The fields for igneous calcite (Bowman, 1998; Hoefs, 2004) and unaltered Rhodope marble (Varti-Matarangas and Eliopoulos, 2005; Boulvais et al., 2007; Eliopoulos and Kilias, 2011) are illustrated on each diagram. Samples from the Olympias deposit: A) marble host-rock; B) gangue carbonate associated replacement sulfide and stylolitic fluid escape structures; C) quartz-rhodochrosite vein-breccias. Samples from the Stratoni fault zone: D) marble host-rock; E) gangue carbonate associated with replacement- and skarn-related sulfide, and stylolitic fluid escape structures from the Madem Lakkos and Mavres Petres deposits; F) quartz-rhodochrosite vein-breccias. Values reported in Gilg (1993) are illustrated by the dotted ellipse.

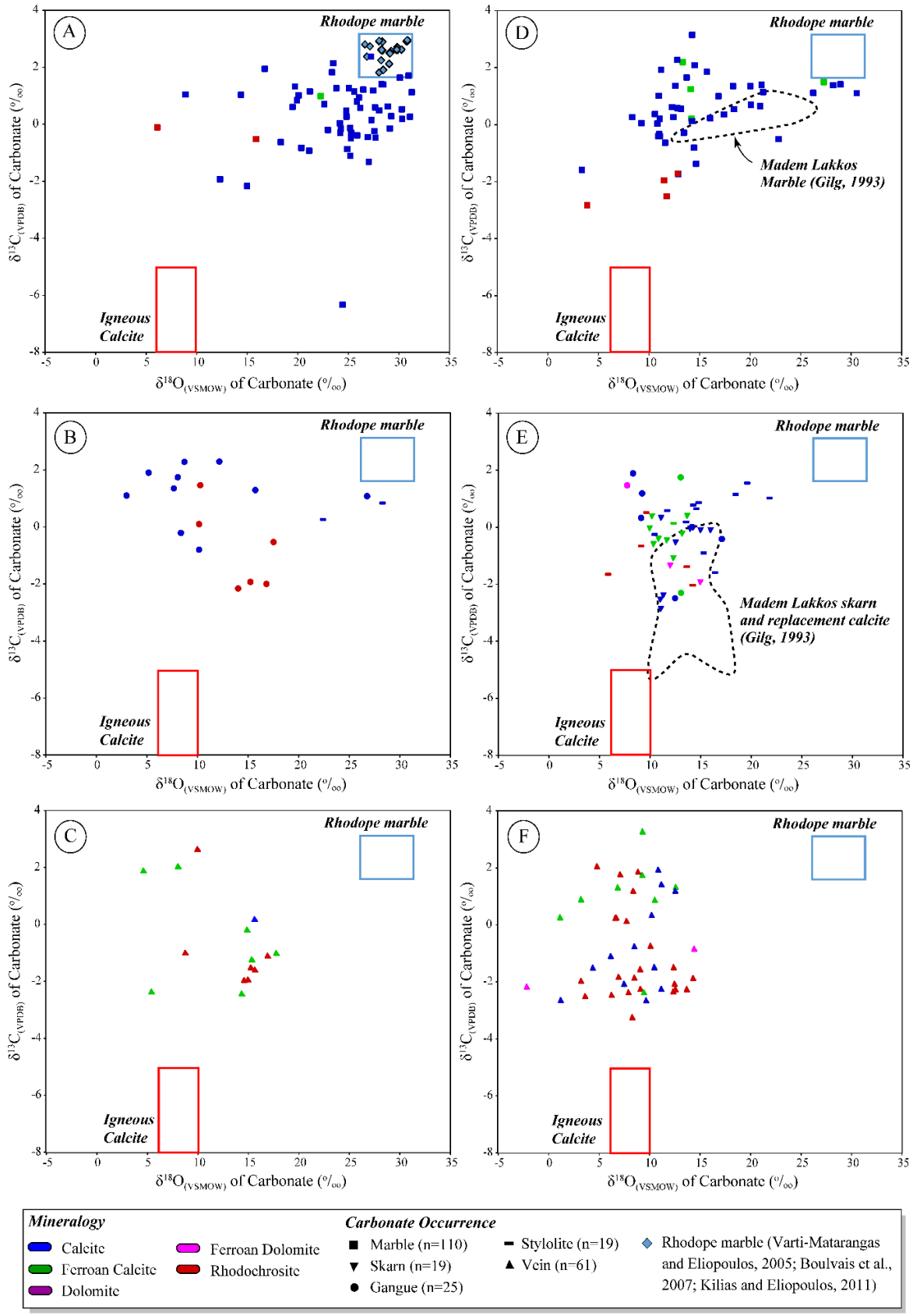
A
Rhodope marble
Igneous Calcite
δ13C(VPDB) of Carbonate (‰)
δ18O(VSMOW) of Carbonate (‰)
D
Rhodope marble
Madem Lakkos Marble (Gilg, 1993)
Igneous Calcite
δ13C(VPDB) of Carbonate (‰)
δ18O(VSMOW) of Carbonate (‰)
B
Rhodope marble
Igneous Calcite
δ13C(VPDB) of Carbonate (‰)
δ18O(VSMOW) of Carbonate (‰)
E
Rhodope marble
Madem Lakkos skarn and replacement calcite (Gilg, 1993)
Igneous Calcite
δ13C(VPDB) of Carbonate (‰)
δ18O(VSMOW) of Carbonate (‰)
C
Rhodope marble
Igneous Calcite
δ13C(VPDB) of Carbonate (‰)
δ18O(VSMOW) of Carbonate (‰)
F
Rhodope marble
Igneous Calcite
δ13C(VPDB) of Carbonate (‰)
δ18O(VSMOW) of Carbonate (‰)
Mineralogy
Calcite
Ferroan Calcite
Dolomite
Ferroan Dolomite
Rhodochrosite
Carbonate Occurrence
Marble (n=110)
Skarn (n=19)
Gangue (n=25)
Stylolite (n=19)
Vein (n=61)
Rhodope marble (Varti-Matarangas and Eliopoulos, 2005; Boulvais et al., 2007; Kilias and Eliopoulos, 2011)

4.7E). Carbonate associated with vein-breccias also display a diverse mineralogy consisting of rhodochrosite and calcite, and including ferroan varieties of calcite and dolomite. Quartz-carbonate vein-breccias exhibit a broad range of $\delta^{13}C$ compositions spanning 3.30‰ to -3.21‰ with isotopically light $\delta^{18}O$ values from 14.40‰ to -6.03‰ (Figure 4.7F).

Lead Isotopes

Lead isotopes can provide important information on the metal source, wallrock or intrusions, and the nature of hydrothermal fluids that resulted in the deposition of sulfide ore (Tosdal et al., 1999). The principal objectives of the Pb isotope study is to determine whether the Pb isotopic compositions of the sulfide orebodies correlate with an igneous intrusion(s) in the district, and whether the Pb isotope composition in the sulfide bodies within the Stratoni fault zone changes with distance from the major intrusive centers, potentially identifying a source of ore fluids. While Pb isotope studies have been conducted previously in the district (Chalkias and Vavelidis, 1989; Mantzos, 1989; Nebel et al., 1991; Frei, 1992, 1995), reevaluation is justified in the context of the revised regional- and deposit-scale geologic framework reported in Siron et al. (2016, 2018). The discussion below is based on previously published data as well as new data from six igneous feldspar samples collected from the late Oligocene Stratoni granodiorite stock, early Miocene porphyry bodies in the Aspro Lakkos area, and the Vathilakkos black-matrix porphyry dike, including ten sulfide samples from the replacement orebodies at the Olympias, Madem Lakkos, and Mavres Petres deposits, and the Piavitsa prospect. Lead isotope data is displayed on conventional uranogenic ($^{207}Pb/^{204}Pb$ vs. $^{206}Pb/^{204}Pb$) and thorogenic ($^{208}Pb/^{204}Pb$ vs. $^{206}Pb/^{204}Pb$) diagrams together with the two-stage Pb evolution curves of Stacey and Kramers (1975), and Chalkias and Vavelidis (1989). The latter is a plumbo-tectonics model that describes the evolution of Pb specific to north Aegean crust. Results described hereafter will be in reference to the latter model curve. Analytical methodology, sample locations, and Pb isotope data are presented in the Appendix.

Previous studies

Previous work in the Kassandra Mining District has contributed a wealth of Pb isotope data from the sulfide orebodies, sulfide associated with the Skouries deposit, and feldspar Pb from the Oligo-Miocene igneous suites and the metamorphic basement units. This comprehensive database permits interpretation of potential source reservoirs for Pb. Frei (1992) determined the Pb isotope composition of the Vertiskos and Kerdilion units in the Skouries and Olympias areas, respectively, based on plagioclase and whole-rock analyses. Analyses from the amphibolite body outcropping south of the Stratoni fault zone were also reported (Figure 4.2). These data are plotted as stippled fields in the uranogenic and thorogenic diagrams in Figure 4.8A-D. Lead isotope compositions of the Kerdilion unit and the amphibolite body define two broad overlapping fields that lie mostly below the average north Aegean crustal growth curve, while the Vertiskos unit mostly plots above this curve, but notably overlaps both the Kerdilion and amphibolite fields where they converge (Figure 4.8A-D).

Frei (1992) also determined igneous Pb isotope ratios from the late Oligocene and early Miocene intrusive suites from plagioclase, K-feldspar, and whole-rock analyses. Lead isotope values plot on both sides of the crustal growth curve in the uranogenic diagram reflecting U/Pb values similar to the average north Aegean crust. However, the thorogenic diagram indicates that Oligo-Miocene magmas in the district have higher Th/U values with respect to north Aegean crust. Lead isotope data from the Stratoni granodiorite stock plot in the field that defines the Kerdilion unit (Figure 4.8A-B), whereas the monzodiorite and granodiorite bodies in the Tsikara and Fisoka areas mostly plot in the field of overlapping metamorphic basement units. Analyses from the early Miocene igneous suite, which includes the Skouries and Aspro Lakkos porphyry stocks, the black-matrix porphyry dikes that occur in the Aspro Lakkos and Tsikara areas, as well as the black-matrix porphyry dike contained within the Vathilakkos fault, displays a restricted range of Pb isotope values that plot in the field that defines the Vertiskos unit (Figure 4.8A-B).

Figure 4.8. Lead isotope data displayed on conventional $^{207}Pb/^{204}Pb$ vs. $^{206}Pb/^{204}Pb$ (uranogenic) and $^{208}Pb/^{204}Pb$ vs. $^{206}Pb/^{204}Pb$ (thorogenic) diagrams. The two-stage crustal Pb evolution curves of Stacey and Kramers (1975) and Chalkias and Vavelidis (1989) are shown for reference and indicated by S/K and C/V, respectively. The stippled fields corresponding to Pb isotope compositions of the metamorphic basement units are adapted from Frei (1992): A-B) lead isotope values of Oligo-Miocene igneous rocks from this study are displayed as squares on the uranogenic (top) and thorogenic (bottom) diagrams with data from Frei (1992) displayed as circles; C-D) lead isotope compositions of galena and pyrite from the carbonate replacement deposits from this study are displayed in red on the uranogenic (top) and thorogenic (bottom) diagrams with published data shown as white polygons (Chalkias and Vavelidis, 1989; Nebel, 1989; Kalogeropoulos et al., 1989). Early Miocene and late Oligocene igneous rocks are represented by dashed and solid ellipses, respectively.

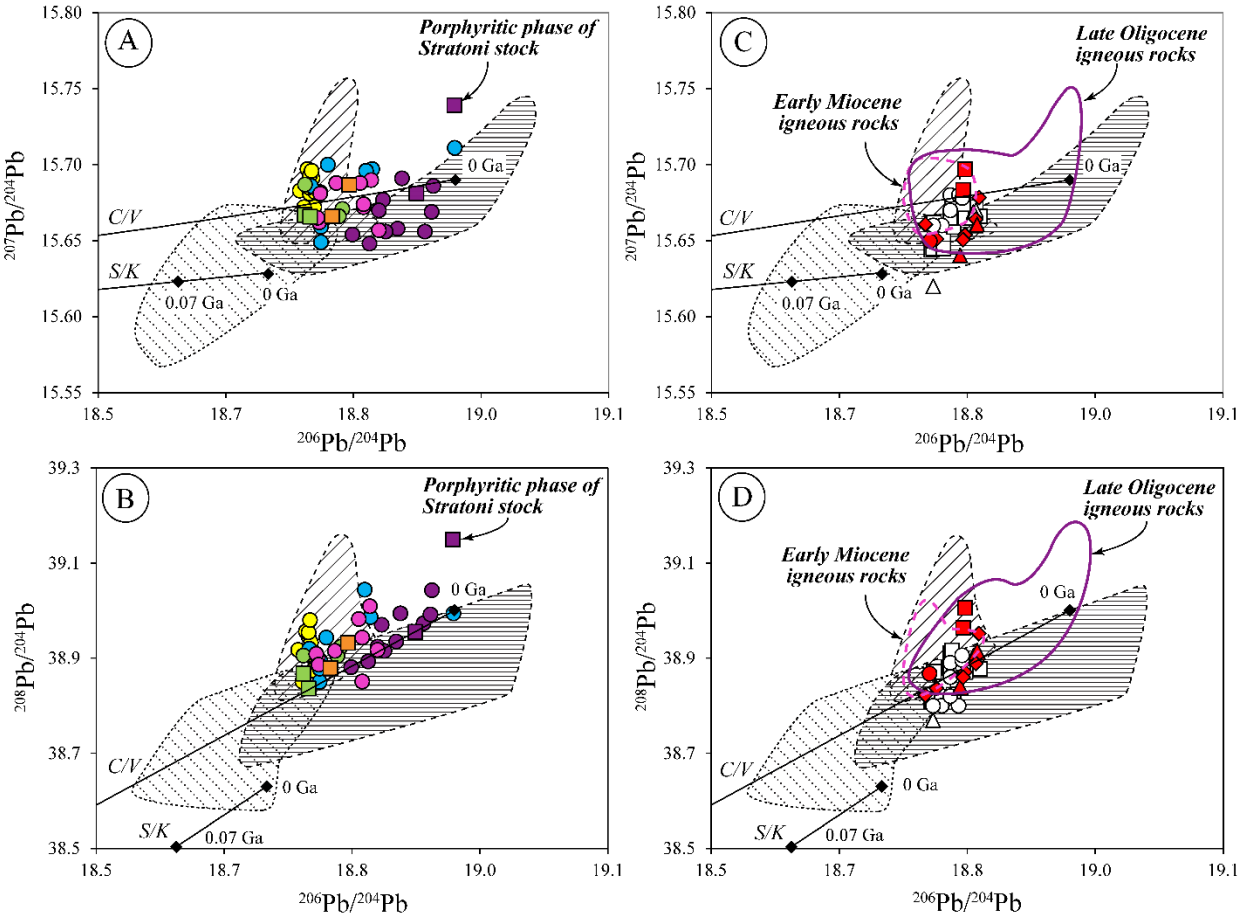

Igneous Rocks: K-feldspar
(Legend for Fig. 4A-B)

- ○ Published data (Frei, 1992; Nebel, 1989)
- □ This study

Early Miocene porphyry stocks and dikes

- Vathilakkos black-matrix porphyry dike
- Aspro Lakkos porphyry stock & black-matrix porphyry dike
- Skouries quartz monzonite porphyry stock, megacrystic K-feldspar porphyry dike

Late Oligocene stocks and dikes

- Fisoka granodiorite-diorite stock and adjacent porphyry dikes
- Stratoni granodiorite stock
- Tsikara monzodiorite

Metamorphic Basement Rocks (Frei, 1992, 1995)

- Biotite and amphibole-bearing biotite gneiss from the Skouries and Aspro Lakkos areas (Vertiskos Unit)
- Amphibolite from the Gomati and Stratoni mafic and ultramafic bodies
- Biotite gneiss and amphibolite from the Olympias and Madem Lakkos areas (Kerdilion Unit)

Sulfide: galena and pyrite
(Legend for Fig. 4C-D)

- ○ Published data (open polygons: Chalkias and Vavelidis, 1989; Nebel, 1989; Kalogeropoulos et al., 1989)

This study

- ■ Madem Lakkos skarn (pyrite)
- ▲ Mavres Petres massive sulfide (galena)
- ● Olympias massive sulfide (galena)
- ◆ Piavitsa semi-massive sulfide (galena and pyrite)

Sulfide Pb isotope compositions of galena were previously reported for the Olympias, Madem Lakkos, and Mavres Petres deposits (Chalkias and Vavelidis, 1989; Kalogeropoulos et al., 1989; Nebel, 1989; Nebel et al., 1991). These data show a restricted range in the uranogenic and thorogenic diagrams, largely correlating with the field defined by overlapping metamorphic basement unit (Figure 4.8C-D). Lead from the sulfide orebodies is isotopically uniform and similar to the igneous feldspar and whole-rock Pb isotope compositions that characterize the Oligo-Miocene igneous rocks within the district (Figure 4.8C-D).

Lead isotope compositions of igneous feldspars and sulfide minerals

Igneous feldspars: Primary K-feldspar phenocrysts from two samples of the late Oligocene Stratoni stock were analyzed for their Pb isotope composition. These samples correspond to zircon U-Pb ages of 25.4 ± 0.2 Ma from the main equigranular granodiorite body and 24.5 ± 0.3 Ma for a porphyritic granodiorite phase located at the northern and topographically highest portion of the intrusive stock (Figure 4.2; Siron et al., 2016). The Pb isotope composition of the equigranular granodiorite phase agrees with previously published results from the Stratoni stock (Frei, 1992). The porphyritic granodiorite phase, however, plots well above the north Aegean crustal growth curve and other Pb isotope values from the Stratoni stock (Figure 4.8A-B) indicating that the porphyritic phase is distinct from the equigranular granodiorite and the Kerdilion unit.

Lead isotope values were also obtained from three early Miocene porphyry samples previously dated by zircon U-Pb methods (Siron et al., 2016). Primary K-feldspar phenocrysts were analyzed from the 19.7 ± 0.1 Ma megacrystic K-feldspar porphyry stock and a crosscutting 19.6 ± 0.1 Ma black-matrix porphyry dike in the Aspro Lakkos area, and the 19.2 ± 0.2 Ma black-matrix porphyry dike hosted by the Vathilakkos fault (Figure 4.2). Lead isotope compositions cluster within the field of overlapping metamorphic basement units (Figure 4.8A-B). This tight distribution of data is broadly consistent with

previously published Pb isotope values from the Skouries porphyry, including trachyte and andesite porphyry dikes peripheral to the Skouries stock and elsewhere in the district (Frei, 1992, 1995).

Sulfide minerals: Lead isotope analyses from galena associated with skarn in the Madem Lakkos deposit plot above the north Aegean crustal growth curve and correspond to the field of the Vertiskos unit, albeit hosted by Kerdilion marbles (Figure 4.8C-D). Skarn-related sulfide contains more radiogenic Pb than the carbonate replacement sulfide. Galena and pyrite from massive sulfide at the Mavres Petres deposit and the Piavitsa prospect are isotopically similar and occur within the field of overlapping metamorphic basement units, and the late Oligocene and early Miocene igneous rocks (Figure 4.8C-D). Lead from galena within the replacement sulfide ore at the Olympias deposit is isotopically similar to the Pb contained in the sulfide from the Stratoni fault zone (Figure 4.8C-D). Boulangerite from a quartz-rhodochrosite vein at the Piavitsa prospect was analyzed to characterize the Pb associated with the late-stage of mineralization. While the Pb isotope composition is coincident with the results from the massive sulfide data, large analytical errors preclude interpretation and it was therefore omitted.

Discussion

District-scale metal zonation as a vector for hydrothermal fluid flow and metal deposition

Distinct mineralogical and metal zonation patterns are evident in the deposits and between the zones of mineralization along the Stratoni fault zone. The southeastern part of the Madem Lakkos deposit is characterized by chalcopyrite-scheelite-bearing skarn spatially associated with aplitic sills. Subordinate skarn development in the gneisses adjacent to the Stratoni granodiorite could indicate that the fluids responsible for the Madem Lakkos skarn body were derived from the east (Figure 4.2). Cubanite-chalcopyrite exsolution textures and abundant magnetite in the southeastern portion of the Madem Lakkos orebody was interpreted by Nicolaou (1964) as a high temperature zone, possibly resulting from a blind intrusive source at depth or the Fisoka stock to the south (Figure 4.2). While Cu is clearly present in the skarn bodies at Madem Lakkos, assays of skarn intersected in historic drilling do not include Cu. Gilg

(1993) reported 0.89% Cu in a drill hole that intercepted skarn, and thus it is likely that Cu was either not systematically assayed, or if obtained, Cu assays were not transferred from the paper logs to the digital database. Skarn reported in the historic database, however, yielded an average Au grade of 0.28 g/t, indicating that the skarn bodies are relatively Au poor compared to replacement mineralization in the district. The mineralized skarn ore also contains minor concentrations of Pb and Zn (0.82% combined) of about equal proportion.

The transition from skarn into sphalerite-galena and pyrrhotite-bearing, pyrite-rich replacement massive sulfide bodies resembles the zonation sequence developed in many carbonate replacement deposits in northern Mexico (Megaw et al., 1988). Pyrrhotite may indicate higher temperatures and a more reduced environment (e.g., Hemley, and Hunt, 1992), consistent with fluid inclusion evidence from Madem Lakkos (Gilg, 1993). Replacement sulfide in the Madem Lakkos deposit contains up to 0.6% Cu, the highest values in the replacement sulfide orebodies within the Stratoni fault zone (Figure 4.9A). Copper mostly occurs in chalcopyrite, as individual grains or as inclusions in sphalerite and pyrite, but also in tetrahedrite-tennantite (Nicolaou, 1964) which commonly form inclusions within galena, as well as bournonite and enargite (Gilg, 1993) also contributing to the elevated Cu grades in the Madem Lakkos deposit. In general, Cu diminishes toward the west (Figure 4.9A) corresponding to lower Cu/Pb and Cu/Zn ratios (Table 4.1). Both Pb and Zn concentrations increase at the Mavres Petres deposit but the lower Pb/Zn ratio relative to the Madem Lakkos sulfide ore indicates increased precipitation of Zn to the west. This pattern, however, conflicts with observed metal zonation patterns developed in other intrusion-related carbonate-hosted replacement deposits (Megaw, 1990; Vikre, 1998).

The Madem Lakkos massive sulfide averages 1.27 g/t Au, almost an order of magnitude higher than skarn-related sulfide. Gold markedly increases to the west, with the highest grades within the Stratoni fault zone occurring at the Mavres Petres deposit (Figure 4.9B). Many carbonate replacement deposits display elevated Au concentrations in proximity to mineral-related intrusions. In the Leadville district of Colorado, the highest Au grades in the replacement sulfide orebodies (>6.8 g/t) occur adjacent

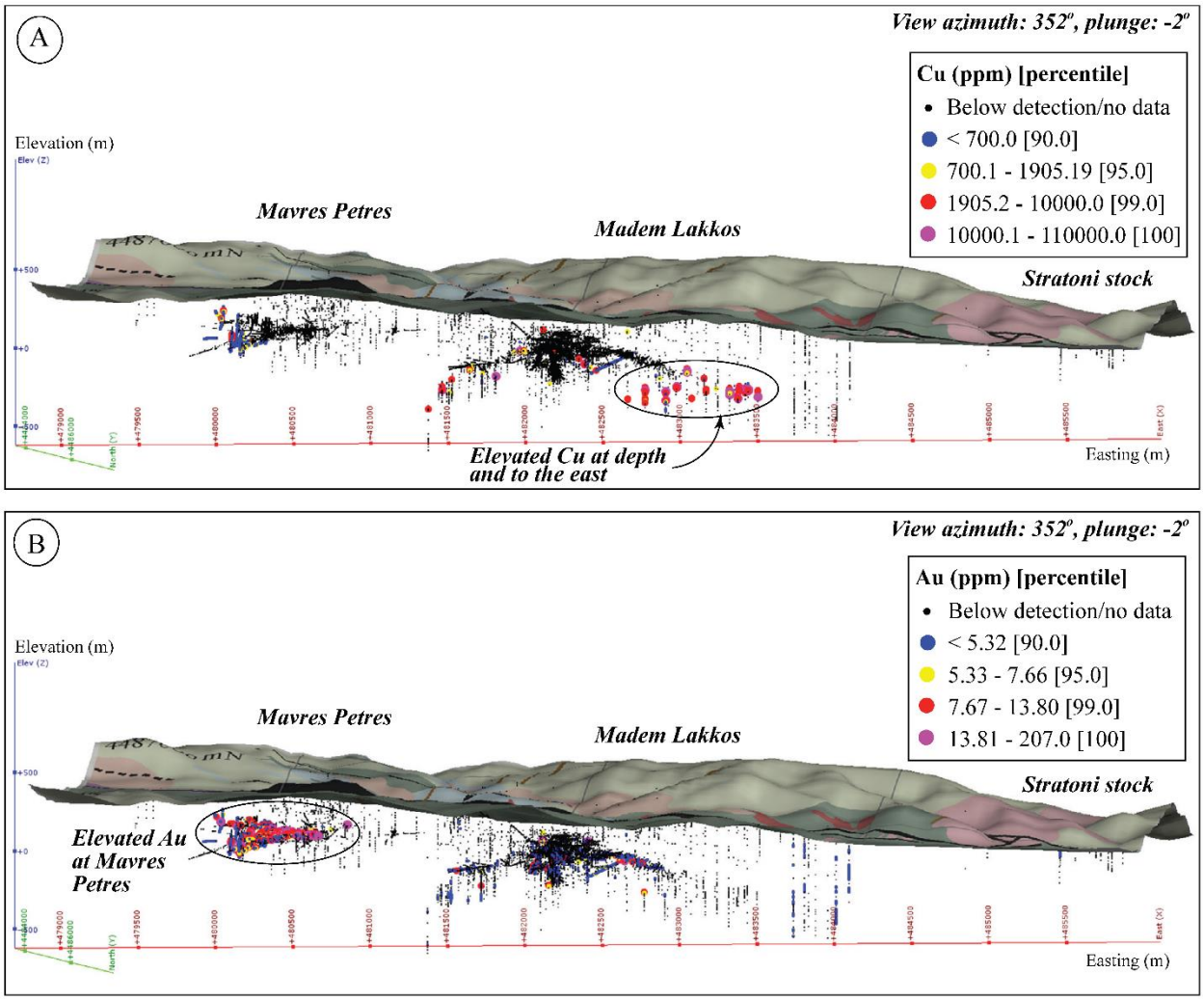

Figure 4.9. Longitudinal view of the Stratoni fault zone displaying drill core geochemical assay data from the Madem Lakkos and Mavres Petres deposits and surrounding area, and illustrating the distribution of (A) Cu values and (B) Au values in parts per million (ppm) for data greater than the 90th percentile.

the Breece Hill stock and in contact with faults that intersect the igneous body at depth (Thompson and Arehart, 1990). However, Au may be enriched in the distal environment such as in the Bingham district of Utah where disseminated Au hosted by carbonate rocks occur at Barneys Canyon, approximately 7.5 km from the Bingham stock (Cunningham et al., 2004). The Mavres Petres deposit occurs more than 2–3 km from the late Oligocene Stratoni and Fisoka stocks (Figure 4.2), and the aplitic dikes and sills that are spatially associated with the sulfide ore at Madem Lakkos were not observed at the Mavres Petres deposit. While early Miocene glomerophyric porphyry dikes occur in the area, these are interpreted to

postdate the sulfide orebody (Siron et al., 2016). The Au- (As, Ag, Sb) enriched sulfide bodies at the Mavres Petres deposit, therefore, either resulted from the efficient transport of Au in hydrothermal solution westward along the Stratoni fault zone, or hydrothermal fluids may have been channelized directly from a nearby source intrusion at depth.

Silver and Mn grades generally increase toward the periphery of many intrusion-related carbonate replacement systems (Megaw, 1998). In the Leadville district, Thompson and Arehart (1990) showed a rise in Ag with a corresponding decrease in Au grade with increasing distance from the Breece Hill stock. The Mavres Petres deposit exhibits a modest increase in Ag with markedly higher Au grades, which corresponds to a lower Ag/Au ratio than at the Madem Lakkos deposit (Table 4.1). Silver also correlates with Pb at both Madem Lakkos ($r = 0.84$) and Mavres Petres ($r = 0.94$); thus, higher galena concentrations corresponds to higher Ag grades. Silicified Mn-rich gossans that outcrop above the Mavres Petres deposit and to the west in the Piavitsa area are the surface equivalent of quartz-rhodochrosite ± rhodonite replacement bodies at depth, and are representative of the vertical and lateral expression of the carbonate replacement system within the Stratoni fault zone. An analogous relationship of Mn-rich alteration outboard from the sulfide replacement orebodies is documented in the Tintic district of Utah (Morris and Lovering, 1979) and the Santa Eulalia camp of northern Mexico (Megaw et al., 1988). Manganese is rarely reported in the historic assays, particularly at the Madem Lakkos deposit. Consequently, outside of mineralogical observations, the drill core data is insufficient to define a zonal geochemical pattern for Mn within the Stratoni fault zone.

Deposit-scale metal zonation patterns are also evident at the Olympias deposit. The sulfides lenses that occur on the eastern portion of the deposit in association with the East fault display the highest Cu values (Figure 4.10A), and correspondingly high Cu/Pb and Cu/Zn ratios (Table 4.1). Anomalously high W and Mo also occurs in the east and, along with elevated Cu, may indicate proximity to an

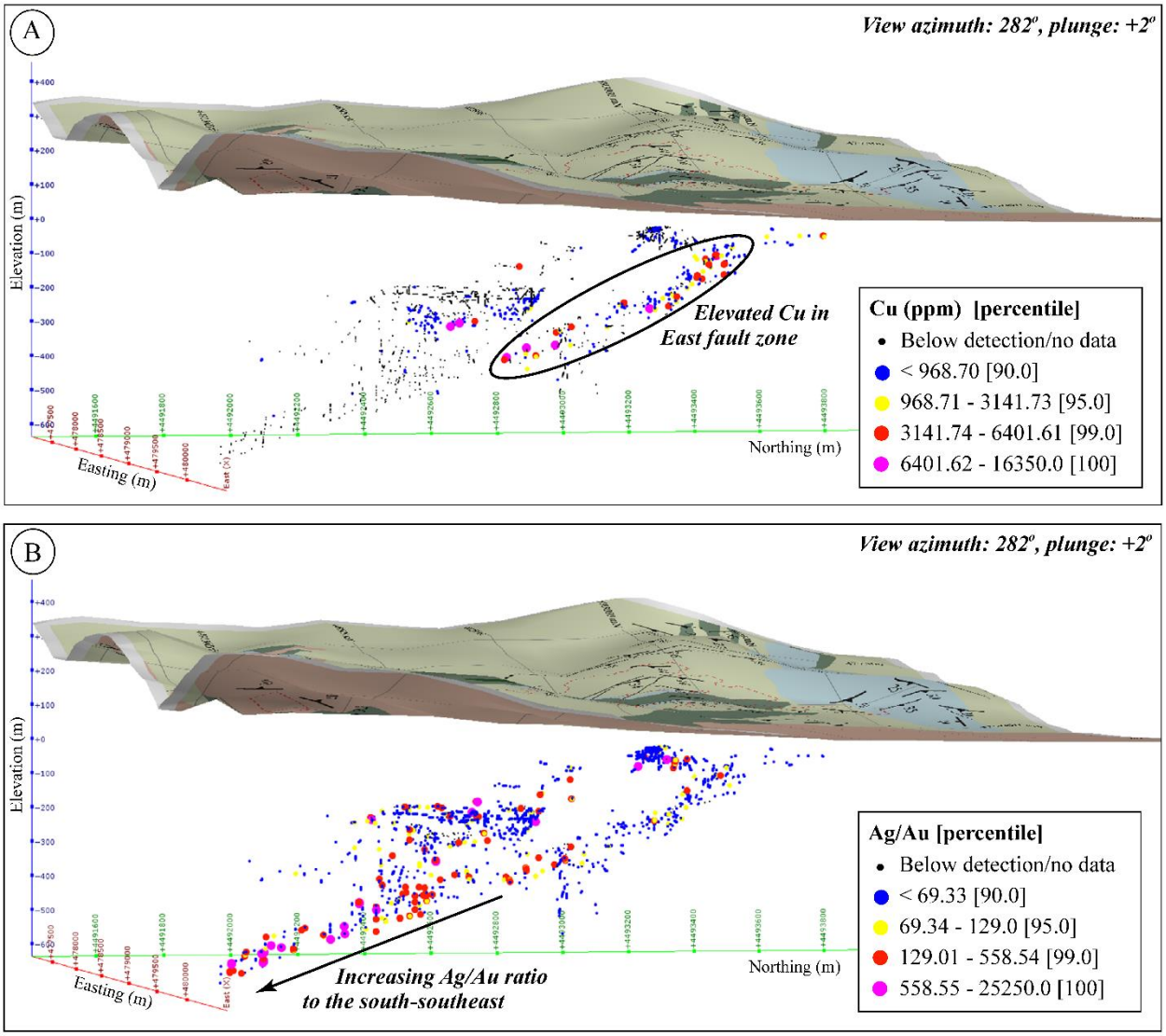

Figure 4.10. Oblique, cross-sectional view of the Kassandra and East fault zones displaying drill core geochemical assay data from the Olympias deposit illustrating (A) Cu values in parts per million (ppm) and (B) Ag/Au ratios for data greater than the 90th percentile.

intrusive source. In general, the sulfide bodies at Olympias are enriched in Au with the highest values focused along the Kassandra and East faults in the upper parts of the deposit. Silver and the Ag/Au ratio increases with depth to the south-southeast (Figure 4.10B), suggesting that the down-plunge extent of the Olympias orebody may be more distal from the hydrothermal fluid source. Manganese is elevated at shallow depths in the north and at the western, up-dip portion of the Kassandra fault; however, this may reflect supergene enrichment as a result of near-surface oxidation. Deposit-scale metal zonation patterns

including elevated Cu-W-Mo in the east, homogenization temperatures exceeding 350ºC, and the presence of syn-mineral granitic breccia dikes, all suggest that the Olympias orebody may have formed relatively close to an intrusive source, potentially located at depth and to the east of known mineralization.

The down-plunge and distal extent of the Olympias orebody inferred by the metal distribution patterns is intriguing since it seems rather unlikely that buoyant hydrothermal fluids would migrate in a downward direction. Two mechanisms that may result in this pattern are considered here. First, is that the Olympias deposit is tilted resulting from either deposit- or regional-scale fault block rotation. While the structural study of the Olympias orebody (Siron et al., 2018) did not identify fault-related block rotation on the deposit-scale, it may be likely that regional-scale tectonic rotation of the Kerdilion unit has occurred since ore formation. The second is a forced convective flow model where hydrothermal fluid is circulating within a confined lithologic horizon in the presence of a steep geothermal gradient resulting in the forced downward migration of a fluid within a dipping layer (e.g., Cambarnous and Bories, 1975; Cathles, 1997). While both scenarios are plausible, further work is required in identifying the controlling mechanism that resulted in this unusual zonation pattern.

Constraints on pressure, temperature, and depth of deposit formation

Microthermometric data reveal a broad zonation pattern from east to west within the deposits hosted by the Stratoni fault zone. Published fluid inclusion data from the Madem Lakkos deposit (Gilg, 1993) revealed decreasing temperatures from ~450ºC with deposition of early skarn and replacement massive sulfide to less than 278ºC for retrograde skarn and 250ºC for the late quartz-rich, disseminated sulfide event. Due to inadequate fluid inclusions, the physiochemical conditions of early replacement sulfide at the Mavres Petres deposit was not determined, and therefore requires further study. The results of this study, however, show relatively low temperatures for the open-space, boulangerite-bearing quartz-rich sulfide phase at the Mavres Petres deposit (~216ºC) suggesting decreasing thermal conditions with

time and toward the west. The Au-bearing base metal-rich quartz-carbonate veins in the Piavitsa area probably belong to the early replacement sulfide phase as inferred from mineralogical similarities and elevated homogenization temperatures, whereas the lower temperature boulangerite-bearing quartz-rhodochrosite veins are similar in texture and mineralogy to the later quartz-rich sulfide phase.

Structural data, relative timing relationships, and geochronological data reported in Siron et al. (2018) showed that replacement sulfide mineralization was coeval with the transition from ductile to semi-brittle north-south extension, while a later period of east-west extension and brittle faulting controlled the emplacement of boulangerite-bearing quartz-rich sulfide and quartz-rhodochrosite vein-breccias. This change in deformation style, contemporaneous with magmatism and hydrothermal fluid flow within the Kassandra and Stratoni fault zones, likely corresponded to a shift from lithostatic to a fluid-dominated hydrostatic pressure regime (e.g., Hedenquist and Arribas, 1997). The fluid inclusion data presented here, combined with the structural evidence shown in Siron et al. (2018), support this mechanism to explain the presence of an immiscible fluid phase at the Madem Lakkos and Olympias deposits. Within the Stratoni fault zone, the documented decrease in fluid inclusion homogenization temperatures from east to west, together with the metal zonation patterns shown above, reinforce the hypothesis of broad-scale hydrothermal fluid flow originating in the east.

At the Madem Lakkos deposit, Gilg (1993) documented CO_2-rich fluid inclusions that homogenized to the liquid and vapor phase, with a coexisting population of highly saline H_2O-rich inclusions containing upwards of 45 weight percent NaCl equivalent. This relationship was previously interpreted to reflect fluid immiscibility resulting from the unmixing of a CO_2-rich parent fluid either by decarbonation reactions or due to a pressure drop in response to boiling. Unmixing of a homogenous fluid as a result of decarbonation is not supported by carbon-oxygen stable isotope models discussed later, and while boiling can result in phase separation, gangue minerals associated the sulfide ore lack the textural evidence for boiling during replacement mineralization (e.g., colloform quartz, adularia, and bladed calcite; Simmons and Browne, 2000; Moncada et al., 2017). The younger quartz-rich sulfide ore and

quartz-rhodochrosite vein-breccias at the Mavres Petres deposit and Piavitsa prospect similarly lack the mineral textures and fluid inclusion evidence necessary to suggest boiling as a mechanism for sulfide deposition. The high salinity fluid inclusions at the Madem Lakkos deposit may therefore reflect one end-member of an immiscible magmatic fluid that was trapped close to its source, and CO_2 may have originated from a magmatic fluid, however, marble is more likely source (Ohmoto and Rye, 1979).

Coexisting H_2O-CO_2, and low-salinity fluid inclusions associated with the quartz-rich sulfide phase at the Olympias deposit similarly indicate fluid phase separation, but lack the mineralogical, textural, and fluid inclusion evidence for boiling. The cluster of H_2O-CO_2 fluid inclusions described in this study exhibit bimodal homogenization behavior, where fluid inclusions homogenize to the liquid phase and by vapor expansion, thus providing empirical evidence for a trapped immiscible fluid. Because this assemblage of fluid inclusions trapped an immiscible fluid, the total homogenization temperature and pressure are interpreted to represent the trapping conditions (Roedder, 1984). An estimated trapping pressure of less than 400 bars was determined by fitting the average homogenization temperature to the P-*X* diagram for coexisting liquid and gas phases in the system H_2O-CO_2 (Figure 4.11; Takenouchi and Kennedy, 1964; Roedder, 1979). This result is consistent with pressure estimates reported in previous studies from the Olympias deposit (Kilias and Kalogeropoulos, 1989; Kilias and Madsen, 1994; Kilias et al., 1996).

The lack of evidence for boiling and an independent geothermometer precluded an empirical determination of the trapping conditions (pressure and temperature) for the fluid inclusions from the Mavres Petres deposit. Nevertheless, an estimated depth of formation was calculated based on fluid inclusion properties in the system H_2O-NaCl (Roedder and Bodnar, 1980), assuming an average salinity of 4 weight percent NaCl and a trapping temperature of 242^{o}C, which is 1σ or approximately 26^{o}C above the average homogenization temperature (Figure 4.12). Under these conditions, the estimated trapping pressure would have been 419 bars, corresponding to a depth of about 4.3 km at hydrostatic conditions (Figure 4.12). The pressure estimates made for the Mavres Petres and Olympias deposits suggest that the

depth of carbonate replacement mineralization was broadly equivalent across the district. Fluid inclusions associated with the quartz-rich sulfide phase at the Olympias deposit, however, contain CO_2 and homogenized at higher temperatures compared to those at Mavres Petres, suggesting that the Olympias sulfide orebodies may have formed closer to a source intrusion and in the presence of an immiscible fluid.

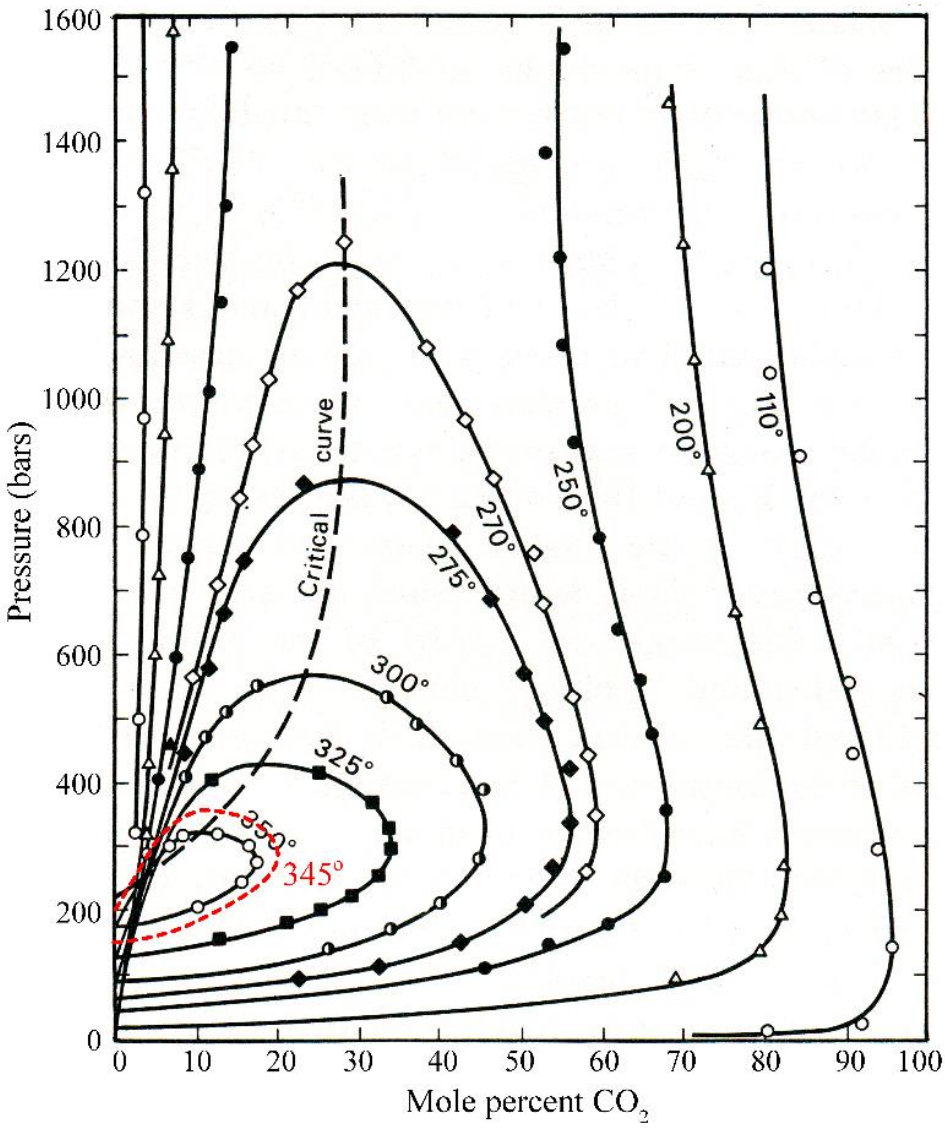

Figure 4.11. Pressure-composition (P-*X*) diagram depicting experimental data on the composition of coexisting gas and liquid phases in the system H_2O-CO_2, modified after Takenouchi and Kennedy (1964) and Roedder (1979). Isotherms are shown by solid black lines with the critical curve represented as a dashed line. The total homogenization temperature of the H_2O-CO_2 fluid inclusion array from the Olympias deposit is illustrated as the red dashed line.

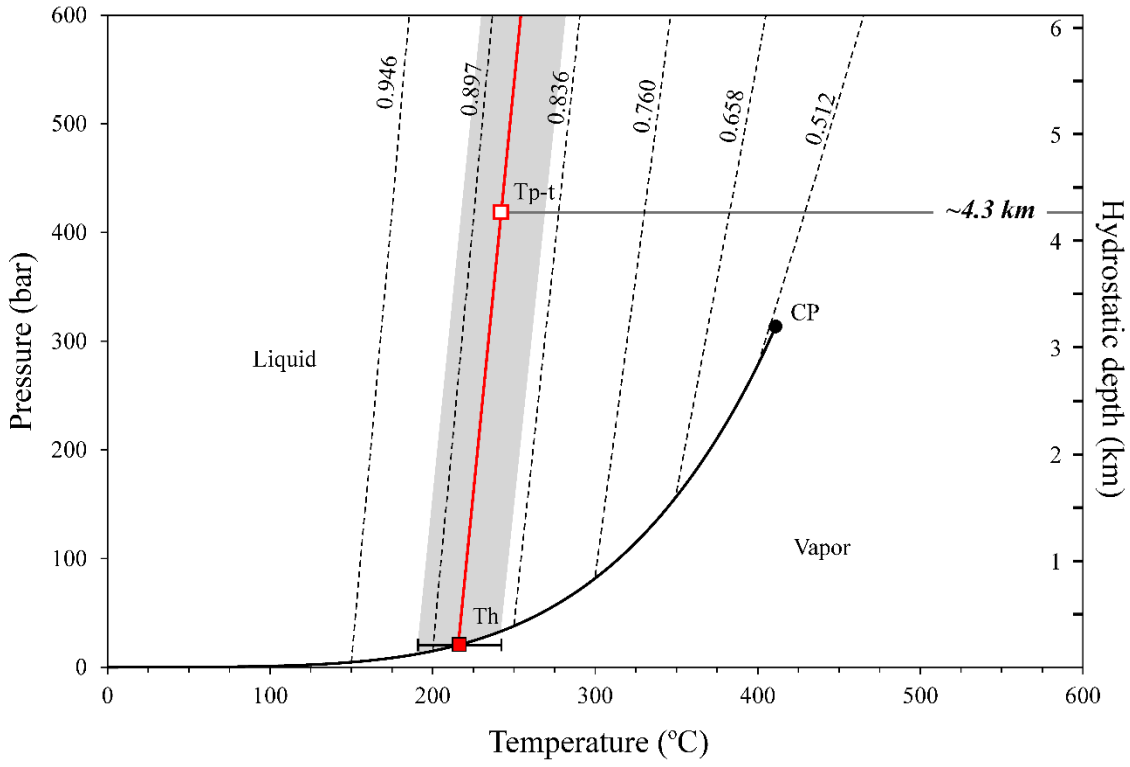

Figure 4.12. Phase diagram for water showing liquid-vapor curves for a water solution containing 4 weight percent NaCl (bold dashed line) with critical point indicated by CP. Selected isochores with labeled densities (g/cm^3) are shown as dashed lines and were calculated using the SoWat program of Driesner (2007). The depth scale corresponds to hydrostatic pressures. The average homogenization temperature (Th) for the quartz-rich sulfide phase at the Mavres Petres deposit is plotted at the 1σ uncertainty represented by error bars and shaded area. The theoretical trapping pressure and temperature (Tp-t) used for the estimated depth calculation is shown as an open box located along the 0.882 g/cm^3 isochore highlighted in red. The approximate depth of ore formation is show at ~4.3 km.

Source of fluids and fluid evolution during ore formation

Carbonate $\delta^{13}C$ and $\delta^{18}O$ isotope and quartz fluid inclusion data permit the modeling of isotopic exchange and fluid mixing processes that occurred during hydrothermal alteration and sulfide deposition. Model curves were calculated using published mass balance equations and fractionation factors for calcite (see Appendix), and are constrained by fluid inclusion total homogenization temperatures from this study and previously published data (Gilg, 1993; Kilias et al., 1996). The models assume an initial marble composition of $\delta^{13}C$ = 2‰ and $\delta^{18}O$ = 31‰, consistent with the range of local unaltered marble and published data from Mount Pangeon and Thassos Island to the north of the Kassandra Mining District

(Varti-Matarangas and Eliopoulos, 2005; Boulvais et al., 2007; Eliopoulos and Kilias, 2011). The models also assume involvement of fluids with magmatic ($\delta^{13}C$ = -7‰ and $\delta^{18}O$ = 6‰) and meteoric ($\delta^{13}C$ = -6‰ and $\delta^{18}O$ = -5‰) compositions.

Isotopic depletion patterns that characterize the Olympias marble (Figure 4.13A) can be interpreted through decarbonation reactions and exchange by means of fluid-rock interaction involving a magmatic fluid at 350ºC. The single-stage (batch) decarbonation curve overlaps with a small cluster of the data, but this exchange process does not produce the necessary $\delta^{13}C$ and $\delta^{18}O$ depletion patterns to explain the distribution of the data. Rayleigh decarbonation, however, may describe the depletion trend on the right-hand side of Figure 4.13A with the extremely $\delta^{13}C$-depleted value either explained by Rayleigh decarbonation at <200ºC or by isotopic exchange with graphite. This is reasonable given the presence of crystalline graphite within the marbles at the Olympias deposit. Coupled $\delta^{13}C$-$\delta^{18}O$ depletion trends within the Olympias marble are largely attributed to fluid-rock interaction, consistent with the interpretations of Kalogeropoulos et al. (1989). The majority of the data plots between the 0.5–0.1X_{CO2} curves indicating that isotopic exchange occurred in the presence of a fluid with relatively high dissolved CO_2 contents. Dispersion of the data along the 0.01X_{CO2} curve, however, could reflect exchange with a carbon-poor fluid, possibly of meteoric origin. Larger $\delta^{13}C$-$\delta^{18}O$ depletion trends correspond to an increase in the water-rock ratio with decreasing CO_2 concentrations (Figure 4.13A). This depletion pattern may be explained by isotopic exchange between marble and a magmatic fluid.

Marbles within the Stratoni fault zone show increasingly depleted $\delta^{13}C$-$\delta^{18}O$ values from east to west. This may reflect fluid-rock interaction principally involving a magmatic fluid at 350ºC (Figure 4.13B). Marbles sampled from drill core at the Madem Lakkos deposit mostly exhibit heavy $\delta^{18}O$ values with data scattering between the 0.2–0.05X_{CO2} curves. This indicates that isotopic exchange was influenced by a fluid with relatively low CO_2 concentrations as compared to the Olympias deposit. The depleted $\delta^{13}C$-$\delta^{18}O$ trend exhibited by marbles in the Mavres Petres and Piavitsa areas is also best

explained by fluid-rock interaction, likely from a fluid of magmatic composition containing $0.1X_{CO2}$ and $0.01X_{CO2}$, respectively (Figure 4.13B). Enriched $\delta^{13}C$ in a sample of marble from the Piavitsa area may reflect isotopic exchange at lower temperatures (e.g., Ohmoto and Rye, 1979). Increased isotopic depletion of marble from east to west may reflect increasing water-rock ratios with decreasing CO_2 concentration from a factor of ~10 at $0.05X_{CO2}$ in the Mavres Petres area to values exceeding 25 at $0.01X_{CO2}$ in the Piavitsa area. Two marble samples from the Mavres Petres deposit, highlighted on the right-hand-side of Figure 4.13B, record highly depleted $\delta^{18}O$ values possibly indicating that magmatic fluid mixed with isotopically light $\delta^{13}C$ and $\delta^{18}O$ fluid, possibly derived from meteoric water.

Gangue carbonate associated with sulfide ore at the Olympias deposit shows a variable isotopic distribution. Data that plots near the shaded region on Figure 4.13C likely precipitated from a magmatic fluid with low CO_2 concentration ($0.1X_{CO2}$) at temperatures between 350–200ºC, consistent with fluid inclusion data. Carbonates showing slightly more depleted values may be explained by the involvement of a magmatic fluid at 350ºC but with a lower dissolved CO_2 concentration ($0.01X_{CO2}$). Gangue carbonate characterized by depleted $\delta^{18}O$ with no $\delta^{13}C$ modification relative to background marble, could have been produced by a carbon-poor fluid at 350ºC (Figure 4.13C). This pattern, however, requires input of an isotopically light $\delta^{18}O$ source that was probably derived from meteoric water. The isotopic composition of carbonate associated with skarn and replacement sulfide from the Madem Lakkos and Mavres Petres deposits is similarly explained by the interaction of marble with a magmatic fluid at 450–200ºC, low dissolved CO_2 concentration ($0.01X_{CO2}$), and high water-rock ratios (Figure 4.13D). The $\delta^{13}C$ and $\delta^{18}O$ signature of stylolites in marble overlap with gangue carbonate (Figure 4.13D) indicating that the mineralizing fluids not only utilized major strands of the Stratoni fault but also infiltrated marble along pressure solution seams.

Crustiform-textured, quartz-rhodochrosite vein-breccias from the Olympias deposit mostly plot within the shaded field defined by a magmatic fluid at 300–200ºC and low CO_2 concentrations

Figure 4.13. Plot of $\delta^{13}C_{VPDB}$ vs. $\delta^{18}O_{VSMOW}$ reported in per mil (‰) for carbonate phases associated with the carbonate replacement deposits from the Kassandra Mining District. Note that the carbonate data in this image is displayed with respect to location (color) and style of occurrence (shape). The fields for igneous calcite (Bowman, 1998; Hoefs, 2004) and unaltered Rhodope marble (Varti-Matarangas and Eliopoulos, 2005; Boulvais et al., 2007; Eliopoulos and Kilias, 2011) are illustrated on each diagram along with a series of $\delta^{13}C$- $\delta^{18}O_{calcite}$ evolution curves. Rayleigh and Batch decarbonation curves are shown as dotted lines with open circles and as a solid line with black tick marks, respectively. Numbers next to the open circles represent the fraction of carbon remaining in the rock. Fluid-rock interaction curves are shown as solid lines and as dashed lines representing magmatic ($\delta^{13}C$ = -7 and $\delta^{18}O$ = 6) and meteoric ($\delta^{13}C$ = -6 and $\delta^{18}O$ = -5) fluids, respectively. Numbers next to the open circles indicate the water-rock ratio. Italicized numbers correspond to the proportion of CO_2 in the fluid with temperatures denoted in bold text. Shaded regions represent a range of temperatures that exist for a family of model curves: A) marbles from the Olympias deposit; B) marbles from the Stratoni fault zone with data from the Madem Lakkos deposit (Gilg, 1993) illustrated by the dotted ellipse; C) gangue carbonate associated massive sulfide and stylolitic fluid escape structures from the Olympias deposit; D) gangue carbonate associated skarn and massive sulfide, along with stylolitic fluid escape structures from the Madem Lakkos and Mavres Petres deposits. Values reported in Gilg (1993) are illustrated by the amoeba-shaped dotted line; E) quartz-rhodochrosite-calcite veins from the Olympias deposit and Stratoni fault zone.

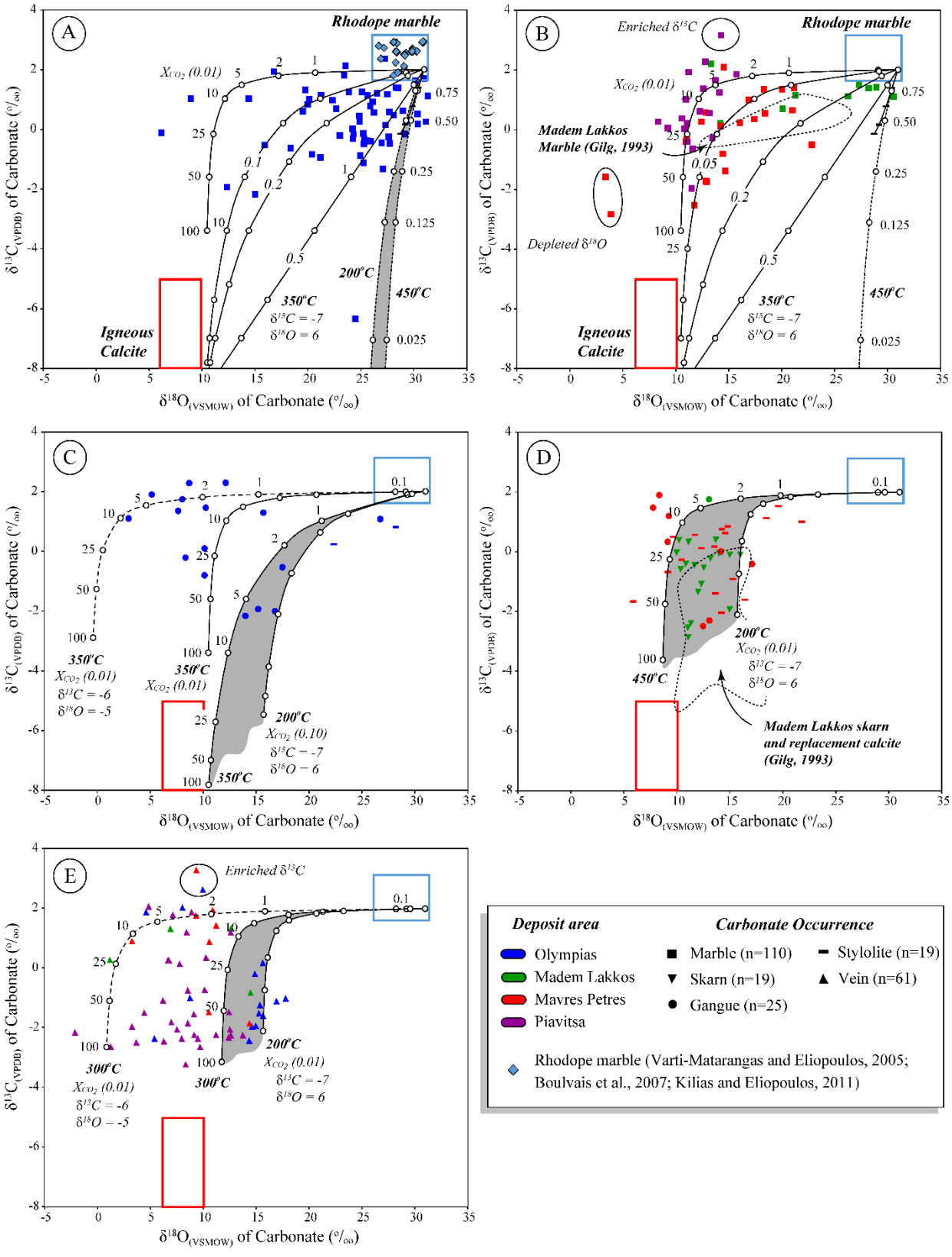
A
Rhodope marble
Igneous Calcite
350°C
δ13C = -7
δ18O = 6
200°C
450°C
B
Enriched δ13C
Rhodope marble
Madem Lakkos Marble (Gilg, 1993)
Depleted δ18O
Igneous Calcite
350°C
δ13C = -7
δ18O = 6
450°C
C
350°C
XCO2 (0.01)
δ13C = -6
δ18O = -5
350°C
XCO2 (0.01)
200°C
XCO2 (0.10)
δ13C = -7
δ18O = 6
350°C
D
200°C
XCO2 (0.01)
δ13C = -7
δ18O = 6
450°C
Madem Lakkos skarn and replacement calcite (Gilg, 1993)
E
Enriched δ13C
300°C
XCO2 (0.01)
δ13C = -6
δ18O = -5
300°C
200°C
XCO2 (0.01)
δ13C = -7
δ18O = 6
δ13C(VPDB) of Carbonate (‰)
δ18O(VSMOW) of Carbonate (‰)
Deposit area
Olympias
Madem Lakkos
Mavres Petres
Piavitsa
Carbonate Occurrence
Marble (n=110)
Skarn (n=19)
Gangue (n=25)
Stylolite (n=19)
Vein (n=61)
Rhodope marble (Varti-Matarangas and Eliopoulos, 2005; Boulvais et al., 2007; Kilias and Eliopoulos, 2011)

($0.01X_{CO2}$), which similarly describes a minor population of quartz-rhodochrosite vein-breccias from the Madem Lakkos, Mavres Petres, and Piavitsa areas (Figure 4.13E). The majority of the quartz-rhodochrosite veins from the district are shifted toward highly depleted $\delta^{18}O$ values, which cannot be achieved from a fluid of magmatic composition at temperatures less than 300ºC. The distribution of the data, however, can be explained by the mixing of a light $\delta^{18}O$ fluid of meteoric composition at lower temperatures between 300–200ºC, consistent with fluid inclusion data.

Source of metals from Pb isotopes

Intrusion-related carbonate replacement deposits commonly show a variety of spatial, geochemical, and isotopic evidence for magmatic-hydrothermal processes and wallrock reactions. Variations in Pb isotopic compositions in many systems reflect a combination of magmatic and wallrock sources of Pb and, by inference, other metals (Tosdal et al., 1999). Sulfide ores from the Kassandra Mining District, however, display a relatively uniform Pb isotopic signature suggesting derivation of Pb from a homogenized reservoir. The overlapping relationship of sulfide Pb isotope compositions may also suggest that the hydrothermal fluids incorporated Pb from multiple sources, potentially including the Kerdilion and Vertiskos units and associated amphibolites, and the late Oligocene igneous suite (Figure 4.8A-D). The Stratoni stock shows the largest distribution of Pb isotope compositions among the late Oligocene igneous suite, broadly reflecting the Pb isotope signature of the Kerdilion unit, while the Tsikara and Fisoka stocks overlap with the fields defining the both, Vertiskos and Kerdilion units (Figure 4.8A-B). This may indicate that Pb within these intrusions was, in part, derived from the metamorphic wallrock (Kalogeropoulos et al., 1989; Nebel et al., 1991), but more likely a homogenized deep crustal source. The early Miocene Skouries and Aspro Lakkos porphyry stock, including the black-matrix porphyry dikes, exhibit a narrow range of Pb isotope values suggesting that the younger igneous suite inherited their Pb isotope signatures from a common source.

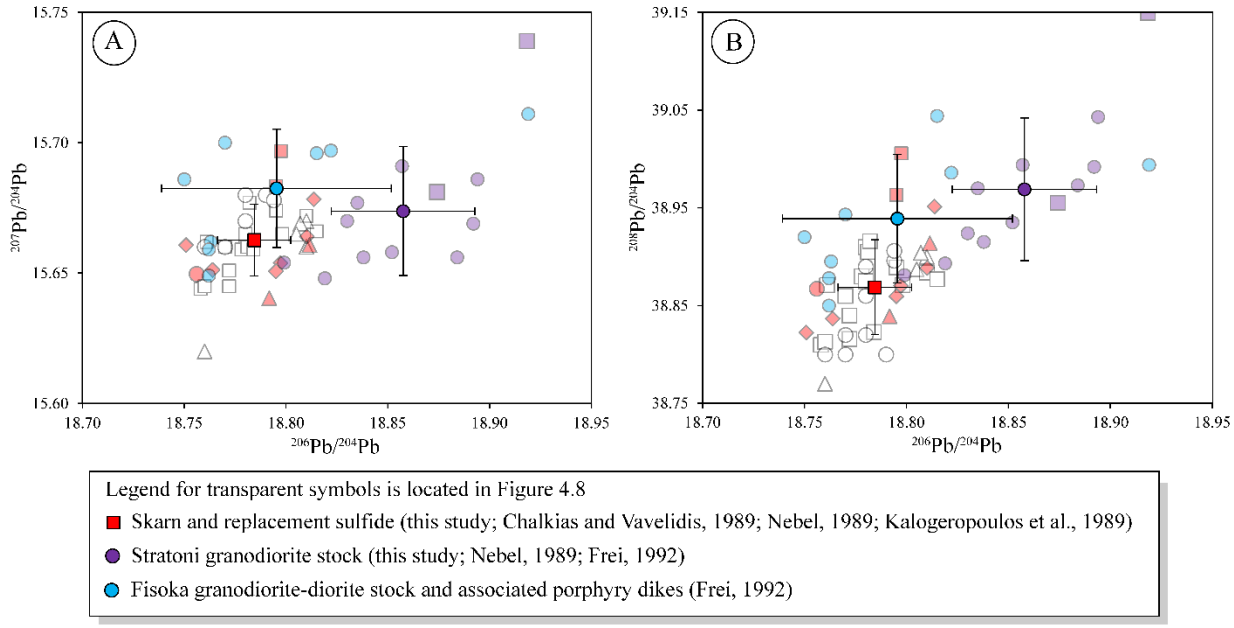

Figure 4.14. Lead isotope data representing the Stratoni and Fisoka stocks, and sulfide ore displayed on $^{207}Pb/^{204}Pb$ vs. $^{206}Pb/^{204}Pb$ (uranogenic) and $^{208}Pb/^{204}Pb$ vs. $^{206}Pb/^{204}Pb$ (thorogenic) diagrams. Transparent symbols illustrate the overlapping distribution of Pb isotope data (see Figure 4.8 for legend), where mean values are plotted as bold symbols with error bars representing 1σ uncertainty.

Previous studies have attempted to fingerprint the causative intrusive source that resulted in skarn and carbonate replacement mineralization within the Stratoni fault zone. Based on Sr and Pb isotope data, Frei (1992) concluded that the Stratoni granodiorite stock did not contribute to the orebodies at the Madem Lakkos deposit. The Pb isotope data of Frei (1992) plotted together with new data show that the $^{207}Pb/^{204}Pb$ and the $^{208}Pb/^{204}Pb$ ratios from the Fisoka and Stratoni stocks overlap with the sulfide dataset at the 1σ confidence level; however, overlapping $^{206}Pb/^{204}Pb$ ratios among sulfide ore and the Fisoka stock may support a genetic relationship (Figure 4.14A-B). When viewed spatially, a Pb isotope zonation pattern is discretely evident with the most radiogenic Pb in the east, associated with the Stratoni stock, and less radiogenic Pb characterizing the Fisoka stock and the sulfide orebodies along the Stratoni fault to the west (Figure 4.15A-B). The limited spatial resolution, however, precludes linking fluid origins with a specific source intrusion. Given the data available, the Pb isotope values are not sufficiently distinct to

Figure 4.15. Map view of the Stratoni fault zone showing the spatial variation of $^{208}Pb/^{204}Pb$ and $^{206}Pb/^{204}Pb$ data from igneous feldspar and sulfide samples. Similar patterns are reflected in the $^{207}Pb/^{204}Pb$ data (not shown). Average values for the Stratoni and Fisoka stocks from Frei (1992) are also indicated. Note that the samples reported in Frei (1992) were not accompanied by precise location data, therefore the data points shown on this image are predicted to approximate the mean of his sampling locations.

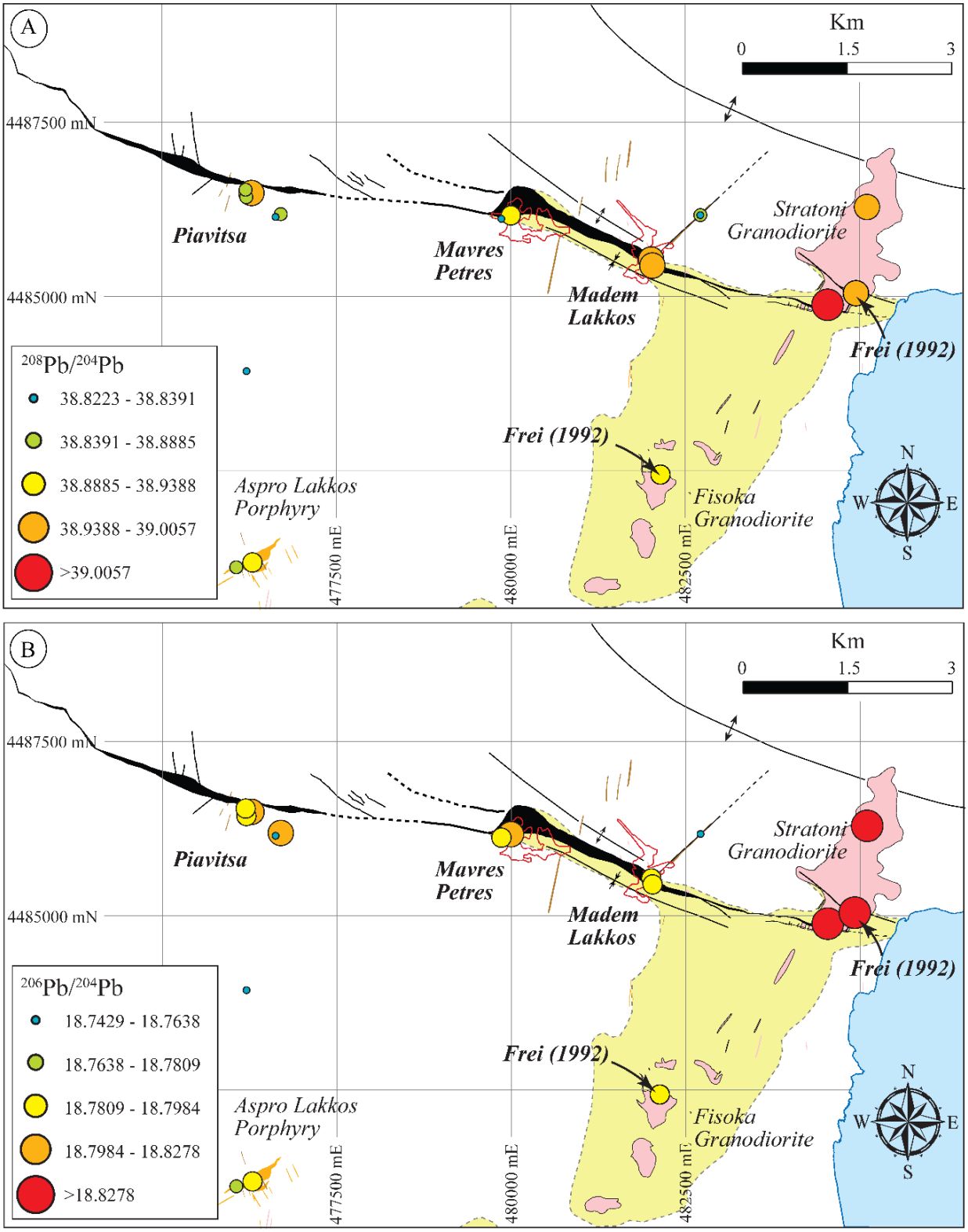
A
Km
0
1.5
3
4487500 mN
4485000 mN
Piavitsa
Mavres
Petres
Madem
Lakkos
Stratoni
Granodiorite
Frei (1992)
Frei (1992)
Aspro Lakkos
Porphyry
Fisoka
Granodiorite
477500 mE
480000 mE
482500 mE
N
W
E
S
208Pb/204Pb
38.8223 - 38.8391
38.8391 - 38.8885
38.8885 - 38.9388
38.9388 - 39.0057
>39.0057
B
Km
0
1.5
3
4487500 mN
4485000 mN
Piavitsa
Mavres
Petres
Madem
Lakkos
Stratoni
Granodiorite
Frei (1992)
Frei (1992)
Aspro Lakkos
Porphyry
Fisoka
Granodiorite
477500 mE
480000 mE
482500 mE
N
W
E
S
206Pb/204Pb
18.7429 - 18.7638
18.7638 - 18.7809
18.7809 - 18.7984
18.7984 - 18.8278
>18.8278

conclude whether the Stratoni or the Fisoka intrusions contributed to the skarn and replacement sulfide orebodies at the Madem Lakkos and Mavres Petres deposits.

District-scale fluid evolution model for carbonate replacement deposition

The distribution of metals and metal ratio patterns, combined with carbon-oxygen isotope and fluid inclusion data, and the relative structural timing and igneous relationships to the sulfide orebodies suggest that the hydrothermal system within the Stratoni fault zone originated from a concealed late Oligocene igneous intrusion in the southeastern sector of the Madem Lakkos deposit (Figure 4.16A), although the Stratoni and Fisoka intrusions cannot be ruled out. Similar patterns evident in the Olympias area support a genetic model that involves a hydrothermal fluid that exploited the Kassandra and East faults, which possibly originated from a local late Oligocene igneous intrusion to the east of the orebody (Figure 4.16B).

Carbon-oxygen isotope and fluid inclusion data, together with previously published sulfur isotope data (0.5 ± 1.7‰; Hahn, 2014) indicate that the early skarn and replacement sulfide within the Stratoni fault zone and the replacement orebodies at the Olympias deposit resulted primarily from a fluid of magmatic origin. The carbonate replacement deposits formed in an environment of rapidly fluctuating fluid conditions, probably due to localized fluid-enhanced overpressure conditions and sudden drops in pressures as fault segments episodically dilated during mineralization (e.g., fault-valve mechanism described by Sibson, 2001). Faults permitted the migration of metal-bearing hydrothermal fluids, where fault-slip events likely facilitating separation of immiscible fluid phases; however, mineral textures and fluid inclusions evidence indicate that the associated pressure decrease may have not been sufficient extensive for boiling to occur (Roedder, 1984; p. 270). The syn-mineral timing of faulting within the Stratoni and Kassandra-East fault zones (Siron et al., 2018), therefore, permits the fault-valve mechanism as a driving force that triggered unmixing of an originally homogeneous parent fluid of magmatic affiliation at the Madem Lakkos and Olympias deposits.

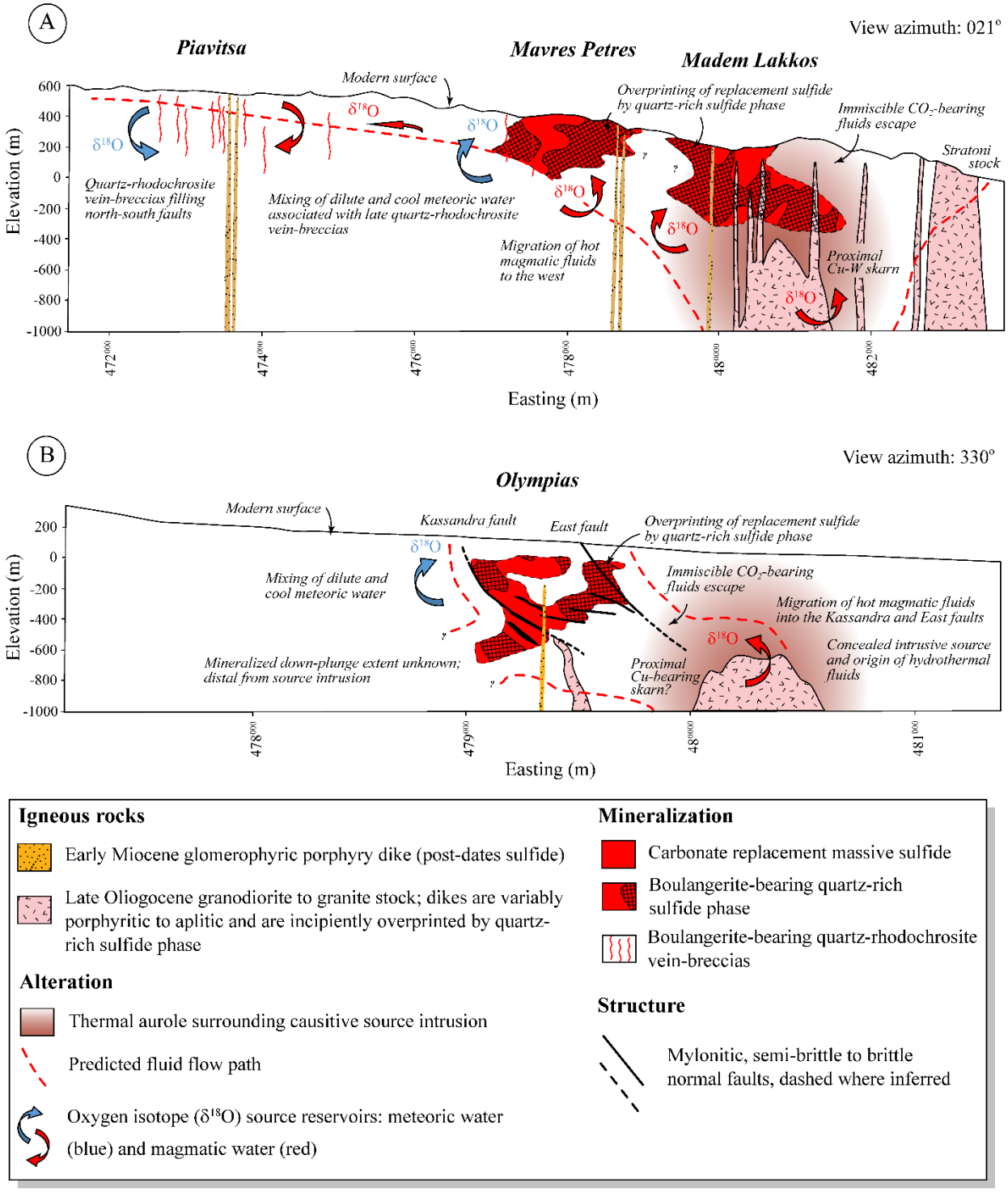

Figure 4.16. Genetic model illustrating the evolution of the carbonate replacement deposits within the Kassandra Mining District: A) long-section view of the Madem Lakkos and Mavres Petres deposits, and the Piavitsa prospect within the plane of the Stratoni fault zone; B) cross-section view of the Olympias deposit.

Mineralization was localized where hydrothermal fluids, mainly confined to faults and preexisting ductile structures, interacted with receptive marble host rocks. Carbonate dissolution resulted in pH neutralization of the hydrothermal fluid, thus inducing precipitation of metals (e.g., Seward and Barnes, 1997). Dissolution of host marble and cooling of the hydrothermal fluid also likely facilitated gangue carbonate deposition as indicated from fluid inclusion data. Isotopically light $\delta^{18}O$ associated with gangue carbonate, and low-salinity fluid inclusions contained in the younger quartz-rich sulfide phase and the quartz-rhodochrosite vein-breccias suggest that the primary magmatic fluid interacted with dilute water of probable meteoric origin during the waning stages of hydrothermal activity. The data show that mixing and cooling of hydrothermal fluids with inferred changes in fluid pH were likely all contributing factors in carbonate replacement mineralization.

Comparisons to other carbonate replacement deposits

The polymetallic sulfide orebodies in the Kassandra Mining District belong to the intrusion-related class of carbonate-hosted replacement deposit, but are distinct when compared to deposits of similar type within the region. The Madem Lakkos, Mavres Petres, and Olympias sulfide ores are characteristically enriched in Au and are hosted by fault-bounded marbles, whereas many replacement-style sulfide deposits in the eastern Mediterranean lack Au in economic quantities (Figure 4.17). While similarly hosted by fault-imbricated marbles, the massive sulfide deposits in the Maden-Thermes district of southern Bulgaria and northeastern Greece, as well as the deposits in the Laviron district of southern Greece are Au deficient (Kaiser-Rohrmeier et al., 2013; Melfos and Voudouris, 2017). Gold is similarly absent in the skarn and replacement sulfide deposits in the Trepča district of Kosovo (Hyseni et al., 2010; Strmić Palinkaš et al., 2013). In contrast, fault-controlled replacement, skarn, and epithermal veins that comprise the Balya deposit in western Turkey are enriched in Au (Yigit, 2012), and appear geologically similar to the Madem Lakkos deposit. It may be the case that Au was not assayed or reported for some of the deposits in the region. For example, Au was not historically reported for the Madem Lakkos and

Mavres Petres deposits despite containing significant concentrations. The sulfide orebodies in the Kassandra Mining District are also comparable to many carbonate-hosted replacement systems in the western United States and northern Mexico (Figure 4.17; Prescott, 1916; Lindgren and Loughlin, 1919; Megaw et al., 1988; Beaty et al., 1990; Vikre, 1998). In terms of metal (Ag-Pb-Zn-Cu) concentration and Au endowment, the sulfide orebodies of the Kassandra Mining District resemble the deposits within the Eureka (Nevada), Bingham (Utah), and Leadville (Colorado) districts.

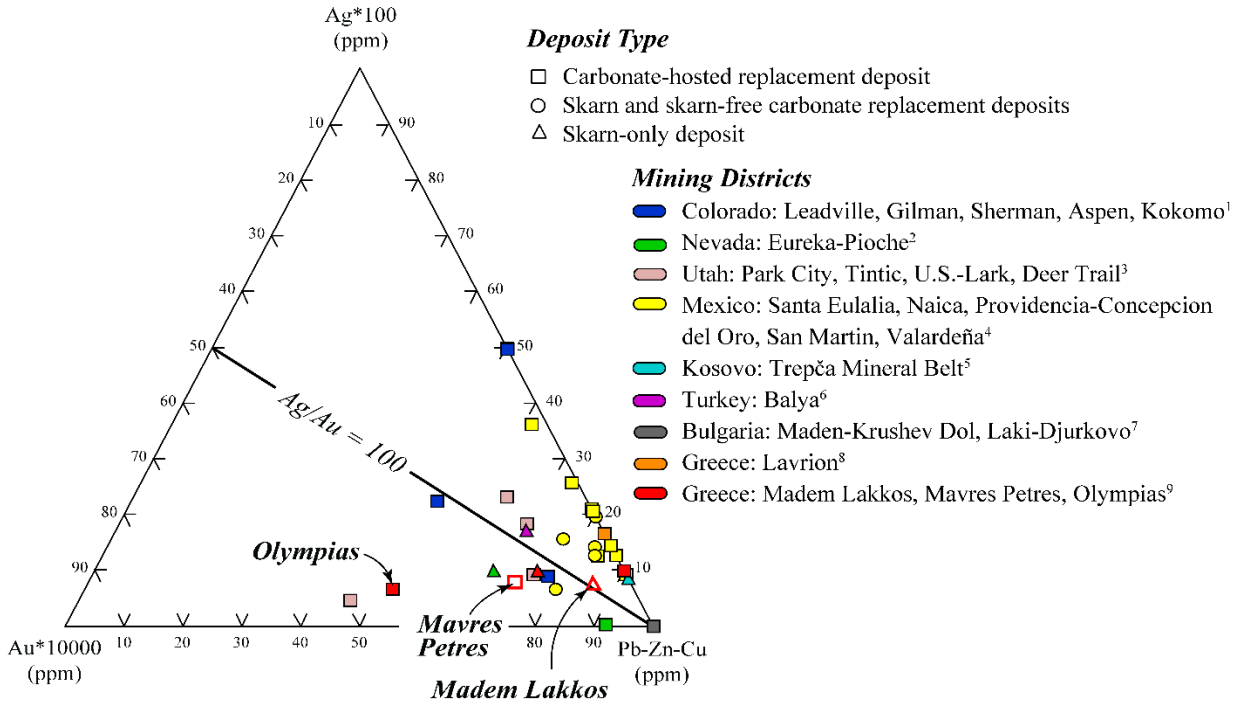

Figure 4.17. Ternary diagram of published grades from selected Ag-Pb-Zn ± Cu ± Au carbonate-hosted replacement districts worldwide: (1) Colorado Mineral Belt (Beaty et al., 1990); (2) Eureka and Pioche districts of Nevada (Shawe and Nolan, 1989; Vikre and Brown, 1999); (3) Park City, Tintic, US-Lark, and Deer Trail districts of Utah (Lindgren and Loughlin, 1919; James, 1973; Beaty et al., 1986; Bromfield, 1989); (4) Mexican deposits located in the Santa Eulalia, Naica, Providencia-Concepcion del Oro, San Martin, and Valardeña districts (Megaw et al., 1988); (5) Trepča Mineral Belt of Kosovo (Mining Journal Special Publication, 2005); (6) Balya deposit on the Biga peninsula of Turkey (Yigit, 2012); (7) Maden-Krushev Dol and Laki-Djurkovo deposits in the Madan-Thermes district of southern Bulgaria (Kaiser-Rohrmeier et al., 2013); (8) Lavrion district in the Attica region of southern Greece (Melfos and Voudouris, 2017); (9) the published grade for the Madem Lakkos deposit is after Nebel et al. (1989) and the current measured and indicated resource grades for the Mavres Petres and Olympias deposits are reported in Eldorado (2017). Open symbols for the Madem Lakkos and Mavres Petres deposits correspond to the average grades from this study. See Appendix for published data.

Conclusions

The polymetallic sulfide orebodies in the Kassandra Mining District belong to the intrusion-related class of carbonate-hosted replacement deposit. These orebodies display geologic similarities to other deposits of comparable type within the Serbo-Macedonian Metallogenic Belt and the Aegean region, but are distinctive in that they are Au-rich. Based on metal grades and Au endowment, the deposits of the Kassandra Mining District resemble the carbonate-hosted sulfide orebodies in the southwestern United States.

Marble contained within the Stratoni fault zone hosts the Madem Lakkos and Mavres Petres deposits, where early skarn in the east transitions into carbonate replacement sulfide orebodies to the west. A younger boulangerite-bearing quartz-rich sulfide phase occurs at each deposit with crosscutting quartz-rhodochrosite vein-breccias culminating late in the mineral paragenesis, which are best developed at the western end of the Stratoni fault zone in the Piavitsa area. The sulfide orebodies at the Olympias deposit are hosted by marbles in contact with, and adjacent to, the Kassandra and East faults, and are mineralogically and paragenetically similar to the Mavres Petres deposit. Estimated fluid conditions determined from fluid inclusion microthermometric measurements suggest that carbonate replacement mineralization occurred at a paleodepth of approximately 4 km, assuming hydrostatic conditions.

Metal distribution patterns within the Stratoni fault zone show elevated Cu in the east, at the Madem Lakkos deposit, with increasing Au, As, Ag, Sb concentrations to the west in the Mavres Petres deposit area. Sulfide ore at the Olympias deposit exhibits elevated Cu values in the east with increasing Ag/Au ratios down-plunge and toward the south. Based on previous fluid inclusion studies, the highest temperatures reported in the Stratoni fault zone are associated with skarn and replacement sulfide ore from the Madem Lakkos deposit (Gilg, 1993). Lower temperatures and salinities are characteristic of the younger quartz-rich sulfide phase and quartz-rhodochrosite veins at the Mavres Petres deposit and Piavitsa prospect, respectively. While similarly exhibiting low salinities, the quartz-rich sulfide phase at the Olympias deposit formed at temperatures intermediate between the Madem Lakkos and Mavres Petres

deposits. Fluid inclusions containing H_2O-CO_2 at the Madem Lakkos and Olympias deposits are interpreted to represent a trapped immiscible fluid phase. A fault-valve mechanism likely resulted in localized and rapid drops in pressure due to slip and dilation along active segments of the Stratoni and Kassandra-East faults, thus enhancing permeability pathways and facilitating separation of a homogenous parent fluid.

Carbon and oxygen isotope patterns developed within the Stratoni fault zone indicate that isotopic exchange was principally controlled by fluid-wallrock interaction, whereas decarbonation and fluid-rock exchange reactions occurred at the Olympias deposit. Gangue carbonates associated with skarn and replacement sulfide from across the district display isotopic compositions intermediate between unaltered marble and igneous values, suggesting the reaction between magmatic hydrothermal fluids and marble. Lower temperatures and salinities of the boulangerite-bearing quartz-rich sulfide phase and quartz-rhodochrosite vein-breccias, and an isotopically light $\delta^{18}O$ signature of gangue carbonate is evidence for dilution of a primary magmatic fluid with water of probable meteoric origin late in the evolution of the hydrothermal system in the Stratoni fault zone and at the Olympias deposit.

The hydrothermal fluids that resulted in the carbonate replacement orebodies within the Stratoni fault zone and at the Olympias deposit were likely derived from late Oligocene igneous activity. Lead isotope compositions of skarn and replacement sulfide overlap with metamorphic basement units and intrusions belonging to the late Oligocene igneous suite, which indicates that sulfide ore likely derived Pb from multiple sources. Based on the Pb isotope data, an inferred causative igneous intrusion responsible for carbonate replacement mineralization in the Stratoni fault zone may be the Fisoka stock, however, this conclusion remains tentative. Structural and igneous relationships to ore, carbon-oxygen stable isotopes, fluid inclusions, and metal distribution patterns are supportive of a zoned, late Oligocene hydrothermal system centered south of the Madem Lakkos deposit and a satellite hydrothermal system located to the east of the Olympias deposit.

Acknowledgements

Eldorado Gold Corporation kindly provided financial support to perform fieldwork and analytical analyses, and provided access to the historic multi-element geochemical drill database from the district. The Hellas Gold geologists in the Madem Lakkos office are thanked for their support while in the field. Janet Gabites at the Pacific Center for Isotopic and Geochemical Research at the University of British Columbia is acknowledged for assisting with the Pb isotope analyses. Greg Dipple at the University of British Columbia and Robert Darling at the State University of New York (Cortland) generously provided the author access to lab facilities and instruction while performing carbon-oxygen isotope and fluid inclusion analyses, respectively. Discussions regarding carbon-oxygen isotope systematics and data interpretation with Louis Derry (Cornell University) and Kaleb Boucher (Teck Resources) were instructive and greatly appreciated. Converstations with Larry Cathles, Louis Derry, and Frank Horowitz (Cornell University) stimulated ideas with regards to the mechanisms of hydrothermal fluid flow. Judith Suzuki (Cornell University) and Kate Carroll (University of British Columbia) are acknowledged for assisting with the carbon-oxygen isotope study, and Malcom Thomas (Cornell University) provided guidance with scanning electron microscopy. ARANZ Geo Limited kindly supplied an academic license of their Leapfrog geological modeling software to the author. This study benefited from the National Science Foundation award number NSF DMR-1719875 to the Cornell Center for Materials Research.

REFERENCES

Arvanitidis, N.D., and Constantinides, D.C., 1994, Ore geology of the Olympias, Madem Lakkos and Mavres Petres polymetallic deposits: Post-congress 2-day field trip to Chalkidiki peninsula (central Macedonia, northern Greece), Congress of the Geological Society of Greece, 7th, Thessaloniki, Greece, May 27-28, 1994, Guidebook, 17 p.

Barker, S.L.L., Dipple, G.M., Hickey, K.A., Lepore, W.A., and Vaughan, J.R., 2011, Applying stable isotopes to mineral exploration: Teaching and old dog new tricks: Economic Geology, v. 108, p. 1-9.

Barker, S.L.L., Dipple, G.M., Dong, F., and Baer, D.S., 2011, Use of laser spectroscopy to measure the $^{13}C/^{12}C$ and $^{18}O/^{16}O$ compositions of carbonate minerals: Analytical Chemistry, v. 83, p. 2220-2226.

Baumgartner, L. P., and Valley, J.W., 2001, Stable isotope transport and contact metamorphic fluid flow: Reviews in Mineralogy and Geochemistry, v. 43, p. 365-413.

Beaty, D.W., Cunningham, C.G., Rye, R.O., Steven, T.A., and Gonzales-Urien, E., 1986, Geology and geochemistry of the Deer Trail Pb-Zn-Ag-Au-Cu manto deposits, Marysvale district, west-central Utah: Economic Geology, v. 81, p. 1932-1952.

Beaty, D.W., Landis, G.P., and Thompson, T.B., 1990, Carbonate-hosted sulfide deposits of the central Colorado mineral belt: Introduction, general discussion, and summary, in Beaty, D.W., Landis, G.P., and Thompson, T.B., eds., Carbonate-hosted sulfide deposits of the central Colorado mineral belt: Economic Geology Monograph 7, p. 1-18.

Beinlich, A., Barker, S.L.L., Dipple, G.M., Gupta, M., and Baer, D.S., Stable isotope (δ13C, δ18O) analysis of sulfide-bearing carbonate samples using laser absorption spectrometry: Economic Geology, v. 112, p. 693-700.

Bodnar, R.J., 1993, Revised equation and table for determining the freezing point depression of H2O-NaCl solutions: Geochimica et Cosmochimica Acta, v. 57, p. 683-684.

Bonev, N., Burg, J.-P., and Ivanov, Z., 2006, Mesozoic-Tertiary structural evolution of an extensional gneiss dome – the Kesebir-kardamos dome, eastern Rhodope (Bulgaria-Greece): International Journal of Earth Science, v. 95, p. 318-340.

Bonev, N., and Dilek, Y., 2010, Geochemistry and tectonic significance of proto-ophiolitic metamafic units from the Serbo-Macedonian and western Rhodope massifs (Bulgaria-Greece): International Geology Review., v. 52, p. 298-335.

Bottinga, Y., 1968, Calculation of fractionation factors for carbon and oxygen exchange in the system calcite-carbon dioxide-water: Journal of Physical Chemistry, v. 72, p. 800-808.

Boulvais, P., Brun, J.-P., and Sokoutis, D., 2007, Fluid circulation related to post-Messinian extension, Thassos Island, north Aegean: Geofluids, v. 7, p. 159-170.

Bowman, J.R., 1998, Stable-isotope systematics of skarns, in Lentz, D.R., ed., Mineralized intrusion-related skarn systems: Mineralogical Association of Canada Short Course Series, v. 26, p. 99-145.

Bowman, J.R., Willett, S.D., and Cook, S.J., 1994, Oxygen isotope transport and exchange during fluid flow: One dimensional models and applications: American Journal of Science, v. 294, p. 1-55.

Bromfield, C.S., 1989, Gold in the Park City mining district, Utah: U.S. Geological Survey Bulletin 1857-C, p. 14-26.

Brun, J.P., and Sokoutis, D., 2007, Kinematics of the southern Rhodope core complex (North Greece): International Journal of Earth Science., v. 96, p. 1079-1099.

Brun, J.P., and Faccenna, C., 2008, Exhumation of high-pressure rocks driven by slab rollback: Earth and Planetary Science Letters, v. 272, p. 1-7.

Brun, J.P., and Sokoutis, D., 2010, 45 m.y. of Aegean crust and mantle flow driven by trench retreat: Geology, v. 38, p. 815-818.

Burg, J.-P., Ivanov, Z., Ricou, L.-E., Dimor, D., and Klain, L., 1990, Implications of shear-sense criteria for the tectonic evolution of the Central Rhodope massif, southern Bulgaria: Geology, v. 18, p. 451-454.

Burg, J.-P., Ricou, L.-E., Ivanov, Z., Godfriaux, I., Dimor, D., and Klain, L., 1996, Syn-metamorphic nappe complex in the Rhodope Massif. Structure and kinematics: Terra Nova, v. 8, p. 6-15.

Burg, J.-P., 2012, Rhodope: from Mesozoic convergence to Cenozoic extension. Review of petro-structural data in the geochronological frame: in Skourtsos, E., and Lister, G.S., eds., The Geology of Greece: Journal of the Virtual Explorer, electronic edition, v. 42(1).

Cambarnous, M. A., and Bories, S. A., 1975, Hydrothermal convection in saturated porous media, Advances in Hydrosciences: Academic Press, v. 10, 77 p.

Cathles, L.M., 1997, Thermal aspects of ore formation, in Barnes, H.L., ed., Geochemistry of hydrothermal ore deposits, 3rd edition: John Wiley and Sons, New York, p. 191-227.

Chalkias, S., and Vavelidis, 1989, Interpretation of lead-isotope data from Greek Pb-Zn deposits, based on an empirical two-stage model: Geological Society of Greece Bulletin, v. 23/2, p. 177-193.

Coplen, T.B., 1994, Reporting of stable hydrogen, carbon, and oxygen isotopic abundances: Pure and Applied Chemistry, v. 66, p. 273-276.

Cunningham, C.G., Austin, G.W., Naeser, C.W., Rye, R.O., Ballantyne, G.H., Stamm, R.G., and Barker, C.E., 2004, Formation of a paleothermal anomaly and disseminated gold deposits associated with the Bingham Canyon porphyry Cu-Au-Mo system, Utah: Economic Geology, v. 99, p. 789-806.

de Boorder, H., Spakman, W., White, S.H., and Wortel, M.J.R., 1998, Late Cenozoic mineralization, orogenic collapse and slab detachment in the European Alpine belt: Earth and Planetary Letters, v. 164, p. 569-575.

Dinter, D.A., 1998, Late Cenozoic extension of the Alpine collisional orogen, northeastern Greece: origin of the north Aegean basin: Geological Society of America Bulletin, v. 110, p. 1208-1230.

Dinter, D.A., and Royden, L., 1993, Late Cenozoic extension in north-eastern Greece: Strymon Valley detachment system and Rhodope metamorphic core complex: Geology, v. 21, p. 45-48.

Dixon, J.E., and Dimitriadis, S., 1984, Metamorphosed ophiolitic rocks from the Serbo-Macedonian Massif near lake Volvi, north-east Greece, in Dixon, J.E., and Robertson, A.H.F., eds., The geological evolution of the eastern Mediterranean: Geological Society of London Special Publication, v. 17, p. 603-618.

Eldorado Gold Corporation, 2017, Resources and reserves: Accessed October 29, 2017, (http://www.eldoradogold.com/assets/resources-and-reserves/).

Eliopoulos, D.G., and Kilias, S.K., 2011, Marble-hosted submicroscopic gold mineralization at Asimotrypes area, Mount Pangeon, southern Rhodope core complex, Greece: Economic Geology, v. 106, p. 751-780.

Engel, A.E.J., Clayton, R.N., and Epstein, S., 1958, Variations in isotopic compositions of oxygen and carbon in Leadville limestone (Mississippian, Colorado) and in its hydrothermal and metamorphic phases: Journal of Geology, v. 66, p. 374-393.

Forward, P., Francis, A., Liddell, N., 2010, Technical report on the Stratoni project Pb-Zn-Ag deposit, northern Greece: European Goldfields Limited, NI 43-101 Report, 54 p.

Frei, R., 1992, Isotope (Pb-Rb-Sr-S-O-C-U-Pb) geochemical investigations of Tertiary intrusions and related mineralizations in the Serbo-Macedonian (Pb-Zn, Sb+Cu-Mo metallogenetic) province in northern Greece: Unpublished Ph.D. thesis, Zürich, Switzerland, ETH, 231 p.

Frei, R., 1995, Evolution of mineralizing fluid in the porphyry copper system of the Skouries deposit, northeast Chalkidiki (Greece): Evidence from combined Pb-Sr and stable isotope data: Economic Geology, v. 90, p. 746-762.

Friedman, I., and O'Neil, J.R., 1977, Compilation of stable isotope fractionation factors of geochemical interest: U.S. Geological Survey Professional Paper 440-KK.

Gautier, P., Brun, J.-P., Moriceau, R., Sokoutis, D., Martinod, J., and Jolivet, L., 1999, Timing, kinematic and cause of Aegean extension: a scenario based on a comparison with simple analogue experiments: Tectonophysics, v. 315, p. 31-72.

Gilg, H.A., 1993, Geochronology (K-Ar), fluid inclusion, and stable isotope (C, H, O) studies of skarn, porphyry copper, and carbonate-hosted Pb-Zn (Ag, Au) replacement deposits in the Kassandra mining district (eastern Chalkidiki, Greece): Unpublished Ph.D. thesis, Zürich, Switzerland, ETH, 153 p.

Gilg, H.A., and Frei, R., 1994, Chronology of magmatism and mineralization in the Kassandra mining area, Greece: The potentials and limitations of dating hydrothermal illites: Geochimica et Cosmochimica Acta, v. 58, p. 2107-2122.

Haines, H.S., 1998, A structural synthesis for sector Vb of the Madem Lakkos polymetallic sulfide deposit – Northeast Greece: Unpublished M.Sc. thesis, London, united Kingdom, The University of London, 81 p.

Hahn, A., 2014, Nature, timing and geodynamic context of polymetallic mineralisation in the Kassandra mining district, North Greece: Unpublished Ph.D. thesis, London, United Kingdom, Kingston University, 351 p.

Hahn, A., Naden, J., Treloar, P.J., Kilias, S.P., Rankin, A.H., and Forward, P., 2012. A new timeframe for the mineralization in the Kassandra mine district, N Greece: deposit formation during metamorphic core complex exhumation: European Mineralogical Conference, v. 1, 1EMC2012-742.

Hedenquist, J.W., and Arribas, A.Jr., 1997, Evolution of an intrusion-centered hydrothermal system: Far Southeast-Lepanto porphyry and epithermal Cu-Au deposits, Philippines: Economic Geology, v. 93, p. 373-404.

Hemley, J.J., and Hunt, J.P., 1992, Hydrothermal ore-forming processes in the light of studies in rock-buffered systems: II. Some general geologic applications: Economic Geology, v. 87, p. 23-43.

Himmerkus, F., Zachariadis, P., Reischmann, T., and Kostopoulos, D.K., 2005, The mafic complexes of the Athos-Volvi-Zone – a suture zone between the Serbo-Macedonian massif and the Rhodope massif?: Geophysical Research Abstracts, v. 7., p. 10, 240.

Himmerkus, F., Reischmann, T., and Kostopoulos, D.K., 2006, Late Proterozoic and Silurian basement units within the Serbo-Macedonian massif, northern Greece: the significance of terrane accretion in the Hellenides, in Robertson, A.H.F., and Mountrakis, D., eds., Tectonic development of the eastern Mediterranean region: Geological Society of London Special Publication, v. 260, p. 35-50.

Himmerkus, F., Anders, B., Reischmann, T., and Kostopoulos, D., 2007, Gondwana-derived terranes in the northern Hellenides, in Hatcher, R.D., Jr., Carlson, M.P., McBride, J.H., and Martínez Catalán, J.R., eds., 4-D framework of continental crust: Geological Society of America Memoir, v. 200, p. 379-390.

Himmerkus, F., Reischmann, T., and Kostopoulos, D.K., 2009, Serbo-Macedonian revisited: a Silurian basement terrane from northern Gondwana in the Internal Hellenides, Greece: Tectonophysics v. 473, p. 20-35.

Himmerkus, F., Zachariadis, P., Reischmann, T., and Kostopoulos, D., 2011, The basement of the Mount Athos Peninsula, northern Greece: insights from geochemistry and zircon ages: International Journal of Earth Sciences., v. 101, p. 1467-1485.

Hitzman, M.W., 1999, Routine staining of drill core to determine carbonate mineralogy and distinguish carbonate alteration textures: Mineralium Deposita, v. 34, p. 794-798.

Hoefs, J., 2004, Stable isotope geochemistry: Berlin, Springer Verlag, 244 p.

Hyseni, S., Durmishaj, B., Fetahaj, B., Shala, F., Berisha, A., and Large, D., 2010, Trepça ore belt and Stan Terg mine – Geological overview and interpretation, Kosovo (SE Europe): Geologija, v. 53, p. 87-92.

Jahn-Awe, S., Froitzheim, N., Nagel, T.J., Frei, D., Georgiev, N., and Pleuger, J., 2010, Structural and geochronological evidence for Paleogene thrusting in the western Rhodopes, SW Bulgaria: elements for a new tectonic model of the Rhodope Metamorphic Province: Tectonics, v. 29, TC3008.

James, A.H., 1973, Lead and zinc resources in Utah: Utah Geological and Mineralogical Survey Special Studies 44, 66 p.

Janković, S., 1997, The Carpatho-Balkanides and adjacent area: a sector of the Tethyan Eurasian metallogenic belt: Mineralium Deposita, v. 32, p. 426-433.

Jolivet, L., and Brun, J.P., 2010, Cenozoic geodynamic evolution of the Aegean region: International Journal of Earth Sciences, v. 99, p. 109-138.

Jolivet, L., Faccenna, C., Huet, B., Labrousse, L., Le Pourhiet, L., Lacombe, O., Lecomte, E, Burov, E, Denele, Y., Brun, J.P., Philippon, M., Paul, A., Salaun, G., Karabulut, H., Piromallo, C., Monie, P., Gueydan, F., Okay, A.I., Oberhansli, R., Pourteau, A., Augier, R., Gadenne, L, and Driussi, O., 2013, Aegean tectonics: Strain localization, slab tearing and trench retreat: Tectonophysics, v. 597-598, p. 1-33.

Kaiser Rohrmeier, M., von Quadt, A., Driesner, T., Heinrich, C.A., Handler, R., Ovtcharova, M., Ivanov, Z., Petrov, P., Sarov, St., and Peytcheva, I., 2013, Post-orogenic extension and hydrothermal ore formation: High-precision geochronology of the central Rhodopian metamorphic core complex (Bulgaria-Greece): Economic Geology, v. 108, p. 691-718.

Kalogeropoulos, S.I., and Economou, G.S., 1987, A study of sphalerite from the carbonate-hosted Pb-Zn sulfide deposits of the eastern Chalkidiki peninsula, northern Greece: Canadian Mineralogist, v. 25, p. 639-646.

Kalogeropoulos, S. I., and Kilias, S.P., 1989, Oxygen (^{18}O) and carbon (^{13}C) isotopic changes in carbonate rocks and minerals in relation to the Olympias Pb-Zn (Au, Ag) sulfide mineralization, E. Chalkidiki, N. Greece: Contribution to metallogeny and exploration: Geological Society of Greece Bulletin, v. 23/2, p. 261-269.

Kalogeropoulos, S.I., Kilias, S.P., Bitzios, D.C., Nicolaou, M., and Both, R.A., 1989, Genesis of the Olympias carbonate-hosted Pb-Zn (Au, Ag) sulfide ore deposit, eastern Chalkidiki peninsula, northern Greece: Economic Geology, v. 84, p. 1210-1234.

Kilias, S.P., and Kalogeropoulos, S.I., 1989, Physiochemical conditions of ore formation of the Olympias Pb-Zn (Au, Ag) sulphide deposit, E. Chalkidiki, based on fluid inclusion studies and arsenopyrite geothermometry. Contribution to metallogeny and exploration: Geological Society of Greece Bulletin, 23/2, p. 271-282.

Kilias, S.P., and Madsen, J. K., 1994, H2O-CO2-NaCl fluid immiscibility in the carbonate-hosted Olympias Pb-Zn (Au, Ag) sulfide deposit, Macedonia, Greece: Bulletin of the Geological Society of Greece, v. 30/1, p. 445-456.

Kilias, S.P., Kalogeropoulos, S.I., and Konnerup-Madsen, J., 1996, Fluid inclusion evidence for the physicochemical conditions of sulfide deposition in the Olympias carbonate-hosted Pb-Zn(Au, Ag) sulfide ore deposit, E. Chalkidiki peninsula, N. Greece: Mineralium Deposita, v. 31, p. 394-406.

Kockel, F., Mollat, H., and Walther, H., 1977, Erläuterungen yur geologischen karte der Chalkidiki und agrenzender Gebiete 1:100,000 (Nord-Griechenland): Bundesanstalt für Geowissenschaften und Rohstoffe, Hannover, p. 1-119.

Kounov, A., Wüthrich, E., Seward, D., Burg, J.P., and Stockli, D., 2015, Low-temperature constraints on the Cenozoic thermal evolution of the southern Rhodope core complex (northern Greece): International Journal of Earth Science, v. 104, p. 1337-1352.

Krenn, K., Bauer, C., Proyer, A., Klözli, U., and Hoinkes, G., 2010, Tectonometamorphic evolution of the Rhodope orogen: Tectonics, v. 29, TC4001.

Krohe, A., and Mposkos, E., 2002, Multiple generations of extensional detachments in the Rhodope mountains (northern Greece): evidence of episodic exhumation of high-pressure rocks, in Blundell, D.L., Neubauer, F., and von Quadt, A., eds., The timing and location of major ore deposits in an evolving orogen: Geological Society of London Special Publication, v. 204, p. 151-178.

Kroll, T., Müller, D., Seifert, T., Herzig, P.M., and Schneider, A., 2002, Petrology and geochemistry of the shoshonite-hosted Skouries porphyry Cu-Au deposit, Chalkidiki, Greece: Mineralium Deposita, v. 37, p. 137-144.

Kydonakis, K., Gallagher, K., Brun, J.-P., Jolivet, M., Gueydan, F., and Kostopoulos, D., 2014, Upper Cretaceous exhumation of the western Rhodope Metamorphic Province (Chalkidiki peninsula, northern Greece): Tectonics, v. 33, p. 1113-1132.

Lindgren, W., and Loughlin, G.F., 1919, Geology and ore deposits of the Tintic mining district, Utah: U.S. Geological Survey Professional Paper 107.

Lips, A.L., 2002, Correlating magmatic-hydrothermal ore deposit formation over time with geodynamic processes in SE Europe: Geological Society of London Special Publication, v. 204, p. 69-79.

Mantzos, L.A., 1989, Geology and lithogeochemistry of the Olympias carbonate-hosted Pb-Zn sulfide deposit, Chalkidiki, Greece: Unpublished Ph.D. thesis, London, United Kingdom, Imperial College, University of London, 404 p.

Moncada, D., Baker, D., and Bodnar, R.J., 2017, Mineralogical, petrographic and fluid inclusion evidence for the link between boiling and epithermal Ag-Au mineralization in the La Luz area, Guanajuato Mining District, México: Ore Geology Reviews, v. 89, p. 143-170.

Morris, H.T., and Lovering, T.S., 1979, General geology and mines of the East Tintic mining district, Utah and Juab counties, Utah: U.S. Geological Survey Professional Paper 1024.

Megaw, P.K.M., 1990, Geology and geochemistry of the Santa Eulalia mining district, Chihuahua, Mexico: Unpublished Ph.D. thesis, Tucson, Arizona, University of Arizona, 461 p.

Megaw, P.K.M., 1998, Carbonate-hosted Pb-Zn-Ag-Cu-Au replacement deposits: An exploration perspective, in Lentz, D.R., ed., Mineralized intrusion-related skarn systems: Mineralogical Association of Canada Short Course Series, v. 26, p. 337-258.

Megaw, P.K.M., Ruiz, J., and Titley, S.R., 1988, High-temperature, carbonate-hosted Ag-Pb-Zn(Cu) deposits of northern Mexico: Economic Geology, v. 83, p. 1856-1885.

Melfos, V., and Voudouris, P., 2017, Cenozoic metallogeny of Greece and potential for precious, critical and rare metals exploration: Ore Geology Reviews, v. 89, p. 1030-1057.

Nabelek, P.I., 1987, General equations for modeling fluid/rock interaction using trace elements and isotopes: Geochimica et Cosmochimica Acta, v. 51, p. 1765-1769.

Nebel, M.L., 1989, Metamorphism and polygenesis of the Madem Lakkos polymetallic sulfide deposit, Chalkidiki, Greece: Unpublished Ph.D. thesis, Golden, Colorado, Colorado School of Mines, 215 p.

Nebel, M.L., Hutchinson, R.W., and Zartman, R.E., 1991, Metamorphism and polygenesis of the Madem Lakkos polymetallic sulfide deposit, Chalkidiki, Greece, Economic Geology., v. 86, p. 81-105.

Neubauer, F., 2002, Contrasting late Cretaceous with Neogene ore provinces in the Alipine-Balkan-Carpathian-Dinaride collision belt, in Blundell, D.L., Neubauer, F., and von Quadt, A., eds., The timing and location of major ore deposits in an evolving orogen: Geological Society of London Special Publication, v. 204, p. 81-102.

Nicolaou, M.N., 1960, L'intrusion granitique dans la région de Stratoni-Olympiade et sa relation avec la métallogenèse: Annales Géologiques des Pays Helléniques, v. 11, p. 214-265.

Nicolaou, M.N., 1964, The mineralogy and micrography of the sulphide ores of Kassandra mines, Greece: Annales Géologiques des Pays Helléniques, v. 16, p. 111-139.

Nicolaou, M., and Kokonis, I., 1980, Geology and development of the Olympias mine, eastern Chalkidiki, Macedonia, Greece, in Jones, M.J., ed., Complex sulfide ores: London Institute of Mining and Metallurgy, p. 260-270.

O'Neil, J.R., Clayton, R.N., and Mayeda, T.K., 1969, Oxygen isotope fractionation of divalent metal carbonates: Journal of Chemical Physics, v. 51, p. 5547-5558.

Ohmoto, H., and Rye, R.O., 1979, Isotopes of sulfur and carbon, in Barnes, H.L., ed., Geochemistry of hydrothermal ore deposits, 2nd edition: John Wiley and Sons, New York, p. 509-567.

Papanikolaou, D., 2013, Tectonostratigraphic models of the Alpine terranes and subduction history of the Hellenides: Tectonophysics, v. 595-596, p. 1-24.

Pavlides, S.B., and Tranos, M.D., 1991, Structural characteristics of two strong earthquakes in the north Aegean: Ierissos (1932) and Agios Efstratios (1968): Journal of Structural Geology, v. 13, p. 205-214.

Pe-Piper, G., and Piper, D.J.W., 2006, Unique features of the Cenozoic igneous rocks of Greece, in Dilek, Y., and Pavlides, S., eds., Postcollisional tectonics and magmatism in the Mediterranean region and Asia: Geological Society of America Special Paper, v. 409, p. 259-282.

Prescott, B., 1916, The main mineral zone of the Santa Eulalia district, Chihuahua: Transactions of the American Institute of Mining Engineers, v. 51, p. 57-99.

Ricou, L.E., Burg, J.-P., Godfriaux, I., Ivanov, Z., 1998, Rhodope and Vardar: the metamorphic and the olistostromic paired belts related to the Cretaceous subduction under Europe: Geodinamica Acta, v. 11, p. 285-309.

Ring, U., Glodny, J., Will, T., Thomson, S., 2010, The Hellenic subduction system: high-pressure metamorphism, exhumation, normal faulting, and large-scale extension: Annual Reviews of Earth and Planetary Sciences, v. 38, p. 45-76.

Roddick, J.C., 1987, Generalized numerical error analysis with applications to geochronology and thermodynamics: Geochimica et Cosmochimica Acta, v. 51, p. 2129-2135.

Roedder E., 1984, Fluid inclusions: Reviews in Mineralogy, v. 12, 644 p.

Roedder, E., 1979, Fluid inclusions as samples of ore fluids, in Barnes, H.L., ed., Geochemistry of hydrothermal ore deposits, 2nd edition: John Wiley and Sons, New York, p. 657-697.

Roedder, E., and Bodnar, R.J., 1980, Geologic pressure determination from fluid inclusion studies: Annual Review of Earth and Planetary Science, v. 8, p. 263-301.

Rumble, D., 1982, Stable isotope fractionation during metamorphic devolatilization reactions, in Ferry, J.M., ed., Characterization of metamorphism through mineral equilibria: Mineralogical Society of America, p. 327-353.

Sagui, C.L., 1928, The ancient mining works of Cassandra, Greece: Economic Geology, v. 23, p. 671-680.

Serafimovski, T., 2000, The Lece-Chalkidiki metallogenic zone: geotectonic setting and metallogenic features: Geologija, v. 42, p. 159-164.

Seward, T.M., and Barnes, H.L., 1997, Metal transport by hydrothermal ore solutions, in Barnes, H.L., ed., Geochemistry of hydrothermal ore deposits, 3rd edition: John Wiley and Sons, New York, p. 435-486.

Shawe, D.R., and Nolan, T.B., 1989, Gold in the Eureka mining district, Nevada: U.S. Geological Survey Bulletin 1857-C, p. 27-37.

Sibson, R.H., 2001, Seismogenic framework for hydrothermal transport and ore deposition, in Richards, J.P., and Tosdal, R.M., eds., Structural controls on ore genesis: Reviews in Economic Geology, v. 14, p. 25-50.

Simmons, S.F., and Browne, P.R.L., 2000, Hydrothermal minerals and precious metals in the Broadlands-Ohaaki geothermal system: implications for understanding low-sulfidation epithermal environments: Economic Geology, v. 95, p. 971-999.

Siron, C.R., Thompson, J.F.H., Baker, T., Friedman, R., Tsitsanis, P., Russell, S., Randall, S., and Mortensen, J., 2016, Magmatic and metallogenic framework of Au-Cu porphyry and polymetallic carbonate-hosted replacement deposits of the Kassandra Mining District, Northern Greece, in Richards, J.P., ed., Tectonics and metallogeny of the Tethyan orogenic belt: Society of Economic Geologists, Special Publication No. 19, p. 29-55.

Siron, C.R., Rhys, D., Thompson, J.F.H., Baker, T., Veligrakis, T., Camacho, A., and Dalampiras, L., 2018, Structural controls on porphyry Au-Cu and Au-rich polymetallic carbonate-hosted replacement deposits of the Kassandra Mining District, northern Greece: Economic Geology, v. 13, p. 309-345.

Sokoutis, D., Brun, J.P., Van Den Driessche, J., and Pavlides, S., 1993, A major Oligo-Miocene detachment in southern Rhodope controlling north Aegean extension: Journal of the Geological Society, London, v. 150, p. 243-246.

Stacey, J.S., and Kramers, J.D., 1975, Approximation of terrestrial lead isotope evolution by a two-stage model: Earth and Planetary Science Letters, v. 26, p. 207-221.

Strmić Palinkaš, S., Palinkaš, L.A., Renac, C., Spangenberg, J.E., Lüders, V., Moldar, F., and Maliqi, G., 2013, Metallogenic model of the Trepča Pb-Zn-Ag skarn deposit, Kosovo: evidence from fluid inclusions, rare earth elements, and stable isotope data: Economic Geology, v. 108, p. 135-162.

Takenouchi, S., and Kennedy, G.C., 1964, The binary system H2O-CO2 at high temperatures and pressures: American Journal of Science, v. 262, p. 1055-1074.

Taylor, H.P., 1971, Oxygen isotope evidence for large-scale interaction between meteoric ground waters and Tertiary granodiorite intrusions, western Cascades Range, Oregon: Journal of Geophysical Research, v. 76, p. 7855-7874.

Taylor, H.P., 1974, The application of oxygen and hydrogen isotope studies to problems of hydrothermal alteration and ore deposition: Economic Geology, v. 69, p. 843-883.

Taylor, H.P., 1979, Oxygen and hydrogen isotope relationships in hydrothermal mineral deposits, in Barnes, H.L., ed., Geochemistry of hydrothermal ore deposits, 2nd edition: John Wiley and Sons, New York, p. 236-277.

Thirlwall, M.F., 2000, Inter-laboratory and other errors in Pb isotope analyses investigated using a 207 Pb–204 Pb double spike: Chemical Geology, v. 163, p. 299-322.

Thompson, T.B., and Arehart, G.B., 1990, Geology and the origin of ore deposits in the Leadville district, Colorado: Part I. Geologic studies of orebodies and wall rocks, in Beaty, D.W., Landis, G.P., and Thompson, T.B., eds., Carbonate-hosted sulfide deposits of the central Colorado mineral belt: Economic Geology Monograph 7, p. 130-155.

Tosdal, R. M., Wooden, J.L., and Bouse, R.M., 1999, Pb isotopes, ore deposits, and metallogenic terranes: Reviews in Economic Geology, v. 12, p. 1-28.

Valley, J. W., 1986, Stable isotope geochemistry of metamorphic rocks: Reviews in Mineralogy and Geochemistry, v. 16, p. 445-489.

Varti-Matarangas, M., and Eliopoulos, D.G., 2005, Petrographic and stable isotope (C, O) studies of the Pangeon Mountain marbles, northern Greece: Implications for metallogenesis, in Mao, J., and Bierlein, F.P., eds., Mineral Deposit Research: Meeting the Global Challenge, Berlin Freiberg, Springer-Verlag, v. 2, p. 931-934.

Vikre, P.G., 1998, Intrusion-related polymetallic carbonate replacement deposits in the Eureka district, Eureka county, Nevada: Nevada Bureau of Mines and Geology Bulletin 110, 52 p.

Vikre, P.G., and Brown, Q.J., 1999, Isotopic characteristics of metal deposits, intrusions, and source rocks in the Pioche district, Lincoln county, Nevada: Economic Geology, v, 94, p. 387-404.

Wawrzenitz, N., and Krohe, A., 1998, Exhumation and doming of the Thassos metamorphic core complex (S Rhodope, Greece): structural and geochronological constrains: Tectonophysics, v. 285, p. 301-312.

Wortel, M.J.R., and Spakman, W., 2000, Subduction and slab detachment in the Mediterranean-Carpathian region: Science, v. 290, p. 1910-1917.

Wüthrich, E., 2009, Low temperature thermochronology of the northern Aegean Rhodope Massif: Unpublished Ph.D. thesis, Zürich, Switzerland, ETH, 210 p.

Yigit, O., 2012, A prospective sector in the Tethyan metallogenic belt: geology and geochronology of mineral deposits in the Biga peninsula, NW Turkey: Ore Geology Reviews, v. 46, p. 118-148.

Zachariadis, P., Kostopoulos, D., Reischmann, T., Himmerkus, F., Matukov, D., and Sergeev, S., 2006, U-Pb ion-microprobe zircon dating of subduction-related magmatism from northern Greece: The ages of the Guevgueli, Thessaloniki and Chalkidiki igneous complexes: Geophysical Research Abstracts, v. 8. 05560.

CHAPTER 5

CONCLUSIONS

Approximately 2500 years of Au and Ag production from the economically important Kassandra Mining District contributed to the prosperity of empires and financed conquests across the region. Activity continues in the district today with the production of Au, Ag, Pb, and Zn from the Mavres Petres and Olympias underground mines, mine development of the Skouries Au-Cu deposit, and exploration at the Piavitsa prospect. The economic and geologic significance of the region has attracted scores of academic and applied researchers with nearly ninety years of published studies. Technological and methodological advancements in geochronology and geochemistry, with a rapidly evolving understanding of the complex geodynamic architecture of the north Aegean realm permitted a geologic reevaluation of the Kassandra Mining District that builds upon previous work. The overarching theme of this research was to establish a revised metallogenic and structural framework of the Kassandra Mining District through geologic mapping, drill core logging, and structural analyses, supported by petrography, ^{40}Ar-^{39}Ar and zircon U-Pb geochronology, whole-rock geochemistry, isotope (C, O, and Pb) geochemistry, fluid inclusion microthermometry, and the evaluation of a comprehensive historic drill core database. The objectives of this study focused on placing constraints on the timing and petrogenesis of Oligo-Miocene magmatism, establish the structural framework of the district, and to determine the source and evolution of the hydrothermal fluid(s) responsible for carbonate replacement mineralization within the district. The following section summarizes the main findings of this research and concludes with recommendations for future work.

Mineral Deposits of the Kassandra Mining District

Marbles within the Stratoni fault zone host the Madem Lakkos and Mavres Petres deposits. Skarn and replacement sulfide orebodies occur in the east, and are spatially associated with porphyritic to aplitic

dikes of probable late Oligocene age (Gilg and Frei, 1994; Haines, 1998). Early skarn principally contains chalcopyrite and scheelite whereas the replacement massive and banded sulfides at Madem Lakkos and Mavres Petres are dominated by sphalerite-galena-pyrite-chalcopyrite and arsenopyrite. An overprinting quartz-rich sulfide phase characterized by a similar sulfide mineral assemblage but containing abundant boulangerite is evident at both deposits. The youngest phase of mineralization manifests as boulangerite-bearing quartz-rhodochrosite ± rhodonite veins and vein-breccias which occur throughout the Stratoni fault zone, but are most extensive at the Piavitsa prospect in the west. The massive and banded sulfide orebodies at the Olympias deposit are hosted by marble lenses that occur between, and within, the Kassandra and East faults, and are spatially associated with mylonitic granite dikes and sills, and an igneous breccia on the western part of the deposit. The Olympias deposit displays geologic relationships, as well as mineralogical and paragenetic similarities to the Mavres Petres deposit.

The Skouries Au-Cu deposit is a multi-phase quartz monzonite porphyry intrusion that forms a narrow stock hosted by gneisses and schists of the Vertiskos unit, and obliquely crosscuts the limb of a district-scale antiform. Four stages of veins and associated alteration are recognized by their relative crosscutting relationships. Pervasive K-feldspar-magnetite alteration of the early quartz monzonite stock and adjacent wallrock was associated with stockwork quartz ± magnetite veins. Introduction of Au-Cu mineralization followed with the emplacement of an intra-mineral porphyry phase, accompanied by K-feldspar-biotite-magnetite alteration with associated quartz-magnetite-chalcopyrite veins and a younger set of sulfide-rich quartz-biotite-chalcopyrite-bornite ± magnetite veins. Quartz-carbonate ± base metal veins culminated as the latest vein event, crosscutting all prior igneous phases, including existing vein and alteration mineral assemblages.

Oligo-Miocene Magmatism

Multi-element whole-rock geochemistry, zircon U-Pb geochronology, and petrology define two distinct igneous suites of late Oligocene and early Miocene age. The Tsikara composite stock consists of

monzogabbros with diorite to granodiorites phases that crystallized around 27 Ma. The younger (24.5 Ma) Fisoka stock is diorite to granodiorite in composition and is associated with a northeast-trending array of quartz-feldspar porphyry and aplite dikes. Two dikes outcropping east of the Madem Lakkos deposit crystallized between 25.5 and 25.7 Ma. The 25.4 to 25.8 Ma Stratoni stock consists of diorite and granodiorite with a porphyritic phase occurring at the topographic top of the intrusive stock. Magmatism resumed after about a 4-5 m.y. hiatus with the emplacement of the Skouries stock and coeval Au-Cu mineralization. Consisting of four quartz monzonite porphyry phases, the Skouries intrusive event is interpreted to have occurred at about 20.6 Ma (Hahn et al., 2012). A glomerophyric porphyry dike at the Piavitsa prospect also crystallized at 20.6 Ma, and is probably coeval with other dikes that exhibit similar texture and geochemistry. Emplacement of the Skouries stock and Au-Cu mineralization was followed by the barren Aspro Lakkos quartz monzonite porphyry at 19.7 Ma and a series of younger subvolcanic trachyandesite (black-matrix) porphyry dikes. Early Miocene magmatism ended by 19.2 Ma with the emplacement of the black-matrix porphyry dike in the Vathilakkos fault.

Both igneous suites belong to the high-K calc-alkaline magmas series, with early Miocene porphyry stocks and dikes having a shoshonitic geochemistry. Geochemical patterns shown by the Sm/Yb ratio and the Eu_n/Eu^* anomaly indicate that plagioclase fractionation was important in the evolution of the late Oligocene igneous suite. In contrast, these ratios together with elevated Sr/Y and La/Yb values, and depleted heavy rare earth element (HREE) patterns indicate amphibole ± garnet fractionation, caused by the presence of abundant water which suppresses plagioclase crystallization. Amphibole and/or garnet fractionation, an indicator of arc magma fertility (Richards, 2011), was therefore an important process within the magmatic source that produced the early Miocene porphyry suite. Enriched light rare earth element (LREE) patterns and extremely elevated large ion lithophile element (LILE) concentrations indicate that both igneous suites, particularly early Miocene magmas, interacted strongly with subduction-enriched continental lithosphere (Pe-Piper et al., 2006).

Oligo-Miocene intrusions in the Kassandra Mining District overlap in time with the Kerdilion and Strymon Valley detachment faults, and exhumation of the southern Rhodope core complex (Dinter et al., 1995; Dinter, 1998; Brun and Sokoutis, 2007; Wüthrich, 2009; Kounov et al., 2015). Unroofing of deep crustal rocks may have been a tectonic process that triggered the ascent of subjacent magmas that exploited crustal-scale structures that delivered magmas and magmatic-hydrothermal fluids to shallow crustal levels within an evolving post-collisional, extensional back arc environment.

Tectonic Implications of the Stratoni Fault Zone

The Stratoni fault zone has been historically viewed as the tectonic boundary separating the Kerdilion unit from the Vertiskos unit (Kockel et al., 1977), the two major lithotectonic assemblages that underlie the Kassandra Mining District. An early interpretation made by the author (Chapter 2) proposed that the Kerdilion unit extends to the south of the Stratoni fault zone and that the southern half of the district was underlain by this metamorphic sequence. This interpretation was revised in Chapter 3 on the basis of detrital zircon ages reported in Hahn (2014); however, the data presented here still shows that the Stratoni fault zone is not a detachment structure as proposed by previous studies (e.g., Haines, 1998). The following lines of geologic evidence support this interpretation: the Kerdilion unit is compositionally gradational with no observable change in metamorphic grade across the Stratoni fault zone; interlayered amphibolites that occur to the south and north of the Stratoni fault zone are geochemically indistinguishable; and ductile structures spanning the Stratoni fault zone display similar patterns suggesting that footwall and hanging wall lithologies were affected by the same phases of deformation. While detrital zircon ages from the southern half of the district are consistent with the Vertiskos unit (Himmerkus et al., 2009; Hahn, 2014), amphibolite geochemistry and structural evidence indicate that the contact between the Kerdilion unit and the much older Vertiskos unit is probably located south of the Stratoni fault zone, and represents an older structure and not a detachment fault as previously proposed.

Structural Framework and Controls on Mineralization

The basement rocks that underlie the Kassandra Mining District have been affected by at least three syn-metamorphic deformation events. The earliest D1 event resulted in a penetrative S1 foliation accompanied by amphibolite-facies metamorphism, followed by a D2 episode which reworked the previous fabric into tight to open F2 folds with a locally developed axial planar S2 cleavage and L2 intersection lineation. District-scale antiforms to the north and south of the Stratoni fault zone are most likely associated with D2 deformation; note that the interpretation of folding events introduced in Chapter 2 was based on preliminary data and revised in Chapter 3. Both D1 and D2 fabrics imply top-to-the-northeast vergence possibly due to regional Eocene or older contraction. A younger D3 event resulted in a steeply dipping S3 cleavage which warps all earlier fabrics. Normal and transtensional faults within the district became active during regional southwest-directed ductile extension likely during the middle Eocene (Wüthrich, 2009; Kounov et al., 2015). Semi-brittle faults that comprise the Stratoni fault zone and those at the Olympias deposit overprint mylonitic extensional fault-related fabrics, and are also superimposed by younger brittle faults.

Kinematic fault-slip data and ^{40}Ar-^{39}Ar geochronology support coeval skarn and carbonate replacement mineralization with north-south extension during the late Oligocene. Younger Au-bearing quartz-rhodochrosite vein and vein-breccias overprint semi-brittle faults and sulfide within the Stratoni fault zone, suggesting that east-west extension was associated with a later stage of hydrothermal activity at the Mavres Petres deposit and the Piavitsa prospect. Post-mineral faults controlled by northeast-southwest extension crosscut the sulfide orebodies within the Stratoni fault zone and are kinematically compatible with middle to late Miocene regional extension (e.g., Dinter, 1998). Brittle faults that overprint all earlier deformation events are characterized by a later stage of north-south directed extension, typical of the modern tectonic environment in the north Aegean region (Pavlides and Tranos, 1991). Fault kinematic patterns and the superposition of fault deformation events within the Stratoni fault zone are similarly developed at the Olympias deposit and elsewhere in the Kassandra Mining District.

The location and morphology of carbonate replacement sulfide was influenced by a preexisting ductile structural architecture, and the interaction of syn-mineral faults with available marble host rocks. The Olympias orebody is controlled by a southeast-plunging L2 intersection lineation and F2 folds interacting with extensional mylonites and semi-brittle shear zones that link the Kassandra and East faults within a marble unit. The Madem Lakkos orebody is controlled by marbles localized within the hinges of folds and syn-mineral strands of the Stratoni fault zone (Gilg and Frei, 1994; Haines, 1998). The Mavres Petres orebody is principally hosted by fault-bounded marble lenses entrained within a strongly carbonaceous segment of the Stratoni fault zone. At the Skouries deposit, the porphyry stock and Au-Cu mineralized veins manifested in response to differential horizontal stresses developed within an anisotropic regional stress field. The shift from north-south to east-west extension from the late Oligocene to early Miocene may have triggered upper crustal emplacement of the Skouries porphyry stock within the steeply dipping limb of a major district-scale antiform.

Fluid Evolution and Timing of Carbonate Replacement Mineralization

Structural crosscutting relationships and U-Pb geochronology suggest that carbonate replacement mineralization within the district occurred syn- to post-emplacement of the late Oligocene Stratoni granodiorite stock at around 25 Ma. The unaltered black-matrix porphyry dike that occurs within the Vathilakkos fault at the Madem Lakkos deposit (Gilg and Frei, 1994; Haines, 1998) and the glomerophyric porphyry dike at the Piavitsa prospect crosscuts mineralized bodies, thus demonstrating that mineralization within the Stratoni fault zone predates early Miocene (19-20 Ma) magmatism. A glomerophyric porphyry dike crosscuts sulfide ore at the Olympias deposit indicating a similar timing of replacement mineralization. Semi-brittle fault deformation was coeval with carbonate replacement mineralization, which occurred from about 24 Ma to 22 Ma based on ^{40}Ar-^{39}Ar geochronology of hydrothermal muscovite. Absolute and relative timing relationships both indicate that late Oligocene magmatism contributed to sulfide deposition within the district.

Within the Stratoni fault zone, chalcopyrite- and scheelite-bearing skarn adjacent to late Oligocene intrusions at the Madem Lakkos deposit transition into Au-bearing replacement sulfide and distal Ag-bearing Mn replacement bodies in the Mavres Petres and Piavitsa areas. Decreasing Cu values with increasing Ag, As, Au, and Sb concentrations are evident from east to west within the Stratoni fault zone, reflecting the path of hydrothermal fluid flow. The Olympias deposit exhibits similar metal concentrations as the Mavres Petres deposit, where elevated Cu grades occur in association with the east ore lenses with increasing Pb, Zn, and Ag/Au ratios to the south indicating the proximal to distal expressions of the hydrothermal system.

Estimated trapping pressures and temperatures deduced from fluid inclusion data suggest that carbonate replacement mineralization occurred at a paleodepth of approximately 4 km, assuming hydrostatic conditions. An inferred immiscible fluid phase present within fluid inclusions from the Madem Lakkos and Olympias deposits (Gilg, 1993; Kilias et al., 1996) probably originated from a homogeneous magmatic fluid derived from a nearby source intrusion at each locality. Localized drops in pressure, likely in response to a fault-valve mechanism, resulted in the infiltration of hydrothermal fluids with concomitant fluid phase separation, dissolution of marble host rocks, and sulfide deposition. Based on fluid inclusion data, the highest temperatures reported in the Stratoni fault zone occur in association with skarn and replacement sulfide from the Madem Lakkos deposit (Gilg, 1993), whereas lower temperatures characterize the younger quartz-rich sulfide phase and quartz-rhodochrosite vein-breccias to the west. Homogenization temperatures from the quartz-rich sulfide phase at the Olympias deposit are intermediate between the Madem Lakkos and Mavres Petres deposits, possibly indicating that mineralization was proximal to a source intrusion.

Carbon and oxygen isotope patterns in the Stratoni fault zone support isotopic exchange principally through fluid-wallrock interaction, whereas decarbonation and fluid-rock exchange reactions were both present at the Olympias deposit. Carbonates associated with skarn and replacement sulfide from across the district have intermediate isotopic compositions between marble and igneous values,

suggesting that the hydrothermal fluids were probably magmatic in origin. The lower temperatures and salinities of the quartz-rich sulfide phase and quartz-rhodochrosite vein-breccias, and an isotopically light $\delta^{18}O$ signature of gangue carbonate is evidence for dilution of a magmatic fluid with meteoric water late in the evolution of the hydrothermal system in the Olympias area and the Stratoni fault zone.

Overlapping Pb isotope values among skarn and replacement sulfide with metamorphic basement units and late Oligocene igneous intrusions indicates that Pb in the sulfide ore was likely derived from multiple sources. Tentatively, the Fisoka stock or a concealed late Oligocene igneous intrusion is considered source responsible for carbonate replacement mineralization in the Stratoni fault zone. Structural and igneous relationships to ore, ^{40}Ar-^{39}Ar ages, carbon-oxygen isotopes, fluid inclusions, and metal distribution patterns presented in this study support a zoned, late Oligocene hydrothermal system originating in the Madem Lakkos area and a satellite hydrothermal system located to the east of the Olympias deposit.

Recommendations for Future Research

Important geologic problems were realized during the course of this research, in which some questions were not pursued either due to limited time and/or the availability of resources. This section outlines areas of possible continued research in the fields of geochronology, igneous geochemistry, fluid flow-thermal modeling, and tectonics, as well as detailed deposit-scale studies that are considered critical in advancing the understanding of the tectono-magmatic and metallogenic evolution of the Kassandra Mining District.

Geochronology and igneous geochemistry

While this study constrained the timing of Oligo-Miocene magmatism, hydrothermal alteration, and structural events within the district, more work is recommended. The aplitic granite dikes and sills that are spatially associated with the sulfide bodies at the Madem Lakkos and Olympias deposits were not

included in this study. However, zircon U-Pb geochronology combined with whole-rock geochemistry may be useful to identify the source intrusion at each location. Unfortunately, the Madem Lakkos mine is no longer accessible, and historic drill core has succumbed to time and may be unsalvageable; thus, recovering aplitic dike intercepts from drill core and locating their position within the deposit may prove to be a challenging task. Zircon U-Pb geochronology and whole-rock geochemical analyses of the mineralized granitic breccia, as well as the glomerophyric porphyry dikes, at the Olympias deposit are also warranted in order to determine the absolute timing and nature of magmatism in the Olympias area. Additional work should focus on drill core samples since exposures within the Olympias mine are thoroughly concealed by shotcrete, thus inhibiting sample collection underground.

Further work is similarly recommended at the Skouries deposit. Recent advances in high-resolution geochronology have revealed remarkably short durations in which mineralized porphyry systems develop (von Quadt et al., 2011). Mass balance calculations and numerical simulations from the 605 Mt Bajo de la Alumbrera porphyry Cu-Au deposit (e.g., Proffett, 2003) showed that volatile release from a magma with subsequent potassic alteration and mineralization occurred in less than 1000 years (Cathles and Shannon, 2007). High-precision geochronology of individual intrusive phases contained within the Bajo de la Alumbrera stock similarly showed that porphyry emplacement and Cu-Au mineralization manifested within a timeframe of just 0.09 m.y. (von Quadt et al., 2011). The published zircon U-Pb and ^{40}Ar-^{39}Ar hydrothermal biotite ages (Hahn et al., 2012) from the Skouries porphyry stock, however, only constrains a single intrusive phase, and therefore the evolution of the magmatic-hydrothermal system is largely undefined. The well-documented intrusive sequence and vein paragenesis within the Skouries stock can be accurately and precisely determined with zircon U-Pb isotope dilution-thermal ionization mass spectrometry (ID-TIMS). Constraining the timing of each intrusive phase may highlight important tectonic and geodynamic processes that facilitated porphyry consolidation and mineralization (Chiaradia et al., 2013).

The intra-mineral porphyry phase of the Skouries stock is coeval with a glomerophyric porphyry dike in the Piavitsa area. Based on a zircon U-Pb age of this dike, it was tentatively assumed that all other glomerophyric porphyry dikes in the district have a similar age. Glomerophyric porphyry dikes clearly postdate the carbonate replacement sulfide event within the Stratoni fault zone and at the Olympias deposit; albeit, many of these dikes are incipiently altered, suggesting that they must have interacted with hydrothermal fluids of some unknown provenance. Other than a temporal relationship, it is unclear if the glomerophyric porphyry dikes share a genetic association with the Skouries stock and Au-Cu mineralization. Additional geochronological and geochemical investigations into the glomerophyric porphyry dike event may resolve this question, and contribute to the understanding of the tectonic evolution of early Miocene shoshonitic magmatism in the district.

Fluid flow and thermal modeling

Mineralogical zonation, metal distributions, stable isotopes, and minimum formation temperatures based on fluid inclusion data imply broad-scale hydrothermal fluid flow that extended for approximately 12 km from east to west along the Stratoni fault zone. Migration of a hydrothermal fluid through temperature or other physical gradient, such as pressure or salinity, drives chemical change and thus ore deposition (Cathles, 1997). The data presented in this study can be used as first-order constraints on a fluid flow-thermal model, in particular, what fluid volumes and velocities were necessary to satisfy the thermal budget of the hydrothermal system within the Stratoni fault zone. Understanding the fluid flow and thermal aspects of this hydrothermal system is of considerable value as it may provide insights into the implications and processes that are necessary for ore formation.

Tectonic and structural investigations

The Kerdilion detachment fault to the west of the Kassandra Mining District is widely considered the principal structure that initially controlled exhumation of the southern Rhodope core complex (Brun

and Sokoutis, 2007). Despite its tectonic importance, a detailed structural-kinematic study of the Kerdilion detachment fault is missing from the published literature. Previous studies have indicated that the Kerdilion detachment fault was active from about the Eocene to the late Oligocene (Brun and Sokoutis, 2007; Wüthrich, 2009; Kounov et al., 2015), overlapping in time with carbonate replacement mineralization within the Stratoni fault zone. However, the relationship between the Kerdilion and Stratoni faults has not been established. Additional work to include the Kerdilion detachment fault into a regional structural model is important for understanding its metallogenic contribution to the Kassandra Mining District and the broader region. While this study showed that the contact between the Vertiskos and Kerdilion units in the Kassandra Mining District is not a detachment fault, additional investigations into the structural relationship between these lithotectonic units is warranted as this contact bears regional tectonic implications.

Fluid inclusion microthermometric data (pressure-temperature and depth of formation estimates) from the carbonate replacement orebodies also provide interesting constraints on the rate of exhumation of the Kerdilion unit. Assuming that the late Oligocene (24-22 Ma) carbonate replacement bodies formed at a depth of approximately 4 km, then the mean exhumation rate would be about 0.17-0.18 mm/year. However, it is unlikely that this rate was constant through time and the controls on this exhumation rate, whether due to erosion or a combination of erosion and tectonic processes remains uncertain. Additional work incorporating microthermometric analyses and ^{40}Ar-^{39}Ar thermochronology from the Kassandra Mining District would contribute to the understanding of extensional tectonics in the Aegean region.

Detailed ore deposit investigations

Structural and geochronological data indicate that the carbonate replacement deposits are likely related to the late Oligocene magmatic event. The timing between carbonate replacement sulfide and the boulangerite-bearing quartz-rich sulfide phase and quartz-rhodochrosite vein-breccias is established through relative crosscutting relationships and ^{40}Ar-^{39}Ar geochronology. The imprecise 26.1 ± 5.3 Ma

arsenopyrite Re-Os age from the Olympias deposit is the only direct age of mineralization in the district (Hahn et al., 2012; Hahn, 2014), and a reevaluation of this age is warranted. Re-Os geochronology has been widely used to accurately and precisely determine the age of mineralization in deposits containing arsenopyrite (e.g., Stein et al., 2007). Since arsenopyrite occurs in association with each stage of carbonate replacement mineralization, including the quartz-rhodochrosite vein-breccias, it is therefore a permissive method that can be used to place additional constraints on the timing and duration of carbonate replacement mineralization.

The carbon and oxygen stable isotope results presented in this study confirmed that a large and structurally-focused hydrothermal system exploited the Stratoni fault zone with an isolated system in the Olympias area. Furthermore, this study contributed to the viability of Off-Axis Integrated Cavity Output Spectroscopy (OA-ICOS) and its implementation as an exploration tool for carbonate replacement deposits (e.g., Barker et al., 2013). However, a detailed carbon-oxygen isotope study in the Stratoni fault zone and at the Olympias deposit is recommended in order to provide the resolution necessary to map isotopic depletion patterns at the deposit-scale. This study may also identify areas of hydrothermal fluid input, thus providing vectoring data that can be used to inform near-mine exploration.

The reason for the highly anomalous concentration of Au in the Kassandra Mining District, whether due to an enriched source and/or efficient transport and trapping mechanisms, remains enigmatic and a fundamental unanswered question. At a more basic level, the nature and location of Au in the carbonate replacement sulfide deposits is largely unresolved. Chryssoulis and Cabri (1990), including a number of unpublished metallurgical reports, indicate that Au occurs in solid solution with pyrite, arsenical pyrite, and arsenopyrite at the Olympias deposit. However, the phase of sulfide ore investigated in these studies was not specified. A mineral chemistry study focused on the paragenetic timing and distribution of Au at the Mavres Petres and Olympias deposits may be fruitful in understanding the requisite geochemical and thermodynamic conditions that governed Au deportment and deposition, and

therefore, evolution of the carbonate replacement orebodies. This study would not only be of academic interest, but also of considerable value for exploration and metallurgical applications.

REFERENCES

Barker, S.L.L., Dipple, G.M., Hickey, K.A., Lepore, W.A., and Vaughan, J.R., 2013, Applying stable isotopes to mineral exploration: Teaching and old dog new tricks: Economic Geology, v. 108, p. 1-9.

Brun, J.P., and Sokoutis, D., 2007, Kinematics of the southern Rhodope core complex (North Greece): International Journal of Earth Science., v. 96, p. 1079-1099.

Cathles, L.M., 1997, Thermal aspects of ore formation, in Barnes, H.L., ed., Geochemistry of hydrothermal ore deposits, 3rd edition: John Wiley and Sons, New York, p. 191-227.

Cathles, L.M., and Shannon, R., 2007, How potassium silicate alteration suggests the formation of porphyry ore deposits begins with the nearly explosive but barren expulsion of large volumes of magmatic water: Earth and Planetary Science Letters, v. 262, p. 92-108.

Chiaradia, M., Schaltegger, U., Spikings, R., Wotzlaw, J.F., and Ovtcharova, M., 2013, How accurately can we date the duration of magmatic-hydrothermal events in porphyry systems?: Economic Geology, v. 108, p. 565-584.

Chryssoulis, S.L., and Cabri, L.J., 1990, Significance of gold mineralogical balances in mineral processing: Transactions of the Institution of Mining and Metallurgy, v. 99, p. C1-C10.

Dinter, D.A., 1998, Late Cenozoic extension of the Alpine collisional orogen, northeastern Greece: origin of the north Aegean basin: Geological Society of America Bulletin, v. 110, p. 1208-1230.

Dinter, D.A., Macfarlane, A., Hames, W., Isachsen, C., Bowring, S., and Royden, L., 1995, U-Pb and 40Ar/39Ar geochronology of the Symvolon granodiorite: implications for the thermal and structural evolution of the Rhodope metamorphic core complex, northeastern Greece: Tectonics, v. 14(4), p. 886-908.

Gilg, H.A., 1993, Geochronology (K-Ar), fluid inclusion, and stable isotope (C, H, O) studies of skarn, porphyry copper, and carbonate-hosted Pb-Zn (Ag, Au) replacement deposits in the Kassandra mining district (eastern Chalkidiki, Greece): Unpublished Ph.D. thesis, Zürich, Switzerland, ETH, 153 p.

Gilg, H.A., and Frei, R., 1994, Chronology of magmatism and mineralization in the Kassandra mining area, Greece: The potentials and limitations of dating hydrothermal illites: Geochimica et Cosmochimica Acta, v. 58, p. 2107-2122.

Hahn, A., 2014, Nature, timing and geodynamic context of polymetallic mineralisation in the Kassandra mining district, North Greece: Unpublished Ph.D. thesis, London, United Kingdom, Kingston University, 351 p.

Hahn, A., Naden, J., Treloar, P.J., Kilias, S.P., Rankin, A.H., and Forward, P., 2012. A new timeframe for the mineralization in the Kassandra mine district, N Greece: deposit formation during metamorphic core complex exhumation: European Mineralogical Conference, v. 1, 1EMC2012-742.

Haines, H.S., 1998, A structural synthesis for sector Vb of the Madem Lakkos polymetallic sulfide deposit – Northeast Greece: Unpublished M.Sc. thesis, London, United Kingdom, The University of London, 81 p.

Himmerkus, F., Reischmann, T., and Kostopoulos, D.K., 2009, Serbo-Macedonian revisited: a Silurian basement terrane from northern Gondwana in the Internal Hellenides, Greece: Tectonophysics v. 473, p. 20-35.

Kilias, S.P., Kalogeropoulos, S.I., and Konnerup-Madsen, J., 1996, Fluid inclusion evidence for the physicochemical conditions of sulfide deposition in the Olympias carbonate-hosted Pb-Zn(Au, Ag) sulfide ore deposit, E. Chalkidiki peninsula, N. Greece: Mineralium Deposita, v. 31, p. 394-406.

Kockel, F., Mollat, H., and Walther, H., 1977, Erläuterungen yur geologischen karte der Chalkidiki und agrenzender Gebiete 1:100000 (Nord-Griechenland): Bundesanstalt für Geowissenschaften Rohstoffe, Hannover, p. 1-119.

Kounov, A., Wüthrich, E., Seward, D., Burg, J.P., and Stockli, D., 2015, Low-temperature constraints on the Cenozoic thermal evolution of the southern Rhodope core complex (northern Greece): International Journal of Earth Science, v. 104, p. 1337-1352.

Pavlides, S.B., and Tranos, M.D., 1991, Structural characteristics of two strong earthquakes in the north Aegean: Ierissos (1932) and Agios Efstratios (1968): Journal of Structural Geology, v. 13, p. 205-214.

Pe-Piper, G., and Piper, D.J.W., 2006, Unique features of the Cenozoic igneous rocks of Greece, in Dilek, Y., and Pavlides, S., eds., Postcollisional tectonics and magmatism in the Mediterranean region and Asia: Geological Society of America Special Paper, v. 409, p. 259-282.

Proffett, J.M., 2003, Geology of the Bajo de la Alumbrera porphyry copper-gold deposit, Argentina: Economic Geology, v. 98, p. 1535-1574.

Richards, J.P., 2011, High Sr/Y arc magmas and porphyry Cu ± Mo ± Au deposits: Just add water: Economic Geology, v. 106, p. 1075-1081.

Stein, H. J., Yang, G., Zimmerman, A., Pandit, M.K., Raut, P.K., and Hannah, J.L., 2007, Re-Os dating of arsenopyrite: Panacea or problematic?: Geological Society of America Abstracts, v. 39, p. 276.

von Quadt, A., Erni, M., Martinek, K., Moll, M., Peytcheva, I., and Heinrich, C.A., 2011, Zircon crystallization and the lifetimes of ore-forming magmatic-hydrothermal systems: Geology, v. 39, p. 731-734.

Wüthrich, E., 2009, Low temperature thermochronology of the northern Aegean Rhodope Massif: Unpublished Ph.D. thesis, Zürich, Switzerland, ETH, 210 p.

APPENDIX I: METHODOLOGY

Zircon U-Pb geochronology

Samples were collected in the field from least altered and weakly weathered surface outcrops. Analyses were conducted at the Pacific Center for Isotopic and Geochemical Research (PCIGR) at the University of British Columbia in Vancouver, Canada. Sample preparation and U-Pb analytical methods are adapted from Tafti et al. (2009). Samples were pulverized using a conventional crushing and grinding circuit. Zircon separation was performed using a Wilfley gravity separation table, heavy liquid, and Frantz magnetic-separator techniques. Zircons greater than about 50 microns in diameter were hand-picked from the mineral separates and were mounted in a thermal-setting epoxy puck beside several grains of the 337.13 ± 0.13 Ma Plešovice zircon standard (Sláma et al., 2008) and the 416.78 ± 0.33 Ma Temora-2 reference zircon (Black et al., 2004). The zircon-embedded epoxy puck was brought to a high polish and the surface washed for 10 minutes with dilute nitric acid and rinsed in ultraclean water prior to analysis. Portions of the grains of the highest quality (e.g., little evidence for alteration, inclusions, or possible inherited cores) were selected for analysis. Each grain was imaged using cathodoluminescence to help guide analysis.

A laser ablation inductively coupled plasma mass spectrometer (LA-ICP-MS) was employed for U-Pb zircon analysis. Samples were mounted into a New Wave UP-213 laser ablation cell coupled with a Thermo Finnigan Element2 single collector, double-focusing, magnetic sector ICP-MS. A laser spot diameter of 30 µm was used at 42% power. Line scans rather than spot analyses were employed to minimize elemental fractionation during the analyses. Background data were measured with the laser shutter closed for ten seconds, followed by data collection with the laser firing for approximately 35 seconds. The time-integrated signals were analysed using Iolite software (Paton et al., 2011), which automatically subtracts background measurements, propagates all analytical errors, and calculates isotopic ratios and dates. Corrections for mass and elemental fractionation were made by bracketing analyses of unknown grains with replicate analyses of the Plešovice zircon standard. Final interpretation and plotting

of the analytical results employed the ISOPLOT v. 3.09 geochronological software of Ludwig (2003). Zircon U-Pb data is located in Table A1.

Whole-rock geochemistry

Eighty-five representative samples of Oligo-Miocene intrusive rocks were collected from surface and drill core for whole rock geochemistry. Least-altered samples were collected where possible; however, some show incipient alteration and weathering that may influence major element chemistry. Whole rock geochemical analyses were completed at Acme labs in Vancouver, British Columbia. Major and minor element analyses were determined by inductively coupled plasma mass spectroscopy (ICP-MS) and inductively coupled plasma optical emission spectroscopy (ICP-OES) after lithium metaborate and tetraborate fusion. Ferrous iron was measured by titration. Analytical accuracy and precision determined from internationally certified reference standards and duplicates, respectively, are within 5 relative percent for major oxides and within 10 relative percent for most minor and trace elements (calculation methods after Piercey, 2014). Whole-rock igneous geochemistry data is located in Tables A2 through A4.

Chapter 3

Structural analysis

Structural measurements were collected using a Brunton compass following the North American strike-dip and right-hand-rule convention. Structural data is presented on a lower-hemisphere, equal-area stereographic projection using Stereonet 9.5 software (Cardozo and Allmendinger, 2013) and contoured using the statistical method of Kamb (1959). Kinematic fault-strain structures were measured following the criteria defined in Nelson (2006). Fault kinematic data is similarly presented in a lower-hemisphere, equal-area stereographic projection using FaultKin 7.0 software (Allmendinger et al., 2012). The infinitesimal strain axes, determined from the statistical Bingham axial distributions, were calculated and

plotted for each fault population following the graphical kinematic method of Marrett and Allmendinger (1990). Structural orientation and fault-kinematic data is located in Tables A5 through A14.

Whole-rock geochemistry and principal component analysis

Whole-rock geochemical analyses of amphibolite samples were completed at Acme labs in Vancouver, British Columbia. Major and minor element analyses were determined by inductively coupled plasma mass spectroscopy (ICP-MS) and inductively coupled plasma optical emission spectroscopy (ICP-OES) after lithium metaborate and tetraborate fusion. Analytical accuracy and precision determined from internationally certified reference standards and duplicates, respectively, are within 5 relative percent for major oxides and within 10 relative percent for most minor and trace elements (calculation methods after Piercey, 2014). Whole-rock geochemistry data for amphibolites is located in Tables A15 and A16.

Immobile element geochemical data (Al, Nb, Nd, Th, Ti, Y, and Zr) from footwall and hanging wall amphibolites in outcrop and drill core have basaltic compositions based on the immobile element ratio classification diagram of Pearce (1996, 2014) (Figure A1A). The degree of similarity between both amphibolite populations was further investigated using principal component analysis. Principal component analysis is a variance-maximizing projection that transforms a set of variables into proportional linear combinations of orthogonal vectors (principal components) which systematically decrease in their degree of variance (Rollinson, 1993). The first two principal components of the seven calculated account for 81% of the explained variance in the data (Figure A1B) and are therefore considered adequate for the principal component interpretation (e.g., Jolliffe, 2002). The first principal component, representing a linear combination of variables with the highest variance, is completely overshadowed by the second principal component, which is represented by a combination of variables with the next highest degree of variance (Figure A1C). The overlapping relationship shown here indicates that the footwall and hanging wall amphibolite populations spanning the Stratoni fault zone display a high level of similarity, and thus are interpreted to be of like origin.

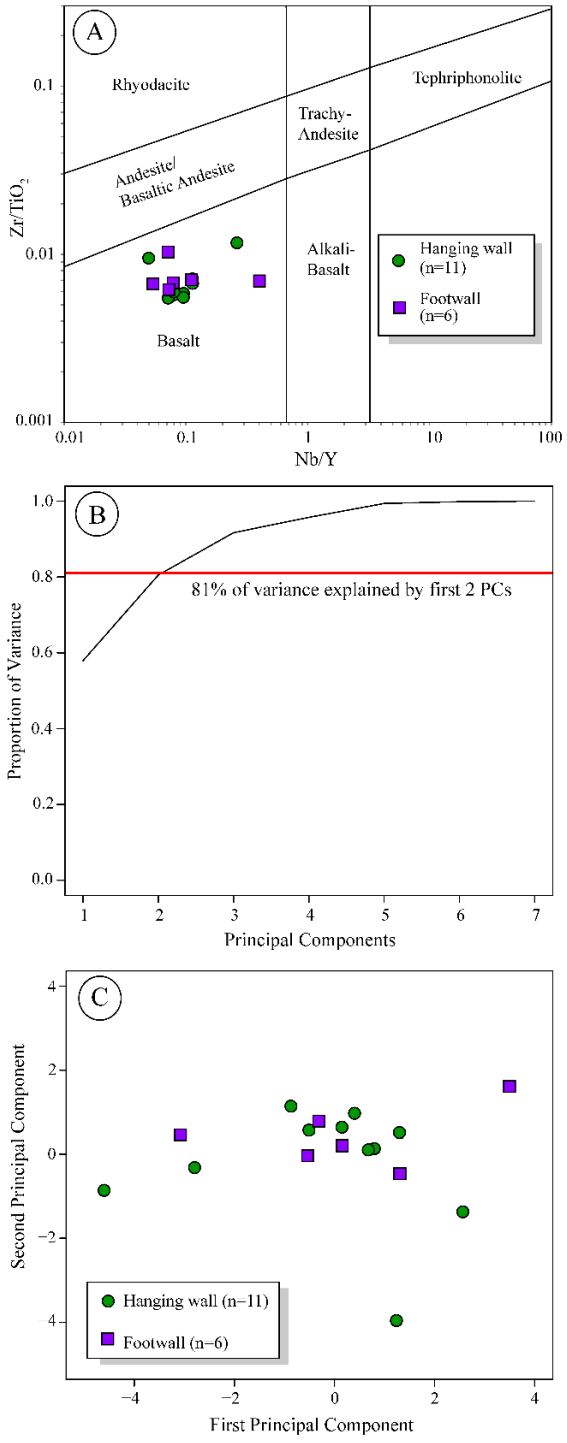

Figure A1. Amphibolite trace element geochemical data: (A) representative footwall (square) and hanging wall (circle) amphibolite samples from the Stratoni fault zone plotted on an immobile element-based discrimination diagram modified after Pearce (1996, 2014); (B) scree plot explaining the percent variance for each of the principal components (PCs). The first two principal components represent a proportion of the variance (81%) as indicated by the horizontal red line; (C) plot of first and second principal components showing the overlap in the footwall and hanging wall amphibolite populations.

^{40}Ar-^{39}Ar geochronology

Samples were prepared and analysed at the ^{40}Ar-^{39}Ar geochronology laboratory at the University of Manitoba in Winnipeg, Canada. The ^{40}Ar-^{39}Ar analytical work in this study was performed using a multi-collector Thermo Fisher Scientific ARGUS VI mass spectrometer, linked to a stainless steel Thermo Fisher Scientific extraction/purification line and Photon Machines (55 W) Fusions 10.6 CO_2 laser. Argon isotopes (with atomic mass ranging from 40 to 37) were measured using Faraday detectors with low-noise (1×10^{12} Ω) resistors. Argon with atomic mass of 36 was measured using a compact discrete dynode detector. The sensitivity for argon measurements is ~6.312×10^{17} moles/fA as determined from measured aliquots of the Fish Canyon Sanidine (Dazé et al., 2003; Kuiper et al., 2008).

Standard and unknown samples were placed into 2 mm-deep wells within 18 mm-diameter aluminium disks, with standards placed strategically so that the lateral neutron flux gradients across the disk could be evaluated. Planar regressions were fit to the standard data and the ^{40}Ar-^{39}Ar neutron fluence parameter (J) was interpolated for the unknown samples. Uncertainties in J are estimated at 0.1 - 0.2% (1s) based on Monte Carlo error analysis of the planar regressions (Best et al., 1995). All specimens were irradiated in the Cadmium-lined, in-core (CLICIT) facility of the Oregon State University TRIGA reactor. Unknown samples, including the Fish Canyon sanidine (Kuiper et al., 2008) and GA1550 biotite (Spell & McDougall, 2003) standards, were irradiated for 7 hours.

Irradiated samples were placed in a Cu sample tray, with a KBr cover slip, and introduced into a stainless steel high-vacuum extraction line and baked with an infrared lamp for 24 hours. Single crystals were either fused or step-heated using the laser. Reactive gases were removed after ~ 3 minutes by three GP-50 SAES getters (two at room temperature and one at 450 °C) prior to being admitted by expansion into an ARGUS VI mass spectrometer. Five argon isotopes were measured simultaneously over a period of 6 minutes. Measured isotope abundances were corrected for extraction-line blanks, which were determined before every sample analysis. Line blanks averaged ~4 fA for atomic mass 40 and ~0.015 fA for atomic mass 36.

Mass discrimination, monitored by online analysis of air pipettes, resulted in a mean D = 1.01312 ± 0.00109 per atomic mass unit based on 28 aliquots interspersed with the unknown samples. A value of 295.5 was used for the atmospheric ^{40}Ar-^{36}Ar ratio (Steiger and Jaëger, 1977) for the purposes of routine measurement of mass spectrometer discrimination using air aliquots, and correction for atmospheric argon in the ^{40}Ar-^{39}Ar age calculation. Corrections are made for neutron-induced ^{40}Ar from potassium, ^{39}Ar and ^{36}Ar from calcium, and ^{36}Ar from chlorine (Roddick, 1983; Renne et al., 1998; Renne and Norman, 2001). Geochronological ^{40}Ar-^{39}Ar data is located in Table A17.

Chapter 4

Fluid inclusion microthermometry

Microthermometric analyses were performed on 7 doubly polished ~200 μm-thick quartz wafers utilizing a Linkham THMS600 heating-freezing stage mounted to a Leica DM750 transmitted light polarizing microscope located at the State University of New York at Cortland. The instrument was calibrated to temperatures ranging from -56.6ºC and 573.0ºC using the internationally recognized FLUID Incorporated synthetic fluid inclusions standards. Accuracy of the thermometric measurements are believed to be within ± 0.3ºC. Microthermometric measurements were only conducted on fluid inclusions that occur in isolation, within isolated clusters, those defining crystal growth zones, or ones that contain an optically observable solid. The inclusions that meet these criteria are considered primary in origin and suitable for analysis (Roedder, 1984). Salinities for inclusions within the system NaCl-H_2O were calculated based on based on the equation of Bodnar (1993) which is reliable for temperatures between -21.2ºC, the eutectic temperature for the system NaCl-H_2O, and 0.0ºC. Salinities based on final clathrate melting temperatures for fluid inclusions in the system H_2O-CO_2-NaCl were calculated based on the equation of Darling (1991). Fluid inclusion microthermometric data is located in Table A18.

Coupled carbon-oxygen isotopes

A total of 234 carbonate mineral samples were collected from 18 drill holes from the Olympias, Madem Lakkos and Mavres Petres deposits, and the Piavitsa prospect. Sampling targeted marble host-rock that appeared visibly unaltered and distal from known mineralization and hydrothermal alteration to establish a local background value. Marble immediately adjacent to sulfide and stylolitic fluid escape structures were sampled, as with carbonate gangue associated with replacement- and skarn-related sulfide, and carbonate from late-stage quartz-rhodochrosite vein and vein breccias. Carbonate mineralogy for each sample was qualitatively determined using the carbonate staining method of Hitzman (1999).

Carbon and oxygen stable isotope analysis employed a laser absorption technique that utilized an Off-Axis Integrated Cavity Output Spectroscopy (OA-ICOS) CO_2 isotope analyzer located at the University of British Columbia in Vancouver, B.C., Canada. Implementation of the OA-ICOS instrument and comparisons with conventional Isotope Ratio Mass Spectrometer is described in Barker et al. (2011) and Beinlich et al. (2017). Sample preparation and analytical procedures follow the methodology prescribed by Barker et al. (2011). Data was corrected based on an experimentally determined CO_2 concentration factor derived from calibrated in-house calcite standards. and not corrected for fractionation due to varying carbonate mineralogy. Analysis of internationally recognized reference materials and internal lab standards allowed isotope ratio values to be converted into conventional delta notation. Calculated $\delta^{13}C$ and $\delta^{18}O$ values are reported as per mil ($^{o}/_{oo}$) and standardized relative to the Vienna Peedee Belemnite (VPDB) and the Vienna Standard Mean Ocean Water (VSMOW), respectively (Coplen, 1994). Analytical accuracy based on repeat analyses of in-house and internationally recognized standards average $0.23^{o}/_{oo}$ for $\delta^{13}C$ and $0.38^{o}/_{oo}$ for $\delta^{18}O$. Carbon and oxygen isotope data is located in Table A19.

Theory and calculations used in the construction of isotope models: Carbon and oxygen stable isotope data are described through isotopic exchange mechanisms controlled by fluid-rock interaction and decarbonation reactions (Bowman et al., 1994; Baumgartner and Valley, 2001; Bowman, 1998). Release

of CO_2 due to decarbonation or volatilization within a carbonate reservoir results in isotopic depletion of the original carbonate rock by equilibrium batch and Rayleigh decarbonation processes (Valley, 1986; Baumgartner and Valley, 2001; Bowman, 1998). Batch decarbonation is a single-stage process where exsolved volatiles isotopically equilibrate with the rock before any fraction is permitted to escape the system. In most natural systems, large volume increases resulting from volatile release would require fluids to continuously escape, therefore, suggesting that equilibrium decarbonation following a batch model is unlikely (Baumgartner and Valley, 2001). Rayleigh decarbonation, however, describes open-system behavior where volatiles are steadily removed from the system as a result of continuous expulsion. While larger $\delta^{13}C$ and $\delta^{18}O$ depletions will result from Rayleigh decarbonation, both processes will only produce approximately 4‰ to 2‰ $\delta^{18}O$ depletion in carbonate rocks (Bowman, 1998).

Isotopic exchange will also result from the infiltration of hydrothermal fluids into a carbonate reservoir described by fluid-rock interaction processes (Taylor, 1971, 1979). Chemical exchange between isotopically distinct reservoirs may produce significant shifts in $\delta^{13}C$ and $\delta^{18}O$ from the original isotopic composition of the carbonate rock. The degree of isotopic depletion requires disequilibrium between the carbonate rocks and the infiltrating fluid (Nabelek, 1987), but also depends on temperature during exchange and the composition of the hydrothermal fluid. Carbonate rocks that interact with large volumes of fluid (e.g., high water-rock ratios) at high temperatures generally show large depletions in $\delta^{18}O$ relative to the original rock composition. Carbon isotopes, however, display a narrower range of values compared to oxygen due to the lower relative abundance of carbon with respect to oxygen within most hydrothermal fluids (Barker et al., 2013).

The mass-balance equation of Valley (1986) and Bowman (1998) was used to calculate the final isotopic composition of calcite resulting from batch CO_2 decarbonation (Eqation 1), whereas a modified version of the Rayleigh equation (Rumble, 1982; Bowman, 1998) was used to model the effects of continuous (Rayleigh) CO_2 decarbonation (Eqation 2). The notations δ_{Cc}^{i} and δ_{Cc}^{f} correspond to the initial

and final δ values of the calcite before and after decarbonation, respectively, and F is the fraction of the element, carbon or oxygen, remaining in the system.

Equation 1. $$\delta_{Cc}^{f} = \delta_{Cc}^{i} - 10^{3} ln\alpha_{(CO_2-Cal)}(1-F)$$

Equation 2. $$\delta_{Cc}^{f} = (\delta_{Cc}^{i} + 10^{3})F^{(\alpha_{CO_2-Cal}-1)} - 10^{3}$$

Isotopic exchange resulting from fluid-rock interaction processes is described by the conventional water (W)–rock (R) ratio mass-balance equation (Eqation 3) of Taylor (1971, 1974, and 1979). The notations δ_R^i and δ_R^f correspond to the initial and final δ value of the rock, respectively, where the $\delta_{H_2O}^f$ notation represents the final δ value of the water. The Δ operator is proportional to the expression $\delta_R^f - \delta_{H_2O}^f$ and is a function of temperature given the relationship in Equation 4. The water-rock mass balance equation is a powerful tool that can be used to interpret the volume of water that has interacted with hydrothermally altered rock. Bowman (1998) shows a modified version of this equation that is solved for $\delta_{H_2O}^f$ and used for the purposes of interpreting the evolution of hydrothermal fluids resulting from fluid-rock interaction. This equation was solved algebraically for δ_{Cc}^f (Equation 5) in order to calculate the final isotopic composition of calcite resulting from fluid-rock interaction.

Equation 3. $$\frac{W}{R} = \frac{\delta_R^f - \delta_R^i}{\delta_{H_2O}^f - (\delta_R^f - \Delta)}$$

Equation 4. $$\Delta = \delta_R^f - \delta_{H_2O}^f \cong 10^3 ln\alpha_{R-H_2O}$$

Equation 5. $$\delta_{Cc}^f = \frac{\left(\frac{W}{R}\right)\left(\frac{C_{H_2O}}{C_R}\right)\delta_{H_2O}^i + (10^3 ln\alpha_{R-W}^j)\left(\frac{W}{R}\right)\left(\frac{C_{H_2O}}{C_R}\right) + \delta_R^i}{\left(\frac{W}{R}\right)\left(\frac{C_{H_2O}}{C_R}\right) + 1}$$

The ratio $\left(\frac{W}{R}\right)$ is the relative proportion of water to rock in the system and the ratio $\left(\frac{C_{H_2O}}{C_R}\right)$ corresponds to the relative carbon or oxygen concentration in the water (C_{H2O}) to that of the rock (C_R). The notation $\delta^i_{H_2O}$ is the initial δ value of the water. The expression α^j_{R-W} represents the fractionation factor between rock and water for carbon or oxygen as represented by the *j* term. The mass-balance equations described above used the oxygen equilibrium fractionation factors for the system calcite-water (O'Neil et al., 1969; Friedman and O'Neil, 1977) and the system CO_2-calcite (Bottinga, 1968) with the carbon equilibrium fractionation factor for the system CO_2-calcite (Ohmoto and Rye, 1979). Each of these fractionation factors are valid for temperatures below 600°C and are considered suitable for use in this study as supported by the range of minimum trapping temperatures measured from fluid inclusions.

Lead isotopes

Lead isotope geochemistry was performed on K-feldspar separates from igneous rocks of late Paleocene to early Miocene age, as determined from zircon U-Pb geochronology. Igneous samples were collected by the author from surface outcrops that have experienced limited effects of alteration and/or weathering. Lead isotope geochemistry was also performed on sulfide minerals including galena, pyrite, and boulangerite from underground exposures (Mavres Petres and Olympias deposits) and drill core intercepts of massive sulfide and quartz-rhodochrosite veins. Sample preparation and analyses were conducted at the Pacific Center for Isotopic and Geochemical Research at the University of British Columbia in Vancouver, B.C. Canada by Dr. Janet Gabites.

Feldspar crystals for trace Pb analysis were hand-picked to total 10-50 mg of sample, which was then leached in dilute hydrochloric acid followed by dilute hydrofluoric/hydrobromic acid to remove surface contamination before dissolution in hydrofluoric acid. Trace Pb analysis of sulfide samples were prepared from 1-20 mg of hand-picked sulfide crystals, which were then leached in dilute nitric acid followed by hydrochloric acid to remove surface contamination before dissolution in dilute nitric acid.

Separation and purification of Pb employed ion exchange column techniques. The dissolved feldspar Pb samples were dried, converted into a chloride complex, and then dissolved in dilute hydrobromic acid. This solution was passed through ion exchange columns where the Pb was eluted in 6N hydrochloric acid. Sulfide crystals were dissolved to dryness in 2N hydrochloric acid, converted into a chloride complex, and washed with 4N hydrochloric acid. The Pb-chloride solution was then re-dried. Approximately 10-25 ng of P-chloride sample was loaded on a rhenium filament using a phosphoric acid-silica gel emitter, and isotopic compositions were determined in peak-switching mode using a modified VG54R thermal ionization mass spectrometer. The measured Pb ratios were corrected for instrumental mass fractionation of 0.08% per amu (Faraday collector) based on repeated measurements of the Standard Isotopic Reference Material NBS-981 and the values in Thirlwall (2000). Errors were numerically propagated including all mass fractionation and analytical uncertainty using the technique of Roddick (1987). All errors are quoted at the 2σ level. The total procedural blank of 64 pg with Pb ratios of 18.2 ($^{206}Pb/^{204}Pb$), 15.5 ($^{207}Pb/^{204}Pb$), and 37.4 ($^{208}Pb/^{204}Pb$) was used for trace Pb chemistry. Lead isotope data is located in Table A20.

APPENDIX II: DATA TABLES

Table A1. Zircon U-Pb LA-ICP-MS analyses for igneous rocks from the Kassandra Mining District

	Isotopic Ratios					Isotopic Ages (Ma)				Background Corrected Mean Counts Per Second							
No.	$^{207}Pb/^{235}U$	2σ	$^{206}Pb/^{238}U$	2σ	ρ	$^{207}Pb/^{235}U$	2σ	$^{206}Pb/^{238}U$	2σ	^{202}Hg	^{204}Pb	^{206}Pb	^{207}Pb	^{208}Pb	^{232}Th	^{235}U	^{238}U
593870 Tsikara Stock																	
Latitude 40.46173, Longitude 23.72401																	
1	0.0251	0.0014	0.00417	0.00011	0.03	25.1	1.4	26.9	0.7	54	-21	4173	186	2020	408965	6633	889959
2	0.0280	0.0016	0.00434	0.00012	0.14	27.9	1.6	27.9	0.8	35	-14	3695	181	1653	347065	5785	757456
3	0.0273	0.0020	0.00432	0.00015	0.16	27.3	1.9	27.8	1.0	66	23	5142	240	1796	389023	7927	1051812
4	0.0279	0.0019	0.00422	0.00013	0.03	28.0	1.9	27.1	0.8	29	22	3734	181	1529	313871	6087	790761
5	0.0280	0.0023	0.00429	0.00014	0.08	27.9	2.2	27.6	0.9	5	6	2354	116	874	182595	3756	487711
6	0.0260	0.0015	0.00419	0.00011	0.10	26.0	1.5	27.0	0.7	22	-2	3492	169	1662	338934	5680	744674
7	0.0266	0.0020	0.00416	0.00012	0.06	26.6	2.0	26.8	0.7	14	9	6242	314	2901	593796	9946	1292610
8	0.0259	0.0016	0.00418	0.00011	0.07	25.9	1.5	26.9	0.7	37	3	3328	152	1159	248436	5417	700692
9	0.0271	0.0017	0.00427	0.00012	0.01	27.1	1.6	27.5	0.8	46	11	3153	144	984	212810	4996	649696
10	0.0268	0.0013	0.00411	0.00010	0.13	26.8	1.3	26.4	0.6	-3	8	5478	271	3175	689871	8938	1187587
11	0.0244	0.0026	0.00399	0.00015	0.04	24.3	2.6	25.7	1.0	20	-16	1298	60	497	98830	2109	286026
12	0.0280	0.0021	0.00420	0.00011	0.11	27.9	2.1	27.0	0.7	44	43	3764	184	1703	375769	6050	787382
13	0.0307	0.0019	0.00418	0.00013	0.03	30.6	1.8	26.9	0.9	116	11	5121	269	2563	519068	8352	1076264
14	0.0264	0.0015	0.00417	0.00012	0.05	26.3	1.5	26.9	0.7	14	19	3617	169	1731	372759	5999	779035
15	0.0270	0.0019	0.00419	0.00012	0.19	26.9	1.9	26.9	0.8	-6	6	2936	142	977	222613	4737	620338
16	0.0250	0.0014	0.00410	0.00011	0.01	25.0	1.4	26.4	0.7	8	-2	4433	198	2099	437467	7346	962565
17	0.0276	0.0018	0.00427	0.00012	0.06	27.5	1.8	27.5	0.8	-15	-7	3066	148	1281	261148	4913	639499
18	0.0265	0.0023	0.00410	0.00015	0.12	26.5	1.5	26.4	1.0	30	10	5873	281	3185	678707	9674	1288768
593871 Tsikara Stock																	
Latitude 40.45619, Longitude 23.72926																	
1	0.0278	0.0038	0.00395	0.00022	0.02	27.5	3.7	25.4	1.4	7	1	1111	58	223	31357	1004	128334
2	0.8240	0.0570	0.09800	0.00440	0.46	610.0	32.0	602.0	26.0	36	-5	52520	3206	5997	34509	1960	258432
3	0.0320	0.0049	0.00413	0.00031	0.04	31.8	4.8	26.5	2.0	13	10	1553	84	225	33051	1401	180775
4	0.0270	0.0019	0.00407	0.00017	0.11	27.0	1.9	26.2	1.1	43	24	12093	579	4592	601031	11790	1466426
5	0.0274	0.0018	0.00410	0.00017	0.48	27.4	1.8	26.4	1.1	23	7	29022	1418	14615	2055165	28244	3536114

Table A1. Zircon U-Pb LA-ICP-MS analyses for igneous rocks from the Kassandra Mining District

	Isotopic Ratios					Isotopic Ages (Ma)				Background Corrected Mean Counts Per Second							
No.	$^{207}Pb/^{235}U$	2σ	$^{206}Pb/^{238}U$	2σ	ρ	$^{207}Pb/^{235}U$	2σ	$^{206}Pb/^{238}U$	2σ	^{202}Hg	^{204}Pb	^{206}Pb	^{207}Pb	^{208}Pb	^{232}Th	^{235}U	^{238}U
6	0.0282	0.0029	0.00436	0.00022	0.15	28.1	2.9	28.0	1.4	42	12	2721	126	752	97156	2480	319831
7	0.0261	0.0023	0.00407	0.00019	0.08	26.1	2.3	26.2	1.2	31	27	3442	165	1191	170206	3462	441641
8	0.0245	0.0019	0.00416	0.00019	0.12	24.7	1.9	26.8	1.2	36	22	4995	225	2198	317100	5160	642319
9	0.0260	0.0023	0.00417	0.00019	0.11	26.1	2.3	26.9	1.2	41	38	3628	167	1034	150538	3680	468561
10	0.0384	0.0025	0.00615	0.00026	0.56	38.2	2.4	39.5	1.6	79	11	39153	1820	1436	154372	27414	3454994
11	0.0277	0.0031	0.00431	0.00021	0.08	27.5	3.1	27.7	1.4	11	15	1640	78	632	90451	1789	230068
12	0.0283	0.0022	0.00438	0.00019	0.14	28.3	2.2	28.2	1.2	28	22	5828	283	2193	343784	6438	812255
13	0.4160	0.0270	0.05420	0.00220	0.39	352.0	20.0	340.0	13.0	39	8	30539	1720	1650	18359	2719	346518
14	0.2850	0.0190	0.03960	0.00160	0.32	255.0	15.0	250.0	10.0	39	6	14592	770	2190	36556	1818	228226
15	0.0303	0.0037	0.00411	0.00023	0.08	30.0	3.6	26.5	1.5	24	24	1161	63	264	45211	1370	172505
16	0.0277	0.0020	0.00414	0.00017	0.14	27.7	2.0	26.7	1.1	-10	2	6817	339	2960	470286	7850	1023108
17	0.0276	0.0024	0.00411	0.00018	0.02	28.0	2.3	26.4	1.2	53	15	3818	184	1597	273316	4538	576281
18	0.0267	0.0018	0.00407	0.00017	0.26	26.8	1.8	26.2	1.1	27	0	16928	801	9044	1593787	20114	2592467
19	0.0271	0.0026	0.00408	0.00020	0.06	27.0	2.6	26.3	1.3	30	6	2860	137	949	162344	3444	440176
20	0.0268	0.0033	0.00405	0.00021	0.06	26.6	3.2	26.1	1.4	35	15	1890	93	508	84531	2231	293770
593882 Tsikara Stock																	
Latitude 40.43350, Longitude 23.72673																	
1	0.0277	0.0009	0.00428	0.00009	0.32	27.8	0.9	27.5	0.6	65	18	19160	939	9748	1929975	28790	3798131
2	0.0263	0.0010	0.00416	0.00010	0.15	26.3	1.0	26.8	0.6	23	-2	12379	586	6048	1275906	19160	2533268
3	0.0265	0.0009	0.00419	0.00009	0.18	26.5	0.9	26.9	0.6	36	-1	12745	603	5384	1144083	19794	2608407
4	0.0272	0.0012	0.00413	0.00010	0.20	27.3	1.2	26.6	0.7	77	5	7749	376	3253	625170	12083	1631500
5	0.0281	0.0011	0.00418	0.00010	0.15	28.1	1.1	26.9	0.6	54	5	9226	465	3696	785187	14518	1904546
6	0.0272	0.0012	0.00414	0.00009	0.25	27.2	1.2	26.6	0.6	60	11	12531	608	5790	1281189	19853	2597589
7	0.0271	0.0009	0.00421	0.00009	0.19	27.1	0.9	27.1	0.6	71	2	14134	685	5683	1181111	21890	2884418
8	0.0276	0.0009	0.00412	0.00009	0.23	27.6	0.9	26.5	0.6	45	4	15934	777	6779	1384704	24764	3280406
9	0.0275	0.0009	0.00411	0.00009	0.30	27.6	0.9	26.5	0.6	97	10	18160	895	8500	1807289	28314	3729511
10	0.0276	0.0012	0.00431	0.00010	0.19	27.6	1.1	27.7	0.6	9	-21	8150	384	3344	681818	12567	1658076

Table A1. Zircon U-Pb LA-ICP-MS analyses for igneous rocks from the Kassandra Mining District

	Isotopic Ratios					Isotopic Ages (Ma)				Background Corrected Mean Counts Per Second							
No.	$^{207}Pb/^{235}U$	2σ	$^{206}Pb/^{238}U$	2σ	ρ	$^{207}Pb/^{235}U$	2σ	$^{206}Pb/^{238}U$	2σ	^{202}Hg	^{204}Pb	^{206}Pb	^{207}Pb	^{208}Pb	^{232}Th	^{235}U	^{238}U
11	0.0280	0.0011	0.00428	0.00010	0.13	28.0	1.0	27.5	0.6	33	1	9765	477	4160	860935	15057	1961334
12	0.0265	0.0010	0.00422	0.00009	0.29	26.6	1.0	27.1	0.6	3	2	12281	562	5026	1093070	19122	2489737
13	0.0268	0.0011	0.00410	0.00009	0.15	26.8	1.1	26.4	0.6	10	9	6283	301	2485	519591	10106	1329100
14	0.0277	0.0011	0.00421	0.00009	0.23	27.7	1.0	27.1	0.6	11	11	12883	630	5362	1088462	20525	2699534
15	0.0269	0.0018	0.00418	0.00010	0.21	27.0	1.2	26.9	0.7	35	5	19986	963	12287	2591243	31465	4199781
16	0.0260	0.0008	0.00417	0.00009	0.17	26.0	0.8	26.8	0.6	25	-9	14689	674	6653	1405344	23387	3112934
17	0.0294	0.0012	0.00419	0.00009	0.25	29.4	1.2	27.0	0.6	4	47	14181	752	7226	1454132	21988	2931370
279446 Fisoka Stock																	
Latitude 40.49469, Longitude 23.79155																	
1	0.0257	0.0013	0.00385	0.00009	0.41	25.7	1.3	24.8	0.6	-54	-5	7197	341	1202	187193	6032	774608
2	0.0246	0.0010	0.00379	0.00009	0.28	24.7	1.0	24.4	0.6	6	0	10410	484	1674	254841	8825	1131185
3	0.0251	0.0012	0.00381	0.00009	0.30	25.1	1.2	24.5	0.6	1	18	8164	384	1293	211206	7045	889746
4	0.0260	0.0018	0.00386	0.00016	0.31	26.1	1.8	24.8	1.0	-3	-13	7992	377	1150	177001	6574	846784
5	0.0250	0.0010	0.00377	0.00010	0.34	25.1	1.0	24.3	0.7	-37	-12	15938	745	2625	444551	13862	1759829
6	0.0253	0.0011	0.00374	0.00009	0.47	25.3	1.1	24.1	0.6	15	-13	12430	606	2218	371445	11160	1410974
7	0.0255	0.0011	0.00377	0.00010	0.36	25.6	1.1	24.3	0.6	1	-9	9541	472	1505	249171	8552	1083740
8	0.0247	0.0012	0.00376	0.00010	0.23	24.7	1.1	24.2	0.7	-18	-2	7153	335	1171	183521	6413	803941
9	0.0259	0.0016	0.00387	0.00015	0.34	25.9	1.6	24.9	1.0	11	-1	9339	452	1538	235591	7982	1024883
10	0.0245	0.0010	0.00378	0.00008	0.37	24.5	1.0	24.3	0.5	-13	-8	13296	623	2519	382994	11784	1503430
11	0.0237	0.0011	0.00373	0.00009	0.24	23.9	1.0	24.0	0.6	2	8	9267	421	1493	236589	8406	1068432
12	0.0259	0.0011	0.00379	0.00009	0.09	25.9	1.1	24.4	0.6	-30	-1	8488	411	1352	213134	7435	960477
13	0.0242	0.0010	0.00379	0.00008	0.38	24.3	1.0	24.4	0.5	-42	4	11269	523	1907	321389	10057	1291714
14	0.0258	0.0010	0.00387	0.00008	0.35	25.8	1.0	24.9	0.5	10	6	13075	636	2981	462162	11912	1480250
15	0.0238	0.0010	0.00382	0.00008	0.16	23.9	1.0	24.6	0.5	-34	-1	8894	404	1559	241208	7770	1005207
16	0.0236	0.0015	0.00391	0.00014	0.23	23.6	1.5	25.2	0.9	-25	16	7516	333	1223	195886	6532	853305
17	0.0253	0.0011	0.00385	0.00010	0.33	25.4	1.1	24.8	0.7	-5	9	8752	408	1390	237663	7821	992237
18	0.0236	0.0011	0.00385	0.00010	0.28	23.6	1.1	24.8	0.7	32	11	8216	372	1190	204495	7246	944427

Table A1. Zircon U-Pb LA-ICP-MS analyses for igneous rocks from the Kassandra Mining District

	Isotopic Ratios					Isotopic Ages (Ma)				Background Corrected Mean Counts Per Second							
No.	$^{207}Pb/^{235}U$	2σ	$^{206}Pb/^{238}U$	2σ	ρ	$^{207}Pb/^{235}U$	2σ	$^{206}Pb/^{238}U$	2σ	^{202}Hg	^{204}Pb	^{206}Pb	^{207}Pb	^{208}Pb	^{232}Th	^{235}U	^{238}U
19	0.0255	0.0012	0.00381	0.00010	0.27	25.6	1.2	24.5	0.7	-22	9	7296	356	1176	204732	6399	837799
20	0.0248	0.0012	0.00379	0.00009	0.33	24.8	1.2	24.4	0.6	41	13	6917	333	1132	178680	6398	813347
679714 Stratoni Stock (Aspro Chomata)																	
Latitude 40.52982, Longitude 23.82598																	
1	0.0256	0.0014	0.00406	0.00010	0.09	25.7	1.4	26.1	0.6	33	17	4078	184	975	149786	3531	451007
2	0.0264	0.0017	0.00407	0.00011	0.26	26.4	1.7	26.2	0.7	9	13	4724	223	1239	207820	4101	520077
3	0.0267	0.0017	0.00414	0.00013	0.11	26.7	1.7	26.6	0.8	-23	18	3952	184	783	119010	3421	429533
4	0.0245	0.0016	0.00402	0.00011	0.11	24.6	1.6	25.8	0.7	25	19	4051	182	1054	169118	3501	446201
5	0.0246	0.0016	0.00384	0.00011	0.09	24.7	1.6	24.7	0.7	27	18	3211	143	749	124686	2928	366972
6	0.0254	0.0014	0.00409	0.00011	0.15	25.5	1.4	26.3	0.7	7	7	7683	356	703	136676	6697	847600
7	0.0257	0.0016	0.00398	0.00010	0.09	25.7	1.6	25.6	0.7	-13	17	4860	224	1261	200664	4253	544623
8	0.0251	0.0013	0.00389	0.00009	0.27	25.2	1.2	25.0	0.6	-32	8	6602	312	1337	214526	5960	764871
9	0.0261	0.0017	0.00403	0.00011	0.16	26.1	1.6	25.9	0.7	15	12	3598	164	858	135748	3187	401340
10	0.0255	0.0015	0.00394	0.00011	0.17	25.6	1.5	25.3	0.7	4	8	3970	183	689	116546	3444	443887
11	0.0254	0.0013	0.00379	0.00010	0.22	25.5	1.3	24.4	0.6	34	-3	9794	462	1850	322018	9132	1153425
12	0.0247	0.0021	0.00389	0.00017	0.22	24.9	2.1	25.0	1.1	18	6	2901	137	675	110863	2622	336475
13	0.0248	0.0013	0.00371	0.00009	0.20	24.8	1.3	23.9	0.6	12	5	5504	264	1076	183219	5203	666731
14	0.0259	0.0011	0.00402	0.00009	0.28	26.0	1.1	25.8	0.6	10	16	8990	426	1726	268651	7938	1011065
15	0.0251	0.0013	0.00378	0.00009	0.29	25.1	1.3	24.3	0.6	30	2	6152	289	1015	177195	5661	720101
16	0.0255	0.0013	0.00382	0.00010	0.19	25.5	1.3	24.6	0.6	14	10	7138	335	1091	183408	6523	825653
17	0.0247	0.0014	0.00374	0.00010	0.04	24.7	1.4	24.1	0.6	25	-25	8126	387	1534	262420	7586	968975
18	0.0247	0.0018	0.00376	0.00011	0.13	24.7	1.8	24.2	0.7	-7	2	4797	225	1214	223121	4457	581764
19	0.0246	0.0014	0.00386	0.00011	0.23	24.7	1.4	24.8	0.7	22	-14	5354	252	886	163067	4956	631798
20	0.0259	0.0022	0.00402	0.00018	0.49	25.9	2.2	25.8	1.2	18	7	5794	272	976	169978	5071	664215

Table A1. Zircon U-Pb LA-ICP-MS analyses for igneous rocks from the Kassandra Mining District

	Isotopic Ratios					Isotopic Ages (Ma)				Background Corrected Mean Counts Per Second							
No.	$^{207}Pb/^{235}U$	2σ	$^{206}Pb/^{238}U$	2σ	ρ	$^{207}Pb/^{235}U$	2σ	$^{206}Pb/^{238}U$	2σ	^{202}Hg	^{204}Pb	^{206}Pb	^{207}Pb	^{208}Pb	^{232}Th	^{235}U	^{238}U
593580 Stratoni Stock																	
Latitude 40.51717, Longitude 23.81934																	
1	0.0254	0.0011	0.00394	0.00010	0.23	25.5	1.1	25.3	0.7	29	4	7875	355	1332	217813	7687	947040
2	0.0248	0.0011	0.00397	0.00010	0.41	24.8	1.1	25.5	0.6	-23	27	7276	318	1169	212482	7007	887890
3	0.0259	0.0014	0.00382	0.00012	0.19	25.9	1.4	24.6	0.8	-4	4	4345	208	799	143189	4328	541349
4	0.0258	0.0019	0.00391	0.00017	0.34	25.8	1.8	25.2	1.1	-4	-4	6745	333	1249	199727	6773	855098
5	0.0266	0.0017	0.00399	0.00013	0.21	26.6	1.7	25.7	0.8	3	1	5556	260	931	147886	5408	673567
6	0.0252	0.0015	0.00383	0.00011	0.25	25.3	1.5	24.7	0.7	-2	16	8309	364	1319	247668	8287	1029549
7	0.0253	0.0010	0.00395	0.00009	0.26	25.3	1.0	25.4	0.6	8	3	7614	348	1313	222006	7304	919356
8	0.0255	0.0017	0.00382	0.00013	0.25	25.6	1.6	24.6	0.8	13	23	7097	344	1157	214641	7319	915898
9	0.0255	0.0010	0.00391	0.00009	0.24	25.5	1.0	25.2	0.6	31	-3	8758	405	1427	255418	8615	1073182
10	0.0267	0.0021	0.00390	0.00019	0.23	26.7	2.1	25.1	1.2	26	0	7365	350	1158	206704	7409	905681
11	0.0249	0.0010	0.00392	0.00009	0.38	24.9	1.0	25.2	0.6	-10	11	10066	454	1746	317602	9849	1243372
12	0.0252	0.0018	0.00410	0.00018	0.37	25.5	1.8	26.4	1.1	-10	2	7163	332	1302	222366	6843	832454
13	0.0262	0.0013	0.00398	0.00010	0.26	26.2	1.2	25.6	0.7	19	28	6247	300	1024	173681	6094	757001
14	0.0255	0.0010	0.00404	0.00009	0.32	25.5	1.0	26.0	0.6	9	8	9238	415	1621	282939	8724	1095468
15	0.0256	0.0011	0.00390	0.00008	0.21	25.7	1.1	25.1	0.5	17	14	5941	280	1132	198340	5925	747077
16	0.0264	0.0011	0.00396	0.00009	0.24	26.5	1.1	25.5	0.6	12	33	8114	379	1308	217420	7963	973851
17	0.0256	0.0012	0.00396	0.00009	0.22	25.7	1.2	25.5	0.6	20	2	5835	269	1023	168635	5652	718277
18	0.0271	0.0016	0.00390	0.00012	0.38	27.1	1.6	25.1	0.8	70	9	8184	404	1432	239280	8270	1015096
19	0.0274	0.0018	0.00408	0.00015	0.19	27.4	1.7	26.2	1.0	76	22	6586	317	1211	197807	6337	782068
20	0.0257	0.0012	0.00398	0.00009	0.13	25.8	1.2	25.6	0.6	7	10	4950	236	1108	194473	4898	601734
679715 Stratoni Quartz-Feldspar Porphyry																	
Latitude 40.51645, Longitude 23.81529																	
1	0.0235	0.0046	0.00400	0.00029	0.09	23.4	4.6	25.7	1.9	4	4	1239	52	200	56143	1158	176897
2	0.0311	0.0049	0.00420	0.00025	0.03	30.5	4.8	27.0	1.6	12	8	791	42	144	35181	731	106131
3	0.0259	0.0014	0.00382	0.00012	0.13	63.0	34.0	32.7	5.5	36	17	166	17	60	6006	112	19252

Table A1. Zircon U-Pb LA-ICP-MS analyses for igneous rocks from the Kassandra Mining District

	Isotopic Ratios					Isotopic Ages (Ma)				Background Corrected Mean Counts Per Second							
No.	$^{207}Pb/^{235}U$	2σ	$^{206}Pb/^{238}U$	2σ	ρ	$^{207}Pb/^{235}U$	2σ	$^{206}Pb/^{238}U$	2σ	^{202}Hg	^{204}Pb	^{206}Pb	^{207}Pb	^{208}Pb	^{232}Th	^{235}U	^{238}U
4	0.0266	0.0046	0.00397	0.00027	0.19	26.4	4.5	25.6	1.7	17	5	976	45	118	36233	932	140568
5	0.0273	0.0068	0.00379	0.00031	0.04	26.1	6.6	24.4	2.0	-1	9	336	18	58	14579	323	49806
6	0.0236	0.0071	0.00438	0.00032	0.04	22.2	7.0	28.1	2.1	20	10	343	14	70	18484	296	43916
7	0.0233	0.0076	0.00391	0.00032	0.04	22.4	7.5	25.1	2.0	9	6	410	18	72	17611	385	57042
8	0.0226	0.0058	0.00406	0.00032	0.11	21.9	5.7	26.1	2.0	7	14	398	18	63	21525	350	54213
9	0.0236	0.0061	0.00400	0.00028	0.04	22.7	5.9	25.7	1.8	-2	11	429	18	97	26065	409	60620
10	0.0242	0.0079	0.00419	0.00042	0.05	23.3	7.8	27.0	2.7	10	16	399	18	60	23127	358	54758
11	0.0218	0.0046	0.00401	0.00022	0.17	21.2	4.5	25.8	1.4	15	12	480	19	74	23764	454	66446
12	0.1622	0.0069	0.02414	0.00072	0.34	151.9	6.0	153.7	4.5	16	8	13531	643	115	3919	2128	309188
13	0.0239	0.0033	0.00384	0.00019	0.08	23.7	3.3	24.7	1.2	8	19	834	38	147	41176	818	119011
14	0.0224	0.0031	0.00400	0.00019	0.16	22.2	3.1	25.7	1.2	6	14	976	37	202	58588	975	135920
15	0.0230	0.0063	0.00408	0.00033	0.08	22.6	6.2	26.3	2.1	27	22	564	28	124	30955	558	82693
16	0.0279	0.0047	0.00393	0.00022	0.11	27.6	4.6	25.3	1.4	11	15	557	31	81	26162	509	77202
17	0.0270	0.0031	0.00400	0.00017	0.05	26.7	3.1	25.8	1.1	11	21	962	47	161	47588	951	138678
18	0.0225	0.0066	0.00406	0.00031	0.09	22.2	6.5	26.1	2.0	12	30	871	33	141	35963	808	119217
19	0.0257	0.0031	0.00396	0.00018	0.01	25.5	3.1	25.5	1.2	1	20	996	49	155	44312	950	138958
20	0.0237	0.0035	0.00398	0.00020	0.06	23.7	3.5	25.6	1.3	14	20	779	35	157	42381	753	110622
679716 Stratoni Quartz-Feldspar Porphyry																	
Latitude 40.51674, Longitude 23.81419																	
1	0.1750	0.0260	0.02540	0.00150	0.08	156.0	23.0	161.8	9.5	-5	-4	1319	68	92	3270	213	30427
2	0.1680	0.0140	0.02450	0.00110	0.35	157.0	12.0	156.0	6.9	6	-1	5198	262	66	2575	799	121967
3	0.1490	0.0140	0.02370	0.00100	0.27	143.0	13.0	150.8	6.4	8	6	3161	144	12	1931	479	75266
4	0.0292	0.0048	0.00414	0.00021	0.13	28.5	4.7	26.6	1.4	-2	1	694	38	90	25819	665	98207
5	0.0448	0.0097	0.00768	0.00058	0.04	45.0	9.7	49.3	3.7	27	1	753	33	16	2212	396	59412
6	0.0380	0.0110	0.00698	0.00069	0.00	36.0	11.0	44.8	4.4	-11	-4	691	29	110	6763	396	61440
7	0.1570	0.0630	0.02690	0.00310	0.33	112.0	54.0	171.0	19.0	9	2	480	22	128	6428	65	10713
8	0.0221	0.0042	0.00382	0.00021	0.11	21.6	4.2	24.6	1.4	0	-2	614	27	93	27084	627	95377

Table A1. Zircon U-Pb LA-ICP-MS analyses for igneous rocks from the Kassandra Mining District

	Isotopic Ratios					Isotopic Ages (Ma)				Background Corrected Mean Counts Per Second							
No.	$^{207}Pb/^{235}U$	2σ	$^{206}Pb/^{238}U$	2σ	ρ	$^{207}Pb/^{235}U$	2σ	$^{206}Pb/^{238}U$	2σ	^{202}Hg	^{204}Pb	^{206}Pb	^{207}Pb	^{208}Pb	^{232}Th	^{235}U	^{238}U
9	0.0202	0.0048	0.00409	0.00024	0.07	19.6	4.7	26.3	1.5	0	3	571	21	71	23351	536	81268
10	0.0223	0.0081	0.00406	0.00041	0.04	21.2	8.0	26.1	2.6	28	3	318	14	64	13747	310	45876
11	0.0240	0.0140	0.00423	0.00051	0.13	21.0	14.0	27.2	3.3	-5	1	276	10	44	18384	244	39300
12	0.0265	0.0038	0.00406	0.00022	0.03	26.1	3.8	26.1	1.4	1	2	797	34	66	23789	753	116163
13	0.0202	0.0029	0.00371	0.00018	0.06	20.1	2.9	23.9	1.1	5	2	1076	43	143	43861	1079	165756
14	0.0226	0.0032	0.00398	0.00020	0.04	22.3	3.2	25.6	1.3	11	8	974	45	152	40105	934	141813
15	0.0269	0.0061	0.00394	0.00027	0.01	25.8	6.0	25.3	1.7	10	4	414	18	61	23998	397	61589
16	0.0253	0.0063	0.00419	0.00028	0.01	24.1	6.1	27.0	1.8	13	8	417	17	98	25988	378	54963
17	0.0201	0.0060	0.00373	0.00024	0.02	19.1	6.0	24.0	1.5	-6	6	362	14	121	29520	373	55105
18	0.0186	0.0091	0.00430	0.00044	0.01	18.3	9.1	27.6	2.8	-3	1	364	14	80	25531	345	52207
19	0.0429	0.0053	0.00650	0.00043	0.27	42.4	5.2	41.8	2.8	11	-1	3283	157	524	102140	1952	284764
20	0.0435	0.0049	0.00663	0.00032	0.12	42.8	4.8	42.6	2.1	31	7	2010	99	262	41150	1203	173218
593567 K-feldspar Porphyry Dike (Skouries Area)																	
Latitude 40.46839, Longitude 23.70576																	
1	0.0196	0.0010	0.00302	0.00007	0.17	19.7	1.0	19.5	0.4	-2	5	17435	823	807	146361	21516	2569489
2	0.0199	0.0008	0.00305	0.00005	0.30	20.0	0.8	19.6	0.4	-13	5	26816	1284	1440	313399	33747	3995966
3	0.0202	0.0008	0.00310	0.00006	0.16	20.4	0.8	19.9	0.4	42	7	23271	1113	1192	259197	28698	3426863
4	0.0476	0.0037	0.00696	0.00020	0.03	47.5	3.6	44.7	1.3	18	11	3726	184	52	4030	2036	240353
5	0.0193	0.0007	0.00300	0.00004	0.21	19.4	0.7	19.3	0.3	2	7	28325	1302	1713	393916	35862	4260058
6	0.0198	0.0009	0.00301	0.00006	0.35	19.9	0.9	19.4	0.4	22	19	27788	1314	1726	347667	35950	4180812
7	0.0195	0.0008	0.00297	0.00005	0.25	19.6	0.8	19.1	0.3	48	9	21893	1032	942	200562	27623	3327040
8	0.0195	0.0007	0.00300	0.00005	0.32	19.6	0.7	19.3	0.3	59	9	27451	1276	1795	373122	34555	4068032
9	0.0199	0.0009	0.00304	0.00006	0.42	20.0	0.9	19.5	0.4	-2	7	22907	1070	1111	217471	29319	3447395
10	0.0197	0.0008	0.00298	0.00005	0.35	19.8	0.8	19.2	0.3	17	7	21711	1034	1018	224390	27824	3306358
11	0.0204	0.0010	0.00304	0.00010	0.16	20.6	1.1	19.6	0.6	1	7	13957	671	1949	422138	17524	2100357
12	0.0207	0.0008	0.00309	0.00006	0.42	20.8	0.8	19.9	0.4	-1	2	27313	1299	2029	448321	33597	3998546
13	0.0202	0.0010	0.00309	0.00007	0.24	20.3	1.0	19.9	0.5	6	-1	15063	703	892	180298	18191	2164897

Table A1. Zircon U-Pb LA-ICP-MS analyses for igneous rocks from the Kassandra Mining District

	Isotopic Ratios					Isotopic Ages (Ma)				Background Corrected Mean Counts Per Second							
No.	$^{207}Pb/^{235}U$	2σ	$^{206}Pb/^{238}U$	2σ	ρ	$^{207}Pb/^{235}U$	2σ	$^{206}Pb/^{238}U$	2σ	^{202}Hg	^{204}Pb	^{206}Pb	^{207}Pb	^{208}Pb	^{232}Th	^{235}U	^{238}U
14	0.0204	0.0009	0.00324	0.00007	0.27	20.5	0.9	20.9	0.4	19	5	15072	695	771	152091	17917	2118810
15	0.0200	0.0008	0.00306	0.00004	0.23	20.1	0.8	19.7	0.3	9	14	25324	1210	1411	313383	32144	3809107
16	0.0194	0.0009	0.00307	0.00006	0.19	19.5	0.9	19.8	0.4	30	6	18655	867	899	196517	24000	2798222
17	0.0202	0.0009	0.00309	0.00005	0.39	20.4	0.9	19.9	0.3	10	5	38913	1853	2724	592340	49472	5859719
18	0.0202	0.0008	0.00314	0.00005	0.44	20.3	0.8	20.2	0.3	8	13	40407	1920	2567	541083	49862	5959411
19	0.0206	0.0014	0.00319	0.00009	0.07	20.7	1.4	20.5	0.6	-19	7	11985	563	3442	796255	14880	1733528
20	0.0204	0.0009	0.00311	0.00007	0.37	20.5	0.9	20.0	0.4	14	31	29607	1414	2099	433521	36843	4377473
593587 Asrpo Lakkos Stock																	
Latitude 40.48301, Longitude 23.71934																	
1	0.0197	0.0008	0.00304	0.00005	0.25	19.8	0.8	19.6	0.4	9	3	14317	672	1339	287476	18443	2161657
2	0.0192	0.0010	0.00300	0.00005	0.06	19.3	1.0	19.3	0.3	2	-3	7272	338	2903	697507	9394	1121933
3	0.0205	0.0009	0.00313	0.00006	0.39	20.6	0.9	20.2	0.4	23	3	27708	1310	1682	338916	34588	4067984
4	0.0202	0.0010	0.00303	0.00007	0.25	20.3	1.0	19.5	0.5	50	2	20152	983	2311	480171	25729	3108348
5	0.0189	0.0018	0.00309	0.00011	0.08	19.0	1.8	19.9	0.7	3	6	3487	155	747	163115	4324	525115
6	0.0200	0.0014	0.00308	0.00009	0.03	20.1	1.4	19.9	0.6	3	-1	2918	137	863	180753	3659	436063
7	0.0205	0.0009	0.00307	0.00007	0.52	20.6	0.9	19.8	0.4	28	16	20905	993	2448	535636	26204	3129683
8	0.0200	0.0009	0.00309	0.00006	0.26	20.1	0.9	19.9	0.4	19	4	14597	671	1448	292346	18179	2151577
9	0.0203	0.0012	0.00304	0.00009	0.10	20.4	1.2	19.6	0.6	17	4	7040	339	461	114892	8905	1055459
10	0.0202	0.0012	0.00314	0.00008	0.20	20.3	1.2	20.2	0.5	39	-1	13271	620	1029	224260	16338	1972132
11	0.0204	0.0012	0.00303	0.00008	0.26	20.5	1.2	19.5	0.5	38	10	15578	754	2092	410650	20292	2410138
12	0.0205	0.0012	0.00317	0.00010	0.26	20.4	1.2	20.4	0.7	13	39	17447	810	6048	1291551	21288	2581447
13	0.0200	0.0016	0.00301	0.00012	0.22	20.1	1.6	19.4	0.8	35	9	7939	387	5320	1182632	10243	1211672
14	0.0204	0.0009	0.00310	0.00006	0.33	20.4	0.9	20.0	0.4	27	12	18322	874	1120	231949	23120	2776520
15	0.0200	0.0009	0.00305	0.00006	0.29	20.1	0.9	19.6	0.4	20	4	19066	883	1290	268916	24459	2879740
16	0.0192	0.0010	0.00305	0.00006	0.24	19.3	0.9	19.7	0.4	10	5	15306	688	1476	309151	19883	2330405
17	0.0198	0.0011	0.00306	0.00009	0.40	19.9	1.1	19.7	0.5	-12	3	16563	787	15279	3457941	21131	2514818
18	0.0194	0.0008	0.00305	0.00004	0.26	19.5	0.8	19.6	0.3	9	-4	29678	1374	3713	877439	38336	4600551

Table A1. Zircon U-Pb LA-ICP-MS analyses for igneous rocks from the Kassandra Mining District

	Isotopic Ratios					Isotopic Ages (Ma)				Background Corrected Mean Counts Per Second							
No.	$^{207}Pb/^{235}U$	2σ	$^{206}Pb/^{238}U$	2σ	ρ	$^{207}Pb/^{235}U$	2σ	$^{206}Pb/^{238}U$	2σ	^{202}Hg	^{204}Pb	^{206}Pb	^{207}Pb	^{208}Pb	^{232}Th	^{235}U	^{238}U
19	0.0214	0.0017	0.00318	0.00013	0.35	21.5	1.6	20.5	0.8	22	14	13392	659	3585	729512	16618	1986451
20	0.0200	0.0008	0.00303	0.00005	0.42	20.1	0.8	19.5	0.3	8	5	32093	1515	2202	508365	41637	4923201
579586 Aspro Lakkos (Black-matrix) Porphyry Dike																	
Latitude 40.48364, Longitude 23.72207																	
1	0.0197	0.0008	0.00304	0.00004	0.39	19.8	0.8	19.6	0.3	6	4	26570	1251	1878	416306	34619	4088387
2	0.0206	0.0009	0.00309	0.00005	0.33	20.7	0.8	19.9	0.3	-2	7	18900	906	984	185767	23397	2826029
3	0.0200	0.0009	0.00310	0.00006	0.28	20.1	0.9	19.9	0.4	5	7	19238	902	1410	282012	24124	2898678
4	0.0193	0.0008	0.00300	0.00005	0.33	19.4	0.8	19.3	0.3	4	6	17104	792	1881	406001	21572	2607851
5	0.0205	0.0012	0.00305	0.00007	0.13	20.6	1.2	19.6	0.5	12	2	6700	315	493	121168	8327	1014770
6	0.0203	0.0010	0.00305	0.00008	0.45	20.4	1.0	19.6	0.5	48	14	24064	1171	2918	665869	31010	3662802
7	0.0200	0.0014	0.00313	0.00008	0.08	20.1	1.4	20.2	0.5	10	6	3601	172	542	125354	4440	525815
8	0.0202	0.0010	0.00318	0.00007	0.26	20.3	1.0	20.5	0.4	65	6	16810	777	1594	325763	20815	2444370
9	0.0201	0.0009	0.00307	0.00006	0.27	20.2	0.9	19.8	0.4	8	5	19135	904	2260	476976	24002	2915846
10	0.0216	0.0009	0.00316	0.00006	0.26	21.7	0.9	20.3	0.4	15	10	17388	871	1548	294655	21687	2537060
11	0.0194	0.0009	0.00306	0.00007	0.18	19.5	0.9	19.7	0.4	-17	5	11761	546	1077	218434	14525	1731716
12	0.0188	0.0016	0.00299	0.00012	0.38	19.1	1.7	19.3	0.8	11	-6	7997	370	6159	1389593	10408	1238968
13	0.0195	0.0008	0.00299	0.00006	0.23	19.6	0.8	19.3	0.4	19	23	14996	714	1979	433421	19647	2307324
14	0.0181	0.0021	0.00318	0.00012	0.15	18.4	2.0	20.5	0.8	4	6	14259	610	1452	325140	18253	1853338
15	0.0199	0.0008	0.00305	0.00005	0.18	20.0	0.8	19.7	0.3	11	6	17095	798	1615	347165	21291	2551646
16	0.0207	0.0010	0.00309	0.00008	0.23	20.7	1.0	19.9	0.5	23	7	15234	726	1108	232787	18652	2218235
17	0.0195	0.0008	0.00304	0.00005	0.25	19.6	0.8	19.6	0.3	11	2	15075	709	1913	425693	18541	2205624
18	0.0196	0.0014	0.00304	0.00007	0.12	19.6	1.3	19.6	0.5	14	4	3252	150	735	169049	4133	496248
19	0.0195	0.0008	0.00299	0.00005	0.18	19.6	0.8	19.3	0.3	-3	8	15995	742	1689	340667	20553	2433351
20	0.0204	0.0011	0.00296	0.00008	0.30	20.5	1.1	19.1	0.5	-16	13	16661	843	1271	209967	21103	2546697

Table A1. Zircon U-Pb LA-ICP-MS analyses for igneous rocks from the Kassandra Mining District

	Isotopic Ratios					Isotopic Ages (Ma)				Background Corrected Mean Counts Per Second							
No.	$^{207}Pb/^{235}U$	2σ	$^{206}Pb/^{238}U$	2σ	ρ	$^{207}Pb/^{235}U$	2σ	$^{206}Pb/^{238}U$	2σ	^{202}Hg	^{204}Pb	^{206}Pb	^{207}Pb	^{208}Pb	^{232}Th	^{235}U	^{238}U
279433 Piavitsa Glomerophyric Porphyry Dike																	
Latitude 40.53294, Longitude 23.71782																	
1	0.0211	0.0007	0.00322	0.00006	0.31	21.2	0.7	20.7	0.4	9	-1	23757	1129	1010	211358	28365	3545045
2	0.0204	0.0006	0.00318	0.00008	0.58	20.5	0.6	20.5	0.5	22	16	27422	1274	998	214246	33041	4169463
3	0.0268	0.0014	0.00418	0.00011	0.25	26.8	1.3	26.9	0.7	14	7	4341	195	1356	231772	3905	497317
4	0.0265	0.0011	0.00410	0.00009	0.21	26.5	1.1	26.4	0.6	16	13	7618	353	2406	402382	7129	900177
5	0.0211	0.0005	0.00322	0.00007	0.63	21.2	0.5	20.7	0.4	3	6	34390	1616	1645	331745	41715	5186725
6	0.0248	0.0014	0.00375	0.00010	0.16	24.8	1.4	24.2	0.7	-8	-1	6028	293	818	147407	6176	774304
7	0.0207	0.0011	0.00313	0.00016	0.59	20.8	1.1	20.1	1.0	35	18	28031	1311	1178	205529	33956	4348802
8	0.0208	0.0007	0.00318	0.00008	0.44	20.9	0.7	20.5	0.5	6	2	21191	998	766	160739	25246	3196212
9	0.0214	0.0010	0.00321	0.00013	0.46	21.5	1.0	20.7	0.9	15	9	19070	924	971	168987	23218	2927948
10	0.0548	0.0022	0.00804	0.00020	0.30	54.0	2.1	51.6	1.3	4	0	7789	382	247	19193	3690	466363
11	0.0275	0.0018	0.00420	0.00013	0.15	27.5	1.8	27.0	0.8	11	8	3350	159	1109	193754	3118	389533
12	0.0202	0.0006	0.00315	0.00008	0.67	20.3	0.6	20.3	0.5	20	-8	39633	1843	4053	855723	48157	6049947
13	0.0209	0.0006	0.00321	0.00006	0.42	21.0	0.6	20.7	0.4	3	7	29005	1355	853	171233	33973	4312900
14	0.0208	0.0006	0.00317	0.00007	0.44	21.0	0.6	20.4	0.4	32	8	23706	1100	880	191547	28915	3600254
15	0.0208	0.0005	0.00322	0.00007	0.48	20.9	0.5	20.8	0.4	-15	5	27496	1269	1130	218903	32414	4082083
16	0.0208	0.0006	0.00327	0.00007	0.55	20.9	0.6	21.0	0.5	31	-3	33885	1542	1415	292940	39221	5000958
17	0.0213	0.0010	0.00324	0.00009	0.48	21.4	1.0	20.9	0.6	31	-4	19225	920	597	118908	23046	2876088
18	0.0212	0.0006	0.00323	0.00007	0.41	21.3	0.6	20.8	0.4	24	16	22841	1076	764	159341	27339	3399071
19	0.0214	0.0006	0.00315	0.00008	0.46	21.6	0.6	20.3	0.5	16	24	34908	1671	1392	265751	41281	5299887
20	0.0430	0.0013	0.00659	0.00012	0.23	42.7	1.3	42.3	0.8	4	8	14090	658	449	48607	8242	1027131
679705 Vathilakkos Black-matrix Porphyry Dike																	
Latitude 40.52872, Longitude 23.79775																	
1	0.3020	0.0110	0.03502	0.00090	0.39	266.0	8.7	221.8	5.6	20	38	33446	2022	5277	84565	3691	458066
2	0.0191	0.0007	0.00297	0.00009	0.48	19.2	0.7	19.1	0.5	33	5	18571	867	897	200829	24164	3024208
3	0.0195	0.0010	0.00299	0.00009	0.35	19.6	1.0	19.3	0.6	24	0	7767	348	249	59257	9908	1244624

Table A1. Zircon U-Pb LA-ICP-MS analyses for igneous rocks from the Kassandra Mining District

	Isotopic Ratios					Isotopic Ages (Ma)				Background Corrected Mean Counts Per Second							
No.	$^{207}Pb/^{235}U$	2σ	$^{206}Pb/^{238}U$	2σ	ρ	$^{207}Pb/^{235}U$	2σ	$^{206}Pb/^{238}U$	2σ	^{202}Hg	^{204}Pb	^{206}Pb	^{207}Pb	^{208}Pb	^{232}Th	^{235}U	^{238}U
4	0.0201	0.0008	0.00302	0.00007	0.44	20.2	0.8	19.5	0.5	6	1	11697	544	581	131502	14875	1865714
5	0.0233	0.0015	0.00348	0.00019	0.76	23.3	1.4	22.4	1.2	6	22	17470	801	1688	309303	19499	2365744
6	0.2915	0.0076	0.03737	0.00072	0.40	258.5	6.0	236.4	4.5	57	24	35074	1976	6193	106188	3533	445255
7	0.2817	0.0083	0.03444	0.00085	0.59	250.0	6.4	218.6	5.3	20	51	54311	3174	12751	225845	6138	754859
8	0.0220	0.0019	0.00299	0.00011	0.13	22.1	1.8	19.3	0.7	27	30	7035	376	469	91585	9269	1166401
9	0.0192	0.0010	0.00287	0.00010	0.44	19.3	1.0	18.4	0.6	52	-6	16954	823	624	108685	22182	2843979
10	0.0199	0.0006	0.00299	0.00006	0.28	20.0	0.6	19.2	0.4	43	11	20874	974	735	149080	26216	3335047
11	0.2648	0.0052	0.03680	0.00064	0.51	238.2	4.2	232.9	4.0	36	7	44190	2278	11840	206276	4501	574651
12	0.0196	0.0006	0.00300	0.00006	0.38	19.8	0.6	19.3	0.4	17	19	18224	852	572	115428	23279	2903102
13	0.0547	0.0026	0.00800	0.00036	0.53	54.0	2.5	51.3	2.3	1	6	19430	962	2068	113779	8873	1157838
14	0.2727	0.0089	0.03660	0.00110	0.69	244.9	6.9	231.8	6.6	52	94	299344	15958	171570	3256944	31195	3891307
15	0.2224	0.0059	0.02884	0.00051	0.42	204.1	4.8	183.3	3.2	36	18	22085	1234	3063	66569	2888	366503
16	0.2685	0.0047	0.03715	0.00061	0.63	242.0	3.7	235.3	3.7	37	23	127506	6750	49011	936778	13462	1644037
17	0.3000	0.0120	0.03970	0.00100	0.39	265.6	9.6	250.8	6.3	40	-1	12116	672	1352	22617	1201	145861
679999 Quartz-Feldspar Pegmatite (Olympias)																	
Latitude 40.59462, Longitude 23.75349																	
1	0.0555	0.0048	0.0086	0.00036	0.16	54.3	4.6	55.2	2.3	0	18	1986	95	152	15988	882	129220
2	0.0539	0.0058	0.0087	0.00039	0.16	52.9	5.7	55.8	2.5	18	18	2250	100	256	31754	978	142322
3	0.0542	0.004	0.00858	0.00034	0.17	54	3.8	55	2.2	6	17	3540	165	487	62007	1550	225986
4	0.0554	0.0061	0.0089	0.00044	0.07	54.8	5.9	57.1	2.8	9	18	1509	63	156	20007	654	95541
5	0.0536	0.0057	0.00859	0.00038	0.12	53.1	5.7	55.1	2.4	9	18	1341	61	125	20103	619	87245
6	0.0566	0.0053	0.00795	0.00039	0.05	55.7	5.1	51.3	2.6	8	21	2612	128	55	6871	1213	178230
7	0.0541	0.0066	0.0087	0.00042	0.02	53.5	6.4	55.8	2.7	22	23	1223	56	129	19053	531	78584
8	0.0597	0.0056	0.00839	0.0004	0.25	58.5	5.4	53.8	2.6	4	15	1700	88	166	19391	764	115473
9	0.0526	0.0056	0.0084	0.00038	0.10	51.3	5.3	53.9	2.4	0	16	1275	62	168	20219	577	86891
10	0.0518	0.0052	0.00854	0.00037	0.17	50.5	5	54.8	2.4	15	17	1427	61	167	22448	617	94871
11	0.0587	0.0057	0.00825	0.00035	0.09	57.6	5.4	53	2.2	14	20	1445	77	270	34820	665	98348

Table A1. Zircon U-Pb LA-ICP-MS analyses for igneous rocks from the Kassandra Mining District

	Isotopic Ratios					Isotopic Ages (Ma)				Background Corrected Mean Counts Per Second							
No.	$^{207}Pb/^{235}U$	2σ	$^{206}Pb/^{238}U$	2σ	ρ	$^{207}Pb/^{235}U$	2σ	$^{206}Pb/^{238}U$	2σ	^{202}Hg	^{204}Pb	^{206}Pb	^{207}Pb	^{208}Pb	^{232}Th	^{235}U	^{238}U
12	0.0564	0.0063	0.00896	0.00043	0.06	54.7	6	57.7	2.7	4	22	1223	56	170	23581	527	76604
13	0.0605	0.0059	0.00865	0.00038	0.01	58.7	5.7	55.5	2.5	-5	23	1343	70	162	23328	609	89099
14	0.0513	0.0043	0.00837	0.00034	0.05	50.6	4.2	53.7	2.1	2	20	4361	198	605	95983	1957	289811
15	0.0582	0.0051	0.00865	0.00037	0.28	57.1	4.9	55.5	2.4	1	13	3483	172	401	54299	1489	226091
16	0.0534	0.0057	0.00861	0.00036	0.05	52	5.4	55.2	2.3	8	22	1359	61	156	22498	596	89288
17	0.0599	0.0031	0.00862	0.00032	0.57	58.9	2.9	55.3	2	4	21	11086	558	2248	292129	4815	714358
18	0.0558	0.0044	0.00865	0.00034	0.24	55	4.3	55.5	2.2	16	17	3199	153	366	47137	1421	211332
19	0.0551	0.0081	0.00852	0.0005	0.13	53.1	7.7	54.9	3.2	1	20	976	44	125	18205	429	65311
20	0.0582	0.0056	0.00863	0.00036	0.15	56.6	5.3	55.4	2.3	6	21	1753	89	128	16872	752	114177
679444 Foliated Granodiorite (Chevalier, Madem Lakkos)																	
Latitude 40.52075, Longitude 23.79534																	
1	0.0584	0.0023	0.00885	0.00024	0.41	57.9	2.3	56.8	1.5	-24	2	25695	1235	3971	322795	11820	1408217
2	0.0617	0.0021	0.00912	0.00019	0.21	60.7	2	58.5	1.2	13	-9	20332	985	4257	327914	8870	1070123
3	0.0588	0.0016	0.00912	0.00013	0.29	58	1.6	58.52	0.83	5	1	20620	971	4410	338348	8967	1076610
4	0.0582	0.0019	0.00893	0.00015	0.23	57.5	1.8	57.29	0.98	1	5	18460	855	4365	306039	8276	978008
5	0.0598	0.0021	0.00901	0.00019	0.28	58.9	2.1	57.8	1.2	-11	8	32392	1521	9354	720938	13857	1648475
6	0.0608	0.0017	0.00909	0.00014	0.23	60	1.7	58.34	0.92	13	1	34113	1651	9482	747989	15252	1783490
7	0.0617	0.0022	0.00916	0.00017	0.10	60.7	2.1	58.8	1.1	-9	3	17845	884	3136	233685	7730	930762
8	0.06	0.0025	0.00912	0.00019	0.18	59.2	2.4	58.5	1.2	22	-19	15736	762	2794	213589	6838	814591
9	0.0606	0.0022	0.0091	0.00024	0.35	59.7	2.1	58.4	1.5	4	1	16694	787	3301	260506	7144	853425
10	0.0581	0.0037	0.0091	0.00024	0.02	57.2	3.6	58.4	1.5	-22	9	11222	535	2063	156758	4935	599297
11	0.0589	0.0018	0.00902	0.00014	0.34	58	1.7	57.86	0.91	9	-18	19721	940	3736	289592	8575	1032452
12	0.0579	0.0018	0.00914	0.00015	0.23	57	1.8	58.69	0.94	-20	4	14949	700	2947	227348	6365	780654
13	0.0572	0.0017	0.00892	0.00015	0.29	56.4	1.6	57.23	0.93	5	1	20434	957	4351	361838	8973	1070550
14	0.0584	0.0018	0.00901	0.00017	0.27	57.5	1.7	57.8	1.1	15	8	22093	1022	4893	398309	9919	1190443
15	0.0612	0.0018	0.00916	0.00014	0.33	60.4	1.7	58.82	0.88	-8	0	21707	1057	6328	458422	9423	1120065
16	0.0592	0.0023	0.00894	0.00017	0.17	58.2	2.2	57.4	1.1	23	-5	7520	361	839	60050	3397	401821

Table A1. Zircon U-Pb LA-ICP-MS analyses for igneous rocks from the Kassandra Mining District

	Isotopic Ratios					Isotopic Ages (Ma)				Background Corrected Mean Counts Per Second							
No.	$^{207}Pb/^{235}U$	2σ	$^{206}Pb/^{238}U$	2σ	ρ	$^{207}Pb/^{235}U$	2σ	$^{206}Pb/^{238}U$	2σ	^{202}Hg	^{204}Pb	^{206}Pb	^{207}Pb	^{208}Pb	^{232}Th	^{235}U	^{238}U
17	0.0586	0.0022	0.00891	0.00019	0.17	57.9	2.1	57.2	1.2	-9	-11	15271	732	3047	244078	6792	829699
18	0.0602	0.002	0.00904	0.00018	0.44	59.4	1.9	58	1.1	22	25	23282	1115	5231	406505	9992	1214567
19	0.0582	0.0018	0.0089	0.00016	0.29	57.3	1.8	57.1	1	46	30	17243	814	4072	323840	7692	922988
20	0.0605	0.0019	0.00897	0.00017	0.29	59.6	1.8	57.6	1.1	29	23	18432	901	5023	400750	8157	988951

Negative values reported for ^{202}Hg and ^{204}Pb indicate that counts are at or below the detection limit

Abbreviations: ρ = correlation parameter (correlation of the relative errors of $^{206}Pb/^{238}U$ and $^{207}Pb/^{235}U$ ratios); controls the shape (and attitude) of error ellipse on Concordia diagrams

Table A2. Sample locations and descriptions for Oligo-Miocene igneous rocks from the Kassandra Mining District

No.	Latitide	Longitude	Area	Field Notes	TAS Lithology
Early Miocene Suite					
593555	40.48163	23.72210	Aspro Lakkos	Megacrystic K-feldspar, plagioclase, quartz phenocrysts, euhedral biotite books; aphanitic K-feldspar-rich? matrix, minor sericite-calcite altered matrix and feldspars	Quartz Monzonite
593556	40.48190	23.72056	Aspro Lakkos	Biotite-plagioclase-K-feldspar phenocrysts; dark gray aphanitic matrix (K-feldspar); non-megacrystic, crosscutting dike	Dacite
593557	40.48185	23.72068	Aspro Lakkos	Megacrystic porphyry; similar to sample 593555 described above	Quartz Monzonite
593558	40.48275	23.72164	Aspro Lakkos	Biotite-plagioclase-K-feldspar phenocrysts; dark gray aphanitic matrix (K-feldspar); non-megacrystic, crosscutting dike; similar to sample 593556 described above	Dacite
593559	40.48426	23.72400	Aspro Lakkos	Megacrystic K-feldspar, plagioclase, quartz phenocrysts, minor biotite; aphanitic K-feldspar-rich? matrix, minor sericite-calcite altered feldspar phenocrysts and matrix	Granodiorite
593560	40.48161	23.71834	Aspro Lakkos	Megacrystic texture; prismatic K-feldspar, sericite altered; euhedral hornblende-biotite phenocrysts; oxidized mafic minerals to limonite; light gray matrix (K-feldspar)	Quartz Monzonite
593561	40.47426	23.72652	Aspro Lakkos	Biotite-plagioclase-K-feldspar phenocrysts; dark gray aphanitic matrix (K-feldspar); non-megacrystic, crosscutting dike	Dacite
593562	40.47606	23.72533	Aspro Lakkos	Quartz eye and feldspar phenocrysts (non-megacrystic); moderate quartz-sericite-pyrite alteration; boxwork texture (oxidized pyrite); minor quartz-veining	Dacite
593563	40.47785	23.72444	Aspro Lakkos	Quartz-feldspar phenocrysts (non-megacrystic); weak quartz-sericite-pyrite altered matrix and phenocrysts; hematite-limonite after pyrite or magnetite	Dacite

Table A2. Sample locations and descriptions for Oligo-Miocene igneous rocks from the Kassandra Mining District

No.	Latitide	Longitude	Area	Field Notes	TAS Lithology
593564	40.47605	23.72299	Aspro Lakkos	K-feldspar phenocrysts, rare K-feldspar megacrysts, crowded texture; phenocrysts are altered to sericite; dark gray-maroon aphanitic matrix (K-feldspar?)	Dacite
593586	40.48364	23.72207	Aspro Lakkos	Fresh, unaltered; quartz-plagioclase-K-feldspar phenocrysts, euhedral biotite phenocrysts (non-megacrystic); dark gray aphanitic K-feldspar-rich matrix	Dacite
593587	40.48301	23.71934	Aspro Lakkos	Megacrystic K-feldspar-plagioclase-quartz phenocrysts; aphanitic matrix, minor sericite-altered matrix and feldspars; limonite replacing mafic minerals or pyrite?	Granodiorite
593567	40.46839	23.70576	Skouries	Megacrystic K-feldspar phenocrysts, crowded texture; K-feldspar matrix with disseminated pyrite; minor planar quartz-pyrite veinlets; sericite altered; late- to post-mineral?	Quartz Monzonite
593568	40.46853	23.70601	Skouries	Megacrystic K-feldspar porphyry similar to sample 593567 described above	Granodiorite
593569	40.46824	23.69938	Skouries	Megacrystic; bi-porphyritic K-feldspar phenocrysts; sericite-altered K-feldspar-plagioclase, aphanitic K-feldspar-rich matrix overprinted by quartz-sericite-pyrite alteration	Granodiorite
593570	40.46882	23.69854	Skouries	Megacrystic; bi-porphyritic K-feldspar-plagioclase phenocrysts; quartz-sericite-altered with disseminated pyrite in matrix	Granodiorite
593571	40.46983	23.69873	Skouries	Prismatic, euhedral K-feldspar-plagioclase phenocrysts, weakly overprinted by sericite; disseminated green mica (Illite?) associated with minor oxidized pyrite	Granodiorite
593573	40.47282	23.70388	Skouries (core)	Megacrystic, K-feldspar phenocrysts; strong pink K-feldspar-altered matrix; moderate disseminated clots of magnetite-chalcopyrite; intra-mineral porphyry	Quartz Monzonite
593574	40.47282	23.70388	Skouries (core)	Fine-grained variety of Skouries porphyry; dark gray-pink matrix (K-feldspar-altered); late-stage, intra-mineral porphyry	Quartz Monzonite

Table A2. Sample locations and descriptions for Oligo-Miocene igneous rocks from the Kassandra Mining District

No.	Latitide	Longitude	Area	Field Notes	TAS Lithology
593575	40.47282	23.70388	Skouries (core)	Megacrystic, K-feldspar-plagioclase phenocrysts; dark matrix, disseminated magnetite-biotite with weak K-feldspar alteration; lacks veins; late-stage, intra-mineral porphyry	Quartz Monzonite
593576	40.47282	23.70388	Skouries (core)	Megacrystic, K-feldspar phenocrysts; strongly K-feldspar-magnetite altered; abundant chalcopyrite-bornite disseminated and in veins; intra-mineral phase	Quartz Monzonite
593577	40.47282	23.70388	Skouries (core)	Megacrystic, K-feldspar-plagioclase phenocrysts; crowded texture; disseminated and veined magnetite-biotite with chalcopyrite-bornite; strong K-feldspar) alteration; intra-mineral phase	Quartz Monzonite
593594	40.47277	23.70206	Skouries (core)	Megacrystic K-feldspar-plagioclase, primary biotite phenocrysts; K-feldspar-altered rims on plagioclase; K-feldspar-magnetite-altered groundmass; intra-mineral phase	Quartz Monzonite
593596	40.47282	23.70388	Skouries (core)	K-feldspar phenocrysts, non-megacrystic; aphanitic to fine-grained K-feldspar-rich matrix; magnetite-biotite-altered with minor chalcopyrite-bornite veinlets; weak sericite overprint; intra-mineral phase	Quartz Monzonite
593597	40.47282	23.70388	Skouries (core)	Intra-mineral K-feldspar porphyry phase; similar to sample 593596 described above	Quartz Monzonite
593583	40.59169	23.75610	Olympias (core)	Euhedral bladed biotite phenocrysts, plagioclase and glomerophyric quartz phenocrysts; dark gray aphanitic (K-feldspar-rich?) matrix; disseminated pyrite, weakly magnetic	Trachy Andesite
279415	40.52925	23.71603	Piavitsa (core)	Fresh, biotite(hornblende?) needle-shaped phenocrysts, feldspar and quartz glomerophyric texture; dark gray K-feldspar-rich matrix; similar to sample 593583 (Olympias) described above	Trachy Andesite
279433	40.53294	23.71782	Piavitsa	Biotite(hornblende?)-feldspar phenocrysts, glomerophyric quartz, overprinted by limonite; green illite/sericite-altered matrix; phenocrysts partially replaced by chlorite-sericite	Trachy Andesite
279436	40.53140	23.71646	Piavitsa	Hornblende-feldspar phenocrysts, glomerophyric quartz eyes with chlorite rims and partially replaced by limonite; sericite-altered plagioclase phenocrysts and matrix	Trachy Andesite

Table A2. Sample locations and descriptions for Oligo-Miocene igneous rocks from the Kassandra Mining District

No.	Latitide	Longitude	Area	Field Notes	TAS Lithology
279437	40.53015	23.71759	Piavitsa	Abundant biotite phenocrysts, glomerophyric quartz, partially replaced by limonite; chlorite after biotite; tan color imparted by sericite-altered matrix	Trachy Andesite
279423	40.53039	23.77777	Stratoni	Biotite-plagioclase phenocrysts, glomerophyric quartz with limonite halos; chlorite after biotite; dark gray aphanitic matrix (K-feldspar?)	Dacite
593579	40.53477	23.78163	Stratoni	Biotite-hornblende?-quartz phenocrysts; round glomerophyric quartz eyes, partially rimmed/replaced by limonite; dark gray K-feldspar-rich? aphanitic matrix	Trachy Andesite
593584	40.52134	23.77258	Stratoni	Biotite-hornblende?-quartz phenocrysts; coarse-grained glomerophyric quartz; flow banding of mafic minerals; dark gray aphanitic (K-feldspar-rich?) matrix; weak sericite alteration; similar to sample 593579 described above	Dacite
679705	40.52872	23.79775	Vathilakkos	Fresh; porphyritic, plagioclase-biotite-hornblende phenocrysts; flow banded; aphanitic (K-feldspar-rich?) matrix; rare K-feldspar megacrysts within outcrop; (non-glomerophyric)	Dacite
Late Oligocene Suite					
593591	40.46216	23.72266	Tsikara	Quartz eye and feldspar (plagioclase/K-feldspar?) phenocrysts; crowded, micro-porphyritic texture; quartz-K-feldspar-rich matrix; sericite-altered	Granodiorite
593599	40.45439	23.72435	Tsikara	Mafic, dark green color imparted by abundant mafic minerals; fine-grained plagioclase and hornblende phenocrysts, equigranular; disseminated pyrite and strongly magnetic	Monzodiorite
593600	40.45767	23.72697	Tsikara	Fresh, mafic; dark green coloration; fine-grained plagioclase-hornblende phenocrysts; equigranular, strongly magnetic	Monzodiorite
593870	40.46173	23.72401	Tsikara	Mafic, dark green color; fine-grained and equigranular; plagioclase-K-feldspar-clinopyroxene-biotite phenocrysts, chlorite after clinopyroxene-biotite; disseminated pyrite and magnetite, strongly magnetic	Diorite

Table A2. Sample locations and descriptions for Oligo-Miocene igneous rocks from the Kassandra Mining District

No.	Latitide	Longitude	Area	Field Notes	TAS Lithology
593871	40.45619	23.72926	Tsikara	Quartz-feldspar (plagioclase/K-feldspar?) phenocrysts; micro-porphyritic texture; green coarse-grained sericite; sericite-clay-altered feldspars and matrix	Granodiorite
593872	40.45180	23.73362	Tsikara	Quartz eye and feldspar phenocrysts, micro-porphyritic texture; dark gray quartz-rich matrix; sericite-altered	Granodiorite
593873	40.45072	23.73309	Tsikara	Quartz eye and feldspar (plagioclase-K-feldspar) phenocrysts, micro-porphyritic texture; dark gray quartz-feldspar-rich matrix; sericite-altered	Granodiorite
593874	40.44544	23.74175	Tsikara	Quartz-feldspar phenocrysts, micro-porphyritic texture; aphanitic groundmass, sericite-altered	Granodiorite
593875	40.44809	23.74568	Tsikara	Dark green, plagioclase-clinopyroxene?(-hornblende?) phenocrysts; equigranular; disseminated magnetite	Monzonite
593876	40.44754	23.74530	Tsikara	Quartz-feldspar phenocrysts; crowded, micro-porphyritic texture; sericite-altered feldspars and matrix	Granodiorite
593881	40.43561	23.72897	Tsikara	Dark green-black coloration; fine-grained plagioclase-clinopyroxene-(hornblende?) phenocrysts; equigranular; disseminated pyrite and magnetite	Monzodiorite
593882	40.43350	23.72673	Tsikara	Fresh, equigranular medium- to coarse-grained plagioclase-K-feldspar-clinopyroxene-biotite phenocrysts; salt-and-pepper color/texture; chlorite-epidote after clinopyroxene-biotite; disseminated magnetite	Monzodiorite
593883	40.45513	23.73494	Tsikara	Plagioclase-biotite-hornblende? phenocrysts; micro-porphyritic texture; magnetic, minor disseminated pyrrhotite	Granodiorite
593884	40.44651	23.72349	Tsikara	Quartz-feldspar phenocrysts, porphyritic texture; fine-grained siliceous matrix; sericite-altered; minor disseminated pyrite (oxidized)	Granodiorite

Table A2. Sample locations and descriptions for Oligo-Miocene igneous rocks from the Kassandra Mining District

No.	Latitide	Longitude	Area	Field Notes	TAS Lithology
593887	40.42392	23.71922	Tsikara	Mafic phase; coarse-grained plagioclase-clinopyroxene-biotite phenocrysts	Monzogabbro
593888	40.42055	23.71982	Tsikara	Mafic phase; coarse-grained, equigranular plagioclase-clinopyroxene-biotite phenocrysts, minor K-feldspar?; disseminated pyrite and magnetite, strongly magnetic	Monzogabbro
593893	40.44598	23.73062	Tsikara	Fine-grained quartz-feldspar (micro-) porphyry texture, siliceous-K-feldspar matrix	Granodiorite
279430	40.50124	23.81567	Fisoka-Stratoni	Euhedral quartz-K-feldspar-plagioclase phenocrysts, aphanitic white, siliceous-K-feldspar-rich? matrix; minor chlorite-sericite after mafic minerals?	Rhyolite
279431	40.50183	23.80770	Fisoka-Stratoni	Crowded porphyry texture; feldspar phenocrysts, aphanitic matrix; coarse-grained sericite-altered	Granodiorite
279432	40.50398	23.80734	Fisoka-Stratoni	Quartz eye-feldspar (plagioclase/K-feldspar) porphyry; sericite-altered; goethite-limonite after mafic minerals or pyrite; minor quartz veins are evident	Granite
279445	40.49492	23.78804	Fisoka	Crowded porphyry texture; feldspar phenocrysts, sericite-altered; limonite-geothite after mafic minerals or pyrite	Granodiorite
279446	40.49469	23.79155	Fisoka	Crowded porphyry texture; feldspars (plagioclase/K-feldspar) and lath-shaped phenocrysts (hornblende?); disseminated oxidized pyrite and boxwork texture	Granodiorite
279447	40.49850	23.79024	Fisoka	Micro-porphyry texture; quartz eye and feldspar (plagioclase/K-feldspar) phenocrysts, minor biotite, sericite-altered	Granodiorite
279448	40.49934	23.79110	Fisoka	Micro-porphyritic texture; feldspar (plagioclase/K-feldspar) phenocrysts; sericite-altered	Granodiorite

Table A2. Sample locations and descriptions for Oligo-Miocene igneous rocks from the Kassandra Mining District

No.	Latitide	Longitude	Area	Field Notes	TAS Lithology
279449	40.49766	23.80076	Fisoka	Crowded porphyry texture; feldspar (plagioclase/K-feldspar) phenocrysts, sericite-limonite-altered with goethite after disseminated pyrite	Granite
593581	40.49331	23.78996	Fisoka	Equigranular, hornblende-plagioclase phenocrysts; chlorite-altered hornblende; patchy epidote intergrown with chlorite and K-feldspar, minor magnetite-biotite alteration	Granodiorite
593582	40.49331	23.78996	Fisoka	Mafic phase; subhedral plagioclase-hornblende phenocrysts; chlorite-epidote after hornblende; minor biotite; aphanitic, dark gray matrix	Gabbroic Diorite
679709	40.48057	23.78372	Fisoka (core)	Porphyritic texture, quartz-plagioclase-biotite phenocrysts; sericite-altered plagioclase, chlorite-epidote-altered biotite; minor magnetite and disseminated pyrite in matrix; least altered of Fisoka drill core	Diorite
679710	40.48057	23.78372	Fisoka (core)	Porphyritic, plagioclase-quartz phenocrysts, resorbed textures in quartz phenocrysts; aphanitic matrix; pervasive chlorite-epidote replacement of mafic minerals; disseminated magnetite and pyrite	Monzodiorite
679711	40.48057	23.78372	Fisoka (core)	Porphyritic, quartz-plagioclase-K-feldspar phenocrysts; sericite-altered plagioclase; pervasive chlorite-epidote-magnetite replacing biotite; chlorite-magnetite-altered; minor disseminated pyrite	Diorite
593592	40.48057	23.78372	Fisoka	Equigranular, quartz-plagioclase-K-feldspar, mottled texture with patches of chlorite-K-feldspar-magnetite; disseminated magnetite and pyrite; selective potassic (K-feldspar) alteration	Granodiorite
593593	40.48057	23.78372	Fisoka	Fine-grained, plagioclase-K-feldspar phenocrysts and unaltered euhedral biotite; aphanitic matrix; patches of K-feldspar-magnetite-epidote-chlorite alteration	Gabbroic Diorite
593877	40.50395	23.80122	Fisoka	Feldspar and anhedral quartz phenocrysts; siliceous matrix; boxwork texture with goethite after pyrite	Granodiorite
593894	40.47027	23.76412	Fisoka	Equigranular, prismatic plagioclase and K-feldspar, chlorite altered hornblende phenocrysts; quartz-feldspar matrix, sericite altered; minor magnetite	Granodiorite

Table A2. Sample locations and descriptions for Oligo-Miocene igneous rocks from the Kassandra Mining District

No.	Latitide	Longitude	Area	Field Notes	TAS Lithology
593895	40.50126	23.80213	Fisoka-Stratoni	Porphyritic; crowded texture, sericite-altered plagioclase phenocrysts in aphanitic (quartz-feldspar?) matrix; no mafic minerals evident	Granodiorite
279441	40.51228	23.81227	Fisoka-Stratoni	Porphyritic; quartz-eye and sericite-altered plagioclase phenocrysts; quartz-rich matrix; no mafic minerals present; secondary limonite-goethite after pyrite	Granodiorite
279442	40.51194	23.81235	Fisoka-Stratoni	Porphyritic; quartz eyes and sericite-altered plagioclase phenocrysts; quartz-rich matrix, no mafic minerals present; limonite-goethite replacing pyrite	Granodiorite
593588	40.51678	23.81293	Fisoka-Stratoni	Porphyritic; quartz eyes and sericite-altered feldspar phenocrysts; disseminated green sericite in matrix; boxwork texture	Granodiorite
679715	40.51645	23.81529	Fisoka-Stratoni	Brecciated porphyry; quartz eyes and sericite-altered feldspar phenocrysts; matrix also replaced by sericite; no mafic minerals evident	Granodiorite
679716	40.51674	23.81419	Fisoka-Stratoni	Post-breccia porphyry dike, crosscutting porphyry breccia (sample 679715); porphyritic texture; quartz eyes and sericite-altered feldspar phenocrysts; green disseminated sericite within fine-grained matrix	Granodiorite
593878	40.50818	23.82518	Fisoka-Stratoni	Fine-grained, micro-porphyritic texture; feldspar-rich; bleached, sericite-altered plagioclase phenocrysts; chlorite-altered mafic minerals; disseminated pyrite; pervasive alteration/weathering	Granite
679713	40.52262	23.82828	Stratoni	Intermediate composition; quartz-plagioclase-K-feldspar-biotite phenocrysts; minor hornblende-clinopyroxene, chlorite-epidote after biotite-hornblende?; disseminated magnetite; weak sericite alteration	Diorite
679714	40.52982	23.82598	Stratoni	Equigranular, quartz-plagioclase-K-feldspar, biotite phenocrysts; disseminated pyrite(± chalcopyrite?); minor magnetite; chlorite-epidote after biotite; secondary $CuCO_3$ staining on biotite	Granodiorite
593551	40.52347	23.82731	Stratoni	Equigranular, quartz-plagioclase-K-feldspar-biotite(hornblende?) phenocrysts; chlorite-altered mafic minerals; disseminated magnetite, strongly magnetic	Monzonite

Table A2. Sample locations and descriptions for Oligo-Miocene igneous rocks from the Kassandra Mining District

No.	Latitide	Longitude	Area	Field Notes	TAS Lithology
593552	40.52894	23.82437	Stratoni	Quartz-plagioclase-K-feldspar with minor biotite-hornblende? Phenocrysts; K-feldspar-quartz matrix, chlorite-epidote after mafic minerals; sericite-alteration associated with quartz-pyrite veins; secondary $CuCO_3$ staining of rock	Granodiorite
593553	40.52449	23.82620	Stratoni	Quartz-plagioclase-K-feldspar-biotite(hornblende?) phenocrysts; chlorite-altered; disseminated magnetite and rare pyrite	Granodiorite
593554	40.53241	23.82587	Stratoni	Quartz-plagioclase-K-feldspar-biotite(hornblende?) phenocrysts; chlorite-epidote-altered mafic minerals; sericite-clay-altered feldspars	Granodiorite
593565	40.52974	23.82431	Stratoni	Porphyritic; quartz-plagioclase-K-feldspar-biotite phenocrysts; chlorite-epidote-altered biotite and sericite-altered feldspars; secondary $CuCO_3$ staining of rock surface; weakly magnetic	Granodiorite
593566	40.52666	23.82523	Stratoni	Porphyritic, crowded texture; quartz-plagioclase-K-feldspar-biotite phenocrysts; sericite after feldspars and chlorite-altered biotite; magnetite in matrix; minor pyrite, $CuCO_3$ staining of rock surface	Granodiorite
593580	40.51717	23.81934	Stratoni	Sub-porphyritic; quartz-plagioclase-K-feldspar phenocrysts; minor biotite-hornblende?; sericite-altered plagioclase and chlorite-epidote replacing biotite-hornblende; minor disseminated pyrite, weakly magnetic	Diorite

Abbreviations: TAS = Total-alkali silica

Table A3. Major oxide and trace element geochemistry for Oligo-Miocene igneous rocks from the Kassandra Mining District

	Wt. (%)												ppm							
No.	SiO_2	Al_2O_3	Fe_2O_3 (T)	MgO	CaO	Na_2O	K_2O	TiO_2	P_2O_5	MnO	Cr_2O_3	LOI	Total	Ba	Sr	Nb	Ta	Ti	Th	U	Y
Early Miocene Suite																					
593555	65.44	15.34	3.02	0.79	2.75	3.33	4.17	0.34	0.24	0.08	0.03	4.10	99.57	1985	862	12	0.9	500	35.6	11.4	18.3
593556	58.21	15.15	4.98	2.25	4.06	2.52	3.95	0.40	0.35	0.10	0.01	7.70	99.64	1405	603	9.3	0.6	460	34.6	12.8	17.2
593557	63.62	16.07	3.24	1.14	2.61	3.32	4.56	0.35	0.20	0.07	0.01	4.30	99.55	2096	856	13.3	0.9	130	44.8	13.7	16.5
593558	61.62	15.66	4.42	1.83	3.14	3.51	3.97	0.43	0.41	0.09	0.01	4.40	99.5	2249	1006	10.1	0.5	450	39	13.3	18.7
593559	66.93	15.73	3.39	0.62	2.17	3.35	3.97	0.30	0.15	0.08	0.02	2.90	99.63	1719	871	9.4	0.7	410	24.5	8.8	18.3
593560	65.30	16.68	3.49	0.66	1.77	3.64	4.53	0.37	0.24	0.08	0.02	2.50	99.28	4190	1028	13.9	0.8	570	46.2	14.7	30.2
593561	63.26	16.01	4.73	1.51	1.99	3.53	4.06	0.47	0.38	0.08	0.01	3.50	99.55	1713	1146	9.1	0.6	940	30.4	13.3	22.1
593562	68.93	16.80	2.26	0.51	0.19	0.12	5.84	0.37	0.15	0.08	0.02	4.40	99.69	1233	221	11.7	0.7	10	30.5	10.4	17.7
593563	68.23	16.63	4.24	0.65	0.09	0.05	4.44	0.36	0.13	0.23	0.01	4.70	99.72	546	107	11.9	0.9	<1	33.6	9.9	19.3
593564	64.69	17.22	3.70	0.37	0.63	1.25	5.25	0.47	0.36	0.08	0.02	5.50	99.49	2940	362	12.6	0.7	30	40.7	15.5	19.4
593586	64.75	16.59	3.68	0.68	2.31	3.73	4.25	0.41	0.34	0.09	0.02	2.60	99.46	2080	1446	12.9	0.8	700	37.8	16.8	18.8
593587	67.86	16.36	2.86	0.21	1.43	3.23	4.12	0.33	0.20	0.07	0.01	2.80	99.51	2217	1091	15.7	0.8	30	43.5	13.9	19.9
593567	65.10	16.15	4.33	1.37	0.76	5.62	2.00	0.49	0.19	<0.01	0.02	3.50	99.53	1356	1122	19.4	0.8	720	67.1	17.3	17.9
593568	69.96	16.38	2.38	0.58	0.06	0.06	2.30	0.48	0.17	<0.01	0.01	7.10	99.47	2885	456	20.1	1.2	10	61.3	16.5	17.7
593569	65.97	16.79	3.55	1.69	0.30	2.09	3.06	0.69	0.23	<0.01	0.02	5.30	99.7	610	470	20.3	1.2	10	53	15.1	20
593570	64.95	15.96	5.83	1.62	0.96	3.71	1.40	0.67	0.32	<0.01	0.03	4.20	99.66	511	697	21.4	1.2	20	66.5	15.2	16.2
593571	64.78	17.25	3.63	2.18	1.35	3.97	2.85	0.48	0.32	<0.01	0.01	2.60	99.45	1926	1087	19.5	1.1	710	64.9	14.8	25.2
593573	65.41	15.31	5.14	1.06	1.61	4.24	4.85	0.34	0.21	0.02	0.03	1.00	99.23	2500	1326	15.8	0.9	980	57.8	13.7	15.6
593574	61.76	13.93	9.04	2.13	1.40	3.00	5.78	0.40	0.24	0.04	0.03	1.50	99.27	1779	795	13.5	0.9	1170	55.1	12.6	15.4
593575	64.18	13.87	9.11	0.81	1.02	3.08	5.75	0.29	0.14	0.02	0.02	1.20	99.49	1959	868	5.7	0.5	600	52.9	11.5	6.4
593576	64.27	14.50	7.56	0.95	1.36	3.40	5.85	0.31	0.17	0.03	0.03	1.00	99.44	2215	972	9.7	0.7	530	51.1	12.6	11
593577	64.88	15.39	5.34	0.98	1.48	4.05	5.58	0.32	0.18	0.04	0.04	0.90	99.21	2458	1229	14.4	1	860	54.6	15.3	15.5
593594	64.15	15.92	4.20	1.30	3.22	4.50	4.11	0.37	0.22	0.04	0.01	1.30	99.38	2425	1571	19.9	0.9	720	55.3	17.3	21.8
593596	62.73	14.19	9.23	0.88	1.15	3.23	6.08	0.29	0.14	0.02	0.01	1.30	99.23	2377	941	8.2	0.9	570	56.7	12	9.1

Table A3. Major oxide and trace element geochemistry for Oligo-Miocene igneous rocks from the Kassandra Mining District

	Wt. (%)												ppm							
No.	SiO_2	Al_2O_3	Fe_2O_3 (T)	MgO	CaO	Na_2O	K_2O	TiO_2	P_2O_5	MnO	Cr_2O_3	LOI	Total	Ba	Sr	Nb	Ta	Ti	Th	U	Y
593597	61.19	14.27	8.67	1.52	1.60	2.36	6.42	0.40	0.23	0.03	0.01	2.60	99.34	1791	737	12.3	0.9	620	65	19	13.7
593583	56.60	13.39	4.07	4.57	5.29	1.94	5.49	0.70	0.37	0.08	0.04	6.70	99.24	1080	3836	14.9	1.2	2500	22.8	9.4	18.5
279415	55.75	13.06	3.97	4.38	4.88	2.71	5.02	0.69	0.36	0.08	0.05	8.70	99.64	1245	268	16	1.1	380	21.8	9.5	16.8
279433	66.50	15.29	4.41	0.83	0.60	0.06	6.33	0.82	0.49	0.44	0.04	3.90	99.76	436	47	18.2	1.5	10	25.9	10.9	22.9
279436	65.75	16.05	3.66	1.87	0.90	4.68	3.22	0.52	0.41	0.07	0.02	2.50	99.62	1105	1110	12	0.6	40	34.9	7.5	14.6
279437	63.80	14.79	4.26	3.47	0.89	1.23	5.13	0.80	0.45	0.06	0.04	4.70	99.61	1406	363	18.9	1.3	30	24.4	11.2	20.1
279423	62.59	15.57	3.86	2.81	2.03	3.04	4.05	0.53	0.18	0.08	0.02	4.10	98.9	1220	379	12.1	1	300	18.2	7.4	19.3
593579	66.47	16.58	3.95	0.62	0.33	2.66	4.98	0.59	0.18	0.08	0.03	3.30	99.77	885	338	12.8	0.9	140	20.7	8.6	16.4
593584	65.12	15.75	3.41	1.99	2.95	3.44	3.64	0.47	0.17	0.08	0.02	2.70	99.74	877	564	9.6	0.9	1510	19.8	5.8	16.4
679705	60.11	14.48	4.36	2.95	5.41	3.25	3.53	0.41	0.44	0.09	0.01	4.40	99.45	1983	1516	8.5	0.6	560	38.6	13.1	19.5
Late Oligocene Suite																					
593591	69.53	17.18	2.69	0.59	0.16	0.04	4.55	0.38	0.15	0.07	0.00	4.50	99.81	337	40	11.9	0.8	<1	32.9	14.2	18.8
593599	51.90	17.88	8.49	4.27	7.41	3.34	2.08	0.97	0.21	0.15	0.01	3.00	99.7	609	758	4.9	0.5	1410	7.4	1.7	21.5
593600	52.36	17.88	9.37	4.66	8.35	3.51	1.78	0.91	0.22	0.17	0.01	0.50	99.68	546	830	4.6	0.3	890	7.8	1.9	23.6
593870	57.35	17.13	7.29	3.26	6.45	3.59	2.18	0.78	0.17	0.14	0.01	1.40	99.74	537	617	6.6	0.5	1390	9.7	2.6	22.7
593871	69.45	17.43	2.70	0.72	0.06	0.06	5.13	0.52	0.06	<0.01	0.01	3.70	99.88	419	50	11.4	1	<1	19.7	6.2	11.7
593872	66.03	19.33	4.32	0.49	0.06	0.20	4.16	0.65	0.06	<0.01	0.00	4.50	99.85	784	65	8.3	0.5	20	14.1	3.9	14.3
593873	63.22	21.76	3.28	0.83	0.05	0.48	5.37	0.59	0.06	<0.01	0.00	4.10	99.78	1136	139	6.8	0.7	20	10.1	2.5	13.8
593874	65.44	17.29	5.03	0.62	0.53	4.38	2.42	0.65	0.13	0.01	0.01	3.30	99.83	430	447	7.7	0.7	40	12.6	4.4	7.2
593875	57.59	17.45	6.93	2.94	4.90	3.59	3.46	0.63	0.27	0.14	0.00	1.80	99.68	800	775	6.7	0.4	890	13	3.4	21.3
593876	70.46	15.99	3.83	0.84	0.08	0.04	4.46	0.40	0.16	<0.01	0.00	3.60	99.84	452	74	6.7	0.6	<1	20.1	4.1	14.4
593881	54.76	17.88	8.30	3.82	7.09	3.54	2.32	0.81	0.25	0.15	0.01	0.80	99.69	626	804	6.9	0.5	1490	10.4	2.6	24.2
593882	56.17	17.07	7.59	3.44	6.22	3.42	2.98	0.78	0.20	0.14	0.01	1.70	99.71	626	665	7.7	0.7	1640	19.9	4.2	25.7
593883	63.24	16.46	5.19	1.76	2.19	2.57	3.04	0.47	0.14	0.12	0.00	4.50	99.72	1032	422	10	0.8	50	21.5	6.7	24

Table A3. Major oxide and trace element geochemistry for Oligo-Miocene igneous rocks from the Kassandra Mining District

	Wt. (%)												ppm							
No.	SiO_2	Al_2O_3	Fe_2O_3 (T)	MgO	CaO	Na_2O	K_2O	TiO_2	P_2O_5	MnO	Cr_2O_3	LOI	Total	Ba	Sr	Nb	Ta	Ti	Th	U	Y
593884	65.17	16.34	7.55	0.79	0.05	0.08	5.02	0.47	0.12	0.07	0.01	4.10	99.78	522	15	9.5	0.7	<1	22.3	7.2	16.8
593887	49.07	16.52	9.34	4.20	6.38	3.54	2.38	0.92	0.23	0.15	0.01	7.00	99.72	610	549	5.6	0.5	2250	8	2.4	23.6
593888	49.61	16.86	10.18	5.32	8.19	2.97	2.43	0.93	0.32	0.18	0.01	2.60	99.62	805	897	5.4	0.4	2540	11.3	2.7	25.7
593893	68.33	18.35	2.49	0.49	0.10	0.12	5.12	0.61	0.08	0.02	<0.002	4.10	99.79	694	36	7.4	0.6	<1	13.6	4	11.9
279430	72.49	15.64	1.39	0.19	0.43	4.29	3.54	0.20	0.01	<0.01	0.02	1.60	99.81	1028	390	7.8	0.3	20	15.2	3.3	5.6
279431	69.27	17.17	3.03	0.61	0.10	0.60	3.97	0.65	0.06	<0.01	0.02	4.30	99.83	715	129	7.7	0.7	10	14.4	3.3	16.6
279432	74.17	15.21	2.82	0.27	0.04	0.20	3.88	0.20	0.05	<0.01	0.03	3.00	99.88	745	38	7.9	0.5	<1	8.9	2.6	4.5
279445	66.65	18.54	4.48	0.58	0.06	0.31	4.28	0.58	0.02	<0.01	0.01	4.40	99.87	563	76	6.8	0.6	10	12	3.4	13.9
279446	66.75	17.06	5.97	0.52	0.07	0.18	4.86	0.56	0.03	<0.01	0.03	3.80	99.81	821	69	6.9	0.8	10	22.7	5.5	15.1
279447	72.45	16.36	1.76	0.61	0.04	0.26	4.71	0.52	0.04	<0.01	0.03	3.10	99.85	646	58	7.3	0.9	20	11	4.1	8.9
279448	68.08	19.09	2.20	0.64	0.06	0.29	5.47	0.65	0.02	<0.01	0.03	3.30	99.84	714	59	6.9	0.4	10	5.2	1.5	17.1
279449	74.76	13.45	3.93	0.36	0.01	0.08	3.96	0.44	0.02	<0.01	0.03	2.90	99.92	223	5	8.8	1.2	10	26.2	3.5	14.2
593581	63.21	15.36	5.96	2.02	3.29	2.89	3.05	0.44	0.15	0.05	0.03	3.30	99.77	639	522	5.8	0.6	800	18.4	2.7	14.4
593582	55.44	16.53	8.23	4.31	6.14	2.85	2.18	0.71	0.33	0.13	0.02	2.80	99.71	518	703	5.6	0.3	2720	15	4.7	24.8
679709	61.32	15.36	5.04	1.78	4.21	3.06	3.48	0.43	0.15	0.08	0.02	4.80	99.72	935	630	6.7	0.7	60	20.6	7.4	15.8
679710	52.35	16.30	9.33	3.86	4.74	2.94	2.39	0.85	0.51	0.09	<0.002	6.40	99.76	525	460	6.8	0.4	400	13.3	5.8	27.6
679711	62.27	15.51	6.98	1.95	3.46	3.07	3.27	0.45	0.16	0.05	0.03	2.60	99.75	621	739	6.4	0.7	950	19.1	4.6	13.9
593592	63.57	15.58	5.28	1.87	2.54	3.32	3.63	0.45	0.15	0.04	0.01	3.30	99.74	624	494	6.7	0.6	60	17.8	2.4	13.9
593593	55.23	17.00	8.63	4.24	6.14	3.12	2.26	0.72	0.33	0.13	0.01	1.90	99.68	604	828	6.4	0.4	2640	14.8	5.6	24.7
593877	69.56	17.07	4.27	0.70	0.29	0.77	3.45	0.47	0.02	<0.01	0.00	3.20	99.83	680	115	8.6	0.8	10	10.4	3.1	13.8
593894	64.45	16.40	5.25	1.85	2.57	3.09	3.59	0.44	0.15	0.04	0.00	1.90	99.74	766	661	6.6	0.7	870	21.5	5	22.1
593895	68.85	17.28	3.84	0.73	0.04	0.21	5.27	0.63	0.06	<0.01	0.00	2.90	99.84	677	45	7.3	0.9	40	9.7	2.6	14.6
279441	69.65	16.64	3.52	0.73	0.12	0.08	4.92	0.50	0.03	0.01	0.04	3.60	99.83	781	17	8.5	0.8	<1	17.1	4.7	8.2
279442	69.30	16.50	3.92	0.71	0.07	0.08	4.90	0.49	0.08	<0.01	0.03	3.70	99.78	746	20	9	0.9	<1	17.8	5.4	8
593588	71.30	15.99	2.34	0.95	0.07	0.13	4.93	0.54	0.07	<0.01	0.03	3.50	99.84	511	20	10.1	0.8	20	12.7	4.2	12.2

Table A3. Major oxide and trace element geochemistry for Oligo-Miocene igneous rocks from the Kassandra Mining District

	Wt. (%)												ppm							
No.	SiO_2	Al_2O_3	Fe_2O_3 (T)	MgO	CaO	Na_2O	K_2O	TiO_2	P_2O_5	MnO	Cr_2O_3	LOI	Total	Ba	Sr	Nb	Ta	Ti	Th	U	Y
679715	66.28	17.75	3.39	1.07	0.12	0.25	5.52	0.66	0.13	0.01	0.03	4.60	99.77	852	88	9.1	0.7	<1	11.5	4.2	13.3
679716	66.44	15.69	5.08	1.07	0.07	0.80	5.41	0.50	0.10	<0.01	0.04	4.60	99.76	731	105	8.6	0.5	20	15.3	6.2	13.4
593878	71.84	16.62	1.42	0.31	0.33	4.58	2.57	0.27	0.09	0.02	0.00	1.80	99.88	271	324	9.8	0.5	<1	23.1	4.5	10.7
679713	58.97	16.92	6.33	2.68	6.02	3.49	2.57	0.54	0.21	0.12	0.02	1.80	99.69	552	761	9.1	0.9	830	21.7	8.2	21.4
679714	64.37	15.87	4.35	2.11	3.19	3.05	3.27	0.44	0.16	0.04	0.00	2.80	99.67	843	676	9.4	1.2	1220	26	7.9	18.6
593551	57.72	17.92	6.60	2.96	6.69	3.64	2.55	0.61	0.21	0.15	0.00	0.70	99.7	643	913	5.9	0.6	2220	16.7	3.6	17
593552	63.50	16.64	4.69	2.10	3.57	3.09	2.93	0.45	0.16	0.05	0.00	2.40	99.54	720	665	8.2	0.7	1070	24.4	7.2	20.9
593553	63.55	16.71	5.01	2.11	3.07	3.01	3.36	0.46	0.14	0.08	0.03	2.00	99.56	718	651	7.9	1	800	31	6.8	20.2
593554	65.51	16.23	4.34	1.90	2.34	2.67	3.57	0.43	0.14	0.04	0.03	2.50	99.67	636	501	8.9	1	810	29.3	11.4	16.8
593565	62.91	16.43	4.77	2.64	1.83	3.04	3.47	0.48	0.16	0.03	0.02	3.40	99.2	1025	602	8.9	0.7	660	24.2	9.1	16.6
593566	64.31	16.62	5.01	1.98	2.94	3.26	3.10	0.45	0.17	0.06	0.03	1.80	99.72	922	687	8.3	0.7	990	26.1	6.3	18.9
593580	62.53	16.51	4.41	1.91	3.28	2.82	4.06	0.51	0.18	0.06	0.02	3.40	99.72	854	687	8.4	0.8	970	27.9	7.7	16

Abbreviations: Wt. % = weight percent; ppm = parts per million; (T) = total

Table A4. Rare earth element geochemistry for Oligo-Miocene igneous rocks from the Kassandra Mining District

	ppm														Ratios				
No.	La	Ce	Pr	Nd	Sm	Eu	Gd	Tb	Dy	Ho	Er	Tm	Yb	Lu	Eu_n/Eu^*	La/Sm	La/Yb	Sm/Yb	Sr/Y
Early Miocene Suite																			
593555	65.5	109.9	13.17	47.3	7.38	1.71	5.37	0.64	3.37	0.56	1.88	0.26	1.77	0.28	0.83	8.88	37.01	4.17	47.09
593556	76.7	142.8	15.89	58.8	8.59	1.86	5.95	0.71	3.4	0.58	1.8	0.27	1.9	0.29	0.80	8.93	40.37	4.52	35.08
593557	74.7	133.8	14.65	50.7	7.58	1.63	5.24	0.66	3.08	0.54	1.51	0.27	1.82	0.29	0.79	9.85	41.04	4.16	51.90
593558	88.7	158.5	17.97	67.2	9.43	2.08	6.56	0.75	3.61	0.63	1.84	0.26	1.66	0.28	0.81	9.41	53.43	5.68	53.79
593559	54.9	83.6	10.66	39.2	5.81	1.32	4.8	0.59	3.07	0.55	1.81	0.25	1.62	0.24	0.76	9.45	33.89	3.59	47.57
593560	186.5	160.6	33.88	122.7	16.55	3.43	11.21	1.31	6.09	1.13	3	0.4	2.67	0.39	0.77	11.27	69.85	6.20	34.04
593561	72.2	127.3	15.39	56.1	8.79	2.07	6.69	0.83	4.09	0.78	2.19	0.3	1.88	0.32	0.83	8.21	38.40	4.68	51.84
593562	54.9	105.8	11.17	42.5	6.54	1.37	4.59	0.57	2.84	0.54	1.77	0.28	1.86	0.35	0.76	8.39	29.52	3.52	12.46
593563	54.1	99.9	10.99	41.1	6.3	1.58	5.03	0.61	3.32	0.58	1.62	0.3	2.26	0.31	0.86	8.59	23.94	2.79	5.53
593564	80.2	155.8	17.12	64.2	9.51	2.13	6.72	0.76	3.41	0.63	1.5	0.27	2.02	0.28	0.81	8.43	39.70	4.71	18.64
593586	72	137.7	15.06	54.7	8.45	2.02	5.85	0.69	3.55	0.65	1.75	0.26	1.86	0.29	0.88	8.52	38.71	4.54	76.91
593587	59.8	128.7	14.67	52.9	7.48	1.9	5.66	0.67	3.52	0.57	1.68	0.29	1.89	0.29	0.89	7.99	31.64	3.96	54.83
593567	142.3	247.8	26.59	90.3	12.05	2.56	7.84	0.82	3.61	0.62	1.95	0.25	1.81	0.32	0.81	11.81	78.62	6.66	62.68
593568	144.6	251.5	27.52	94.1	12.68	2.54	8.09	0.83	3.8	0.61	1.76	0.26	2.14	0.33	0.77	11.40	67.57	5.93	25.75
593569	144.1	271.7	30.54	106.5	15.96	2.99	9.9	1.04	4.37	0.69	1.95	0.31	2.33	0.4	0.73	9.03	61.85	6.85	23.51
593570	145.1	263.8	30.18	108	15.75	3.54	9.46	0.9	3.56	0.53	1.67	0.26	2.04	0.35	0.89	9.21	71.13	7.72	43.01
593571	136.2	244.1	26.91	95.7	13.73	2.47	8.56	1.07	5.5	0.88	2.41	0.37	2.34	0.37	0.70	9.92	58.21	5.87	43.12
593573	42.3	86.6	10.87	39.5	6.46	1.46	4.53	0.55	2.84	0.48	1.4	0.21	1.35	0.23	0.83	6.55	31.33	4.79	85.00
593574	39.1	83.2	9.95	38.5	6.21	1.35	4.57	0.57	2.68	0.53	1.45	0.23	1.48	0.22	0.77	6.30	26.42	4.20	51.64
593575	14.2	26.7	3.29	12.4	2.05	0.63	1.53	0.18	0.9	0.19	0.55	0.1	0.74	0.15	1.09	6.93	19.19	2.77	135.61
593576	30.9	59.8	6.56	23.6	4.16	1	2.84	0.36	1.54	0.32	0.94	0.14	0.98	0.2	0.89	7.43	31.53	4.24	88.33
593577	38.7	80.1	9.72	36.5	5.8	1.24	4.23	0.53	2.78	0.46	1.39	0.21	1.42	0.23	0.77	6.67	27.25	4.08	79.31
593594	83.1	174.6	19.09	68.2	10.34	2.05	6.49	0.78	3.92	0.72	2.07	0.29	2.05	0.34	0.77	8.04	40.54	5.04	72.04
593596	15.7	34.3	3.91	15.1	2.76	0.88	1.98	0.26	1.22	0.25	0.78	0.11	0.97	0.14	1.15	5.69	16.19	2.85	103.45

Table A4. Rare earth element geochemistry for Oligo-Miocene igneous rocks from the Kassandra Mining District

	ppm														Ratios				
No.	La	Ce	Pr	Nd	Sm	Eu	Gd	Tb	Dy	Ho	Er	Tm	Yb	Lu	Eu_n/Eu^*	La/Sm	La/Yb	Sm/Yb	Sr/Y
593597	48.5	93.1	10.19	38.4	6.28	1.2	4.22	0.51	2.45	0.46	1.26	0.2	1.4	0.22	0.71	7.72	34.64	4.49	53.77
593583	53.1	103.6	12.2	45.8	7.24	1.41	5	0.64	3.22	0.52	1.63	0.24	1.83	0.27	0.72	7.33	29.02	3.96	207.33
279415	50.6	105.1	12.18	46.4	6.87	1.5	5.02	0.62	3.13	0.53	1.51	0.24	1.65	0.25	0.78	7.37	30.67	4.16	15.96
279433	58.1	123.5	14.01	54	8.5	1.78	5.86	0.76	4.04	0.66	1.97	0.29	2.02	0.33	0.77	6.84	28.76	4.21	2.07
279436	93	179.6	19.41	70.2	10.15	2.25	6.09	0.7	3.24	0.52	1.42	0.21	1.34	0.2	0.87	9.16	69.40	7.57	76.01
279437	56.8	115.6	13.39	48	7.7	1.58	5.58	0.71	3.43	0.64	1.9	0.26	2.05	0.3	0.74	7.38	27.71	3.76	18.06
279423	40.7	74.4	8.49	31	4.83	1.11	3.91	0.59	3.45	0.6	1.97	0.29	1.77	0.3	0.78	8.43	22.99	2.73	19.62
593579	39.5	74.8	8.03	26.6	4.36	1.04	3.57	0.51	2.8	0.55	1.63	0.28	1.92	0.29	0.81	9.06	20.57	2.27	20.62
593584	38.7	66.2	7.49	26.9	4.1	0.97	3.75	0.52	2.94	0.53	1.7	0.26	1.96	0.3	0.76	9.44	19.74	2.09	34.36
679705	97.8	192	22.5	80.6	11.45	2.53	7.41	0.83	3.36	0.62	1.66	0.24	1.67	0.32	0.84	8.54	58.56	6.86	77.74
Late Oligocene Suite																			
593591	54.9	104.8	11.16	40	6.46	1.35	4.55	0.58	2.93	0.61	1.74	0.28	1.94	0.32	0.76	8.50	28.30	3.33	2.11
593599	23	44.3	5.47	22.4	4.64	1.31	4.49	0.67	4.17	0.77	2.38	0.33	2.05	0.34	0.88	4.96	11.22	2.26	35.25
593600	26.8	54.7	6.32	25	5.43	1.32	5.07	0.74	4.33	0.84	2.49	0.36	2.42	0.38	0.77	4.94	11.07	2.24	35.15
593870	29.2	58.4	6.12	22.9	4.6	1.12	4.7	0.73	4.1	0.83	2.44	0.36	2.68	0.38	0.74	6.35	10.90	1.72	27.17
593871	40.7	68.4	6.24	20.8	3.13	0.52	2.47	0.31	2.07	0.39	1.45	0.22	1.64	0.28	0.57	13.00	24.82	1.91	4.26
593872	19	36.1	3.67	12.9	2.57	0.69	2.81	0.46	2.57	0.58	1.78	0.28	2.08	0.31	0.78	7.39	9.13	1.24	4.57
593873	38.9	64.2	6.71	24.3	3.74	0.78	3.06	0.38	2.36	0.45	1.42	0.23	1.65	0.26	0.70	10.40	23.58	2.27	10.07
593874	23	36.1	3.3	11	1.42	0.34	1.36	0.19	1.36	0.25	0.78	0.14	1.15	0.2	0.75	16.20	20.00	1.23	62.07
593875	33.4	69.1	7.44	29.2	5.25	1.29	4.97	0.71	4.06	0.77	2.16	0.34	2.27	0.36	0.77	6.36	14.71	2.31	36.40
593876	33	63.8	6.79	27.8	4.51	0.87	3.56	0.49	2.95	0.5	1.44	0.2	1.56	0.23	0.66	7.32	21.15	2.89	5.13
593881	30	60.7	6.89	27.6	5.3	1.35	5.04	0.76	4.13	0.84	2.46	0.37	2.57	0.39	0.80	5.66	11.67	2.06	33.23
593882	35.4	69.6	7.62	29.2	5.75	1.32	5.46	0.77	4.43	0.83	2.67	0.37	2.47	0.39	0.72	6.16	14.33	2.33	25.89
593883	37.3	70.2	7.29	25.5	5.08	1.06	4.44	0.69	3.84	0.78	2.18	0.34	2.33	0.37	0.68	7.34	16.01	2.18	17.57

Table A4. Rare earth element geochemistry for Oligo-Miocene igneous rocks from the Kassandra Mining District

	ppm														Ratios				
No.	La	Ce	Pr	Nd	Sm	Eu	Gd	Tb	Dy	Ho	Er	Tm	Yb	Lu	Eu_n/Eu^*	La/Sm	La/Yb	Sm/Yb	Sr/Y
593884	33	65.4	6.63	24.1	4.02	0.68	3.52	0.58	3.18	0.66	2.08	0.31	2.09	0.31	0.55	8.21	15.79	1.92	0.90
593887	25.9	54.2	6.35	26.7	5.89	1.33	5.44	0.79	4.38	0.91	2.48	0.38	2.41	0.37	0.72	4.40	10.75	2.44	23.28
593888	38.8	76.5	8.39	35.3	6.96	1.65	6.47	0.91	4.71	0.89	2.59	0.36	2.4	0.34	0.75	5.57	16.17	2.90	34.91
593893	47	83.9	9.61	34.3	5.69	1.17	3.82	0.44	2.25	0.44	1.54	0.22	1.75	0.34	0.77	8.26	26.86	3.25	2.99
279430	22.7	40.5	4.14	13.8	2.1	0.51	1.42	0.18	0.87	0.22	0.62	0.08	0.69	0.09	0.90	10.81	32.90	3.04	69.59
279431	35.1	60.1	6.39	21.8	3.5	0.87	3.11	0.5	3.04	0.58	1.68	0.27	2.01	0.27	0.81	10.03	17.46	1.74	7.75
279432	22.8	39.3	3.9	12.8	1.79	0.43	1.11	0.14	0.77	0.12	0.4	0.07	0.63	0.11	0.93	12.74	36.19	2.84	8.53
279445	29.1	52.6	5.31	19.3	3.43	0.76	3.02	0.46	2.72	0.52	1.56	0.23	1.6	0.24	0.72	8.48	18.19	2.14	5.45
279446	33.9	59.8	6.45	23.7	3.72	0.9	3.44	0.47	2.58	0.56	1.7	0.24	1.73	0.28	0.77	9.11	19.60	2.15	4.54
279447	33.2	57.9	5.85	20.8	3.12	0.69	2.42	0.28	1.68	0.32	0.85	0.16	1.28	0.2	0.77	10.64	25.94	2.44	6.55
279448	29.4	55.8	6.33	23.7	4.01	1.19	3.76	0.5	2.98	0.6	1.92	0.29	1.88	0.28	0.94	7.33	15.64	2.13	3.46
279449	38.6	72	7.37	27	4.04	0.92	3.07	0.42	2.09	0.48	1.58	0.27	1.65	0.33	0.80	9.55	23.39	2.45	0.33
593581	17.2	31.4	3.64	14.9	2.91	0.83	2.79	0.43	2.35	0.48	1.62	0.22	1.53	0.24	0.89	5.91	11.24	1.90	36.26
593582	36.1	67.5	8.03	33	6.19	1.62	5.44	0.79	4.28	0.83	2.41	0.38	2.4	0.35	0.85	5.83	15.04	2.58	28.35
679709	34.6	59.5	6.49	23.9	4.43	1.03	3.23	0.48	2.57	0.57	1.58	0.29	1.83	0.32	0.83	7.81	18.91	2.42	39.88
679710	29.2	58.8	7.15	28.5	6.67	1.17	5.94	0.92	5.12	0.98	2.96	0.46	3.02	0.43	0.57	4.38	9.67	2.21	16.66
679711	12.4	24.2	2.75	10.2	2.35	0.69	2.35	0.39	1.78	0.34	1.27	0.17	1.56	0.23	0.90	5.28	7.95	1.51	53.17
593592	18.1	36	3.7	14.3	2.79	0.88	2.83	0.46	2.54	0.5	1.47	0.23	1.78	0.26	0.96	6.49	10.17	1.57	35.55
593593	36	74.7	8.29	32.2	6.27	1.44	5.72	0.84	4.23	0.81	2.25	0.35	2.35	0.36	0.74	5.74	15.32	2.67	33.51
593877	22.1	43.2	4.05	14.3	2.37	0.51	2.2	0.31	2.19	0.44	1.53	0.23	1.72	0.28	0.68	9.32	12.85	1.38	8.35
593894	38.7	74.3	7.45	27.5	5.27	1.28	4.99	0.74	4.28	0.81	2.48	0.34	2.41	0.38	0.76	7.34	16.06	2.19	29.89
593895	35.5	68.5	7.18	26	4.85	0.91	3.6	0.47	2.8	0.53	1.8	0.26	2	0.29	0.67	7.32	17.75	2.43	3.10
279441	24.2	44.4	4.63	16.1	2.73	0.53	1.99	0.27	1.45	0.34	0.89	0.15	1.35	0.2	0.70	8.86	17.93	2.02	2.07
279442	26.9	46.9	5.09	16.8	2.92	0.61	2.42	0.31	1.63	0.33	0.9	0.16	1.15	0.2	0.70	9.21	23.39	2.54	2.48
593588	38.4	64.1	6.45	22.5	3.26	0.57	2.71	0.33	1.7	0.41	1.24	0.22	1.55	0.21	0.59	11.78	24.77	2.10	1.61

Table A4. Rare earth element geochemistry for Oligo-Miocene igneous rocks from the Kassandra Mining District

	ppm														Ratios			
No.	La	Ce	Pr	Nd	Sm	Eu	Gd	Tb	Dy	Ho	Er	Tm	Yb	Lu	Eu_n/Eu^*	La/Sm	La/Yb	Sm/Yb	Sr/Y
679715	33.3	64.2	6.72	21.4	4.31	0.89	2.94	0.51	3.02	0.58	1.38	0.19	1.42	0.23	0.76	7.73	23.45	3.04	6.63
679716	28	56.2	5.75	17.3	4.04	0.88	3.38	0.49	2.67	0.58	1.58	0.22	1.59	0.21	0.73	6.93	17.61	2.54	7.84
593878	56.5	101.1	10.15	34.9	5.14	1.18	3.56	0.42	2.22	0.39	1.04	0.15	1.09	0.18	0.84	10.99	51.83	4.72	30.26
679713	33.1	66.5	7.04	26.3	4.99	1.09	4.62	0.61	3.76	0.8	1.75	0.27	2.36	0.36	0.69	6.63	14.03	2.11	35.55
679714	37.6	66.2	6.02	24.8	4.22	1.01	3.38	0.51	2.66	0.56	1.9	0.24	1.95	0.33	0.82	8.91	19.28	2.16	36.35
593551	33.3	58.6	6.55	24	3.97	1.13	4.05	0.59	3.04	0.6	1.74	0.29	1.68	0.28	0.86	8.39	19.82	2.36	53.68
593552	36.6	65.2	6.82	25.7	4.18	1.18	3.94	0.58	3.48	0.75	2.01	0.33	2.21	0.33	0.89	8.76	16.56	1.89	31.81
593553	36.5	63.7	6.88	24.5	4.41	1.1	4.11	0.59	3.4	0.72	1.85	0.29	2.19	0.36	0.79	8.28	16.67	2.01	32.25
593554	38.3	67	6.84	22.8	4	0.8	3.44	0.52	3.09	0.63	1.81	0.28	1.79	0.27	0.66	9.58	21.40	2.23	29.80
593565	36.8	65.4	6.53	24.2	4.14	0.96	3.32	0.5	2.78	0.56	1.62	0.29	2.06	0.31	0.79	8.89	17.86	2.01	36.29
593566	29.6	52.5	5.62	20.5	4.01	0.88	3.76	0.56	3.04	0.6	2.04	0.32	2.25	0.36	0.69	7.38	13.16	1.78	36.34
593580	35.5	62.7	6.79	24.2	4.03	1.05	3.61	0.49	3.13	0.57	1.69	0.27	1.83	0.32	0.84	8.81	19.40	2.20	42.92

Abbreviations: Wt. % = weight percent; ppm = parts per million

Table A5. S1 foliation measurements

Domain	Latitude	Longitude	Station No.	Strike	Dip
S1 Foliation					
Olympias	40.59466	23.75281	2014_510	108	26
Olympias	40.58663	23.75317	2014_981	355	48
Olympias	40.57765	23.74571	2014_987	85	35
Olympias	40.57775	23.74684	2014_988	20	50
Olympias	40.57801	23.74758	2014_989	335	20
Olympias	40.57849	23.74793	2014_991	20	50
Olympias	40.57553	23.74440	2014_993	30	35
Olympias	40.57156	23.74219	2014_994	14	25
Olympias	40.57160	23.75767	2014_996	15	20
Olympias	40.57271	23.75823	2014_997	340	50
Olympias	40.57442	23.75864	2014_999	330	75
Olympias	40.57534	23.75893	2014_1000	335	60
Olympias	40.57552	23.75911	2014_1001	330	70
Olympias	40.59249	23.74204	2014_1002	355	20
Olympias	40.59514	23.74315	2014_1007	16	35
Olympias	40.59597	23.74370	2014_1013	25	25
Olympias	40.59659	23.74829	2014_1024	354	25
Olympias	40.59662	23.74839	2014_1027	5	30
Olympias	40.59688	23.74873	2014_1034	350	40
Olympias	40.59705	23.74882	2014_1041	10	35
Olympias	40.59733	23.74886	2014_1049	45	30
Olympias	40.60173	23.73599	2013_215	135	33
Olympias	40.60124	23.73624	2013_217	135	25
Olympias	40.60080	23.73621	2013_218	120	17
Olympias	40.60117	23.73605	2013_219	126	35
Olympias	40.60128	23.73589	2013_221	135	45
Olympias	40.60166	23.73555	2013_223	70	15

Domain	Latitude	Longitude	Station No.	Strike	Dip
S1 Foliation					
Stratoni FW	40.55552	23.77158	2013_919	132	55
Stratoni FW	40.55556	23.77166	2013_920	101	65
Stratoni FW	40.55559	23.77175	2013_921	132	79
Stratoni FW	40.55709	23.77241	2013_940	159	72
Stratoni FW	40.55694	23.77239	2013_941	160	89
Stratoni FW	40.55700	23.77043	2013_943	166	68
Stratoni FW	40.55681	23.77206	2013_1007	340	69
Stratoni FW	40.55719	23.77088	2013_1009	136	81
Stratoni FW	40.55719	23.77027	2013_1013	160	70
Stratoni FW	40.55737	23.77043	2013_1014	95	24
Stratoni FW	40.55785	23.77056	2013_1016	220	35
Stratoni FW	40.54778	23.77089	2013_1041	120	29
Stratoni FW	40.54660	23.77429	2013_1046	110	24
Stratoni FW	40.54724	23.77547	2013_1051	112	39
Stratoni FW	40.54762	23.77529	2013_1052	126	59
Stratoni FW	40.54807	23.77509	2013_1053	75	25
Stratoni FW	40.54912	23.77569	2013_1056	125	25
Stratoni FW	40.54980	23.77599	2013_1058	126	45
Stratoni FW	40.55021	23.77592	2013_1059	100	85
Stratoni FW	40.55004	23.77766	2013_1061	112	44
Stratoni FW	40.55014	23.77795	2013_1062	217	61
Stratoni FW	40.55037	23.77829	2013_1063	120	50
Stratoni FW	40.55064	23.77846	2013_1064	101	70
Stratoni FW	40.55081	23.77828	2013_1065	114	71
Stratoni FW	40.55177	23.77858	2013_1068	140	45
Stratoni FW	40.55409	23.77657	2013_1070	124	71
Stratoni FW	40.55427	23.77714	2013_1071	135	64

Table A5. S1 foliation measurements

Domain	Latitude	Longitude	Station No.	Strike	Dip
S1 Foliation					
Olympias	40.60201	23.73545	2013_226	75	21
Olympias	40.60216	23.73533	2013_228	120	30
Olympias	40.60217	23.73523	2013_230	97	14
Olympias	40.60214	23.73490	2013_231	93	35
Olympias	40.60214	23.73464	2013_233	115	27
Olympias	40.60231	23.73438	2013_234	92	25
Olympias	40.60244	23.73394	2013_236	128	47
Olympias	40.60221	23.73370	2013_239	74	21
Olympias	40.60168	23.73304	2013_240	101	15
Olympias	40.60143	23.73255	2013_242	88	20
Olympias	40.60134	23.73234	2013_245	67	16
Olympias	40.60057	23.73156	2013_250	124	25
Olympias	40.60038	23.73139	2013_254	76	25
Olympias	40.60039	23.73090	2013_257	96	25
Olympias	40.60056	23.73082	2013_258	130	35
Olympias	40.60133	23.73100	2013_259	40	15
Olympias	40.60216	23.73056	2013_261	132	25
Olympias	40.60217	23.73108	2013_262	115	25
Olympias	40.60228	23.73132	2013_263	127	26
Olympias	40.60263	23.73168	2013_264	138	34
Olympias	40.60336	23.73085	2013_265	144	30
Olympias	40.60396	23.73103	2013_267	123	20
Olympias	40.60423	23.73059	2013_269	137	26
Olympias	40.60442	23.72959	2013_270	107	26
Olympias	40.60443	23.72898	2013_271	100	20
Olympias	40.60423	23.72872	2013_273	115	23
Olympias	40.60395	23.72810	2013_274	125	14

Domain	Latitude	Longitude	Station No.	Strike	Dip
S1 Foliation					
Stratoni FW	40.55414	23.77677	2013_1072	122	70
Stratoni FW	40.55365	23.77640	2013_1074	106	66
Stratoni FW	40.54874	23.75495	2013_1076	92	45
Stratoni FW	40.54849	23.75527	2013_1078	106	55
Stratoni FW	40.54808	23.75636	2013_1079	110	65
Stratoni FW	40.54814	23.75685	2013_1080	90	65
Stratoni FW	40.54824	23.75737	2013_1082	107	80
Stratoni FW	40.54933	23.75667	2013_1084	105	46
Stratoni FW	40.54966	23.75668	2013_1086	92	59
Stratoni FW	40.54992	23.75654	2013_1087	93	60
Stratoni FW	40.55031	23.75659	2013_1088	40	33
Stratoni FW	40.55062	23.75658	2013_1089	268	66
Stratoni FW	40.55079	23.75650	2013_1090	320	41
Stratoni FW	40.55053	23.75921	2013_1093	110	18
Stratoni FW	40.55126	23.76069	2013_1098	131	28
Stratoni FW	40.55143	23.76099	2013_1099	101	30
Stratoni FW	40.55172	23.76184	2013_1100	96	55
Stratoni FW	40.54954	23.76305	2013_1103	150	42
Stratoni FW	40.54851	23.76405	2013_1105	145	28
Stratoni FW	40.54637	23.76587	2013_1107	145	50
Stratoni FW	40.53953	23.76384	2013_1113	71	30
Stratoni FW	40.53976	23.76596	2013_1118	322	36
Stratoni FW	40.53988	23.76621	2013_1119	300	29
Stratoni FW	40.53958	23.76849	2013_1123	285	20
Stratoni FW	40.53944	23.76866	2013_1124	295	45
Stratoni FW	40.53942	23.76924	2013_1126	52	50
Stratoni FW	40.54024	23.76913	2013_1127	285	60

Table A5. S1 foliation measurements

Domain	Latitude	Longitude	Station No.	Strike	Dip
S1 Foliation					
Olympias	40.60225	23.72817	2013_275	85	40
Olympias	40.60138	23.72835	2013_278	120	40
Olympias	40.60119	23.72818	2013_279	104	71
Olympias	40.60050	23.72732	2013_283	66	56
Olympias	40.60046	23.72708	2013_284	100	44
Olympias	40.59982	23.72772	2013_285	105	51
Olympias	40.59991	23.72796	2013_288	135	52
Olympias	40.59994	23.72882	2013_289	61	45
Olympias	40.59622	23.73098	2013_294	260	54
Olympias	40.59382	23.73328	2013_305	330	46
Olympias	40.59368	23.73315	2013_306	320	50
Olympias	40.59265	23.73262	2013_312	335	35
Olympias	40.59229	23.73296	2013_313	345	37
Olympias	40.59261	23.73370	2013_314	25	31
Olympias	40.59139	23.73446	2013_316	0	30
Olympias	40.59086	23.73444	2013_318	0	32
Olympias	40.59026	23.73511	2013_321	3	38
Olympias	40.59082	23.73561	2013_323	6	50
Olympias	40.59118	23.73664	2013_330	24	41
Olympias	40.59115	23.73725	2013_332	5	21
Olympias	40.59148	23.73767	2013_333	23	30
Olympias	40.59152	23.73818	2013_334	11	55
Olympias	40.59146	23.73941	2013_338	10	27
Olympias	40.59142	23.73976	2013_339	11	21
Olympias	40.59141	23.74033	2013_341	2	40
Olympias	40.59314	23.74051	2013_354	188	88
Olympias	40.59410	23.74038	2013_359	206	86

Domain	Latitude	Longitude	Station No.	Strike	Dip
S1 Foliation					
Stratoni FW	40.54192	23.76946	2013_1131	299	85
Stratoni FW	40.54192	23.77711	2013_1133	125	54
Stratoni FW	40.54223	23.77631	2013_1134	146	75
Stratoni FW	40.54288	23.77439	2013_1136	105	45
Stratoni FW	40.54220	23.77313	2013_1137	296	80
Stratoni FW	40.54210	23.77280	2013_1138	314	70
Stratoni FW	40.53672	23.79182	2013_1144	102	30
Stratoni FW	40.53683	23.79009	2013_1147	114	50
Stratoni FW	40.53784	23.78712	2013_1152	125	35
Stratoni FW	40.54184	23.78200	2013_1158	262	24
Stratoni FW	40.54171	23.78157	2013_1159	120	44
Stratoni FW	40.54068	23.78060	2013_1161	140	75
Stratoni FW	40.54051	23.77956	2013_1163	290	39
Stratoni FW	40.54152	23.77767	2013_1168	299	25
Stratoni FW	40.53700	23.78666	2013_1174	135	60
Stratoni FW	40.53729	23.78464	2013_1178	105	26
Stratoni FW	40.53756	23.78354	2013_1180	310	51
Stratoni FW	40.53818	23.78340	2013_1183	291	60
Stratoni FW	40.53830	23.78298	2013_1184	145	56
Stratoni FW	40.53799	23.78271	2013_1186	117	76
Stratoni FW	40.53699	23.78223	2013_1188	110	78
Stratoni FW	40.53640	23.78225	2013_1189	70	29
Stratoni FW	40.53613	23.78246	2013_1190	229	30
Stratoni FW	40.53648	23.77514	2013_1197	298	54
Stratoni FW	40.53706	23.77453	2013_1201	301	35
Stratoni FW	40.53753	23.77438	2013_1204	296	50
Stratoni FW	40.53777	23.77470	2013_1207	317	56

Table A5. S1 foliation measurements

Domain	Latitude	Longitude	Station No.	Strike	Dip
S1 Foliation					
Olympias	40.59486	23.74043	2013_363	73	51
Olympias	40.59491	23.74043	2013_364	62	44
Olympias	40.59496	23.74073	2013_365	62	41
Olympias	40.59377	23.74172	2013_370	350	31
Olympias	40.59440	23.74272	2013_371	206	86
Olympias	40.59439	23.74275	2013_372	85	54
Olympias	40.59460	23.74291	2013_374	27	31
Olympias	40.59459	23.74284	2013_375	213	86
Olympias	40.59519	23.74312	2013_378	200	81
Olympias	40.59558	23.74335	2013_383	35	75
Olympias	40.59562	23.74343	2013_384	214	85
Olympias	40.59705	23.74552	2013_388	36	31
Olympias	40.59736	23.74774	2013_396	139	65
Olympias	40.59660	23.74737	2013_399	50	29
Olympias	40.59658	23.74688	2013_400	59	25
Olympias	40.59664	23.74835	2013_404	60	23
Olympias	40.59687	23.74871	2013_410	341	44
Olympias	40.59736	23.74890	2013_414	40	25
Olympias	40.59879	23.74480	2013_416	350	24
Olympias	40.59456	23.75326	2013_417	120	12
Olympias	40.59463	23.75356	2013_420	59	56
Olympias	40.59457	23.75360	2013_421	81	31
Olympias	40.59629	23.75118	2013_423	336	39
Olympias	40.59726	23.75179	2013_427	97	44
Olympias	40.59690	23.74783	2013_431	84	24
Olympias	40.59703	23.74787	2013_432	10	30
Olympias	40.59707	23.74780	2013_433	115	68

Domain	Latitude	Longitude	Station No.	Strike	Dip
S1 Foliation					
Stratoni FW	40.53857	23.77470	2013_1210	124	30
Stratoni FW	40.53746	23.77593	2013_1212	315	67
Stratoni FW	40.53714	23.77677	2013_1216	310	70
Stratoni FW	40.53737	23.77734	2013_1218	335	55
Stratoni FW	40.53757	23.77787	2013_1219	325	75
Stratoni FW	40.53687	23.77810	2013_1222	330	46
Stratoni FW	40.53640	23.77883	2013_1223	142	16
Stratoni FW	40.53625	23.78039	2013_1225	314	88
Stratoni FW	40.53636	23.78127	2013_1228	335	69
Stratoni FW	40.53500	23.78140	2013_1230	105	60
Stratoni FW	40.52906	23.79032	2013_1233	100	75
Stratoni FW	40.53006	23.78918	2013_1236	87	54
Stratoni FW	40.52999	23.78884	2013_1238	132	68
Stratoni FW	40.52998	23.78827	2013_1239	135	80
Stratoni FW	40.53076	23.78812	2013_1241	131	75
Stratoni FW	40.53094	23.78820	2013_1242	154	69
Stratoni FW	40.53181	23.78798	2013_1246	133	71
Stratoni FW	40.53213	23.78824	2013_1247	130	74
Stratoni FW	40.53283	23.78732	2013_1248	130	85
Stratoni FW	40.53308	23.78701	2013_1250	121	56
Stratoni FW	40.53270	23.78683	2013_1251	121	40
Stratoni FW	40.53258	23.78545	2013_1255	140	76
Stratoni FW	40.53325	23.78506	2013_1256	140	78
Stratoni FW	40.53418	23.78523	2013_1261	104	40
Stratoni FW	40.53413	23.78490	2013_1263	142	85
Stratoni FW	40.53622	23.78350	2013_1268	273	54
Stratoni FW	40.53596	23.78345	2013_1269	326	62

Table A5. S1 foliation measurements

Domain	Latitude	Longitude	Station No.	Strike	Dip
S1 Foliation					
Olympias	40.59888	23.74575	2013_434	30	54
Olympias	40.59903	23.74531	2013_436	29	31
Olympias	40.59922	23.74477	2013_437	25	30
Olympias	40.59902	23.74463	2013_438	36	35
Olympias	40.59716	23.75091	2013_439	27	24
Olympias	40.59606	23.75013	2013_442	18	21
Olympias	40.59587	23.74983	2013_443	355	33
Olympias	40.59579	23.74964	2013_444	351	39
Olympias	40.59566	23.74937	2013_447	352	35
Olympias	40.59449	23.74746	2013_448	340	50
Olympias	40.59436	23.74786	2013_449	27	35
Olympias	40.59424	23.74855	2013_450	39	36
Olympias	40.59389	23.74858	2013_452	30	25
Olympias	40.59226	23.74918	2013_458	340	50
Olympias	40.59982	23.72887	2013_464	48	65
Olympias	40.59975	23.72880	2013_465	56	71
Olympias	40.59881	23.72850	2013_466	54	50
Olympias	40.59838	23.72824	2013_469	55	28
Olympias	40.60003	23.72833	2013_470	70	29
Olympias	40.60001	23.72807	2013_471	90	40
Olympias	40.59977	23.72744	2013_472	107	45
Olympias	40.60009	23.72733	2013_473	65	49
Olympias	40.60021	23.72703	2013_474	74	51
Olympias	40.60206	23.72826	2013_480	107	42
Olympias	40.60192	23.72773	2013_482	79	27
Olympias	40.60172	23.72734	2013_484	65	42
Olympias	40.60160	23.72704	2013_488	160	55

Domain	Latitude	Longitude	Station No.	Strike	Dip
S1 Foliation					
Stratoni FW	40.53519	23.78306	2013_1273	140	84
Stratoni FW	40.53430	23.78238	2013_1275	100	50
Stratoni FW	40.53193	23.77686	2013_1277	171	30
Stratoni FW	40.53248	23.77708	2013_1278	129	65
Stratoni FW	40.53319	23.77712	2013_1283	12	21
Stratoni FW	40.53345	23.77689	2013_1284	140	40
Stratoni FW	40.53350	23.77688	2013_1285	305	55
Stratoni FW	40.53408	23.77712	2013_1287	339	42
Stratoni FW	40.53406	23.77716	2013_1288	55	25
Stratoni FW	40.53422	23.77711	2013_1289	114	35
Stratoni FW	40.53438	23.77697	2013_1290	99	40
Stratoni FW	40.52871	23.79080	2013_1296	115	60
Stratoni FW	40.52919	23.79231	2013_1300	136	88
Stratoni FW	40.52971	23.79219	2013_1302	118	65
Stratoni FW	40.52984	23.79238	2013_1305	119	55
Stratoni FW	40.52878	23.79328	2013_1308	104	75
Stratoni FW	40.52854	23.79426	2013_1312	108	77
Stratoni FW	40.52952	23.79509	2013_1316	110	50
Stratoni FW	40.52853	23.79573	2013_1318	101	66
Stratoni FW	40.52852	23.79638	2013_1319	108	79
Stratoni FW	40.52845	23.79664	2013_1320	116	35
Stratoni FW	40.52873	23.79746	2013_1323	90	69
Stratoni FW	40.52829	23.79754	2013_1326	118	64
Stratoni FW	40.52763	23.79791	2013_1327	110	47
Stratoni FW	40.52683	23.79718	2013_1329	118	50
Stratoni FW	40.52586	23.79650	2013_1332	110	70
Stratoni FW	40.52472	23.79742	2013_1338	96	35

Table A5. S1 foliation measurements

Domain	Latitude	Longitude	Station No.	Strike	Dip
S1 Foliation					
Olympias	40.60157	23.72724	2013_489	89	47
Olympias	40.60170	23.72684	2013_490	76	40
Olympias	40.60178	23.72668	2013_492	86	24
Olympias	40.60179	23.72648	2013_493	104	24
Olympias	40.60177	23.72604	2013_494	77	26
Olympias	40.60164	23.72583	2013_495	80	26
Olympias	40.60175	23.72547	2013_497	126	18
Olympias	40.60192	23.72539	2013_498	125	20
Olympias	40.60204	23.72505	2013_499	120	25
Olympias	40.60128	23.72385	2013_500	254	25
Olympias	40.60115	23.72338	2013_502	110	16
Olympias	40.60109	23.72295	2013_504	130	28
Olympias	40.60086	23.72254	2013_506	106	34
Olympias	40.60051	23.72244	2013_507	96	40
Olympias	40.59985	23.72226	2013_509	110	23
Olympias	40.59935	23.72204	2013_510	307	39
Olympias	40.59951	23.72212	2013_511	285	80
Olympias	40.59700	23.72157	2013_513	299	24
Olympias	40.59653	23.72161	2013_515	300	28
Olympias	40.60451	23.73027	2013_517	148	26
Olympias	40.60119	23.73228	2013_519	106	19
Olympias	40.60203	23.73629	2013_522	136	20
Olympias	40.60237	23.73629	2013_524	115	17
Olympias	40.60269	23.73627	2013_525	106	16
Olympias	40.60306	23.73595	2013_527	100	20
Olympias	40.60361	23.73638	2013_528	110	29
Olympias	40.60390	23.73689	2013_529	105	30

Domain	Latitude	Longitude	Station No.	Strike	Dip
S1 Foliation					
Stratoni FW	40.52498	23.79868	2013_1339	112	26
Stratoni FW	40.53165	23.77664	2013_1342	154	36
Stratoni FW	40.53116	23.77658	2013_1345	127	74
Stratoni FW	40.53071	23.77623	2013_1347	121	46
Stratoni FW	40.53050	23.77595	2013_1349	136	50
Stratoni FW	40.53034	23.77560	2013_1350	145	45
Stratoni FW	40.53021	23.77520	2013_1354	150	77
Stratoni FW	40.53026	23.77681	2013_1356	126	28
Stratoni FW	40.53015	23.77679	2013_1357	109	46
Stratoni FW	40.53007	23.77482	2013_1358	120	34
Stratoni FW	40.53079	23.77385	2013_1361	160	60
Stratoni FW	40.53098	23.77358	2013_1363	155	80
Stratoni FW	40.53110	23.77347	2013_1364	154	84
Stratoni FW	40.53134	23.77284	2013_1369	340	74
Stratoni FW	40.53100	23.77284	2013_1371	305	56
Stratoni FW	40.53076	23.77284	2013_1372	310	76
Stratoni FW	40.53008	23.77267	2013_1375	170	64
Stratoni FW	40.52977	23.77253	2013_1376	140	67
Stratoni FW	40.53358	23.76843	2013_1378	40	46
Stratoni FW	40.53403	23.76801	2013_1380	66	27
Stratoni FW	40.53428	23.76759	2013_1381	112	61
Stratoni FW	40.53449	23.76718	2013_1383	70	51
Stratoni FW	40.53455	23.76689	2013_1384	126	35
Stratoni FW	40.53363	23.76800	2013_1386	112	54
Stratoni FW	40.53357	23.76746	2013_1388	260	73
Stratoni FW	40.53296	23.76881	2013_1390	138	40
Stratoni FW	40.53305	23.76917	2013_1392	94	21

Table A5. S1 foliation measurements

Domain	Latitude	Longitude	Station No.	Strike	Dip
S1 Foliation					
Olympias	40.60319	23.73715	2013_530	110	40
Olympias	40.60305	23.73729	2013_531	100	21
Olympias	40.60206	23.73849	2013_532	79	21
Olympias	40.60219	23.73893	2013_533	70	21
Olympias	40.60229	23.73896	2013_534	152	45
Olympias	40.60239	23.73912	2013_535	50	27
Olympias	40.60258	23.73931	2013_536	118	16
Olympias	40.60340	23.74023	2013_537	122	39
Olympias	40.60363	23.74055	2013_538	124	28
Olympias	40.60320	23.74226	2013_539	100	24
Olympias	40.60284	23.73975	2013_540	103	16
Olympias	40.60264	23.73954	2013_542	55	57
Olympias	40.60282	23.73818	2013_543	103	15
Olympias	40.60360	23.73702	2013_544	75	20
Olympias	40.60173	23.73611	2013_545	150	51
Olympias	40.59102	23.75564	2013_548	340	55
Olympias	40.59153	23.75622	2013_549	0	24
Olympias	40.59157	23.75649	2013_550	355	54
Olympias	40.59024	23.75286	2013_553	4	35
Olympias	40.58991	23.75252	2013_554	0	47
Olympias	40.58885	23.75194	2013_556	0	80
Olympias	40.58883	23.75071	2013_560	356	49
Olympias	40.58908	23.74959	2013_563	23	45
Olympias	40.58898	23.74917	2013_564	337	65
Olympias	40.58898	23.74893	2013_566	335	74
Olympias	40.58897	23.74838	2013_567	334	51
Olympias	40.58892	23.74837	2013_568	354	40

Domain	Latitude	Longitude	Station No.	Strike	Dip
S1 Foliation					
Stratoni FW	40.53302	23.76934	2013_1393	109	42
Stratoni FW	40.53277	23.76819	2013_1396	26	19
Stratoni FW	40.53281	23.76780	2013_1399	77	21
Stratoni FW	40.53278	23.76770	2013_1402	31	30
Stratoni FW	40.53288	23.76699	2013_1405	40	45
Stratoni FW	40.53337	23.76648	2013_1406	330	30
Stratoni FW	40.53313	23.76578	2013_1407	37	29
Stratoni FW	40.53305	23.76568	2013_1408	294	45
Stratoni FW	40.53295	23.76562	2013_1409	271	50
Stratoni FW	40.53225	23.76632	2013_1413	95	36
Stratoni FW	40.53233	23.76609	2013_1415	315	64
Stratoni FW	40.53207	23.76538	2013_1416	305	49
Stratoni FW	40.53185	23.76455	2013_1418	64	55
Stratoni FW	40.53256	23.76706	2013_1419	20	46
Stratoni FW	40.52740	23.83583	2013_1420	94	46
Stratoni FW	40.52791	23.83564	2013_1421	55	29
Stratoni FW	40.52878	23.83559	2013_1422	76	60
Stratoni FW	40.52903	23.83593	2013_1424	310	67
Stratoni FW	40.52919	23.83742	2013_1425	94	85
Stratoni FW	40.52957	23.83790	2013_1428	270	68
Stratoni FW	40.52972	23.83804	2013_1429	316	65
Stratoni FW	40.52968	23.83836	2013_1430	288	54
Stratoni FW	40.52902	23.83847	2013_1431	105	86
Stratoni FW	40.52867	23.83848	2013_1433	291	55
Stratoni FW	40.52811	23.83956	2013_1434	95	69
Stratoni FW	40.52754	23.83958	2013_1436	93	40
Stratoni FW	40.52718	23.84080	2013_1439	85	52

Table A5. S1 foliation measurements

Domain	Latitude	Longitude	Station No.	Strike	Dip
S1 Foliation					
Olympias	40.58892	23.74729	2013_569	358	27
Olympias	40.58897	23.74623	2013_570	3	29
Olympias	40.58918	23.74544	2013_571	8	16
Olympias	40.58809	23.74613	2013_572	345	34
Olympias	40.58791	23.74536	2013_573	24	32
Olympias	40.58798	23.74442	2013_576	0	39
Olympias	40.58828	23.74374	2013_577	32	46
Olympias	40.58799	23.74241	2013_579	14	35
Olympias	40.58818	23.74187	2013_580	15	24
Olympias	40.58853	23.74144	2013_581	4	40
Olympias	40.58897	23.74289	2013_582	1	36
Olympias	40.58876	23.74423	2013_585	350	44
Olympias	40.58896	23.74366	2013_586	8	36
Olympias	40.58918	23.74247	2013_587	15	35
Olympias	40.58962	23.74174	2013_589	10	36
Olympias	40.58957	23.74111	2013_591	10	35
Olympias	40.59014	23.74042	2013_592	359	31
Olympias	40.59042	23.73977	2013_595	351	35
Olympias	40.58983	23.73942	2013_596	355	30
Olympias	40.59019	23.73871	2013_599	15	24
Olympias	40.59015	23.73794	2013_601	356	28
Olympias	40.58999	23.73719	2013_604	0	35
Olympias	40.59037	23.73663	2013_610	356	27
Olympias	40.59041	23.74929	2013_617	352	60
Olympias	40.58885	23.75122	2013_618	350	69
Olympias	40.58968	23.75195	2013_620	0	54
Olympias	40.57643	23.75929	2013_628	352	29

Domain	Latitude	Longitude	Station No.	Strike	Dip
S1 Foliation					
Stratoni FW	40.52673	23.84111	2013_1441	114	69
Stratoni FW	40.52572	23.84142	2013_1443	90	63
Stratoni FW	40.52601	23.84192	2013_1446	105	48
Stratoni FW	40.52632	23.84297	2013_1449	112	56
Stratoni FW	40.52605	23.84313	2013_1450	70	85
Stratoni FW	40.52547	23.84431	2013_1453	86	55
Stratoni FW	40.52517	23.84508	2013_1454	86	50
Stratoni FW	40.52525	23.84582	2013_1457	100	51
Stratoni FW	40.52599	23.84620	2013_1459	323	70
Stratoni FW	40.52663	23.84704	2013_1460	81	80
Stratoni FW	40.52712	23.84759	2013_1461	296	71
Stratoni FW	40.52729	23.84798	2013_1463	75	75
Stratoni FW	40.52818	23.84844	2013_1467	289	84
Stratoni FW	40.53032	23.84809	2013_1471	294	75
Stratoni FW	40.52794	23.83392	2013_1473	100	69
Stratoni FW	40.52881	23.83224	2013_1477	274	80
Stratoni FW	40.52332	23.82774	2013_1492	225	40
Stratoni FW	40.52055	23.82897	2013_1495	350	50
Stratoni FW	40.51706	23.81889	2013_1527	265	54
Stratoni FW	40.53257	23.83215	2013_1551	279	40
Stratoni FW	40.53224	23.83083	2013_1554	117	15
Stratoni FW	40.53397	23.82615	2013_1566	85	36
Stratoni FW	40.53483	23.82477	2013_1568	118	66
Stratoni FW	40.53553	23.82408	2013_1571	99	85
Stratoni FW	40.52140	23.81075	2013_1579	55	25
Stratoni FW	40.52147	23.81081	2013_1580	92	26
Stratoni FW	40.51932	23.80943	2013_1586	312	30

Table A5. S1 foliation measurements

Domain	Latitude	Longitude	Station No.	Strike	Dip
S1 Foliation					
Olympias	40.57558	23.75908	2013_632	322	75
Olympias	40.57537	23.75891	2013_633	335	51
Olympias	40.57250	23.75843	2013_644	345	45
Olympias	40.57184	23.75727	2013_652	359	25
Olympias	40.57167	23.75727	2013_653	24	28
Olympias	40.56650	23.75385	2013_664	9	28
Olympias	40.56444	23.75270	2013_666	315	85
Olympias	40.56455	23.75190	2013_667	315	83
Olympias	40.56448	23.75137	2013_668	4	20
Olympias	40.56448	23.75078	2013_671	327	66
Olympias	40.56462	23.75059	2013_672	1	44
Olympias	40.56501	23.75017	2013_674	335	59
Olympias	40.56526	23.75048	2013_677	337	81
Olympias	40.56507	23.75036	2013_678	320	35
Olympias	40.56490	23.75040	2013_679	330	50
Olympias	40.56545	23.74982	2013_681	345	29
Olympias	40.56528	23.74961	2013_682	305	51
Olympias	40.56638	23.74918	2013_683	8	54
Olympias	40.56544	23.75062	2013_685	315	64
Olympias	40.56534	23.75070	2013_686	311	75
Olympias	40.56693	23.75149	2013_688	340	67
Olympias	40.56716	23.75108	2013_689	158	75
Olympias	40.56742	23.75091	2013_690	325	75
Olympias	40.56753	23.75104	2013_692	325	86
Olympias	40.56782	23.75136	2013_694	322	74
Olympias	40.57980	23.75765	2013_704	330	65
Olympias	40.58005	23.75764	2013_705	330	60
Stratoni FW	40.51810	23.81202	2013_1591	130	45
Stratoni FW	40.51849	23.81212	2013_1593	235	25
Stratoni FW	40.52579	23.81310	2013_1597	130	30
Stratoni FW	40.52358	23.81082	2013_1603	55	51
Stratoni FW	40.52340	23.81010	2013_1604	75	69
Stratoni FW	40.52324	23.80879	2013_1607	73	24
Stratoni FW	40.52304	23.80460	2013_1613	92	40
Stratoni FW	40.52353	23.80418	2013_1615	88	35
Stratoni FW	40.52353	23.80355	2013_1616	104	34
Stratoni FW	40.52374	23.80310	2013_1617	137	45
Stratoni FW	40.52267	23.80216	2013_1620	260	26
Stratoni FW	40.52310	23.80100	2013_1622	240	21
Stratoni FW	40.52321	23.80006	2013_1625	270	30
Stratoni FW	40.52344	23.79906	2013_1627	58	22
Stratoni FW	40.52287	23.80497	2013_1631	291	5
Stratoni FW	40.52231	23.80661	2013_1636	105	5
Stratoni FW	40.52204	23.80711	2013_1637	94	25
Stratoni FW	40.52199	23.80768	2013_1638	86	30
Stratoni FW	40.52202	23.80879	2013_1640	85	32
Stratoni FW	40.53421	23.82100	2013_1641	95	70
Stratoni FW	40.53436	23.82083	2013_1642	105	40
Stratoni FW	40.53477	23.81993	2013_1644	95	46
Stratoni FW	40.53522	23.81908	2013_1645	85	37
Stratoni FW	40.53525	23.81861	2013_1646	100	55
Stratoni FW	40.53509	23.81792	2013_1647	130	71
Stratoni FW	40.53513	23.81697	2013_1648	110	50
Stratoni FW	40.53510	23.81684	2013_1649	130	50

Table A5. S1 foliation measurements

Domain	Latitude	Longitude	Station No.	Strike	Dip
S1 Foliation					
Olympias	40.57666	23.75939	2013_708	18	37
Olympias	40.57540	23.76092	2013_716	326	71
Olympias	40.57529	23.76162	2013_717	32	26
Olympias	40.57447	23.76301	2013_719	32	17
Olympias	40.56844	23.75104	2013_723	337	55
Olympias	40.56820	23.75065	2013_724	335	38
Olympias	40.56823	23.75036	2013_725	340	85
Olympias	40.56828	23.74963	2013_728	344	66
Olympias	40.56854	23.74914	2013_729	329	59
Olympias	40.56887	23.74911	2013_730	345	32
Olympias	40.56908	23.74827	2013_733	319	52
Olympias	40.56946	23.74802	2013_734	355	55
Olympias	40.56938	23.74742	2013_735	335	73
Olympias	40.57054	23.74510	2013_737	349	70
Olympias	40.57058	23.74520	2013_738	95	42
Olympias	40.57063	23.74516	2013_739	346	82
Olympias	40.57067	23.74531	2013_741	355	40
Olympias	40.57042	23.74348	2013_742	328	65
Olympias	40.57019	23.74393	2013_743	355	76
Olympias	40.57068	23.74204	2013_750	70	29
Olympias	40.57190	23.74234	2013_757	335	81
Olympias	40.57207	23.74204	2013_759	344	61
Olympias	40.57249	23.74221	2013_761	348	45
Olympias	40.57375	23.74350	2013_765	335	49
Olympias	40.57500	23.74499	2013_766	0	34
Olympias	40.57516	23.74525	2013_769	26	60
Olympias	40.57583	23.74576	2013_770	345	55

Domain	Latitude	Longitude	Station No.	Strike	Dip
S1 Foliation					
Stratoni FW	40.53495	23.81551	2013_1651	85	30
Stratoni FW	40.53494	23.81506	2013_1653	91	60
Stratoni FW	40.53388	23.81472	2013_1657	110	55
Stratoni FW	40.53408	23.81281	2013_1660	106	31
Stratoni FW	40.53138	23.81379	2013_1662	265	45
Stratoni FW	40.53161	23.80737	2013_1667	160	55
Stratoni FW	40.53055	23.80297	2013_1671	70	36
Stratoni FW	40.53434	23.80004	2013_1677	135	77
Stratoni FW	40.53632	23.79768	2013_1679	94	29
Stratoni FW	40.53667	23.79419	2013_1682	80	21
Stratoni FW	40.53634	23.79356	2013_1683	82	35
Stratoni FW	40.53602	23.79190	2013_1684	105	60
Stratoni FW	40.53300	23.73370	2014_P679	270	50
Stratoni FW	40.54300	23.69140	2014_P096	294	25
Stratoni FW	40.55820	23.66880	2014_P620	295	10
Stratoni FW	40.55230	23.67780	2014_P249	306	74
Stratoni FW	40.54200	23.69300	2014_P119	328	18
Stratoni FW	40.53360	23.72620	2014_P263	93	16
Stratoni FW	40.53890	23.70500	2014_P356	95	35
Stratoni FW	40.54640	23.68270	2014_P179	100	10
Stratoni FW	40.55330	23.67430	2014_P237	110	17
Stratoni FW	40.55720	23.67010	2014_P334	118	45
Stratoni FW	40.55450	23.67260	2014_P221	120	32
Stratoni FW	40.53540	23.70800	2014_P378	120	40
Stratoni FW	40.54600	23.68570	2014_P602	120	44
Stratoni FW	40.53320	23.73020		120	40
Stratoni FW	40.54340	23.69110	2014_P093	125	29

Table A5. S1 foliation measurements

Domain	Latitude	Longitude	Station No.	Strike	Dip
S1 Foliation					
Olympias	40.57599	23.74606	2013_771	355	14
Olympias	40.57666	23.74853	2013_778	135	31
Olympias	40.57685	23.74884	2013_779	82	24
Olympias	40.57685	23.74908	2013_782	140	24
Olympias	40.57715	23.74973	2013_785	359	70
Olympias	40.57681	23.75143	2013_789	10	51
Olympias	40.57650	23.75194	2013_792	345	81
Olympias	40.57611	23.75279	2013_795	333	25
Olympias	40.57510	23.75421	2013_798	359	76
Olympias	40.57452	23.75492	2013_801	0	53
Olympias	40.57486	23.75559	2013_806	344	50
Olympias	40.57528	23.74469	2013_808	355	24
Olympias	40.57553	23.74434	2013_810	3	34
Olympias	40.57581	23.74410	2013_811	356	31
Olympias	40.57618	23.74469	2013_812	25	55
Olympias	40.57663	23.74505	2013_819	358	25
Olympias	40.57709	23.74569	2013_820	340	38
Olympias	40.57735	23.74569	2013_821	121	46
Olympias	40.57757	23.74567	2013_822	65	26
Olympias	40.57792	23.74572	2013_826	46	75
Olympias	40.57786	23.74574	2013_827	125	78
Olympias	40.57807	23.74638	2013_832	5	45
Olympias	40.57763	23.74668	2013_833	25	26
Olympias	40.57767	23.74682	2013_834	354	28
Olympias	40.57796	23.74731	2013_835	4	31
Olympias	40.57804	23.74764	2013_837	317	34
Olympias	40.57841	23.74778	2013_840	335	31

Domain	Latitude	Longitude	Station No.	Strike	Dip
S1 Foliation					
Stratoni FW	40.53730	23.71700	2014_P418	125	20
Stratoni FW	40.54160	23.69320	2014_P098	130	40
Stratoni FW	40.53500	23.71600	2014_P420	130	40
Stratoni FW	40.54120	23.70450	2014_P357	135	30
Stratoni FW	40.55050	23.67850	2014_P257	140	24
Stratoni FW	40.54170	23.71100	2014_P394	140	30
Stratoni FW	40.56070	23.66500	2014_P610	140	40
Stratoni FW	40.54210	23.70860	2014_P367	150	22
Stratoni FW	40.53620	23.71480	2014_P413	150	38
Stratoni FW	40.56250	23.66330	2014_P615	150	32
Stratoni FW	40.55070	23.68020	2014_P250	158	40
Stratoni FW	40.54230	23.69240	2014_P115	200	20
Stratoni FW	40.53710	23.71130	2014_P402	205	65
Stratoni FW	40.54040	23.69950	2014_P0791	260	36
Stratoni HW	40.49330	23.79613	2015_1298	105	85
Stratoni HW	40.49366	23.79626	2015_1299	285	80
Stratoni HW	40.49438	23.79706	2015_1300	125	84
Stratoni HW	40.48646	23.79812	2015_1391	350	85
Stratoni HW	40.48654	23.79846	2015_1392	340	85
Stratoni HW	40.48436	23.80058	2015_1393	173	65
Stratoni HW	40.48455	23.80000	2015_1394	4	76
Stratoni HW	40.48515	23.79805	2015_1395	346	86
Stratoni HW	40.48574	23.79729	2015_1397	344	86
Stratoni HW	40.48588	23.79490	2015_1400	354	60
Stratoni HW	40.48505	23.79291	2015_1401	341	65
Stratoni HW	40.48700	23.79094	2015_1402	326	77
Stratoni HW	40.48767	23.79098	2015_1403	330	48

Table A5. S1 foliation measurements

Domain	Latitude	Longitude	Station No.	Strike	Dip
S1 Foliation					
Olympias	40.57843	23.74796	2013_841	351	50
Olympias	40.57853	23.74813	2013_842	330	51
Olympias	40.57855	23.74815	2013_843	325	79
Olympias	40.57940	23.74871	2013_847	345	15
Olympias	40.58037	23.74886	2013_849	359	44
Olympias	40.58076	23.74880	2013_850	355	30
Olympias	40.58153	23.74886	2013_852	354	48
Olympias	40.58173	23.74887	2013_853	355	60
Olympias	40.58193	23.74892	2013_854	354	65
Olympias	40.57359	23.76268	2013_858	355	50
Olympias	40.56994	23.76438	2013_866	350	24
Olympias	40.56816	23.76539	2013_868	125	28
Olympias	40.56469	23.76544	2013_872	11	34
Olympias	40.56418	23.76531	2013_873	2	34
Olympias	40.58301	23.74942	2013_885	16	39
Olympias	40.58322	23.75010	2013_887	24	20
Olympias	40.58403	23.75151	2013_889	10	20
Olympias	40.58408	23.75166	2013_890	356	46
Olympias	40.58403	23.75185	2013_891	16	62
Olympias	40.58408	23.75254	2013_893	10	34
Olympias	40.58426	23.75262	2013_894	10	62
Olympias	40.58478	23.75103	2013_897	358	50
Olympias	40.58478	23.75095	2013_898	36	28
Olympias	40.58504	23.75124	2013_899	11	38
Olympias	40.58625	23.75237	2013_900	15	30
Olympias	40.58622	23.75236	2013_901	105	38
Olympias	40.58659	23.75300	2013_903	356	47

Domain	Latitude	Longitude	Station No.	Strike	Dip
S1 Foliation					
Stratoni HW	40.50559	23.80193	2015_1404	310	81
Stratoni HW	40.50067	23.77181	2015_1407	305	66
Stratoni HW	40.50040	23.77191	2015_1408	290	69
Stratoni HW	40.49761	23.76717	2015_1409	286	20
Stratoni HW	40.49555	23.76611	2015_1410	270	50
Stratoni HW	40.49377	23.76480	2015_1411	304	36
Stratoni HW	40.49266	23.76317	2015_1412	288	40
Stratoni HW	40.48997	23.76328	2015_1413	299	36
Stratoni HW	40.48801	23.76369	2015_1415	300	40
Stratoni HW	40.48714	23.76298	2015_1417	70	44
Stratoni HW	40.48638	23.76276	2015_1418	314	67
Stratoni HW	40.48675	23.76293	2015_1419	87	81
Stratoni HW	40.48580	23.76245	2015_1420	314	30
Stratoni HW	40.48728	23.76046	2015_1421	287	64
Stratoni HW	40.48802	23.75945	2015_1422	305	45
Stratoni HW	40.49448	23.75856	2015_1423	274	51
Stratoni HW	40.48782	23.75725	2015_1427	244	61
Stratoni HW	40.48647	23.75725	2015_1432	302	44
Stratoni HW	40.51112	23.81295	2015_1466	115	65
Stratoni HW	40.51167	23.81278	2015_1467	34	42
Stratoni HW	40.51184	23.81266	2015_1468	320	90
Stratoni HW	40.51258	23.81194	2015_1469	260	35
Stratoni HW	40.51313	23.81146	2015_1470	33	46
Stratoni HW	40.51083	23.72012	2015_1481	299	44
Stratoni HW	40.50849	23.72070	2015_1483	345	36
Stratoni HW	40.50948	23.72099	2015_1484	293	60
Stratoni HW	40.52226	23.72358	2015_1487	220	44

Table A5. S1 foliation measurements

Domain	Latitude	Longitude	Station No.	Strike	Dip
S1 Foliation					
Olympias	40.58666	23.75321	2013_905	345	54
Olympias	40.58725	23.75398	2013_907	10	40
Olympias	40.58782	23.75445	2013_909	352	65
Olympias	40.58256	23.75815	2013_913	351	50
Olympias	40.56408	23.76690	2013_923	8	45
Olympias	40.56373	23.76710	2013_925	2	81
Olympias	40.56372	23.76737	2013_926	354	35
Olympias	40.56314	23.76758	2013_927	8	30
Olympias	40.56291	23.76797	2013_929	350	42
Olympias	40.56267	23.76820	2013_930	344	55
Olympias	40.56177	23.76930	2013_931	350	48
Olympias	40.56155	23.76921	2013_932	300	45
Olympias	40.56185	23.77013	2013_934	305	65
Olympias	40.56190	23.77106	2013_936	354	65
Olympias	40.56020	23.77049	2013_937	349	49
Olympias	40.55993	23.77056	2013_938	126	55
Olympias	40.55972	23.77040	2013_939	345	50
Olympias	40.56455	23.75002	2013_944	295	44
Olympias	40.56361	23.74873	2013_950	347	24
Olympias	40.56284	23.74830	2013_951	322	75
Olympias	40.56231	23.74754	2013_953	355	55
Olympias	40.55919	23.74747	2013_959	120	41
Olympias	40.55798	23.74725	2013_960	138	84
Olympias	40.55756	23.74855	2013_963	200	56
Olympias	40.55831	23.74953	2013_966	350	55
Olympias	40.56066	23.74902	2013_969	15	35
Olympias	40.56162	23.74953	2013_972	294	68
Stratoni HW	40.52412	23.72340	2015_1488	264	30
Stratoni HW	40.51342	23.72260	2015_1620	236	28
Stratoni HW	40.51376	23.72292	2015_1622	152	27
Stratoni HW	40.51307	23.72248	2015_1625	184	36
Stratoni HW	40.51202	23.72231	2015_1628	283	19
Stratoni HW	40.51129	23.72220	2015_1630	299	47
Stratoni HW	40.51071	23.72165	2015_1631	297	29
Stratoni HW	40.50930	23.72260	2015_1638	281	24
Stratoni HW	40.50765	23.72202	2015_1645	339	30
Stratoni HW	40.50565	23.72241	2015_1648	284	29
Stratoni HW	40.50712	23.80954	2015_1733	247	53
Stratoni HW	40.50755	23.80990	2015_1734	274	39
Stratoni HW	40.47212	23.81823	2015_1768	139	55
Stratoni HW	40.47695	23.81562	2015_1769	123	59
Stratoni HW	40.47722	23.81545	2015_1770	144	75
Stratoni HW	40.47882	23.81467	2015_1771	114	75
Stratoni HW	40.47964	23.81449	2015_1772	141	81
Stratoni HW	40.48202	23.81253	2015_1773	169	40
Stratoni HW	40.48679	23.81242	2015_1774	341	83
Stratoni HW	40.48888	23.81344	2015_1775	348	80
Stratoni HW	40.49251	23.81340	2015_1776	171	44
Stratoni HW	40.49312	23.81323	2015_1777	204	83
Stratoni HW	40.49619	23.81419	2015_1778	346	86
Stratoni HW	40.46289	23.77948	2015_1779	34	56
Stratoni HW	40.46269	23.77915	2015_1785	3	54
Stratoni HW	40.46409	23.77453	2015_1786	25	37
Stratoni HW	40.46552	23.77346	2015_1787	11	36

Table A5. S1 foliation measurements

Domain	Latitude	Longitude	Station No.	Strike	Dip
S1 Foliation					
Olympias	40.56146	23.75053	2013_974	31	24
Olympias	40.56173	23.75129	2013_976	120	45
Olympias	40.56189	23.75158	2013_980	85	15
Olympias	40.56259	23.75228	2013_981	70	45
Olympias	40.56276	23.75396	2013_986	305	38
Olympias	40.56150	23.75742	2013_991	135	24
Olympias	40.56014	23.75748	2013_994	120	45
Olympias	40.55836	23.75634	2013_998	130	62
Olympias	40.55719	23.75946	2013_1000	110	54
Olympias	40.55856	23.76844	2013_1021	135	74
Olympias	40.55892	23.76671	2013_1027	145	49
Olympias	40.55842	23.76624	2013_1029	115	64
Skouries	40.46704	23.71736	2015_1168	43	41
Skouries	40.46841	23.71948	2015_1169	34	40
Skouries	40.46794	23.71996	2015_1171	320	30
Skouries	40.46796	23.72000	2015_1172	324	33
Skouries	40.46629	23.72103	2015_1175	74	21
Skouries	40.46600	23.72100	2015_1176	356	20
Skouries	40.46296	23.72177	2015_1178	70	21
Skouries	40.46426	23.71991	2015_1182	90	35
Skouries	40.46374	23.71982	2015_1183	106	42
Skouries	40.46362	23.71961	2015_1184	130	88
Skouries	40.46303	23.71931	2015_1185	43	20
Skouries	40.46262	23.71905	2015_1186	101	34
Skouries	40.46179	23.71853	2015_1188	89	26
Skouries	40.45885	23.71726	2015_1189	89	39
Skouries	40.45799	23.71699	2015_1190	65	33

Domain	Latitude	Longitude	Station No.	Strike	Dip
S1 Foliation					
Stratoni HW	40.46695	23.77225	2015_1790	10	40
Stratoni HW	40.46853	23.77068	2015_1791	27	26
Stratoni HW	40.46830	23.76023	2015_1792	22	26
Stratoni HW	40.47334	23.76719	2015_1794	38	46
Stratoni HW	40.47402	23.76767	2015_1795	36	46
Stratoni HW	40.47469	23.76644	2015_1796	54	62
Stratoni HW	40.47806	23.76594	2015_1798	336	47
Stratoni HW	40.47912	23.76615	2015_1799	346	59
Stratoni HW	40.46844	23.76976	2015_1800	327	41
Stratoni HW	40.46795	23.76835	2015_1801	357	30
Stratoni HW	40.46994	23.76593	2015_1802	20	39
Stratoni HW	40.47029	23.76375	2015_1803	345	34
Stratoni HW	40.47200	23.76065	2015_1805	6	46
Stratoni HW	40.51698	23.79027	2015_1829	261	31
Stratoni HW	40.51568	23.78975	2015_1830	314	20
Stratoni HW	40.51605	23.79230	2015_1833	47	30
Stratoni HW	40.50814	23.82514	2015_1882	171	88
Stratoni HW	40.52938	23.77012	2014_81	320	20
Stratoni HW	40.52896	23.77041	2014_84	50	55
Stratoni HW	40.52873	23.77046	2014_87	44	76
Stratoni HW	40.52979	23.76932	2014_89	89	36
Stratoni HW	40.52964	23.76858	2014_96	285	33
Stratoni HW	40.52951	23.76842	2014_99	310	40
Stratoni HW	40.53000	23.76730	2014_106	320	35
Stratoni HW	40.53037	23.76738	2014_107	90	59
Stratoni HW	40.53073	23.76729	2014_117	340	35
Stratoni HW	40.51646	23.81758	2014_139	1	65

Table A5. S1 foliation measurements

Domain	Latitude	Longitude	Station No.	Strike	Dip
S1 Foliation					
Skouries	40.45759	23.71674	2015_1191	76	25
Skouries	40.45613	23.71739	2015_1193	95	50
Skouries	40.45493	23.71707	2015_1196	84	35
Skouries	40.45366	23.71737	2015_1199	75	30
Skouries	40.45312	23.71963	2015_1202	76	57
Skouries	40.45411	23.72352	2015_1203	74	48
Skouries	40.45408	23.72351	2015_1204	74	41
Skouries	40.44585	23.74792	2015_1242	65	68
Skouries	40.44573	23.74805	2015_1243	50	57
Skouries	40.44592	23.75080	2015_1244	64	45
Skouries	40.44581	23.75103	2015_1245	66	45
Skouries	40.44583	23.75231	2015_1246	74	72
Skouries	40.44597	23.75482	2015_1250	60	61
Skouries	40.44565	23.75530	2015_1251	63	61
Skouries	40.44548	23.75528	2015_1252	64	81
Skouries	40.44820	23.74572	2015_1254	110	70
Skouries	40.44165	23.74607	2015_1438	72	54
Skouries	40.44218	23.74538	2015_1439	85	35
Skouries	40.44244	23.74514	2015_1440	91	40
Skouries	40.44289	23.74387	2015_1441	75	50
Skouries	40.43665	23.74302	2015_1442	104	65
Skouries	40.43777	23.74194	2015_1445	90	51
Skouries	40.43779	23.74013	2015_1447	89	48
Skouries	40.43751	23.73941	2015_1448	86	54
Skouries	40.43691	23.73863	2015_1449	80	51
Skouries	40.43476	23.73669	2015_1450	72	34
Skouries	40.43409	23.73538	2015_1451	130	36

Domain	Latitude	Longitude	Station No.	Strike	Dip
S1 Foliation					
Stratoni HW	40.51710	23.81447	2014_143	65	45
Stratoni HW	40.51541	23.80731	2014_157	4	35
Stratoni HW	40.51525	23.80710	2014_160	24	20
Stratoni HW	40.51774	23.80349	2014_161	317	59
Stratoni HW	40.52576	23.78242	2014_207	135	10
Stratoni HW	40.52557	23.78334	2014_212	101	18
Stratoni HW	40.52156	23.79002	2014_246	103	35
Stratoni HW	40.52153	23.79006	2014_247	97	65
Stratoni HW	40.52146	23.79033	2014_248	270	85
Stratoni HW	40.52144	23.79039	2014_250	100	45
Stratoni HW	40.52126	23.79140	2014_251	65	50
Stratoni HW	40.52131	23.79160	2014_253	65	35
Stratoni HW	40.52133	23.79187	2014_254	99	40
Stratoni HW	40.52097	23.79373	2014_260	90	30
Stratoni HW	40.52068	23.79572	2014_264	150	30
Stratoni HW	40.52062	23.79643	2014_271	115	37
Stratoni HW	40.52055	23.79632	2014_272	120	33
Stratoni HW	40.52060	23.79602	2014_273	88	45
Stratoni HW	40.52285	23.78304	2014_292	109	34
Stratoni HW	40.52328	23.78334	2014_293	100	45
Stratoni HW	40.52476	23.78428	2014_296	290	45
Stratoni HW	40.51741	23.80233	2014_343	295	80
Stratoni HW	40.51792	23.80172	2014_344	105	60
Stratoni HW	40.51878	23.80108	2014_346	350	47
Stratoni HW	40.51861	23.80024	2014_347	35	40
Stratoni HW	40.53163	23.75140	2014_348	33	45
Stratoni HW	40.53142	23.75605	2014_360	112	65

Table A5. S1 foliation measurements

Domain	Latitude	Longitude	Station No.	Strike	Dip
S1 Foliation					
Skouries	40.43418	23.73494	2015_1452	100	36
Skouries	40.43373	23.73406	2015_1453	94	36
Skouries	40.43344	23.73361	2015_1458	110	46
Skouries	40.43368	23.73264	2015_1460	105	51
Skouries	40.43451	23.73138	2015_1462	108	29
Skouries	40.43521	23.73109	2015_1463	115	26
Skouries	40.43484	23.73040	2015_1464	120	49
Skouries	40.44106	23.72355	2015_1472	71	69
Skouries	40.44017	23.72428	2015_1473	67	69
Skouries	40.43939	23.72418	2015_1474	32	36
Skouries	40.43711	23.70451	2015_1501	126	72
Skouries	40.43747	23.70373	2015_1502	126	55
Skouries	40.43774	23.70322	2015_1503	101	71
Skouries	40.43806	23.70100	2015_1504	103	64
Skouries	40.43816	23.70045	2015_1505	66	35
Skouries	40.43877	23.70004	2015_1506	129	72
Skouries	40.43813	23.69937	2015_1508	276	28
Skouries	40.43825	23.69963	2015_1509	121	84
Skouries	40.43701	23.70508	2015_1512	120	49
Skouries	40.43712	23.70632	2015_1513	86	61
Skouries	40.43745	23.70626	2015_1514	120	34
Skouries	40.43912	23.70669	2015_1517	99	54
Skouries	40.43954	23.70781	2015_1519	108	34
Skouries	40.43952	23.70888	2015_1520	105	39
Skouries	40.44133	23.70931	2015_1521	90	44
Skouries	40.44262	23.71023	2015_1523	83	46
Skouries	40.44378	23.71182	2015_1524	79	58

Domain	Latitude	Longitude	Station No.	Strike	Dip
S1 Foliation					
Stratoni HW	40.53120	23.75717	2014_363	345	35
Stratoni HW	40.53136	23.74846	2014_364	141	20
Stratoni HW	40.53258	23.74327	2014_368	40	35
Stratoni HW	40.53371	23.74537	2014_373	320	35
Stratoni HW	40.53418	23.74403	2014_374	150	40
Stratoni HW	40.52866	23.74327	2014_377	285	30
Stratoni HW	40.52899	23.74176	2014_378	91	60
Stratoni HW	40.53237	23.73998	2014_389	322	45
Stratoni HW	40.53243	23.73956	2014_393	110	75
Stratoni HW	40.53124	23.74503	2014_396	90	25
Stratoni HW	40.53162	23.74395	2014_398	152	20
Stratoni HW	40.53168	23.74390	2014_399	105	26
Stratoni HW	40.53134	23.72320	2014_409	292	35
Stratoni HW	40.49597	23.81460	2014_423	190	88
Stratoni HW	40.49797	23.81682	2014_424	185	80
Stratoni HW	40.49801	23.81541	2014_425	165	70
Stratoni HW	40.49965	23.81474	2014_429	171	80
Stratoni HW	40.50091	23.81525	2014_430	153	85
Stratoni HW	40.50189	23.81559	2014_434	150	66
Stratoni HW	40.50227	23.81477	2014_435	155	81
Stratoni HW	40.50261	23.81189	2014_437	120	75
Stratoni HW	40.50220	23.80907	2014_438	135	77
Stratoni HW	40.50160	23.80776	2014_440	290	55
Stratoni HW	40.53306	23.71687	2014_461	50	45
Stratoni HW	40.53140	23.71644	2014_493	160	25
Stratoni HW	40.53258	23.71567	2014_495	115	50
Stratoni HW	40.52963	23.76688	2014_507	33	30

Table A5. S1 foliation measurements

Domain	Latitude	Longitude	Station No.	Strike	Dip
S1 Foliation					
Skouries	40.44457	23.71215	2015_1525	81	31
Skouries	40.44650	23.71203	2015_1527	77	51
Skouries	40.44700	23.71263	2015_1530	74	42
Skouries	40.44805	23.71417	2015_1531	54	36
Skouries	40.44935	23.71543	2015_1532	81	56
Skouries	40.44998	23.71619	2015_1533	85	38
Skouries	40.45186	23.71683	2015_1534	80	39
Skouries	40.45295	23.71727	2015_1535	75	18
Skouries	40.44563	23.72020	2015_1539	76	51
Skouries	40.44666	23.72072	2015_1540	75	51
Skouries	40.39739	23.79732	2015_1658	11	50
Skouries	40.39808	23.79669	2015_1659	226	49
Skouries	40.39916	23.79614	2015_1660	101	68
Skouries	40.42108	23.71963	2015_1666	102	79
Skouries	40.42458	23.72053	2015_1668	113	40
Skouries	40.42565	23.72144	2015_1669	295	58
Skouries	40.42571	23.72163	2015_1670	294	73
Skouries	40.42661	23.72249	2015_1672	95	75
Skouries	40.42710	23.72270	2015_1673	149	52
Skouries	40.42766	23.72319	2015_1676	124	37
Skouries	40.45695	23.66274	2015_1679	237	84
Skouries	40.45730	23.66288	2015_1680	229	43
Skouries	40.45934	23.66470	2015_1683	127	17
Skouries	40.46045	23.66578	2015_1685	79	27
Skouries	40.46072	23.66599	2015_1686	74	28
Skouries	40.46089	23.66646	2015_1687	91	49
Skouries	40.46128	23.66680	2015_1690	88	53
Stratoni HW	40.51134	23.81299	2014_512	100	60
Stratoni HW	40.51184	23.81259	2014_513	121	80
Stratoni HW	40.51259	23.81213	2014_515	190	80
Stratoni HW	40.51268	23.81195	2014_516	310	80
Stratoni HW	40.51316	23.81145	2014_517	40	80
Stratoni HW	40.55755	23.66777	2014_520	330	14
Stratoni HW	40.55752	23.66700	2014_521	104	28
Stratoni HW	40.55734	23.66688	2014_523	135	28
Stratoni HW	40.55669	23.66775	2014_526	85	5
Stratoni HW	40.55675	23.66674	2014_527	130	30
Stratoni HW	40.55633	23.66661	2014_528	320	35
Stratoni HW	40.55602	23.66641	2014_530	90	20
Stratoni HW	40.55545	23.66596	2014_532	104	35
Stratoni HW	40.55485	23.66527	2014_533	245	30
Stratoni HW	40.55383	23.66497	2014_534	130	36
Stratoni HW	40.55278	23.66490	2014_535	50	40
Stratoni HW	40.55202	23.66511	2014_536	125	40
Stratoni HW	40.57358	23.65507	2014_541	225	20
Stratoni HW	40.57401	23.65477	2014_542	220	15
Stratoni HW	40.57362	23.65168	2014_544	345	20
Stratoni HW	40.57331	23.65078	2014_547	100	50
Stratoni HW	40.57450	23.64910	2014_548	275	24
Stratoni HW	40.57471	23.64848	2014_550	240	40
Stratoni HW	40.57537	23.64545	2014_552	286	42
Stratoni HW	40.57488	23.64361	2014_554	85	12
Stratoni HW	40.57435	23.64220	2014_559	340	20
Stratoni HW	40.57444	23.63844	2014_561	270	25

Table A5. S1 foliation measurements

Domain	Latitude	Longitude	Station No.	Strike	Dip
S1 Foliation					
Skouries	40.46179	23.66658	2015_1691	94	42
Skouries	40.46246	23.66684	2015_1692	91	61
Skouries	40.46279	23.66853	2015_1698	125	53
Skouries	40.46355	23.66902	2015_1700	117	64
Skouries	40.46384	23.66938	2015_1701	134	54
Skouries	40.46422	23.66938	2015_1702	128	53
Skouries	40.46630	23.66911	2015_1703	146	40
Skouries	40.46581	23.66932	2015_1705	123	60
Skouries	40.46575	23.66889	2015_1706	120	61
Skouries	40.46527	23.66900	2015_1707	133	44
Skouries	40.46510	23.66919	2015_1709	130	41
Skouries	40.46704	23.66874	2015_1711	134	45
Skouries	40.46788	23.66865	2015_1713	138	52
Skouries	40.46814	23.66874	2015_1714	146	34
Skouries	40.47169	23.67311	2015_1715	127	36
Skouries	40.47211	23.67312	2015_1716	123	25
Skouries	40.47559	23.67727	2015_1717	131	39
Skouries	40.47555	23.67688	2015_1718	129	44
Skouries	40.48046	23.68213	2015_1721	36	14
Skouries	40.48036	23.68178	2015_1723	343	21
Skouries	40.47970	23.68007	2015_1726	225	24
Skouries	40.47970	23.68002	2015_1727	205	21
Skouries	40.47842	23.68519	2015_1728	277	41
Skouries	40.47902	23.68425	2015_1729	254	23
Skouries	40.47912	23.68415	2015_1730	150	4
Skouries	40.47960	23.68387	2015_1731	229	13
Skouries	40.47871	23.68561	2015_1732	246	14
Stratoni HW	40.57394	23.63998	2014_562	270	25
Stratoni HW	40.56867	23.65049	2014_588	230	20
Stratoni HW	40.56880	23.64943	2014_595	225	30
Stratoni HW	40.51453	23.77293	2014_611	315	45
Stratoni HW	40.47840	23.78107	2014_612	20	40
Stratoni HW	40.47815	23.78278	2014_614	2	40
Stratoni HW	40.48454	23.78771	2014_979	335	30
Stratoni HW	40.48945	23.78621	2014_980	335	60
Stratoni HW	40.52113	23.77108	2014_1050	300	35
Stratoni HW	40.52107	23.77121	2014_1051	35	88
Stratoni HW	40.52111	23.77126	2014_1052	302	35
Stratoni HW	40.52143	23.77228	2014_1053	276	45
Stratoni HW	40.52143	23.77239	2014_1054	295	40
Stratoni HW	40.52117	23.77347	2014_1057	305	48
Stratoni HW	40.52110	23.77361	2014_1058	296	26
Stratoni HW	40.52061	23.77487	2014_1060	295	30
Stratoni HW	40.51978	23.77860	2014_1062	305	53
Stratoni HW	40.51963	23.77870	2014_1063	315	41
Stratoni HW	40.52040	23.77802	2014_1064	305	75
Stratoni HW	40.52052	23.77774	2014_1065	307	70
Stratoni HW	40.52049	23.77716	2014_1066	310	75
Stratoni HW	40.52055	23.77734	2014_1067	305	69
Stratoni HW	40.51899	23.78037	2014_1068	356	65
Stratoni HW	40.51900	23.78026	2014_1070	335	56
Stratoni HW	40.51901	23.78016	2014_1071	340	45
Stratoni HW	40.51906	23.77989	2014_1072	323	70
Stratoni HW	40.51911	23.77966	2014_1073	355	55

Table A5. S1 foliation measurements

Domain	Latitude	Longitude	Station No.	Strike	Dip
S1 Foliation					
Skouries	40.43186	23.70508	2015_1840	137	51
Skouries	40.43270	23.70429	2015_1842	88	52
Skouries	40.42067	23.72172	2015_1847	86	46
Skouries	40.42022	23.72239	2015_1848	95	51
Skouries	40.41742	23.75254	2015_1849	14	24
Skouries	40.42296	23.75394	2015_1850	87	43
Skouries	40.41240	23.76134	2015_1851	239	24
Skouries	40.40497	23.78366	2015_1853	44	37
Skouries	40.42032	23.72058	2015_1857	103	52
Skouries	40.47468	23.65090	2015_1864	36	88
Skouries	40.47354	23.65425	2015_1865	135	52
Skouries	40.47543	23.65543	2015_1866	125	41
Skouries	40.47648	23.65578	2015_1870	130	64
Skouries	40.47720	23.65715	2015_1871	154	38
Skouries	40.47728	23.65722	2015_1872	143	48
Skouries	40.47752	23.65781	2015_1876	161	36
Skouries	40.47859	23.65974	2015_1877	158	47
Skouries	40.47865	23.65993	2015_1879	155	49
Skouries	40.47666	23.65616	2015_1880	125	52
Skouries	40.42396	23.71891	2015_1883	161	26
Skouries	40.48467	23.72557	2014_586	310	40
Skouries	40.48357	23.71962	2014_615	320	30
Skouries	40.48337	23.71955	2014_616	315	40
Skouries	40.48239	23.71862	2014_621	300	45
Skouries	40.48243	23.71866	2014_622	294	50
Skouries	40.48258	23.72178	2014_634	302	50
Skouries	40.48702	23.72192	2014_638	305	60

Domain	Latitude	Longitude	Station No.	Strike	Dip
S1 Foliation					
Stratoni HW	40.51915	23.77955	2014_1074	336	60
Stratoni HW	40.51685	23.78235	2014_1075	15	35
Stratoni HW	40.51701	23.78214	2014_1076	25	50
Stratoni HW	40.51648	23.78237	2014_1077	320	35
Stratoni HW	40.51550	23.78242	2014_1078	350	45
Stratoni HW	40.51437	23.78276	2014_1080	330	50
Stratoni HW	40.51022	23.78568	2014_1081	95	50
Stratoni HW	40.51024	23.78561	2014_1082	56	75
Stratoni HW	40.51027	23.78549	2014_1083	88	70
Stratoni HW	40.50871	23.78577	2014_1084	105	80
Stratoni HW	40.50856	23.78573	2014_1086	120	75
Stratoni HW	40.50821	23.78592	2014_1087	135	55
Stratoni HW	40.50824	23.78813	2014_1089	270	50
Stratoni HW	40.50806	23.78830	2014_1091	285	67
Stratoni HW	40.50654	23.78877	2014_1092	262	40
Stratoni HW	40.50606	23.78953	2014_1093	205	65
Stratoni HW	40.50606	23.78960	2014_1094	177	65
Stratoni HW	40.51678	23.81302	2014_1147	133	29
Stratoni HW	40.53240	23.75161	2014_1149	100	10
Stratoni HW	40.50160	23.77760	2014_PT1	272	38
Stratoni HW	40.50120	23.77740	2014_PT2	340	70
Stratoni HW	40.50080	23.77670	2014_PT3	300	50
Stratoni HW	40.49930	23.77860	2014_PT4	288	80
Stratoni HW	40.49860	23.78260	2014_PT5	108	60
Stratoni HW	40.49860	23.78350	2014_PT6	118	80
Stratoni HW	40.49860	23.78410	2014_PT7	80	50
Stratoni HW	40.49860	23.78430	2014_PT8	120	55

Table A5. S1 foliation measurements

Domain	Latitude	Longitude	Station No.	Strike	Dip
S1 Foliation					
Skouries	40.48694	23.72079	2014_644	295	58
Skouries	40.48692	23.72056	2014_645	290	60
Skouries	40.48684	23.71984	2014_649	305	73
Skouries	40.48644	23.72405	2014_651	115	60
Skouries	40.48566	23.72411	2014_655	100	55
Skouries	40.48485	23.72616	2014_657	330	25
Skouries	40.48510	23.72684	2014_658	56	30
Skouries	40.48574	23.72750	2014_661	320	30
Skouries	40.48602	23.72557	2014_664	270	65
Skouries	40.48710	23.72523	2014_667	300	90
Skouries	40.48722	23.72434	2014_668	120	30
Skouries	40.48155	23.72263	2014_670	340	55
Skouries	40.48131	23.72169	2014_674	305	75
Skouries	40.48163	23.72146	2014_676	340	77
Skouries	40.48377	23.72370	2014_682	80	27
Skouries	40.48236	23.72409	2014_685	260	45
Skouries	40.47938	23.71402	2014_686	95	40
Skouries	40.47805	23.71291	2014_689	280	60
Skouries	40.47794	23.71361	2014_693	305	45
Skouries	40.47749	23.71406	2014_694	275	60
Skouries	40.47740	23.71475	2014_697	265	60
Skouries	40.47746	23.71556	2014_698	320	30
Skouries	40.47868	23.71668	2014_699	95	57
Skouries	40.47883	23.71705	2014_700	95	85
Skouries	40.47934	23.71745	2014_706	90	80
Skouries	40.47966	23.71764	2014_707	295	70
Skouries	40.48064	23.71860	2014_709	265	55

Domain	Latitude	Longitude	Station No.	Strike	Dip
S1 Foliation					
Stratoni HW	40.49830	23.78520	2014_PT9	100	85
Stratoni HW	40.49840	23.78530	2014_PT10	145	85
Stratoni HW	40.49890	23.78120	2014_PT11	160	38
Stratoni HW	40.49790	23.78520	2014_PT12	125	60
Stratoni HW	40.49720	23.78660	2014_PT13	320	60
Stratoni HW	40.49720	23.78720	2014_PT14	350	50
Stratoni HW	40.49780	23.78370	2014_PT15	260	75
Stratoni HW	40.49670	23.78180	2014_PT16	305	50
Stratoni HW	40.49580	23.78230	2014_PT17	110	60
Stratoni HW	40.49560	23.78240	2014_PT18	308	60
Stratoni HW	40.49540	23.78200	2014_PT19	300	58
Stratoni HW	40.49560	23.78040	2014_PT20	305	75
Stratoni HW	40.49560	23.78020	2014_PT21	308	88
Stratoni HW	40.49760	23.78230	2014_PT22	95	28
Stratoni HW	40.49730	23.77950	2014_PT23	285	80
Stratoni HW	40.49570	23.77960	2014_PT24	320	65
Stratoni HW	40.49440	23.78080	2014_PT25	115	45
Stratoni HW	40.49430	23.78060	2014_PT26	295	80
Stratoni HW	40.49770	23.78440	2014_PT27	288	80
Stratoni HW	40.49770	23.78440	2014_PT28	144	68
Stratoni HW	40.49770	23.78450	2014_PT29	255	72
Stratoni HW	40.49990	23.79170	2014_PT30	30	30
Stratoni HW	40.50060	23.79610	2014_PT31	45	30
Stratoni HW	40.49920	23.79170	2014_PT32	305	60
Stratoni HW	40.49930	23.79560	2014_PT33	110	64
Stratoni HW	40.49930	23.79570	2014_PT34	132	65
Stratoni HW	40.50090	23.79710	2014_PT35	40	20

Table A5. S1 foliation measurements

Domain	Latitude	Longitude	Station No.	Strike	Dip
S1 Foliation					
Skouries	40.48097	23.71843	2014_713	265	40
Skouries	40.46493	23.70856	2014_715	70	20
Skouries	40.46500	23.70857	2014_716	91	34
Skouries	40.46694	23.71749	2014_717	10	25
Skouries	40.46745	23.71783	2014_718	330	75
Skouries	40.47295	23.72505	2014_719	270	60
Skouries	40.47392	23.72435	2014_720	275	35
Skouries	40.47429	23.72589	2014_721	280	50
Skouries	40.47425	23.72666	2014_724	285	70
Skouries	40.47714	23.72406	2014_731	110	65
Skouries	40.47764	23.72420	2014_732	115	75
Skouries	40.47798	23.72395	2014_733	300	60
Skouries	40.47325	23.70425	2014_735	300	35
Skouries	40.47491	23.72065	2014_738	300	55
Skouries	40.47606	23.72326	2014_743	100	75
Skouries	40.47701	23.72320	2014_744	85	66
Skouries	40.47763	23.72363	2014_747	290	75
Skouries	40.46631	23.70436	2014_749	330	47
Skouries	40.46675	23.70434	2014_751	335	27
Skouries	40.46732	23.70433	2014_758	332	20
Skouries	40.46866	23.70634	2014_767	325	25
Skouries	40.46984	23.70721	2014_772	105	25
Skouries	40.47019	23.70773	2014_775	305	55
Skouries	40.47072	23.70820	2014_777	295	55
Skouries	40.47125	23.70897	2014_786	285	60
Skouries	40.47212	23.70922	2014_789	295	55
Skouries	40.47267	23.71015	2014_792	305	65

Domain	Latitude	Longitude	Station No.	Strike	Dip
S1 Foliation					
Stratoni HW	40.50090	23.79750	2014_PT36	70	32
Stratoni HW	40.50100	23.79770	2014_PT37	85	18
Stratoni HW	40.50060	23.79800	2014_PT38	50	65
Stratoni HW	40.50040	23.79820	2014_PT39	52	60
Stratoni HW	40.50010	23.79840	2014_PT40	95	75
Stratoni HW	40.49990	23.79850	2014_PT41	85	72
Stratoni HW	40.49950	23.79900	2014_PT42	91	75
Stratoni HW	40.49920	23.79930	2014_PT43	275	82
Stratoni HW	40.49900	23.79960	2014_PT44	102	75
Stratoni HW	40.49890	23.79980	2014_PT45	75	70
Stratoni HW	40.49940	23.80030	2014_PT46	82	70
Stratoni HW	40.49910	23.80060	2014_PT47	100	78
Stratoni HW	40.49740	23.78740	2014_PT48	345	58
Stratoni HW	40.49760	23.78780	2014_PT49	350	65
Stratoni HW	40.49790	23.78860	2014_PT50	320	55
Stratoni HW	40.49810	23.78990	2014_PT51	352	80
Stratoni HW	40.49840	23.79080	2014_PT52	20	75
Stratoni HW	40.49830	23.79270	2014_PT53	22	70
Stratoni HW	40.49840	23.79370	2014_PT54	60	75
Stratoni HW	40.49790	23.79520	2014_PT55	308	52
Stratoni HW	40.49790	23.79640	2014_PT56	155	78
Stratoni HW	40.49790	23.79650	2014_PT57	275	38
Stratoni HW	40.49680	23.78790	2014_PT58	130	78
Stratoni HW	40.49660	23.78800	2014_PT59	125	78
Stratoni HW	40.49600	23.78870	2014_PT60	10	57
Stratoni HW	40.49510	23.78800	2014_PT61	345	60
Stratoni HW	40.49570	23.78970	2014_PT62	80	78

Table A5. S1 foliation measurements

Domain	Latitude	Longitude	Station No.	Strike	Dip
S1 Foliation					
Skouries	40.47270	23.71028	2014_793	290	90
Skouries	40.47340	23.71109	2014_795	305	75
Skouries	40.47417	23.71144	2014_798	290	80
Skouries	40.47467	23.71227	2014_799	100	73
Skouries	40.47493	23.71253	2014_801	115	80
Skouries	40.47566	23.71308	2014_804	295	65
Skouries	40.48366	23.71860	2014_806	300	35
Skouries	40.48354	23.71759	2014_816	285	70
Skouries	40.48336	23.71719	2014_819	296	60
Skouries	40.48313	23.71673	2014_827	270	60
Skouries	40.48358	23.71422	2014_840	305	27
Skouries	40.48376	23.71322	2014_846	310	33
Skouries	40.48425	23.71208	2014_852	315	55
Skouries	40.48099	23.71149	2014_855	300	68
Skouries	40.47969	23.71075	2014_861	100	40
Skouries	40.47971	23.70976	2014_863	90	70
Skouries	40.47987	23.70898	2014_868	95	75
Skouries	40.47989	23.70866	2014_870	110	70
Skouries	40.47962	23.70863	2014_875	335	50
Skouries	40.47962	23.70839	2014_879	295	85
Skouries	40.47988	23.70732	2014_888	120	75
Skouries	40.47993	23.70701	2014_890	135	62
Skouries	40.47980	23.70552	2014_898	125	55
Skouries	40.46732	23.70056	2014_900	110	20
Skouries	40.46701	23.70019	2014_902	155	25
Skouries	40.46768	23.69947	2014_903	150	38
Skouries	40.46797	23.69934	2014_904	105	30

Domain	Latitude	Longitude	Station No.	Strike	Dip
S1 Foliation					
Stratoni HW	40.49550	23.79010	2014_PT63	122	80
Stratoni HW	40.49590	23.78880	2014_PT64	70	70
Stratoni HW	40.49550	23.78960	2014_PT65	102	65
Stratoni HW	40.49540	23.79010	2014_PT66	255	70
Stratoni HW	40.49880	23.79990	2014_PT67	285	80
Stratoni HW	40.49860	23.80010	2014_PT68	81	70
Stratoni HW	40.49860	23.80010	2014_PT69	95	72
Stratoni HW	40.49860	23.80020	2014_PT70	245	40
Stratoni HW	40.49760	23.80080	2014_PT71	262	30
Stratoni HW	40.49760	23.80080	2014_PT72	345	60
Stratoni HW	40.49740	23.80080	2014_PT73	270	60
Stratoni HW	40.49720	23.79860	2014_PT74	290	50
Stratoni HW	40.49770	23.79800	2014_PT75	214	40
Stratoni HW	40.49800	23.79700	2014_PT76	282	68
Stratoni HW	40.49370	23.79370	2014_PT77	322	60
Stratoni HW	40.49270	23.79420	2014_PT78	308	60
Stratoni HW	40.49350	23.79400	2014_PT79	290	65
Stratoni HW	40.49210	23.79350	2014_PT80	312	55
Stratoni HW	40.49310	23.79520	2014_PT81	332	48
Stratoni HW	40.49260	23.79570	2014_PT82	345	61
Stratoni HW	40.49270	23.79610	2014_PT83	318	70
Stratoni HW	40.49430	23.78790	2014_PT84	333	67
Stratoni HW	40.49380	23.78150	2014_PT85	2	80
Stratoni HW	40.49210	23.78750	2014_PT86	315	50
Stratoni HW	40.49080	23.78780	2014_PT87	328	68
Stratoni HW	40.49460	23.79750	2014_PT88	150	72
Stratoni HW	40.49460	23.79780	2014_PT89	150	75

Table A5. S1 foliation measurements

Domain	Latitude	Longitude	Station No.	Strike	Dip
S1 Foliation					
Skouries	40.46826	23.69908	2014_906	125	40
Skouries	40.46932	23.69836	2014_908	150	10
Skouries	40.47311	23.69767	2014_909	297	35
Skouries	40.47428	23.69811	2014_912	235	25
Skouries	40.47690	23.69766	2014_913	295	20
Skouries	40.47730	23.69702	2014_918	296	35
Skouries	40.47783	23.69683	2014_921	305	41
Skouries	40.47008	23.69848	2014_922	310	45
Skouries	40.46972	23.69866	2014_923	281	46
Skouries	40.47154	23.70408	2014_928	308	14
Skouries	40.46956	23.72450	2014_930	314	55
Skouries	40.47081	23.72212	2014_931	290	30
Skouries	40.46885	23.72240	2014_932	304	25
Skouries	40.46818	23.72139	2014_935	273	16
Skouries	40.48049	23.69769	2014_940	118	30
Skouries	40.48000	23.69631	2014_949	299	75
Skouries	40.47948	23.69638	2014_953	305	82
Skouries	40.47947	23.69692	2014_957	125	56
Skouries	40.47787	23.69692	2014_959	314	40
Skouries	40.47753	23.69627	2014_969	324	30
Skouries	40.48237	23.72477	2014_1121	295	75
Skouries	40.48269	23.72571	2014_1122	255	40
Skouries	40.48325	23.72630	2014_1123	105	44
Skouries	40.48287	23.72679	2014_1124	305	54
Skouries	40.48050	23.68898	2015_SKL15	290	30
Skouries	40.47787	23.69251	2015_SKL10	294	25
Skouries	40.47979	23.68973	2015_SKL14	294	35
Stratoni HW	40.49460	23.79800	2014_PT90	132	80
Stratoni HW	40.49450	23.79840	2014_PT91	138	78
Stratoni HW	40.49000	23.78840	2014_PT92	335	51
Stratoni HW	40.49370	23.79620	2014_PT93	348	60
Stratoni HW	40.49380	23.78150	2014_PT94	320	70
Stratoni HW	40.49350	23.78190	2014_PT95	308	75
Stratoni HW	40.49290	23.78190	2014_PT96	292	70
Stratoni HW	40.49230	23.78300	2014_PT97	288	75
Stratoni HW	40.49210	23.78360	2014_PT98	310	58
Stratoni HW	40.49180	23.78450	2014_PT99	296	70
Stratoni HW	40.49130	23.78490	2014_PT100	312	68
Stratoni HW	40.49080	23.78480	2014_PT101	320	45
Stratoni HW	40.49080	23.78380	2014_PT102	322	72
Stratoni HW	40.48500	23.78190	2014_PT103	338	52
Stratoni HW	40.48420	23.78250	2014_PT104	340	52
Stratoni HW	40.48380	23.78430	2014_PT105	340	42
Stratoni HW	40.48540	23.77980	2014_PT106	325	60
Stratoni HW	40.48430	23.78090	2014_PT107	240	68
Stratoni HW	40.48380	23.78120	2014_PT108	312	64
Stratoni HW	40.48280	23.78050	2014_PT109	324	50
Stratoni HW	40.48310	23.78150	2014_PT110	300	55
Stratoni HW	40.48200	23.78230	2014_PT111	345	50
Stratoni HW	40.48200	23.78430	2014_PT112	352	58
Stratoni HW	40.48130	23.78430	2014_PT113	295	50
Stratoni HW	40.47900	23.77900	2014_PT114	344	50
Stratoni HW	40.47860	23.78110	2014_PT115	332	58
Stratoni HW	40.47820	23.78310	2014_PT116	340	32

Table A5. S1 foliation measurements

Domain	Latitude	Longitude	Station No.	Strike	Dip
S1 Foliation					
Skouries	40.47912	23.69078	2015_SKL13	296	55
Skouries	40.47999	23.69643	2015_SKL1	300	60
Skouries	40.47763	23.69285	2015_SKL8	300	45
Skouries	40.47790	23.69241	2015_SKL11	300	45
Skouries	40.47941	23.69614	2015_SKL4	304	50
Skouries	40.47796	23.69390	2015_SKL6	304	45
Skouries	40.47772	23.69267	2015_SKL9	304	45
Skouries	40.48225	23.68717	2015_SKL16	304	42
Skouries	40.47823	23.69223	2015_SKL12	306	40
Skouries	40.47748	23.69689	2015_SKL5	332	45
Skouries	40.47767	23.69348	2015_SKL7	336	42
Skouries	40.46122	23.66682	2015_SKL42	30	60
Skouries	40.45690	23.65823	2015_SKL47	84	15
Skouries	40.46162	23.66668	2015_SKL38	86	20
Skouries	40.46198	23.66656	2015_SKL39	90	55
Skouries	40.45697	23.65826	2015_SKL49	94	22
Skouries	40.46082	23.66666	2015_SKL41	100	68
Skouries	40.47239	23.67319	2015_SKL24	108	35
Skouries	40.46359	23.66927	2015_SKL35	110	70
Skouries	40.46243	23.66692	2015_SKL40	110	54
Skouries	40.47937	23.69714	2015_SKL3	116	30
Skouries	40.46402	23.66948	2015_SKL34	118	50
Skouries	40.47554	23.67690	2015_SKL23	122	40
Skouries	40.46500	23.66925	2015_SKL33	124	50
Skouries	40.46128	23.66684	2015_SKL43	124	45
Skouries	40.46544	23.66917	2015_SKL31	126	44
Skouries	40.46527	23.66916	2015_SKL32	128	55
Stratoni HW	40.47930	23.78450	2014_PT117	325	20
Stratoni HW	40.47980	23.78460	2014_PT118	305	30
Stratoni HW	40.48240	23.77960	2014_PT119	305	40
Stratoni HW	40.48210	23.77880	2014_PT120	330	40
Stratoni HW	40.48180	23.77810	2014_PT121	308	50
Stratoni HW	40.48830	23.78610	2014_PT122	235	32
Stratoni HW	40.48950	23.78630	2014_PT123	318	52
Stratoni HW	40.48750	23.79130	2014_PT124	300	76
Stratoni HW	40.48500	23.79310	2014_PT125	342	75
Stratoni HW	40.48530	23.79340	2014_PT126	315	30
Stratoni HW	40.48590	23.79500	2014_PT127	340	75
Stratoni HW	40.47970	23.80090	2014_PT128	342	78
Stratoni HW	40.48260	23.78940	2014_PT129	340	65
Stratoni HW	40.53640	23.70020	2014_P073	270	46
Stratoni HW	40.56880	23.64940	2014_P682	270	32
Stratoni HW	40.57540	23.64550	2014_P646	286	42
Stratoni HW	40.53030	23.71730	2014_P423	290	30
Stratoni HW	40.52940	23.72930		290	40
Stratoni HW	40.53050	23.74020	2014_P443	298	35
Stratoni HW	40.54940	23.67630	2014_P159	300	40
Stratoni HW	40.57450	23.64910	2014_P642	300	23
Stratoni HW	40.52940	23.72440		300	40
Stratoni HW	40.52750	23.72020		300	40
Stratoni HW	40.54550	23.68250	2014_P177	302	80
Stratoni HW	40.53300	23.69370	2014_P153	305	50
Stratoni HW	40.55110	23.66970	2014_P224	308	20
Stratoni HW	40.52900	23.73950	2014_P459	308	20

Table A5. S1 foliation measurements

Domain	Latitude	Longitude	Station No.	Strike	Dip
S1 Foliation					
Skouries	40.45628	23.65926	2015_SKL48	130	65
Skouries	40.46676	23.66863	2015_SKL28	134	55
Skouries	40.46605	23.66932	2015_SKL30	138	50
Skouries	40.46774	23.66866	2015_SKL25	139	55
Skouries	40.46694	23.66878	2015_SKL27	142	50
Skouries	40.46629	23.66915	2015_SKL29	142	40
Skouries	40.46744	23.66865	2015_SKL26	144	55
Skouries	40.46273	23.66858	2015_SKL37	152	45
Skouries	40.47977	23.68672	2015_SKL17	154	45
Skouries	40.47918	23.68563	2015_SKL18	158	35
Skouries	40.46310	23.66897	2015_SKL36	170	45
Skouries	40.48040	23.68265	2015_SKL20	12	42
Skouries	40.45733	23.66288	2015_SKL45	30	45
Skouries	40.47983	23.68067	2015_SKL21	34	42
Skouries	40.45691	23.66241	2015_SKL44	44	60
Skouries	40.45642	23.66040	2015_SKL46	48	70
Skouries	40.48012	23.69644	2015_SKL2	60	60
Skouries	40.47871	23.68561	2015_SKL19	64	12
Skouries	40.47969	23.68004	2015_SKL22	71	33
Skouries	40.48571	23.72648	2015_PG228	259	34
Skouries	40.48625	23.72497	2015_PG227	271	64
Skouries	40.48610	23.72557	2015_PG230	282	22
Skouries	40.48725	23.72465	2015_PG225	286	41
Skouries	40.48695	23.72525	2015_PG226	303	56
Skouries	40.48731	23.72447	2015_PG224	304	41
Stratoni FW	40.56095	23.81851	2015_1344	274	30
Stratoni FW	40.56346	23.81939	2015_1347	300	20

Domain	Latitude	Longitude	Station No.	Strike	Dip
S1 Foliation					
Stratoni HW	40.53840	23.68910	2014_P141	312	58
Stratoni HW	40.54070	23.68390	2014_P149	312	40
Stratoni HW	40.53600	23.69710	2014_P037	318	38
Stratoni HW	40.53350	23.69700	2014_P052	320	87
Stratoni HW	40.54220	23.68890	2014_P113	320	40
Stratoni HW	40.54790	23.68030	2014_P183	324	64
Stratoni HW	40.54730	23.67940	2014_P188	324	64
Stratoni HW	40.53720	23.69640	2014_P044	325	67
Stratoni HW	40.53660	23.68020	2014_P150	328	68
Stratoni HW	40.54460	23.67270	2014_P349	328	60
Stratoni HW	40.54300	23.68320	2014_P173	330	50
Stratoni HW	40.54610	23.67460	2014_P344	332	60
Stratoni HW	40.55240	23.66690	2014_P307	335	25
Stratoni HW	40.55100	23.67470	2014_P242	338	80
Stratoni HW	40.54820	23.67500	2014_P341	340	80
Stratoni HW	40.55130	23.67280	2014_P241	25	50
Stratoni HW	40.53100	23.73360		50	90
Stratoni HW	40.53260	23.71580	2014_P427	60	38
Stratoni HW	40.53130	23.72710		90	30
Stratoni HW	40.53270	23.73870	2014_P454	98	35
Stratoni HW	40.53100	23.73330		110	60
Stratoni HW	40.53170	23.69680	2014_P001	120	83
Stratoni HW	40.55270	23.67030	2014_P216	120	26
Stratoni HW	40.55680	23.66670	2014_P626	130	30
Stratoni HW	40.55010	23.66850	2014_P328	140	25
Stratoni HW	40.55390	23.66190	2014_P325	150	38
Stratoni HW	40.55090	23.66540	2014_P321	161	58

Table A5. S1 foliation measurements

Domain	Latitude	Longitude	Station No.	Strike	Dip
S1 Foliation					
Stratoni FW	40.55927	23.81754	2015_1545	257	20
Stratoni FW	40.55924	23.81737	2015_1546	259	29
Stratoni FW	40.55814	23.81673	2015_1549	306	27
Stratoni FW	40.55775	23.81699	2015_1551	304	33
Stratoni FW	40.55722	23.81711	2015_1552	256	25
Stratoni FW	40.55765	23.81565	2015_1555	305	44
Stratoni FW	40.55837	23.81439	2015_1558	288	11
Stratoni FW	40.55875	23.81309	2015_1563	298	10
Stratoni FW	40.55871	23.81300	2015_1564	294	11
Stratoni FW	40.55927	23.81218	2015_1565	259	24
Stratoni FW	40.55966	23.81104	2015_1566	285	21
Stratoni FW	40.55969	23.80937	2015_1567	319	16
Stratoni FW	40.55881	23.81000	2015_1568	275	21
Stratoni FW	40.55803	23.81092	2015_1569	266	54
Stratoni FW	40.55673	23.81065	2015_1570	298	36
Stratoni FW	40.55601	23.81006	2015_1571	316	11
Stratoni FW	40.55563	23.80883	2015_1572	275	24
Stratoni FW	40.55488	23.80943	2015_1574	321	25
Stratoni FW	40.55437	23.80986	2015_1575	284	24
Stratoni FW	40.55451	23.80687	2015_1578	281	26
Stratoni FW	40.55484	23.80572	2015_1579	309	35
Stratoni FW	40.55494	23.80531	2015_1580	310	31
Stratoni FW	40.55461	23.80481	2015_1584	293	84
Stratoni FW	40.55371	23.80539	2015_1586	296	56
Stratoni FW	40.55292	23.80255	2015_1589	311	14
Stratoni FW	40.55333	23.80151	2015_1590	154	16
Stratoni FW	40.55353	23.80119	2015_1591	136	5

Domain	Latitude	Longitude	Station No.	Strike	Dip
S1 Foliation					
Stratoni HW	40.52830	23.72460		220	30
Stratoni HW	40.52770	23.73680		240	60
Stratoni HW	40.52540	23.72580		240	20
Stratoni HW	40.53140	23.72580		240	80
Stratoni HW	40.53090	23.71860		250	10
Stratoni HW	40.53140	23.72320		250	30
Stratoni HW	40.52467	23.72331	2015_PG110	8	71
Stratoni HW	40.49626	23.71669	2015_PG141	9	26
Stratoni HW	40.50722	23.74743	2015_PG96	10	41
Stratoni HW	40.50111	23.73862	2015_PG188	22	3
Stratoni HW	40.50121	23.74293	2015_PG185	34	13
Stratoni HW	40.50870	23.72125	2015_PG32	40	10
Stratoni HW	40.51279	23.71919	2015_PG25	45	10
Stratoni HW	40.49799	23.70397	2015_PG121	49	56
Stratoni HW	40.51208	23.72217	2015_PG156	53	22
Stratoni HW	40.49500	23.74670	2015_PG195	54	28
Stratoni HW	40.49439	23.71500	2015_PG145	56	40
Stratoni HW	40.50577	23.73584	2015_PG169	56	32
Stratoni HW	40.51093	23.75531	2015_PG90	60	16
Stratoni HW	40.49513	23.74825	2015_PG194	63	44
Stratoni HW	40.49483	23.71578	2015_PG144	65	31
Stratoni HW	40.50854	23.73113	2015_PG50	70	10
Stratoni HW	40.50129	23.74410	2015_PG183	84	54
Stratoni HW	40.51584	23.72242	2015_PG41	90	8
Stratoni HW	40.50902	23.71091	2015_PG79	90	63
Stratoni HW	40.51284	23.74288	2015_PG92	90	25
Stratoni HW	40.51112	23.73383	2015_PG48	95	27

Table A5. S1 foliation measurements

Domain	Latitude	Longitude	Station No.	Strike	Dip
S1 Foliation					
Stratoni FW	40.55401	23.80116	2015_1596	300	16
Stratoni FW	40.55672	23.80101	2015_1604	324	46
Stratoni FW	40.55706	23.80098	2015_1605	314	45
Stratoni FW	40.55957	23.79828	2015_1609	322	14
Stratoni FW	40.55979	23.79706	2015_1610	320	31
Stratoni FW	40.53754	23.84248	2015_1736	293	72
Stratoni FW	40.53669	23.84728	2015_1738	314	50
Stratoni FW	40.53674	23.84801	2015_1739	288	62
Stratoni FW	40.53763	23.85009	2015_1740	286	79
Stratoni FW	40.53899	23.85602	2015_1741	249	90
Stratoni FW	40.53952	23.85714	2015_1742	278	84
Stratoni FW	40.53989	23.85784	2015_1743	277	56
Stratoni FW	40.54014	23.85897	2015_1744	267	69
Stratoni FW	40.54165	23.86087	2015_1745	274	64
Stratoni FW	40.54300	23.86044	2015_1746	271	55
Stratoni FW	40.54212	23.86229	2015_1747	267	64
Stratoni FW	40.54671	23.85833	2015_1749	262	45
Stratoni FW	40.54747	23.85735	2015_1750	267	44
Stratoni FW	40.54823	23.85658	2015_1751	254	66
Stratoni FW	40.55006	23.85428	2015_1752	275	80
Stratoni FW	40.55097	23.85283	2015_1754	265	56
Stratoni FW	40.55154	23.85250	2015_1756	269	52
Stratoni FW	40.54942	23.84838	2015_1757	273	50
Stratoni FW	40.54930	23.84744	2015_1758	263	56
Stratoni FW	40.55006	23.84653	2015_1759	276	56
Stratoni FW	40.55322	23.84343	2015_1760	284	66
Stratoni FW	40.55424	23.84302	2015_1761	269	36

Domain	Latitude	Longitude	Station No.	Strike	Dip
S1 Foliation					
Stratoni HW	40.50730	23.73008	2015_PG51	95	42
Stratoni HW	40.49839	23.69872	2015_PG126	96	26
Stratoni HW	40.50887	23.72118	2015_PG31	110	5
Stratoni HW	40.51302	23.73594	2015_PG47	110	42
Stratoni HW	40.49390	23.71066	2015_PG132	110	79
Stratoni HW	40.49753	23.71709	2015_PG153	112	21
Stratoni HW	40.51975	23.70984	2015_PG64	115	66
Stratoni HW	40.49875	23.73973	2015_PG212	115	84
Stratoni HW	40.52009	23.72359	2015_PG5	118	50
Stratoni HW	40.50144	23.72432	2015_PG56	120	28
Stratoni HW	40.50622	23.69691	2015_PG101	121	41
Stratoni HW	40.50783	23.69383	2015_PG106	121	54
Stratoni HW	40.52555	23.72284	2015_PG12	125	44
Stratoni HW	40.49556	23.71719	2015_PG142	129	18
Stratoni HW	40.50359	23.71640	2015_PG149	131	35
Stratoni HW	40.49312	23.71260	2015_PG134	134	63
Stratoni HW	40.50068	23.69837	2015_PG137	134	66
Stratoni HW	40.50012	23.73998	2015_PG189	134	47
Stratoni HW	40.49978	23.73995	2015_PG190	134	43
Stratoni HW	40.52427	23.71458	2015_PG62	135	80
Stratoni HW	40.49698	23.70313	2015_PG167	136	58
Stratoni HW	40.51087	23.71224	2015_PG78	140	47
Stratoni HW	40.51727	23.72780	2015_PG112	143	26
Stratoni HW	40.51202	23.69289	2015_PG107	144	79
Stratoni HW	40.52079	23.70410	2015_PG63	150	39
Stratoni HW	40.50955	23.70798	2015_PG81	150	80
Stratoni HW	40.51448	23.75259	2015_PG86	155	20

Table A5. S1 foliation measurements

Domain	Latitude	Longitude	Station No.	Strike	Dip
S1 Foliation					
Stratoni FW	40.55441	23.84367	2015_1762	285	37
Stratoni FW	40.53857	23.81198	2015_1858	114	88
Stratoni FW	40.53927	23.81165	2015_1859	255	74
Stratoni FW	40.53939	23.81186	2015_1860	311	47
Stratoni FW	40.54044	23.81183	2015_1861	288	89
Stratoni FW	40.54097	23.81326	2015_1862	271	65
Stratoni FW	40.54154	23.81394	2015_1863	275	74
Stratoni FW	40.53551	23.71018	2014_40	103	34
Stratoni FW	40.53584	23.70930	2014_53	89	32
Stratoni FW	40.53594	23.70880	2014_54	87	66
Stratoni FW	40.53573	23.70915	2014_57	70	20
Stratoni FW	40.54894	23.68158	2014_58	170	40
Stratoni FW	40.54899	23.68108	2014_60	194	46
Stratoni FW	40.55053	23.68039	2014_61	169	34
Stratoni FW	40.55071	23.68022	2014_62	173	26
Stratoni FW	40.54623	23.68535	2014_64	72	24
Stratoni FW	40.51717	23.81788	2014_132	350	70
Stratoni FW	40.51904	23.81174	2014_147	105	20
Stratoni FW	40.51906	23.81148	2014_148	90	35
Stratoni FW	40.51953	23.81117	2014_149	105	50
Stratoni FW	40.51851	23.81188	2014_150	285	6
Stratoni FW	40.51943	23.80606	2014_168	115	15
Stratoni FW	40.51960	23.80581	2014_175	101	25
Stratoni FW	40.52118	23.81099	2014_179	105	40
Stratoni FW	40.52045	23.81191	2014_180	130	21
Stratoni FW	40.52033	23.81191	2014_183	105	40
Stratoni FW	40.52031	23.81215	2014_186	110	20

Domain	Latitude	Longitude	Station No.	Strike	Dip
S1 Foliation					
Stratoni HW	40.50006	23.70072	2015_PG168	155	68
Stratoni HW	40.50750	23.71857	2015_PG33	160	5
Stratoni HW	40.51825	23.72293	2015_PG35	165	75
Stratoni HW	40.50497	23.70621	2015_PG117	171	49
Stratoni HW	40.48747	23.75733	2015_PG191	174	44
Stratoni HW	40.50619	23.72947	2015_PG52	175	18
Stratoni HW	40.52541	23.72285	2015_PG111	176	4
Stratoni HW	40.51341	23.72260	2015_PG155	176	24
Stratoni HW	40.51645	23.71011	2015_PG77	180	35
Stratoni HW	40.52486	23.71578	2015_PG114	183	18
Stratoni HW	40.52496	23.72310	2015_PG11	185	70
Stratoni HW	40.49998	23.74572	2015_PG179	197	36
Stratoni HW	40.49937	23.74596	2015_PG175	200	22
Stratoni HW	40.50197	23.70334	2015_PG164	206	37
Stratoni HW	40.50666	23.73771	2015_PG98	210	26
Stratoni HW	40.50093	23.74538	2015_PG181	215	38
Stratoni HW	40.50053	23.74424	2015_PG184	215	14
Stratoni HW	40.50312	23.74761	2015_PG201	215	13
Stratoni HW	40.49723	23.71682	2015_PG154	221	82
Stratoni HW	40.49352	23.74613	2015_PG178	225	36
Stratoni HW	40.50687	23.70762	2015_PG82	230	28
Stratoni HW	40.52190	23.72346	2015_PG3	234	44
Stratoni HW	40.50928	23.74048	2015_PG97	235	41
Stratoni HW	40.49780	23.75077	2015_PG203	238	43
Stratoni HW	40.51512	23.72086	2015_PG20	240	22
Stratoni HW	40.51306	23.72265	2015_PG44	240	18
Stratoni HW	40.49724	23.74917	2015_PG199	240	58

Table A5. S1 foliation measurements

Domain	Latitude	Longitude	Station No.	Strike	Dip
S1 Foliation					
Stratoni FW	40.52029	23.81223	2014_187	101	14
Stratoni FW	40.52025	23.81234	2014_189	108	25
Stratoni FW	40.52023	23.81238	2014_190	110	31
Stratoni FW	40.52016	23.81247	2014_193	93	24
Stratoni FW	40.52014	23.81255	2014_194	100	40
Stratoni FW	40.52012	23.81252	2014_196	102	20
Stratoni FW	40.53038	23.77872	2014_203	90	44
Stratoni FW	40.53053	23.77851	2014_204	130	40
Stratoni FW	40.53061	23.77809	2014_205	127	35
Stratoni FW	40.53065	23.77782	2014_206	120	42
Stratoni FW	40.52544	23.78439	2014_224	317	24
Stratoni FW	40.52553	23.78463	2014_225	315	30
Stratoni FW	40.52567	23.78548	2014_229	310	30
Stratoni FW	40.52585	23.78658	2014_231	275	46
Stratoni FW	40.52605	23.78672	2014_232	305	30
Stratoni FW	40.52675	23.78642	2014_234	35	30
Stratoni FW	40.52689	23.78597	2014_237	105	25
Stratoni FW	40.52783	23.78422	2014_240	264	27
Stratoni FW	40.52776	23.78405	2014_241	255	40
Stratoni FW	40.52877	23.78250	2014_242	125	36
Stratoni FW	40.52711	23.78529	2014_244	235	41
Stratoni FW	40.52580	23.78740	2014_245	94	48
Stratoni FW	40.52966	23.77996	2014_275	101	20
Stratoni FW	40.52762	23.78043	2014_279	290	20
Stratoni FW	40.52772	23.78001	2014_280	135	30
Stratoni FW	40.52756	23.77951	2014_281	110	55
Stratoni FW	40.52910	23.78158	2014_283	346	40

Domain	Latitude	Longitude	Station No.	Strike	Dip
S1 Foliation					
Stratoni HW	40.51458	23.73610	2015_PG46	245	15
Stratoni HW	40.49710	23.74624	2015_PG197	249	74
Stratoni HW	40.51393	23.72103	2015_PG22	250	12
Stratoni HW	40.50126	23.74305	2015_PG173	250	35
Stratoni HW	40.50166	23.74438	2015_PG182	259	49
Stratoni HW	40.48651	23.75690	2015_PG192	259	36
Stratoni HW	40.51690	23.70971	2015_PG76	260	28
Stratoni HW	40.51168	23.74632	2015_PG93	260	42
Stratoni HW	40.51300	23.72218	2015_PG161	262	51
Stratoni HW	40.50116	23.74922	2015_PG200	264	39
Stratoni HW	40.48945	23.72368	2015_PG223	269	48
Stratoni HW	40.52643	23.72212	2015_PG13	270	40
Stratoni HW	40.51452	23.71945	2015_PG23	270	45
Stratoni HW	40.50465	23.72856	2015_PG53	270	25
Stratoni HW	40.50001	23.74577	2015_PG174	271	49
Stratoni HW	40.48609	23.75771	2015_PG193	272	39
Stratoni HW	40.52298	23.73223	2015_PG16	275	40
Stratoni HW	40.52352	23.72956	2015_PG17	275	45
Stratoni HW	40.51824	23.74900	2015_PG74	275	65
Stratoni HW	40.51590	23.75073	2015_PG85	275	75
Stratoni HW	40.49813	23.74594	2015_PG176	276	24
Stratoni HW	40.49398	23.73170	2015_PG214	279	47
Stratoni HW	40.49273	23.72325	2015_PG219	279	68
Stratoni HW	40.52530	23.73967	2015_PG69	280	30
Stratoni HW	40.49795	23.74620	2015_PG177	280	65
Stratoni HW	40.48988	23.72370	2015_PG222	280	57
Stratoni HW	40.49136	23.73821	2015_PG211	284	37

Table A5. S1 foliation measurements

Domain	Latitude	Longitude	Station No.	Strike	Dip
S1 Foliation					
Stratoni FW	40.52999	23.78006	2014_284	120	35
Stratoni FW	40.53099	23.77928	2014_285	110	55
Stratoni FW	40.53129	23.77923	2014_289	150	50
Stratoni FW	40.52347	23.78896	2014_294	260	30
Stratoni FW	40.52150	23.79492	2014_301	30	30
Stratoni FW	40.52198	23.79227	2014_302	145	55
Stratoni FW	40.52255	23.79091	2014_305	120	45
Stratoni FW	40.52449	23.79173	2014_307	110	15
Stratoni FW	40.52411	23.79070	2014_308	137	16
Stratoni FW	40.53150	23.77180	2014_311	315	36
Stratoni FW	40.52638	23.78834	2014_327	95	25
Stratoni FW	40.52563	23.78973	2014_330	120	28
Stratoni FW	40.52476	23.78664	2014_334	320	20
Stratoni FW	40.52486	23.78625	2014_335	300	40
Stratoni FW	40.52428	23.78869	2014_336	216	36
Stratoni FW	40.52492	23.78808	2014_337	240	39
Stratoni FW	40.52057	23.80422	2014_339	216	10
Stratoni FW	40.52010	23.79971	2014_342	100	19
Stratoni FW	40.53301	23.73365	2014_404	101	45
Stratoni FW	40.53288	23.73438	2014_405	105	55
Stratoni FW	40.53217	23.73201	2014_406	84	59
Stratoni FW	40.53272	23.72060	2014_412	95	50
Stratoni FW	40.53283	23.72079	2014_414	105	44
Stratoni FW	40.53199	23.72853	2014_415	65	65
Stratoni FW	40.54407	23.83290	2014_418	260	35
Stratoni FW	40.54268	23.83313	2014_419	280	45
Stratoni FW	40.54138	23.83171	2014_420	252	35

Domain	Latitude	Longitude	Station No.	Strike	Dip
S1 Foliation					
Stratoni HW	40.49117	23.72357	2015_PG220	284	33
Stratoni HW	40.50076	23.74567	2015_PG180	286	53
Stratoni HW	40.51683	23.69364	2015_PG108	289	40
Stratoni HW	40.51856	23.72983	2015_PG113	289	39
Stratoni HW	40.50320	23.72771	2015_PG55	290	88
Stratoni HW	40.50072	23.72405	2015_PG57	290	55
Stratoni HW	40.49046	23.72457	2015_PG221	292	57
Stratoni HW	40.50835	23.72099	2015_PG140	293	60
Stratoni HW	40.49805	23.74621	2015_PG198	293	46
Stratoni HW	40.50420	23.70671	2015_PG116	294	20
Stratoni HW	40.49875	23.69823	2015_PG127	294	9
Stratoni HW	40.51107	23.72206	2015_PG158	294	43
Stratoni HW	40.49724	23.73202	2015_PG215	294	74
Stratoni HW	40.49369	23.72359	2015_PG218	294	44
Stratoni HW	40.51708	23.72181	2015_PG39	295	65
Stratoni HW	40.49351	23.70858	2015_PG128	295	82
Stratoni HW	40.49061	23.73112	2015_PG216	296	37
Stratoni HW	40.50917	23.72218	2015_PG159	298	18
Stratoni HW	40.49615	23.71020	2015_PG130	299	48
Stratoni HW	40.47944	23.74518	2015_PG206	299	46
Stratoni HW	40.49430	23.72429	2015_PG217	299	57
Stratoni HW	40.51273	23.71917	2015_PG24	300	10
Stratoni HW	40.50776	23.71849	2015_PG147	300	39
Stratoni HW	40.51116	23.69334	2015_PG103	301	61
Stratoni HW	40.49085	23.73907	2015_PG210	301	38
Stratoni HW	40.48825	23.74043	2015_PG209	303	33
Stratoni HW	40.52632	23.73758	2015_PG66	305	32

Table A5. S1 foliation measurements

Domain	Latitude	Longitude	Station No.	Strike	Dip
S1 Foliation					
Stratoni FW	40.53860	23.83370	2014_421	250	44
Stratoni FW	40.53427	23.71322	2014_441	75	40
Stratoni FW	40.53607	23.71345	2014_452	115	35
Stratoni FW	40.53716	23.71299	2014_453	135	35
Stratoni FW	40.53914	23.71089	2014_454	110	45
Stratoni FW	40.54133	23.70993	2014_457	35	26
Stratoni FW	40.53434	23.71535	2014_458	140	55
Stratoni FW	40.53458	23.71525	2014_459	122	45
Stratoni FW	40.56257	23.66299	2014_497	172	30
Stratoni FW	40.55940	23.66842	2014_518	220	20
Stratoni FW	40.55815	23.66889	2014_519	232	24
Stratoni FW	40.55354	23.67391	2014_1095	77	20
Stratoni FW	40.55347	23.67634	2014_1103	1	50
Stratoni FW	40.55481	23.67457	2014_1104	305	15
Stratoni FW	40.53627	23.74131	2014_1126	109	65
Stratoni FW	40.53583	23.74253	2014_1131	94	20
Stratoni FW	40.53834	23.74436	2014_1139	63	30
Stratoni FW	40.53877	23.74426	2014_1141	105	50
Stratoni FW	40.53773	23.74397	2014_1145	110	50
Stratoni FW	40.53617	23.74589	2014_1150	130	10
Stratoni FW	40.53499	23.74886	2014_1151	102	44
Stratoni FW	40.55792	23.83829	2013_133	110	24
Stratoni FW	40.55756	23.83982	2013_146	99	7
Stratoni FW	40.55790	23.84010	2013_147	150	25
Stratoni FW	40.55804	23.84037	2013_151	100	25
Stratoni FW	40.55873	23.84432	2013_156	105	33
Stratoni FW	40.55882	23.84497	2013_161	96	26

Domain	Latitude	Longitude	Station No.	Strike	Dip
S1 Foliation					
Stratoni HW	40.49486	23.71673	2015_PG143	305	36
Stratoni HW	40.51200	23.72222	2015_PG157	305	14
Stratoni HW	40.49932	23.71734	2015_PG152	306	50
Stratoni HW	40.50161	23.73945	2015_PG186	306	74
Stratoni HW	40.49374	23.71478	2015_PG139	309	59
Stratoni HW	40.49374	23.71478	2015_PG146	309	59
Stratoni HW	40.48270	23.74051	2015_PG204	309	51
Stratoni HW	40.52779	23.73121	2015_PG18	310	18
Stratoni HW	40.50833	23.70950	2015_PG80	310	60
Stratoni HW	40.50787	23.74707	2015_PG94	310	25
Stratoni HW	40.50341	23.70428	2015_PG163	310	87
Stratoni HW	40.50028	23.70292	2015_PG166	310	50
Stratoni HW	40.49707	23.70026	2015_PG125	311	37
Stratoni HW	40.50393	23.71752	2015_PG148	311	59
Stratoni HW	40.47942	23.74616	2015_PG205	313	37
Stratoni HW	40.50112	23.74266	2015_PG171	314	71
Stratoni HW	40.49912	23.73805	2015_PG213	314	68
Stratoni HW	40.50090	23.70761	2015_PG119	315	75
Stratoni HW	40.49861	23.70668	2015_PG120	316	82
Stratoni HW	40.51113	23.69452	2015_PG102	319	59
Stratoni HW	40.50941	23.69342	2015_PG104	319	54
Stratoni HW	40.50310	23.69614	2015_PG138	319	43
Stratoni HW	40.50313	23.71582	2015_PG150	319	74
Stratoni HW	40.50045	23.73695	2015_PG170	319	79
Stratoni HW	40.51046	23.70132	2015_PG99	320	79
Stratoni HW	40.50870	23.70585	2015_PG100	320	68
Stratoni HW	40.48006	23.74433	2015_PG207	322	21

Table A5. S1 foliation measurements

Domain	Latitude	Longitude	Station No.	Strike	Dip
S1 Foliation					
Stratoni FW	40.56026	23.85230	2013_162	115	31
Stratoni FW	40.56000	23.85304	2013_165	100	39
Stratoni FW	40.56001	23.85460	2013_173	103	11
Stratoni FW	40.55966	23.85559	2013_177	115	12
Stratoni FW	40.55908	23.85767	2013_187	340	24
Stratoni FW	40.55894	23.85829	2013_189	94	34
Stratoni FW	40.55791	23.85865	2013_190	292	40
Stratoni FW	40.57081	23.82270	2013_194	290	20
Stratoni FW	40.57043	23.82309	2013_195	285	24
Stratoni FW	40.57021	23.82324	2013_197	284	33
Stratoni FW	40.56872	23.82383	2013_204	297	21
Stratoni FW	40.56778	23.82457	2013_209	282	25
Stratoni FW	40.56770	23.82504	2013_211	301	22
Stratoni FW	40.55538	23.77266	2013_917	140	72
Stratoni FW	40.55563	23.77250	2013_918	129	72

Domain	Latitude	Longitude	Station No.	Strike	Dip
S1 Foliation					
Stratoni HW	40.51769	23.69455	2015_PG109	324	49
Stratoni HW	40.49915	23.71812	2015_PG151	324	67
Stratoni HW	40.49353	23.70629	2015_PG123	325	46
Stratoni HW	40.49243	23.71111	2015_PG133	325	54
Stratoni HW	40.50200	23.73855	2015_PG187	326	53
Stratoni HW	40.51370	23.75284	2015_PG87	330	68
Stratoni HW	40.49586	23.70537	2015_PG124	330	56
Stratoni HW	40.49536	23.71075	2015_PG131	330	64
Stratoni HW	40.49880	23.69990	2015_PG136	330	38
Stratoni HW	40.50513	23.70543	2015_PG118	336	41
Stratoni HW	40.52348	23.73644	2015_PG68	340	12
Stratoni HW	40.50830	23.69366	2015_PG105	340	54
Stratoni HW	40.50028	23.70413	2015_PG165	343	51
Stratoni HW	40.52398	23.72359	2015_PG10	350	87
Stratoni HW	40.50983	23.74629	2015_PG95	350	32

Abbreviations: HW = hanging wall of Stratoni fault zone; FW = footwall of Stratoni fault zone

Table A6. S2 foliation measurements

Domain	Latitude	Longitude	Station No.	Strike	Dip
S2 Foliation					
Olympias	40.59479	23.74299	2014_1009	110	30
Olympias	40.59492	23.74304	2014_1010	103	35
Olympias	40.59686	23.74860	2014_1029	35	30
Olympias	40.59683	23.74864	2014_1033	30	30
Olympias	40.59687	23.74869	2014_1037	30	28
Olympias	40.59714	23.74885	2014_1043	25	31
Olympias	40.59724	23.73175	2013_293	115	35
Olympias	40.59570	23.73052	2013_295	67	30
Olympias	40.59532	23.73092	2013_296	266	46
Olympias	40.59522	23.73086	2013_297	114	17
Olympias	40.59550	23.73115	2013_298	100	23
Olympias	40.59545	23.73143	2013_299	82	11
Olympias	40.59514	23.73228	2013_300	117	35
Olympias	40.59440	23.73362	2013_302	116	60
Olympias	40.59408	23.73353	2013_304	140	80
Olympias	40.59340	23.73279	2013_311	64	16
Olympias	40.59197	23.73441	2013_315	110	24
Olympias	40.59109	23.73449	2013_317	70	30
Olympias	40.59085	23.73450	2013_319	127	50
Olympias	40.59075	23.73459	2013_320	130	34
Olympias	40.59077	23.73561	2013_324	110	84
Olympias	40.59085	23.73577	2013_326	99	34
Olympias	40.59096	23.73600	2013_327	75	16
Olympias	40.59117	23.73656	2013_329	81	38
Olympias	40.59146	23.73810	2013_335	77	22
Olympias	40.59140	23.73861	2013_337	96	21
Olympias	40.59156	23.74138	2013_344	95	30

Domain	Latitude	Longitude	Station No.	Strike	Dip
S2 Foliation					
Olympias	40.58957	23.74209	2013_588	75	28
Olympias	40.58956	23.74114	2013_590	75	44
Olympias	40.59001	23.73930	2013_598	76	24
Olympias	40.59013	23.73692	2013_611	100	29
Olympias	40.59027	23.73774	2013_612	73	24
Olympias	40.56555	23.76575	2013_870	80	34
Olympias	40.56533	23.76579	2013_871	47	45
Olympias	40.56515	23.76598	2013_881	75	41
Olympias	40.59713	23.74880	2013_1817	5	30
Skouries	40.48624	23.72388	2014_654	285	15
Skouries	40.48159	23.72260	2014_671	145	15
Skouries	40.48290	23.72404	2014_684	130	30
Skouries	40.47805	23.71291	2014_690	100	25
Skouries	40.47519	23.72624	2014_726	105	15
Skouries	40.47561	23.72150	2014_740	95	20
Skouries	40.47354	23.71113	2014_796	140	20
Skouries	40.47538	23.71285	2014_802	130	15
Skouries	40.47543	23.71291	2014_803	100	35
Skouries	40.48090	23.71137	2014_854	95	48
Skouries	40.47970	23.70957	2014_864	135	15
Skouries	40.47977	23.70595	2014_896	125	20
Skouries	40.48027	23.69656	2014_946	300	20
Skouries	40.47993	23.69629	2014_951	100	25
Skouries	40.47975	23.69620	2014_952	105	20
Skouries	40.47991	23.69636	2014_972	122	25
Skouries	40.48002	23.69649	2014_975	95	25
Skouries	40.48008	23.69645	2014_976	95	21

Table A6. S2 foliation measurements

Domain	Latitude	Longitude	Station No.	Strike	Dip
S2 Foliation					
Olympias	40.59182	23.74131	2013_347	95	5
Olympias	40.59319	23.74041	2013_356	63	25
Olympias	40.59411	23.74038	2013_361	114	21
Olympias	40.59455	23.74044	2013_362	80	24
Olympias	40.59395	23.74105	2013_367	60	30
Olympias	40.59345	23.74090	2013_368	130	14
Olympias	40.59500	23.74315	2013_377	41	50
Olympias	40.59556	23.74338	2013_382	335	33
Olympias	40.59659	23.74808	2013_403	25	34
Olympias	40.59687	23.74869	2013_409	47	28
Olympias	40.59226	23.74917	2013_459	86	64
Olympias	40.59627	23.72930	2013_462	107	5
Olympias	40.59624	23.73094	2013_463	104	34
Stratoni HW	40.46295	23.77925	2015_1780	55	40
Stratoni HW	40.46301	23.77927	2015_1783	81	58
Stratoni HW	40.46263	23.77925	2015_1784	75	56
Stratoni HW	40.53036	23.76739	2014_108	105	65
Stratoni HW	40.53034	23.76739	2014_109	110	70
Stratoni HW	40.51521	23.80713	2014_159	335	50
Stratoni HW	40.52554	23.78343	2014_214	61	30
Stratoni HW	40.52555	23.78341	2014_215	60	43
Stratoni HW	40.57405	23.65477	2014_543	185	35
Stratoni HW	40.56875	23.65028	2014_590	260	25
Stratoni HW	40.52145	23.77249	2014_1055	335	60
Stratoni HW	40.52064	23.77460	2014_1059	55	40
Stratoni HW	40.52897	23.74175	2014_1146	105	30

Abbreviations: HW = hanging wall of Stratoni fault zone; FW = footwall of Stratoni fault zone

Table A7. S3 foliation measurements

Domain	Latitude	Longitude	Station No.	Strike	Dip
S3 Foliation					
Olympias	40.59470	23.75285	2014_508	116	67
Olympias	40.59454	23.75270	2014_509	305	75
Olympias	40.58631	23.75242	2014_982	140	70
Olympias	40.57832	23.74766	2014_990	290	80
Olympias	40.57643	23.74442	2014_992	310	70
Olympias	40.57144	23.74210	2014_995	270	70
Olympias	40.57445	23.75847	2014_998	310	70
Olympias	40.59580	23.74364	2014_1012	132	65
Olympias	40.59596	23.74364	2014_1014	110	55
Olympias	40.59753	23.74762	2014_1019	115	85
Olympias	40.59683	23.74864	2014_1031	120	69
Olympias	40.59683	23.74852	2014_1032	122	75
Olympias	40.59688	23.74870	2014_1035	120	84
Olympias	40.59685	23.74872	2014_1038	135	65
Olympias	40.59689	23.74873	2014_1039	138	60
Olympias	40.59690	23.74873	2014_1040	125	69
Olympias	40.59707	23.74884	2014_1042	140	65
Olympias	40.59719	23.74884	2014_1048	138	70
Olympias	40.59748	23.74765	2013_394	150	78
Olympias	40.59683	23.74870	2013_407	310	86
Olympias	40.59729	23.74888	2013_412	217	75
Olympias	40.59754	23.74764	2013_430	140	78
Olympias	40.59391	23.74858	2013_453	290	79
Olympias	40.59305	23.74776	2013_455	293	45
Olympias	40.60024	23.72710	2013_475	165	74
Olympias	40.59993	23.72805	2013_477	203	81
Olympias	40.60112	23.72333	2013_503	160	35
Skouries	40.47755	23.65783	2015_1875	130	64
Skouries	40.47867	23.65961	2015_1878	126	72
Skouries	40.47968	23.70640	2014_894	110	84
Skouries	40.47983	23.70603	2014_895	122	80
Skouries	40.47991	23.70547	2014_899	121	80
Skouries	40.48051	23.69763	2014_939	125	70
Skouries	40.48051	23.69741	2014_942	138	85
Skouries	40.48044	23.69714	2014_945	130	85
Skouries	40.48002	23.69627	2014_950	125	80
Skouries	40.47939	23.69694	2014_956	145	81
Skouries	40.47989	23.69642	2014_971	300	75
Skouries	40.48000	23.69647	2014_974	295	70
Skouries	40.48007	23.69649	2014_977	305	60
Stratoni FW	40.55352	23.80125	2015_1592	120	70
Stratoni FW	40.55349	23.80117	2015_1593	125	79
Stratoni FW	40.55335	23.80119	2015_1594	123	81
Stratoni FW	40.55350	23.80128	2015_1595	119	80
Stratoni FW	40.55493	23.80089	2015_1598	322	81
Stratoni FW	40.55493	23.80082	2015_1599	130	90
Stratoni FW	40.55949	23.79841	2015_1606	155	86
Stratoni FW	40.55951	23.79849	2015_1607	151	79
Stratoni FW	40.55942	23.79849	2015_1608	154	88
Stratoni FW	40.55981	23.79689	2015_1611	120	88
Stratoni FW	40.56269	23.66320	2014_498	135	52
Stratoni FW	40.56253	23.66332	2014_499	120	70
Stratoni FW	40.55959	23.66847	2014_537	325	77
Stratoni FW	40.55382	23.67365	2014_1096	100	61

Table A7. S3 foliation measurements

Domain	Latitude	Longitude	Station No.	Strike	Dip
S3 Foliation					
Olympias	40.59932	23.72231	2013_512	345	25
Olympias	40.58982	23.75210	2013_558	120	32
Olympias	40.58920	23.74974	2013_562	138	52
Olympias	40.57527	23.75894	2013_634	304	78
Olympias	40.57440	23.75853	2013_635	287	44
Olympias	40.57344	23.75889	2013_638	124	50
Olympias	40.57279	23.75864	2013_642	295	67
Olympias	40.57255	23.75831	2013_645	116	67
Olympias	40.57169	23.75736	2013_654	117	50
Olympias	40.57579	23.75973	2013_713	82	21
Olympias	40.57456	23.76285	2013_718	124	70
Olympias	40.57433	23.76328	2013_720	275	30
Olympias	40.57408	23.76295	2013_721	312	23
Olympias	40.57064	23.74213	2013_749	315	40
Olympias	40.57125	23.74180	2013_753	305	35
Olympias	40.57245	23.76267	2013_861	86	13
Olympias	40.56162	23.74963	2013_973	346	56
Olympias	40.56149	23.75048	2013_975	170	86
Olympias	40.56160	23.75106	2013_977	155	85
Olympias	40.56180	23.75162	2013_978	333	75
Olympias	40.56190	23.75159	2013_979	346	80
Olympias	40.56306	23.75326	2013_982	156	84
Olympias	40.56307	23.75344	2013_983	150	85
Olympias	40.56271	23.75405	2013_984	156	85
Olympias	40.56170	23.75471	2013_987	155	80
Olympias	40.56218	23.75500	2013_988	335	75
Olympias	40.56230	23.75533	2013_989	154	70

Domain	Latitude	Longitude	Station No.	Strike	Dip
S3 Foliation					
Stratoni FW	40.55071	23.68027	2014_1098	150	40
Stratoni FW	40.55240	23.67777	2014_1099	130	88
Stratoni FW	40.55241	23.67777	2014_1100	131	85
Stratoni FW	40.55240	23.67779	2014_1101	125	85
Stratoni FW	40.55482	23.67466	2014_1105	105	65
Stratoni FW	40.53583	23.74257	2014_1130	133	74
Stratoni FW	40.53627	23.74189	2014_1136	122	50
Stratoni FW	40.55731	23.77046	2013_1015	155	55
Stratoni FW	40.55816	23.77031	2013_1017	160	45
Stratoni FW	40.53919	23.76902	2013_1125	2	62
Stratoni FW	40.53698	23.78938	2013_1148	332	65
Stratoni FW	40.53703	23.78525	2013_1176	130	79
Stratoni FW	40.53738	23.78471	2013_1177	325	80
Stratoni FW	40.53601	23.78247	2013_1191	133	80
Stratoni FW	40.52969	23.78956	2013_1234	319	80
Stratoni FW	40.53007	23.78932	2013_1235	330	61
Stratoni FW	40.53093	23.78824	2013_1243	299	56
Stratoni FW	40.53111	23.78791	2013_1244	333	30
Stratoni FW	40.53328	23.78711	2013_1249	348	69
Stratoni FW	40.53252	23.78668	2013_1252	332	76
Stratoni FW	40.53321	23.78507	2013_1257	300	61
Stratoni FW	40.53371	23.78537	2013_1258	290	63
Stratoni FW	40.53411	23.78526	2013_1260	344	65
Stratoni FW	40.53417	23.78423	2013_1264	337	60
Stratoni FW	40.53514	23.78396	2013_1265	299	64
Stratoni FW	40.53535	23.78387	2013_1266	300	90
Stratoni FW	40.53623	23.78351	2013_1267	315	90

Table A7. S3 foliation measurements

Domain	Latitude	Longitude	Station No.	Strike	Dip
S3 Foliation					
Olympias	40.56105	23.75599	2013_990	184	77
Olympias	40.55946	23.75693	2013_996	344	86
Olympias	40.55725	23.75931	2013_1001	170	65
Olympias	40.55885	23.76893	2013_1022	150	74
Olympias	40.55920	23.76878	2013_1023	152	88
Olympias	40.55929	23.76862	2013_1024	149	76
Skouries	40.44197	23.70914	2015_1522	90	85
Skouries	40.45302	23.71714	2015_1536	105	70
Skouries	40.45726	23.66283	2015_1681	93	65
Skouries	40.47570	23.67720	2015_1719	101	80
Skouries	40.47568	23.67725	2015_1720	91	79
Skouries	40.48029	23.68159	2015_1722	99	53
Skouries	40.47988	23.68073	2015_1724	107	63
Skouries	40.47984	23.68040	2015_1725	94	63
Skouries	40.47578	23.65520	2015_1867	282	76
Skouries	40.47572	23.65507	2015_1868	110	62
Skouries	40.47603	23.65502	2015_1869	120	75
Skouries	40.47775	23.65777	2015_1873	121	74
Skouries	40.47765	23.65767	2015_1874	121	81
Stratoni FW	40.52943	23.79303	2013_1307	321	65
Stratoni FW	40.52128	23.81084	2013_1582	106	80
Stratoni HW	40.50988	23.72223	2015_1636	115	71
Stratoni HW	40.50837	23.72245	2015_1642	284	70
Stratoni HW	40.50834	23.72249	2015_1643	246	74
Stratoni HW	40.50675	23.72217	2015_1646	277	69
Stratoni HW	40.50641	23.72224	2015_1647	310	63
Stratoni HW	40.55735	23.66699	2014_522	295	50
Stratoni HW	40.55736	23.66693	2014_524	305	75
Stratoni HW	40.55737	23.66701	2014_525	290	54
Stratoni HW	40.55637	23.66658	2014_529	105	35
Stratoni HW	40.55564	23.66619	2014_531	135	72
Stratoni HW	40.57356	23.65170	2014_545	310	65
Stratoni HW	40.57335	23.65070	2014_546	110	75
Stratoni HW	40.57446	23.64898	2014_549	145	65
Stratoni HW	40.57535	23.64544	2014_553	140	60
Stratoni HW	40.57490	23.64350	2014_557	310	73
Stratoni HW	40.51898	23.78036	2014_1069	145	55

Abbreviations: HW = hanging wall of Stratoni fault zone; FW = footwall of Stratoni fault zone

Table A8. F2 axial plane measurements

Domain	Latitude	Longitude	Station No.	Strike	Dip
F2 Axial Plane					
Olympias	40.59719	23.74880	2014_1045	145	14
Olympias	40.59986	23.72751	2013_287	15	75
Olympias	40.59341	23.73295	2013_308	170	29
Olympias	40.60160	23.72695	2013_487	175	26
Olympias	40.60216	23.73493	2013_521	10	35
Olympias	40.60044	23.73093	2013_547	5	22
Olympias	40.59031	23.75291	2013_552	120	47
Olympias	40.59021	23.73777	2013_603	320	56
Olympias	40.57146	23.74214	2013_755	136	19
Olympias	40.57245	23.74221	2013_763	170	48
Olympias	40.60232	23.73376	2013_1809	325	15
Olympias	40.59474	23.74291	2013_1811	345	30
Olympias	40.59685	23.74864	2013_1812	359	15
Skouries	40.43876	23.69989	2015_1507	95	60
Skouries	40.48696	23.71993	2014_648	140	26
Skouries	40.48635	23.72411	2014_652	290	15
Skouries	40.48649	23.72487	2014_665	105	20
Skouries	40.47939	23.71409	2014_688	90	15
Skouries	40.47549	23.72611	2014_728	85	16
Skouries	40.47738	23.72350	2014_746	85	18
Skouries	40.47115	23.70913	2014_785	315	55
Skouries	40.47978	23.70657	2014_893	131	45
Skouries	40.48042	23.69727	2014_943	125	15
Skouries	40.48002	23.69627	2014_947	125	15
Skouries	40.47942	23.69652	2014_954	135	30
Skouries	40.47942	23.69652	2014_955	315	7
Skouries	40.47973	23.70658	2014_1114	130	45
Stratoni FW	40.55788	23.83827	2013_129	80	40
Stratoni FW	40.55795	23.83795	2013_131	298	90
Stratoni FW	40.55812	23.84044	2013_152	74	60
Stratoni FW	40.56029	23.85217	2013_163	105	66
Stratoni FW	40.56006	23.85315	2013_167	79	59
Stratoni FW	40.56003	23.85454	2013_172	93	64
Stratoni FW	40.55969	23.85533	2013_176	245	16
Stratoni FW	40.55951	23.85610	2013_179	84	64
Stratoni FW	40.55961	23.85630	2013_181	89	45
Stratoni FW	40.55953	23.85652	2013_182	125	41
Stratoni FW	40.55902	23.85771	2013_186	298	17
Stratoni FW	40.57022	23.82320	2013_199	100	9
Stratoni FW	40.56855	23.82386	2013_205	84	54
Stratoni FW	40.56847	23.82374	2013_206	115	15
Stratoni FW	40.54673	23.76651	2013_1111	138	25
Stratoni FW	40.54092	23.76891	2013_1130	130	32
Stratoni FW	40.53299	23.77725	2013_1281	100	20
Stratoni FW	40.52870	23.79178	2013_1299	125	20
Stratoni FW	40.52508	23.79592	2013_1335	305	25
Stratoni FW	40.53278	23.76760	2013_1401	95	45
Stratoni FW	40.53292	23.76564	2013_1411	270	26
Stratoni FW	40.52571	23.84143	2013_1445	86	64
Stratoni FW	40.52766	23.84807	2013_1465	90	15
Stratoni FW	40.52992	23.84806	2013_1470	90	10
Stratoni FW	40.51934	23.80955	2013_1549	115	19
Stratoni HW	40.49417	23.75854	2015_1424	310	51
Stratoni HW	40.48650	23.75693	2015_1431	269	65

Table A8. F2 axial plane measurements

Domain	Latitude	Longitude	Station No.	Strike	Dip
F2 Axial Plane					
Skouries	40.47998	23.69642	2014_973	125	30
Skouries	40.47969	23.70646	2014_1111	305	50
Skouries	40.48099	23.72230	2014_1118	135	33
Stratoni FW	40.53139	23.77961	2014_287	155	32
Stratoni FW	40.52379	23.79163	2014_306	140	20
Stratoni FW	40.55348	23.67377	2014_1097	70	15
Stratoni FW	40.55748	23.83965	2013_145	95	76

Domain	Latitude	Longitude	Station No.	Strike	Dip
F2 Axial Plane					
Stratoni HW	40.51089	23.72169	2015_1632	299	9
Stratoni HW	40.46262	23.77915	2015_1781	83	54
Stratoni HW	40.52946	23.76856	2014_98	260	31
Stratoni HW	40.53052	23.76747	2014_111	130	30
Stratoni HW	40.57488	23.64361	2014_555	70	10
Stratoni HW	40.56881	23.64983	2014_593	250	25
Stratoni HW	40.51738	23.81210	2013_1543	85	12

Abbreviations: HW = hanging wall of Stratoni fault zone; FW = footwall of Stratoni fault zone

Table A9. F2 hinge line measurements

Domain	Latitude	Longitude	Station No.	Trend	Plunge
F2 Hinge Line					
Olympias	40.59719	23.74880	2014_1046	145	20
Olympias	40.60228	23.73376	2013_237	145	20
Olympias	40.60429	23.72880	2013_272	170	19
Olympias	40.59985	23.72753	2013_286	192	44
Olympias	40.59342	23.73289	2013_307	175	14
Olympias	40.59342	23.73288	2013_310	146	14
Olympias	40.59309	23.74051	2013_355	165	7
Olympias	40.59337	23.74045	2013_357	180	19
Olympias	40.59457	23.74282	2013_373	130	26
Olympias	40.59469	23.74289	2013_376	165	25
Olympias	40.59682	23.74859	2013_405	156	20
Olympias	40.59683	23.74867	2013_406	171	15
Olympias	40.59707	23.74877	2013_411	145	22
Olympias	40.60162	23.72697	2013_486	175	16
Olympias	40.60044	23.73144	2013_518	175	12
Olympias	40.60212	23.73492	2013_520	160	16
Olympias	40.60269	23.73974	2013_541	160	21
Olympias	40.60045	23.73093	2013_546	185	30
Olympias	40.59032	23.75289	2013_551	155	19
Olympias	40.59022	23.73785	2013_602	145	19
Olympias	40.57255	23.75832	2013_646	174	8
Olympias	40.56504	23.75032	2013_675	155	24
Olympias	40.56531	23.75046	2013_676	159	10
Olympias	40.56695	23.75150	2013_687	326	8
Olympias	40.56744	23.75103	2013_691	329	19
Olympias	40.57143	23.74205	2013_754	161	21
Olympias	40.57248	23.74223	2013_762	170	2

Domain	Latitude	Longitude	Station No.	Trend	Plunge
F2 Fold Hinge Line					
Stratoni FW	40.52715	23.78562	2014_243	200	24
Stratoni FW	40.52774	23.78025	2014_282	98	38
Stratoni FW	40.53140	23.77960	2014_288	155	10
Stratoni FW	40.55788	23.83824	2013_130	240	18
Stratoni FW	40.55729	23.83893	2013_140	250	19
Stratoni FW	40.55744	23.83956	2013_144	90	21
Stratoni FW	40.55811	23.84045	2013_153	70	9
Stratoni FW	40.56006	23.85317	2013_166	270	16
Stratoni FW	40.55969	23.85534	2013_175	275	24
Stratoni FW	40.55959	23.85632	2013_180	259	9
Stratoni FW	40.55906	23.85763	2013_185	295	7
Stratoni FW	40.56864	23.82381	2013_212	90	6
Stratoni FW	40.54877	23.77521	2013_1055	147	10
Stratoni FW	40.54921	23.77588	2013_1057	115	8
Stratoni FW	40.54953	23.75647	2013_1085	125	4
Stratoni FW	40.54673	23.76649	2013_1110	135	5
Stratoni FW	40.54103	23.76903	2013_1129	130	5
Stratoni FW	40.53305	23.77714	2013_1280	94	9
Stratoni FW	40.52867	23.79185	2013_1298	110	12
Stratoni FW	40.52826	23.79357	2013_1310	121	5
Stratoni FW	40.52856	23.79684	2013_1322	100	12
Stratoni FW	40.52509	23.79591	2013_1334	108	12
Stratoni FW	40.53277	23.76755	2013_1400	105	14
Stratoni FW	40.53291	23.76558	2013_1410	85	12
Stratoni FW	40.52568	23.84142	2013_1444	86	30
Stratoni FW	40.52766	23.84808	2013_1464	90	22
Stratoni FW	40.53002	23.84824	2013_1469	90	18

Table A9. F2 hinge line measurements

Domain	Latitude	Longitude	Station No.	Trend	Plunge
F2 Hinge Line					
Skouries	40.43837	23.69984	2015_1510	101	20
Skouries	40.43839	23.69986	2015_1511	101	4
Skouries	40.48637	23.72410	2014_653	290	10
Skouries	40.48651	23.72488	2014_666	105	7
Skouries	40.47939	23.71409	2014_687	90	5
Skouries	40.47556	23.72613	2014_729	85	5
Skouries	40.48045	23.69734	2014_944	305	5
Skouries	40.47974	23.70646	2014_1112	305	20
Skouries	40.47971	23.70666	2014_1115	310	5
Skouries	40.48098	23.72232	2014_1119	135	5
Stratoni FW	40.53580	23.71018	2014_47	40	32
F2 Fold Hinge Line					
Stratoni FW	40.51938	23.80954	2013_1548	292	24
Stratoni HW	40.49416	23.75861	2015_1425	310	25
Stratoni HW	40.51089	23.72169	2015_1633	299	6
Stratoni HW	40.46262	23.77915	2015_1782	81	31
Stratoni HW	40.52946	23.76856	2014_97	80	20
Stratoni HW	40.53052	23.76747	2014_110	130	20
Stratoni HW	40.53075	23.76729	2014_118	60	27
Stratoni HW	40.57488	23.64361	2014_556	70	5
Stratoni HW	40.56881	23.64983	2014_594	250	5
Stratoni HW	40.51740	23.81208	2013_1542	268	25

Abbreviations: HW = hanging wall of Stratoni fault zone; FW = footwall of Stratoni fault zone

Table A10. L2 Intersection lineation (S1-S2) measurements

Domain	Latitude	Longitude	Station No.	Trend	Plunge
L2 Intersection Lineation					
Olympias	40.58499	23.75113	2014_983	160	35
Olympias	40.58493	23.75105	2014_984	150	35
Olympias	40.59501	23.74313	2014_1008	145	25
Olympias	40.59746	23.74770	2014_1018	149	22
Olympias	40.59662	23.74823	2014_1025	140	21
Olympias	40.59676	23.74862	2014_1028	130	20
Olympias	40.59687	23.74870	2014_1036	135	29
Olympias	40.59715	23.74884	2014_1044	135	28
Olympias	40.59719	23.74890	2014_1047	140	17
Olympias	40.59690	23.74869	2013_408	136	26
Olympias	40.58981	23.75211	2013_559	165	25
Olympias	40.56423	23.74980	2013_947	170	15
Olympias	40.55768	23.74721	2013_962	150	28
Olympias	40.56274	23.75392	2013_985	156	45
Skouries	40.44457	23.71215	2015_1526	234	16
Skouries	40.48245	23.71869	2014_623	118	5
Skouries	40.48158	23.72264	2014_672	330	5
Skouries	40.47810	23.71295	2014_691	110	5
Skouries	40.47750	23.71406	2014_695	95	10
Skouries	40.47527	23.72624	2014_727	100	4
Skouries	40.47491	23.72063	2014_739	100	11
Skouries	40.47100	23.70920	2014_784	100	10
Skouries	40.48333	23.71716	2014_822	110	25
Skouries	40.48092	23.71137	2014_853	112	9
Skouries	40.47968	23.71037	2014_858	110	14
Skouries	40.47959	23.70829	2014_880	105	10
Skouries	40.47961	23.70815	2014_882	290	15
Skouries	40.47978	23.70666	2014_891	120	6
Skouries	40.47749	23.69703	2014_920	124	5
Skouries	40.46827	23.72144	2014_936	280	5
Skouries	40.48058	23.69758	2014_938	115	9
Skouries	40.47790	23.69692	2014_958	134	5
Skouries	40.47756	23.69618	2014_970	140	12
Skouries	40.47968	23.70632	2014_1113	118	10
Skouries	40.47975	23.70894	2014_1117	115	25
Skouries	40.48097	23.72234	2014_1120	125	7
Stratoni FW	40.53627	23.74107	2014_1125	136	25
Stratoni FW	40.53627	23.74192	2014_1127	140	26
Stratoni FW	40.53876	23.74423	2014_1142	138	20
Stratoni FW	40.53715	23.78235	2013_1187	107	22
Stratoni FW	40.52513	23.84504	2013_1455	121	25
Stratoni FW	40.52152	23.81079	2013_1578	35	9

Abbreviations: HW = hanging wall of Stratoni fault zone; FW = footwall of Stratoni fault zone

Table A11. Quartz-magnetite and Cu-bearing veins in the Skouries stock

Domain	Latitude	Longitude	Station No.	Strike	Dip
Quartz-Magnetite Veins					
Skouries	40.47288	23.70289	2014_584	325	65
Skouries	40.47288	23.70289	2014_640	195	85
Skouries	40.47288	23.70289	2014_659	180	75
Skouries	40.47288	23.70289	2014_675	210	60
Skouries	40.47288	23.70289	2014_678	345	75
Skouries	40.47288	23.70289	2014_679	340	80
Skouries	40.47288	23.70289	2014_708	5	75
Skouries	40.47288	23.70289	2014_723	196	70
Skouries	40.47288	23.70289	2014_753	200	80
Skouries	40.47288	23.70289	2014_759	305	70
Skouries	40.47288	23.70289	2014_809	10	90
Skouries	40.47288	23.70289	2014_810	68	75
Skouries	40.47288	23.70289	2014_811	356	75
Skouries	40.47288	23.70289	2014_812	350	90
Skouries	40.47288	23.70289	2014_813	205	85
Skouries	40.47288	23.70289	2014_824	170	65
Skouries	40.47288	23.70289	2014_839	195	85
Skouries	40.47288	23.70289	2014_859	220	75
Skouries	40.47288	23.70289	2014_889	350	80
Skouries	40.47288	23.70289	2014_911	95	49
Skouries	40.47288	23.70289	2014_924	70	81
Skouries	40.47288	23.70289	2014_925	212	82
Skouries	40.47288	23.70289	2014_1200	15	82
Skouries	40.47288	23.70289	2014_1201	20	75
Skouries	40.47288	23.70289	2014_1202	19	75
Skouries	40.47288	23.70289	2014_1203	25	76
Skouries	40.47288	23.70289	2014_1204	2	80

Domain	Latitude	Longitude	Station No.	Strike	Dip
Quartz-Magnetite Veins					
Skouries	40.47298	23.70285	2014_DR26	320	12
Skouries	40.47298	23.70285	2014_DR27	264	68
Skouries	40.47298	23.70285	2014_DR28	56	85
Skouries	40.47298	23.70285	2014_DR29	64	82
Skouries	40.47298	23.70285	2014_DR30	218	34
Skouries	40.47298	23.70285	2014_DR31	340	84
Skouries	40.47298	23.70285	2014_DR32	138	66
Skouries	40.47298	23.70285	2014_DR33	164	75
Skouries	40.47298	23.70285	2014_DR34	12	32
Skouries	40.47298	23.70285	2014_DR35	164	82
Skouries	40.47298	23.70285	2014_DR36	204	86
Skouries	40.47298	23.70285	2014_DR37	56	84
Skouries	40.47298	23.70285	2014_DR38	66	68
Skouries	40.4733	23.70361	2014_DR39	116	83
Skouries	40.4733	23.70361	2014_DR40	106	38
Skouries	40.4733	23.70361	2014_DR41	192	81
Skouries	40.4733	23.70361	2014_DR42	171	84
Skouries	40.4733	23.70361	2014_DR43	74	72
Skouries	40.4733	23.70361	2014_DR44	197	86
Skouries	40.4733	23.70361	2014_DR45	224	85
Skouries	40.4733	23.70361	2014_DR46	182	85
Skouries	40.4733	23.70361	2014_DR47	46	81
Skouries	40.4733	23.70361	2014_DR48	147	76
Skouries	40.4733	23.70361	2014_DR49	147	86
Skouries	40.4733	23.70361	2014_DR50	320	10
Skouries	40.4733	23.70361	2014_DR51	6	84
Skouries	40.4733	23.70361	2014_DR52	97	82

Table A11. Quartz-magnetite and Cu-bearing veins in the Skouries stock

Domain	Latitude	Longitude	Station No.	Strike	Dip
Quartz-Magnetite Veins					
Skouries	40.47288	23.70289	2014_1205	24	74
Skouries	40.47288	23.70289	2014_1206	349	80
Skouries	40.47288	23.70289	2014_1207	10	82
Skouries	40.47288	23.70289	2014_1208	25	86
Skouries	40.47288	23.70289	2014_1209	27	82
Skouries	40.47288	23.70289	2014_1210	20	80
Skouries	40.47288	23.70289	2014_1211	25	81
Skouries	40.47288	23.70289	2014_1212	5	87
Skouries	40.47288	23.70289	2014_1213	35	88
Skouries	40.47288	23.70289	2014_1214	26	80
Skouries	40.47288	23.70289	2014_1215	20	77
Skouries	40.47288	23.70289	2014_1219	325	84
Skouries	40.47288	23.70289	2014_1220	351	76
Skouries	40.47288	23.70289	2014_1221	355	76
Skouries	40.47288	23.70289	2014_1222	16	81
Skouries	40.47288	23.70289	2014_1223	24	80
Skouries	40.47288	23.70289	2014_1224	10	84
Skouries	40.47288	23.70289	2014_1225	35	80
Skouries	40.47288	23.70289	2014_1227	91	80
Skouries	40.47288	23.70289	2014_1228	245	81
Skouries	40.47288	23.70289	2014_1229	110	75
Skouries	40.47288	23.70289	2014_1230	90	67
Skouries	40.47288	23.70289	2014_1231	221	79
Skouries	40.47288	23.70289	2014_1232	255	84
Skouries	40.47288	23.70289	2014_1233	39	76
Skouries	40.47288	23.70289	2014_1234	35	89
Skouries	40.47288	23.70289	2014_1235	65	75

Domain	Latitude	Longitude	Station No.	Strike	Dip
Quartz-Magnetite Veins					
Skouries	40.4733	23.70361	2014_DR53	283	85
Skouries	40.4733	23.70361	2014_DR54	283	87
Skouries	40.4733	23.70361	2014_DR55	282	85
Skouries	40.4733	23.70361	2014_DR56	96	86
Skouries	40.4733	23.70361	2014_DR57	175	86
Skouries	40.4733	23.70361	2014_DR58	7	76
Skouries	40.4733	23.70361	2014_DR59	42	88
Skouries	40.4733	23.70361	2014_DR60	204	83
Skouries	40.4733	23.70361	2014_DR61	205	86
Skouries	40.4733	23.70361	2014_DR62	42	87
Skouries	40.4733	23.70361	2014_DR63	76	51
Skouries	40.4733	23.70361	2014_DR64	71	87
Skouries	40.4733	23.70361	2014_DR65	56	72
Skouries	40.4733	23.70361	2014_DR66	57	84
Skouries	40.4733	23.70361	2014_DR67	174	86
Skouries	40.4733	23.70361	2014_DR68	195	83
Skouries	40.4733	23.70361	2014_DR69	215	81
Skouries	40.4733	23.70361	2014_DR70	224	86
Skouries	40.4733	23.70361	2014_DR71	216	87
Skouries	40.4733	23.70361	2014_DR72	214	56
Skouries	40.4733	23.70361	2014_DR73	234	76
Skouries	40.4733	23.70361	2014_DR74	243	33
Skouries	40.4733	23.70361	2014_DR75	213	74
Skouries	40.4733	23.70361	2014_DR76	28	84
Skouries	40.4733	23.70361	2014_DR77	219	80
Skouries	40.4733	23.70361	2014_DR78	221	81
Skouries	40.4733	23.70361	2014_DR79	208	80

Table A11. Quartz-magnetite and Cu-bearing veins in the Skouries stock

Domain	Latitude	Longitude	Station No.	Strike	Dip
Quartz-Magnetite Veins					
Skouries	40.47288	23.70289	2014_1236	84	75
Skouries	40.47288	23.70289	2014_1237	85	85
Skouries	40.47288	23.70289	2014_1238	78	76
Skouries	40.47288	23.70289	2014_1239	55	75
Skouries	40.47298	23.70285	2014_DR1	97	74
Skouries	40.47298	23.70285	2014_DR2	76	84
Skouries	40.47298	23.70285	2014_DR3	83	86
Skouries	40.47298	23.70285	2014_DR4	84	85
Skouries	40.47298	23.70285	2014_DR5	85	86
Skouries	40.47298	23.70285	2014_DR6	82	88
Skouries	40.47298	23.70285	2014_DR7	84	83
Skouries	40.47298	23.70285	2014_DR8	324	5
Skouries	40.47298	23.70285	2014_DR9	75	88
Skouries	40.47298	23.70285	2014_DR10	69	87
Skouries	40.47298	23.70285	2014_DR11	56	84
Skouries	40.47298	23.70285	2014_DR12	47	78
Skouries	40.47298	23.70285	2014_DR13	63	65
Skouries	40.47298	23.70285	2014_DR14	262	88
Skouries	40.47298	23.70285	2014_DR15	268	89
Skouries	40.47298	23.70285	2014_DR16	224	26
Skouries	40.47298	23.70285	2014_DR17	28	85
Skouries	40.47298	23.70285	2014_DR18	72	86
Skouries	40.47298	23.70285	2014_DR19	57	88
Skouries	40.47298	23.70285	2014_DR20	63	87
Skouries	40.47298	23.70285	2014_DR21	242	18
Skouries	40.47298	23.70285	2014_DR22	32	31
Skouries	40.47298	23.70285	2014_DR23	143	81

Domain	Latitude	Longitude	Station No.	Strike	Dip
Quartz-Magnetite Veins					
Skouries	40.4733	23.70361	2014_DR80	209	85
Skouries	40.4733	23.70361	2014_DR81	175	84
Skouries	40.4733	23.70361	2014_DR82	38	42
Skouries	40.4733	23.70361	2014_DR83	39	36
Skouries	40.4733	23.70361	2014_DR84	138	79
Skouries	40.4733	23.70361	2014_DR85	134	79
Skouries	40.4733	23.70361	2014_DR86	44	43
Skouries	40.4733	23.70361	2014_DR87	174	86
Skouries	40.4733	23.70361	2014_DR88	152	24
Skouries	40.4733	23.70361	2014_DR89	332	82
Skouries	40.4733	23.70361	2014_DR90	188	87
Skouries	40.4733	23.70361	2014_DR91	216	18
Skouries	40.4733	23.70361	2014_DR92	248	26
Skouries	40.4733	23.70361	2014_DR93	8	85
Skouries	40.4733	23.70361	2014_DR94	5	84
Skouries	40.4733	23.70361	2014_DR95	214	86
Skouries	40.4733	23.70361	2014_DR96	352	87
Skouries	40.4733	23.70361	2014_DR97	11	85
Skouries	40.4733	23.70361	2014_DR98	354	86
Skouries	40.4733	23.70361	2014_DR99	5	83
Skouries	40.4733	23.70361	2014_DR100	6	86
Skouries	40.4733	23.70361	2014_DR101	23	86
Skouries	40.4733	23.70361	2014_DR102	338	36
Skouries	40.4733	23.70361	2014_DR103	3	86
Skouries	40.4733	23.70361	2014_DR104	48	62
Skouries	40.4733	23.70361	2014_DR105	32	85
Skouries	40.4733	23.70361	2014_DR106	29	76

Table A11. Quartz-magnetite and Cu-bearing veins in the Skouries stock

Domain	Latitude	Longitude	Station No.	Strike	Dip
Quartz-Magnetite Veins					
Skouries	40.47298	23.70285	2014_DR24	63	86
Skouries	40.47298	23.70285	2014_DR25	76	85
Cu-bearing Veins					
Skouries	40.47288	23.70289	2014_1300	24	75
Skouries	40.47288	23.70289	2014_1301	10	90
Skouries	40.47288	23.70289	2014_1302	37	82
Skouries	40.47288	23.70289	2014_1303	55	90
Skouries	40.47288	23.70289	2014_1304	17	85
Skouries	40.47288	23.70289	2014_1305	202	79
Skouries	40.47288	23.70289	2014_1306	24	85
Skouries	40.47288	23.70289	2014_1307	189	84
Skouries	40.47288	23.70289	2014_1308	15	90
Skouries	40.47288	23.70289	2014_1309	85	83
Skouries	40.47288	23.70289	2014_1310	85	80
Skouries	40.47288	23.70289	2014_1311	325	87
Skouries	40.47288	23.70289	2014_1312	200	86
Skouries	40.47288	23.70289	2014_1313	26	80
Skouries	40.47288	23.70289	2014_1314	32	89
Skouries	40.47288	23.70289	2014_1315	35	76
Skouries	40.47288	23.70289	2014_1316	36	70
Skouries	40.47288	23.70289	2014_1317	29	70
Skouries	40.47288	23.70289	2014_1318	30	89
Skouries	40.47288	23.70289	2014_1319	42	50
Skouries	40.47288	23.70289	2014_1320	27	32
Skouries	40.47288	23.70289	2014_1321	20	70
Skouries	40.47288	23.70289	2014_1335	304	75
Skouries	40.47288	23.70289	2014_1336	40	80
Skouries	40.4733	23.70361	2014_DR107	4	37
Cu-bearing Veins					
Skouries	40.47288	23.70289	2014_1337	36	84
Skouries	40.47288	23.70289	2014_1338	60	14
Skouries	40.47298	23.70285	2014_DR108	84	85
Skouries	40.47298	23.70285	2014_DR109	286	66
Skouries	40.47298	23.70285	2014_DR110	250	72
Skouries	40.47298	23.70285	2014_DR111	67	79
Skouries	40.47298	23.70285	2014_DR112	64	83
Skouries	40.47298	23.70285	2014_DR113	127	83
Skouries	40.47298	23.70285	2014_DR114	64	87
Skouries	40.47298	23.70285	2014_DR115	57	68
Skouries	40.4733	23.70361	2014_DR116	171	10
Skouries	40.4733	23.70361	2014_DR117	186	82
Skouries	40.4733	23.70361	2014_DR118	274	86
Skouries	40.4733	23.70361	2014_DR119	286	87
Skouries	40.4733	23.70361	2014_DR120	186	81
Skouries	40.4733	23.70361	2014_DR121	124	68
Skouries	40.4733	23.70361	2014_DR122	194	68
Skouries	40.4733	23.70361	2014_DR123	195	86
Skouries	40.4733	23.70361	2014_DR124	198	68
Skouries	40.4733	23.70361	2014_DR125	188	24
Skouries	40.47288	23.70289	2014_1322	4	86
Skouries	40.47288	23.70289	2014_1323	201	76
Skouries	40.47288	23.70289	2014_1324	195	79
Skouries	40.47288	23.70289	2014_1325	210	88
Skouries	40.47288	23.70289	2014_1326	88	86

Table A11. Quartz-magnetite and Cu-bearing veins in the Skouries stock

Domain	Latitude	Longitude	Station No.	Strike	Dip
Cu-bearing Veins					
Skouries	40.47288	23.70289	2014_1327	95	86
Skouries	40.47288	23.70289	2014_1328	90	88
Skouries	40.47288	23.70289	2014_1329	65	84
Skouries	40.47288	23.70289	2014_1330	66	79
Skouries	40.47288	23.70289	2014_1331	55	75
Skouries	40.47288	23.70289	2014_1332	66	76
Skouries	40.47288	23.70289	2014_1333	31	74
Skouries	40.47288	23.70289	2014_1334	59	80
Skouries	40.4733	23.70361	2014_DR126	211	34
Skouries	40.4733	23.70361	2014_DR127	166	85
Skouries	40.4733	23.70361	2014_DR128	66	74
Skouries	40.4733	23.70361	2014_DR129	148	36
Skouries	40.4733	23.70361	2014_DR130	234	88
Skouries	40.4733	23.70361	2014_DR131	236	87
Skouries	40.4733	23.70361	2014_DR132	230	89
Skouries	40.4733	23.70361	2014_DR133	56	81
Skouries	40.4733	23.70361	2014_DR134	76	74
Skouries	40.4733	23.70361	2014_DR135	199	75
Skouries	40.4733	23.70361	2014_DR136	58	72
Skouries	40.4733	23.70361	2014_DR137	126	86
Skouries	40.4733	23.70361	2014_DR138	5	78

Table A12. Pyrite-bearing veins surrounding the Skouries stock

Domain	Latitude	Longitude	Station No.	Strike	Dip
Pyrite Veins					
Skouries	40.47997	23.71775	2014_703	340	88
Skouries	40.47999	23.71766	2014_704	345	80
Skouries	40.47945	23.71775	2014_705	4	72
Skouries	40.48096	23.71897	2014_711	175	80
Skouries	40.48157	23.71904	2014_712	15	65
Skouries	40.46748	23.70452	2014_762	75	40
Skouries	40.46788	23.70527	2014_763	165	80
Skouries	40.46851	23.70588	2014_765	300	85
Skouries	40.46934	23.70674	2014_771	305	30
Skouries	40.47023	23.708	2014_776	170	80
Skouries	40.47073	23.70865	2014_780	295	84
Skouries	40.47103	23.70872	2014_781	290	80
Skouries	40.47092	23.70893	2014_782	295	70
Skouries	40.4719	23.70928	2014_788	300	80
Skouries	40.47228	23.70956	2014_790	25	75
Skouries	40.47303	23.71044	2014_794	170	88

Table A13. Porphyry dikes surrounding the Skouries stock

Domain	Latitude	Longitude	Station No.	Strike	Dip
K-feldspar Porphyry Dikes					
Skouries	40.47327	23.70425	2014_734	275	70
Skouries	40.47296	23.70418	2014_736	265	90
Skouries	40.46827	23.69936	2014_905	30	70
Skouries	40.46881	23.69855	2014_907	215	80
Skouries	40.47329	23.70427	2014_926	245	60
Skouries	40.47309	23.70421	2014_927	200	80
Skouries	40.472	23.70358	2014_929	290	64
Skouries	40.4733	23.70361	2014_DR52	35	85
Skouries	40.4733	23.70361	2014_DR91	6	84
Skouries	40.47298	23.70285	2014_DR31	343	86
Skouries	no coordinate		2014_SK07	190	74

Table A14. Fault-kinematic measurements and field descriptions

Domain	Fault Style	Slip	Latitude	Longitude	Strike	Dip	Trend	Plunge	Field Notes
Olympias	Brittle	L.L.	Level -203, Olympias underground		345	65	359	27	Kassandra fault zone; sighted; prominent, second (later) set of slickensides on gouged fault surface exposed underground
Olympias	Brittle	N	Level -203, Olympias underground		345	65	75	65	Kassandra fault zone; sighted; gouged fault scarp exposed underground
Olympias	Brittle	N	40.58407	23.74591	351	56	72	56	Kassandra fault zone, surface exposure; quartz mineral fibers indicate normal, top to the east
Olympias	Brittle	R.L.	40.58827	23.75061	359	66	165	28	Brittle fault zone approx. 8-10m wide within granitic and quartzo-feldspathic biotite gneiss; individual faults are clay-rich and contain mostly angular quartz and feldspar clasts; normal sense of shear
Olympias	Brittle	R.L.	40.58803	23.75081	330	84	143	50	East fault zone; continued exposure of East fault, clay consisting of kaolinite and paragonitic illite (Terraspec)
Olympias	Brittle	L.L.	40.58029	23.75782	344	79	356	48	East fault zone; mostly brittle, strong clay alteration of granitic gneiss; thin kaolinitic gouge lenses containing clasts of angular granite gneiss
Olympias	Breccia	N	40.58043	23.75799	199	85	1	74	Fault breccia, 4-5cm wide shear surface associated with intense silification; contains chaotic arrangement of angular granite gneiss clasts, matrix supported by chalcedonic quartz
Olympias	Breccia	N	40.58043	23.75799	20	82	58	77	Same as above

Table A14. Fault-kinematic measurements and field descriptions

Domain	Fault Style	Slip	Latitude	Longitude	Strike	Dip	Trend	Plunge	Field Notes
Olympias	Breccia	N	40.58043	23.75799	194	69	315	66	Same as above
Olympias	Breccia	N	40.57909	23.75770	211	59	343	51	Fault breccia, 20-30cm wide with pervasive silification associated with Mn-FeOx staining; clay-altered clasts of granite gneiss with arsenopyrite-pyrite, matrix-supported by chalcedonic quartz; normal sense of shear
Olympias	Vein Breccia	N	40.57616	23.82139	4	85	49	83	Fault vein-breccia, 0.5 m wide; colloform-crustiform, open-space quartz vein infilled by chalcedonic quartz; breccia contains angular clasts of clay-altered granite gneiss, contains arsenopyrite-pyrite-sphalerite; normal sense of shear
Olympias	Vein Breccia	N	40.57616	23.82139	19	77	84	76	Same as above
Stratoni	Semi-brittle	R.L.	40.52928	23.77030	31	35	161	28	Splay of Stratoni fault; carbonaceous semi-ductile shear fabric; internal riedel fractures and folds show normal displacement
Stratoni	Semi-brittle	R.L.	40.52928	23.77029	28	44	164	34	Extension of fault described above
Stratoni	Semi-brittle	N	40.52967	23.76908	79	30	148	28	Splay of Stratoni fault; strong internal shear fabric with graphitic gouge; oblique shear fabric and riedel fractures show normal displacement
Stratoni	Semi-brittle	N	40.53059	23.76724	98	31	197	31	Stratoni fault; internal shear fabric containing clasts of graphitic schist; green mica is pervasive

Table A14. Fault-kinematic measurements and field descriptions

Domain	Fault Style	Slip	Latitude	Longitude	Strike	Dip	Trend	Plunge	Field Notes
Stratoni	Semi-brittle	L.L.	40.51744	23.82349	26	56	35	13	Mineralized semi-brittle cataclastic fault crosscutting granodiorite; pervasive Mn-FeO and sericite-pyrite-galena
Stratoni	Semi-brittle	R.L.	40.52538	23.78380	30	35	175	22	Splay of the Stratoni fault; semi-brittle fabric and riedel fractures oblique to shear plane; Mn-Fe gossan on HW side in marble
Stratoni	Semi-brittle	N	40.52055	23.79656	104	40	219	37	Stratoni fault, major surface; drainage gives cross sectional view; pervasive semi-brittle shear fabric defined by green sericite and graphitic gouge; parallel series of shears internal to fault
Stratoni	Semi-brittle	L.L.	40.53093	23.76724	200	27	202	1	NE-SW fault; semi-brittle shear fabric with graphitic bands; clasts of amphibolite and granite gneiss; limonite-sericite-Mn replacement; mineralized
Stratoni	Semi-brittle	R.L.	40.53420	23.71331	10	44	169	19	Splay to main Stratoni fault; carbonaceous semi-brittle cataclastic fault defined by oblique graphite-sericite shear fabric
Stratoni	Semi-brittle	N	40.53324	23.71681	107	31	165	27	Stratoni fault zone, major surface; oblique internal shear fabric; graphitic, green sericite and sulfide-bearing, in part siliceous, massive MnO-quartz replacement on immediate HW
Stratoni	Semi-brittle	R.L.	40.53048	23.76692	35	40	212	3	Splay of Stratoni fault; semi-brittle cataclastic breccia with internal oblique shear fabric defined by graphitic-green sericite gouge and riedel fractures
Stratoni	Semi-brittle	R.L.	40.53307	23.71553	55	45	225	10	Semi-brittle fault surface; riedel fractures oblique to shear planes; difficult to access

Table A14. Fault-kinematic measurements and field descriptions

Domain	Fault Style	Slip	Latitude	Longitude	Strike	Dip	Trend	Plunge	Field Notes
Stratoni	Semi-brittle	N	40.51921	23.82145	130	40	207	39	Stratoni fault; grooves marks on shear surface and steps in limonite-clay altered surface suggest normal movement
Stratoni	Semi-brittle	N	40.53588	23.70895	100	35	200	34	Stratoni fault; grooved and striated fault surface coated in MnO; cutting into Mn-SiO2 mineralized breccia; syn to post mineral?
Stratoni	Semi-brittle	N	40.52310	23.78110	107	36	228	32	Stratoni fault cutting marble with weak cataclasite in fault plane, interlayered amphibolite; fault gouge minor
Stratoni	Semi-brittle	N/R.L.	40.52680	23.76840	39	62	179	50	Splay of Stratoni fault; carbonaceous rock exposed along the fault close to HW amphibolite; carbonaceous with oblique foliation and riedel shear fabric
Stratoni	Semi-brittle	N/L.L.	40.52680	23.76620	78	30	142	27	Stratoni fault; minor carbonaceous shear zone, internal shear structure and intense alteration
Stratoni	Semi-brittle	N	40.52960	23.76500	112	36	174	32	Stratoni fault; major carbonaceous shear zone; E-W fault developed in massive sulfide lenses
Stratoni	Semi-brittle	N	40.53320	23.70710	83	39	196	35	Stratoni fault; minor carbonaceous shear zone in the Piavitsa area; in contact with graphitic schist
Stratoni	Semi-brittle	N	40.52900	23.72650	105	64	217	62	Stratoni fault; major carbonaceous shear zones exposed in the Mn pits; containing several units within the fault zone

Table A14. Fault-kinematic measurements and field descriptions

Domain	Fault Style	Slip	Latitude	Longitude	Strike	Dip	Trend	Plunge	Field Notes
Stratoni	Semi-brittle	N	40.52840	23.76550	196	39	313	36	Stratoni fault; minor carbonaceous shear zone containing a complex internal structure
Stratoni	Semi-brittle	R.L.	40.53578	23.70912	155	60	325	16	Stratoni fault; semi-brittle shear zone; limonite-sericite-MnO-altered internal shear fabric
Stratoni	Semi-brittle	N/R.L.	40.53061	23.77602	130	45	269	33	Sub-parallel semi-brittle fault in amphibolite, adjacent to granite gneiss; internal riedel shear fractures
Stratoni	Brittle	N/R.L.	40.52578	23.78252	120	50	257	39	Stratoni fault exposed within marble outcrop; calcite mineral fibers indicating direction of fault movement; groove marks and mineral fibers give same rake
Stratoni	Brittle	N/R.L.	40.52569	23.78285	110	40	248	30	Stratoni fault exposed within marble outcrop; grooved surface with extension fractures
Stratoni	Brittle	N/R.L.	40.52572	23.78278	107	46	240	37	Stratoni fault exposed within marble outcrop; m-scale grooves on surface; extension fractures
Stratoni	Brittle	N/R.L.	40.52567	23.78293	125	49	255	42	Stratoni fault exposed within marble outcrop; surface displays calcite mineral fibers in direction of slip
Stratoni	Brittle	N/R.L.	40.52577	23.78280	110	41	236	35	Stratoni fault exposed within marble outcrop; deep grooves and calcite mineral fibers indicating normal displacement

Table A14. Fault-kinematic measurements and field descriptions

Domain	Fault Style	Slip	Latitude	Longitude	Strike	Dip	Trend	Plunge	Field Notes
Stratoni	Brittle	N	40.51649	23.81512	106	48	165	44	Stratoni-parallel, post-mineral fault cross cutting porphyry dike; small pencil-thin groove/striations on fault surface
Stratoni	Brittle	N	40.51650	23.81497	114	45	187	43	Stratoni fault parallel, post-mineral fault cross cutting porphyry dike
Stratoni	Brittle	N	40.52550	23.78342	92	70	176	70	Late, post-mineral fault with slickensides on slip surface; dip-slip indicated by groove marks
Stratoni	Brittle	N/L.L.	40.53132	23.75420	89	62	118	43	Fault scarp; poorly preserved slickensides rake between 45-50 degrees on weathered crust of granite gneiss
Stratoni	Brittle	N	40.53129	23.75387	91	77	194	77	Fault scarp with faint slickensides on outcrop surface crosscutting granite gneiss
Stratoni	Brittle	N	40.52130	23.79061	93	49	153	45	Post-mineral brittle fault; overprinting sericite-altered early generation of syn-mineral fault
Stratoni	Brittle	N/L.L.	40.52130	23.79061	126	55	164	42	Same as above
Stratoni	Brittle	L.L.	40.52417	23.79177	210	69	224	32	Vathilakkos fault; brittle cataclastic fault surface in contact between black-matrix porphyry dike and granite gneiss; riedel fractures and slickenline preserved

Table A14. Fault-kinematic measurements and field descriptions

Domain	Fault Style	Slip	Latitude	Longitude	Strike	Dip	Trend	Plunge	Field Notes
Stratoni	Brittle	L.L.	40.52415	23.79179	216	65	227	23	Vathilakkos fault; same as above
Skouries	Brittle	R.L.	40.46274	23.66815	148	52	308	23	Brittle cataclastic fault outcropping on road to Skouries; highly polished and deeply grooved fault surface; quartz-sericite-clay gouge; Gomati fault zone
Skouries	Brittle	R.L.	40.46275	23.66807	145	57	307	26	Same as above; Gomati fault zone
Skouries	Brittle	R.L.	40.46266	23.66813	121	66	299	5	Same as above; Gomati fault; early slickensides are clearly crosscut by later groove marks showing dip-slip movement

Abbreviations: N = normal fault; L.L. = left-lateral fault; R.L. = right-lateral fault

Table A15. Sample locations and descriptions for amphibolites within the Stratoni fault zone

No.	Latitide	Longitude	Drill Hole	Structural Position	Field Descriptions	TAS-proxy Lithology
279401	40.53362	23.69707	PVD135 (32.2m)	Hanging wall	Amphibolite gneiss containing black to green hornblende-actinolite with localized plagioclase porphyroblasts	Basalt
279403	40.53362	23.69707	PVD135 (104.5m)	Hanging wall	Amphibolite gneiss containing green actinolitic amphibole intergrown with plagioclase and minor disseminated pyrrhotite	Basalt
279406	40.53362	23.69707	PVD135 (228.5m)	Hanging wall	Amphibolite gneiss containing intergrown amphibole and plagioclase, with disseminated garnet porphyroblasts	Basalt
279407	40.53362	23.69707	PVD135 (269.3)	Hanging wall	Amphibolite gneiss composed mostly of actinolite; contains minor, thin carbonate veinlets resulting in localized chlorite alteration of actinolite	Basalt
279411	40.53323	23.70484	PVD131 (129.3)	Hanging wall	Amphibolite contained within lenses within biotite-graphitic gneiss	Basalt
279413	40.52925	23.71603	PVD93 (122.9)	Hanging wall	Amphibolite gneiss composed of coarse-grained green actinolite and intergrown plagioclase defining S1 fabric; minor disseminated pyrite	Basalt
279414	40.52925	23.71603	PVD93 (204.0)	Hanging wall	Amphibolite gneiss, coarse-grained amphibole/actinolite and intergrown plagioclase	Basalt
279416	40.53069	23.71133	PVD124 (204.1)	Hanging wall	Amphibolite gneiss (no field description)	Basalt
279422	40.53046	23.77550		Footwall	Amphibolite gneiss containing coarse-grained actinolite, intergrown with plagioclase, disseminated pyrite and trace pyrrhotite	Basalt
279425	40.52286	23.78265		Hanging wall	Amphibolite gneiss containing fine-grained actinolite with minor disseminated pyrite; affected by minor carbonate-chlorite alteration	Basalt

Table A15. Sample locations and descriptions for amphibolites within the Stratoni fault zone

No.	Latitide	Longitude	Drill Hole	Structural Position	Field Descriptions	TAS-proxy Lithology
279426	40.53461	23.76714		Footwall	Amphibolite gneiss consisting of strongly foliated and coarse-grained green amphibole and intergrown plagioclase with disseminated pyrite	Basalt
279429	40.54141	23.83182		Footwall	Amphibolite gneiss containing equigranular actinolite and segregated plagioclase layers; minor disseminated pyrite and pyrrhotite	Basalt
679700	40.60266	23.72824		Footwall	Amphibolite gneiss composed of strongly foliated, fine- to medium-grained and intergrown actinolite-chlorite and plagioclase	Basalt
2000052	40.49600	23.81453		Hanging wall	Amphibolite gneiss composed of fine-grained actinolite and intergrown plagioclase; plagioclase also segregated into thin layers	Basalt
2000059	40.50720	23.77009		Hanging wall	Amphibolite gneiss composed of fine-grained actinolite and intergrown plagioclase; plagioclase also exists as mineral segregations	Basalt
2000063	40.53907	23.85495		Footwall	Amphibolite gneiss composed of fine-grained actinolite (and minor pyroxene?), may have undergone minor serpentinization?	Basalt
2000064	40.53995	23.85787		Footwall	Amphibolite gneiss consists of medium-grained black amphibole (hornblende) and intergrown plagioclase	Basalt

Abbreviations: TAS = Total-alkali silica

Table A16. Major oxide and trace element geochemistry for amphibolites within the Stratoni fault zone

	Wt. (%)												ppm						
No.	SiO_2	Al_2O_3	Fe_2O_3(T)	MgO	CaO	Na_2O	K_2O	TiO_2	P_2O_5	MnO	Cr_2O_3	LOI	Total	Al	Nb	Nd	Th	Ti	Y	Zr
279401	45.31	14.04	11.08	6.86	13.13	2.69	0.82	1.44	0.13	0.18	0.02	4.10	99.76	14600	2.7	9.5	0.3	2150	29.0	84.0
279403	47.01	14.31	12.32	8.03	11.29	2.74	0.55	1.55	0.09	0.19	0.02	1.60	99.76	13600	2.4	8.8	0.2	2960	30.7	89.0
279406	48.27	13.51	15.69	5.82	8.78	2.68	0.31	2.40	0.33	0.23	0.01	1.70	99.75	13900	5.9	20.0	0.7	2180	53.3	160.7
279407	48.29	15.68	9.09	8.45	12.64	2.18	0.40	0.89	0.09	0.15	0.06	1.80	99.78	19700	1.7	5.9	0.2	1820	18.3	49.2
279411	48.60	14.50	11.90	8.89	9.35	2.52	0.40	1.39	0.10	0.20	0.03	1.80	99.73	11500	1.9	8.9	0.1	1110	26.5	81.2
279413	49.48	14.75	10.59	7.73	7.69	3.95	0.35	1.29	0.09	0.17	0.03	3.60	99.76	18100	1.8	8.4	0.3	1050	25.4	73.0
279414	52.51	14.19	8.90	8.72	10.02	1.68	0.07	0.45	0.05	0.15	0.06	2.90	99.77	28600	0.7	6.8	0.7	440	14.5	42.6
279416	51.02	15.08	11.81	6.69	8.75	3.56	0.14	1.54	0.13	0.19	0.03	0.80	99.77	9600	2.0	9.5	0.4	1160	28.7	84.3
279422	50.26	16.68	9.07	7.16	9.28	3.75	0.55	1.36	0.12	0.17	0.03	1.30	99.77	8300	1.4	10.9	0.8	1230	26.7	90.5
279425	51.16	14.17	7.18	5.59	9.68	2.83	0.33	0.53	0.06	0.15	0.04	8.10	99.82	27100	3.5	9.0	2.1	560	13.7	61.9
279426	53.54	17.37	8.52	5.57	9.19	2.94	0.29	0.73	0.05	0.17	0.02	1.40	99.8	12500	1.2	7.9	1.0	970	17.3	75.0
279429	48.21	13.77	14.36	6.86	9.54	2.77	0.48	2.39	0.17	0.26	0.02	0.90	99.74	9800	3.6	14.9	0.4	2060	47.0	161.3
679700	50.57	15.09	10.32	7.90	8.57	4.08	0.33	1.22	0.12	0.18	0.04	1.40	99.85	9400	3.3	12.3	0.6	910	30.5	85.9
2000052	50.06	15.26	12.64	5.24	8.93	4.04	0.35	1.79	0.19	0.22	0.01	1.00	99.78	9700	4.5	16.7	0.7	1850	40.8	127.5
2000059	49.14	16.35	10.45	7.70	9.29	3.56	0.23	1.15	0.07	0.17	0.06	1.60	99.77	11000	1.9	8.7	0.7	1140	24.5	68.5
2000063	56.65	2.88	6.72	18.69	12.37	0.37	0.17	0.08	<0.01	0.16	0.17	1.30	99.66	1200	1.8	1.4	0.2	40	4.2	5.5
2000064	49.82	15.15	10.65	7.05	10.11	3.45	0.79	1.34	0.11	0.21	0.03	1.00	99.77	7700	2.2	9.9	0.5	1730	31.2	82.2

Abbreviations: Wt. % = weight percent; ppm = parts per million

Table A17. ^{40}Ar-^{39}Ar analyses of hydrothermal white micas from the Olympias deposit and the Piavitsa area

		Relative Isotopic abundances (fAmps)*								
Step	Power (%)	Ar40	± 1σ	Ar39	± 1σ	Ar38	± 1σ	Ar37	± 1σ	Ar36
OL559-252 Muscovite (Olympias)										
Latitude 40.580727, Longitude 23.748835, Depth 252m										
J-value = 0.0018031 ± 2.14 x 10 $^{-6}$ (1σ)										
1	0.2	71.83994	0.06718	6.03957	0.06445	0.08566	0.02763	0.02586	0.02614	0.08871
2	0.4	31.33073	0.06303	3.25585	0.06088	0.03877	0.02857	0.01044	0.02905	0.02284
3	0.6	89.00174	0.06935	10.36982	0.06024	0.21240	0.03146	-0.00092	0.02647	0.04657
4	0.7	103.13600	0.07464	12.42050	0.05858	0.13368	0.02993	0.08910	0.02733	0.05326
5	0.8	95.72699	0.07919	11.42901	0.06239	0.12435	0.03015	0.08596	0.02677	0.04862
6	1	139.67770	0.07485	16.09387	0.05997	0.18371	0.02901	0.03087	0.02605	0.08825
7	1.5	275.20240	0.08772	31.59277	0.06370	0.35877	0.02978	-0.00266	0.02731	0.19285
8	2	193.13300	0.07379	20.22348	0.06198	0.28830	0.02752	-0.03347	0.02736	0.17707
9	2.5	16.88862	0.06095	1.64958	0.06164	-0.02770	0.03106	0.05670	0.02586	0.01840
10	5	18.31651	0.06395	1.68361	0.06471	0.01476	0.02859	0.03297	0.02704	0.02180

Plateau age (steps 4-8): 79.96% ^{39}Ar released

Table A17. ^{40}Ar-^{39}Ar analyses of hydrothermal white micas from the Olympias deposit and the Piavitsa area

									Isotopic Ages	
Step	± 1σ	Ca/K	± 1σ	Cl/K	± 1σ	40Ar*/39Ar(K)	± 1σ	40Ar* (%)	Age (Ma)	± 1σ
1	0.00165	0.03597	0.03729	-0.00226	0.01362	7.55143	0.11994	63.52116	24.4	0.4
2	0.00109	0.02685	0.07691	-0.00468	0.02612	7.54617	0.17881	78.46531	24.4	0.6
3	0.00141	-0.00119	0.02203	0.02155	0.00903	7.25157	0.06129	84.54155	23.4	0.2
4	0.00138	0.06072	0.01901	-0.00651	0.00717	7.03451	0.04977	84.76564	22.7	0.2
5	0.00134	0.06374	0.02025	-0.00616	0.00785	7.11681	0.05529	85.01914	23.0	0.2
6	0.00166	0.01595	0.01401	-0.00528	0.00537	7.05468	0.04369	81.33428	22.8	0.1
7	0.00222	-0.00116	0.00749	-0.00578	0.00281	6.90257	0.02967	79.28886	22.3	0.1
8	0.00202	-0.01461	0.01173	0.00118	0.00405	6.95769	0.04159	72.90031	22.5	0.1
9	0.00115	0.29434	0.13666	-0.09012	0.05614	6.94783	0.34297	67.89601	22.4	1.1
10	0.00107	0.16761	0.13980	-0.01701	0.05054	7.05591	0.34164	64.89088	22.8	1.1
								Age:	**22.6**	**0.3**

*Corrected for blank, mass discrimination, and radioactive decay

Sensitivity = $6.312 \times 10^{-17} \pm 1.047 \times 10^{-18}$ (mol/fAmp)

Table A17. ^{40}Ar-^{39}Ar analyses of hydrothermal white micas from the Olympias deposit and the Piavitsa area

		Relative Isotopic abundances (fAmps)*								
Step	Power (%)	Ar40	± 1σ	Ar39	± 1σ	Ar38	± 1σ	Ar37	± 1σ	Ar36
PVD131-290 Muscovite (Piavitsa)										
Latitude 40.530625, Longitude 23.703084, Depth 290m										
J-value = 0.0018068 ± 2.12 x 10 $^{-6}$ (1σ)										
1	0.2	123.08330	0.07676	13.49960	0.05966	0.11247	0.02892	0.27349	0.02720	0.06072
2	0.4	103.07940	0.07264	11.52225	0.06392	0.11430	0.02885	0.05783	0.02483	0.04063
3	0.6	172.27310	0.08253	20.24445	0.06135	0.24829	0.02876	0.04886	0.02742	0.06624
4	0.7	112.82630	0.07269	13.09870	0.06195	0.11037	0.02914	0.18415	0.02813	0.05615
5	0.8	85.71493	0.07209	9.57025	0.06083	0.10630	0.02809	0.14625	0.02499	0.05234
6	1.0	98.41150	0.07682	10.57060	0.06022	0.16281	0.03149	-0.03434	0.02573	0.07211
7	1.5	132.69400	0.07751	14.22429	0.06179	0.24327	0.03098	0.13719	0.02786	0.08449
8	2.0	81.22196	0.07095	8.33145	0.06041	0.09129	0.03112	0.02773	0.02825	0.04205
9	2.5	35.03067	0.06619	3.29201	0.05906	0.01229	0.03172	0.01674	0.02677	0.01511
10	3.0	17.43299	0.06023	1.84299	0.05937	-0.06432	0.02916	0.01706	0.02688	0.01091
11	4.0	20.62348	0.06258	1.93858	0.06446	0.01608	0.02747	0.01091	0.02681	0.01427
12	5.0	9.83271	0.06616	0.90395	0.06110	0.06815	0.03020	0.02777	0.02641	0.01151

Plateau age (steps 4-6): 62.10% ^{39}Ar released

Table A17. ^{40}Ar-^{39}Ar analyses of hydrothermal white micas from the Olympias deposit and the Piavitsa area

									Isotopic Ages	
Step	± 1σ	Ca/K	± 1σ	Cl/K	± 1σ	40Ar*/39Ar(K)	± 1σ	40Ar* (%)	Age (Ma)	± 1σ
1	0.00128	0.17645	0.01785	-0.01367	0.00638	7.79081	0.04803	85.49568	25.2	0.2
2	0.00114	0.04341	0.01908	-0.00854	0.00745	7.90101	0.05616	88.37090	25.6	0.2
3	0.00144	0.02066	0.01200	-0.00161	0.00423	7.53884	0.03428	88.64608	24.4	0.2
4	0.00139	0.12260	0.01906	-0.01328	0.00662	7.34719	0.05000	85.34729	23.8	0.2
5	0.00137	0.13338	0.02319	-0.00615	0.00874	7.34106	0.06652	82.01124	23.8	0.2
6	0.00140	-0.02890	0.02161	0.00555	0.00887	7.28844	0.06109	78.33568	23.6	0.2
7	0.00159	0.08417	0.01741	0.01097	0.00648	7.57235	0.05048	81.22017	24.5	0.2
8	0.00119	0.02878	0.03016	-0.00637	0.01112	8.25327	0.07729	84.70990	26.7	0.2
9	0.00100	0.04423	0.07237	-0.02706	0.02868	9.28045	0.19680	87.26460	30.0	0.6
10	0.00103	0.08096	0.12998	-0.13975	0.04733	7.70634	0.30869	81.51820	24.9	1.0
11	0.00098	0.04909	0.12328	-0.01534	0.04219	8.46035	0.33087	79.57287	27.4	1.1
12	0.00090	0.27008	0.26133	0.17624	0.10022	7.12349	0.58626	65.52165	23.1	1.9
								Age:	**24.0**	**0.6**

*Corrected for blank, mass discrimination, and radioactive decay

Sensitivity = $6.312 \times 10^{-17} \pm 1.047 \times 10^{-18}$ (mol/fAmp)

Table A18. Primary fluid inclusions in quartz from the sulfide deposits in the Kassandra Mining District

Sample No.	Type	Daughter minerals	Tm_{ice} (°C)	Salinity (wt.% NaCl equiv.)[1,2]	Tm_{CO2} (°C)	Tm_{clath}(°C)	Th_{CO2} (°C)	Th_{total} (°C)	Mode
Olympias: OL593 (189m)									
OL593A01-1	CO2	soild	-	1.64	-57.3	9.2	18.4	344.5	L
OL593A01-2	CO2	soild	-	0.21	-56.9	9.9	17.7	345.9	V
OL593A01-3	CO2	soild	-	1.24	-56.9	9.4	18.3	345.4	V
OL593B01-1			-5.6	8.68				303.0	L
OL593B01-2			-5.6	8.68				-	
OL593B01-3			-5.4	8.41				313.6	L
OL593B01-4			-5.6	8.68				303.9	L
OL593B01-5			-5.5	8.55				316.2	L
OL593B01-6			-5.6	8.68				320.9	L
OL593B01-7			-5.5	8.55				305.2	L
OL593C01-1			-4.6	7.31				299.8	L
OL593D0-1			-5.4	8.41				310.3	L
OL593E01-1			-3.6	5.86				294.4	L
OL593F01-1			-5.8	8.95				310.6	L
OL593G01-1			-	-				345.6	L
OL593H01-1			-5.4	8.41				329.7	L
OL593I01-1			-4.5	7.17				-	
OL593J01-1			-1.8	3.06				298.1	L
OL593K01-1			-2.5	4.18				340.8	L
OL593K01-2		clear solid	-1.4	2.41				345.9	L
OL593L01-1			-2.0	3.39				282.4	L
OL593M01-1			-2.8	4.65				288.6	L
OL593N01-1			-3.7	6.01				294.1	L
OL593N01-2			-	-				302.5	L
OL593N01-3		clear solid	-3.4	5.56				306.2	L
OL593N01-4			-	-				312.9	L
OL593N01-5			-	-				341.0	L
OL593O01-1			-2.0	3.39				329.7	L

Table A18. Primary fluid inclusions in quartz from the sulfide deposits in the Kassandra Mining District

Sample No.	Type	Daughter minerals	Tm_{ice} (°C)	Salinity (wt.% NaCl equiv.)[1,2]	Tm_{CO2} (°C)	Tm_{clath}(°C)	Th_{CO2} (°C)	Th_{total} (°C)	Mode
OL593P01-1	CO2		-	0.83	-57.7	9.6		345.3	V
OL593P01-2	CO2	clear solid	-	1.44	-57.6	9.3	14.4	345.2	V
OL593P01-3	CO2			1.44	-57.7	9.3		347.1	V
OL593P01-4	CO2	clear solid		1.04	-57.5	9.5		345.3	V
Olympias: OL542-147									
OL542A01-1			-4.4	7.02				342.3	L
OL542B01-1		solid	-4.0	6.45				356.1	L
OL542B01-2		solid	-	-				365.3	L
OL542C01-1			-3.2	5.26				247.6	L
OL542D01-1			-1.9	3.23				291.6	L
OL542D01-2			-1.8	3.06				227.8	L
OL542D01-3		clear solid	-2.3	3.87				327.7	L
OL542D01-4			-3.4	5.56				240.9	L
OL542D01-5			-4.2	6.74				270.9	L
OL542D01-6			-3.5	5.71				266.2	L
OL542E01-1		opaque solid	-4.9	7.73				331.1	L
OL542F01-1			-5.2	8.14				334.5	L
OL542G01-1			-4.0	6.45				333.6	L
OL542G01-2			-4.8	7.59				325.2	L
Mavres Petres: MPUG264									
MP264A01-1		clear solid	-2.2	3.71				261.6	L
MP264B01-1		clear solid	-3.1	5.11				243.4	L
MP264C01-1			-2.3	3.87				172.4	L
MP264C01-2			-2.3	3.87				169.6	L
MP264D01-1			-2.0	3.39				209.2	L
MP264D01-2			-2.1	3.55				208.9	L
MP264E01-1		clear solid	-3.0	4.96				245.5	L

Table A18. Primary fluid inclusions in quartz from the sulfide deposits in the Kassandra Mining District

Sample No.	Type	Daughter minerals	Tm_{ice} (°C)	Salinity (wt.% NaCl equiv.)[1,2]	Tm_{CO2} (°C)	Tm_{clath}(°C)	Th_{CO2} (°C)	Th_{total} (°C)	Mode
MP264F01-1			-2.9	4.80				220.9	L
MP264G01-1			-2.4	4.03				192.8	L
MP264H01-1			-2.6	4.34				173.4	L
MP264H01-2			-2.1	3.55				190.3	L
MP264I01-1		clear solid	-2.7	4.49				241.8	L
MP264J01-1			-1.3	2.24				291.6	L
MP264K01-1			-2.3	3.87				211.9	L
MP264K01-2		clear solid	-2.4	4.03				225.6	L
MP264K01-3		opaque solid	-2.3	3.87				228.9	L
MP264K02-1			-2.6	4.34				236.0	L
MP264L01-1			-2.6	4.34				178.0	L
MP264M01-1			-2.7	4.49				188.4	L
MP264M01-2			-2.6	4.34				179.7	L
MP264M01-3			-2.6	4.34				232.2	L
MP264N01-1			-0.1	0.18				203.0	L
MP264O01-1			-1.9	3.23				230.2	L
MP264P01-1			-1.2	2.07				219.3	L
MP264P01-2			-1.5	2.57				220.5	L
MP264P01-3			-1.6	2.74				218.7	L
Mavres Petres: MP748 (34m)									
MP748A01-1			-2.5	4.18				227.4	L
MP748B01-1			-3.2	5.26				233.1	L
MP748B01-2			-3.2	5.26				234.8	L
MP748C01-1			-1.4	2.41				228.6	L
MP748D01-1			-2.7	4.49				233.2	L
MP748E01-1			-2.6	4.34				231.6	L
MP748F01-1			-3.0	4.96				204.9	L
MP748G01-1			-3.1	5.11				179.4	L

Table A18. Primary fluid inclusions in quartz from the sulfide deposits in the Kassandra Mining District

Sample No.	Type	Daughter minerals	Tm_{ice} (°C)	Salinity (wt.% NaCl equiv.)[1,2]	Tm_{CO2} (°C)	Tm_{clath}(°C)	Th_{CO2} (°C)	Th_{total} (°C)	Mode
MP748H01-1			-2.1	3.55				236.4	L
MP748H01-2			-2.1	3.55				-	
MP748I01-1		opaque solid	-1.3	2.24				185.1	L
MP748J01-1			0.2	0.35				220.8	L
MP748J01-2			-1.7	2.90				194.7	L
MP748J01-3			-1.7	2.90				206.7	L
MP748K01-1			-3.0	4.96				236.9	L
MP748L01-1			-2.8	4.65				217.9	L
MP748M01-1			-1.1	1.91				219.2	L
MP748N01-1			-0.5	0.88				144.7	L
MP748O01-1			-	-				219.7	L
MP748P01-1			-7.7	11.34				216.3	L
MP748Q01-1		clear solid	-6.9	10.36				226.6	L
MP748Q01-2			-8.2	11.93				233.8	L
MP748Q01-3		clear solid	-6.9	10.36				230.7	L
MP748Q01-4			-	-				226.3	L
MP748R01-1			-4.9	7.73				224.8	L
MP748R01-2			-4.1	6.59				209.5	L
MP748S01-1		clear solids	-2.9	4.80				230.5	L
Piavitsa: PHG78 (156m)									
PHG78A01-1			-3.5	5.71				265.9	L
PHG78A01-2			-3.6	5.86				242.6	L
PHG78A02-1			-1.6	2.74				247.1	L
PHG78A02-2			-0.9	1.57				252.3	L
PHG78A03-1			-	-				258.3	L
PHG78B01-1			-2.1	3.55				226.5	L
PHG78C01-1			-3.2	5.26				272.3	L
PHG78C01-2		solid	-3.2	5.26				272.1	L

Table A18. Primary fluid inclusions in quartz from the sulfide deposits in the Kassandra Mining District

Sample No.	Type	Daughter minerals	Tm_{ice} (°C)	Salinity (wt.% NaCl equiv.)[1,2]	Tm_{CO2} (°C)	Tm_{clath}(°C)	Th_{CO2} (°C)	Th_{total} (°C)	Mode
PHG78C02-3			-2.6	4.34				274.2	L
PHG78C02-4			-2.6	4.34				268.7	L
PHG78C02-5			-	-				271.9	L
PHG78D01-1		solid	-1.7	2.90				284.4	L
PHG78E01-1			-2.7	4.49				289.8	L
PHG78E01-2		solid	-1.4	2.41				291.8	L
PHG78F01-1			-3.5	5.71				283.8	L
PHG78G01-1		solid	-2.3	3.87				286.5	L
PHG78H01-1			-2.3	3.87				256.8	L
PHG78I01-1		solid	-2.2	3.71				258.4	L
PHG78J01-1			-2.8	4.65				266.9	L
PHG78K01-1		solid	-	-				248.4	L
PHG78L01-1			-4.2	6.74				277.3	L
PHG78L01-2			-	-				272.4	L
Piavitsa: PHG78 (95m)									
PHG78-95A01-1			-2.6	4.34				280.1	L
PHG78-95B01-1			-2.7	4.49				285.8	L
PHG78-95C01-1			-2.3	3.87				238.0	L
PHG78-95D01-1			-1.5	2.57				288.6	L
PHG78-95D01-2			-1.6	2.74				294.9	L
PHG78-95E01-1			-2.9	4.80				249.9	L
PHG78-95F01-1			-	-				258.8	L
PHG78-95F01-2		solid	-	-				256.9	L
PHG78-95G01-1			-2.6	4.34				266.4	L
PHG78-95H01-1			-2	3.39				287.7	L
PHG78-95I01-1		solid	-2.3	3.87				251.3	L
PHG78-95J01-1		clear solid	-1.8	3.06				261.6	L
PHG78-95K01-1			-1.9	3.23				253.9	L

Table A18. Primary fluid inclusions in quartz from the sulfide deposits in the Kassandra Mining District

Sample No.	Type	Daughter minerals	Tm_{ice} (^oC)	Salinity (wt.% NaCl equiv.)[1,2]	Tm_{CO2} (^oC)	Tm_{clath}(^oC)	Th_{CO2} (^oC)	Th_{total} (^oC)	Mode
PHG78-95L01-1		clear solid	-1.8	3.06				267.8	L
PHG78-95L01-2			-1.80	3.06				268.7	L
PHG78-95L01-3			-1.90	3.23				268.7	L
PHG78-95L01-4			-1.8	3.06				266.4	L
PHG78-95M01-1			-2.1	3.55				251.8	L
Piavitsa: PVD124-162									
PVD124A01-1			-2.7	4.49				236.4	L
PVD124A01-2			-2.2	3.71				229.7	L
PVD124A01-3			-2.9	4.80				238.3	L
PVD124B01-1		clear and opaque solid	-2.1	3.55				219.3	L
PVD124B01-2			-2	3.39				225.6	L
PVD124B01-3			-2	3.39				239.7	L
PVD124C01-1			-3.6	5.86				232.8	L
PVD124C01-2			-3.7	6.01				237.9	L
PVD124D01-1			-3.6	5.86				199.3	L
PVD124E01-1			-2.1	3.55				234.9	L

[1]Salinity for H_2O-rich inclusions was calculated using the equation in Bodnar (1993) and is suitable for temperatures between 0.0^oC and 21.2^oC (the eutectic temperature for the system NaCl-H_2O).

[2]Salinity for CO_2-rich inclusion was calculated using the equation in Darling (1991) and is suitable for temperatures between the peritectic temperature for CO_2 (-10.0^oC) and 10.0^oC.

Abbreviations: Tm_{ice} = ice melting temperature; equiv. = equivalent; Tm_{CO2} = dry ice melting temperature; Tm_{clath} = clathrate melting temperature; Th_{CO2} = homogenization temperature of CO_2 phase; Th_{total} = total homogenization temperature; L = liquid; V = vapor

Table. A19. Carbon and oxygen isotope data of carbonate minerals from the sulfide deposits of the Kassandra Mining District

Drill Hole	Latitude	Longitude	Depth	$\delta^{13}C_{VPDB}$	1σ	$\delta^{18}O_{VSMOW}$	1σ	Style	Mineral[1]
Olympias									
OL-826	478453	4493042	44.3	-1.93		12.31		Marble	*Cal*
			44.3	-2.17		14.98		Marble	*Cal*
			56.2	1.18		27.46		Marble	*Cal*
			58.2	0.46		24.79		Marble	*Cal*
			63.8	-2.00		16.79		Gangue	*Rds*
			64.8	-0.87		24.89		Marble	*Cal*
			67.2	-2.16		13.99		Gangue	*Rds*
			73.0	-0.38		25.58		Marble	*Cal*
			74.5	-0.53		17.49		Gangue	*Rds*
			83.1	1.08		26.74		Gangue	*Cal*
			92.6	-1.58		15.59		Vein	*Rds*
			105.2	-1.09		16.85		Vein	*Rds*
			110.4	-1.93		15.20		Gangue	*Rds*
			127.9	-1.94		14.53		Vein	*Rds*
			136.4	0.59		27.64		Marble	*Cal*
OL-757	478426	4493048	48.5	-6.33		24.43		Marble	*Cal*
			51.0	-0.52		15.88		Marble	*Rds*
			56.2	-0.98		8.69		Vein	*Rds*
			60.6	-0.93		21.13		Marble	*Cal*
			64.5	-1.50		15.19		Vein	*Rds*
			73.4	-1.92		14.90		Vein	*Rds*
OL-652	478827	4492220	230.3	2.37		27.24		Marble	*Cal*
			235.5	-0.45		26.91		Marble	*Cal*
			239.5	1.94		16.74		Marble	*Cal*
			248.3	-1.11		25.20		Marble	*Cal*
			253.7	-0.21		8.33		Gangue	*Cal*

Table. A19. Carbon and oxygen isotope data of carbonate minerals from the sulfide deposits of the Kassandra Mining District

Drill Hole	Latitude	Longitude	Depth	$\delta^{13}C_{VPDB}$	1σ	$\delta^{18}O_{VSMOW}$	1σ	Style	Mineral[1]
			278.4	1.74		8.02		Gangue	*Cal*
			283.8	1.29		15.69		Gangue	*Cal*
			299.1	1.15		21.19		Marble	*Cal*
			313.0	0.79		25.84		Marble	*Cal*
			313.1	1.10		2.95		Gangue	*Cal*
			337.0	-0.20		22.97		Marble	*Cal*
			341.7	-0.80		10.13		Gangue	*Cal*
			364.4	-0.39		25.87		Marble	*Cal*
			374.0	1.26		25.06		Marble	*Cal*
OL-593	478740	4492440	139.5	0.26		24.83		Marble	*Cal*
			142.5	1.35		7.63		Gangue	*Cal*
			153.7	-0.48		25.25		Marble	*Cal*
			169.8	-0.63		18.32		Marble	*Cal*
			185.9	0.03		24.16		Marble	*Cal*
			190.6	2.29		12.13		Gangue	*Cal*
			192.0	0.62		28.91		Marble	*Cal*
			205.1	1.03		14.38		Marble	*Cal*
			207.6	1.32		19.72		Marble	*Cal*
			213.0	1.21		26.48		Marble	*Cal*
			217.5	1.01		20.08		Marble	*Cal*
			221.5	1.39		28.45		Marble	*Cal*
			227.7	-0.13		25.17		Marble	*Cal*
			231.9	1.26		23.82		Marble	*Cal*
			239.5	-0.16		24.26		Marble	*Cal*
			245.0	-0.47		27.68		Marble	*Cal*
			248.9	-0.15		29.10		Marble	*Cal*

Table. A19. Carbon and oxygen isotope data of carbonate minerals from the sulfide deposits of the Kassandra Mining District

Drill Hole	Latitude	Longitude	Depth	$\delta^{13}C_{VPDB}$	1σ	$\delta^{18}O_{VSMOW}$	1σ	Style	Mineral[1]
OL-634	478827	4492220	153.0	1.89	0.26	4.55	0.57	Vein	Fe Cal
			168.0	2.04	0.26	7.98	0.57	Vein	Fe Cal
			194.0	1.40	0.26	28.27	0.57	Marble	Cal
			211.0	2.64	0.26	9.90	0.57	Vein	Rds
			213.0	0.10	0.26	10.13	0.57	Gangue	Rds
			215.0	0.48	0.26	28.05	0.57	Marble	Cal
			227.0	1.46	0.26	10.24	0.57	Gangue	Rds
			230.0	1.90	0.16	5.14	0.22	Gangue	Cal
			232.0	-0.30	0.26	24.20	0.57	Marble	Cal
			238.0	1.04	0.26	8.91	0.57	Marble	Cal
			258.0	0.60	0.26	19.48	0.57	Marble	Cal
			261.0	0.98	0.26	22.27	0.57	Marble	Fe Cal
			280.0	-0.11	0.26	6.12	0.57	Marble	Rds
			281.5	1.14	0.26	25.58	0.57	Marble	Cal
			291.0	0.84	0.26	19.92	0.57	Marble	Cal
			306.0	0.93	0.26	26.06	0.57	Marble	Cal
OL-992	478376	4493216	12.0	0.57	0.09	26.18	0.52	Marble	Cal
			27.0	0.70	0.09	22.63	0.52	Marble	Cal
			37.5	-1.00	0.09	17.71	0.52	Vein	Fe Cal
			39.5	-0.30	0.09	25.28	0.52	Marble	Cal
			45.5	-2.41	0.09	14.28	0.52	Vein	Fe Cal
			49.0	-1.22	0.09	15.29	0.52	Vein	Fe Cal
			55.0	2.28	0.09	8.68	0.52	Gangue	Cal
			59.0	-2.34	0.09	5.34	0.52	Vein	Fe Cal
			68.0	-0.83	0.09	20.35	0.52	Marble	Cal
			79.0	1.70	0.26	30.95	0.57	Marble	Cal
			87.0	0.19	0.26	15.56	0.57	Vein	Cal
			88.5	0.84	0.26	28.27	0.57	Stylolite	Cal

Table. A19. Carbon and oxygen isotope data of carbonate minerals from the sulfide deposits of the Kassandra Mining District

Drill Hole	Latitude	Longitude	Depth	$\delta^{13}C_{VPDB}$	1σ	$\delta^{18}O_{VSMOW}$	1σ	Style	Mineral[1]
			102.5	1.63	0.26	30.09	0.57	Marble	Cal
			116.0	0.15	0.26	27.28	0.57	Marble	Cal
			124.5	0.26	0.26	22.38	0.57	Stylolite	Cal
			133.0	2.14	0.26	23.50	0.57	Marble	Cal
			138.5	-0.24	0.26	27.57	0.57	Marble	Cal
			139.5	-0.18	0.26	14.82	0.57	Vein	Fe Cal
			148.5	1.82	0.26	23.38	0.57	Marble	Cal
			155.7	0.18	0.26	30.31	0.57	Marble	Cal
			168.0	0.26	0.26	31.09	0.57	Marble	Cal
			192.0	1.12	0.26	31.27	0.57	Marble	Cal
			215.5	-1.32	0.26	27.02	0.57	Marble	Cal
			234.5	0.28	0.26	29.24	0.57	Marble	Cal
			270.0	0.52	0.26	30.30	0.57	Marble	Cal
Madem Lakkos									
ML-222	481991	4485810	12.5	-0.81	0.17	14.40	0.34	Vein	Fe Dol
			22.5	-1.92	0.16	14.96	0.22	Skarn	Fe Dol
			64.5	1.50	0.28	27.25	0.73	Marble	Fe Cal
			66.0	0.70	0.28	20.05	0.73	Marble	Cal
			68.0	1.15	0.28	21.25	0.73	Marble	Cal
			68.8	-1.07	0.19	12.29	0.14	Skarn	Fe Cal
			70.0	-0.21	0.16	13.16	0.22	Skarn	Fe Cal
			71.8	-0.39	0.28	10.83	0.59	Skarn	Fe Cal
			73.0	-0.58	0.19	10.33	0.14	Skarn	Fe Cal
			73.4 (a)	-0.02	0.19	9.95	0.14	Skarn	Fe Cal
			73.4 (b)	-0.44	0.19	11.64	0.14	Skarn	Fe Cal
			75.0	1.75	0.28	13.04	0.59	Gangue	Fe Cal
			80.5	-2.53	0.28	11.01	0.59	Skarn	Cal
			81.5	0.34	0.28	11.08	0.59	Skarn	Cal

Table. A19. Carbon and oxygen isotope data of carbonate minerals from the sulfide deposits of the Kassandra Mining District

Drill Hole	Latitude	Longitude	Depth	$\delta^{13}C_{VPDB}$	1σ	$\delta^{18}O_{VSMOW}$	1σ	Style	Mineral[1]
			82.0	-2.38	0.28	11.30	0.59	Skarn	Cal
			84.5	-0.01	0.16	14.20	0.22	Skarn	Fe Dol
			81.5	1.35	0.16	12.58	0.22	Vein	Fe Cal
ML-141	481948	4485794	7.0 (a)	-0.09	0.28	14.98	0.06	Skarn	Cal
			7.0 (b)	-0.04	0.28	13.96	0.06	Skarn	Cal
			7.0 (c)	-2.85	0.28	11.06	0.06	Skarn	Cal
ML-255	no coordinate		48.5	-1.33	0.19	11.98	0.14	Skarn	Fe Dol
			67.0	1.39	0.17	28.16	0.34	Marble	Cal
			68.0	1.42	0.17	28.89	0.34	Marble	Cal
			134.5	1.12	0.28	26.21	0.06	Marble	Cal
			136.5 (a)	0.21	0.28	14.17	0.06	Marble	Fe Cal
			136.5 (b)	2.20	0.28	13.30	0.06	Marble	Fe Cal
			144.0	1.11	0.16	30.50	0.22	Marble	Cal
			146.5	-0.09	0.28	15.97	0.06	Skarn	Cal
			146.9	-0.52	0.28	12.52	0.06	Skarn	Cal
			155.4 (a)	0.41	0.17	13.66	0.34	Skarn	Fe Cal
			155.4 (b)	0.40	0.28	10.18	0.06	Skarn	Fe Cal
			157.0	0.29	0.19	1.14	0.14	Vein	Fe Cal
			158.6	1.34	0.16	6.84	0.22	Vein	Fe Cal
Mavres Petres									
MP-756	479869	4485963	3.0	0.78	0.28	14.27	0.06	Stylolite	Cal
			8.0	0.87	0.28	14.82	0.06	Stylolite	Cal
			14.0	0.19	0.28	13.57	0.06	Stylolite	Cal
			24.0	-1.59	0.17	16.44	0.34	Stylolite	Cal
			38.5	1.15	0.28	18.47	0.06	Stylolite	Cal
			45.3	-0.50	0.28	22.79	0.06	Marble	Cal

Table. A19. Carbon and oxygen isotope data of carbonate minerals from the sulfide deposits of the Kassandra Mining District

Drill Hole	Latitude	Longitude	Depth	$\delta^{13}C_{VPDB}$	1σ	$\delta^{18}O_{VSMOW}$	1σ	Style	Mineral[1]
			48.9	-0.90	0.28	15.31	0.06	Stylolite	Cal
			55.0	1.03	0.28	21.84	0.06	Stylolite	Cal
			63.0	1.40	0.28	21.11	0.06	Marble	Cal
			63.3	-0.66	0.28	9.14	0.06	Stylolite	Rds
			64.2	1.45	0.28	11.16	0.06	Vein	Cal
			66.3	0.52	0.28	9.64	0.06	Stylolite	Rds
			70.0	1.96	0.28	10.84	0.06	Vein	Cal
MP-758	479868	4485962	2.0	-1.46	0.28	10.46	0.59	Vein	Cal
			10.5	2.09	0.28	14.49	0.59	Marble	Cal
			14.0	0.27	0.28	12.39	0.59	Marble	Cal
			16.0	-0.40	0.28	10.89	0.59	Marble	Cal
			20.0	0.59	0.28	11.71	0.59	Stylolite	Cal
			24.0	0.23	0.28	16.02	0.59	Marble	Cal
			27.5	0.55	0.28	18.37	0.59	Marble	Cal
			29.5	0.65	0.28	20.96	0.59	Marble	Cal
			30.0	-1.38	0.16	13.65	0.22	Stylolite	Rds
			34.0	-0.25	0.19	10.46	0.14	Stylolite	Cal
			38.0	-2.51	0.28	11.71	0.59	Marble	Rds
			40.5	-2.82	0.28	3.86	0.59	Marble	Rds
			42.3	-1.65	0.28	5.86	0.59	Stylolite	Rds
			44.5	-2.03	0.17	14.23	0.34	Stylolite	Rds
			46.0	1.36	0.17	19.99	0.34	Marble	Cal
			48.7	-1.73	0.28	12.88	0.59	Marble	Cal
			50.5	0.36	0.17	17.38	0.34	Marble	Cal
			52.5	1.00	0.28	16.84	0.59	Marble	Cal
			53.5	-1.71	0.28	12.80	0.59	Marble	Rds
			55.0	0.13	0.16	14.21	0.22	Marble	Cal
			57.0 (a)	0.65	0.19	14.59	0.14	Stylolite	Cal

Table. A19. Carbon and oxygen isotope data of carbonate minerals from the sulfide deposits of the Kassandra Mining District

Drill Hole	Latitude	Longitude	Depth	$\delta^{13}C_{VPDB}$	1σ	$\delta^{18}O_{VSMOW}$	1σ	Style	Mineral[1]
			57.0 (b)	-0.80	0.28	14.41	0.59	Marble	Cal
			60.0	1.36	0.28	18.28	0.59	Marble	Cal
			64.0	-1.37	0.28	14.63	0.59	Marble	Cal
			66.0	-1.58	0.28	3.34	0.59	Marble	Cal
			68.3	-0.31	0.28	10.98	0.59	Marble	Cal
			69.5	-2.30	0.16	13.07	0.22	Gangue	Fe Cal
			81.7	1.47	0.17	7.75	0.34	Gangue	Fe Dol
MP-759	479875	4485960	3.5	0.33	0.16	9.13	0.22	Gangue	Cal
			26.6	-0.41	0.16	17.11	0.22	Gangue	Cal
			40.0	1.89	0.17	8.33	0.34	Gangue	Cal
			50.1	0.01	0.17	14.16	0.34	Gangue	Cal
			80.4	1.19	0.17	9.23	0.34	Gangue	Cal
			100.0	-2.49	0.16	12.48	0.22	Gangue	Cal
			102.8	0.58	0.16	12.79	0.22	Marble	Cal
MP-748	479745	4486226	37.3	-1.84	0.16	14.30	0.22	Vein	Rds
			47.4	0.14	0.17	12.34	0.34	Stylolite	Fe Cal
			52.7	0.92	0.16	3.22	0.22	Vein	Fe Cal
MP-527	479933	4486087	21.0	1.55	0.16	19.61	0.22	Stylolite	Cal
			34.2	0.90	0.17	10.51	0.34	Vein	Fe Cal
			36.0	1.78	0.17	9.26	0.34	Vein	Fe Cal
			37.5	3.30	0.17	9.29	0.34	Vein	Fe Cal
Piavitsa									
PHG-78	476700	4486192	87.0	-0.73	0.17	8.49	0.34	Vein	Cal
			88.3	-2.22	0.26	9.09	0.32	Vein	Rds
			92.0	-2.34	0.26	7.91	0.32	Vein	Rds

Table. A19. Carbon and oxygen isotope data of carbonate minerals from the sulfide deposits of the Kassandra Mining District

Drill Hole	Latitude	Longitude	Depth	$\delta^{13}C_{VPDB}$	1σ	$\delta^{18}O_{VSMOW}$	1σ	Style	Mineral[1]
			96.5	-2.04	0.26	12.46	0.32	Vein	Rds
			99.5	1.80	0.17	7.08	0.34	Vein	Rds
			100.3	1.22	0.26	8.37	0.32	Vein	Rds
			103.0	-2.23	0.17	13.67	0.34	Vein	Rds
			106.0	-1.94	0.26	3.22	0.32	Vein	Rds
			142.0	-3.21	0.26	8.28	0.32	Vein	Rds
			146.5	2.08	0.26	4.79	0.32	Vein	Rds
			147.0	0.16	0.26	7.72	0.32	Vein	Rds
			152.5	-1.80	0.26	6.93	0.32	Vein	Rds
			159.0	0.28	0.26	6.70	0.32	Vein	Rds
			165.0	1.89	0.17	8.85	0.34	Vein	Rds
			173.0	-2.47	0.26	3.63	0.32	Vein	Rds
			209.0	-2.23	0.26	12.55	0.32	Vein	Rds
			209.3	-2.31	0.17	12.33	0.34	Vein	Rds
			214.0	-2.04	0.26	7.47	0.32	Vein	Cal
			225.0	0.27	0.17	6.61	0.34	Vein	Rds
			269.0	-1.46	0.26	12.37	0.32	Vein	Rds
			301.0	0.27	0.26	8.32	0.32	Marble	Cal
			307.0	1.02	0.17	10.93	0.34	Marble	Cal
			327.0	2.28	0.26	12.76	0.32	Marble	Cal
			332.0	1.93	0.17	11.17	0.34	Marble	Cal
			338.0	-0.63	0.17	11.57	0.34	Marble	Cal
PHG-70	476280	4486494	97.0	-1.48	0.28	4.38	0.73	Vein	Cal
			105.0	-2.14	0.28	-2.15	0.73	Vein	Fe Dol
			156.0	-2.61	0.28	1.21	0.73	Vein	Cal
			201.0	-2.62	0.28	9.65	0.73	Vein	Cal
			208.0	-1.95	0.28	11.47	0.73	Marble	Rds
			210.5	-1.53	0.17	9.06	0.34	Vein	Rds

Table. A19. Carbon and oxygen isotope data of carbonate minerals from the sulfide deposits of the Kassandra Mining District

Drill Hole	Latitude	Longitude	Depth	$\delta^{13}C_{VPDB}$	1σ	$\delta^{18}O_{VSMOW}$	1σ	Style	Mineral[1]
			211.0	-2.22	0.28	11.15	0.73	Vein	Cal
			226.0	-2.13	0.28	-6.03	0.73	Vein	Rds
			240.0	-0.71	0.28	10.08	0.73	Vein	Rds
PVD-135	474197	4486744	154.3	-1.83	0.30	8.49	0.21	Vein	Rds
			273.1	-2.43	0.30	6.23	0.21	Vein	Rds
			333.5	-1.07	0.30	6.15	0.21	Vein	Cal
			381.8	-2.34	0.30	9.43	0.21	Vein	Fe Cal
			385.8	-0.28	0.30	13.42	0.21	Marble	Cal
			387.2	0.37	0.30	10.20	0.21	Vein	Cal
			389.0	0.06	0.30	9.22	0.21	Marble	Cal
			390.2	1.25	0.30	14.09	0.21	Marble	Fe Cal
			402.8	0.56	0.30	13.15	0.21	Marble	Cal
			403.5	1.37	0.30	12.57	0.21	Marble	Cal
			405.1	0.04	0.30	10.80	0.21	Marble	Cal
			407.0	-0.40	0.30	11.05	0.21	Marble	Cal
			408.0	3.16	0.30	14.24	0.21	Marble	Cal
			409.0 (a)	0.21	0.30	11.03	0.21	Marble	Cal
			409.0 (b)	1.22	0.30	12.53	0.21	Vein	Cal
			417.8	0.38	0.17	10.56	0.34	Marble	Cal
			481.3	1.66	0.17	13.69	0.34	Marble	Cal
PVD-131	474853	4486696	255.4	1.86	0.26	15.69	0.32	Marble	Cal
			265.6	0.62	0.26	12.24	0.32	Marble	Cal

[1]Abbreviations: Cal = calcite; Fe Cal = ferroan calcite; Fe Dol = ferroan dolomite; Dol = dolomite; Rds = rhodochrosite. Mineralogy determined from carbonate stain methods (Hitzman, 1999). Minerals denoted by italics are field observations.

Table A20. Lead isotope data from igneous intrusions and the replacement sulfide deposits of the Kassandra Mining District

						Isotopic Results					
No.	Deposit	Drillhole (depth)	Latitude	Longitude	Mineral	$^{206}Pb/^{204}Pb$	2σ (%)	$^{207}Pb/^{204}Pb$	2σ (%)	$^{208}Pb/^{204}Pb$	2σ (%)
Carbonate Replacement and Vein Sulfide											
ML-102	Madem Lakkos	ML+24in.8	corrdinate uncertain		Galena (skarn)	18.79737	0.02291	15.69685	0.02085	39.00569	0.02487
ML-105	Madem Lakkos	ML+24in.11	corrdinate uncertain		Galena (skarn)	18.79499	0.01391	15.68346	0.01133	38.96328	0.01516
MP-101	Mavres Petres	Underground 232m level			Pyrite	18.79166	0.03264	15.64043	0.02346	38.83914	0.03551
MP-110	Mavres Petres	Underground 115m level			Galena	18.81144	0.00575	15.66068	0.00470	38.91376	0.00655
PS-100	Piavitsa	Surface sample	40.50579	23.71920	Galena	18.76385	0.05156	15.65116	0.05165	38.83667	0.05165
P-107-a	Piavitsa	PHG70 (223m)	40.52885	23.71994	Galena	18.79729	0.00385	15.65384	0.00313	38.87035	0.00481
P-107-b	Piavitsa	PHG70 (223m)	40.52885	23.71994	Galena	18.79502	0.01120	15.65068	0.01104	38.85941	0.01149
P-108	Piavitsa	PHG70 (222m)	40.52885	23.71994	Galena	18.81366	0.00420	15.67832	0.00283	38.95141	0.00486
P-111	Piavitsa	PHG78 (97m)	40.52613	23.72492	Pyrite	18.75081	0.03301	15.66068	0.01723	38.82231	0.03940
P-106	Piavitsa	PHG78 (209m)	40.52613	23.72492	Boulangerite	18.81015	0.04408	15.66410	0.02976	38.88849	3.09842
OL-104	Olympias	Underground 195m level			Galena	18.75602	0.01068	15.64970	0.00939	38.86721	0.01164
Late Paleocene Granodiorite Dikes											
279444		Surface sample	40.52075	23.79534	K-feldspar	18.86163	0.01775	15.71336	0.01728	39.05829	0.01878
279424		Surface sample	40.52544	23.78417	K-feldspar	18.82785	0.05699	15.73873	0.05509	38.98866	0.05782
Late Oligocene Stratoni Stock											
679714		Surface sample	40.52982	23.82598	K-feldspar	18.87411	0.02210	15.68122	0.02195	38.95512	0.02215
593580		Surface sample	40.51717	23.81934	K-feldspar	18.91844	0.12519	15.73911	0.11364	39.14924	0.12832
Early Miocene Porphyry Suite											
679705a		Surface sample	40.52872	23.79775	K-feldspar	18.74295	0.01183	15.66707	0.01138	38.86725	0.01245
679705b		Surface sample	40.52872	23.79775	K-feldspar	18.74923	0.02060	15.66575	0.02050	38.83624	0.02076
593586		Surface sample	40.48364	23.72207	K-feldspar	18.79523	0.01280	15.68670	0.00984	38.93174	0.01415
593587		Surface sample	40.48301	23.71934	K-feldspar	18.77492	0.03088	15.66600	0.03010	38.87857	0.03155

Table A21. Published metal grades for selected carbonate replacement districts from North America and Eastern Europe

District	Ore style	Grade					Reference
		Pb (%)	Zn (%)	Cu (%)	Ag (g/t)	Au (g/t)	
Colorado, USA							
Leadville	manto (chimney)	4.2	3	0.2	320	3.65	Beaty et al., 1990
Gilman	manto (chimney)	3	7.3	0.05	120	1.8	"
Aspen	manto-breccia	8	2	0.02	1000	0	"
Sherman	breccia	0.8	4	0.1	485	0	"
Kokomo	manto	3	7.3	0.05	120	1.8	"
Nevada, USA							
Eureka	skarn-manto	6	10.5	0.15	250	5.47	Shawe and Nolan, 1989
Pioche	manto	3	7.8	0	3.9	0.94	Vikre and Brown, 1999
Utah, USA							
Tintic	manto	6.2	0.1	1.4	78.1	8.23	Lindgren and Loughlin, 1919
Park City	manto	8.1	4.45	0.39	473.46	2.72	Bromfield, 1989
Bingham (U.S.-Lark)	manto	4.91	2.07	0.91	97.71	1.66	James, 1973
Marysvale (Deer Trail)	manto	5	12	0.6	468.75	3.13	Beaty et al., 1986
Nothern Mexico							
Santa Eulalia	manto	8	5	<0.1	350	0	Megaw et al., 1988
	chimney	5	12	<0.1	250	0	"
	skarn	2	3	0.1	125	0	"
Providencia-Concepcion del oro	manto (chimney)	6.5	13	0	200	0	"
	manto	8	6	0.2	500	0.2	"
	skarn	1	0.6	2	30	0.6	"
Naica	skarn	4.5	3.8	0.4	150	0.3	"
	manto (chimney)	7	6	0.3	200	0.5	"
San Martin	skarn	0.6	5.3	1.24	146	0.7	"
	manto (chimney)	2.9	3.2	0.2	164	0	"
Velardeña	skarn	4	5	2.5	175	0.5	"
	manto (chimney)	4	7	0.2	190	0	"
	manto	7	3.8	<1	700	0.5	"
	manto	20	27	0	0	0	"

Table A21. Published metal grades for selected carbonate replacement districts from North America and Eastern Europe

District	Ore style	Grade					Reference
		Pb (%)	Zn (%)	Cu (%)	Ag (g/t)	Au (g/t)	
Turkey							
Balya	skarn-manto	8 (Pb+Zn)		0	200	1.5	Yigit, 2012
Kosovo (Trepca Mineral Belt)							
Trepča	skarn-manto	5.46	5.64	0	116	0	Hyseni et al., 2010
Bulgaria-Greece (Maden-Thermes)							
Maden-Krushev Dol	manto	2.54	2.1	0	0	0	Kaiser-Rohrmeier et al., 2013
Laki-Djurkovo	manto	2.9	2.16	0	0	0	"
Greece (Attica and Kassandra)							
Lavrion	manto (chimney)	20 (Pb+Zn)		0	400	0	Melfos and Voudouris, 2017
Madem Lakkos	skarn-manto	4	4	0.15	110	1.6	Nebel et al., 1989
Madem Lakkos	skarn-manto	6.94	8.34	0.6	145.96	1.19	(this study)
Mavres Petres	manto	8.1	11	0	212	0	Eldorado, 2017
Mavres Petres	manto	7.67	10.27	0.04	197.7	4.87	(this study)
Olympias	manto	4.9	6.5	0	146	8.97	Eldorado, 2017